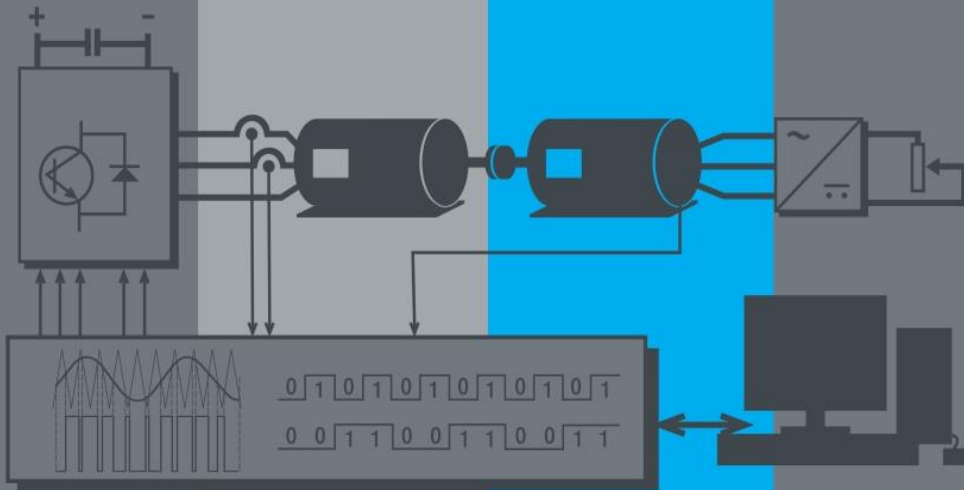




## UPT MONOGRAPHS



# ELECTRIC DRIVES UPT SELECTED CONTRIBUTIONS

Sorin Muşuroi (ed.)



Editura POLITEHNICA

# ADVANCED ELECTRIC DRIVES AN UPT SELECTION

Prof. **Sorin Mușuroi** (ed.)



**UPT**  
MONOGRAPHS

Descrierea CIP a Bibliotecii Naționale a României:

**Advanced Electric Drives - An UPT Selection,**

**trad.:** Lect dr. ing. **Marcela Farcașiu;**

**editor:** Prof. **Mușuroi Sorin.**

Colectiv autori:

Dorin Popovici, Ciprian Șorândaru, Cristian Lascu,

Codruța M. Ancuți, Marcus Svoboda, N. Olărescu

Timișoara, Editura Politehnica, 2020

Conține bibliografie. - Index

ISBN 978-606-35-0393-1

**I. Marcela Farcașiu** (trad.)

**II. Mușuroi Sorin** (ed.)

CIP description of the National Library of Romania:

**Advanced Electric Drives - An UPT Selection**

Translator: Lect dr. ing. **Marcela Farcașiu;**

Editor: Prof. **Mușuroi Sorin.**

Authors:

Dorin Popovici, Ciprian Șorândaru, Cristian Lascu,

Codruța M. Ancuți, Marcus Svoboda, N. Olărescu

Timișoara, Editura Politehnica - Publishing House,  
2020

Includes bibliography. - Index

ISBN 978-606-35-0393-1

**I. Marcela Farcașiu** (translator)

**II. Mușuroi Sorin** (editor)

# ADVANCED ELECTRIC DRIVES AN UPT SELECTION



**UPT**  
MONOGRAPHS

Prof. **Sorin Mușuroi** (ed.)

Copyright © Politehnica Publishing House, 2020

**Editura Politehnica - Publishing House**

Bd. Vasile Pârvan nr. 2B  
300223 Timișoara, România  
Ph./Fax. +4 0256 404677  
E-mail: editura@upt.ro

**Reader:**

Prof. Univ. Dr. Nicolae MUNTEAN

**Translator:**

Lect dr. ing. Marcela Farcașiu

**Editorial Advisor:** Prof. Dr. Ing. Sabin IONEL

**Editor:** Claudia MIHALI

**Good to print:** 15.11.2020

**ISBN** 978-606-35-0393-1

## FOREWORD

The entry into the new century of the Politehnica University of Timișoara is very well intertwined with the new century of electrical engineering studies in our university. This first century means modernization of the city or region, a lot of opportunities for development local or regional companies, attracting important funds for developing or preparing human resources for the industry in Banat, Romania or all over the world.



My thoughts on this double celebration go both to the teachers or administrative staff who in this first century of university or faculty have managed to ensure a higher technical education here and to the whole generations of graduates or students who understood that they are the representatives of a prestigious institution, which contributed not only by providing highly trained engineers to the regional socio-economic environment, but also by its important roles played in the research area or academic community.

We are ending a century of existence at the university level or at the faculty level looking back with pride and, although the period is not very favorable, looking forward with confidence. A trust that requires a lot of work, creativity, innovation, but having as main asset a human resource aware of the important mission it has. If this period is a little different, it offers us a series of opportunities that will materialize through essential transformations in education, pedagogy, research and our university must be prepared to face these changes, as Romanian society used to do in this first century.

How will the new century look like for our academic community? Will we have at our home big screens through which we will participate to classes anywhere in the world? Or will we have glasses for this? Will we use cars or will have autonomous vehicles? We know now but, it is obvious that our knowledge and our power of innovation will have a central place in our world's future. Therefore, I finally-want to thanks all for their efforts in building over the first century a strong faculty in our university and to wish to the entire academic community of the Faculty of Electrical Engineering good health, as many achievements as possible and:

"Happy anniversary!"

Timișoara, 11.11.2020

**Associate Professor Florin DRĂGAN, PhD,  
Rector of Politehnica University of Timișoara**

A handwritten signature in blue ink, appearing to be 'F. Drăgan'.



# CONTENT

<b>Foreword</b>	5
<b>1. Introduction</b>	11
<b>Author: S. Muşuroi</b>	
1.1 Remember: Education in Banat. The Polytechnic School of Timișoara	11
1.2 One hundred years of electrical education in Timișoara	14
1.3 Founders of Timișoara's School of Electric Drives	16
1.4 References	20
<b>2. Startup, braking and speed control in classic DC electric drives</b>	21
<b>Authors: D. Popovici, S. Muşuroi, M. Svoboda</b>	
2.1 Introduction	21
2.2 The DC motor mathematical model	22
2.3 Physical characteristics of DC motors	30
2.4 Static converters feeding DC machines	33
2.5 Motion control of DC motor drivers	79
2.6 References	110
<b>3. Scalar control of induction motor drives</b>	111
<b>Authors: S. Muşuroi, D. Popovici, M. Svoboda</b>	
3.1 General considerations	111
3.2 Functional equations and mechanical characteristics	113
3.3 Static converters fed induction machines	134



3.4 Scalar speed control of induction machines by change of voltage / current supply frequency	149
3.5 References	164
<b>4. Vector control of induction motor drives</b>	<b>166</b>
<b>Author: C. Lascu</b>	
4.1 Introduction	166
4.2 State-space models of induction machines	168
4.3 Direct vector control	177
4.4 Indirect vector control	191
4.5 Direct torque control	192
4.6 Linear direct torque control	201
4.7 Sliding mode direct torque control	206
4.8 State observers for induction motor drives	215
4.9 References	229
<b>5. Scalar control of permanent magnet synchronous motor drives</b>	<b>231</b>
<b>Authors: V.N. Olărescu, C.M. Ancuți, S. Mușuroi</b>	
5.1 Introductory elements	231
5.2 General equations of PMSM. The dynamic model	233
5.3 V/f control methods	261
5.4 Conclusion	269
5.5 References	269

<b>6. Sensorless vector control of permanent magnet synchronous motor drives</b>	271
<b>Author: C.M. Ancuți</b>	
6.1 Introduction	271
6.2 Novel Method for Flux Weakening Control of PMSMs	275
6.3 Optimal Current Referencers for Four-Quadrant Operation of PMSM Drive Systems	287
6.4 Conclusions	306
6.5 References	306
<b>7. Sensorless - vector control of PM -assisted reluctance synchronous motor drives</b>	310
<b>Authors: C.M. Ancuți, S. Mușuroi, C. Șorândaru, M. Svoboda</b>	
7.1 Introduction	310
7.2 PM-RSM design aspects	314
7.3 PM-RSM rotor's geometry variants	318
7.4 Implementation of a PM – RSM motion sensorless vector control	332
7.5 Conclusion	341
7.6 References	342
<b>8. Switched reluctance motor drives</b>	344
<b>Authors: C. Șorândaru, M. Svoboda</b>	
8.1 The switching reluctance motor. General presentation	344
8.2 Design considerations of the SRM	350
8.3 Power converters for switched reluctance machines	367
8.4 Control structures and strategies for SRM drives	374

8.5 SRM control systems developed at the Faculty of Electrical Engineering of Timisoara	392
8.6 Perspectives on using the SRM in electric drive systems	397
8.7 References	399
<b>9. Power factor correction in single-phase switching power sources used in electrical drives</b>	<b>402</b>
<b>Authors: D. Popovici, S. Muşuroi, C.M. Ancuţi, M. Svoboda, C. Şorândaru</b>	
9.1 Introduction	402
9.2 The Power Factor definition	403
9.3 Actual publications for single - phase PFC	404
9.4 Evaluation of the relevant publications	436
9.5 Conclusion	470
9.6 References	471

# 1 INTRODUCTION

## 1.1 Remember: Education in Banat. The Polytechnic School of Timișoara

Higher education institutions are of overwhelming importance for their contribution to the development of the education, knowledge and scientific progress of a society. The twentieth century's Banat land was a region developed industrially and economically, with high intellectual potential and diversity in the craft fields. At the beginning of this century, the historical Banat met all the conditions for the establishment of a Higher School in order to stimulate its progress.

This auspicious time allowed the mayor of Timișoara, Carol Telbisz, to send a report to the Hungarian government on 6 November 1906, proposing the establishment of a Polytechnic School in Timișoara, the second largest of this type after Budapest. The Hungarian government's answer came only in 1911 and it was not favorable. The letters were constantly sent until 1912, when the City Council addressed Dr. Kornel Zelovich, from the Budapest Polytechnic, the request to support the establishment of the Polytechnic School in Timișoara. On 26 July 1916, he wrote a document and sent it to the Municipal Council. The report was then sent by the Municipal Council to the Budapest government. New attempts to convince the Hungarian government were continued in the following year, but the beginning of the world war put an end to all these efforts.

After the establishment of the Romanian administration in Banat in 1919, the idea of founding a Polytechnic School in Timișoara became a major concern for the intelligent part of society within Banat and decision-making bodies. In the autumn of 1919, "Banat's Cultural Association" was founded, having Bishop Miron Cristea as president, and Traian Lalescu and Cornel Cornean, as vice-presidents. The main objective of the Association, which grouped the most important personalities within Banat, was the establishment of a Polytechnic School in Timișoara. One of the main supporters of the Romanian culture, Emanuil Ungureanu, is the one who made the first steps in this respect. The Mayor of Timișoara, Stan Vidrighin, joined this endeavor, being supported by the entire City Council.

The request of the intellectuals in Banat received efficient support and complete understanding from the Governing Council, within which the Cult Division was led by Valeriu Braniște. Together with Stan Vidrighin and Emanuil Ungureanu, Valeriu Braniște wrote a Memorandum and submitted it to the Governing Council on 27 February 1920, in which the need for the establishment of the Polytechnic School in Timișoara was motivated, "the city being an important industrial center, having a developed economic

life, superior to other urban centers and, in this respect, no other city in the Greater Romania could be likened to it" [2]. A broad publishing support accompanied these efforts, through articles published by the Romanian intellectuals, such as Traian Birăescu, Ascaniu Crișan and Traian Lalescu.

After the dissolution of the Governing Council on 10 April 1920, Valeriu Braniște, Onisifor Ghibu and Alexandru Rusu drafted a "Will" stating: "the consistent pursuit of the study program started by us until its full completion represents a holy obligation to the nation, to our homeland and to the humanity" [2].

All documents regarding the establishment of the Polytechnic School in Timișoara were submitted by Mayor Stan Vidrighin to the Ministry of Public Affairs, which gave a favorable response on 24 September 1920.

On 16 October 1920, under the chairmanship of the General Secretary of the Ministry of Public Affairs, Eng. P. Panaitescu, the council authorizing the establishment of the Polytechnic School in Timișoara convened. Among the participants were S. Vidrighin, T. Lalescu, G. Panait, A. Beleş and C. Teodorescu. In accordance with the Decree-Law of 10 June 1920, a Law on the organization of the higher technical education decreed by King Ferdinand I, on 21 October 1920, the Romanian government approved the establishment of the Polytechnic School of Timișoara, a decision published on 22 October 1920, in the Journal no. 3191 of the Council of Ministers of the Greater Romania.

The Decree-Law signed on 11 November 1920 by King Ferdinand I stated: "We hereby approve the establishment of the Polytechnic School of Timișoara on 15 November 1920, which will operate in accordance with the provisions of the Decree-Law no. 2521 of 10 June 1920 on the establishment and organization of polytechnic schools in Romania". Thus, the dream of the people within Banat was accomplished after 15 years of endless efforts.

King Ferdinand I is also remembered for the famous sentence he said later, during his visit to the young Polytechnic School:

**"It is not the walls that make a school, but the spirit that reigns in it".**

The news of the establishment of a Polytechnic School in Timișoara had a great impact on the country. On 2 December 1920, in the "Country" newspaper, the writer Camil Petrescu wrote the following: "The news that, at last, Timișoara will have a higher education school meant to give an academic vibe to the capital of Banat, was received with profound gratitude by all of our society layers. It is undeniable that this school, through its high cultural level, will contribute a lot to make Timișoara the intellectual center we all want it to become".

The first Rector of the Polytechnic School of Timișoara was Professor Traian Lalescu. His first and foremost concerns were related to the gathering of funds needed to carry out the

activity and the foundation of a library. Being involved in too many activities, in the second year of school, between 1921 and 1922, Prof. Traian Lalescu resigned from the rectorate, Professor Victor Vâlcovici becoming the new rector. There were two specializations in those years: mine-metallurgy and electromechanical engineering, with 117 students, 89 in the first year and 28 in the preparatory year. In the first academic year, opened on 29 November 1920, the teaching staff were chosen with great care from among the leading intellectuals from Banat: Prof. T. Lalescu, Eng. C. Teodorescu, Col. Gh. Buicliu, Architect Victor Vlad, C. Stăncescu, PhD, Eng., C. Căndea, PhD, A. Kaldor, Prof. Aug. Coman, Mihai Popescu, Mihai Vasiliu and others [3].

In the meantime, the necessary documents were prepared in order to build a University Technical Center. The general plan was drawn up by the architect Victor Vlad, requesting the assistance of Prof. A. Ruster from Charlottenburg and of Architect Krauss, Prof., from Vienna. In September 1922, Architect Duiliu Marcu started the construction of the Mechanical pavilion, completed and inaugurated on 11 November 1923 [4]. Today, this building is declared a national heritage site.

In 1933, the Electromechanical Engineering and the Mine-Metallurgy Engineering were created. On 28 January 1937, the Polytechnic School board approved the Regulation for conferring the "PhD" degree. The first PhD degree was awarded to engineer Stefan Nădășan, in 1939.

In the first decades, a significant number of intellectuals of within Banat have contributed to the establishment of the Polytechnic School of Timișoara, enthusiastically participating in the building of a higher education institution at a European level and becoming thus its founders. Some of them are mentioned here: Victor Vlad (architect), Marin Bănărescu (thermal machines), Pompiliu Nicolau (hydraulics and hydraulic plants), Valeriu Alaci (mathematics), Plauțius Andronescu (electrotechnical engineering), Corneliu Mikloși (modern welding technologies), Koloman Bakony (materials technology).

The period of the Second World War also marked the activity of the Polytechnic School of Timișoara, which continued its education under the leadership of the Rector Plauțius Andronescu, who fought daily for the survival of the school. During those troubled years, the Faculty of Civil Engineering was founded, in 1941, and after the education reform of 1948, the Faculty of Electromechanical Engineering split into two distinct faculties: the Faculty of Mechanical Engineering and the Faculty of Electrotechnical Engineering. The Faculty of Industrial Chemistry Engineering was also established during that time. The Polytechnic School was renamed the Polytechnic Institute of Timișoara, comprising four faculties: Mechanical Engineering, Electrotechnical Engineering, Civil Engineering and Industrial Chemistry Engineering. In 1962, the Faculty of Agricultural Mechanisation Engineering was also added to the list, being transferred from Craiova.

In 1970 - fifty years since the foundation of the Polytechnic Institute - the institution was already made up of 5 faculties and 24 specializations. The same year, it was named "Traian Vuia", in the memory of the world aviation pioneer.

## 1.2 One hundred years of electrical education in Timișoara

The beginnings of the electrotechnical higher education in Timișoara coincide with the beginnings of the Polytechnic School of Timișoara. 15 November 1920 is the date of the establishment of the Polytechnic School in Timișoara, which started its activity with the training of engineers in the specializations of Electromechanical Engineering (Mechanics and Electricity) and Mine and Metallurgy, respectively. At the beginning, the higher education institution included 15 members of the academic staff and 117 students.

In 1925, the Department of Electricity was established, its leader being Emeritus Professor Plauțius Andronescu, who had returned from Switzerland, where he worked as a private teaching doctor at the Polytechnic of Zurich. Professor Plauțius Andronescu introduced the Polytechnic of Timișoara to the modern way of presenting the theoretical basics of Electrotechnics course. In 1928, Professor Plauțius Andronescu set up the first electrical laboratory in the Polytechnic School, equipped with modern equipment and instruments, which was located for several years in the pavilion of the Faculty of Mechanical Engineering. In 1952, the laboratory was almost entirely transferred and developed in one location belonging to the Faculty of Electrical Engineering, in the Horațiu Square.

In 1927, Remus Bazilius Răduleț graduated from the Polytechnic School of Timișoara, later becoming a member of the Romanian Academy and the President of the International Electrotechnical Commission.

In 1933, as the number of students and academic staff in the Polytechnic School of Timișoara had increased, two faculties were established, namely, the Faculty of Mechanical Engineering and Electricity (Electromechanical Engineering) - which coordinated the training of engineers in the specialization of electromechanical engineering, and the Faculty of Mine-Metallurgy Engineering, which ensured the training of engineers in the specialization of mine and metallurgy.

An important step ahead in the development of the Polytechnic School took place in 1948 when, through the education reform, the Polytechnic School of Timișoara became the Polytechnic Institute, comprising four faculties, namely: Mechanical Engineering, Electrotechnical Engineering, Civil Engineering and Industrial Chemistry Engineering, summing up 12 specializations, with an initial academic duration of four years and, then, of five years.

At the beginning, the Faculty of Electrotechnical Engineering included the following departments: Fundamentals of Electrotechnical Engineering, Electric Machines, Uses of Electrical Energy, Electrical Measurements.

Since 2002, the Faculty of Electrotechnical Engineering has changed its name into the Faculty of Electrotechnical and Electrical Energy Engineering. Currently, the faculty consists of two departments: the Department of Electrical Engineering and the Department of Power Systems Engineering.

The founders of the Polytechnic School of Timișoara considered that a university teacher should be kept up-to-date with the news of science in the field and should carry out, in addition to the teaching activity, a continuous scientific activity. With this objective in mind, since 1925, the scientific bulletin entitled "Bulletin Scientifique de l'École Polytechnique de Timișoara" has been published, including articles where the results of the scientific research of the academic staff were presented. This bulletin was published annually. Prof. Plauțius Andronescu, PhD, Eng., was part of the editorial staff of the 1943 edition, as vice-president.

Starting with 1948, the bulletin was renamed: "Bulletin Scientifique et Technique de la Polytechnique de Timișoara". Among the members of the editorial committee was also Prof. Remus Răduleț, PhD, Eng., of the Faculty of Electrical Engineering. From 1949, the bulletin was called: "The Bulletin of Science and Technology of the Polytechnic Institute of Timișoara". Since 1956, this bulletin has started to appear in the "New Series" edition, with two issues per year. From the Faculty of Electrotechnical Engineering, Acad. Corneliu Mikloși, Prof., and Prof. Alexandru Rogojan, PhD, Eng., were part of the editorial board. The first scientific and technical bulletin of the Polytechnic Institute of Timișoara, the electrotechnical specialization, appeared in 1970, the editorial team being made up of Mihai Brașovan, PhD, Eng. - editor-in-chief, Prof. Ioan Novac, PhD, Eng. - deputy editor, Prof. Nicolae Bogoevici, PhD, Eng., Prof. Ovidiu Crișan, PhD, Eng., Prof. Toma Dordea, PhD, Eng., Reader Tiberiu Muresan, PhD, Eng., Prof. Alexandru Rogojan, PhD, Eng., Prof. Iacob Suciuc, PhD, Eng., Reader Vlad Văzdăuțeanu, PhD, Eng. - editorial secretary.

It should be mentioned that, since 2000, the Scientific Bulletin of the Polytechnic University of Timișoara, the electrotechnical engineering section has been published in two series: the "Energy" series and the "Journal of Electrical Engineering" series, the latter representing the first Bulletin of the Polytechnic University of Timișoara published in electronic form. The editorial board for the Energy series consisted of A. Baia, M. Biriescu, A. Butta, I. Bucătariu, V. Dușa, I. Ionel, Șt. Kilyeni, B. Luștrea, M. Nemeș, A. Pană, F. Șurianu, A. Vasilievici, I. Vetreș. For the series published in the electronic form, the editorial board was made up of Prof. Ion Boldea, PhD, Eng. – director, Prof. Nicolae Muntean, PhD, Eng. – editor-in-chief; Prof. Dumitru Radu, PhD, Eng. - Deputy Chief Editor; PhD student Sever Scridon - secretary.

Postgraduate training was ensured through a PhD stage. The first PhD diploma in electrical engineering was awarded in 1961 to engineer Gheorghe Reusz, who, under the supervision of Acad. Corneliu Mikloși, Prof., defended the thesis entitled "Electric Drives in Mills".

Starting with 1990, within the Faculty of Electrotechnical Engineering, engineers have been trained in the fundamental field of engineering sciences, including the fields of electrical engineering and power systems engineering, respectively.



## 1.3 Founders of Timișoara's School of Electric Drives

### 1.3.1 Academician Corneliu MIKLOȘI, Professor

Acad. Corneliu Mikloși, Prof. was a remarkable teacher of the Faculty of Electrotechnical Engineering of Timișoara, who marked for decades the technical and scientific life of the city. He was born on 5 March 1887, in Covășanț, Arad county. He was the son of the Orthodox priest Ioan Mikloși and of his wife Melania. He had a brother, Emil.

He first attended the primary school in his hometown and, then, the one from Arad. Between 1897 and 1905, he continued his studies at the "Moise Nicoara" high school in Arad, in the classical section, receiving the "remarkable" grade at the baccalaureate exam, in 1905. With the perseverance that characterized his entire life, he has managed to speak seven modern languages and to perfectly master two classical languages, Latin and Greek.

During 1905 – 1906, he was enrolled at the Faculty of Electrotechnical Engineering of the Karlsruhe Polytechnic and, then, obtaining a Gojdu scholarship, he continued his university studies, between 1906 and 1909, at the Faculty of Mechanical Engineering at the Technical University of Budapest, where he received the bachelor of science degree, majoring in mechanical engineering, with the "with honors" distinction, in 1909. He joined the faculty as a lecturer, being chosen by the remarkable Professor A. Rejtö. During his military service, he wrote his PhD thesis, which he defended in May 1912, being conferred thus the PhD scientific title in technical sciences with the "with honors" distinction, based on the dissertation: "Observations on Testing the Materials for Transmission Belts".

He returned into the educational field in 1916, teaching the course of Mechanical Technology at the Technical University of Budapest.

In 1918, he submitted his habilitation thesis entitled "On the Formation of Alloys", and, in 1919, he received the highest degree of teaching doctor.

Although with a brilliant situation and beautiful prospects in his university career, after the Act of the Union of 1 December 1918, Corneliu Mikloși returned to his country, joining from December 1919 to March 1920 the Depot of the Romanian Railways in Arad. In March 1920, he was appointed as chief engineer and then director of the Municipal Tramways in Timișoara, which, from 1922, merging with the Electrical Factory, would form the Electromechanical Enterprises in Timișoara, led by the professor for 30 years. His main concerns as a director revolved around the modernization and the economic efficiency of the company. Thus, in order to ensure a civilized public transport, he modernized the tram park through designing and executing way of the new models of bogie trams, he made automatic tram switches, he introduced, for the first time in the country, in Timișoara, the trolleybus, better known in the region as "firobus". Among the achievements of the director Corneliu Mikloși, it is worth mentioning the supply of the city of Timișoara with a network of electric clocks, mounted in all the main crossroads of the city, the "mother" clock being in the director's office, controlled by his Swiss chronometer. He initiated and

designed - for the purpose of modernizing the electrical network - the operating frequency of 42 Hz to the current one of 50 Hz, he also installed converters for the tram network supply and the list can go on.

Between 1925 and 1930, he was a Professor at the Polytechnic School of Timișoara, teaching the course of Mechanical Technology and Industrial Alloys and, at the same time, between 1927 and 1928, at the Technical University of Budapest, where he taught the course of Metallography. It is worth noticing that, in 1924, at his retirement, Professor A. Rejtő recommended Corneliu Mikloși as his successor to the chair, although Corneliu Mikloși had already left Budapest in 1919.

Promoter of modern technologies, he established in Timișoara, in 1936, the "Centre for the Support of Welding", a research and teaching center in the field of welding, established in collaboration with the Polytechnic School of Timișoara. A special achievement in the field of welding was, in his time, the construction, in 1936, of the boilers' room of the Electrical Factory of Timișoara, initiated and designed by the Academician C. Mikloși, Professor.

In 1947, he returned to the academic life and led the Departments of Electricity and Welding until his retirement. Corneliu Mikloși has taught several specialized courses at the Faculty of Electrotechnical Engineering: Applications of Electricity, Electric Drives, Rolling Stock, Electric Transportation, Power Stations. For all these courses, he wrote course books, which were published by the Polytechnic Institute of Timișoara, the said courses being of great help for the students in order to prepare their exams. They are as follows: Production, Distribution and Applications of Electricity (vol. I and II in 1949), Course on Power Plants (vol. I in 1949, vol. II in 1951), Course on the Applications of Electricity in Industry (vol. I in 1952, vol. II in 1953), Electromechanical Equipment for Industrial Enterprises (Didactic and Pedagogical Publishing House, Bucharest 1961), Electric Transportation - in collaboration with Prof. C. Șora - (Didactic and Pedagogical Publishing House, Bucharest 1961).

As a teacher, Academician C. Mikloși, Professor was a model of scientific competence, seriousness in work, punctuality and fairness towards students. A good organiser, he laid the foundations and led the works for designing and equipping the electric drive laboratories at the Polytechnic Institute of Timișoara.

Academician C. Mikloși, Professor was the first professor of the Faculty of Electrotechnical Engineering who received the right to supervise PhD theses. In this activity, he was able to contribute to the higher education of some engineers, who later became tireless researchers and teachers, among whom we can mention Prof. Aurel Nanu, Prof. Mihai Brașovan, Prof. Traian Sălăgean, Prof. Toma Dordea, Prof. Eugen Seracin, Prof. Ioan Șora.

His scientific research activity has been extremely fruitful. His first scientific concerns were related to the field of mechanical technology, studying the influence of the deformation speed on the characteristics of the military posts determined by the split test; then he studied the wear of the gears, designing a machine to investigate these uses, the results of the study being published in Berlin and Budapest; the method recommended by

him was subsequently adopted by Physikalisch - Technische Reichsanstalt in Berlin. Other problems pursued were the transmission of the rotational motion through belts and gears, the wear of brake pads, the study of the characteristic of cast iron for shoes, the quality of the coal used in power plants, the financial and economic problems related to electricity pricing, etc.

A special original scientific contribution is brought by C. Mikloși, PhD, in the field of welding, research in this field starting after the First World War. The semi-automatic installation for welding the "Taurus" rail type, patented in Romania and Switzerland and made available upon request for Germany and China, is originally designed by engineer C. Mikloși. Professor C. Mikloși also focused on the application of low-frequency currents to welding, which brought significant improvements in electricity savings and power factor improvements.

Academician Corneliu Mikloși, Professor, PhD, was a man with a high moral reputation, who dedicated his entire life to the research in the field of technical and technological sciences, combining his interest in technique with a love for culture, thinking and deep meditation regarding the human existence and the supreme human values.

The appreciation of his scientific activity and his contribution to the development of the modern technology led, in 1955, to his election as a full member of the Romanian Academy. Academician Corneliu Mikloși, Professor, died on 10 August 1963.

### **1.3.2 Emeritus Professor Mihai BRAȘOVAN, PhD, Eng.**

Emeritus Professor Mihai Brașovan, PhD, Eng., was born in Banat in 1908. He brilliantly graduated the Faculty of Electromechanical Engineering at the Polytechnic School of Timișoara in 1934, continuing as an assistant at the Department of Fundamentals of Electrical Engineering. From 1934 until his retirement, Professor Mihai Brașovan worked at the Polytechnic Institute of Timișoara, successively occupying the positions of assistant, lecturer, reader and, since 1963, the position of full professor at the Department of Applications of Electricity. In 1962, he defended his PhD thesis at the Polytechnic Institute of Timișoara and, in the same year, he was also head of the Department of Applications of Electricity.

The way in which Professor Mihai Brașovan fulfilled his teaching, scientific and educational tasks over the years, as well as his personal conduct, attracted great appreciation from both his fellow teachers and his students. Professor Mihai Brașovan distinguished himself through the high level and the clarity of his lectures. During his almost 40 years of activity, he taught several subjects, such as: Electromechanical Drives, Uses of the Electrical Energy, Electric and Thermal Phenomena, Electric Drives, for which he had written and published many course books, guides and collections of problems that are well-known due to his concise presentation style and to the very clear and scientifically-proven content. Whenever the opportunity arose, the former students, who were guided in their training activity as engineers by Professor Mihai Brașovan, expressed

their gratitude for the valuable scientific and technical knowledge gained from their former teacher. Furthermore, his remarkable scientific, teaching and educational activity brought him the esteem of all his collaborators, who considered him as one of the most valuable scientists and teachers in the higher education in our country.

The same tireless work in the field of scientific research characterized Professor Mihai Braşovan during his four decades of activity, completed by numerous published papers, protocols for collaborative work with the industry, and contracts, all highly appreciated and very valuable for both the design field, as well as for practical reasons. His research activity was mainly oriented towards the electric drives field, where Emeritus Professor Mihai Braşovan, PhD, Eng., has made significant contributions to establishing new design methods for the electric drives and to introducing modern systems for the electric drives in the industry.

Professor Mihai Braşovan has also contributed to the field of the electrification of railways and welding.

Due to his outstanding work, Professor Mihai Braşovan received the right to supervise PhD theses in 1963 and many valuable engineers defended their PhD theses under his leadership.

As a high appreciation for the long and valuable activities he carried out, in 1970, Professor Mihai Braşovan, PhD, Eng., was awarded the title of Emeritus Professor.

From an administrative point of view, between 1963 and 1976, he held the position of head of the Department of Application of Electricity and of Vice-dean of the Faculty of Electrotechnical Engineering in Timişoara. He died in 1976.

### **1.3.3 Professor Eugen SERACIN, PhD, Eng.**

Professor Eugen Seracin, PhD, Eng., was born on 28 November 1928, in Drobeta Turnu-Severin. In 1952, he graduated the Faculty of Electrotechnical Engineering at the Polytechnic Institute of Timişoara. He defended his PhD thesis in 1970, obtaining the PhD degree in the same year. During his prestigious teaching activity, he taught many courses such as: Electric Drives, Design of the Electric Drives, Electromechanical Equipment for Industrial Enterprises, Applications of Electricity, Electric Transportation, Lighting, Electromechanical Drives.

The teaching and pedagogical mastery of Professor Eugen Seracin is attested by the numerous classes of students who attended his very clear and precise courses. The constant concerns of Professor Eugen Seracin were both the content of the courses and the way of transferring the knowledge to the students, with an emphasis on the understanding of the concepts and their practical uses. These concerns are reflected in his 12 electric drive books and manuals, published by the most prestigious publishers in the country.

Professor Eugen Seracin also distinguished himself in the field of scientific research through more than 80 papers published in the country and abroad and 38 research contracts, their focus being on the experimental confirmation of the theoretical research

and on their consistent application into practice. The merits of Professor Eugen Seracin also extended to the field of National Electric Drives Conferences, a beautiful tradition of the Romanian School of Electric Drives, by organizing a flawless conference in Timisoara, in 1987, and by having an important contribution to all the other editions of the conference. The scientific prestige assigned to him was also highlighted by his position of PhD theses supervisor, guiding with great competence a large number of specialists from the faculty and the industry. The Professor is also well-known through his different professional achievements in the field of optimal computation of electric drives depending on the operating service, electric drive systems with linear machines used on rolling bridges and new design methods for the electric drives.

Professor Eugen Seracin also maintained in the department a breath of academic air, characterized by cooperation and peer harmony, based on respect and exigency. In time, his modesty and honesty, as well as the gratitude shown to his forerunners, Academician Corneliu Mikloși and Professor Mihai Brașovan, who represented his role models in his entire activity, were also noticed. Last but not least, his love for nature and sports should be appreciated. He dedicated memorable moments to those hobbies and remarkably educated the students in the spirit of "Mens Sana in Corpore Sano", teaching them to worship the mountains, in general, and the Carpathians, in particular. Between 1968 and 1972, he was the Vice-dean of the Faculty of Electrotechnical Engineering in Timișoara. He died in 2013.

The present monograph is intended to be a praise brought to the School of Electric Drives of the Faculty of Electrical and Power Systems Engineering, a valuable link of Politehnica University of Timișoara, through the achievements of the teachers and of the research that have served for a century in this field. In order to be a really useful work for students and specialists in the field, the monograph treats the electric drive systems in their complexity, focusing on the problems related to starting, braking, speed variation and reversing, as well as on the possibility of an optimal operation and energy recovery.

## 1.4 References

- [1] I. Munteanu, "Universitatea „Politehnica” din Timișoara la 80 de ani, Ctitori ai Școlii Politehnice din Timișoara", Editura Politehnica, Timișoara, 2001.
- [2] T. Dordea, P. Andea, N. Muntean, S. Mușuroi, "90 de ani de învățământ electric la Timișoara – Monografie", Editura Orizonturi Universitare, Timișoara, 2010.
- [3] C. De Sabata, "Universitatea Politehnica Timișoara, Oameni, idei, fapte", Editura Excelsior Timișoara, 1997.
- [4] F. Goga, "Împlinirea unui vis. Școala Politehnica din Timișoara. Ani de frământări și de eroism", Timișoara, 1985.

## 2.1 Introduction

The nowadays industrial performances rely heavily on the progress in making flexible, reliable and especially easy to operate electric drives. The use of conventional DC machines in electric drives was due to their ability to allow easy and wide speed regulation. At the same time, the automatic regulation systems for this type of machines use the principle of cascade regulation which has the advantage of being able to limit the armature current, thus ensuring the protection of the drive. At the same time, static AC–DC converters were developed, making possible the almost exclusively use of these machines in adjustable electric drives.

Throughout this period, DC excited electric drives have developed both technically and economically. The rapid progress recorded by the power electronics field, namely of the DC–AC converters, has made possible the replacement of the DC drives with AC drives, initially, with asynchronous motors [1].

It is, however, difficult to draw a clear dividing line between the DC electric drives and AC ones, in both cases, due to the large and varied number of adjustable drives. A relatively simpler economic factor and the nowadays control equipment's advocate the fact that DC drives as being favored. The efficiency of the DC electric drives is relatively high [2].

The increase of the electric drives qualitative requirements and of the magnetic and electro-insulating materials performances, together with the development of power electronics have led to a DC motor re-launch. And this is due to the adaptability of DC machines in various electric drives types. These machines continue to be used in various applications, such as industrial robots, numerical control machines, computer peripherals and scientific and aerospace applications.

In this chapter, the main aspects related to electric drive systems, consisting of conventional DC motors with electromagnetic excitation, will be synthetically presented. There will be problems related to the mechanical characteristics, starting, braking and speed variation. The main converters types used for powering the machines, will also be presented synthetically, namely the AC–DC ones and the DC–DC, respectively. The achievements obtained in this field by the teaching staff of the Department of Electrical Engineering will also be highlighted.

## 2.2 The DC motor mathematical model

The analysis of the motor operation is based on the equations deduced in various situations and on the simplifying assumptions. A DC motor with separate electromagnetic excitation will be taken into consideration in what follows (see Fig. 2.1).

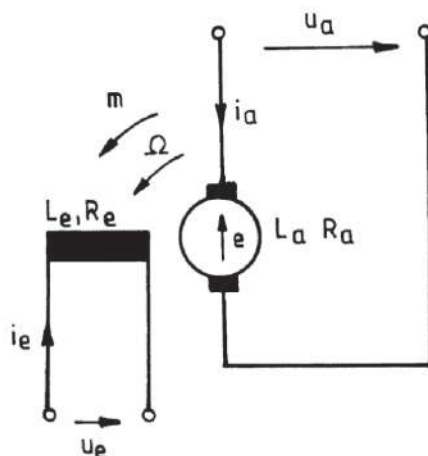


Fig. 2.1 DC motor with separate electromagnetic excitation.

The machine behavior in motor operation mode is described by the following equations:

$$\begin{aligned}
 u_e &= R_e \cdot i_e + \frac{d}{dt}(L_e \cdot i_e), \\
 u_a &= R_a \cdot i_a + \frac{d}{dt}(L_a \cdot i_a) + e, \\
 e &= k \cdot \phi \cdot \Omega, \\
 m &= k \phi \cdot i_a, \\
 m - m_v - m_r &= J \frac{d\Omega}{dt}, \quad m_v + m_r = m_R, \\
 \phi &= f(i_e)
 \end{aligned}
 \tag{2.1}$$

where:  $R_e$  and  $R_a$  are the excitation winding total resistance and the armature circuit total resistance, respectively;  $L_e$ ,  $L_a$  are the excitation winding total inductance and the armature total inductance, respectively;  $u_e$  and  $u_a$  are the instantaneous values of the voltages at the excitation winding terminals and armature winding terminals;  $i_e$  and  $i_a$  are the current instantaneous values through the armature winding or excitation winding;  $e$  is the magneto motive force induced by the excitation field.

When writing the relationships (2.1), **the transient electromagnetic regime** that takes place inside the machine windings (excitation + armature), due to the variation of currents

and fluxes as well as **the mechanical transient regime** of the machine rotor due to the angular velocity variation were considered. The brushes were considered to be placed in the neutral axis.

The first two equations are the result of applying the electromagnetic induction law along the armature and excitation windings circuits. When the brushes are placed in the neutral axis, there is no mutual inductance between the excitation winding and the armature winding.

Both  $L_e$  and  $L_a$  were introduced, but as derivatives, as they are variable with the load, as a consequence of the machine saturation variation.

The total flux  $\psi_e = L_e \cdot i_e$  (chained to the excitation windings turns) has two components: the dispersion component  $L_{e\sigma} i_e$  and the main component  $\psi_{eh}$  that penetrates the rotor and is proportional to the polar flux  $\phi$ . It can be written as:

$$\psi_e = L_e \cdot i_e = \psi_{e\sigma} + \psi_{eh} = L_{e\sigma} \cdot i_e + L_{eh} \cdot i_e \quad (2.2)$$

$$L_{eh} \cdot i_e = C \cdot \phi \quad (2.3)$$

where  $L_{eh}$  is the main inductance  $L_{eh} = f(i_e)$  and  $C$  is the proportionality constant.

Since  $L_a$  generally varies within the restricted limits, it can be admitted that  $L_a \approx ct$  and therefore,

$$\frac{d(L_a \cdot i_a)}{dt} = L_a \frac{di_a}{dt} \quad (2.4)$$

The third and fourth equations represent the expressions of the magneto motive force induced by rotation and of the electromagnetic torque, respectively. In these relationships,  $k$  is a non-dimensional constant that depends on the machine construction:

$$k = \frac{p \cdot N}{\pi \cdot 2a} \quad (2.5)$$

where  $p$  represents the number of pair poles,  $N$  is the number of turns and  $a$  is the pairs number of the winding paths.

The fifth relation represents the fundamental motion equation, where  $J$  is the moment of inertia for the machine together with the working mechanism related to the machine shaft, and  $m_r$  is the total instantaneous torque that can be decomposed into two components: the viscous friction torque  $m_v = F \cdot \Omega$  and the torque, independent of speed,  $m_r$ .

The DC motors have two operating modes:

- a) the constant flux regime ( $\phi = \text{const.}$ );
- b) the constant armature voltage regime ( $U_a = \text{const.}$ ).



### 2.2.1 The armature control of the DC motor

The armature control of the DC motor is characterized by a constant excitation flux. In the case of steady-state regime, by customizing the relation (2.1), the equation of the mechanical characteristic is obtained:

$$m = \frac{K}{R_a} u_a - \frac{K^2}{R_a} \Omega = k_M u_a - F_e \Omega \quad (2.6)$$

where  $K=k \cdot \phi [Wb]$  the machine constant (for motors with separate and parallel excitation,  $\phi = \text{const.}$ ).

The amplification voltage-torque coefficient  $k_M = \frac{K}{R_a}$  and  $F_e = \frac{K^2}{R_a} = k_M \cdot K$ , the electric viscous friction coefficient, characterize the behavior of a particular motor. The linearity of the characteristics (2.6) is important for the operation of the drive system. Extremely important is also the minimum value of the voltage control  $U_m$ , for which the motor is idling.

For voltage values  $< U_m$ , the motor does not respond to a control signal, the physical causes being the friction in the bearings, the rotor preferential position due to electrical or mechanical machine imbalances, etc. For quality motors,  $U_m < 3\%$  from the maximum control voltage. The control characteristics, the dependence  $m=f(u)$  with speed parameter are shown in Fig. 2.2 and should be as linear as possible. The developed effective power can be written as:

$$P_u = m\Omega = (k_M u_a - F_e \Omega) \Omega \quad (2.7)$$

It should be noted that the effective power is zero during startup ( $\Omega=0$ ) and idle ( $m=0$ ) and has a maximum deduced from:

$$\frac{dP_u}{dt} = 0 \quad \text{at} \quad \Omega = \frac{k_M}{2F_e} = \frac{\Omega_0}{2} \quad (2.8)$$

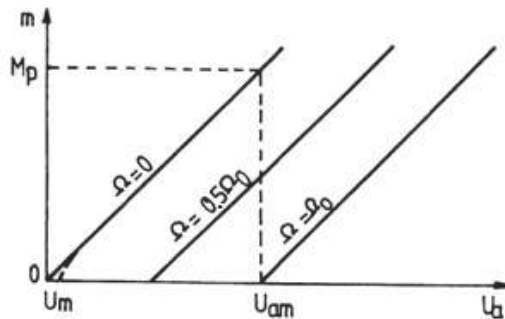


Fig. 2.2 The control characteristics of the DC motors with control on the armature.

The variation characteristic is depicted in Fig. 2.3 and shows that the motor's critical parameters are the maximum starting torque  $M_p$ , the maximum developed power  $P_m$  and the idling velocity  $\Omega_0$  corresponding to the maximum control signal  $U_{amr}$ , without also specifying the nominal parameters such as power and speed.

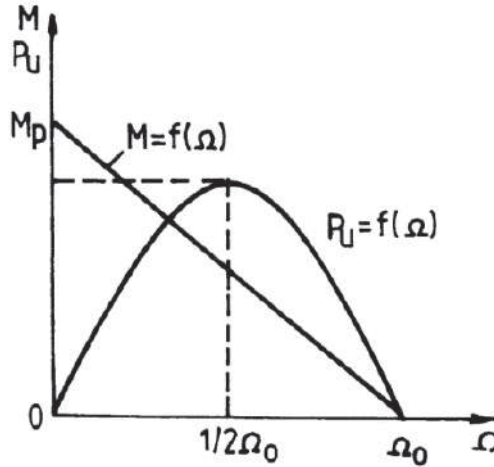


Fig. 2.3 Variation of the effective power based on the speed.

In the dynamic mode, the relationships (2.1) can be directly entered into the operation, considering that, in general,  $\Omega(s)=s \cdot \theta(s)$ , where  $\theta$  is the position angle of the motor shaft:

$$\begin{aligned}
 e(s) &= K \cdot s \cdot \theta(s) \\
 u_a(s) &= K \cdot s \cdot \theta(s) + R_a(1 + sT_a)i_a(s) \\
 m(s) &= K i_a(s) \\
 m(s) &= F_m(1 + sT_m)s\theta(s) + m_r(s)
 \end{aligned} \tag{2.9}$$

where  $T_a=L_a/R_a$  – is the time constant of the armature circuit, and  $T=J/F_m$  – is the electromechanical constant of the motor and the load.

By eliminating the current in the first three relationships in (2.9) and by introducing  $k_M$  and  $F_e$  it can be written that:

$$m(s) = \frac{K}{R_a} \cdot u_a(s) - \frac{K^2}{R_a} \frac{s\theta(s)}{1 + sT_a} = \frac{k_M}{1 + sT_a} u_a(s) - \frac{F_e \cdot s\theta(s)}{1 + sT_a}, \tag{2.10}$$

and introducing the last relationship in (2.9), it yields:

$$\frac{k_M}{1 + sT_a} u_a(s) - m_r(s) = \frac{F_e}{1 + sT_a} \left[ 1 + \frac{F_m}{F_e} (1 + sT_m)(1 + sT_a) \right] s\theta(s), \tag{2.11}$$

relationship that allows the presentation of the motor transfer function through a block diagram as depicted in Fig. 2.4.a.

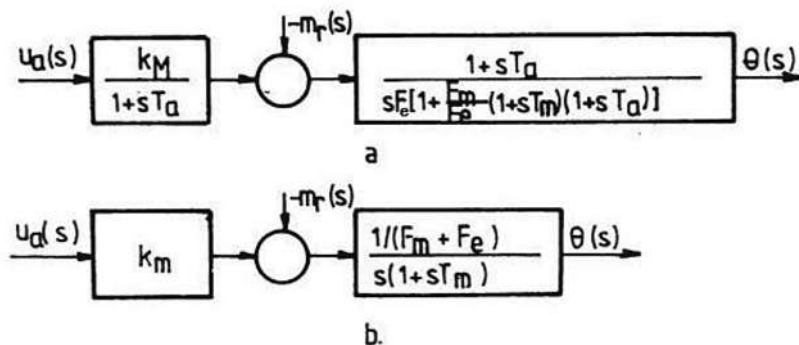


Fig. 2.4 Block diagram of the DC motor: a) complete scheme; b) simplified scheme.

If  $T_a \ll T_m$  in the relationship (2.11), some simplifications could be made and therefore, the simplified block scheme in Fig. 2.4.b is obtained. In the absence of a static torque, the simplified transfer function obtains the form:

$$G_m(s) = \frac{\theta(s)}{u_a(s)} = \frac{k_M}{F \cdot s(1 + sT_m)}, \quad (2.12)$$

where:  $F = F_e + F_m$ , which shows that the DC motor with controlled armature behaves dynamically as a set of two elements, an aperiodic inertial one, with the time constant  $T_m$  and an integrator. This model can be used in most cases [3].

### 2.2.2 The DC motor with controlled excitation

This motor is encountered in many situations due to the reduced power of the control circuit, which represents few percentages from the armature control power. For a constant supply voltage of the armature,  $U_a = ct$ , the control of the excitation leads to inappropriate mechanical characteristics. By specifying the relationship (2.1) for the steady-state regime, the following equations are obtained:

$$\begin{aligned} U_a &= e + R_a i_a \\ u_e &= R_e i_e \\ e &= k' \cdot \Omega i_e \end{aligned} \quad (2.13)$$

the last relationship being written assuming the linearization of the magnetizing characteristic  $\phi = f(i_e)$ . Taking into account the expression of the electromagnetic torque  $m = k' \cdot i_a \cdot i_e$ , the expression of the mechanical characteristics of the DC motor with control on excitation, at a constant rotor voltage, is deduced:

$$m = \frac{k'U_a u_e}{R_a R_e} - \frac{k'^2 u_e^2}{R_a R_e^2} \Omega \quad (2.14)$$

It is noted that the starting torque, term which is independent of  $\Omega$ , varies with the first order of the control voltage at the same time with the characteristic slope with the second order of this voltage. Fig. 2.5 shows two characteristics illustrating a situation incompatible with a drive system, namely that two different values for the control voltage correspond to the same operating point.

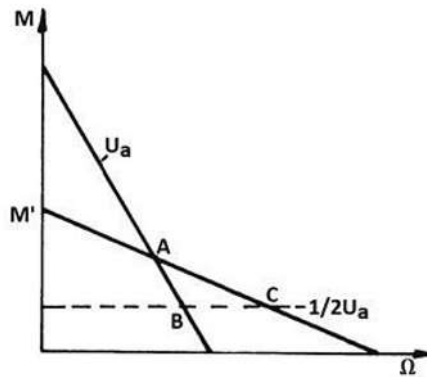


Fig. 2.5 Mechanical characteristics of the DC motor with control on excitation.

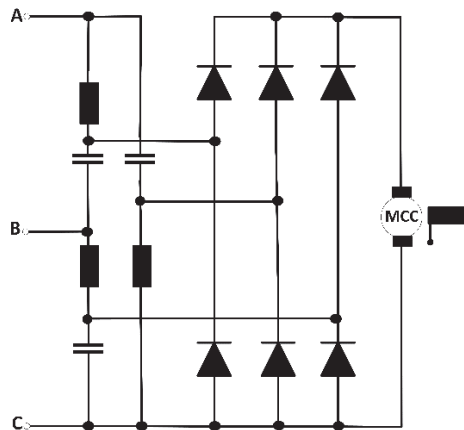


Fig 2.6 The Boucherot scheme for feeding the armature of the DC motor.

The command for the excitation becomes interesting and is used when feeding the rotor from a constant current source, see Fig. 2.6. Since a constant voltage source is generally characterized by a very low impedance and a constant output voltage in a given variation range of the supplied current, the constant current source is characterized by a very high impedance and a variable output voltage in the same range. In addition, if, for a

constant voltage source, the most favorable operation mode is the no-load one and the most unfavorable is the short circuit one; for the constant current source is the opposite way: the short circuit is favorable, and the no-load mode is usually not tolerated. The constant current source is based on the Boucherot type circuit, Fig. 2.6 is built using an electronically controlled semiconductor power plant.

In the steady state, it can be written:

$$m = k'' i_e = k \frac{u_e}{R_e} = k_M u_e \tag{2.15}$$

In Fig. 2.7.a, the regulation characteristic is shown, with the observation that, in the upper zone, due to the saturation, it deviates from the line. In Fig. 2.7.b., the mechanical characteristics show stiffness because  $F_e = 0$ , which is a minor disadvantage compared to the armature control method because the improvement of the stationary regime can be done by means of a negative speed feedback, assuming a linear magnetizing characteristic.

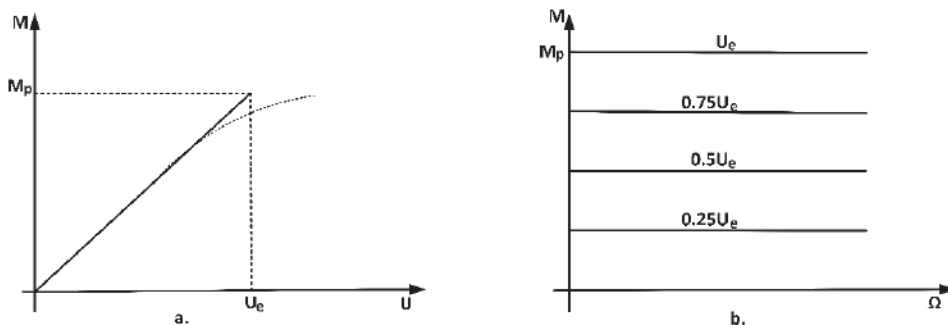


Fig. 2.7 Characteristics of DC motors with control on excitation: a) control characteristics; b) mechanical characteristics.

The major disadvantage of the method is that the excitation circuit has a much larger time constant than the armature circuit and, therefore, from a dynamic point of view, the system has lower performances than the armature control.

### 2.2.3 The DC motor with series excitation

The DC motor with series excitation is used to position loads that require large starting torques and where linear mechanical characteristics are not absolutely needed. The DC series motor has a drawback due to the inability to sense the sign change of the command signal. This inconvenience is constructively solved as depicted in Fig. 2.8 with two excitation windings and a diode so that, regardless of the current direction, the excitation flux has the same path.

Assuming linear field operation, the equations in steady-state are:

$$u_a = i_a(R_a + R_e) + e; \quad e = k i_a \Omega; \quad m = k i_a \phi = k i_a^2 \quad (2.16)$$

Fig. 2.9 shows the mechanical characteristics evidentiating their nonlinear character. Considering the motor running at low angular speeds around the pause position ( $\Delta\Omega$ ), the characteristics can be approximated by a straight line, so it can be written:

$$m = k_1 i_a = M_p - F_e \Omega; \quad e = k_1 \Omega \quad (2.17)$$

and similar to the DC armature-controlled motor, for a low static torque compared to the starting one, the transfer function with constant coefficients is deduced:

$$G_m(s) = \frac{\theta(s)}{u_a(s)} = \frac{\frac{1}{k_1}}{s \left[ 1 + \frac{F_m}{F_e} (s + sT_e)(1 + sT_m) \right]} \quad (2.18)$$

where  $F_e = k_1 / (R_a + R_e)$  is the slope of the linearized mechanical characteristic:  $T_e = (L_a + L_e) / (R_a + R_e)$ .

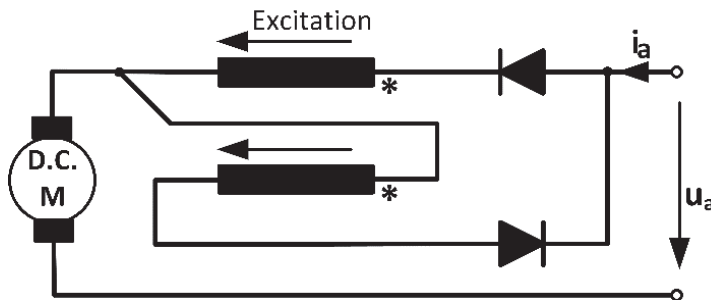


Fig. 2.8 The DC series motor scheme.

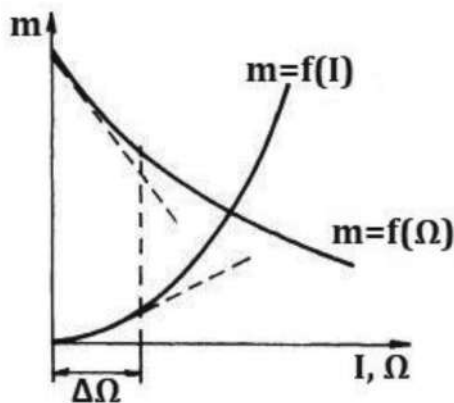


Fig. 2.9 Characteristics of the DC series motor.

## 2.3 Physical characteristics of DC motors

There are situations where a more accurate model is needed, one which also considers, for example, the variation of some parameters, the induction reaction, the brush voltage drop, etc.

For a more accurate DC motor model, the relationship (2.1) can be written as:

$$\begin{aligned}
 u_a &= e_0 + R_a(i_a) \cdot i_a + L_a(i_a) \cdot \frac{di_a}{dt} + \varepsilon(i_a, i_e) + \Delta u_p(i_a) \\
 e_0 &= k\phi_0\Omega; \phi_0 = f(i_e); m = \frac{e \cdot i_a}{\Omega} = \frac{e_0 + \varepsilon(i_a, i_e)}{\Omega} \cdot i_a \\
 m &= J \frac{d\Omega}{dt} + m_r + F_m(\Omega) \cdot \Omega
 \end{aligned} \tag{2.19}$$

in which  $\Delta u_p$  represents the brush voltage drop,  $F_m$  is the mechanical frictions depending on the speed and  $\varepsilon$  is the decrease of the electromotive force due to the armature reaction. For the DC motors with electromagnetic excitation, the armature reaction is important, especially for high excitation currents, and for those DC motors with permanent magnets excitation, the effect of the armature reaction can be neglected.

The variations of the brush voltage drops are non-linear, depending on the load current. For good quality brushes cases and currents greater than 30% of  $I_N$ , this voltage drop can be approximated by 1 [V].

The rotor resistance depends on the winding temperature and, therefore, indirectly, on the load current. It can be simply determined by knowing the coefficient of the torque resistivity variation with temperature, knowing that a variation of the rotor temperature from 25 [°C] to 155 [°C] leads to an electric resistance increase of 50% [33].

Also, the rotor circuit inductance is not constant and varies with the load current more for a DC motor with electromagnetic excitation and less for those with permanent magnets.

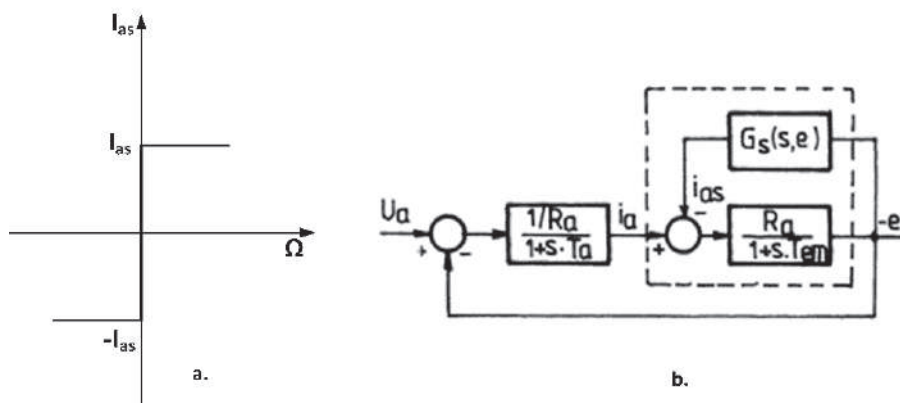


Fig. 2.10 a) Static torque characteristic; b) the corresponding structural scheme of the DC motor.

For motors operating in a very wide speed range (between 1 and 5000 [rpm]), the block diagram in Fig. 2.4.a is not appropriate, especially for very small rotations close to zero. At these speeds, the most important component of the resistive torque is the static friction torque, which has a nonlinear relay type characteristic, as depicted in Fig. 2.10 a.

The machine equations, (2.19), are customized as:

$$\begin{aligned} u_a &= R_a i_a + L_a \frac{di_a}{dt} + e \\ e &= k_1 \Omega \\ m - m_r &= k_1 (i_a - i_{as}) = J \frac{d\Omega}{dt} \end{aligned} \quad (2.20)$$

in which  $i_{as}$  represents the current corresponding to the static torque  $m_r$ . They all together lead to the block diagram in Fig. 2.10b, in which  $G_s(s,e)$  represents the speed-dependent transfer function between the current corresponding to the static torque and the electromotive voltage. For the function to be linear, it is necessary for the pulse of the excitation signal, in the case of a frequency analysis, to fulfill the condition:

$$\omega \ll \frac{1}{T_m} \ll 3\omega \quad (2.21)$$

which is equivalent to the fact that the system's cutting pulse  $\omega_m = \frac{1}{T_m}$  is between the first and the third harmonic of the  $i_{as}$  response. Knowing the static torque  $m_r$  and using the relationship  $m_r = k_1 \cdot k_{\theta s}$ , it is possible to determine the minimum current required for the machine startup. In case of a periodically disturbing signal, this current has the allure shown in Fig. 2.11. Given the particular form of this current, it can be decomposed into Fourier series and, considering only the first harmonic, it results:

$$i_{as}(1) = \frac{4}{\pi} I_{as} \quad (2.22)$$

For each value of  $e$ , there can be found a  $G_{s1}$  transfer factor corresponding to the first harmonic,

$$G_{s1}(e) = \frac{4I_{as}}{\pi e} \quad (2.23)$$



which has a hyperbolic variation of  $e$ ,  $i_{as}$  being constant. Thus, considering  $sT_m \gg 1$ , with the determined  $G_s(s, e)$  in Fig. 2.10. b, the equivalent system of the interrupted contour becomes:

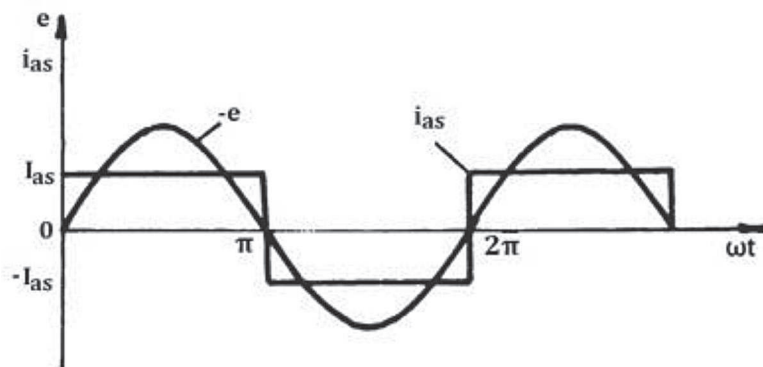


Fig. 2.11 Time variation of  $e(\omega t)$  and  $i_{as}(\omega t)$ .

$$H(s) = \frac{\frac{R_a}{sT_m}}{1 + \frac{R_a}{sT_m} \cdot G_{s1}(e)} = \frac{1}{G_{s1}(e)} \cdot \frac{1}{1 + \frac{sT_m}{R_a G_{s1}(e)}} \quad (2.24)$$

and the block diagram of the servomotor becomes as depicted in Fig. 2.12, where the product  $R_a G_{s1}(e)$  depends of the machine minimum starting voltage,

$$R_a \cdot G_{s1}(e) = \frac{4}{\pi} \cdot \frac{U_{as}}{e} \quad (2.25)$$

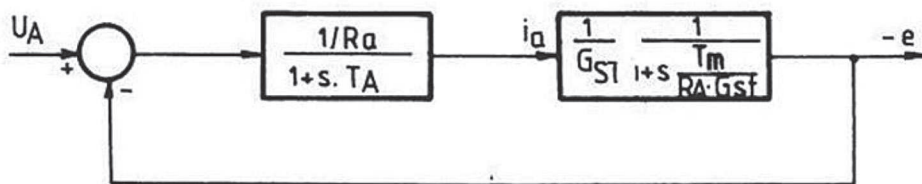


Fig. 2.12 Block diagram for the linearized model.

It is found that, at a very low speed, the factor  $1 / G_{s1}(e)$  is very small, which is equivalent to breaking the loop on the direct path. A decrease in the electromechanical time constant, a decrease which must be taken into account when choosing the parameters of the controller is also noted. From the presented model, there is a need for **adaptive regulators** to ensure the correct operation of the motors in a wide speed range with modifiable parameters depending on a slow variable, e.g. the average rotation speed.

Even in stationary mode, for a well-filtered continuous supply, the electromagnetic torque is not constant, but exhibits a variation as in Fig. 2.13 due to the switching, due to the variation of the magnetic reluctance in the slots, etc. At very low speeds, these torque ripples are manifested in the load oscillating speed, being extremely difficult to remove them.

Therefore, a torque ripples coefficient is used to determine the quality of the DC motors,

$$k_o = \frac{M_{\max} - M_{\min}}{M_{\max} + M_{\min}} \quad (2.26)$$

which has values  $\leq 1 - 2\%$  for motors in a control range  $\geq 1: 10000$  [rpm]. For this purpose, constructive solutions such as the inclination of the rotor slots and the increase of the number of commutator segments are used, etc.

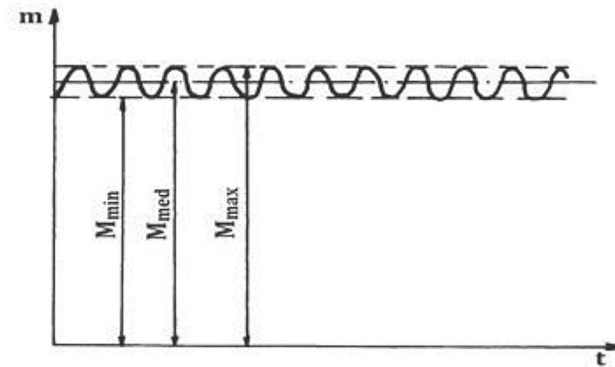


Fig.2.13 Time varying electromagnetic torque.

In conclusion, it is noted that the DC motors performances related to torque, speed, heat, etc., can be found in the special catalogues of the building motors companies.

## 2.4 Static converters feeding DC machines

### 2.4.1 Converters with natural commutation

This group of converters includes an extremely vast solution based on natural commutation. As the network or the machine can supply the switching voltage, three major classes of applications are distinguished:

- converters with commutation from the network, operating in rectifier and inverter mode;
- frequency converters with direct network commutation (cyclo-converters);
- converters with commutation from the load, usually operating in the inverter mode.

In this paragraph, the group of rectifiers and inverters with network commutation is synthetically treated. The approach is based on the vast experience and work accomplishments achieved by the Department of Electrical Engineering [4].

The rectifiers convert the energy from AC into DC. They can operate in one, two or four quadrants. These variants together with a clear delimitation of the quadrants in the voltage and current space coordinates are represented in Fig. 2.14. Due to the unidirectional current conduction property through the thyristors, the current at the rectifier output can have only one sense. As it will be shown next, it is, however, possible for a continued variation of the voltage from a maximum positive value to a negative maximum value by changing the control angle.

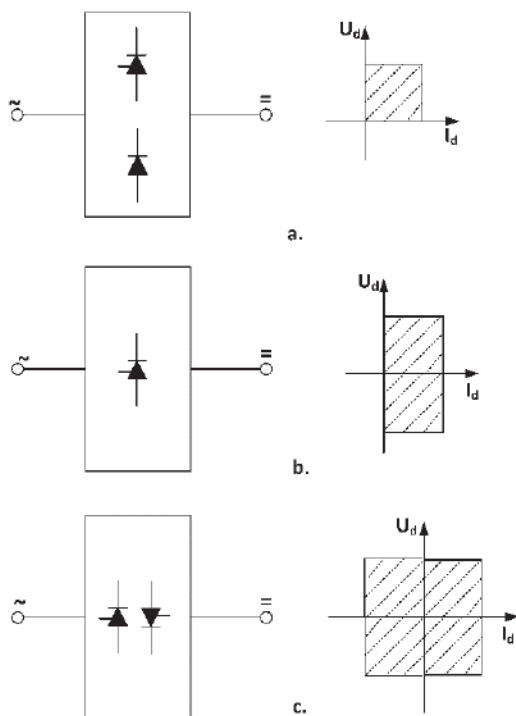


Fig.2.14 Converters with direct network commutation, the main types: a) rectifiers with a single-quadrant (semi-detached or un-decked); b) two-quadrant rectifiers; c) four-quadrant rectifiers.

For the inverter operation mode, however, there is an important condition to be satisfied: the load must be **active**, i.e. it has an electromotive voltage. This is the only way in which the current could be maintained positive through the valves, while the load voltage is negative.

The four-quadrant converters are obtained by setting up two anti-parallel two-quadrant converters and by allowing the reversal of both the output voltage and the current.

### 2.4.1.1 Two-quadrant converters

This category consists of a series of schemes that are widely used in power electronics, providing both voltage polarities and one sense for the current. Rectifier operation means  $i_d > 0, u_d > 0$ , while  $u_d < 0, i_d > 0$  characterizes the inverter operation mode.

The ideal theory of these converters is presented below and it supposes to neglect the commutation and to consider that the overlapping interval at the anode is negligible and that it does not influence the progress of the phenomena. The valves are also considered as ideal components.

a. Single-phase converter with null

One of the most used rectifier schemes is that of the midpoint rectifier or null, as shown in Fig. 2.15.

The two thyristors are connected in the secondary of the mono-phase transformer with a median point, the load being connected between the thyristors cathodes and the median point.

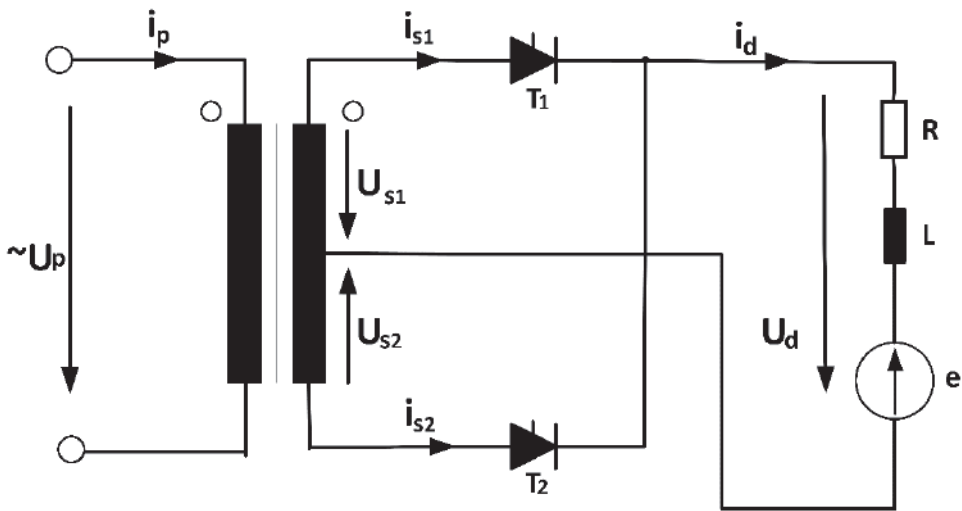


Fig.2.15 Single-phase converter with null.

For the two-quadrant operation, the load must have an electromotive voltage (usually a DC machine or a battery).

It is assumed that the load circuit has a strong inductive character,  $L \rightarrow \infty$ , which means that the load current can be considered constant  $i_d = I_d = Ct$ . With the notations from Fig. 2.15, the voltages expressions in the primary and secondary of the transformers are:

$$\begin{aligned} u_p &= U_{pm} \cdot \sin \omega t = \sqrt{2} \cdot U_p \cdot \sin \omega t \\ u_{s1} &= -u_{s2} = U_{sm} \cdot \sin \omega t = \sqrt{2} \cdot U_s \cdot \sin \omega t \end{aligned} \quad (2.27)$$

By priming the thyristors, the secondary of the transformer is connected to the load. The rectified voltage is obtained by sequentially controlling the two thyristors on a half period of the supply voltage, where the continuous voltage presents two pulses.

The thyristors can only be primed if they are polarized directly. The natural amortization point is at the beginning of each half period, Fig. 2.16 a. Thus, the operation is identical to that of an uncontrolled (diode) rectifier. It yields to that the diode schemes are particular operation cases of those containing thyristors.

In the blocked state, the voltage drop on the thyristor is:

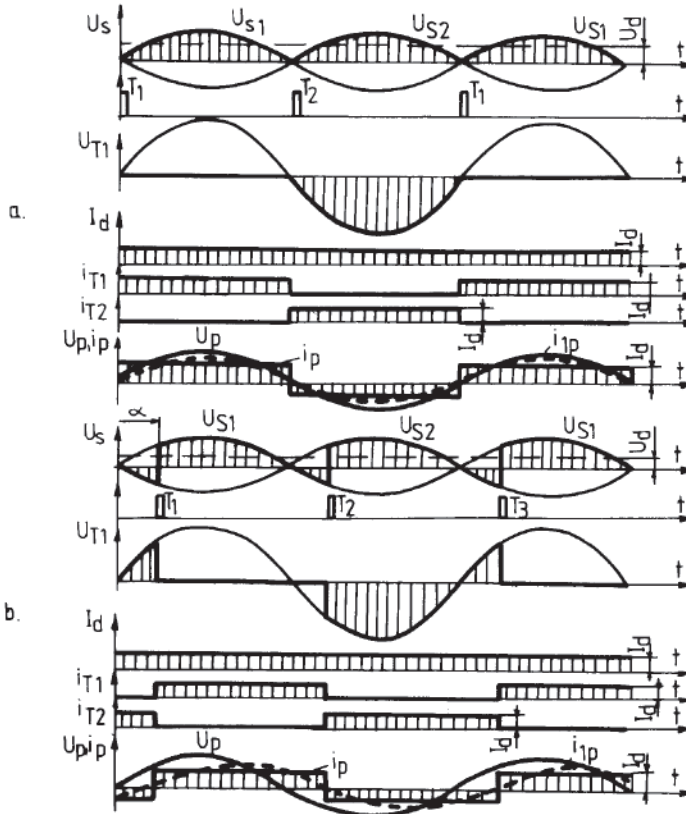


Fig. 2.16 Voltages and currents variations at single-phase converter with null: a)  $\alpha = 0$  (natural priming); b)  $\alpha = 45^\circ$ .

In the blocked state, the voltage drop on the thyristor is:

$$u_{T1} = u_{s1} - u_{s2} = 2 \cdot U_{sm} \cdot \sin \omega t \quad (2.28)$$

having a maximum value of:

$$U_{T_{max}} = 2 \cdot U_{sm} \quad (2.29)$$

If a priming at a command angle  $\alpha \neq 0^\circ$  is considered, Fig. 2.16.b, the rectified voltage is:

$$\begin{aligned} u_d &= u_{s1} = U_{sm} \cdot \sin \omega t, & \alpha < \omega t < \pi + \alpha \\ u_d &= u_{s2} = -U_{sm} \cdot \sin \omega t, & \pi + \alpha < \omega t < 2\pi + \alpha \end{aligned} \quad (2.30)$$

An increase in the control angle  $\alpha$  causes a decrease in the rectified average voltage and, at the same time, the fundamental of the transformer's primary current will deviate from the supply mains voltage ( $\phi_1 = \alpha$ ).

The rectified average voltage of the converter is:

$$U_d = \frac{1}{\pi} \cdot \int_{\alpha}^{\pi+\alpha} U_{sm} \cdot \sin \omega t \cdot d(\omega t) = \frac{2}{\pi} \cdot U_{sm} \cdot \cos \alpha = \frac{2\sqrt{2}}{\pi} \cdot U_s \cdot \cos \alpha = U_{d0} \cdot \cos \alpha \quad (2.31)$$

where  $U_{d0}$  represents the maximum ideal rectified voltage.

It can be seen from the relationship (2.31) that for  $\alpha = 90^\circ$ , the average value of the rectified voltage is null and for  $\alpha > 90^\circ$ , the rectified average voltage becomes negative and the converter operates in the inverter mode. In this situation, the load must maintain the sense of current through thyristors, which is possible only if  $e$  has reversed its polarity and if  $e > U_d$ . In this situation, the energy is transferred from the load to the source. If the load is represented by a DC machine, it will be driven from the outside, in reverse direction, at a speed that causes an electromotive voltage greater than the average value of the rectified voltage; in other words, the DC machine will operate as a generator. The current must therefore satisfy the inequality in all the circumstances:

$$I_d = \frac{U_d - e}{R} > 0 \quad (2.32)$$

with the observation that, due to the assumption that  $L \rightarrow \infty$ , the filter inductance does not appear in the relationship (2.32).

It means that, in the rectifier mode, the inequalities are valid:

$$\begin{aligned} U_d &> e > 0 \\ P &= U_d \cdot I_d > 0 \end{aligned} \quad (2.33)$$

and in inverter operation mode:

$$\begin{aligned} U_d &< e < 0 \\ P &= U_d \cdot I_d < 0 \end{aligned} \quad (2.34)$$

For the transformer sizing, a series of useful design relationships can be deduced. Considering the transformation ratio, in general, to be:

$$k_t = \frac{N_1}{N_2} \quad (2.35)$$

where  $N_1$  and  $N_2$  are the total number of turns in the primary of the transformer and half turns in the transformer secondary, respectively, and, also, considering for simplification that  $k_r = 1$ , the following expressions are obtained:

$$\begin{aligned} U_p = U_s &= \frac{\pi}{2\sqrt{2}} \cdot U_{d0} \\ I_p = I_d & \\ I_s &= \sqrt{\frac{1}{2\pi} \cdot \int_0^\pi I_d^2 \cdot d(\omega t)} = \frac{I_d}{\sqrt{2}} \end{aligned} \quad (2.36)$$

The apparent power of the transformer results as an average value of the apparent powers in the primary and secondary of the transformer:

$$\begin{aligned} S_t &= \frac{1}{2} \cdot (S_p + S_s) = \frac{1}{2} \cdot (U_p \cdot I_p + U_s \cdot I_s) = \\ &= \frac{1}{2} \cdot \left( \frac{\pi}{2\sqrt{2}} + 2 \cdot \frac{\pi}{2\sqrt{2}} \cdot \frac{1}{\sqrt{2}} \right) \cdot U_{d0} \cdot I_d \cong 1.34 \cdot P_{d0} \end{aligned} \quad (2.37)$$

It is noted that, at the single-phase converter with null, the power transformer is oversized by 34% in comparison with the power in the DC circuit due to the fact that it is poorly used. Indeed, the secondary windings operate only for a half-period.

The apparent power absorbed from the mains is:

$$S_r = S_p = \frac{\pi}{2\sqrt{2}} \cdot U_{d0} \cdot I_d \cong 1.11 \cdot P_{d0} \quad (2.38)$$

Thus, less than that for which the transformer is to be dimensioned. In conclusion, the scheme can only be used at low powers, which do not exceed the kW order, due to the transformer's cost and gauge.

Generally, for the grid-connected converters, the shape factor  $k_f$  and wave factor  $K_u$  are defined as:

$$k_f = \frac{U_{def}}{U_d}; \quad k_u = \frac{U_{def}}{U_d} \quad (2.39)$$

where  $U_d$  is the average value of the rectified voltage,  $U_{def}$  is the effective value of the rectified voltage and  $U_{def-}$  is the effective value of the rectified voltage alternating component, and:

$$U_{def} = \sqrt{U_{def-}^2 - U_d^2} = U_d \cdot \sqrt{k_f^2 - 1} = k_u \cdot U_d \quad (2.40)$$

These sizes qualitatively characterize the rectified voltage.

b. Single-phase bridge converter

This converter is usually preferred to the null converter because it can be connected directly to the network, without using a transformer. Even if the transformer is still used, this is done very efficiently. The operation of the bridge converter is based on the diagram in Fig. 2.17. The converter is comprised of two converters with null, the load being connected between P and N. In a half-period, the thyristors  $T_1$  and  $T_2$  lead, and in the other half period,  $T_3$  and  $T_4$  lead. Considering a reference null, it can be noticed that the rectified voltage is:

$$u_d = u_{dp} - u_{dN} \quad (2.41)$$

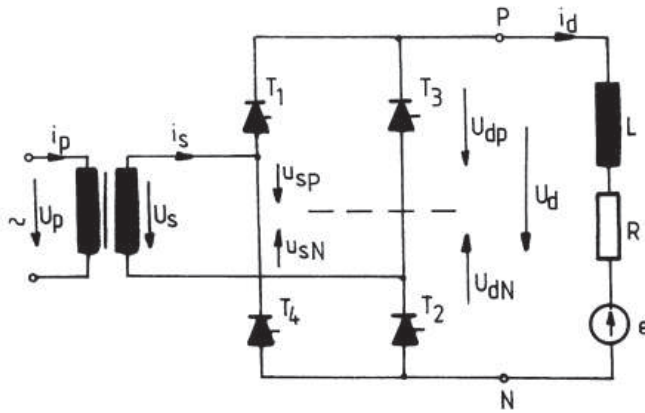


Fig. 2.17 Single-phase bridge converter.

The average voltages are:

$$u_{dp} = \frac{1}{\pi} \cdot \int_{\alpha_p}^{\pi+\alpha_p} \frac{1}{2} \cdot U_{sm} \cdot \sin \omega t d(\omega t) = \frac{U_{sm}}{\pi} \cdot \cos \alpha_p$$

$$u_{dN} = -\frac{U_{sm}}{\pi} \cdot \cos \alpha_N \quad (2.42)$$

$$u_d = u_{dp} - u_{dN} = \frac{U_{sm}}{\pi} \cdot (\cos \alpha_p + \cos \alpha_N)$$

In the case of a symmetrical command, almost exclusively used,  $\alpha_p = \alpha_N = \alpha$  and the average rectified voltage:

$$U_d = \frac{2}{\pi} \cdot U_{sm} \cdot \cos \alpha = \frac{2\sqrt{2}}{\pi} \cdot U_s \cdot \cos \alpha = U_{d0} \cdot \cos \alpha \quad (2.43)$$



The waveforms are shown in Fig. 2.18.

The voltage at which the thyristors are required to enter in conduction is half of the null converter voltage.

The apparent power of the power transformer is:

$$S_t = \frac{1}{2} \cdot (S_p + S_s) = S_p = S_s = \frac{\pi}{2\sqrt{2}} \cdot U_{d0} \cdot I_d \cong 1.11 \cdot P_{d0} \quad (2.44)$$

therefore, it is oversized by only 11% of the maximum useful power.

The apparent power absorbed by the mains is equal to that of the transformer:

$$S = S_t = S_p \cong 1.11 \cdot P_{d0} \quad (2.45)$$

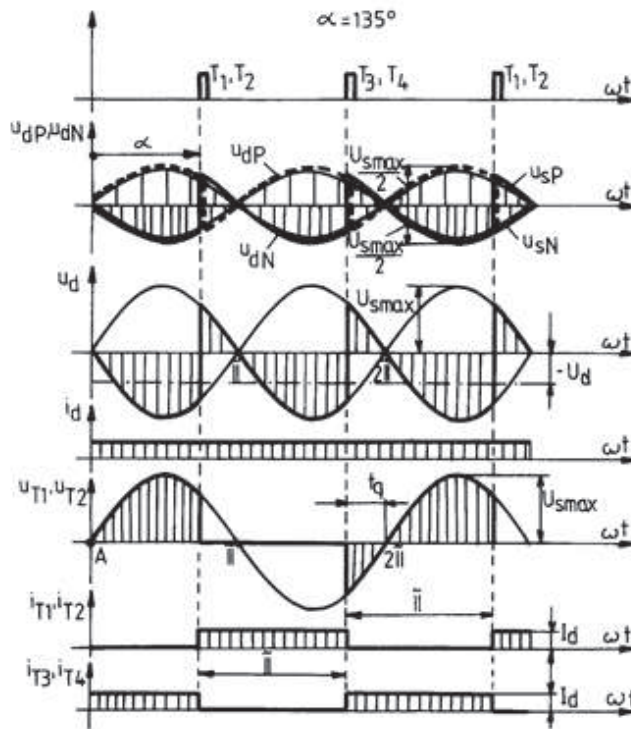


Fig. 2.18 Variation of voltages and currents in the single-phase bridge converter for  $\alpha=135^\circ$ .

The essential difference between the bridge and the null schemes is that the bridge circuit always closes the current through two thyristors located in the two parts of the bridge and, therefore, at the symmetrical command, two commutations of the same voltage switching take place simultaneously.

c. Three-phase converter with null

The use of the three-phase voltage system allows an increase in the number of pulses: 3, 6 and multiples. The converters are supplied with ordinary or special transformers with various wiring connections. The three-phase neutral converter is a three-pulse converter, Fig. 2.19.

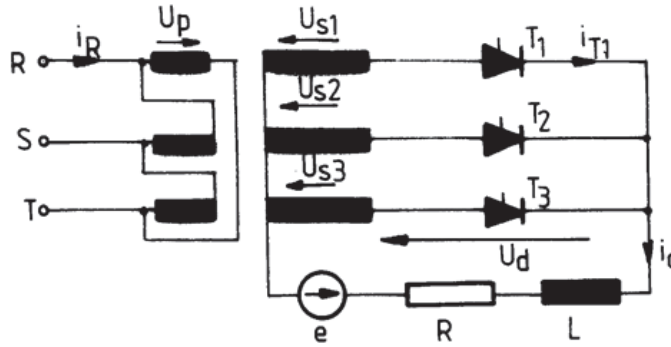


Fig.2.19 Three-phase neutral converter.

The three thyristors lead successively by connecting each phase with the load only once over a period of  $2\pi/3$ .

The converter voltages and currents waveforms are shown in Fig. 2.20.

The maximum voltage that occurs on a locked thyristor, polarized directly or vice versa is:

$$U_{T\max} = \sqrt{3} \cdot U_{sm} = \sqrt{6} \cdot U_s \quad (2.46)$$

that is equal to the maximum value of the line voltage.

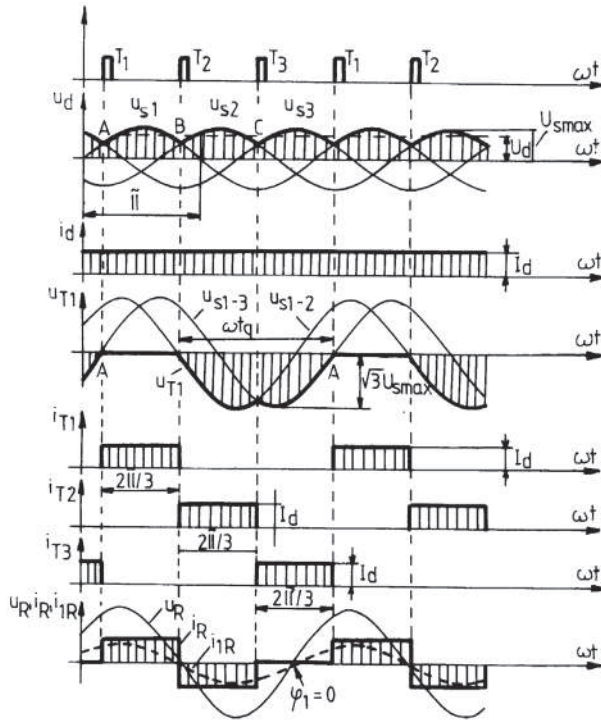
The rectified average voltage has the expression:

$$\begin{aligned} U_d &= U_{d0} \cdot \cos \alpha \\ U_{d0} &= \frac{3\sqrt{6}}{2\pi} \cdot U_s \end{aligned} \quad (2.47)$$

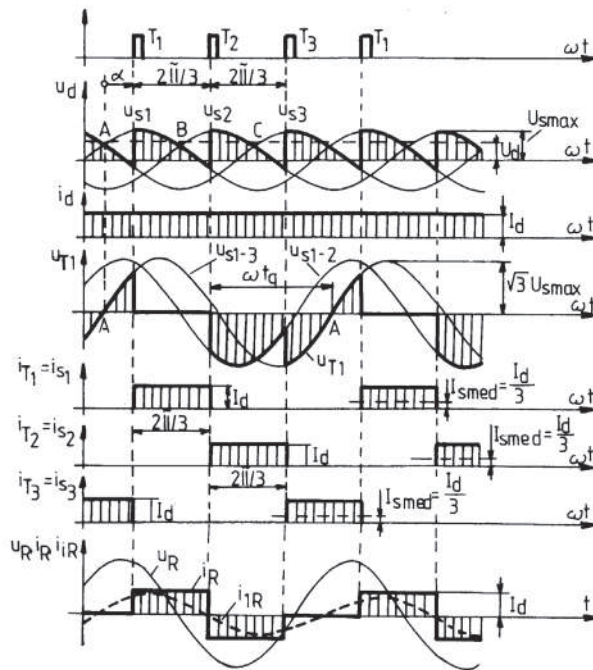
The rectified voltage decreases as the command angle increases; for  $\alpha > \pi/6$ , in the rectified voltage waveforms, negative electric arcs appear in the voltages from the secondary of the transformer, and for  $\alpha > 5\pi/6$  ( $150^\circ$ ) the rectified voltage reaches only negative portions.

The three-phase neutral converter allows the current to flow in the transformer's secondary in one direction, its average value being:

$$I_{smed} = \frac{1}{2\pi} \cdot \int_{\alpha}^{2\pi/3+\alpha} I_d(\omega t) = \frac{I_d}{3} \quad (2.48)$$



a.



b.

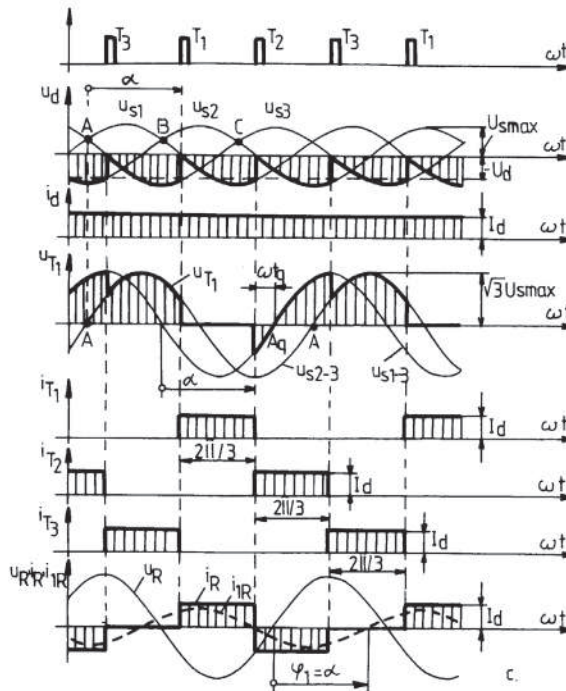


Fig. 2.20 Variation of voltages and currents for a three-phase neutral converter: a)  $\alpha = 0^\circ$  (natural priming); b)  $\alpha = 45^\circ$ ; c)  $\alpha = 150^\circ$ .

The apparent power of the transformer is:

$$S_r = \frac{1}{2} \cdot (3S_p + 3S_s) = \frac{1}{2} \cdot \left( 3 \cdot \frac{2\pi}{3\sqrt{6}} \cdot \frac{\sqrt{2}}{3} + 3 \cdot \frac{2\pi}{3\sqrt{6}} \cdot \frac{\sqrt{3}}{3} \right) \cdot U_{d0} \cdot I_d \approx 1.35 \cdot P_{d0} \quad (2.49)$$

which means an increase of 35% of the maximum power  $P_{d0}$ . The apparent power absorbed by the mains transformer is  $S_r = S_p = 3U_p I_p \approx 1.21 P_{d0}$ .

The three-phase neutral scheme has the disadvantage of oversizing the transformer due to the poor use of the secondary windings, which limits the power obtained with these converters to the order of [kW] [4].

d. Three-phase bridge converter

The improvement of the rectified voltage shape and of the transformer power factor is done by using the three-phase bridge converter depicted in Fig. 2.21. This is equivalent to two three-phase neutral converters connected in series, P and N. In this case, the transformer's null is not used, and there is also the possibility of removing the transformer if the grid voltage matches the load requirements. The rectified voltages  $u_{dP}$  and  $u_{dN}$  relate to a virtual null. The operation of the three-phase bridge converter impose to the two thyristors to be in conduction in each moment, one of the P group and one of the N group, but obviously from different phases. The value of the rectified voltage is:



component. The current in the transformer's primary winding is identical to the one in the secondary one. Considering  $kt = 1$ , the sizing's characterizing the transformer are:

$$u_p = u_s = \frac{\pi}{3\sqrt{6}} \cdot U_{d0}$$

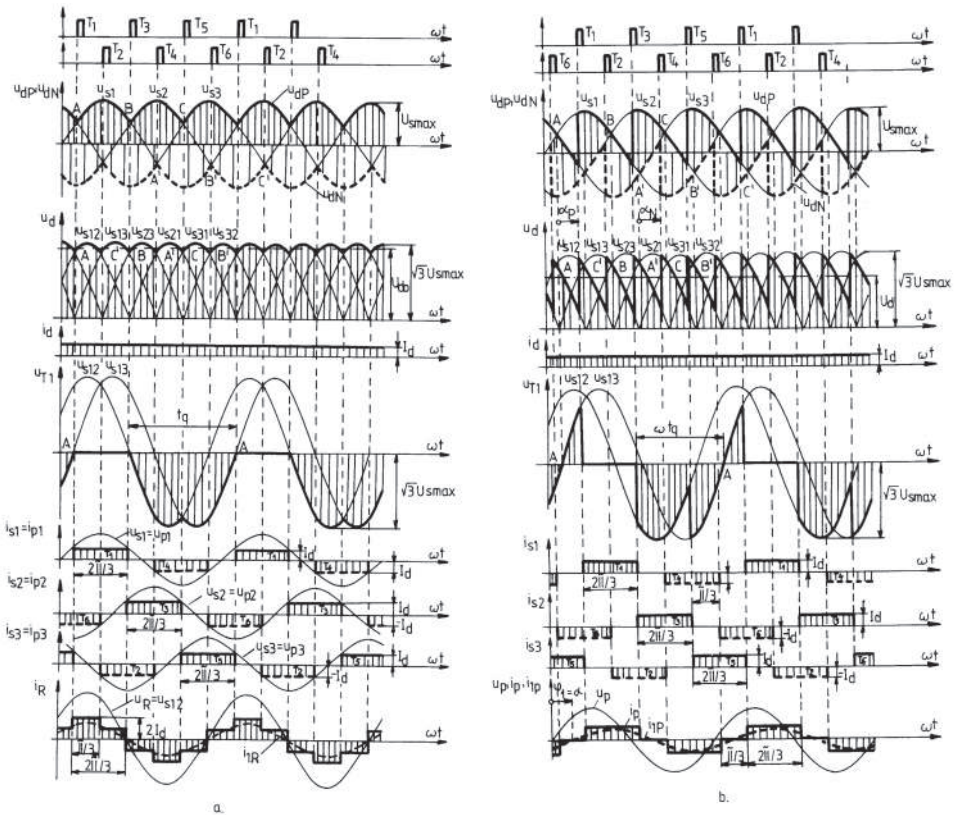
$$I_p = I_s = \sqrt{\frac{1}{2\pi} \cdot \int_0^{4\pi/3} I_d^2 \cdot d(\omega t)} = \sqrt{\frac{2}{3}} \cdot I_d \quad (2.52)$$

With these sizes, the apparent power of the transformer is:

$$S_t = 3 \cdot U_p \cdot I_p = 3 \cdot U_s \cdot I_s = \frac{\pi}{3\sqrt{6}} \cdot \sqrt{\frac{2}{3}} \cdot U_{d0} \cdot I_d \cong 1.05 \cdot P_{d0} \quad (2.53)$$

It is noticed that the transformer is properly used, its apparent power being only 5% higher than the maximum useful power  $P_{d0}$ . When the transformer's windings are star connected, the same value for its apparent power is obtained.

It can be concluded that the three-phase bridge scheme is the most efficient scheme, with such converters having a wide spread of up to hundreds of [kW].



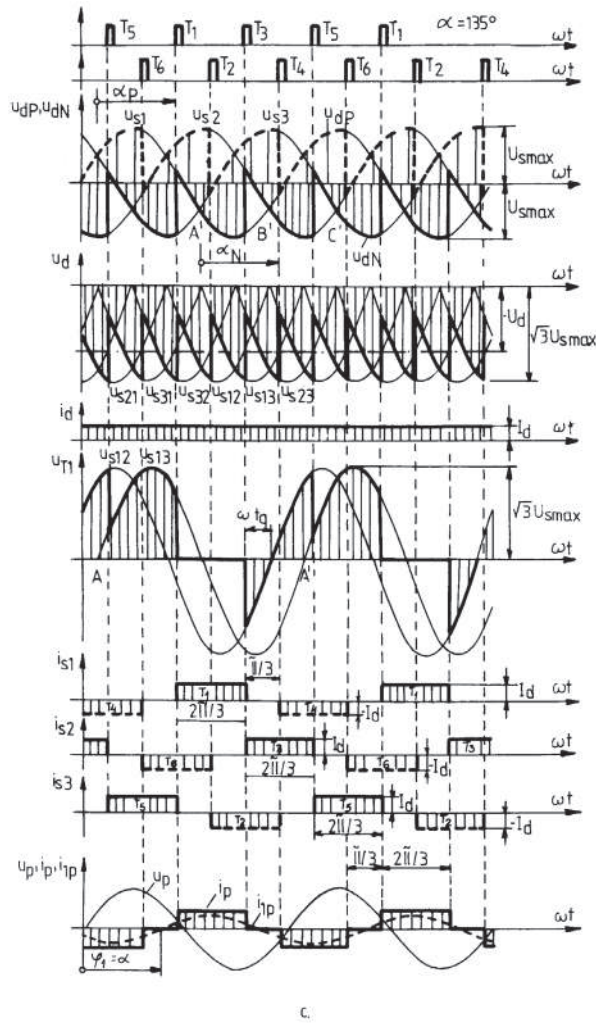


Fig. 2.22 Variation of voltages and currents for a bi-phase bridge converter: a)  $\alpha = 0^\circ$  (natural priming); b)  $\alpha = 45^\circ$ ; c)  $\alpha = 135^\circ$ .

e. Converter schemes with an increased number of pulses

In practice, in the high power static converters field, other schemes that have the number of pulses  $\geq 6$  are also used.

Fig. 2.23 shows a 6-pulse converter with midpoint M6 / 30, where the star-connected transformer's secondary windings form a hexagonal system. This scheme is not identical to the parallel connection of two of the three-pulse converter schemes, its performance being similar to the three-phase bridge converter in terms of continuous voltage waveforms. One of its drawbacks is similar to the one of the other median point schemes, i.e. inefficient operation of the transformer. In other words, it is oversized.

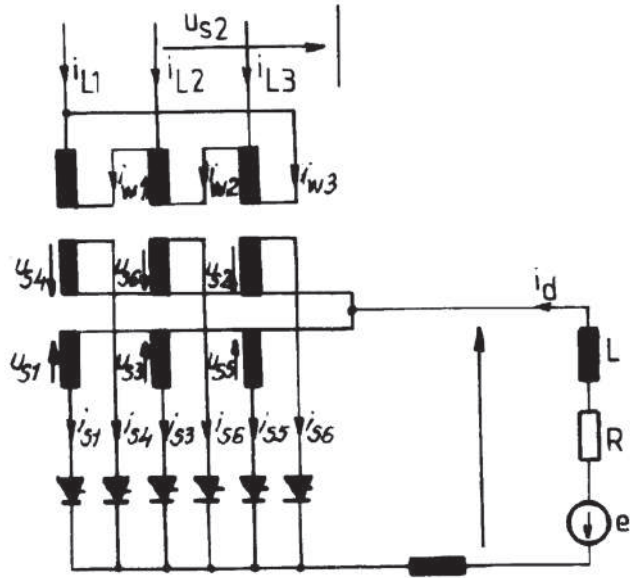


Fig.2.23 6-pulse converter with mid-point.

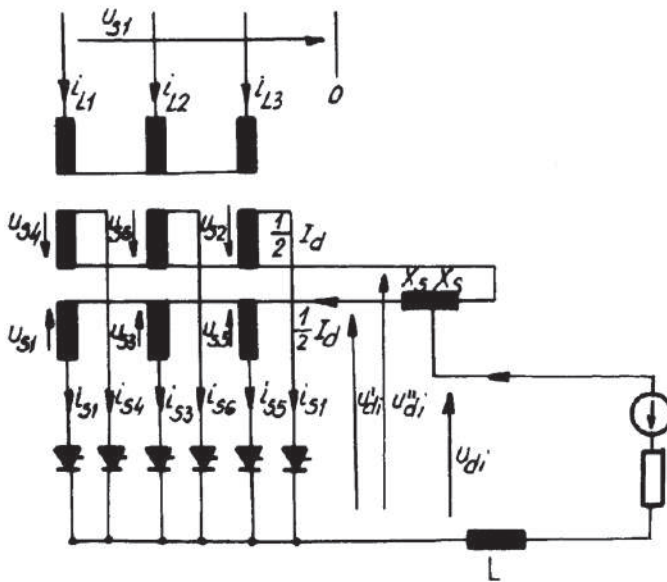


Fig. 2.24 6-pulse converter and absorption coil.

Another variant is the diagram in Fig. 2.24. Here, the two sections of the converter operate in parallel through an inductive voltage divider. Basically, it is an induction coil with a mid-point socket, called an **absorption coil**, whose computing power is relatively small, because there is no continuous flux in it.



The absorption coil scheme has the advantage that the current transition time corresponds to  $120^\circ$  and offers a better use of the valves and of the transformer.

At very high powers, two 6-pulse converters are connected in parallel through an absorption coil, obtaining a 12-pulse converter, Fig. 2.25.

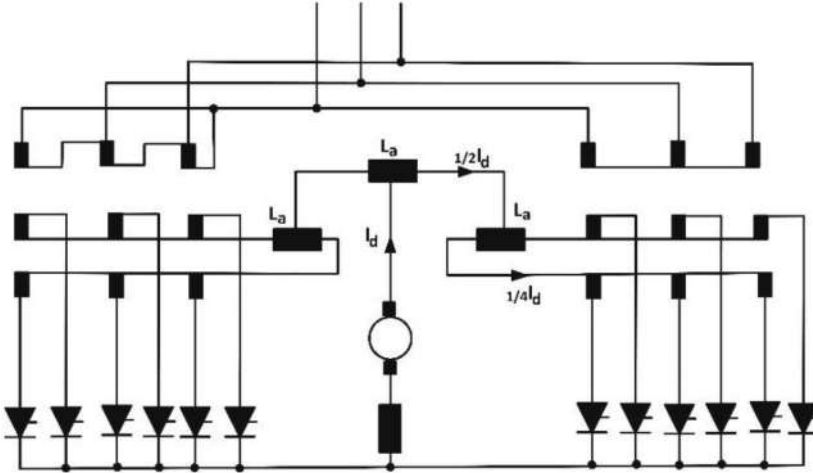


Fig 2.25 12-pulse converter with three absorption coils.

If a high continuous voltage is required, which implies a higher number of valves connected in series, the 12-pulse converter would represent the solution, as depicted in Fig. 2.26. It uses bifurcated bridge converters. Only one transformer having two secondaries is needed. This means that the phase shift between voltages is  $30^\circ$ .

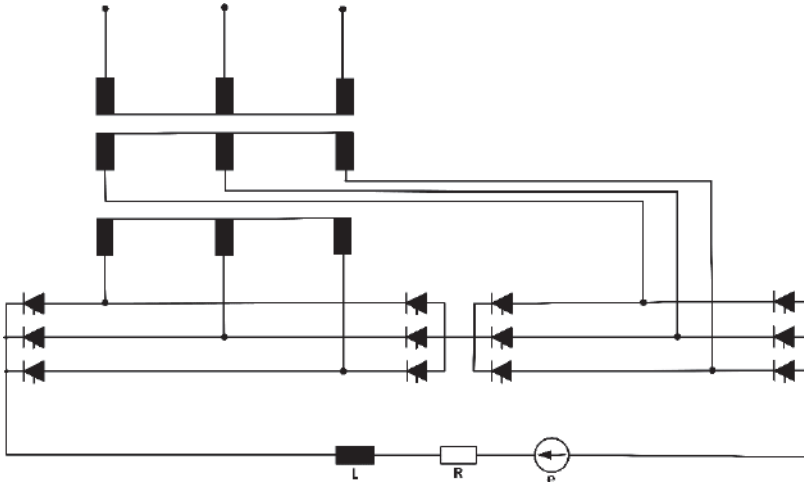


Fig. 2.26 12-pulse converter that uses two bridges connected in series.

Due to the serial connection instead of a parallel connection, the absorption coil is eliminated [4].

### 2.4.1.2 One-quadrant converters

There are many power receivers that require unidirectional DC current and voltage, these converters operate in one-quadrant. This category, which is a particular case of the two-quadrant converters, includes converters for which several thyristors are replaced by diodes. In general, a mains direct commutation converter could operate in one-quadrant if it contains at least one diode in its structure. Operation in one-quadrant is also specific to the two-quadrant converters that feed passive load, i.e. without its own electromotive voltage. Particularly, for the one-quadrant converters that can operate only in rectifier mode, the name "rectifier" is appropriate for them.

#### a. Single-phase half-controlled bridge rectifier

This converter can be built in two variants, as an asymmetrical or symmetrical bridge, depending on the location of the diodes.

**The asymmetrical bridge** is shown in Fig. 2.27. We can consider the rectifier composed of two null converters, of which P is ordered and N is not ordered. The voltage  $u_d$  consists of  $u_{dP}$  and  $u_{dN}$ , measured in relation with the fictitious null. The relationships (2.41) and (2.42) remain valid, with the remarks that the control angle  $\alpha_{NP} = \alpha$  for the P side and  $\alpha_N = 0$  for the diodes side.

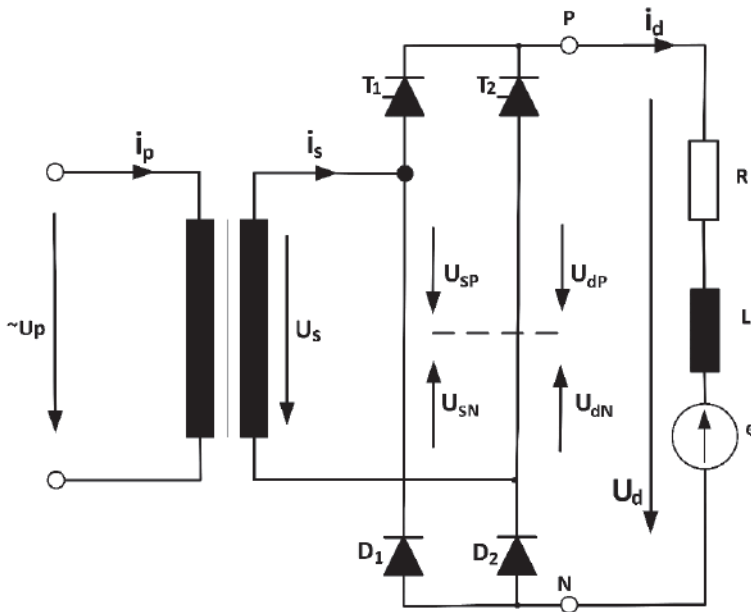


Fig. 2.27 Single-phase rectifier in asymmetrical bridge.

The load voltage value is null if two valves on the same vertically side of the bridge drive simultaneously. The rectified voltage contains only positive portions and can be modified using:

$$u_d = \frac{U_{sm}}{\pi} \cdot (1 + \cos \alpha) = U_{d0} \cdot \frac{1 + \cos \alpha}{1} \quad (2.54)$$

Basically, the control angle  $\alpha$  cannot reach  $180^\circ$  because for this to happen, it would mean involving the application of a reverse voltage on the interval  $t_q > t_{rev}$  for blocking the thyristor. If  $t_q < t_{rev}$ , there may be a chance for the bridge to flip-flop, i.e. the blocked thyristor to re-enter the conduction without being controlled, resulting in a rise of the load voltage and, implicitly, in a forced current occurrence. Fig. 2.28 shows the variation of currents and voltages for the asymmetrical bridge.

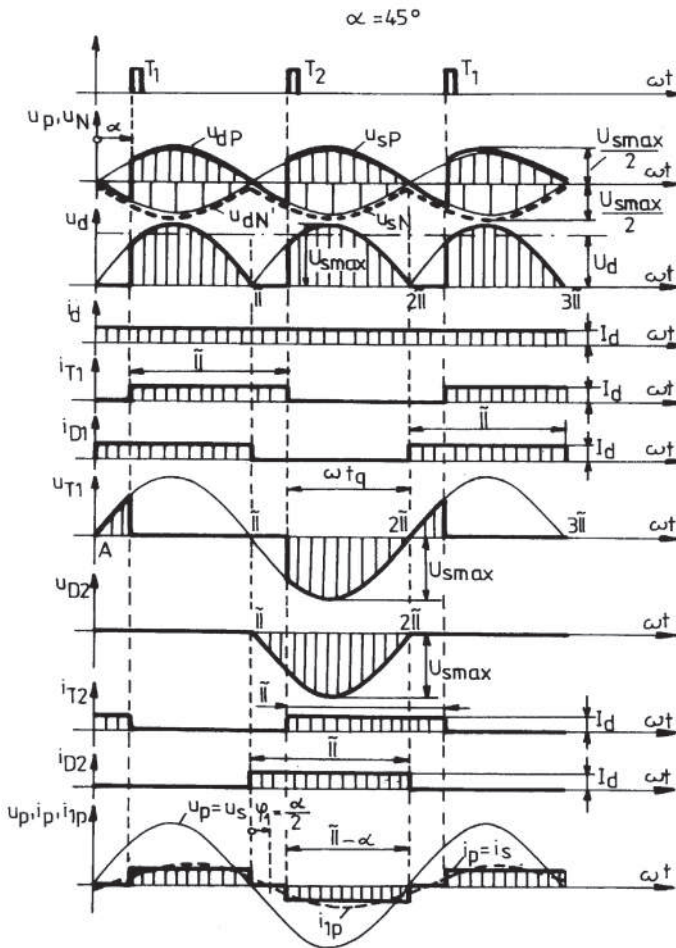


Fig. 2.28 Currents and voltages for an asymmetrical bridge with  $\alpha = 45^\circ$ .

To avoid the rectifier tipping and to trigger operation at voltages  $U_d \cong 0$ , a **freewheeling diode** completes the diagram, absorbing the load current from the valve pairs  $T_1 - D_2$  and  $T_2 - D_1$ , respectively, every time the voltage  $U_d$  becomes 0.

**The semi-controlled symmetrical bridge**, Fig. 2.29, contains thyristors and diodes on the same side, and, thus, the fast diode is no longer needed, because the diodes take over its role together.

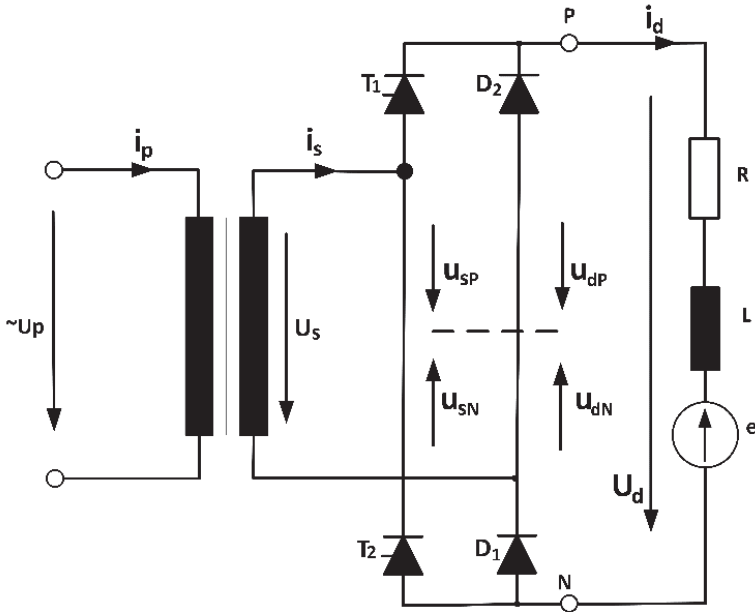


Fig. 2.29 Single-phase rectifier in symmetrical bridge.

None of the half-bridges, P or N, is fully-controlled by the neutral converters and, consequently, the rectified average voltage is determined over a half-period.

$$u_d = \frac{1}{\pi} \cdot \int_{\alpha}^{\pi} U_{sm} \cdot \sin \omega t (d\omega t) = \frac{U_{sm}}{\pi} \cdot (1 + \cos \alpha) = U_{d0} \cdot \frac{1 + \cos \alpha}{2} \quad (2.55)$$

Fig. 2.30 shows the variation of currents and voltages for the semi-controlled symmetrical bridge. It can be seen that the shape of the rectified voltage is the same as for the asymmetrical bridge, but there is a major difference in the duration of conduction of the thyristors and diodes. The thyristors are in conduction on  $\pi - \alpha$  and the diodes on  $\pi + \alpha$ .

The voltage demand is the same for all valves.

The phase-shift between the commanded fundamental and the transformer voltage is similar to the one in the asymmetrical bridge  $\varphi_1 = \alpha/2$ .

Also, in the symmetrical semi-controlled bridge, there is no tilting danger due to the inverse polarization of the thyristors over a voltage semi period, the diodes also taking over the role of a fast diode alternatively.

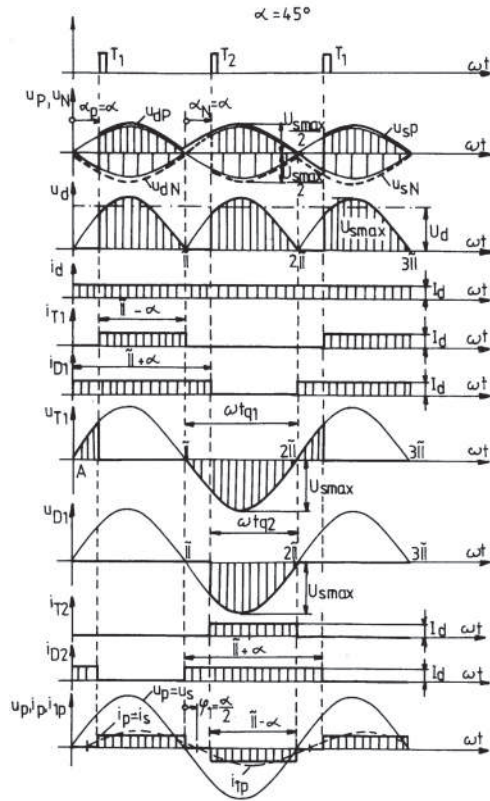


Fig. 2.30 Variation of currents and voltages for  $\alpha = 45^\circ$  for the semi-controlled symmetrical bridge.

b. Three-phase rectifier in semi-controlled bridge

By replacing the thyristors in one part of the diode bridge, a semi-controlled three-phase rectifier is obtained, Fig. 2.31. This rectifier can be considered as consisting of two neutral three-phase converters, one commanded (P) and one non-commanded (N).

The diodes are opened at the natural priming points ( $\alpha_N = 0$ ) and the thyristors are primed in pairs by the command angle.

Fig. 2.32 shows the variation of the currents and the voltages for three-phase rectifier with half-controlled bridge. It is noted that, for  $\alpha < 60^\circ$ , the rectified instantaneous voltage is not cancelled, the valves in the two parts switching at different times. For  $\alpha = 60^\circ$ , the priming moments for the thyristors and diodes coincide and the instantly rectified voltage  $u_d$  is cancelled three times over a period. For  $\alpha > 60^\circ$ , voltage breaks occur and the greater  $\alpha$  is, the longer they are. During the cancellation of the rectified voltage, Fig. 2.32.b, the valves pairs on the same side,  $T_1$ - $D_1$ ,  $T_2$ - $D_2$ ,  $T_3$ - $D_3$ , ensure the discharge of the  $i_d$  current, playing the role of a fast diode. On these time intervals, the current absorbed from the mains is null.

The rectified voltage is computed by using:

$$u_d = u_{dp} - u_{dN} = \frac{3 \cdot \sqrt{6}}{2\pi} \cdot u_s (1 + \cos \alpha) = U_{d0} \cdot \frac{1 + \cos \alpha}{2} \quad (2.56)$$

similar to (2.55), but  $U_{d0}$  has the value of (2.52).

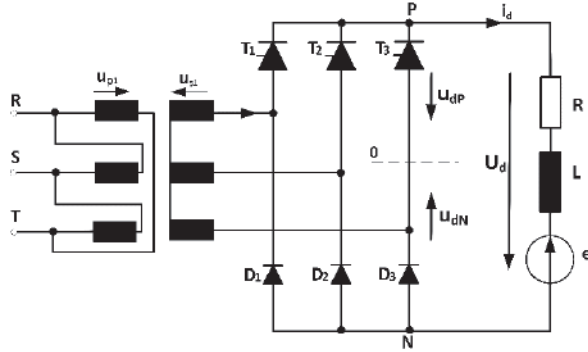


Fig.2.31 Three-phase rectifier with half-controlled bridge.

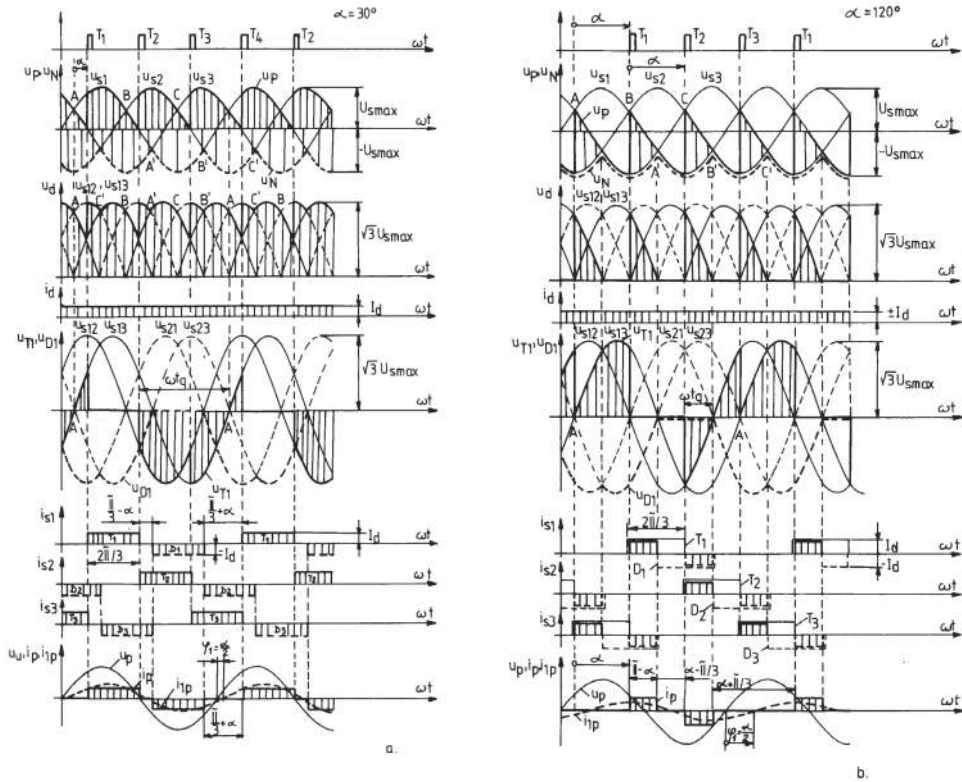


Fig. 2.32 Variation of currents and voltages for a)  $\alpha = 30^\circ$ ; b)  $\alpha = 120^\circ$ .

All the other considerations, shown at the three-phase controlled bridge converters regarding the valves' maximum voltage, the currents and voltages in the primary and secondary transformer's windings and its sizing, remain valid here, too. There is a phase-shift between the fundamental current phase of the transformer and voltage of  $\varphi_1 = \alpha/2$ . In this case, the maximum control angle cannot reach  $180^\circ$  due to the bridge swinging. To remedy this, there are two solutions: using a fast diode or supplying the bridge from the transformer's secondary circuit with different voltages [4].

c. Fast diodes rectifiers

Installing a fast diode prevents the inverter from tipping at high command angles. Installing a fast diode to the two quadrants converters provides it with the possibility to operate only in rectifier mode, which actually means operation in one quadrant. The fast diode enters in conduction mode by short-circuiting the load whenever the rectified voltage  $u_d$  becomes negative. Practically, the fast diode "cuts" the negative portions of the rectified voltage, cancelling them. For this reason, this diode is also known in the literature as **the null diode**.

**The single-phase bridge rectifier with null diode** is shown in Fig. 2.33. The currents and voltages can be seen in Fig. 2.34.

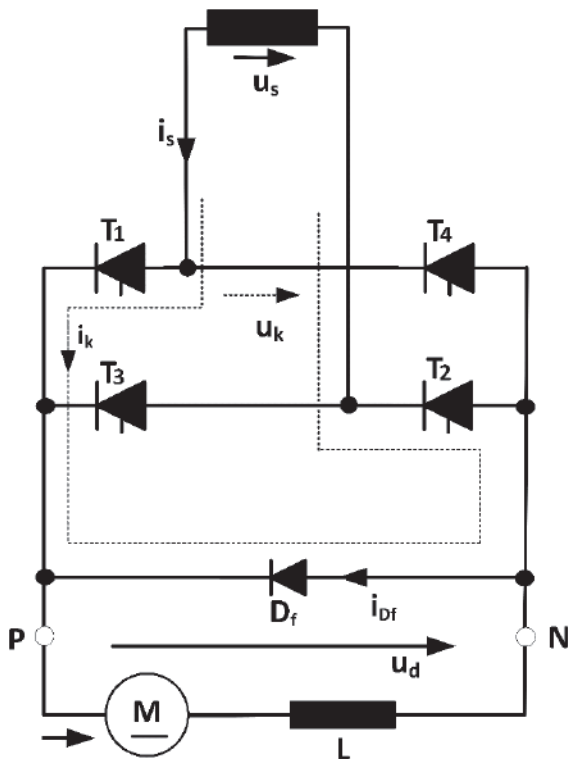


Fig. 2.33 Single-phase rectifier with null diode bridge.

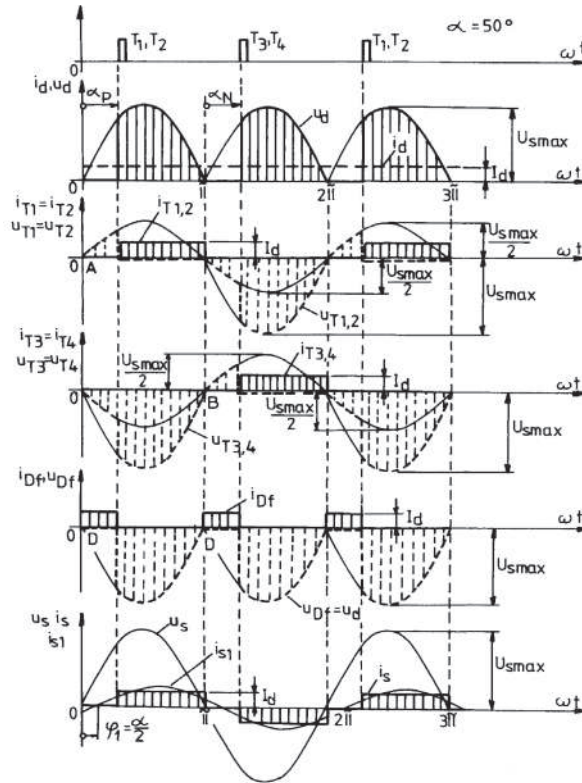


Fig. 2.34 Currents and voltages for a single-phase controlled bridge with null diode.

The requests are the same, but on the diode conduction period, the thyristors are polarized inversely at the voltage  $u_s/2$ . For the remaining half-period  $\pi - \alpha$ , the voltage  $u_s$  is applied to the blocked thyristor.

**The single-phase rectifier with null and fast diode**, Fig. 2.35, contains only few valves and has variations in currents and voltages similar to the previous scheme.

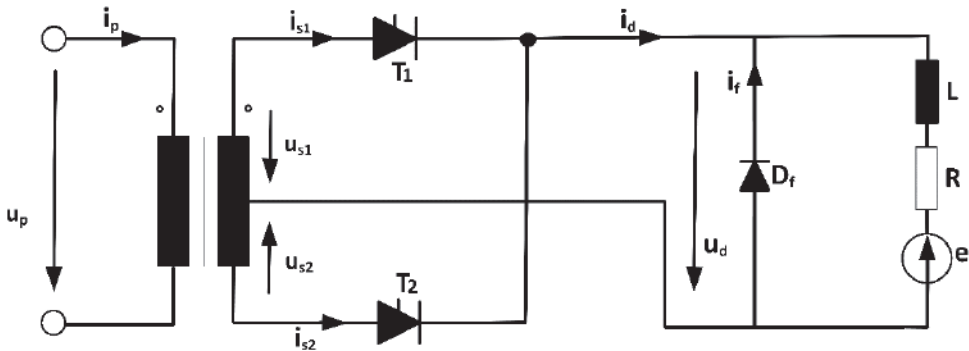


Fig. 2.35 Single-phase rectifier with null and fast diode.



The waveforms of currents and voltages are shown in Fig. 2.36.

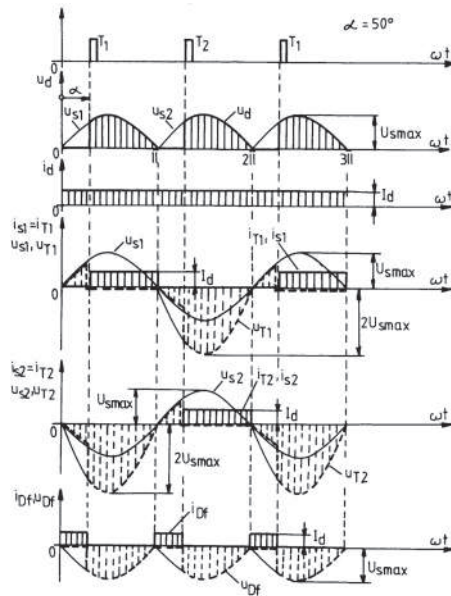


Fig. 2.36 Variation of currents and voltages for the single-phase rectifier with null and fast diode, for  $\alpha = 45^\circ$ .

**The three-phase rectifier with null and fast diode**, Fig. 2.37, is characterized by the fact that the diode enters in conduction only if  $u_d < 0$ , which also means that for control angles  $\alpha > \pi/6$ . For angles  $\alpha < \pi/6$ , the fast diode has no role, the waveforms of currents and voltages being similar to the three-phase converter with null diode. For  $\alpha > \pi/6$ , the variation of currents and voltages is shown in Fig. 2.38.

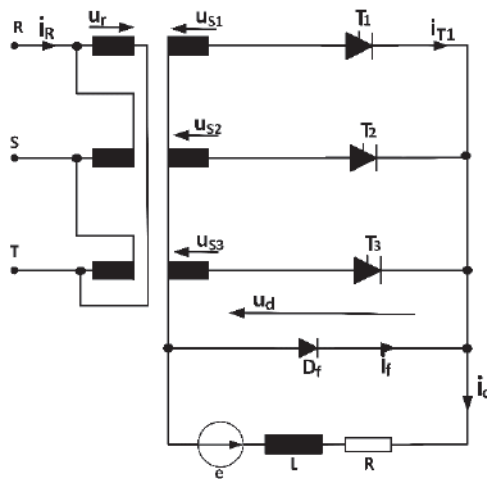


Fig. 2.37 Three-phase rectifier with null and fast diode.

Theoretically, the maximum control angle is  $\alpha_{\max} = 5\pi/6$ , because the range in which  $u_d > 0$  is between the natural priming moment ( $\alpha = 0$ ) and the moment when  $u_s$  is cancelled.

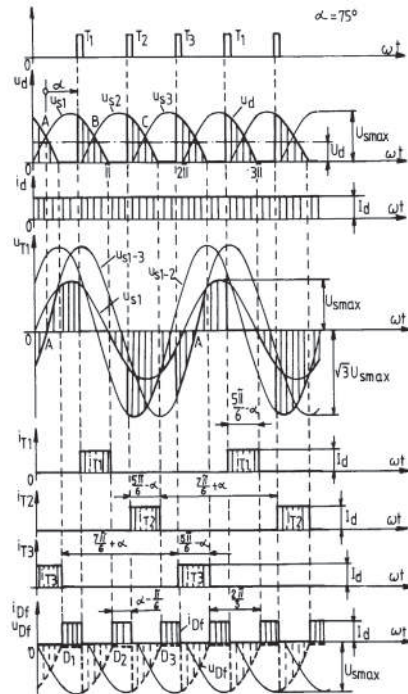


Fig. 2.38 Variation of currents and voltages for the three-phase rectifier with null diode for  $\alpha = 75^\circ$ .

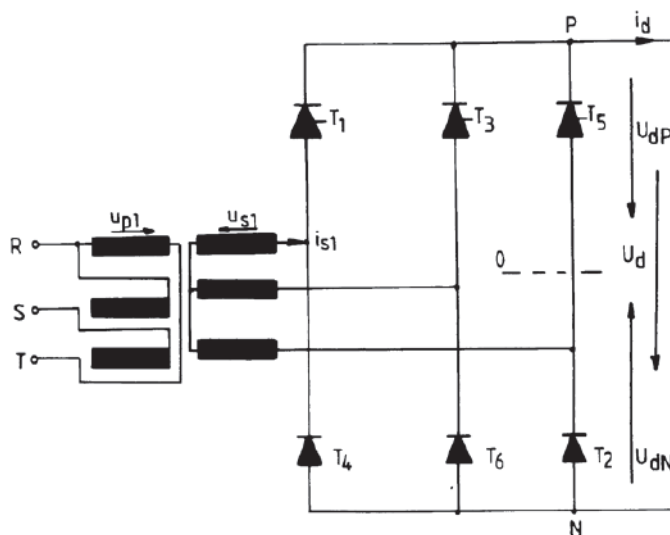


Fig. 2.39 Three-phase bridge rectifier with null diode.



### 2.4.1.3 Four quadrants converters

Reversible electric drives [5] use four-quadrant converters, obtained by coupling two two-quadrant converters, one for each current direction. The four-quadrant converters allow the operation of the DC machine in any mode and quadrant, without any other auxiliary elements.

The two two-quadrant converters A and B, Fig. 2.41, are controlled with the angles  $\alpha_A$  and  $\alpha_B$ , the diodes in the Fig. showing the direction of the current. The current through the drive is:

$$I_m = I_{dA} - I_{dB} \quad (2.57)$$

Where  $I_{dA}$  and  $I_{dB}$  are the average current values for the converters A and B. The sense of the current through the machine is determined by the result of this relationship. The converters being mounted in antiparallel, it means that the voltage at the machine terminals is:

$$U_M = U_{dA} = -U_{dB} \quad (2.58)$$

where the rectified average voltages  $U_{dA} = -U_{dB}$  are:

$$\begin{aligned} U_{dA} &= U_{d0} \cdot \cos \alpha_A \\ U_{dB} &= U_{d0} \cdot \cos \alpha_B \\ \alpha_A + \alpha_B &> 180^\circ \end{aligned} \quad (2.59)$$

From the relationships (2.58) and (2.59), it results that, between the control angles of the two converters A and B, there must be the relationship:

$$\alpha_A = \alpha_B = 180^\circ \quad (2.60)$$

By neglecting the machine and converters' losses, each operating quadrant of the converter corresponds to a machine operating quadrant, in voltage and current coordinates.

The four-quadrant converters, according to the operating mode of each component converter, are classified in:

- without circulating currents, in which case the characteristics of a quadrant are obtained by the operation of a single converter, the other converter being blocked;
- with circulating currents means the simultaneous operation of both converters regardless of the quadrant.

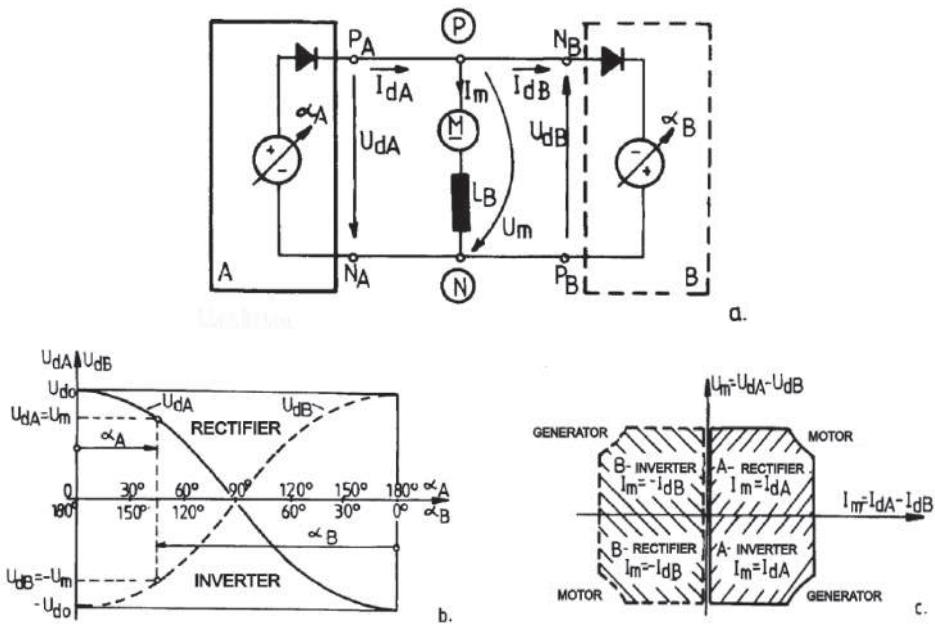


Fig.2.41 Four quadrants converters: a) scheme of principle; b) command characteristics; c) operating modes of the fed machine.

a. Four-quadrant converters without circulating currents

The most commonly used scheme is presented in Fig. 2.42, where two bridges are connected in antiparallel, one being in conduction and the other blocked. The locking of one of the converters can be done in two ways:

- suppressing the command pulses;
- modifying the phase of the command pulses in such a way as to avoid the occurrence of the circulating currents.

For the second way, the next condition must be met:

$$\alpha_A + \alpha_B > 180^\circ \tag{2.61}$$

which involves the occurrence of an instantaneous rectified voltage opposing to the current flow between the two converters. The converters without circulating currents are preferred at high power, due to the low number of circuit elements. It is necessary, at the command of these converters, to notice the load zero-crossing currents in order to decide which one of the two converters will enter into conduction and which one will be blocked, respectively. There are two possibilities for doing this. The first one is to track the current from the DC side and, after the zero-crossing, the two component converters to exchange places. It is necessary for a dead time to lock the valves of the converter that was in the conduction and then to prime the other one. Another variant follows the variation of the

current on the alternating current side and, at the zero-crossing of one phase, triggers the procedure of blocking the conduction of the converter and then the priming of the other one. The dead time is approx. 10 ms in both situations.

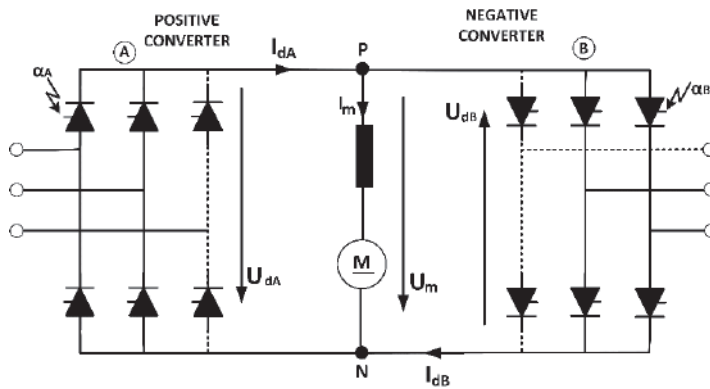


Fig.2.42 Four-quadrant converter without circulating currents; --- mono-phase; three-phase ---.

The four-quadrant non-current converter has another advantage. Because one of the component converters is always locked, their power supply can be done from the same secondary transformer.

For the four quadrant of the  $U_m, I_m$  coordinate system, the operation takes place as shown in Fig. 2.43.

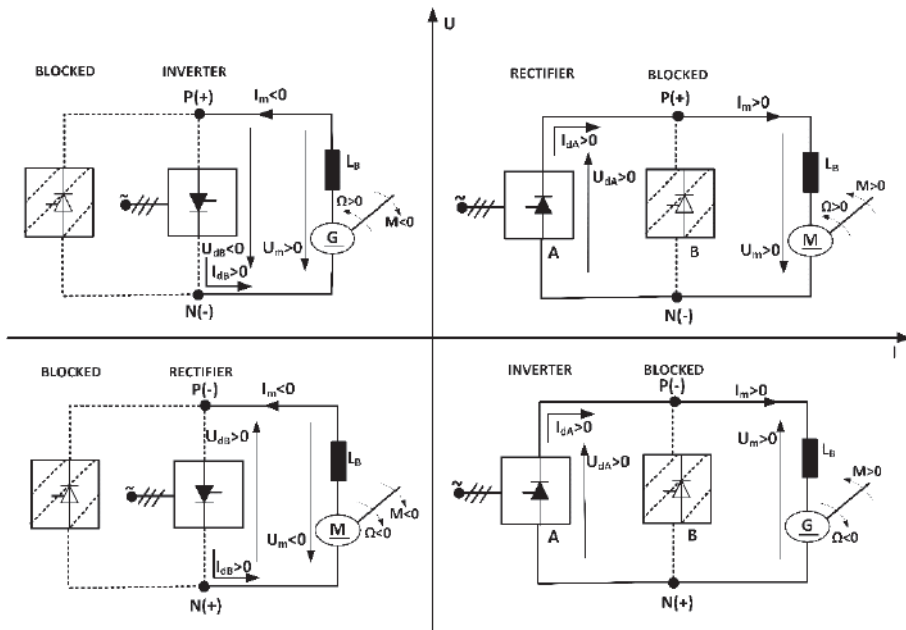


Fig. 2.43 Operating modes of a DC machine fed by a four-quadrant converter.

In quadrant I, the converter B is blocked. The converter A will work as a rectifier with:

$$\begin{aligned} I_{dA} &= I_m > 0 \\ U_{dA} &= U_m > 0 \end{aligned} \quad (2.62)$$

For the machine, this implies:

$$\Omega > 0 \quad M > 0 \quad (2.63)$$

i.e., the machine works as a motor.

In quadrant II, the converter A is blocked and the converter B acts as an inverter:

$$\begin{aligned} I_{dB} &= -I_m > 0 \\ U_{dB} &= -U_m < 0 \end{aligned}$$

and:

$$\Omega > 0 \quad M < 0 \quad (2.64)$$

which means that the machine works as a power generator, pushing energy to the network.

In quadrant III, the converter B works as a rectifier, the converter A is locked and the machine works as a reverse motor:

$$\begin{aligned} I_{dB} &= -I_m > 0 \\ U_{dB} &= -U_m > 0 \end{aligned} \quad (2.65)$$

and

$$\Omega < 0 \quad M < 0$$

In quadrant IV, the converter A acts as an inverter, the converter B is locked and the machine acts as a generator:

$$\begin{aligned} I_{dA} &= I_m > 0 \\ U_{dA} &= U_m < 0 \end{aligned} \quad (2.66)$$

and:

$$\Omega < 0 \quad M > 0$$

the energy transfer being from the machine to the network.

The proper operation of the four-quadrant converter poses problems with low loads, where a discontinuous conduction may appear with a current break [5], [6].

b. Four quadrant converters with circulating currents

The drawback of the discontinuous conduction, occurring in the converters without circulating currents can be eliminated if both two-quadrant converters are simultaneously commanded in such a way as to provide a current flow between them. This current keeps the converters in permanent conduction over the entire operating range. The linear system operating the control system is much simplified.

The command of the two converters A and B, Fig. 2.41.a, is done in such a way that, between P and N, for each converter, the same average voltage is achieved. As the two converters are connected with different polarities, it means that each time a converter works as a rectifier and the other as an inverter. In this case, the relationship (2.60) is rigorously respected. Although the equality between the average voltages is noticed, the instantaneous values of the voltages are not equal,  $u_{dA} \neq u_{dB}$ . The difference between these instantaneous voltages determines the circulating currents between the two converters and must be limited by the inductors placed between the two converters. The voltage difference has a sinusoidal variation and forces a circulating current  $i_C$  with a pulsating variation:

$$u_C = u_{dA} - (-u_{dB}) = u_{dA} + u_{dB} \quad (2.67)$$

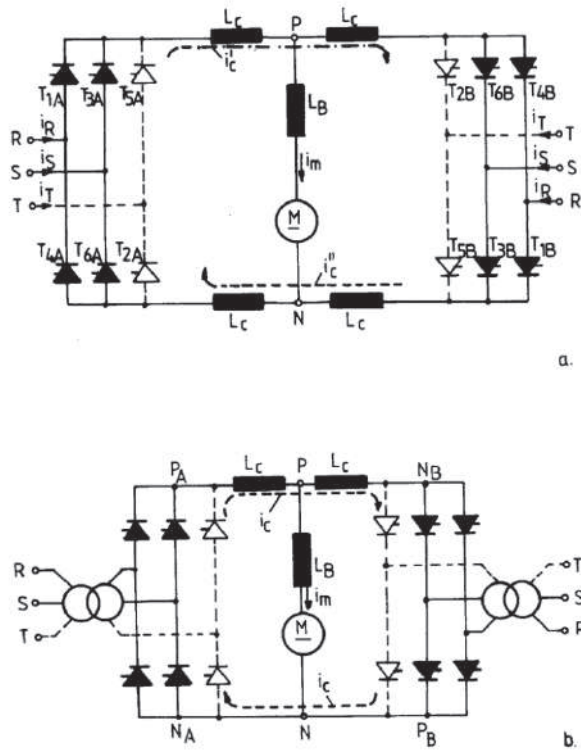


Fig. 2.44 Four-quadrant converters with circulating currents: a) – antiparallel assembly; b) – cross assembly.



The assemblies used for the four quadrant and circulating currents converters are shown in Fig. 2.44.

The antiparallel assembly has converters connected to the same alternating voltage source, in which case two circulating currents  $i'_c$  and  $i''_c$  are established and four  $L_c$  coils are required, Fig. 2.44.a.

The built-in cross assembly has converters connected to two separate sources, or to the same transformer with two galvanically separated secondary windings. In this case, there is only one circulating current  $i_c$ , which requires only two  $L_c$  coils for being limited, mounted on the same side of the circuit, as shown in Fig. 2.44.b.

## 2.4.2 Forced commutation DC converters

These converters, known in the literature also as DC voltage variators, [7], transfer the electricity directly between a DC source and a DC consumer, or vice versa. The conversion takes place directly without an intermediate AC circuit.

### 2.4.2.1 Common schemes of DC voltage variators

#### 2.4.2.1.1 Functioning principle, classification

The simplest DC voltage variation scheme is shown in Fig. 2.45 and it consists of a static switching element Q that connects and disconnects the load to the voltage source, periodically, generating the voltage pulses. The switching element can be any electronic device: an bipolar transistor, an MOSFET or IGBT, a GTO thyristor or an ordinary thyristor. Its major applications are in the electrical traction field for controlling motors on electric vehicles and precise adjustment of parameters (currents, voltages) to consumers fed into the DC. If the DC voltage converter is made with thyristors, they must be equipped with extinguishing circuits.

It is noted that the diode D allows the load current to close when the switching element Q is blocked. The absence of this diode, also called a diode, causes dangerous overvoltage's due to the stored magnetic energy occurring when the inductive load is disconnected abruptly.

The control frequency and the duration of the load connection at the source are variable depending on the operating mode. Usually, the operation is periodic with the frequency  $f = 1 / T$ , see Fig. 2.45.b. During the time  $t_1$ , Q is also closed and the load is fed with the voltage U, and on  $t_2$ , Q is open and the voltage on the load is null (actually, it is equal to the voltage drop on the diode D, while being in conduction).

Average load voltage can be calculated with:

$$u_{med} = \frac{1}{T} \int_0^{t_1} U dt = \frac{t_1}{T} \cdot U = a \cdot U \quad (2.68)$$

in which we have noted the non-dimensional ratio  $t_1/T$ , which is also called the **relative duration of conduction**.

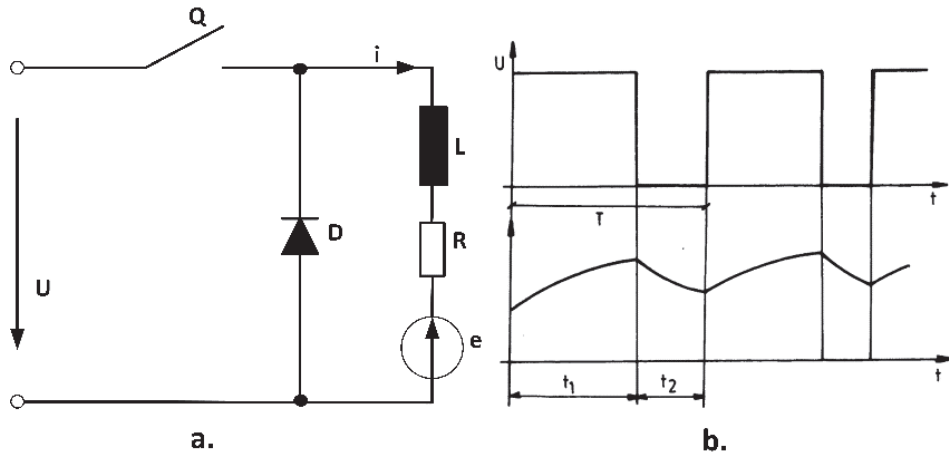


Fig. 2.45 DC voltage variator: a) principle diagram; b) variation of voltage and current across the load.

The classification of DC converters with forced commutation can be done after the ratio between the output voltage and the supply voltage.

In the case of a circuit as the one depicted in Fig. 2.45, the average output voltage is less than or equal to the supply voltage, the relation (2.68). Such a converter in series with the load is known as **the step-down (or buck) converter**.

A converter in parallel with the load provides an output voltage greater than or equal to the input voltage. In the literature, it is known as **the step-up (or boost) converter**.

Based on the two basic types, combinations of converters such as the buck-boost and Cuk converters can be made and will be presented in the following paragraphs.

It should also be noted that DC voltage variables can work, just like the above-mentioned converters, in a single quadrant, or two or four quadrants. In addition, as it will be shown, multiple pulse schemes can also be designed to reduce the content of higher harmonics.

#### 2.4.2.1.2 The series DC voltage variator

The schematic diagram for this converter is shown in Fig. 2.45. Based on the relationship (2.68), the average voltage over the load changes linearly with the relative conduction period.

Thyristor DC voltage variators are characterized by the appearance of an extinguishing circuit that locks the static switch. There is a wide variety of schemes that currently have a more limited use due to the use of power transistors.

The voltage switch with the extinguishing circuit in parallel to the main thyristor is shown in Fig. 2.46. The thyristor  $T_1$  is blocked by the extinguishing circuit composed of  $C$ ,  $T_2$ ,  $L$  and  $D_1$ .

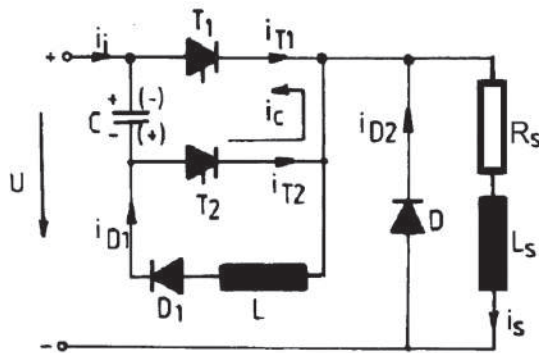


Fig. 2.46 DC voltage variator with parallel extinguishing circuit.

The waveforms of the variator with parallel extinguishing circuit are shown in Fig. 2.47.

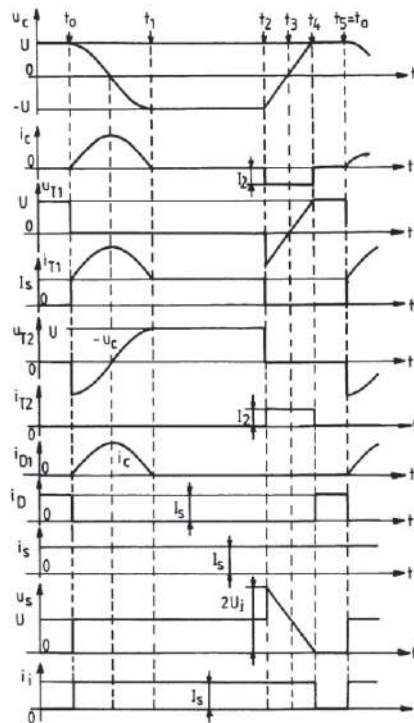


Fig. 2.47 Waveforms for the variator with parallel extinguishing circuit.

The operation of the practical schemes is slightly different, in the sense that, in the electric traction, particularly, the circuit presents an inductance of the supply line, between

the voltage source and the variator, as shown in Fig. 2.48 a. The operation of the variator is affected as it accumulates energy when the capacitor discharges through the path consisting of  $D$ ,  $L$ ,  $D_1$ ,  $C$  and the source. If the line inductance  $L_1$  is to be considered, the diode  $D_1$  is replaced by the thyristor  $T_3$  that will be commanded simultaneously with  $T_1$ .

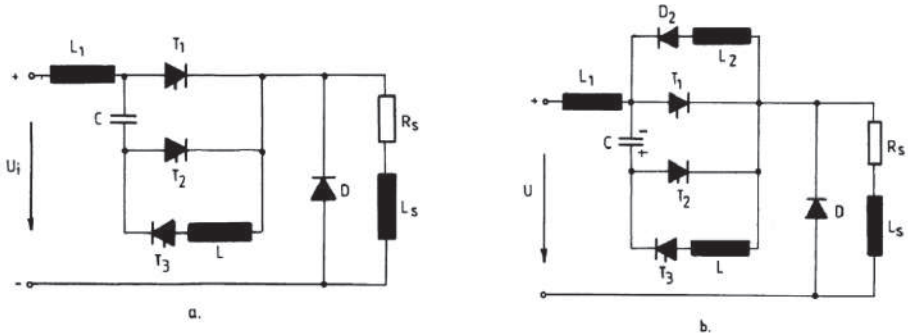


Fig. 2.48 Variants of the scheme in fig. 2.46: a) scheme with three thyristors for annihilating the influence of the source inductance; b) circuit with auxiliary capacitor for the circuit recharging.

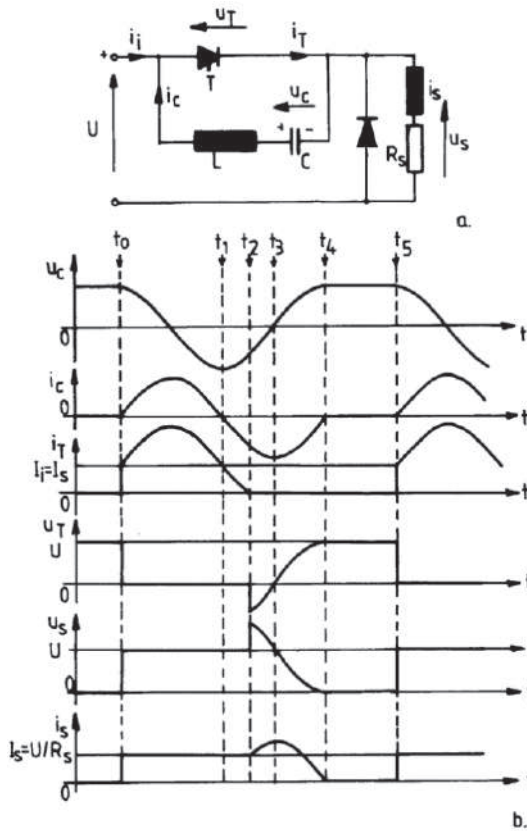


Fig. 2.49 Variator with a thyristor: a) scheme; b) waveforms.

The period for the capacitor recharging depends on the load current. Under low load conditions, this process expands unacceptably, making the scheme operation difficult. In order to recharge the capacitor independently of the load circuit, the diagram in Fig. 2.48.b is used, to which the  $D_2, L_2$  assembly is added. If we consider the capacitor  $C$  charged with the shown polarity, at the priming of  $T_2$ ,  $C$  is discharged over the load, but also over the oscillating circuit  $L_2, D_2, C$ , the last one being a priority.

A particular case is the single-thyristor variator having the scheme shown in Fig. 2.49 a. In parallel to the thyristor, there is only one oscillating circuit LC. The charging of the capacitor  $C$  at the value  $U$  is done through a damped oscillation, through  $L, C$  and the load with the polarity shown in the below Fig. 2.49. Then, the scheme will be ready for operation.

In Fig. 2.50, other variants for parallel extinguishing circuits are presented. The scheme in Fig. 2.50.a uses as an extinguishing circuit the scheme in Fig. 2.49. In fact, the blocking of the thyristor  $T_1$  is done in two steps: first, by priming  $T_2$ ,  $C$  is discharged through  $T_2$  and then, this is blocked when the current crosses zero. The oscillating process continues with the second step closing the current of the oscillating circuit through  $L, C, D_1, T_1$ , and thus blocking  $T_1$ . The repolarization current of  $C$  is then closed through the load. A capacitor discharge over the source is prevented by the  $D_1$  diode, which allows the current to flow in only one direction.

The scheme in Fig. 2.50.b uses, for the capacitor repolarization, a bridge of thyristors, which are commanded sequentially two by two:  $T_2$  and  $T_5$ , and  $T_3$  and  $T_4$ , respectively.

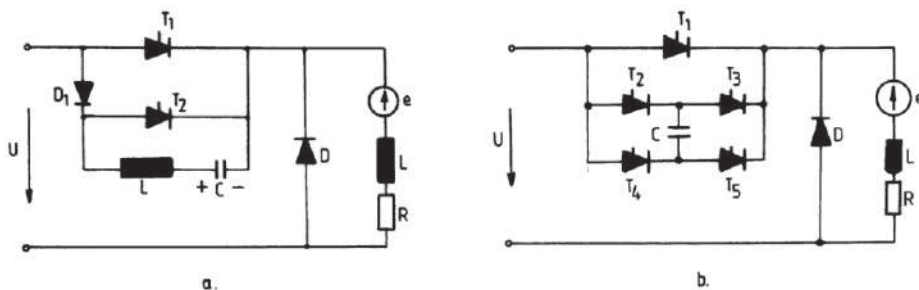


Fig. 2.50 Variants of parallel extinguishing circuits: a) with a thyristor and an oscillating circuit; b) with bridge capacitor.

Other schemes use the extinguishing circuit in parallel to the source or to the load. Fig. 2.51.a shows a circuit diagram of the extinguishing circuit in parallel to the source, which is also known as an extinguishing circuit on the cathode. The principle of the extinguishing of the main thyristor  $T_1$  is based on increasing the potential of the cathode that becomes "more positive" relative to the anode. By connecting the scheme to the voltage source, the capacitor  $C$  is oscillating charged by  $L$  and  $D_2$ . The LC circuit must be dimensioned in such a way that the capacitor  $C$  is charged at a voltage  $u_c > U$  (e.g.  $u_c = 1.5 U$ ), in which case the  $D_2$  diode is blocked and the circuit is ready for operation.

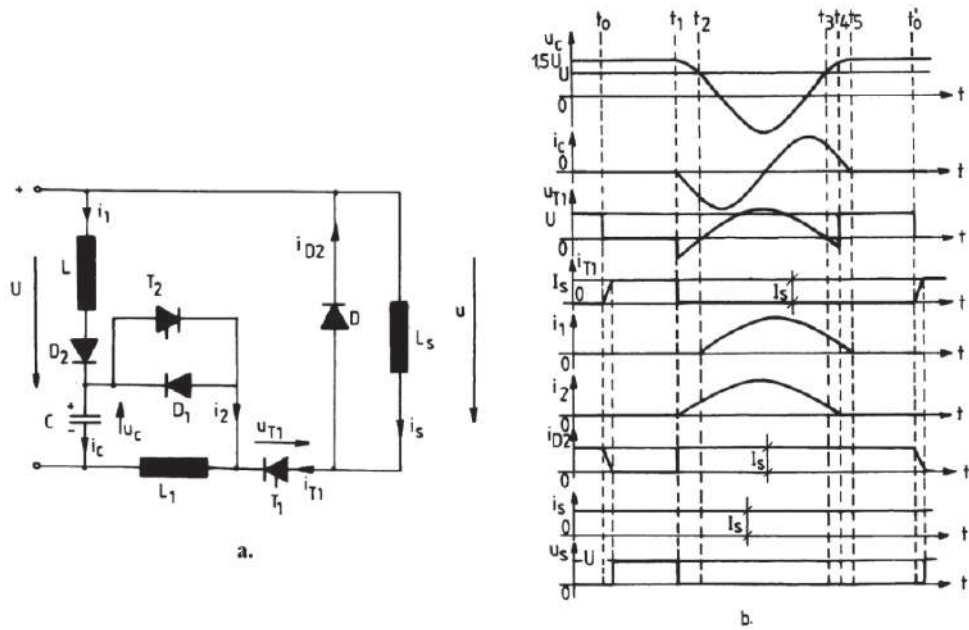


Fig. 2.51 Variator with extinguishing circuit on the cathode (parallel extinguishing circuit): a) schematic diagram; b) waveforms.

The extinguishing circuit can be placed in parallel to the load as in Fig. 2.52. Here, too, for the capacitor there is an oscillating charging at a voltage higher than the supply voltage thus blocking the thyristor  $T_1$  at the priming of  $T_2$ .

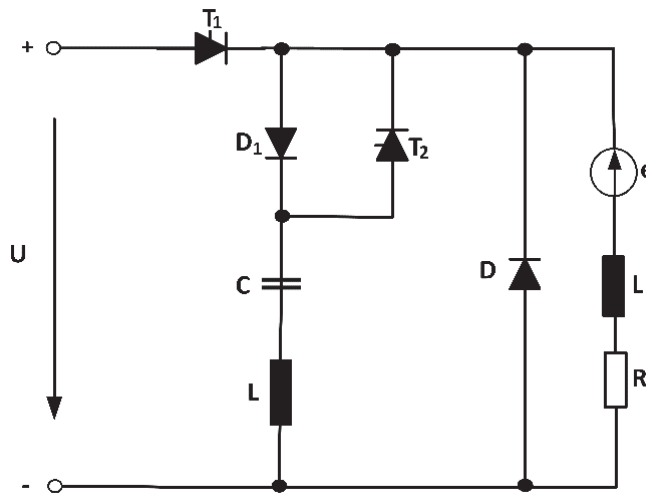


Fig.2.52 Variator with extinguishing circuit in parallel to the load.

### 2.4.2.1.3 The parallel DC voltage variator

The principle diagram for the parallel DC voltage variator is shown in Fig. 2.53.a. The load voltage should be always higher than the supply voltage, otherwise the diode  $D$  would be open (the capacitance  $C$  is large enough to keep the load voltage constant). When  $T$  is open, the diode is locked and the load is isolated from the source and  $C$  is discharged over  $R_s$ . In this situation, the source supplies energy to the inductance  $L$ . During the blocking period of  $T$ , the load receives energy from both the inductance and the source. The inductance  $L$  gives to the supply power source a character of current generator, while the load has a resistive character. In addition, the variation of the current through  $L$  causes a voltage at its terminals to make terminal  $A_1$  more positive than  $A_2$  (Fig. 2.53.a). Consequently, the voltage at the load terminals will be higher than  $U$  and the capacitor  $C$  will be charged to this value. The energy accumulated in the inductance in the  $t_1$  period, which represents the conduction interval of  $T_1$ , is transferred to the load in the  $T-t_1$  period. In steady-state, the load voltage stabilizes at  $U_s$  value. The capacitance  $C$  value determines the voltage pulsation  $\Delta U_s$ .

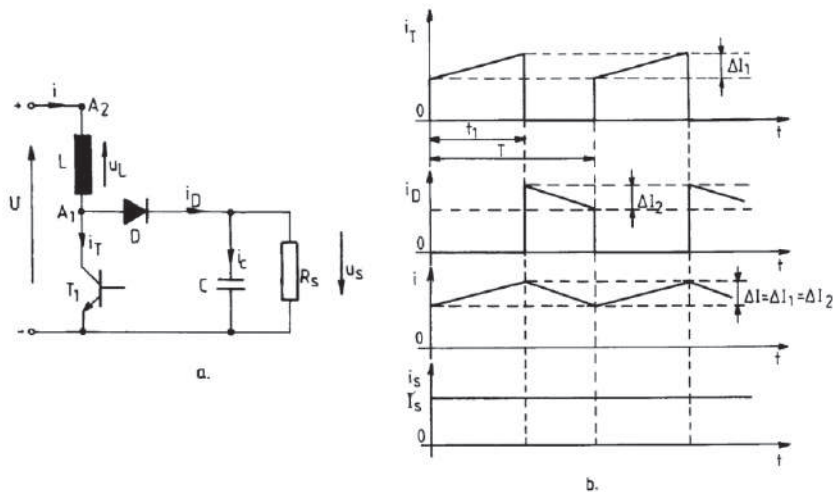


Fig. 2.53 Parallel voltage variator: a) principle diagram; b) current variation.

If  $\Delta U_s \ll U_s$  is considered, the variations of the currents waveforms are shown in Fig.2.53.b. During a continuous conduction, the voltage value  $U_s$  is determined by putting an equality condition between the current variations (of increasing or decreasing) throughout the inductance  $L$ . Finally, the expression [4] is obtained:

$$U_s = \frac{U}{1-a} \quad (2.68)$$

where  $a$  is the relative conduction duration,  $a = t_1 / T$ .

If the elements in the scheme are assumed without losses, the input and output powers are equal, resulting in:

$$\frac{U}{U_s} = \frac{I_D}{I} = 1 - a \quad (2.69)$$

At the limit of the continuous conduction, the current  $I$  has the allure in Fig. 2.54.a.

The maximum current is:

$$I_{\max} = \frac{U \cdot t_1}{L} \quad (2.70)$$

and the average current value at the conduction limit continues:

$$I_1 = \frac{U \cdot t_1}{2 \cdot L} = \frac{(1-a) \cdot U_s \cdot t_1}{2 \cdot L} = \frac{U_s}{2 \cdot L} \cdot (1-a) \cdot a \cdot T \quad (2.71)$$

The maximum average current value at the conduction limit is:

$$I_{1\max} = \frac{U_s \cdot T}{8 \cdot L} \quad (2.72)$$

and is obtained for  $a = 0.5$ . The average value of the current  $I_D$  at the conduction limit is obtained from (2.69) and (2.71):

$$I_{D1} = (1-a) \cdot I_1 = \frac{U_s}{2 \cdot L} = (1-a)^2 \cdot a \cdot T \quad (2.73)$$

The discontinuous conduction mode appears for load current  $I_0$  values higher than  $I_{D1}$ . The maximum current  $I_{Dc}$  at the continuous conduction limit is obtained for  $a = 1/3$  and has the value:

$$I_{D1\max} = \frac{2 \cdot U_s \cdot T}{27 \cdot L} \quad (2.74)$$

The currents variation  $I$  and  $I_D$ , or different average conduction times, is shown in Fig. 2.54.b.

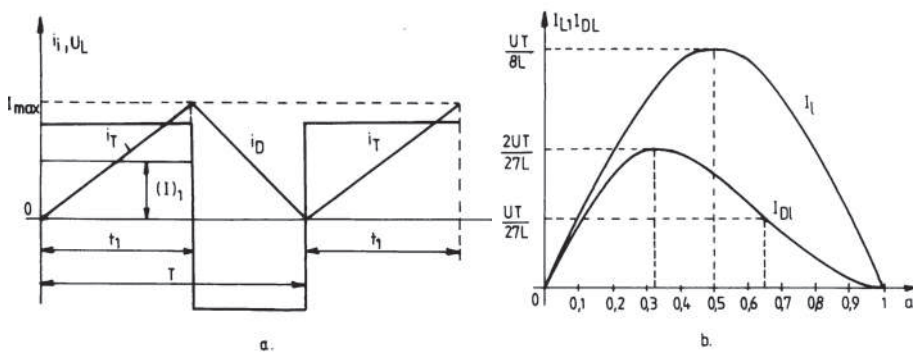


Fig. 2.54 Explanatory for the currents at the limit of continuous conduction: a) current variation; b) average values for  $I$  and  $I_D$  depending on the current variation from point a).



A proper operation is the one of continuous conduction (no current break). The load voltage pulse decreases with the increase of the control frequency and the time constant  $\tau$ , thus increasing the capacitor value  $C$ .

### 2.4.2.1.4 The Buck-Boost Converter

This converter can operate either by lifting or lowering the voltage and its main application refers to the switching power sources. Here, the output voltage may be higher or lower than the input voltage. In addition, it is also possible to output a negative polarity relative to the input reference terminal. The principle scheme, which consists of the connection between the two converters, buck and boost, is shown in Fig. 2.55.a. The operating mode depends on the conduction period provided by  $T_1$  and  $T_2$ . The buck converter ( $T_1, D_1$ ) is connected in series with a boost converter ( $T_2, D_2$ ).  $T_1$  and  $T_2$  are commanded simultaneously. In the period  $t_1$ , when  $T_1$  and  $T_2$  are closed,  $i = i_{L1}$  and the inductance  $L$  accumulates magnetic energy. By opening the switches  $T_1$  and  $T_2$ , the diodes  $D_1$  and  $D_2$  enter into conduction mode and this magnetic energy is transferred to the load by discharging the inductance  $L$ ,  $i_{L2} = i_s$ . The current variation through inductance  $L$  is shown in Fig. 2.55.b.

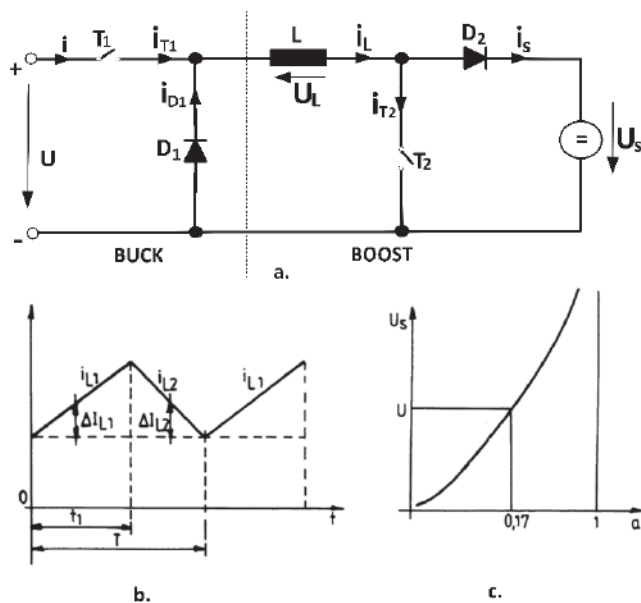


Fig. 2.55 Buck-Boost Converter: a) principle diagram; b) inductance current  $L$ ; c) voltage variation according to point a).

The load voltage over the duration of conduction has the expression:

$$U_s = \frac{a}{1-a} \cdot U \quad (2.75)$$

The relationship (2.75) shows that for:

- $a \in (0, 0.5)$   $U_s \in (0, U)$  - the converter reduces the voltage;
- $-a \in (0.5, 1)$   $U_s > U$  - the converter raises the voltage, Fig. 2.55.c.

By reducing the switching elements with one and the number of diodes as well thus rearranging the elements as in Fig. 2.56, the practical schemes become simpler. The operation is identical to that of the converter in Fig. 2.55, but the load voltage and the source voltage have opposite signs. In the deduction of the following relationships, this reversal of the output voltage is not taken into account because it does not cause any substantial changes. In the continuous conduction mode, when all the circuit elements are ideal, the input and output powers are equal.

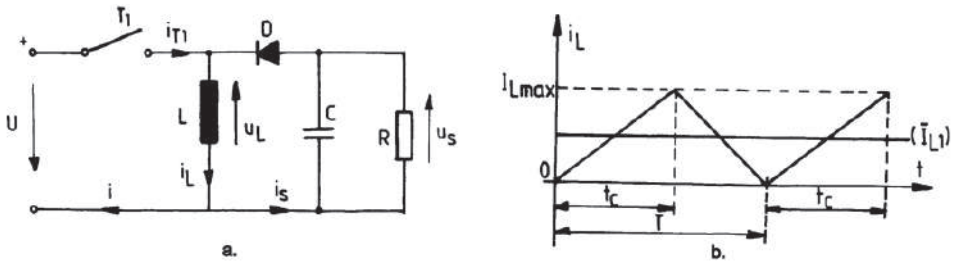


Fig.2.56 Practical Buck-Boost Converter: a) principle diagram; b) inductance current  $i_L$ .

At the limit of continuous driving, the current  $i_L$  through the inductance  $L$  has the allure depicted in Fig. 2.56.b.

Maximum and average currents at the driving limit:

$$I_{Smed} = (1-a)^2 \cdot \frac{U_s \cdot T}{2 \cdot L} \quad (2.76)$$

$$I_{Smax} = \frac{U_s \cdot T}{2 \cdot L}$$

#### 2.4.2.1.5 The Cuk converter

For this converter, named after its inventor, the capacitor  $C$  plays both the role of energy storage and of transfer between input and output, just as for the Buck-Boost converter the inductance plays the same. These converters can transfer energy between two sources of the same type: the Buck-Boost converter between two voltage sources and the Cuk converter between a current generator and a current receiver. The scheme is shown in Fig. 2.57.a. The  $L$  and  $L_s$  inductors give to the source and to the load the character of a generator and of a receiver, respectively. This should be understood as, for one period comparable to the control period  $T$ , the source currents and load currents do not change, but they are constant. The capacitor  $C$  is considered to be charged with the polarity shown in the

Fig.2.57.a. If T is closed for a time  $t_1$ , the capacitor is discharged across  $L_s, R_s$  while diode D is blocked. The waveforms are shown in Fig. 2.57.b.

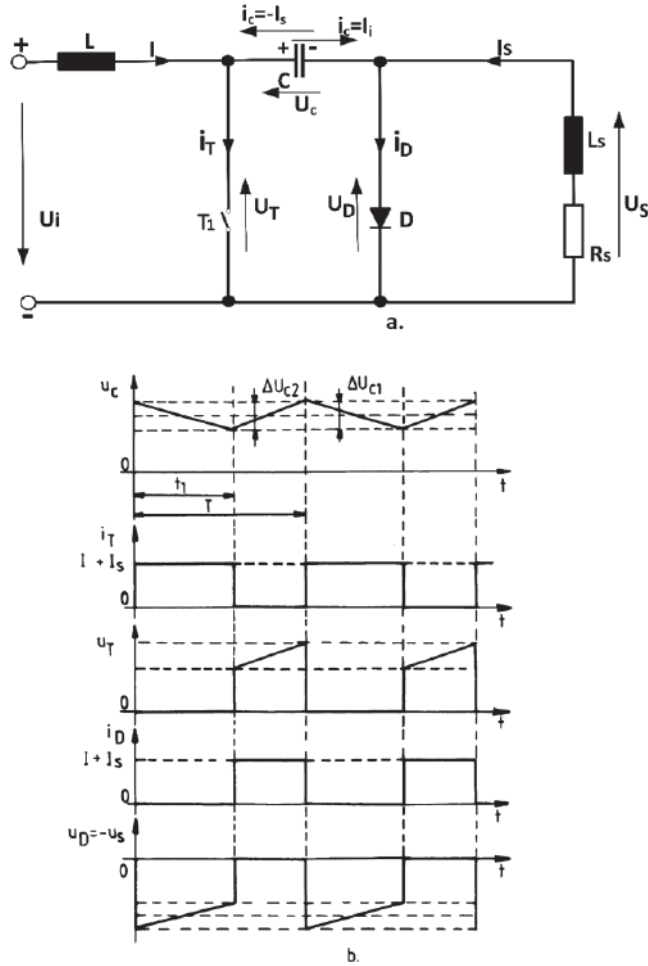


Fig. 2.57 The Cuk converter: a) principle diagram; b) waveforms.

The capacitor voltage variations across the two periods are equal,  $\Delta u_{c1} = \Delta u_{c2}$ , which implies:

$$\frac{I}{I_s} = \frac{a}{1-a} \quad (2.77)$$

If the elements of the scheme are assumed not to have losses, then the average input and output powers are equal and, consequently, the relation (2.77) can be extended to the average voltages:

$$\frac{U_s}{U} = \frac{I}{I_s} = \frac{a}{1-a} \quad (2.78)$$

### 2.4.2.2 Reversible DC voltage variators

The schemes presented in the previous paragraph are characterized by a unilateral power flow, from source to load, corresponding to the operation in one quadrant. However, there are situations that require operation in two or even four quadrants. This kind of converters will be examined next.

#### 2.4.2.2.1 Two quadrant DC voltage variators

These variators perform the reversing of either the voltage or the current. The reversible voltage variators provide a voltage  $\pm U_s$  and a load current  $I_s$  of the same sense, by operating in quadrants I and IV, Fig. 2.58. The reversible current variators provide the same  $U_s$  voltage, while the load current can be  $\pm I_s$ , operating in quadrants I and II, Fig. 2.60.

Fig. 2.58 shows two different topologies of voltage variators, but operating the same.

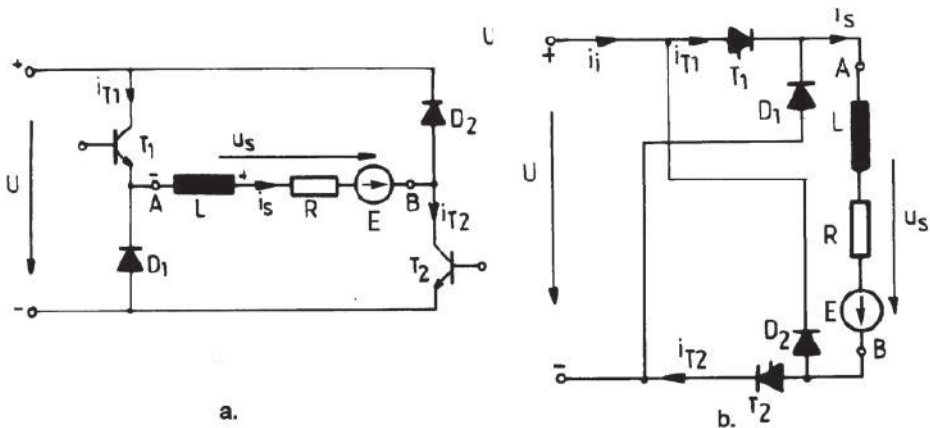


Fig. 2.58 Reversible voltage variators: a) with transistors; b) with GTO thyristors.

$T_1$  and  $T_2$  are simultaneously commanded both in conduction and blocking modes. During the conduction of  $T_1$  and  $T_2$ , the  $U$  voltage is applied to the load. When  $T_1$  and  $T_2$  are blocked,  $D_1$  and  $D_2$  are in conduction and the voltage  $-U$  is applied to the load. The sense of the current remains unchanged. The waveforms are shown in Fig. 2.59.

The average voltage across the load is:

$$U_s = \frac{t_1}{T} \cdot U - \frac{(T-t_1)}{T} \cdot U = (2a-1) \cdot U \quad (2.79)$$

It is noted that for  $a > 0.5$   $U_s > 0$ , which means that the variator is operating in quadrant I, Fig. 6.20.a, and for  $a < 0.5$   $U_s < 0$ , corresponding to the operation in quadrant IV, Fig. 2.59.b.

The reversible current variator has the principle diagram shown in Fig. 2.60. Switches  $T_1$  and  $T_2$  may be transistors or thyristors. The scheme consists of two variants, one in series ( $T_1, D_2$ ) and the other one in parallel ( $T_2, D_1$ ).

For positive load currents  $I_s > 0$ , the variator generates a voltage  $U_s = a \cdot U$ .

Considering the circuit elements to be ideal ones, the input and output powers are equal and consequently:

$$\frac{U_s}{U} = \frac{I}{I_s} = a \quad (2.80)$$

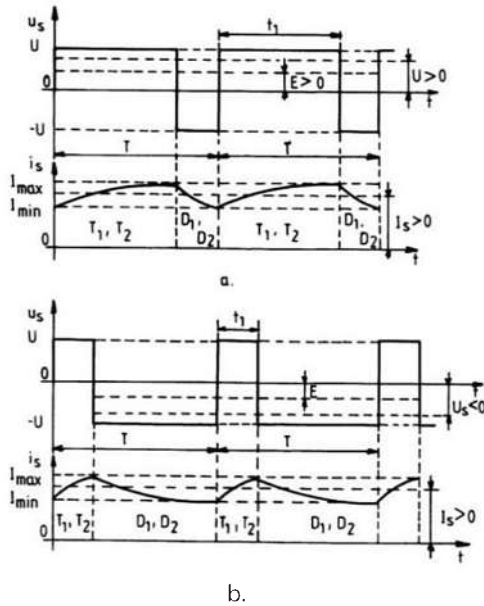


Fig.2.59 Waveforms in the case of a reversible voltage variator: a) operation in quadrant I; b) operation in quadrant IV.

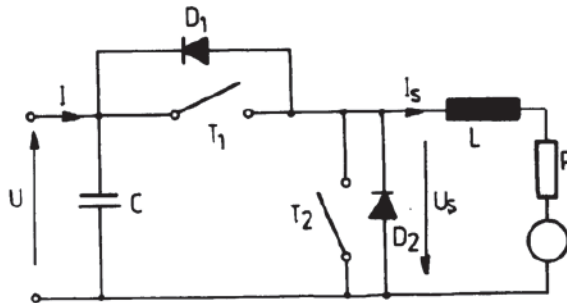


Fig. 2.60 Reversible current variator.

#### 2.4.2.2.2 Four quadrant DC voltage variators

Changes or additions to the two-quadrant schemes yield to four quadrant converter schemes, as shown in Fig. 2.61. In Fig. 2.61.a, the load is connected with one end at the median socket of the voltage source. Depending on the voltage at the load terminals, the current is absorbed from the upper or lower half of the voltage source.

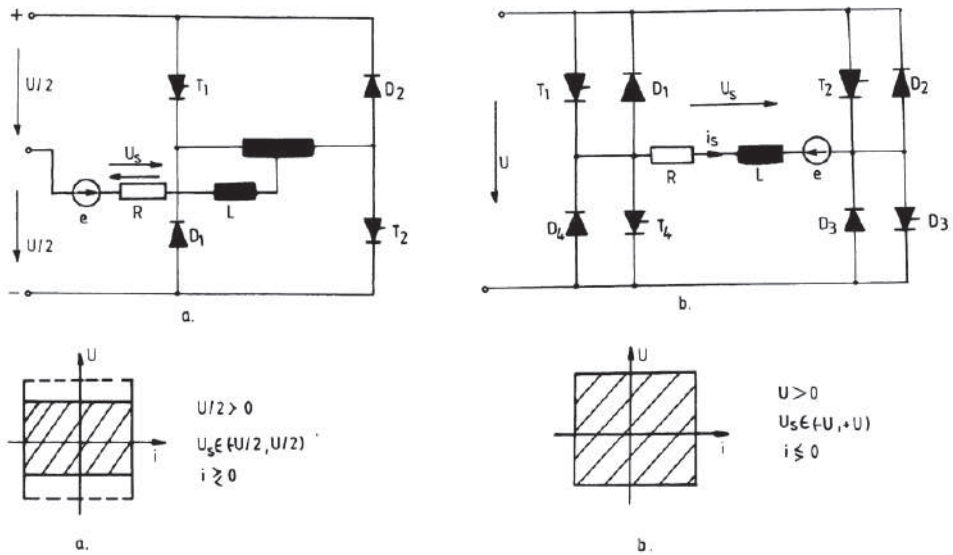


Fig. 2.61 Four-quadrant variators: a) the median scheme; b) the bridge scheme.

The bridge scheme, Fig. 2.61.b, no longer requires access to the source median socket and extends the control range across the entire supply voltage range. For this reason, the variant in Fig. 2.61.b is used more frequently and it will be presented next. The  $T_1, T_2, T_3$  and  $T_4$  valves can be either thyristors or transistors, controlled for both the priming and locking modes. However, due to the diodes connected in the antiparallel with the valves, a distinction has to be made between the valve command and the valve's ability to take over the load current.

If a valve is controlled, it can drive (or not) the load current according to its switching off direction, by means of its antiparallel diode. It is known that the valve is in conduction mode only if it "drives" the current. On the same vertical circuit branch, the two valves cannot be simultaneously in conduction in order not to short-circuit the source. There are two control strategies for the four-quadrant voltage variators from Fig. 2.61.b:

- **The bipolar voltage control**, in which  $T_1, T_4$  and  $T_2, T_3$ , respectively, are simultaneously controlled both in conduction and blocked modes (voltage modulation);
- **The unipolar voltage control**, in which the valves on each vertical branch are controlled independently of each other (double voltage modulation).

In the case of a bipolar voltage control, the current and voltage waveforms are shown in Fig. 2.62. The average voltage across the load is obtained with:

$$U_s = \frac{1}{T} \left( \int_0^{t_1} U dt - \int_{t_1}^T U dt \right) = U(2a - 1) \quad (2.81)$$

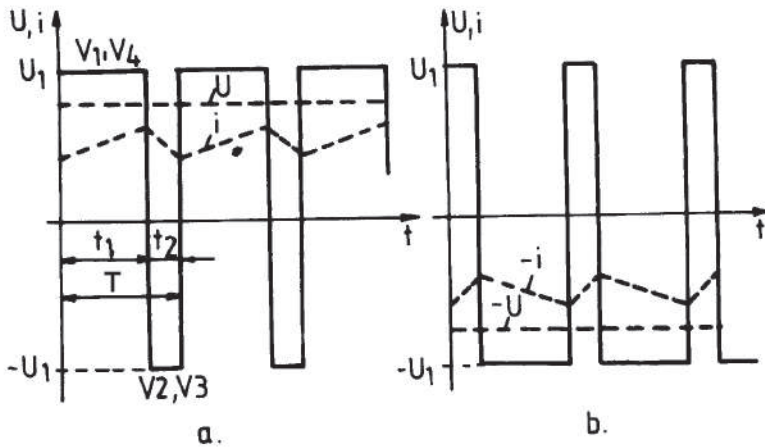


Fig. 2.62 Waveforms of the average voltages across the load in two cases: a)  $a=t_1/T > 0.5$ ; b)  $a < 0.5$ .

The bipolar command has two major inconveniences. The main one is the doubled number of commutations in one period, due to the simultaneous command of the two valves, which leads to increased losses. In addition, because the output voltage "jumps" from  $+U$  to  $-U$ , the ripple in the load current waveform is higher. For these reasons, a unipolar voltage control is used, Fig. 2.63, which reduces the number of commutations while one of the two valves in series is maintained in conduction.

For a first quadrant operation (I),  $T_3$  is maintained in conduction,  $T_1$  is pulse-controlled, and  $T_2$  and  $T_4$  are blocked. Operation in the second quadrant (II) is also performed by  $T_3$  being in conduction mode and  $T_4$  being pulse-controlled.  $T_1$  and  $T_2$  are blocked. In the third quadrant (III),  $T_4$  is maintained in conduction mode and the pulse control is performed by  $T_2$ .  $T_1$  and  $T_3$  are blocked. Finally, in the fourth quadrant (IV),  $T_4$  is in conduction mode,  $T_3$  is pulse-controlled, and  $T_1$  and  $T_2$  are blocked.

Choosing the inverter control frequency is a matter of compromise. On one hand, the frequency should be as large as possible to ensure minimum pulsations in the load current waveform, but on the other hand an increased frequency yields to higher switching losses in the valves. For the nowadays transistors, the control frequency exceeds 20 kHz, eliminating the specific acoustic noise from the operation.

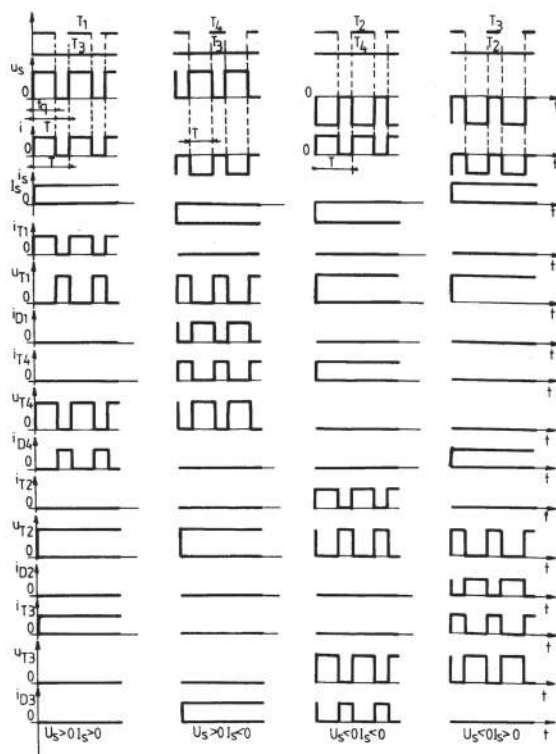


Fig. 2.63 Unipolar command waveforms.

## 2.5 Motion control of DC motor drivers

### 2.5.1 Starting in DC motor electric drives systems

#### 2.5.1.1 DC motor drives with parallel and separate excitation

The resistance and inductance of the armature circuit have low values at low machine speeds during start-up, which leads to high currents. A current that is too high has undesirable effects on the operation of the entire drive system:

- the destruction of the machine windings insulation due to the released heat;
- the inappropriate switching and the possible occurrence of the circular fire at the collector;
- the high stress of the brushes and of the bonding on winding conductors;
- the large torque values that can cause inadmissible mechanical stresses;
- the increased demand for the supply equipment.

Therefore, measures are required to limit the starting current to admissible values, determined also by the start-up times. In terms of the resistive torque, the start-up can take



place as follows: at no load, at half load, at nominal load and at a load higher than the rated load. The influence of the inertia on the transient processes' duration is emphasized by the inertia factor defined as follows:

$$IF = \frac{(J_M + J_{TL})}{J_M} = 1 + \frac{J_{TL}}{J_M}, \quad (2.82)$$

where  $J_M$  is the machine inertia moment and  $J_{TL}$  is the inertia moment of the other movable parts reported to the machine shaft [8].

In practice, the following start-up methods are used [9]:

- direct connection to the main supply;
- attaching additional resistors in series with the armature circuit;
- variation of the supply voltage without using a starting rheostat.

a. Start-up by direct connection to the main supply

It is a very simple and cost-effective start-up method. But, the very high starting current,  $I_p = (8.5 - 13.8)I_N$ , at no load and with 15-33 % higher at nominal loads or higher, make it suitable for low power start-up applications, powered by fixed voltage networks [10].

b. Start-up using resistors

It is a simple method to implement, but presents the disadvantage of the losses in the starting rheostat, which has the role of limiting the current to an admissible value. The resistance changes in steps, so that the current could vary between two limits:  $I_{max} = (1.5-2.5)I_N$  and  $I_{min} = (1.1-1.2)I_N$ .

For example, Fig. 2.64 shows the diagram of a three-stage rheostat  $R_1$ ,  $R_{ij}$  and  $R_{ij}$  and Fig. 2.65 shows the evolution of the operating point in the impedance of the rheostatic start-up process in the  $\Omega$ -M plane.

At point A, with  $\Omega = 0$  and  $I_a = I_{max}$  results  $R_3 + R_a = \frac{U}{I_{max}}$ . The machine accelerates as

long as the developed torque  $M > M_R$ . In  $A_1$ , when the current becomes  $I_a = I_{min}$ , the resistance  $R_{ij} = R_3 - R_2$  is removed from the armature circuit by closing the contact  $K_3$ . In this way, the operating point moves into point B on the characteristic corresponding to the  $I_{max}$  current. The resistance  $R_2$  is determined by:

$$R_2 = \frac{(U - K \cdot \Omega_B)}{I_{max}} - R_a \quad (2.83)$$

where  $K$  is the machine constant.

The calculation of the other resistors is similar to the one presented above.

In the case of a  $n$  start-up steps, the relation between the armature resistance  $R_a$ , the value of the  $n$  step of the resistance  $R_n$  and the currents  $I_{max}$  and  $I_{min}$  is given by the relation:

$$\frac{(R_a + R_n)}{R_a} = \left( \frac{I_{max}}{I_{min}} \right)^n = \lambda^n \quad (2.84)$$

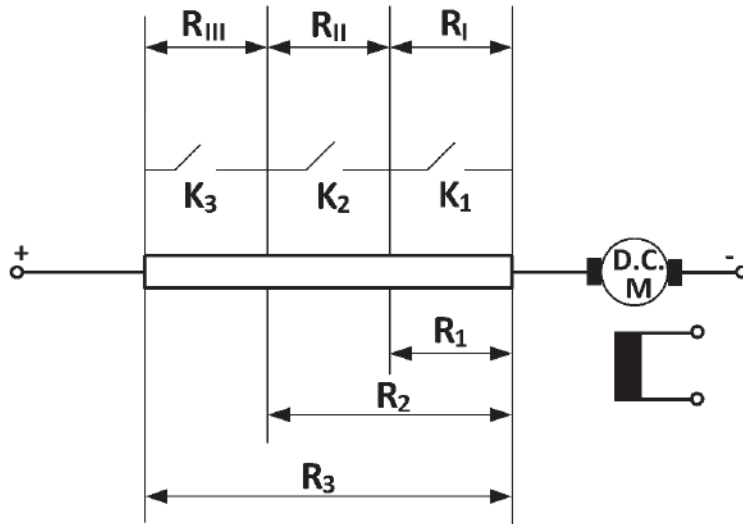


Fig. 2.64 The main scheme during the rheostatic start-up.

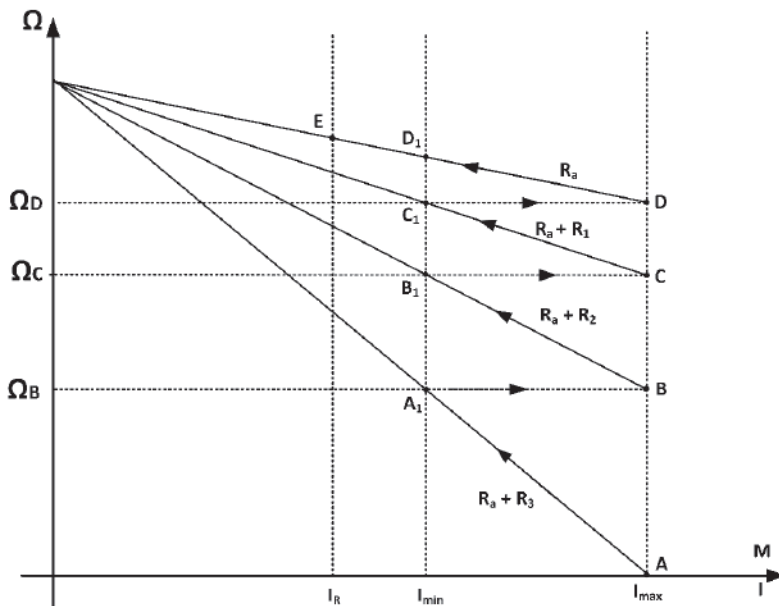


Fig. 2.65 Explanatory to the start-up using resistors.

c. Start-up by increasing the supply voltage

This method, in which the increase of the supply voltage is done from a low or zero voltage value to the nominal voltage value, eliminates the disadvantages of the previous methods. The supply voltage can be changed automatically so that the current stays constant during the start-up, resulting in a minimal power consumption, a low start-up time and in no shocks. Fig. 2.66 presents: a. the principle scheme of such a drive system; b. the phenomena evolution on the static characteristics; c. the transient process graphical diagram.

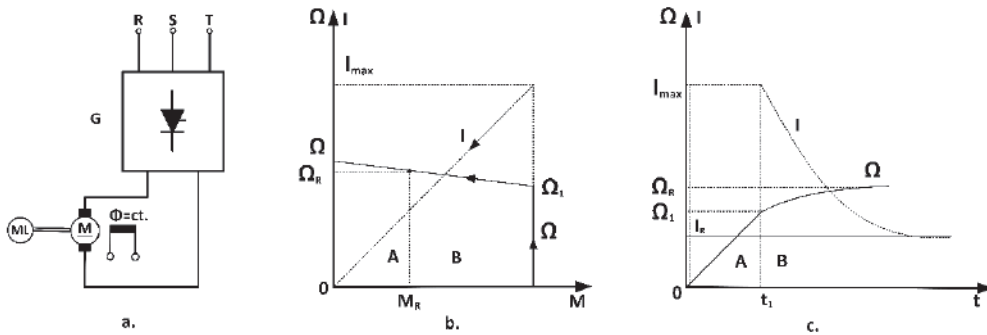


Fig. 2.66 Start-up by modifying the voltage.

The two stages of the start-up can be observed: A). the torque is constant, the speed is increasing linearly over time; B) the torque decreases linearly on the static characteristic, the velocity increases exponentially over time and the current decreases exponentially over time [8].

A cascade speed control scheme that can perform a start-up at current  $I_a = \text{const.}$  is presented in Fig. 2.67 [11]. The scheme is provided with a static converter, either a rectifier or a DC voltage variator. The regulators are of proportional type and saturable.

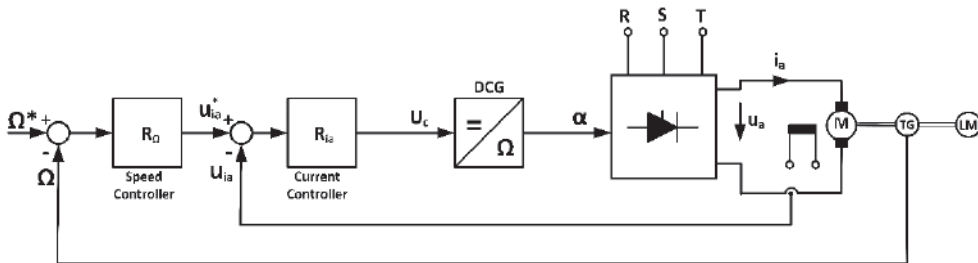


Fig. 2.67 Cascade speed control scheme that can achieve constant current start-up.

The current transducer in the armature circuit can be of the Hall type. The scheme ensures an automatic start-up at constant current up to the imposed stationary speed  $\Omega^*$ , which significantly reduces the start-up time and reduces the Joule losses since only the  $R_s$  remains in the circuit.

### 2.5.1.2 Electric drives equipped with DC machines with serial and mixed excitation circuit

The limitation of stresses, the processes and the start-up times in terms of resistive torque are similar to those of the DC machines with separate excitation case.

The start-up with resistors is calculated so that the current varies between a maximum  $I_{max}$  limit and a minimum  $I_{min}$  limit. The phenomenon as well as the electrical scheme are similar to the case of the DC machine with parallel excitation.

**The start-up** can also be realized by **continuous or step by step voltage changing**. As an example, we present the case of vehicles with multiple drive machines, whose start-up is done by switching from the serial connection to the parallel connection following a certain algorithm. The electrical scheme and the connection sequence of the contacts are shown in Fig. 2.68.

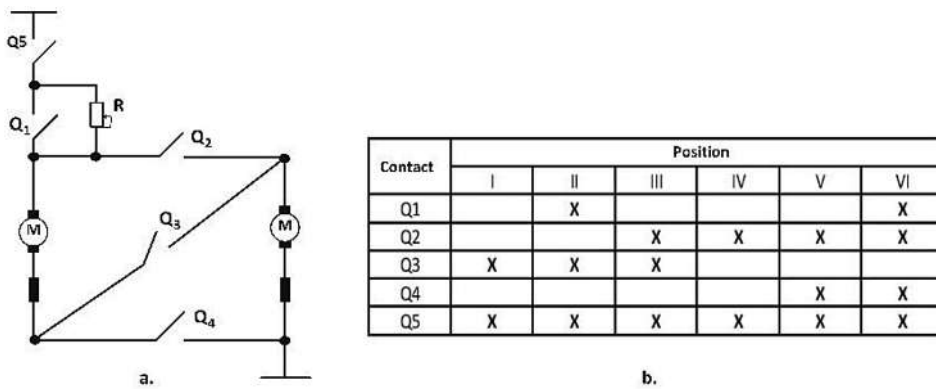


Fig. 2.68 Start-up by changing the voltage in two steps; a) the electrical scheme; b) the connection sequence.

## 2.5.2 Braking in electric drive systems equipped with DC machines

### 2.5.2.1 Electric drives equipped with DC machines with separate and parallel excitation circuit

The braking phenomena can be explained by referring to two widespread working mechanisms: the translation mechanism, characterized by the reactive torque, and the lifting mechanism, characterized by the active torque. Three classic braking methods are known in the literature: the regenerative braking, the dynamic braking and the electromagnetic braking.

#### a. The regenerative braking

Let us consider the case of a vehicle operating in the motor regime at point A on the natural characteristic of quadrant I as shown in Fig. 2.69. If the route tilts so that the vehicle descends without the help of the electric machine, its speed will rise above the value of the idling speed  $\Omega_0$  and the operating point will move to B.

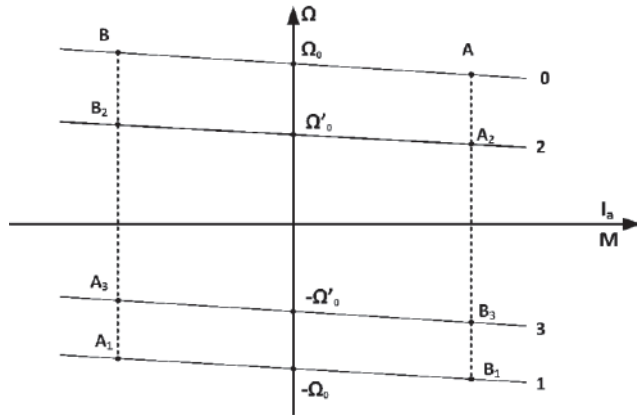


Fig. 2.69 Explanatory to the regenerative braking.

Under these conditions, the value of the electromotive voltage  $|E| = K\Omega$  becomes greater than the voltage at the terminals  $U = K\Omega_0$  and the following relationship:

$$K \cdot \Omega_0 - K \cdot \Omega = R_a \cdot I_a \quad (2.85)$$

highlights the change of the armature's current direction and thus of the torque direction  $M$ , which becomes a braking torque. Thus, the energy taken from the descending vehicle is transmitted to the grid by the electric machine operating as a generator.

Although it is the most economical braking method, the regenerative braking can only be applied at higher speeds than  $\Omega_0$ . The regenerative braking range can be extended to lower speeds by feeding the DC electric machine from a variable voltage source, so that the velocity  $\Omega_0$  changes, for example to  $\Omega'_0$ , obtaining the operating point  $B_2$  on characteristic 2 for the same torque. Similarly, for the reverse rotation direction, the regenerative braking operation points  $B_1$  and  $B_3$  are obtained.

The characteristics having the allure 2 or 3 are obtained, for example, by feeding the DC electric machine from the three-phase network via a converter consisting of two thyristor-controlled rectifiers  $G_1$  and  $G_2$ , as shown in Fig. 2.70.

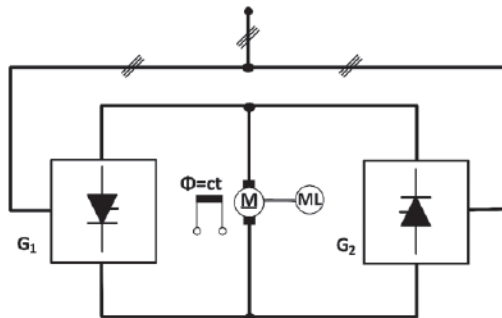


Fig. 2.70 Electric scheme in the case of the regenerative braking of a three-phase powered electric drive.

When operating in the motor mode in quadrant I, the drive machine M is fed through the rectifier  $G_1$  and  $G_2$  is blocked or operates as a currentless inverter. When operating as a regenerative brake in quadrant II, the current direction changes, so that the machine M will supply power to the grid via  $G_2$ , which will operate in the inverter mode, while  $G_1$  will be locked or will operate as a currentless rectifier.

In the case of a DC power source supply, continuous voltage variators are used to recover energy at different speeds, see Fig. 2.71.

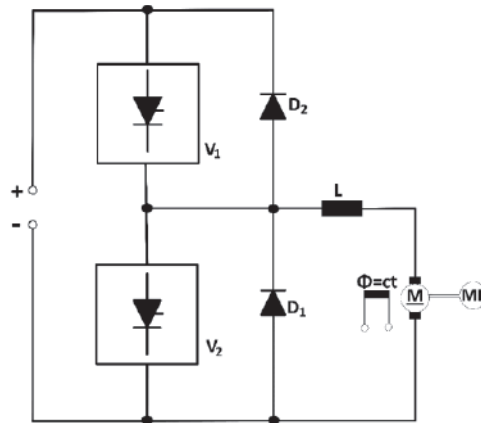


Fig. 2.71 Electric scheme in the case of the regenerative braking of a DC power source-fed electric drive.

In the motor operating mode, the machine M is fed by  $V_1$ , while  $V_2$  is permanently locked. When  $V_1$  is blocked, the current circulates through the discharging diode  $D_1$ . When operating as a brake,  $V_1$  is permanently locked. When  $V_2$  drives, the current increases at a rate determined by the inductance L and the energy received at the machine shaft is being stored in the coil L as magnetic energy. While  $V_2$  is blocked, the electromotive voltage of the machine M, to which the induced coil voltage is added, exceeds the voltage of the source and the diode  $D_2$  opens and the current  $I_a$  changes its direction. Under these conditions, the energy received at the machine M shaft and the magnetic energy stored in the coil will be transmitted to the power source.

For the lifting mechanisms, the regenerative braking occurs at the weight dip. For this purpose, the voltage U is reversed. The torque direction remains the same for both the dip and the lifting cases. The operation is stabilized in quadrant IV at a velocity  $\Omega < 0$  and  $|\Omega| > |\Omega_0|$ , respectively, in point B<sub>1</sub>, Fig. 2.69 [8].

b. The dynamic (rheostatic) braking

In the literature, this method is mostly known under the name of **dynamic braking**. It is done by disconnecting the armature from the grid and connecting it to a resistor, on which the machine dissipates the energy by operating as a generator. During this time, the excitation remains connected to the network, as shown in Fig. 2.72.

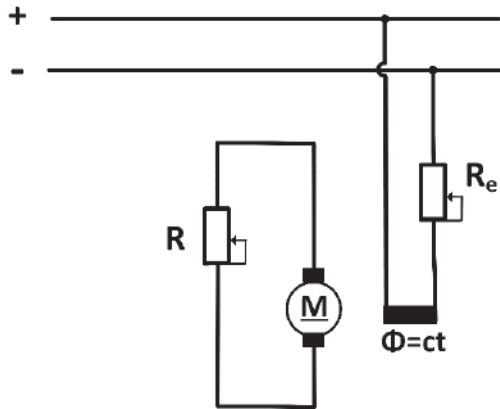


Fig 2.72 Electric scheme in the case of the dynamic (rheostatic) braking of a DC power source-fed electric drive.

The grid voltage becomes  $U = 0$ , and thus the mechanical characteristic equation is:

$$\Omega = -[(R_a + R) \cdot M] / K^2 \quad (2.86)$$

The mechanical characteristics are represented in Fig. 2.73.

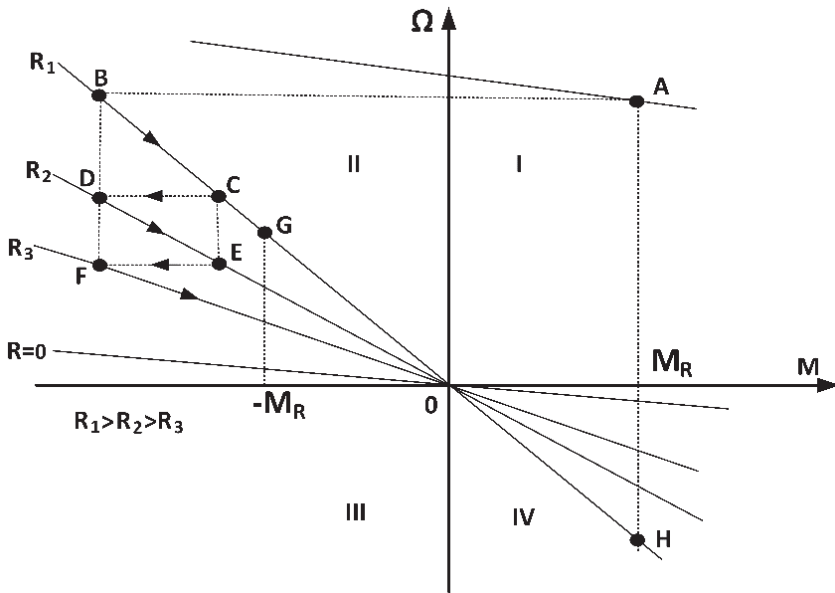


Fig. 2.73 Mechanical characteristics for the rheostatic braking case.

The case of a vehicle that moves horizontally is considered in what follows. When braking for vehicle stopping, the operating point switches from the point A corresponding to the motor mode operation to the point B corresponding to the generator mode

operation and then travels the broken BCDEFO line until it stops. The braking effect decreases proportionally with the deceleration. Therefore, in order to maintain the torque between the boundaries defined by the BCDEF trajectory, the external resistance  $R$  must be reduced in steps, resulting the braking characteristics of the  $R_1$ ,  $R_2$  and  $R_3$  resistors. If the vehicle is to be lowered by braking on an inclined plan, the operating point shall stabilize in  $G$ , where  $M_G = -M_R$ . The characteristic with the most powerful braking effect corresponds to the minimum value of the total resistance,  $R_a$ , i.e.  $R = 0$ . To obtain zero speed, a mechanical brake is required.

Braking when lowering a weight corresponds to the operation in quadrant IV. In equation 2.86, the torque is inserted with a positive sign, e.g. the H point on the characteristic.

Using the electric circuit diagram in Fig. 2.74 a, the braking current variation limit may be so close that it remains almost constant or varies according to a particular law. The forced commutated  $V_1$  converter acts as a static contactor and thus the high braking resistance  $R$  is intermittently short-circuited. This resistance behaves as a variable resistance that depends on the conduction (lead) duration  $t_i$  or on the blocking duration  $t_r$  of the main switching device from the  $V_1$  converter. During the current  $t_i$ , the current increases exponentially by  $V_1$  and in the  $t_r$ , the pulse decreases exponentially through  $R$ , as seen in Fig. 2.74 b.

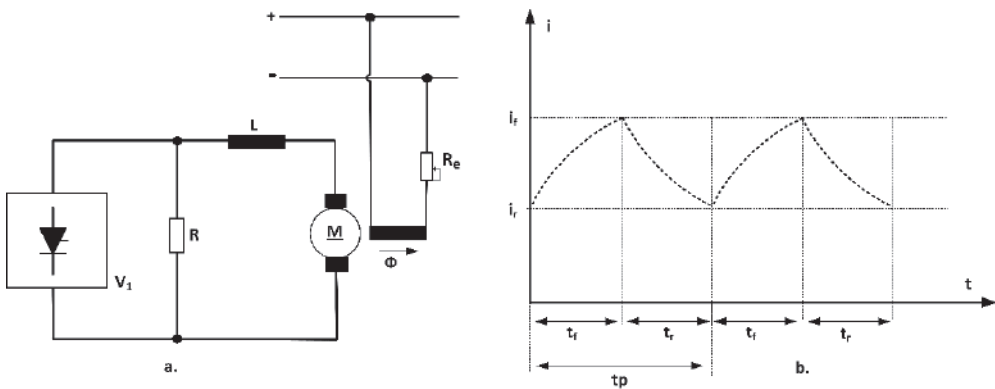


Fig. 2.74 Rheostatic braking using the static converter  $V_1$ .

In conclusion, the rheostatic braking has the advantage of the simplicity of the electric circuit. A disadvantage is represented by the losses in the braking resistance [8].

### c. The electromagnetic braking

In the literature, this braking method is also known as **braking through opposing connections, electric braking or simply braking**. Its feature consists of the fact that the electromotive force has the same sense as the voltage at the terminals, their sum determining the current in the armature circuit which needs to be limited.



The electromagnetic braking is practiced in two ways:

a. In the case of lifting mechanisms, characterized by the active torque, for example, if  $M_R=M_D$ , an additional resistance  $R_f$  is inserted into the armature circuit, dimensioned so that to stabilize the operation at negative speed  $-\Omega_D$  and the operating point to travel along the trajectory ABCD, presented in Fig. 2.75, in order to get on the characteristic 1 in the CD braking area;

b. In the case of translational mechanisms, characterized by a reactive torque, for example, for  $M_R=M_E$ , the voltage polarity at the terminals is reversed and an  $R_f$  resistance is inserted into the armature to limit the current so as to obtain a negative torque on characteristic 2, in the FG braking area. It is either stopping the vehicle according to the EFG trajectory or reversing it according to the EFGH trajectory, if  $|M_G| > |M_R|$ , in which case the operation stabilizes in the motor operation mode in point H.

Based on the relation 2.1, corresponding to the cases an and b, we can write the relationships:

$$\begin{aligned} U + E_D &= (R_a + R_f) \cdot I_a \quad \text{- for the case a)} \\ -U - E_F &= (R_a + R_f) \cdot I_a \quad \text{- for the case b)} \end{aligned} \tag{2.87}$$

From (2.87), the resistance  $R_f$  or the current  $I_a$  can be determined.

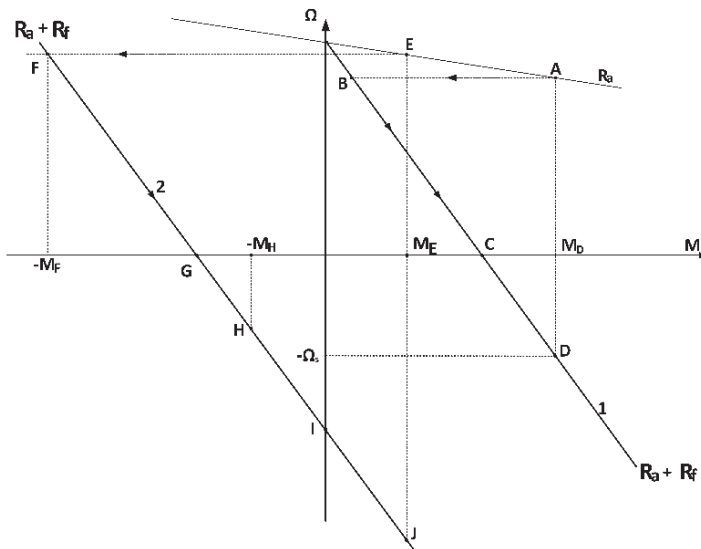


Fig. 2.75 Electromagnetic braking.

The braking effect is strong even at low speeds. However, there is a danger of undesirable reversal, the stiffness of the characteristics is reduced and the losses are high as the power taken from the grid through the machine shaft dissipates in the resistors [8].

### 2.5.2.2 Electric drives equipped with DC machines with serial and mixed excitation circuit

#### a. The regenerative braking

In the case of electric drives equipped with DC machines with serial excitation circuit, the regenerative braking cannot be applied as it is usually done for the other types of DC machines, because the natural mechanical characteristic does not travel the quadrant II (see Fig. 2.9). One solution is to bind the excitation separately to the network. However, large losses in the current limiting the resistance of the excitation circuit occur. In the electric drives with more identical machines, a more favorable solution is to bind the excitation circuits in series using a single resistance. A more cost-effective solution is to use the power supply from a separate low-voltage source.

Another economical solution for the braking is achieved by using continuous voltage variators. An extensive study of this problem was carried out in the Department of Electrical Engineering of Politehnica University of Timisoara. The technical solutions obtained in the studies [12, 13, 14, 15] are summarized below.

For the regenerative braking, the DC voltage variator is connected in parallel to the drive machine (see Fig. 2.76).

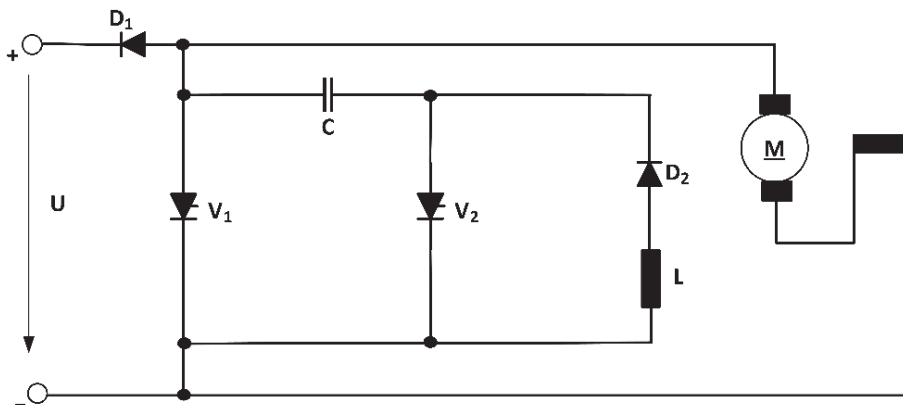


Fig. 2.76 Regenerative braking using a DC voltage variator.

When the thyristor  $V_1$  drives, the machine is short-circuited and the current increases and when  $V_1$  is blocked, the current is switched to the source and decreases. The kinetic energy of the drive is converted into electromagnetic energy inside the machine and, at the opening of the diode  $D_1$ , a part of it is sent to the source. In this process, the machine inductance plays an important role. Thus, the inductance is charged with electromagnetic energy when the current increases and  $V_1$  is primed and the inductance is discharged when  $D_1$  is in conduction. Therefore, for the analytical study of the regenerative braking process, the elements of the machine circuit such as the resistance, the inductance and the electromotive voltage must be fully taken into account.

In principle, there are good energy recovery possibilities with this scheme for both cases of series and separate excitation DC machines. In the DC machine with serial excitation, however, additional measures must be taken in order to excite the machine at the beginning of the braking process. The easiest way is the partial excitation of the machine with a second separated excitation circuit, similar to the self-excitation circuit specific to the DC machines with mixed excitation. The scheme in Fig. 2.77.a shows how it is possible to excite by using an additional voltage source  $G$  via the diode  $D_2$ . When the excitation process is primed and the current in the machine circuit reaches its nominal values, the voltage drop on the excitation winding becomes greater than the voltage provided by the source  $G$  and it is disconnected by blocking the diode  $D_2$ . Instead of the voltage source, a shocking excitation can also be used, by discharging a capacitor through the excitation winding. In the scheme in Fig. 2.77.b, a resistor  $R$  is connected between the excitation winding and the source, thus providing for the thyristor  $V_1$  priming a higher current than the one needed for machine maintenance and excitation. The diode  $D_2$  blocks the current through the rotor and resistance  $R$ . With this procedure, the machine self-excitation already occurs at approx. 10 % of rated speed at a correct dimensioning of the resistance. After the braking process has been started, the resistance is disconnected.

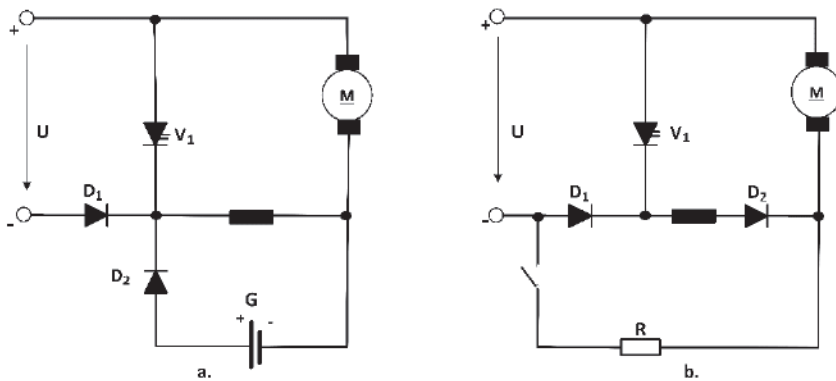


Fig. 2.77 Excitation of the DC machine with serial excitation at braking; a) from an additional source; b) from the voltage source.

Another issue that needs to be addressed in the case of the regenerative braking of the DC machine with serial excitation is to avoid instability at high speed operation, which may occur when the machine's electromotive voltage becomes greater than the source voltage, which leads to the direct polarization of the diode  $D_1$ . In this case, the braking process can no longer be controlled by the continuous voltage variator. A stable operation can be provided by additional resistance, as seen in Fig. 2.78 a.

In this case, the stability is ensured at the expense of a part of the recovery energy that is dissipated over the stabilizing resistance. When lowering the speed below a certain limit, the resistance  $R$  may be short-circuited. It is possible to remove the instability without additional losses by modifying the regenerative braking scheme according to the one

presented in Fig. 2.78.b, which results in the automatic field weakening at high speeds. In order for the field weakening to take place, the scheme requires an expansion of the variator control band in correlation with the excitation circuit time constant, especially at low frequencies, which complicates the control and filtering parts.

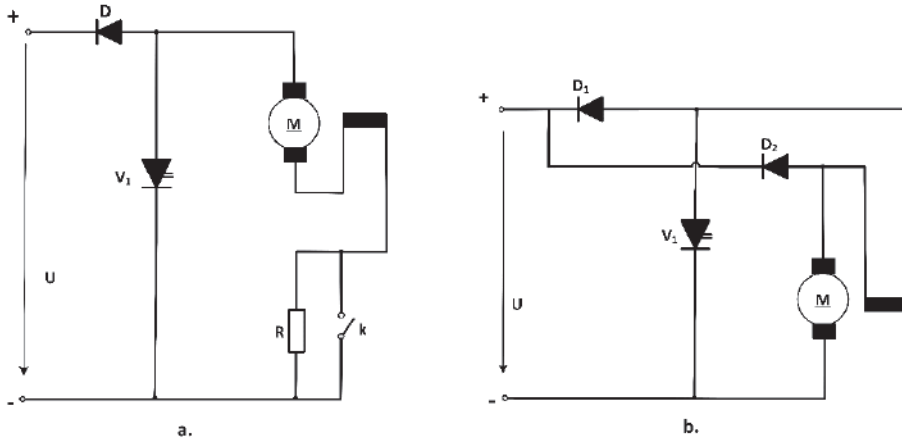


Fig. 2.78 Removing instability: a) using an additional resistance; b) through flux weakening.

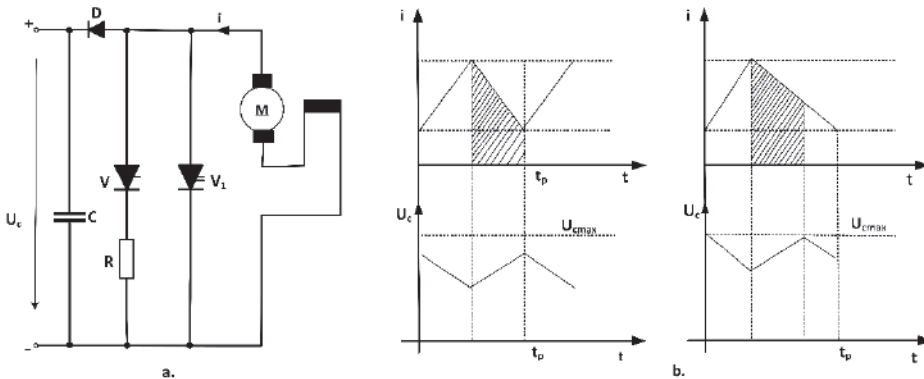


Fig. 2.79 a) Regenerative-rheostatic braking; b) recovered current variation (shaded area) and  $U_c$  voltage.

An essential condition for the machine's proper operation during the regenerative braking mode is the possibility of the power supply network to fully take over the recovered energy. If this energy is not fully absorbed, then, in few operation periods, it accumulates in the extinguishing capacitor, producing severe consequences for the semiconductor elements due to their stress at much higher voltages than normal ones. One way of avoiding this situation is to use mixed, regenerative and rheostatic braking, as shown in Fig. 2.79. The braking resistor is connected in parallel and is inserted into the thyristor  $V$  circuit. As long as the voltage on the power supply capacitor's filter does not

exceed the value  $U_{cmax}$ , the regenerative brake is inhibited. If the voltage rises above this value, which means that the recovered energy cannot be fully transmitted to the grid, the resistance  $R$  is connected.

It should be noted that the thyristor  $V$  does not require an extinguishing circuit, being turned off by priming the main thyristor in the continuous voltage variator.

b. The rheostatic or dynamic braking

This method is especially used in the case of the DC machines with serial excitation circuit by binding the excitation over a resistor  $R$ , according to Fig. 2.80, so that the current direction through the excitation winding remains the same in order to avoid the demagnetization of the poles. The machine self-excitation occurs due to the remaining magnetic field. In the case of a vehicle braking, the speed keeps its sense and the direction of the armature current changes according to the relation (2.1) written for  $U = 0$ :

$$-E = (R_a + R) \cdot I_a \tag{2.88}$$

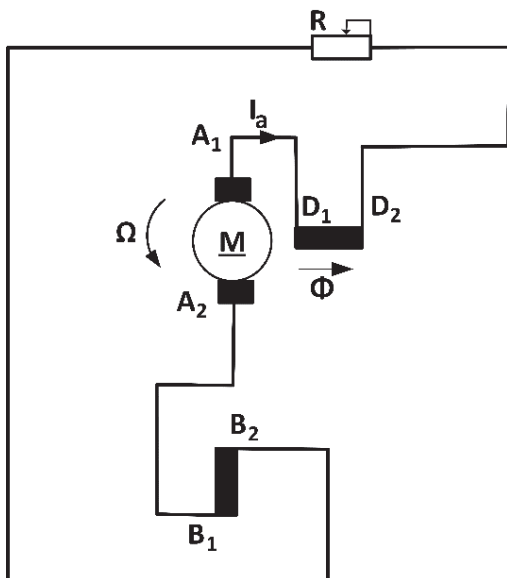


Fig. 2.80 Dynamic braking scheme.

The equation (2.88) highlights the machine requirement to develop friction torque, to dissipate the current over the resistance  $R$ , respectively: the existence of the operating point  $P$  on the characteristic shown in Fig. 2.81 at the intersection of the characteristic  $E=f(I_a)$  of constant speed  $\Omega_1$  with the straight line  $(R_a + R) I_a = f(I_a)$ . For a speed  $\Omega_3 < \Omega_1$ , the two characteristics no longer intersect. In order to obtain a braking torque, the resistance must be reduced to  $R'' < R'$ , resulting the new operating point  $P_3$ .

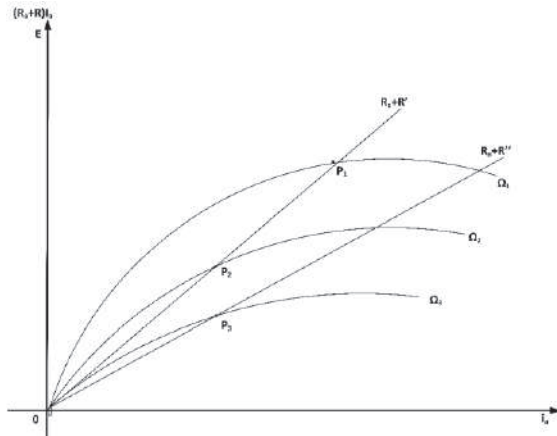


Fig. 2.81 Characteristics corresponding to the rheostatic braking method.

The disadvantages of the method are the losses in the resistance and the cancellation of the braking torque at  $\Omega = 0$ . For a fine adjustment of the braking system, the diagram presented in Fig. 2.82 is recommended.

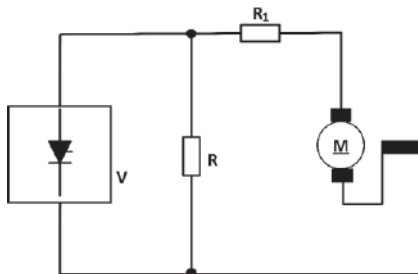


Fig. 2.82 Rheostatic braking using a static contactor.

c. The electromagnetic braking

This method is specific to the DC machines with parallel excitation circuit. The electrical scheme is shown in Fig. 2.83 a, while the characteristics in Fig. 2.83.b.

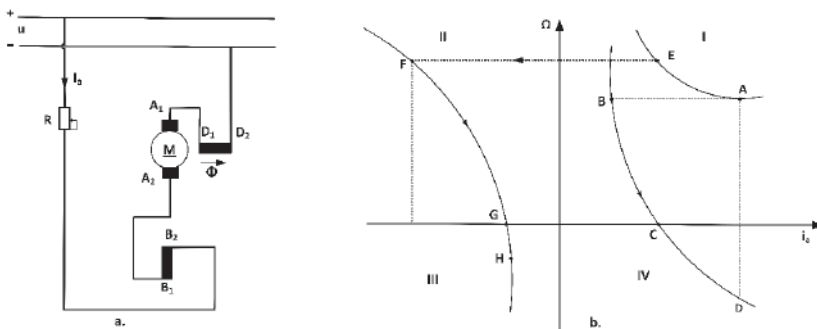


Fig. 2.83 Electromagnetic braking: a) connection scheme; b) characteristics.

## 2.5.3 Speed change in electric drives equipped with DC machines

### 2.5.3.1 Electric drives equipped with DC machines with parallel and separate excitation circuit

#### a. Speed change through resistors

The method is easy to accomplish; however, it presents the disadvantage of losses in the resistance. In case the resistance is serially interleaved, soft mechanical characteristics of the same speed  $\Omega_0$  are obtained. If the resistance is mounted in parallel with the inductance, it is also possible to modify the idling speed  $\Omega_0$ .

#### b. Speed changing through field weakening

The field weakening is accomplished by the implementation of the schemes shown in Fig. 2.84.

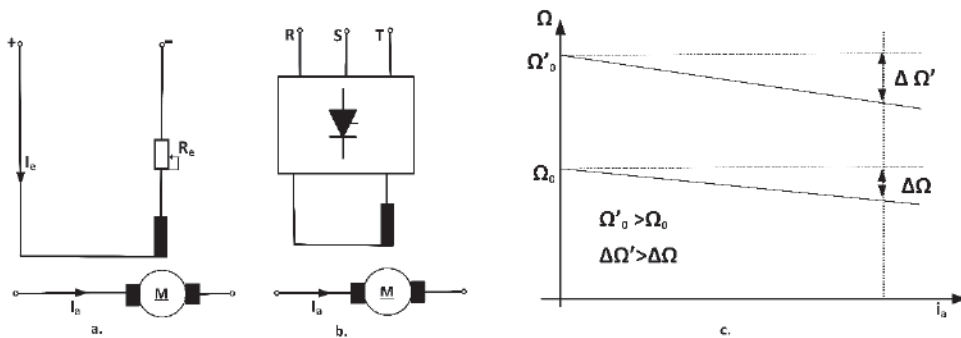


Fig. 2.84 Speed variation through field weakening: a) and b) electrical schemes; c) mechanical characteristics.

The losses in the resistance  $R_e$  are small or practically null for the scheme presented in Fig. 2.84 b.

The equation of the mechanical characteristic is:

$$\Omega = \frac{U}{k \cdot \Phi} - \frac{(R_a \cdot M)}{(k \cdot \Phi)^2} \quad (2.89)$$

The previous relation shows that  $\Omega_0$  and  $\Delta\Omega$  increase with the flux decreasing. The method is advantageous for achieving speeds above the rated speed, noting the advantage of the possibility of a continuous command in a low power circuit, especially when using controlled rectifiers. In industrial applications, the method is often used combined with speed changing through modifying the armature voltage, providing a great speed-changing range.

c. Speed variation through voltage changing

The voltage change is made at the armature terminals in order to reduce the speed, while maintaining the excitation constant. Therefore, the method does not apply to the DC machine with parallel excitation. The equation of the mechanical characteristic:

$$\Omega = \frac{U}{K} - \frac{(R_a \cdot M)}{K^2} \quad (2.90)$$

shows that at  $M = \text{const.}$ ,  $\Omega_0$  decreases and  $\Delta\Omega$  remains constant.

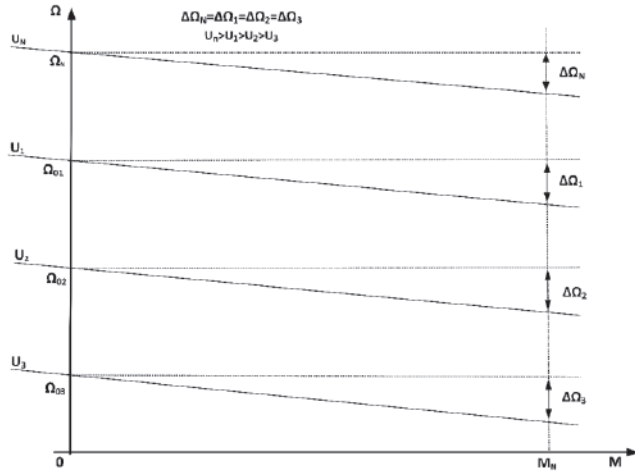


Fig. 2.85 Mechanical characteristics for the case of the armature voltage change.

The mechanical characteristics are parallel to the natural characteristic, providing the best possibilities for speeding up to wide and economic limits. Thus, with small losses, sometimes even negligible, the method is widely used in practice.

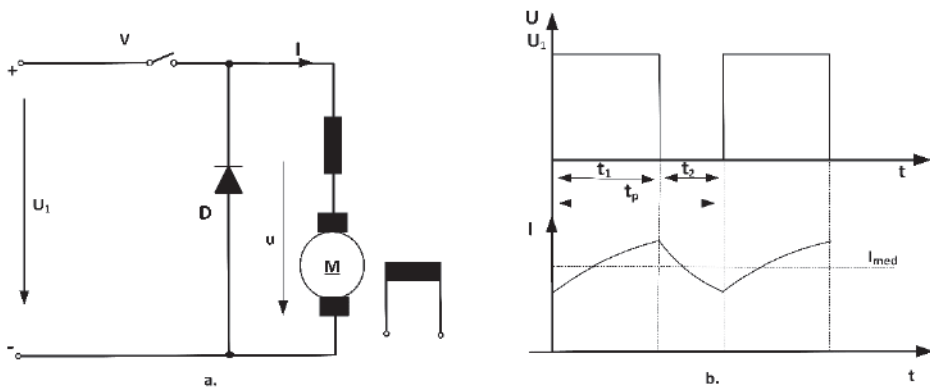


Fig. 2.86 Speed variation through voltage pulses: a) scheme of principle; b) current and voltage variation.



One way of changing the speed between 0 and the rated speed is **to power supply the machine with a pulse train**. Its schematic diagram is shown in Fig. 2.86. The machine is powered constantly by a constant voltage for a period  $t_1$  followed by a period  $t_2$  in which the voltage at the machine terminals is null.

The devices used for the machine power supply with pulses are the continuous voltage variators [16, 17]. The voltage variators with power transistors (see Fig. 2.87a) are basically simple, the command being performed by the alternating saturation of the transistor  $V_2$  for the  $V_1$  to conduct and of the transistor  $V_3$ , respectively, for blocking the transistor  $V_1$ . Note that the voltage source  $\pm U_c$  must be galvanically separated from the main circuit. The thyristor voltage variators (see Fig. 2.87 b) operate by alternating control of the thyristors  $V_1$  and  $V_2$ .

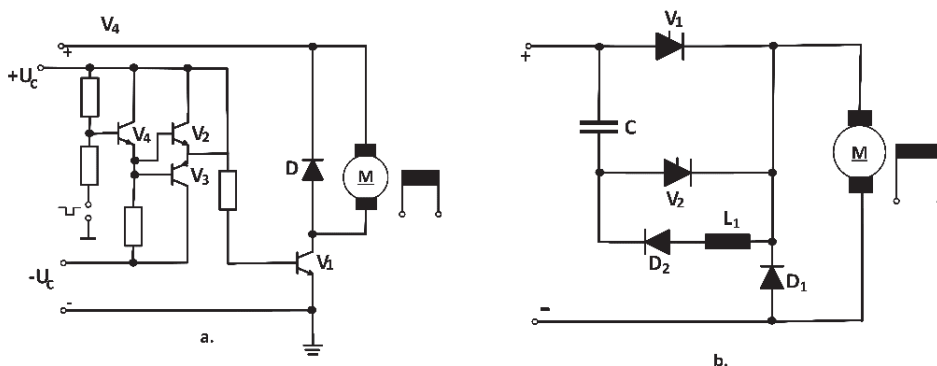


Fig. 2.87 Continuous voltage variators. a) using transistors; b) using thyristors.

The mean value of the voltage supplied by the variable voltage converter is:

$$u = \left(\frac{t_1}{t_p}\right) \cdot U_1 = a \cdot U_1 \tag{2.91}$$

where  $a$  is the relative driving time. The voltage change is performed by acting on  $t_1$  and  $t_p$  (command parameters) as follows:

- for variable  $t_p$  and constant  $t_1$  - frequency control;
- for constant  $t_p$  and variable  $t_1$  – pulse width modulation control;
- for  $t_1$  and  $t_p$  variable - as in the case of bi-positioning current control.

### 2.5.3.2 Electric drives equipped with DC machines with serial excitation circuit

#### a. Speed variation using resistors

The method is easy to accomplish, but presents the disadvantages of losses in resistances, soft operating characteristics and unlimited idling speed. By binding a resistance in parallel

with the armature, more favorable operating characteristics are obtained, eliminating the danger of motor packing at idling.

b. Speed variation through field weakening

In the case of electric drives equipped with DC machines with serial excitation, the field weakening is implemented according to the scheme presented in Fig. 2.88.a and Fig. 2.88.b.

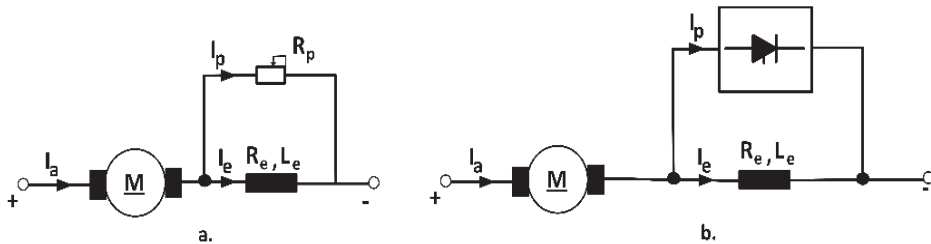


Fig. 2.88 Speed variation through field weakening: a) and b) scheme variants.

The degree of field weakening is characterized by the ratio:

$$\alpha = \frac{I_e}{I_a} \leq 1 \quad (2.92)$$

Fig. 2.88.b shows the undesired oscillations of the current  $I_a$ , which cannot be prevented [18]. The method is cost-effective, the losses are small, but it only allows for the speeding up [11].

c. Speed variation through voltage changing

This method is the most cost-effective one, because the losses are being very low. Still, its practical implementation is more complicated. At a given current, the speed changes almost proportionally with the voltage at the terminals. Thus, the speeds  $\Omega$  and  $\Omega_x$  corresponding to the voltages at the terminals  $U$  and  $U_x$  are in the range of:

$$\frac{\Omega_x}{\Omega} = \frac{(U_x - R_a \cdot I_a)}{(U - R_a \cdot I_a)} \quad (2.93)$$

The above relationship shows that the speed changes to a greater degree than proportional to the voltage [11].

## 2.5.4 Automatic speed adjustment control systems

**Changing the speed** means changing it from one value to another according to the requirements of the production process or unwanted drive parameters variation. **The speed control** involves the operation of maintaining a speed at a certain prescribed value based on a required operating programme. Thus, if the speed modification can be

achieved in both the drive systems and the control systems, then the speed control is achieved only in the automatic control systems by the intervention of the reaction, **which is their fundamental feature.**

Fig. 2.89 shows a cascade speed control system using DC machines with separate excitation circuit.

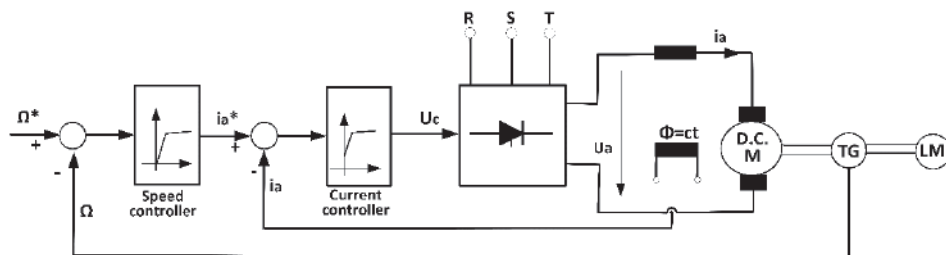


Fig. 2.89 Cascade speed control system.

The control system allows maintain the prescribed angular speed  $\Omega^*$  regardless of the machine load. The command voltage  $u_c$  is the result of the error  $i_a^* - i_a$  processing by the controller P. The magnitudes at the input of the current controller come from the upper hierarchical loop:  $i_a^*$  is the prescribed value and  $i_a$  is the measured value. The imposed value  $i_a^*$  is the result of the speed error processing,  $\Omega^* - \Omega$ .

## 2.5.5 Automatic positioning systems

### 2.5.5.1 Linear positioning systems

In general, the position control realized with DC motors is done with specialized equipment and a greatest tradition in this field can be testified. The most commonly used method is the cascade control, meaning that the current loop is subordinate to the speed loop and the speed loop to the position loop, respectively. In this way, the reference for the current loop is the output of the speed controller, and the output of the position controller is the reference speed for the speed loop.

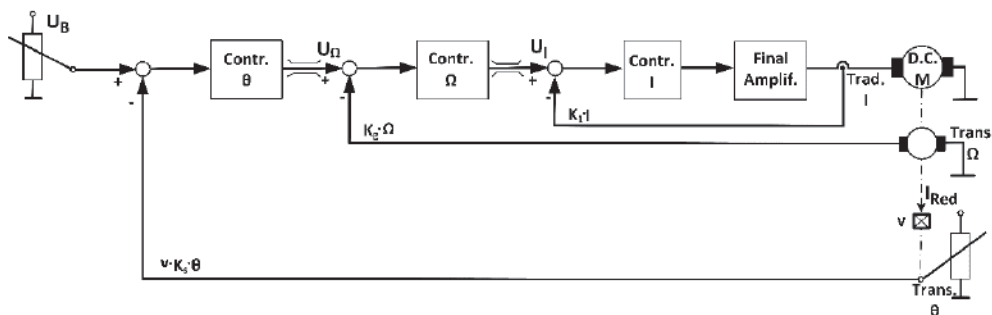


Fig. 2.90 Scheme of cascade position loop control.

The schematic diagram is presented in Fig. 2.90. The limitation of the speed and current variation through the armature is done at the output of the regulators through special limiting circuits containing Zener diodes.

For the control scheme computation, the current, speed and position loops are successively considered in the block diagram in Fig. 2.91. Here, you can clearly see the filter time constants on the current and speed loops, which mainly cannot be compensated.

a. The current loop

The external transfer function of the loop, having as output the armature current and as input the armature voltage is (see Fig. 2.91):

$$Y_{IU}(s) = \frac{i_a(s)}{u_a(s)} = \frac{1}{R_a + s \cdot L_a} = \frac{F + s \cdot J}{(F + s \cdot J) \cdot (R_a + s \cdot L_a) + K^2} \quad (2.94)$$

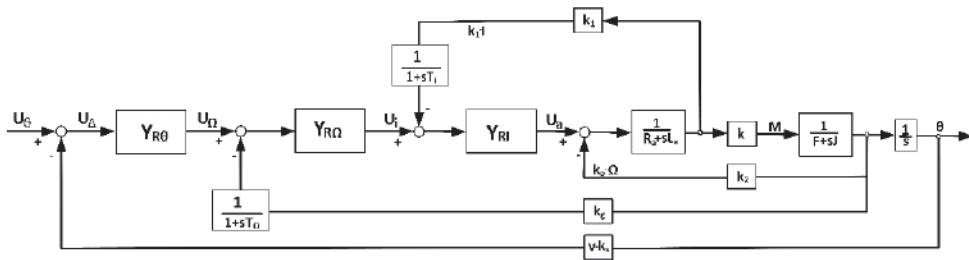


Fig. 2.91 System block diagram.

Fig. 2.92.a shows the block diagram of the current loop, in which the transfer function of the current regulator to be determined has been noted with  $Y_{RI}(s)$ . For the conventional DC motors, it can be considered that  $F = 0$  and, once the cascade regulation is often used in such motor types, the relation (2.94) can be rewritten:

$$Y_{IU}(s) = \frac{s \cdot T_m / R_a}{1 + s \cdot T_m + s^2 \cdot T_m \cdot T_a} = \frac{1 / R_a}{\frac{1}{s \cdot T_m} + 1 + s \cdot T_a} \approx \frac{1 / R_a}{1 + s \cdot T_a} \quad (2.95)$$

in which it was noted:  $T_m = \frac{J \cdot R_a}{K^2}$ ,  $T_a = \frac{L_a}{R_a}$  and it was taken into account that

$T_m \gg T_a$ .

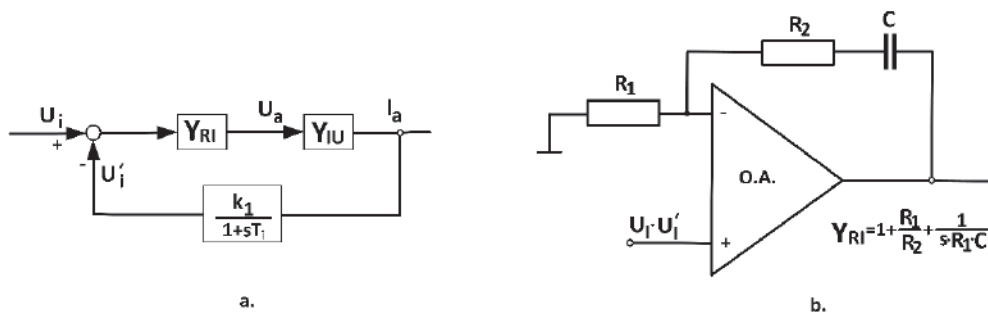


Fig. 2.92 Current loop: a) block diagram; b) current regulator PI.

It is defined:

$$Y_{exi}(s) = Y_{iU}(s) \cdot \frac{k_1}{1 + s \cdot T_i} = \frac{k_1}{R_a} \cdot \frac{1}{(1 + s \cdot T_i) \cdot (1 + s \cdot T_a)} \quad (2.96)$$

The current regulator is chosen according to the module's criterion, imposing to the current loop an optimal structure described by:

$$Y_{d\,opt}(s) = \frac{1}{s \cdot 2 \cdot T_\Sigma \cdot (1 + s \cdot T_\Sigma)} \quad (2.97)$$

in which  $T_\Sigma$  represents the sum of the small time constants, mainly uncompensable in the loop,  $T_\Sigma = T_i$ . The transfer function of PI controller type is obtained from:

$$Y_{pi}(s) = \frac{Y_{d\,opt}(s)}{Y_{exi}(s)} = \frac{R_a}{k_1} \cdot \frac{1 + s \cdot T_a}{s \cdot 2 \cdot T_i} = k_p + \frac{k_I}{s} \quad (2.98)$$

where it was noted:

$$k_p = \frac{R_a \cdot T_a}{k_1 \cdot 2 \cdot T_i} = \frac{L_a}{2 \cdot k_1 \cdot T_i} \quad (2.99)$$

$$k_I = \frac{R_a}{2 \cdot T_i \cdot k_1}$$

The schema of the controller is shown in Fig. 2.92.b and its adjustment assumes the choice of values for  $R_1, R_2$  și  $C$  such as:

$$k_p = 1 + \frac{R_2}{R_1}; \quad k_I = \frac{1}{R_1 \cdot C} \quad (2.100)$$

The loop optimization being made according to the module criterion, it means that, at a step signal variation at the input of the loop, the response is defined based on the relation (2.97) with an overshoot of 4.3 % and a set time of  $4.72 T_{\Sigma}$ , without oscillations after this time and a stationary error [3].

b. The speed loop

The speed loop scheme, in which the subordinate current loop is included, optimized according to the module criterion, is shown in Fig. 2.93. The internal current loop is assimilated to an element having the optimal transfer function:

$$Y_{opt}(s) = \frac{Y_{d\,opt}(s)}{1 + Y_{d\,opt}(s)} = \frac{1}{1 + 2 \cdot T_i \cdot s + 2 \cdot T_i^2 \cdot s^2} \quad (2.101)$$

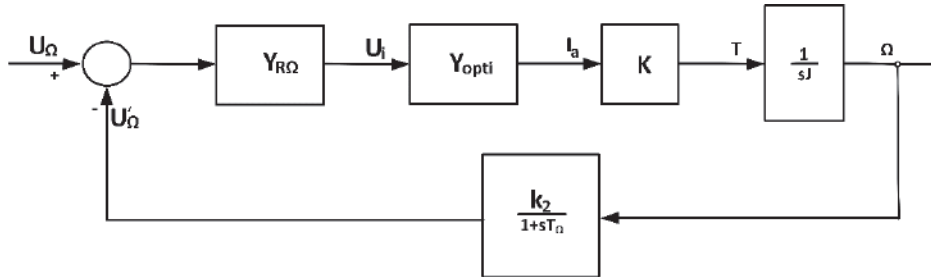


Fig. 2.93 Block scheme of the speed loop.

Similar to the relation (2.96), for the speed loop, the following results:

$$Y_{ex\Omega}(s) = Y_{opt}(s) \cdot \frac{k}{s \cdot I} \cdot \frac{k_2}{1 + s \cdot T_{\Omega}} = \frac{R_a \cdot k_2 / k}{s \cdot T_m \cdot (1 + s \cdot T_{\Omega}) \cdot (1 + 2 \cdot T_i \cdot s + 2 \cdot T_i^2 \cdot s^2)} \quad (2.102)$$

and considering that  $T_{\Sigma\Omega} = T_{\Omega} + T_i$  is the sum of the small irretrievable time constants, the external transfer function is approximated by:

$$Y_{ex\Omega}(s) \cong \frac{R_a \cdot k_2 / k}{s \cdot T_m \cdot (1 + s \cdot T_{\Sigma\Omega})} \quad (2.103)$$

The speed controller is chosen according to the symmetry criterion, implying that the loop is optimal for a ramp input signal:

$$Y_{d\,opt\,\Omega}(s) = \frac{1 + s \cdot 4 \cdot T_{\Sigma\Omega}}{s \cdot 4 \cdot T_{\Sigma\Omega}} \cdot \frac{2}{s \cdot (1 + s \cdot T_{\Sigma\Omega})} \quad (2.104)$$

causing an optimal variation of 4.3% overshooting, no-oscillation reversal and zero stationary error at ramp signal. The speed controller has the transfer function:

$$Y_{R\Omega}(s) = \frac{Y_{d\text{opt}}(s)}{1 + Y_{\text{ext}\Omega}(s)} = \frac{1 + s \cdot 4 \cdot T_{\Sigma\Omega}}{s \cdot \frac{R_a \cdot k_2 \cdot 2 \cdot T_{\Sigma\Omega}}{k \cdot T_m}} \quad (2.105)$$

being also of PI type (Fig. 2.92 b), having the constants [3]:

$$k_p = \frac{2 \cdot k \cdot T_m}{R_a \cdot k_2}; \quad k_I = \frac{k \cdot T_m}{R_a \cdot k_2 \cdot 8 \cdot T_{\Sigma\Omega}^2} \quad (2.106)$$

c. The position loop

If the previous regulators operate correctly, there is no stationary error, the position controller can be selected as being of proportional type [19]. There are some particularities in the position loop because, in practice, no overshooting is allowed in reaching a prescribed position. Therefore, the ideal feature of a position controller should be as shown in Fig. 2.94, as a saturation parabola, better said, with variable amplification factor and, in addition, with very high amplification at very low deviations.

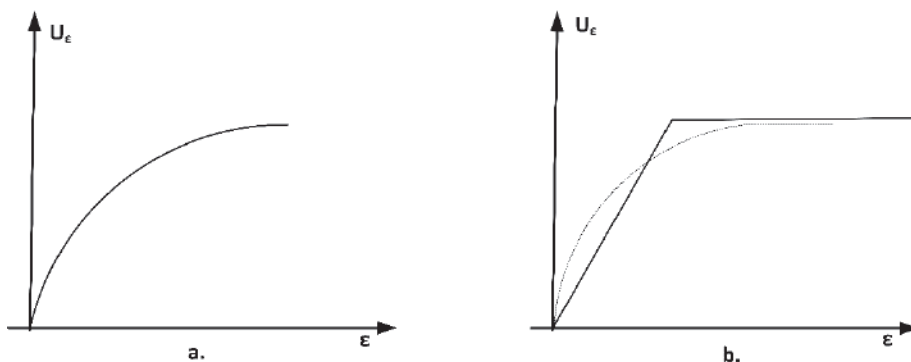


Fig. 2.94 Characteristic of the static position controller: a) ideal; b) real.

$$A = \lim_{\epsilon \rightarrow 0} \frac{U_\epsilon}{\epsilon} = \lim_{\epsilon \rightarrow 0} \frac{k_3}{\sqrt{\epsilon}} = \infty \quad (2.107)$$

Such a controller cannot be implemented and is replaced by the proportional type controller, as shown in Fig. 2.94.b. Another issue of the loop position, to which the previous mentioned loops subordinate, occurs when a variable prescription is given,  $X_i = \alpha t$ . It can be demonstrated [20] that, at such a prescription, a stationary error occurs when,  $t \rightarrow \infty$ ,

$$u_e^* = \frac{\alpha}{k_d} \quad (2.108)$$

$k_d$  is the global open loop amplification. As this amplification does not have an infinite value, it results that this stationary error is finite and it can be appreciated as a quality factor for the drive systems. In order to compensate it, a correction factor  $k_c$ , as shown in Fig. 2.95, is introduced in parallel to the speed controller.

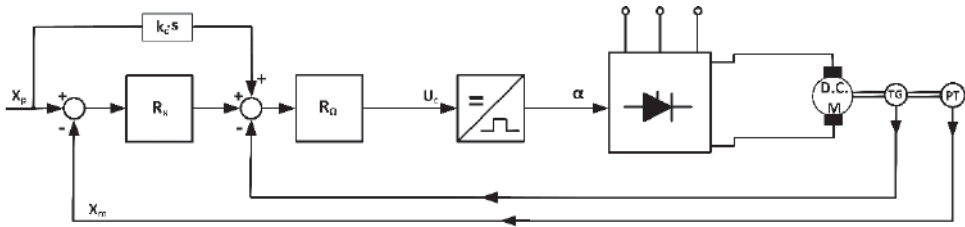


Fig. 2.95 Structure of a positioning system with correction.

The cascade regulation still has a disadvantage, namely that the response is even slower as there are several subordinate loops. It can be shown [19] that the time constant equivalent to the loop is multiplied by a factor greater than two for each additional reaction loop. Therefore, it is preferable, excluding the positioning systems with conventional drive motors, which need to be protected, to give up to the current loop, as in presented in Fig. 2.95.

### 2.5.5.2. Non-linear positioning systems

Position control systems having at least one non-linear behavioral element are called non-linear systems. The most widespread non-linear element is the one having the relay-type feature. In various applications, the valves positioning to control the debit use the single position loop system shown in Fig. 2.96.

The grid control device GCD together with the grid switching converter, all have a non-linear character, in general. This is done using the control scheme in Fig. 2.97 a, which is part of the GCD. The  $u_c$  error signal is introduced into a non-linear element consisting of a double comparator (CLB 2711), a Schmitt trigger (CDB 413), a logic block and a transistor for the sense establishment. The feeding of the armature is done by two antiparallel thyristors that compose a bidirectional half-wave rectifier, the command for one or the other sense being obtained by closing the contacts I, D via the signals provided by the logic block, shown in Fig. 2.97.a. The voltage comparator and the trigger form a non-linear element with the "window-type" characteristic represented in Fig. 2.98.a.

$$u_e = \begin{cases} 1, & u_c > U_{c1}, & u_c < U_{c2} \\ 0, & U_{c2} < u_c, & U_{c1} > u_c \end{cases} \quad (2.109)$$



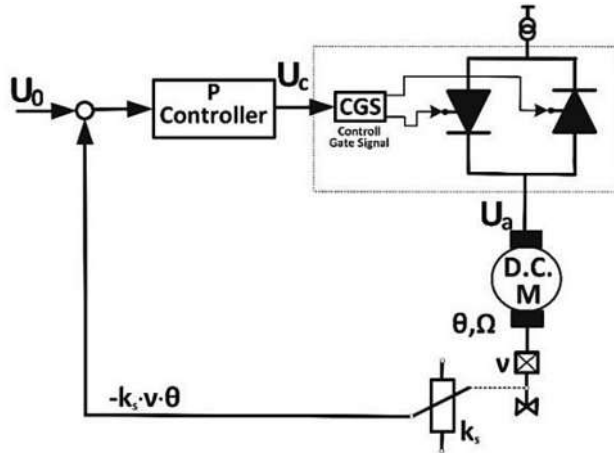


Fig. 2.96 Schematic diagram of the non-linear position loop system of a DC motor drive.

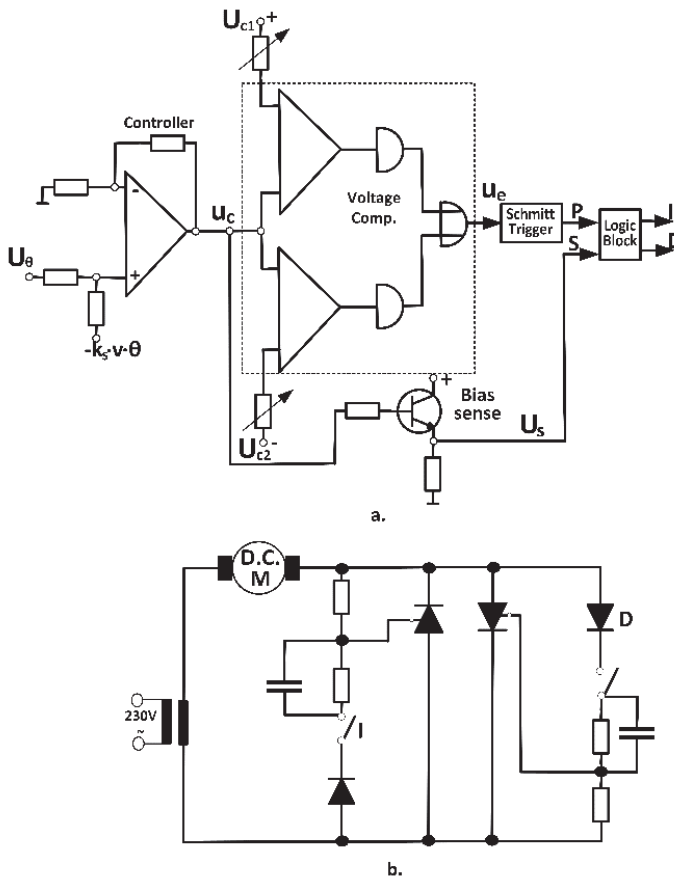


Fig. 2.97 Positioning scheme of a DC motor drive: a) the command; b) the power feeding.

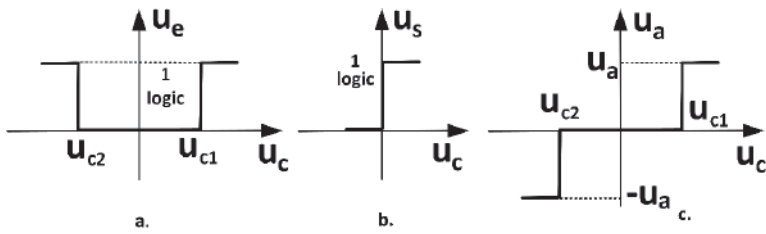


Fig. 2.98 Non-linear characteristics: a) comparator; b) sense; c) assemblage.

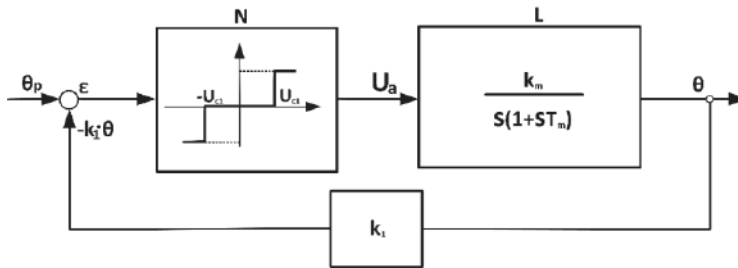


Fig. 2.99 Simplified block scheme of the system.

The element setting the sense has the characteristic from Fig. 2.98.b, and the two logical signals  $u_e$  and  $u_s$  provide the logical functions:

$$\begin{aligned} I &= P \cdot \bar{S} \\ D &= P \cdot S \end{aligned} \quad (2.110)$$

The function  $u_a = f(u_c)$  of the armature voltage according to the command is non-linear and can be written as:

$$u_a = \begin{cases} U_a, & u_c > U_{c1} \\ 0, & U_{c2} > u_c > U_{c1} \\ -U_a, & u_c < U_{c2} \end{cases} \quad (2.111)$$

and is represented in Fig. 2.98.c. Considering the other elements of the system as being linear, the block diagram of the system in Fig. 2.99 is obtained, in which the inductance of the motor was neglected. It contains both the non-linear element  $N(U_e)$  and the linear element corresponding to the machine. The system response is shown in Fig. 2.100. The existence of the insensibility threshold causes the system to exhibit a stationary error  $\varepsilon$ , due to the fact that  $u_e$  ranges between  $\pm U_{c1}$  and the motor is practically disconnected and operates uncontrollably. By accepting a maximum error of  $\varepsilon_{\max}$ , the relationship between the  $U_{c1}$  threshold and the error is:

$$U_{c1} = k_A \cdot \varepsilon_{\max} \quad (2.112)$$

where  $k_A$  is the global amplification factor.

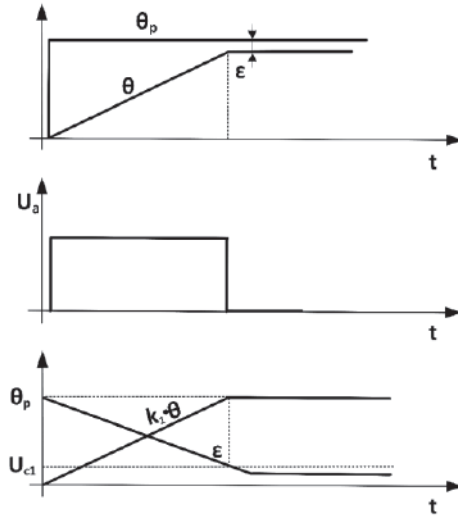


Fig. 2.100 System response to a step (ideal) signal input.

It is noted that the reduction of  $U_{cl}$  or the increase in amplification has as result the loss of the system stability. That is why this issue needs to be further studied. The stability study can be carried out starting from the transfer function of the closed-loop system,

$$Y(s) = \frac{N(u_\varepsilon) \cdot Y_m \cdot \frac{1}{s}}{1 + N(u_\varepsilon) \cdot Y_m \cdot \frac{1}{s} \cdot k_1} \quad (2.113)$$

The solution of the equation that cancels the denominator in the complex plan is:

$$\frac{Y_m \cdot k_1}{s} = -\frac{1}{N(u_\varepsilon)} \quad (2.114)$$

and gives system instability points. The two members of the equation will be represented in the plane Y by making  $s=j\omega$ . For the linear part, replacing the  $Y_m$  transfer function of the motor, it results:

$$\frac{k_1 \cdot Y_m}{s} \Big|_{s=j\omega} = -\frac{k_m \cdot T_m \cdot k_1}{1 + \omega^2 \cdot T_m^2} - j \cdot \frac{k_m \cdot k_1}{\omega \cdot (1 + \omega^2 \cdot T_m^2)} \quad (2.115)$$

and for the non-linear part, being a real function, it will occupy in the plane Y the negative part of the real axis starting with the abscissa,

$$\frac{1}{N_{\min}} = -\left(\frac{U_a}{U_{cl}}\right)^{-1} \quad (2.116)$$

where  $N_{min}$  represents the minimum non-linear function. The representation of the relationships (2.115) and (2.116) is shown in Fig. 2.101 a. The system is clear stable, there is no intersection between the two curves. If the inductance  $L_a$  is taken into account, the problem is complicated by inserting an additional pole on the direct loop by complicating the  $Y_m$  transfer function. The curve  $k_i Y_m/s$  also travels the quadrant II, as shown in Fig. 2.101 b.

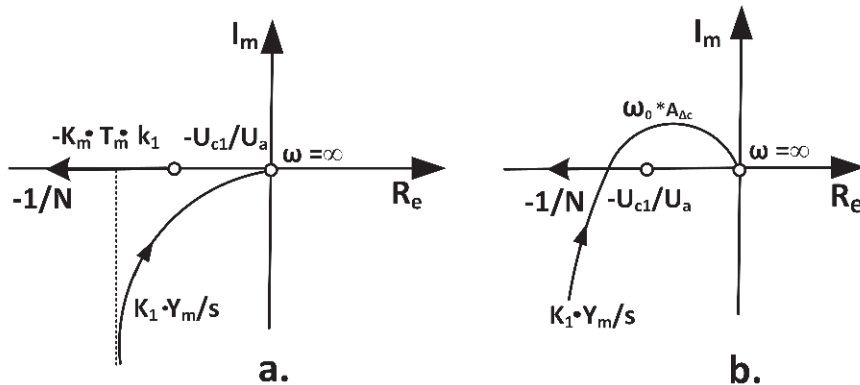


Fig. 2.101 Explanatory to the stability study:  $L_a = 0$ ; b.  $L_a \neq 0$ .

The two curves intersect through points that can be determined analytically or graphically. To bring the system to the stable area, either  $\frac{1}{N}$  moves to the left or  $k_i y_m/s$  moves to the right to avoid their intersection. The problem is solved by adjusting the transmission ratio  $k_i$  or the  $U_{c1}$  threshold.

### 2.5.5.3 Incremental positioning systems

The incremental positioning feature is that the programmed distance is obtained based on a required speed profile. For this reason, incremental positioning schemes are speed control systems with an additional position loop for positioning cycle termination. The principle of such a positioning system is shown in Fig. 2.102. When applying a starting impulse, the system receives a voltage  $U_c$  the maximum deviation  $u_c$  and the DC motor accelerates to the speed  $\Omega_L$ . During this time, the motion transducer produces a number of pulses counted by the counter. When the required distance is reached, a stop impulse cancelling the reference value  $U_c$  is given. The deviation is less than 0 and the machine brakes until it stops. Between the start and stop pulses, the position loop is disconnected, with only the speed control being performed. The displacement obtained is:

$$\theta_L = \Omega_L \cdot \left[ \frac{1}{2} \cdot (t_a + t_f) + t_m \right] \quad (2.117)$$

where the notations are those in Fig. 2.102. Consideration must be given to the additional movement during braking. This displacement generates a non-cumulative error that is part of the shaded area of the speed profile (see Fig. 2.102.b).

The positioning error is, therefore, proportional to the braking movement:

$$\theta_f = \frac{1}{2} \cdot \Omega_L \cdot t_f \quad (2.118)$$

In order to reduce  $\theta_f$  as much as possible for a given speed  $\Omega_L$ , it is necessary to reduce the braking duration, which requires the use of a low inertia and a maximum allowable current DC motor. It is further assumed that the load is a wagon having the radius  $r$ , the peripheral speed  $v$ , the friction torque  $M_r$  and the total moment of inertia  $J$ . The distance travelled during braking is:

$$S_f = \frac{J}{2 \cdot r_c} \cdot \frac{v^2}{M_r + k \cdot \frac{U_a}{R_a}} \quad (2.119)$$

being deduced from the motion equation. The influence of  $v$ ,  $M_r$ ,  $R_a$ ,  $U_a$  parameters variation over the distance  $S_f$  is investigated, based on the known relationship from the errors calculation:

$$\Delta S_f = \frac{\partial S_f}{\partial v} \cdot \Delta v + \frac{\partial S_f}{\partial M_r} \cdot \Delta M_r + \frac{\partial S_f}{\partial U_a} \cdot \Delta U_a + \frac{\partial S_f}{\partial R_a} \cdot \Delta R_a \quad (2.120)$$

After performing the partial derivatives, it results:

$$\Delta S_f = \frac{J}{2r_c} \cdot \left\{ \frac{2}{M_r + k \cdot \frac{U_a}{R_a}} \cdot \Delta v + \frac{v^2}{(M_r + k \cdot \frac{U_a}{R_a})^2} \cdot \left( -\Delta M_r - k \cdot \frac{\Delta U_a}{R_a} + \frac{k \cdot U_a}{R_a^2} \cdot \Delta R_a \right) \right\} \quad (2.121)$$

The parameters  $U_a$  and  $R_a$  have the greatest influence on the  $S_f$  variation and, therefore, constant current control (torque) during the transient process is required. An improvement in accuracy is obtained if the speed control is subordinated to the position control, as shown in Fig. 2.103. The system performs a positioning following a trapezoidal speed profile. Once the motor is started, the counter countdown begins. Its content is converted to a continuous CAN signal, giving a signal proportional to the content of the counter, representing the analogue position deviation. At the beginning  $u_c - u_r = \max$ . and the motor accelerates in response to a step signal.



## 2.6 References

- [1] I. Țopa, L. Diaconu "Acționări electrice reglabile cu mașini de curent continuu", Matrix Rom, București, 2009.
- [2] R. Măgureanu "Mașini și acționări electrice. Tendințe actuale", Editura Tehnică, București, 1988.
- [3] S. Mușuroi, D. Popovici "Acționări electrice cu servomotoare", Editura Politehnică, Timișoara, 2006.
- [4] D. Popovici "Bazele convertoarelor statice", Editura Politehnică, Timișoara, 1999.
- [5] B. Bose "Power electronics and Variable Frequency Drives", IEEE Press, New York, 1997.
- [6] A. Kelemen, M. Imecs "Electronică de putere", Editura Didactică și Pedagogică, București, 1983.
- [7] M. Meyer "Mutatoare cu comutație forțată", Editura Tehnică, București, 1970.
- [8] E. Seracin, D. Popovici, "Tehnica acționărilor electrice", Editura Tehnică, București, 1985.
- [9] A. Fransua, R. Măgureanu "Mașini și acționări electrice", Editura Tehnică, București, 1986.
- [10] A. Fransua, R. Măgureanu, M. Tocaci "Mașini și acționări electrice". Culegere de probleme, Editura Didactică și Pedagogică, București, 1980.
- [11] I. F. Soran "Sisteme de acționare electrică", Matrix Rom, București, 2010.
- [12] D. Popovici "Frânarea recuperativă cu variatoare de tensiune continuă la mașinile de curent continuu". Teză de doctorat, I.P. "Traian Vuia", Timișoara, 1980.
- [13] D. Popovici "Calculul energiei recuperative la frânarea vehiculelor autonome în impulsuri". EEA-Electrotehnica 26, 5, 170-174, 1978.
- [14] D. Popovici, P. Scăreanu "Stabilirea parametrilor comenzii variatorului de tensiune continuă la alimentarea unei mașini de curent continuu", Bul. Șt. și tehn. al IP "Traian Vuia", Timișoara, Seria Electrotehnica, 22, 1, 174-176, 1977.
- [15] D. Popovici, P. Scăreanu "Aplicații de calcul din utilizările energiei electrice în Fortran", IP "Traian Vuia", Timișoara, 1975.
- [16] D. Comșa, S. Darie, V. Maier, M. Chindriș "Proiectarea instalațiilor electrice industriale", Editura Didactică și Pedagogică, București, 1981.
- [17] I. Străinescu "Variatoare statice de tensiune continuă", Editura Tehnică, București, 1983.
- [18] L. Cantemir, M. Orișor "Tracțiune electrică", Editura Didactică și Pedagogică, București, 1971.
- [19] D. V. Vasiliev, B.A. Mitrofanov "Calculul și proiectarea sistemelor de urmărire". Editura Tehnică, București, 1966.
- [20] R. Schönfeld, E. Habiger "Automatisierte Elektroantriebe". VEB Verlag Technik, Berlin, 1981.
- [21] A. Bitoleanu, ș.a. "Convertoare statice", Editura INFOMED, Craiova, 1997.
- [22] A. Kelemen, M. Imecs "Acționări electrice". Editura Didactică și Pedagogică, București, 1979.
- [23] I. Boldea "Transformatoare și mașini electrice", Editura Politehnică, Timișoara, 2001.
- [24] R. Schönfeld, E. Habiger "Automatisierte Elektroantriebe", VEB Verlag Technik, Berlin,

## 3.1 General considerations

The modernization of technological processes, the massive implementation of automation, robotics and new generations of programmed machine tools in all industry branches, require the use of rapid, accurate and economically efficient electric drive systems, in the conditions of an optimum functional behavior.

In the context of an accelerated technical progress, electric car drives must provide a high performance at starting, braking, reversing, and speed change and control, and a correlation of the movements between mechanisms of the same plant. All these technical requirements have created the premises for the development of complex drives, mainly by using static converters with semiconductor components, which ensure the automatic control of the production processes with low energy consumption [1].

Nowadays, variable speed drives, electronically powered in both the hard and the soft circuits, are one of the most important levers to boost the technical progress in a modern industry. The recent evolution of power electronics as well as the rapid dynamics recorded in the microcontroller field, the digital signal processors (DSP) field, and the digital signal controllers (DSC) field, which is actually a combination of the first two, make the use of variable speed electric drives become more attractive than ever.

Today, the variable electric drives involve both DC and AC machines.

The DC electric machines were the first electric machines to be used and their electric drive systems, especially the ones with variable speed, dominated the field of electric drives for more than a century [2]. The increasing qualitative requirements for the automated control systems and the development of power electronics have resulted in a continuous use of the DC motors. The adaptability of the DC motors in different electric power drive systems should be highlighted. Derived or separated DC electric drives are the most used in practice due to their good capabilities of: changing and varying speed, starting, reversing, economical electric braking and automatic driving.

Despite all undeniable advantages these motor types have, their use in today's drive systems is, somehow limited by a few drawbacks. Thus, in the DC, the power is transmitted to the rotor by the slipping contacts of the brush-collector system, which limits their nominal power to 10 – 15 MW. The rated voltage, and hence the speed, is limited (maximum 1500 V) by the maximum allowable voltage between the two collector lamellas, which



cannot exceed 20-24 V due to switching considerations. The presence of the collector also leads to an increase in the cost price of the DC car, reducing its reliability in comparison, for example, with induction motors with a short-circuited rotor. In addition, the existence of the "brush-collector" mobile contacts is directly responsible for the wear of both the collector and the brushes in time. These phenomena make the functional parameters of the DC motor move away from the nominal, optimistic ones.

Removing the negative aspects associated with the switching: wear, spark and electromagnetic noise, it often involves complex construction of DC motors by introducing of a commutation winding (sometimes even of a compensating winding) and by achieving a precise brush positioning, with negative consequences on the cost price.

The three-phase induction motors have experienced a rapid and widespread expansion in the electric drives and the reasons - very well-known from the literature - are the following [2]:

- the distribution of the electricity is currently done by using a three-phase alternative voltages system, this being the most economical system; low-power asynchronous motors can be coupled to a direct network without using intermediate elements;
- induction motors (especially those with a short-circuited rotor) are characterized by a simple and robust construction, being also recognized as the most reliable electric motors.

Compared to the DC motors, short-circuited rotor asynchronous motors are distinguished by numerous advantages, - briefly presented below -, which make their use in electric drives attractive.

Thus, by removing sensitive components (e.g. the collector-brush system), short-circuited rotor induction motors are safe to operate, having a virtually constant rotational speed at the given load and inertia moments of the moving parts (rotor) lower to those of the DC motors. They can operate at higher speeds for long periods without maintenance, requiring only AC power supply. The value of the stator voltage is not limited by the commutation.

The advantage of the induction motors over the DC motors is also due to economic reasons. The price of short-circuited rotor asynchronous motors is much lower (the ratio of power [kW] / weight [kg] is practically double as opposed to that of the DC motors).

Due to the technical and economic advantages mentioned above, the induction motor is currently being widely used in easy drive systems, which is the reason why it has been built into a wide range of power and speed. The use of these motors in variable speed drive systems has, however, been limited until recently, only because of the difficulties concerning the control and the cost of static frequency converters.

Recent achievements in the field of tuning technology, the development of power electronics in general and of microelectronics, particularly, have made the short-circuited rotor asynchronous motor to gain an increased interest in the demanding control systems area.

Modern control, scalar or field-oriented performance techniques are currently used being as control strategies for converters built using semiconductor elements (IGBT or MOS transistors).

As a conclusion of the above-mentioned facts, it can be stated that the field of variable electric drives, involving induction machines fed directly by static frequency converters, represents an important subject for the industry specialists due to the technical-economic advantages they may provide.

## 3.2 Functional equations and mechanical characteristics

### 3.2.1 Equations in phase coordinates

The equations in phase coordinates will be established for a wound three-phase induction machine, to which both the stator and the rotor have cylindrical symmetry. The symmetrical cage rotor can be reduced to a symmetrical three-phase winding. Next, the indices A, B, C for the three stator phases and a, b, c for the rotor phases will be used.

In Fig. 3.1, the model of the considered machine in phase coordinates is represented. The reference axes of the stator  $R_s$  and of the rotor  $R_r$ , were considered to be superposed to the axis A of the stator and to the axis a of the rotor, respectively. The rotor has the angular speed in electrical terms, its position being indicated by the angle measured between the axes  $R_s$  and  $R_r$ .

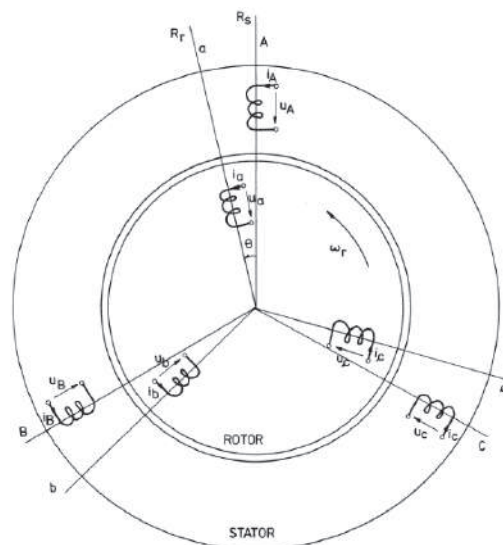


Fig. 3.1 The physical model of a wound three-phase induction machine.

The assumed hypotheses are the neglect of saturation and iron losses, the constant air gap and the consideration of the magnetic field distribution along the air gap as being sinusoidal. By respecting the association of the positive senses corresponding to the

receiver, the voltage equations and flux equations in instantaneous quantities can be written in a matrix form as follows [3]:

$$[u] = [R] \cdot [i] + \frac{d}{dt} [\psi] \quad (3.1)$$

and

$$[\psi] = [L] \cdot [i], \quad (3.2)$$

where the voltages matrix and the currents matrix form:

$$[u] = \begin{bmatrix} u_A \\ u_B \\ u_C \\ \hline u_a \\ u_b \\ u_c \end{bmatrix}; \quad [i] = \begin{bmatrix} i_A \\ i_B \\ i_C \\ \hline i_a \\ i_b \\ i_c \end{bmatrix}, \quad (3.3)$$

and the resistances matrix:

$$[R] = \begin{bmatrix} R_A & 0 & 0 & | & 0 & 0 & 0 \\ 0 & R_A & 0 & | & 0 & 0 & 0 \\ 0 & 0 & R_A & | & 0 & 0 & 0 \\ \hline 0 & 0 & 0 & | & R_a & 0 & 0 \\ 0 & 0 & 0 & | & 0 & R_a & 0 \\ 0 & 0 & 0 & | & 0 & 0 & R_a \end{bmatrix} \quad (3.4)$$

In (3.4),  $R_A$  is the phase resistance of the stator winding and  $R_a$  is the phase resistance of the rotor winding. Machine symmetry allows the consideration of  $R_A = R_B = R_C$  and  $R_a = R_b = R_c$ , respectively.

The inductances matrix  $[L]$  is then determined.

The real inductances that characterize the physical model of the considered machine are: the total inductance corresponding to a stator phase  $L_{AA}$  and to a rotor phase  $L_{aa}$ ; the mutual inductance between two stator phases  $L_{AB}$  and between two rotor phases  $L_{ab}$ ; the mutual inductance between a stator and a rotor phase  $L_{Aa}$ , respectively.

The total inductances of  $L_{AA}$  and  $L_{aa}$  can be written as:

$$L_{AA} = L_{AA\sigma} + L_{AAu} \quad (3.5)$$

respectively:

$$L_{aa} = L_{aa\sigma} + L_{aau} \quad (3.6)$$

Where  $L_{AA\sigma}$  and  $L_{aa\sigma}$  are the leakage inductances of the stator and rotor phases, and  $L_{AAu}$  and  $L_{aau}$  are the main inductances of a stator phase and of a rotor phase, respectively. These main inductances refer to the case of single-phase power supply and are defined based on the main field passing through the air gap. Therefore, it can be written that:

$$L_{AAu} = L_{AAh} \text{ and } L_{aau} = L_{aah} \quad (3.7)$$

where  $L_{AAh}$  and  $L_{aah}$  are the main inductances of a stator phase and of a rotor phase in the case of single-phase power supply, respectively.

Between the total machine own inductances of the stator and rotor phases there are the relationships:

$$L_{AA} = L_{BB} = L_{CC} , \quad (3.8)$$

$$L_{aa} = L_{bb} = L_{cc} \quad (3.9)$$

The following relationships define the mutual inductances between two windings disposed and on the stator:

$$L_{AB} = L_{AB\sigma} + L_{ABu} , \quad (3.10)$$

and on the rotor, respectively:

$$L_{ab} = L_{ab\sigma} + L_{abu} \quad (3.11)$$

where  $L_{AB\sigma}$ ,  $L_{ab\sigma}$  are the mutual leakage inductances between two stator and rotor phases and  $L_{ABu}$ ,  $L_{abu}$  are the mutual main inductances between two stator and rotor phases.

Taking into account the cylindrical symmetry of the machine, the relationships can be written as:

For  $\alpha_s = \frac{2\pi}{3p}$  (the center angle between the stator phases),

$$L_{ABu} = L_{BCu} = L_{CAu} = L_{AAh} \cos \frac{2\pi}{3} = -\frac{L_{AAh}}{2} \quad (3.12)$$

And for  $\alpha_s = \frac{4\pi}{3p}$ :

$$L_{ACu} = L_{BAu} = L_{CBu} = L_{AAh} \cos \frac{4\pi}{3} = -\frac{L_{AAh}}{2}, \quad (3.13)$$

respectively.

For the rotor, similar relationships are obtained. Thus:

for  $\alpha_r = \frac{2\pi}{3p}$  (center angle between rotor phases),

$$L_{abu} = L_{bcu} = L_{cau} = L_{aah} \cos \frac{2\pi}{3} = -\frac{L_{aah}}{2}, \quad (3.14)$$

and for  $\alpha_r = \frac{4\pi}{3p}$ ,

$$L_{acu} = L_{bau} = L_{cbu} = L_{aah} \cos \frac{4\pi}{3} = -\frac{L_{aah}}{2}. \quad (3.15)$$

Taking into account the relationships (3.12), (3.13), (3.14) and (3.15), the relationships (10) and (11) can be written down as follows:

$$L_{AB} = -L_{AB\sigma} - \frac{1}{2}L_{AAh}, \quad (3.16)$$

$$L_{ab} = -L_{ab\sigma} - \frac{1}{2}L_{aah}. \quad (3.17)$$

The stator-rotor mutual inductances are defined according to the relationships:

$$L_{Aa} = L_{Bb} = L_{Cc} = L_m \cos \theta \quad (3.18)$$

$$L_{Aa} = L_{Bb} = L_{Cc} = L_m \cos\left(\theta + \frac{2\pi}{3}\right) \quad (3.19)$$

$$L_{Aa} = L_{Bb} = L_{Cc} = L_m \cos\left(\theta - \frac{2\pi}{3}\right) \quad (3.20)$$

$$L_{aA} = L_{bB} = L_{cC} = L_m \cos(-\theta) = L_m \cos \theta \quad (3.21)$$

$$L_{bA} = L_{cB} = L_{aC} = L_m \cos\left(-\theta + \frac{4\pi}{3}\right) = L_m \cos\left(\theta + \frac{2\pi}{3}\right) \quad (3.22)$$

$$L_{bA} = L_{cB} = L_{aC} = L_m \cos\left(-\theta + \frac{4\pi}{3}\right) = L_m \cos\left(\theta + \frac{2\pi}{3}\right) \quad (3.23)$$

In the above relationships,  $L_m$  represents the maximum mutual inductance between a stator phase and a rotor phase, when the axes associated to the two windings coincide.

The equation system (3.1) is nonlinear because both currents and inductances vary over time, depending on the position of the rotor, which complicates the study. The linearization of the system can be accomplished by using appropriate transformations in order to obtain a set of equations in which the inductances are no longer dependent on the rotor position or time.

### 3.2.2 The transformed equations of the three-phase asynchronous machine. The $dq0$ model

The transition from the machine model in phase coordinates to the  $dq0$  model of a three-phase asynchronous machine is based on the Park transformation.

The  $dq0$  system is thus, placed at a moment in time when the  $d$ -axis is phase-shifted with an angle  $\theta_s$  to the axis  $R_s$  and with an angle  $\theta_r$  to the axis  $R_r$  (see Fig. 3.2) [3].

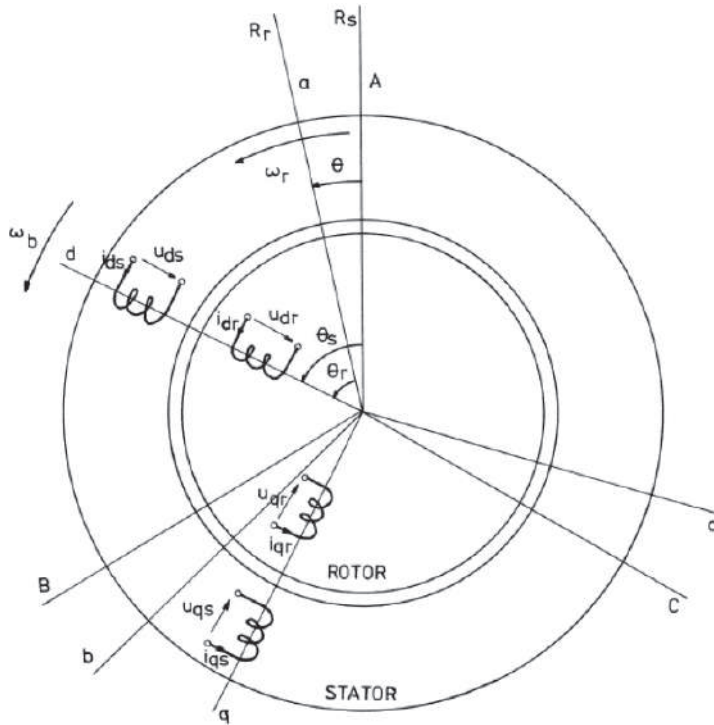


Fig. 3.2 Turning from the real machine model to the equivalent machine model.

The direct transformation matrix  $[T_{dq0}]$  has the form in (3.24) and its inverse  $[T_{dq0}^{-1}]$  is expressed in (3.25).

$$[T_{dq0}] = \frac{2}{3} \cdot \begin{bmatrix} \cos \theta_s & \cos\left(\theta_s - \frac{2\pi}{3}\right) & \cos\left(\theta_s + \frac{2\pi}{3}\right) & 0 & 0 & 0 \\ -\sin \theta_s & -\sin\left(\theta_s - \frac{2\pi}{3}\right) & -\sin\left(\theta_s + \frac{2\pi}{3}\right) & 0 & 0 & 0 \\ \frac{1}{2} & \frac{1}{2} & \frac{1}{2} & 0 & 0 & 0 \\ 0 & 0 & 0 & \cos \theta_r & \cos\left(\theta_r - \frac{2\pi}{3}\right) & \cos\left(\theta_r + \frac{2\pi}{3}\right) \\ 0 & 0 & 0 & -\sin \theta_r & -\sin\left(\theta_r - \frac{2\pi}{3}\right) & -\sin\left(\theta_r + \frac{2\pi}{3}\right) \\ 0 & 0 & 0 & \frac{1}{2} & \frac{1}{2} & \frac{1}{2} \end{bmatrix} \quad (3.24)$$

$$[T_{dq0}^{-1}] = \begin{bmatrix} \cos \theta_s & -\sin \theta_s & 1 & 0 & 0 & 0 \\ \cos\left(\theta_s - \frac{2\pi}{3}\right) & -\sin\left(\theta_s - \frac{2\pi}{3}\right) & 1 & 0 & 0 & 0 \\ \cos\left(\theta_s + \frac{2\pi}{3}\right) & -\sin\left(\theta_s + \frac{2\pi}{3}\right) & 1 & 0 & 0 & 0 \\ 0 & 0 & 0 & \cos \theta_r & -\sin \theta_r & 1 \\ 0 & 0 & 0 & \cos\left(\theta_r - \frac{2\pi}{3}\right) & -\sin\left(\theta_r - \frac{2\pi}{3}\right) & 1 \\ 0 & 0 & 0 & \cos\left(\theta_r + \frac{2\pi}{3}\right) & -\sin\left(\theta_r + \frac{2\pi}{3}\right) & 1 \end{bmatrix} \quad (3.25)$$

The transition from the actual (phase) quantities to the equivalent quantities  $dq0$  is done using the relationships:

$$\begin{aligned} [\mathbf{u}_{dq0}] &= [T_{dq0}] \cdot [\mathbf{u}] , \\ [\mathbf{i}_{dq0}] &= [T_{dq0}] \cdot [\mathbf{i}] , \\ [\boldsymbol{\psi}_{dq0}] &= [T_{dq0}] \cdot [\boldsymbol{\psi}] , \end{aligned} \quad (3.26)$$

After performing the operations and grouping, the relationships established for the voltages and fluxes, for the equivalent machine the following system of equations is obtained [3]:

$$\begin{aligned}
 u_{ds} &= R_s i_{ds} + \frac{d\psi_{ds}}{dt} - \omega_b \psi_{qs} , \\
 u_{qs} &= R_s i_{qs} + \frac{d\psi_{qs}}{dt} + \omega_b \psi_{ds} , \\
 u_{os} &= R_s i_{os} + \frac{d\psi_{os}}{dt} , \\
 u_{dr} &= R_r i_{dr} + \frac{d\psi_{dr}}{dt} - (\omega_b - \omega_r) \psi_{qr} , \\
 u_{qr} &= R_r i_{qr} + \frac{d\psi_{qr}}{dt} + (\omega_b - \omega_r) \psi_{dr} , \\
 u_{or} &= R_r i_{or} + \frac{d\psi_{or}}{dt} , \\
 \psi_{ds} &= L_s i_{ds} + L_{sr} i_{dr} , \\
 \psi_{qs} &= L_s i_{qs} + L_{sr} i_{qr} , \\
 \psi_{os} &= L_{os} i_{os} , \\
 \psi_{dr} &= L_r i_{dr} + L_{sr} i_{ds} , \\
 \psi_{qr} &= L_r i_{qr} + L_{sr} i_{qs} , \\
 \psi_{or} &= L_{or} i_{or} ,
 \end{aligned} \tag{3.27}$$

as well as for the electromagnetic torque:

$$m = \frac{3}{2} p (\psi_{ds} i_{qs} - \psi_{qs} i_{ds}) \tag{3.28}$$

and for the motion equation, respectively:

$$m - m_R = \frac{J}{p} \cdot \frac{d^2 \theta}{dt^2} \tag{3.29}$$

$m_R$  is the resistant torque load.

In (3.27),  $R_s$  and  $R_r$  represent the resistances of the windings corresponding to the two armatures,  $L_s$  and  $L_r$  are the total inductances of the stator and of the rotor windings,



respectively; and  $L_{sr}$  is the mutual inductance between the stator and the rotor.  $L_s$ ,  $L_r$  and  $L_{sr}$  are the cyclic inductances, represented by the windings in the resulting field.  $L_{os}$  and  $L_{or}$  are the zero sequence inductances of the stator and of the rotor windings, respectively.

The relationships between the equivalent parameters and the actual physical phase parameters is shown below. Thus, the resistances can be written as:

$$R_s = R_A \text{ and } R_r = R_a \quad (3.30)$$

The total inductance of the stator winding is composed of the main inductance  $L_{sh}$  (cyclic) and the leakage inductance  $L_{s\sigma}$  (cyclic):

$$L_s = L_{s\sigma} + L_{hs}, \quad (3.31)$$

where:

$$L_{s\sigma} = L_{AA\sigma} + L_{AB\sigma}, \quad (3.32)$$

$$L_{hs} = \frac{3}{2} L_{AAh}. \quad (3.33)$$

$L_{hs}$  is the main inductance of the machine stator phase when the machine is three-phase fed, unlike  $L_{AAh}$ , which represents the main inductance of the stator phase in the case of single-phase voltage supply. Both inductances are defined based on the main field passing through the air gap [4]. Introducing (3.32) and (3.33) into (3.31) yields:

$$L_s = L_{AA\sigma} + L_{AB\sigma} + \frac{3}{2} L_{AAh} \quad (3.34)$$

The mutual inductance between the stator and the rotor is also defined based on the main field:

$$L_{sr} = \frac{3}{2} L_m \quad (3.35)$$

The homopolar inductance of the stator winding is introduced based on the relationships:

$$L_{os} = L_{AA\sigma} + 2L_{AB\sigma} \quad (3.36)$$

Similarly, the following rotor equations are obtained:

$$L_r = L_{\sigma r} + L_{hr} = L_{aa\sigma} + L_{ab\sigma} + \frac{3}{2} L_{aah} \quad (3.37)$$

$$L_{or} = L_{aa\sigma} + 2L_{ab\sigma} \quad (3.38)$$

Relationships (3.27) receive different shapes of expression depending on how the reference system is chosen.

Thus, if the reference system is fixed to the rotor, then  $\omega_b = \omega_r$  and the following relationships result in:

$$\begin{aligned}
 u_{ds} &= R_s i_{ds} + \frac{d\psi_{ds}}{dt} - \omega_r \psi_{qs} , \\
 u_{qs} &= R_s i_{qs} + \frac{d\psi_{qs}}{dt} + \omega_r \psi_{ds} , \\
 u_{os} &= R_s i_{os} + \frac{d\psi_{os}}{dt} , \\
 u_{dr} &= R_r i_{dr} + \frac{d\psi_{dr}}{dt} , \\
 u_{qr} &= R_r i_{qr} + \frac{d\psi_{qr}}{dt} , \\
 u_{or} &= R_r i_{or} + \frac{d\psi_{or}}{dt} .
 \end{aligned} \tag{3.39}$$

If the reference system is fixed to the stator, then  $\omega_b=0$  and the following expressions are obtained:

$$\begin{aligned}
 u_{ds} &= R_s i_{ds} + \frac{d\psi_{ds}}{dt} , \\
 u_{qs} &= R_s i_{qs} + \frac{d\psi_{qs}}{dt} , \\
 u_{os} &= R_s i_{os} + \frac{d\psi_{os}}{dt} , \\
 u_{dr} &= R_r i_{dr} + \frac{d\psi_{dr}}{dt} + \omega_r \psi_{qr} , \\
 u_{qr} &= R_r i_{qr} + \frac{d\psi_{qr}}{dt} - \omega_r \psi_{dr} , \\
 u_{or} &= R_r i_{or} + \frac{d\psi_{or}}{dt} .
 \end{aligned} \tag{3.40}$$

For the synchronous reference system, when  $\omega_b = \omega_s$  (synchronous angular velocity), the followings results are obtained:

$$\begin{aligned}
 u_{ds} &= R_s i_{ds} + \frac{d\psi_{ds}}{dt} - \omega_s \psi_{qs} , \\
 u_{qs} &= R_s i_{qs} + \frac{d\psi_{qs}}{dt} + \omega_s \psi_{ds} , \\
 u_{os} &= R_s i_{os} + \frac{d\psi_{os}}{dt} , \\
 u_{dr} &= R_r i_{dr} + \frac{d\psi_{dr}}{dt} - (\omega_s - \omega_r) \psi_{qr} , \\
 u_{qr} &= R_r i_{qr} + \frac{d\psi_{qr}}{dt} + (\omega_s - \omega_r) \psi_{dr} , \\
 u_{or} &= R_r i_{or} + \frac{d\psi_{or}}{dt} .
 \end{aligned} \tag{3.41}$$

### 3.2.3 The phasor model of three-phase asynchronous machines

The equations are written starting from the model in the phase coordinates.

By marking the stator phase fluxes with  $\psi_A, \psi_B, \psi_C$  and the rotor phase fluxes with  $\psi_a, \psi_b, \psi_c$  the spatial phasors of stator flux  $\underline{\psi}_s$ , of rotor flux  $\underline{\psi}_r$  and of stator current  $i_s$  and rotor current  $i_r$ , respectively, are introduced with the following relationships [3]:

$$\underline{\psi}_s = \frac{2}{3} (\psi_A + a\psi_B + a^2\psi_C) , \tag{3.42}$$

$$\underline{\psi}_r = \frac{2}{3} (\psi_a + a \cdot \psi_b + a^2\psi_c) , \tag{3.43}$$

$$\underline{i}_s = \frac{2}{3} (i_A + ai_B + a^2i_C) , \tag{3.44}$$

$$\underline{i}_r = \frac{2}{3} (i_a + ai_b + a^2i_c) . \tag{3.45}$$

The flux from a certain stator phase of the machine is defined by both the three-phase stator and the rotor currents system. Thus, for the fluxes of stator phases *A*, *B* and *C*, the following relationships can be written [3]:

$$\psi_A = L_s i_A + i_a L_m \cos \theta + i_b L_m \cos \left( \theta + \frac{2\pi}{3} \right) + i_c L_m \cos \left( \theta - \frac{2\pi}{3} \right) \tag{3.46}$$

$$\psi_B = L_S i_B + i_a L_m \cos\left(\theta - \frac{2\pi}{3}\right) + i_b L_m \cos\theta + i_c L_m \cos\left(\theta + \frac{2\pi}{3}\right) \quad (3.47)$$

$$\psi_C = L_S i_C + i_a L_m \cos\left(\theta + \frac{2\pi}{3}\right) + i_b L_m \cos\left(\theta - \frac{2\pi}{3}\right) + i_c L_m \cos\theta \quad (3.48)$$

The spatial phasor of the stator resulting flux is obtained by computing the fluxes of the three-stator phases given by the relationships (3.46), (3.47) and (3.48) using (3.42) and taking into account (3.44):

$$\underline{\psi}_s = L_s \underline{i}_s + L_{sr} \underline{i}_r e^{j\theta} \quad (3.49)$$

Similarly, for the spatial phasor of the resulting rotor flux, the following relationships are obtained:

$$\underline{\psi}_r = L_r \underline{i}_r + L_{sr} \underline{i}_s e^{-j\theta} \quad (3.50)$$

The equations of stator and rotor voltages, written with the aid of the spatial phasors have the following shape [3]:

$$\underline{u}_s = R_s \underline{i}_s + \frac{d\underline{\psi}_s}{dt} \quad (3.51)$$

$$\underline{u}_r = R_r \underline{i}_r + \frac{d\underline{\psi}_r}{dt} \quad (3.52)$$

The equation (3.51) is valid in the stator coordinate system, while the relationship (3.52) is valid in the coordinate system relative to the rotating rotor, whose real axis coincides with the  $\alpha$  phase axis. The analysis of electric machines uses a common axis system for both the stator and the rotor variables assuming that the  $dq$  coordinate system rotates with the angular velocity (see Fig. 3.3).

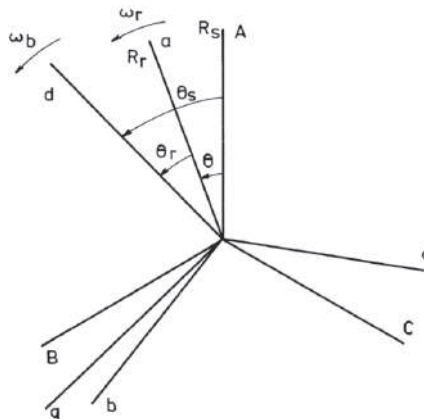


Fig. 3.3 The  $dq$  coordinate system associated with stator and rotor windings.

By transposing equations (3.51) and (3.52) into the  $dq$  coordinate system, their independence from the angle  $\theta$ , which determines the position of the rotor relative to the stator, is ensured. The following notations  $\underline{u}_s^{dq}$ ,  $\underline{i}_s^{dq}$ ,  $\underline{\psi}_s^{dq}$ ,  $\underline{u}_r^{dq}$ ,  $\underline{i}_r^{dq}$  and  $\underline{\psi}_r^{dq}$  are used for defining the spatial phasors of both the stator and the rotor voltages, the currents and the fluxes in the new coordinate system. After performing the calculations, the following results in [3]:

$$\underline{u}_s^{dq} = R_s \underline{i}_s^{dq} + \frac{d\underline{\psi}_s^{dq}}{dt} + j\underline{\psi}_s^{dq} \frac{d\theta_s}{dt} = R_s \underline{i}_s^{dq} + \frac{d\underline{\psi}_s^{dq}}{dt} + j\omega_b \underline{\psi}_s^{dq}, \quad (3.53)$$

$$\underline{u}_r^{dq} = R_r \underline{i}_r^{dq} + \frac{d\underline{\psi}_r^{dq}}{dt} + j\underline{\psi}_r^{dq} \frac{d(\theta_s - \theta)}{dt} = R_r \underline{i}_r^{dq} + \frac{d\underline{\psi}_r^{dq}}{dt} + j(\omega_b - \omega_r) \underline{\psi}_r^{dq}.$$

$$\begin{aligned} \underline{\psi}_s^{dq} &= L_s \underline{i}_s^{dq} + L_{sr} \underline{i}_r^{dq} \\ \underline{\psi}_r^{dq} &= L_r \underline{i}_r^{dq} + L_{sr} \underline{i}_s^{dq}. \end{aligned} \quad (3.54)$$

The index "dq" can be neglected because the form of the differential equations indicates the coordinate system in which the variables are written. This gives a simplification of the writing, relationships (53) and (54) becoming:

$$\begin{aligned} \underline{u}_s &= R_s \underline{i}_s + \frac{d\underline{\psi}_s}{dt} + j\omega_b \underline{\psi}_s, \\ \underline{u}_r &= R_r \underline{i}_r + \frac{d\underline{\psi}_r}{dt} + j(\omega_b - \omega_r) \underline{\psi}_r, \end{aligned} \quad (3.55)$$

respectively,

$$\begin{aligned} \underline{\psi}_s &= L_s \underline{i}_s + L_{sr} \underline{i}_r \\ \underline{\psi}_r &= L_r \underline{i}_r + L_{sr} \underline{i}_s. \end{aligned} \quad (3.56)$$

By considering appropriate particular values for  $\omega_b$ , equations (3.55) can be translated into any desired reference system.

Thus, for  $\omega_b = 0$  the voltages equations in the reference system fixed to the stator are obtained:

$$\begin{aligned} \underline{u}_s &= R_s \underline{i}_s + \frac{d\underline{\psi}_s}{dt}, \\ \underline{u}_r &= R_r \underline{i}_r + \frac{d\underline{\psi}_r}{dt} - j\omega_r \underline{\psi}_r. \end{aligned} \quad (3.57)$$

If the reference system is fixed with the rotor, then  $\omega_b = \omega_r$  and the equations (3.55) become:

$$\begin{aligned}\underline{u}_s &= R_s \underline{i}_s + \frac{d\underline{\psi}_s}{dt} + j\omega_r \underline{\psi}_s, \\ \underline{u}_r &= R_r \underline{i}_r + \frac{d\underline{\psi}_r}{dt}.\end{aligned}\tag{3.58}$$

For  $\omega_b = \omega_s$ , the following expressions in the synchronous reference system can be obtained:

$$\begin{aligned}\underline{u}_s &= R_s \underline{i}_s + \frac{d\underline{\psi}_s}{dt} + j\omega_s \underline{\psi}_s, \\ \underline{u}_r &= R_r \underline{i}_r + \frac{d\underline{\psi}_r}{dt} + j(\omega_s - \omega_r) \underline{\psi}_r.\end{aligned}\tag{3.59}$$

And for the torque, some equations highlighting the representative phasors of the fluxes and currents can be established. Thus:

$$m = \frac{3}{2} p \operatorname{Re} \left[ j \underline{\psi}_s \underline{i}_s^* \right] = \frac{3}{2} p \left| \underline{\psi}_s x \underline{i}_s \right|\tag{3.60}$$

or,

$$m = \frac{3}{2} p \operatorname{Re} \left[ -j \underline{\psi}_r \underline{i}_r^* \right] = \frac{3}{2} p \left| \underline{i}_r x \underline{\psi}_r \right|\tag{3.61}$$

where and are the complex phasors conjugated to and, respectively.

Next, the real rotor is replaced by an equivalent rotor used for computation. Equations (3.55) and (3.56) take the following shape:

$$\begin{aligned}\underline{u}_s &= R_s \underline{i}_s + \frac{d\underline{\psi}_s}{dt} + j\omega_b \underline{\psi}_s, \\ \underline{u}'_r &= R'_r \underline{i}'_r + \frac{d\underline{\psi}'_r}{dt} + j(\omega_b - \omega_r) \underline{\psi}'_r.\end{aligned}\tag{3.62}$$

and

$$\begin{aligned}\underline{\psi}_s &= L_s \underline{i}_s + L_{hs} \underline{i}'_r \\ \underline{\psi}'_r &= L'_r \underline{i}'_r + L_{hs} \underline{i}_s\end{aligned}\tag{3.63}$$

respectively,

where,

$$L_s = L_{\sigma s} + L_{hs} \quad (3.64)$$

$$L_r' = L_{\sigma r'} + L_{hs} \quad (3.65)$$

The variables marked by "'" correspond to the equivalent rotor used for computation. By introducing rotor quantities in p.u., the mutual cyclic inductance  $L_{sr}$  is replaced by the main cyclic inductance  $L_{hs}$ . This should be written as follows:

$$\underline{i}_m' = \underline{i}_s' + \underline{i}_r' \quad (3.66)$$

The main machine flux becomes:

$$\underline{\psi}_{hs}' = \underline{\psi}_{hr}' = L_{hs} (\underline{i}_s' + \underline{i}_r') = L_{hs} \underline{i}_m' \quad (3.67)$$

Between the variables relating to the rotor in p.u. and those relating to the real rotor, there are relationships, such as:

$$R_r' = K_e K_i R_r \quad (3.68)$$

$$L_r' = K_e K_i L_r \quad (3.69)$$

$$L_{hs} = K_i L_{sr} \quad (3.70)$$

$$\underline{u}_r' = K_e \underline{u}_r \quad (3.71)$$

$$\underline{i}_r' = \frac{1}{K_i} \underline{i}_r \quad (3.72)$$

$$\underline{\psi}_r' = K_e \underline{\psi}_r \quad (3.73)$$

In the above relationships,  $K_i$  is machine currents transformation ratio, and  $K_e$  represents the voltages transformation ratio.

If in (3.62) the flux derivatives are eliminated, the following voltages equations are obtained, (with  $p=d/dt$ ):

$$\begin{aligned} \underline{u}_s' &= R_s' \underline{i}_s' + pL_{\sigma s}' \underline{i}_s' + pL_{hs}' \underline{i}_m' + j\omega_b \underline{\psi}_s', \\ \underline{u}_r' &= R_r' \underline{i}_r' + pL_{\sigma r}' \underline{i}_r' + pL_{hs}' \underline{i}_m' + j(\omega_b - \omega_r) \underline{\psi}_r'. \end{aligned} \quad (3.74)$$

These equations correspond to the equivalent scheme presented in Fig. 3.4.

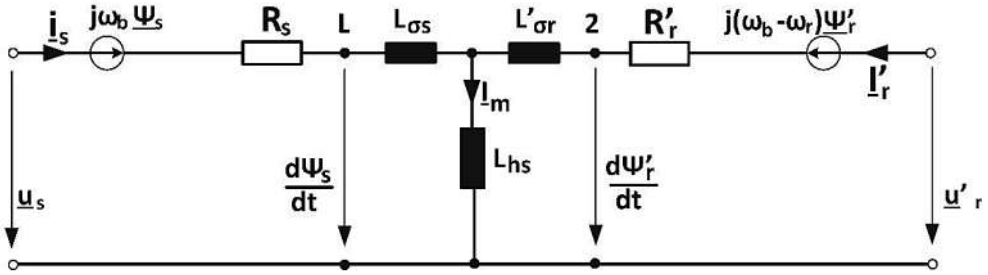


Fig. 3.4 The equivalent scheme of the induction machine during transients.

### 3.2.4. Mechanical characteristics of three-phase asynchronous machines

It is further considered that the machine is supplied by a symmetrical sinusoidal voltages system. In these conditions, the stator and rotor currents also form symmetrical sinusoidal systems and the resulting air gap rotating field is circular.

To put it simply, the notation "1" is used for the stator and "2" for the rotor. Thus:  $L_{\sigma s} = L_{1\sigma}$ ,  $L_{\sigma r} = L_{2\sigma}$ ,  $R_s = R_1$  and  $R_r = R_2$ . Therefore, the steady-state equations of the asynchronous machine are:

$$\begin{aligned} \underline{U}_1 &= \underline{Z}_1 \underline{I}_1 - \underline{U}_{e1} \\ \underline{U}'_2 &= -\underline{Z}'_2 \underline{I}'_2 + \underline{U}_{e1} \\ \underline{U}_{e1} &= -jX_{1m} \underline{I}_{01} \\ \underline{I}_{01} &= \underline{I}_1 + \underline{I}'_2 \end{aligned} \quad (3.75)$$

where :

$$\begin{aligned} \underline{Z}_1 &= R_1 + jX_1 \quad , \quad X_1 = \omega_1 L_{1\sigma} \\ \underline{Z}'_2 &= K_e K_i \underline{Z}_2 = \frac{R'_2}{s} + jX'_2 \\ R'_2 &= K_e K_i R_2 \quad , \quad X'_2 = K_e K_i X_2 = K_e K_i \omega_1 L_{2\sigma} \\ X_{1m} &= \omega_1 L_{hs} \end{aligned} \quad (3.76)$$

$X_{1m}$  being the magnetizing reaction corresponding to the main magnetic machine field.

The machine slip "s" is defined by the relationship:



$$s = \frac{\omega_1 - \omega_r}{\omega_1} \quad (3.77)$$

The usual T equivalent scheme of the machine is shown in Fig. 3.5.

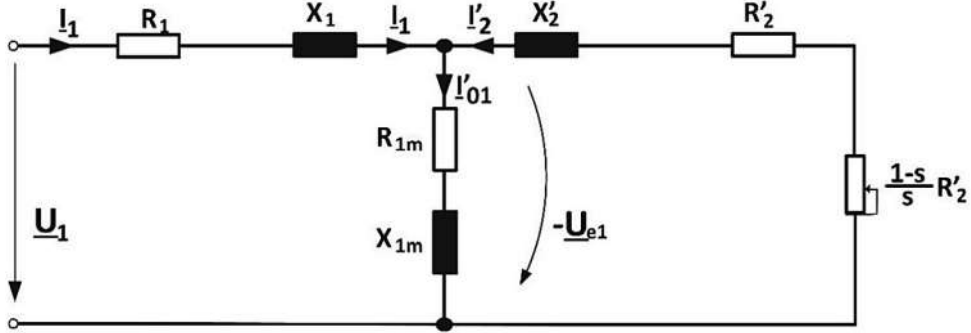


Fig. 3.5 The usual T equivalent scheme of the three-phase asynchronous machine.

In steady state, the electromagnetic motor torque  $M$  has the expression:

$$M = \frac{3p}{\omega_1} \cdot \frac{\frac{R_2'}{s} U_1^2}{(R_1 + C_1 \frac{R_2'}{s})^2 + (X_1 + C_1 X_2')^2} \quad (3.78)$$

where  $C_1 = 1 + \frac{X_1}{X_{1m}}$  = machine constant.

The critical slip  $s_k$  is determined by the condition  $\frac{dM}{ds} = 0$ . It yields to [6]:

$$s_k = \frac{C_1 R_2'}{\sqrt{R_1^2 + (X_1 + C_1 X_2')^2}} \quad (3.79)$$

and

$$M_k = \frac{3pU_1^2}{2\omega_1 C_1 \left[ R_1 + \sqrt{R_1^2 + (X_1 + C_1 X_2')^2} \right]}, \quad (3.80)$$

respectively.

Fig. 3.6 shows the mechanical characteristics of the three-phase asynchronous machine as follows: for various rotor resistances and, in Fig. 3.7, the mechanical characteristics of the three-phase asynchronous machine for various supply voltages.

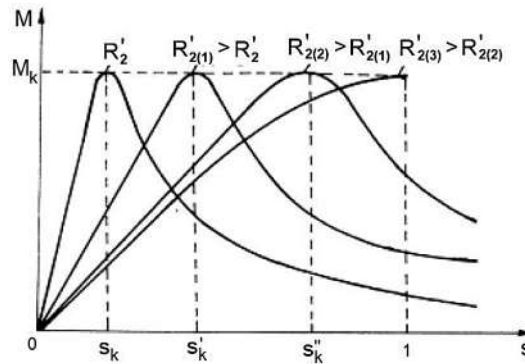


Fig. 3.6 Mechanical characteristics of three-phase asynchronous machines for various rotor resistors.

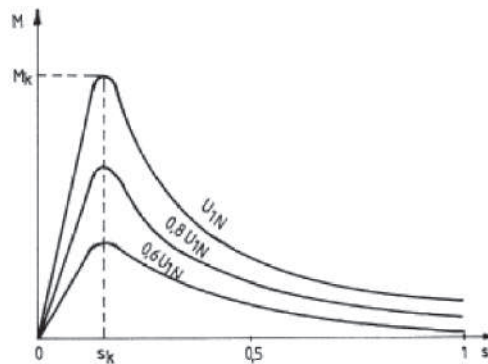


Fig. 3.7 Mechanical characteristics of three-phase asynchronous machines for different supply voltages.

### 3.2.5 The mathematical model of the three-phase induction machines in steady-state

This paragraph represents the synthesis of the theoretical and experimental researches carried out in the Department of Electrical Engineering of the Faculty of Electrical Engineering and Power Systems Engineering of Timisoara. The objectives of the study were mainly focused on the behavior of the induction machine in the presence of a deforming (non-sinusoidal) regime. Actually, they consist of analytically determining a mathematical model associated with short-circuited rotor three-phase asynchronous machines in steady-state and fed through static frequency converters. In what follows, the model and the influence of the converter's role on the machine parameters and characteristics is presented [3], [7], [8], [9].

If the induction machine is fed through a converter, a series of higher harmonics will be found in its supply voltage waveform, yielding to the difference of both its parameters and functional characteristic quantities from those of sinusoidal supplying case. These higher harmonics of odd time will result in a deforming regime in the machine, with generally unfavorable effects in its operation.

The following considerations are based on the simplifying assumptions:

- only the fundamental space harmonic of the winding is considered;
- saturation is neglected, if we take into consideration the fact that the machine parameters are not influenced by the saturation phenomenon depending on the load, so there are no time quantities through it.

The above-mentioned research has shown that, under non-sinusoidal feeding conditions, the three-phase induction machine can be associated with an equivalent scheme corresponding to all the harmonics that occur. The scheme works at the fundamental frequency  $f_{1(i)}$  and is presented in Fig. 3.8. The influence of higher harmonics is found in the particular parameters values, valid for a given load.

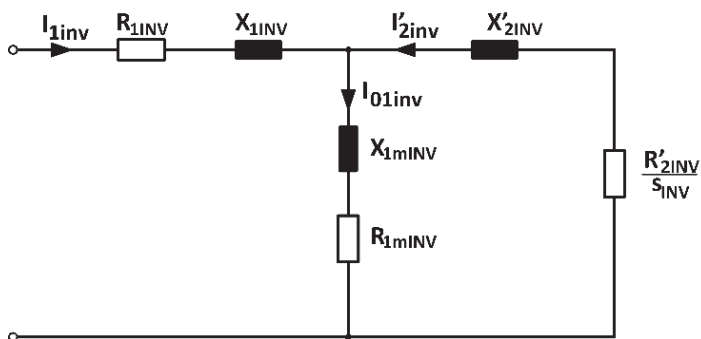


Fig. 3.8 Diagram of the three-phase asynchronous machine fed through an inverter.

According to this scheme, it can be formally considered that in the case of the machine feeding through the converter (the parameters corresponding to this situation are marked with the index "INV") behaves as if it would be fed through a sine wave voltage system of fundamental frequency,  $f_{1(i)}$ :

$$\begin{aligned}
 u_A &= \sqrt{2}U_{1(INV)} \sin \omega_1 t, \\
 u_B &= \sqrt{2}U_{1(INV)} \sin \left( \omega_1 t - \frac{2\pi}{3} \right), \\
 u_C &= \sqrt{2}U_{1(INV)} \sin \left( \omega_1 t + \frac{2\pi}{3} \right).
 \end{aligned} \tag{3.81}$$

where,

$$U_{1(INV)} = \sqrt{U_{1(1)}^2 + \sum_{v \neq 1} U_{1(v)}^2} \quad (3.82)$$

$U_{1(v)}$  is the phase supply voltage corresponding to the time harmonics of order  $v$ .

The equivalent parameters of the scheme were calculated for the fundamental frequency, taking into account all the higher odd time harmonics present in the supply voltage.

Thus, the equivalent resistance of the stator winding  $R_{1(INV)}$ , corresponding to all the harmonics including the fundamental, is determined by the condition that the resistance losses  $p_{Cu1(INV)}$  are the same as when considering all the "v" resistances corresponding to the harmonics,  $R_{1(v)}$ . This equivalent resistance  $R_{1(INV)}$  has the value:

$$R_{1(inv)} = R_{1(1)} = R_1 \quad (3.83)$$

and is traversed by the current:

$$I_{1(INV)} = \sqrt{I_{1(1)}^2 + \sum_{v \neq 1} I_{1(v)}^2} \quad (3.84)$$

The stator winding reactance corresponding to the fundamental  $X_{1(1)}$ , determined for the fundamental frequency  $f_{1(1)}$  and the stator winding reactance corresponding to the higher harmonics  $X_{1(v)}$ , determined for the frequencies  $f_{1(v)} = v f_1$ , is replaced by an equivalent reactance,  $X_{1(inv)}$  determined for the fundamental frequency. This equivalent reactance, traversed by the current  $I_{1(inv)}$  requires the same reactive power  $Q_{Cu1(INV)}$  as the "v" reactance  $X_{1(v)}$ , each determined at  $f_{1(v)}$  and travelled by the current  $I_{1(v)}$ . Following equivalence is obtained:

$$X_{1(CSF)} = k_{x1} X_1 \quad (3.85)$$

where:

$$k_{x1} = \frac{1 + \sum_{v \neq 1} \frac{1}{v} \cdot \left( \frac{1}{f_{1r} x_{sc}^*} \right)^2 \cdot \left( \frac{U_{1(v)}}{U_{1(1)}} \right)^2}{1 + \sum_{v \neq 1} \frac{1}{v^2} \cdot \left( \frac{1}{f_{1r} x_{sc}^*} \right)^2 \cdot \left( \frac{U_{1(v)}}{U_{1(1)}} \right)^2} \quad (3.86)$$

In (3.86),  $x_{sc}^* = \frac{X_{sc}}{Z_{(1)}}$  is the reported short-circuit impedance corresponding to the frequency  $f_1 = f_{1n}$  (usually,  $f_{1n} = 50$  Hz,  $X_{sc} = X_1 + X_2'$  and  $f_{1r} = \frac{f_1}{f_{1L}}$  ( $f_{1L}$  is the fundamental frequency at which the reactances  $X_1$  and  $X_2'$  were determined).

Similarly, for the rotor phase, the equivalent resistance and reactance relative to the stator, determined for the fundamental frequency, which corresponds to all the harmonics, including the base, the following expressions are obtained:

$$R'_{2(CSF)} = k_{R'_2} R'_2 \quad (3.87)$$

$$X'_{2(CSF)} = k_{X'_2} X'_2 \quad (3.88)$$

where  $k_{R'_2}$  and  $k_{X'_2}$  are defined by the following relationships:

$$k_{R'_2} = \frac{\frac{k_{r(CSF)}}{k_r} + \frac{R'_{2i}}{R'_{2c}} \cdot \frac{1}{k_r}}{1 + \frac{R'_{2i}}{R'_{2c}} \cdot \frac{1}{k_r}} \quad (3.89)$$

$$k_{X'_2} = \frac{\frac{k_{x(CSF)}}{k_x} + \frac{X'_{2i}}{X'_{2c}} \cdot \frac{1}{k_x}}{1 + \frac{X'_{2i}}{X'_{2c}} \cdot \frac{1}{k_x}} \quad (3.90)$$

In the above relationships,  $R'_{2c}$  is the resistance of the rotor phase winding laid in notches and relative to the stator (determined at fundamental frequency);  $R'_{2i}$  is the resistance of the rotor phase winding with negligible film effect and relative to the stator (determined at fundamental frequency);  $X'_{2c}$  is the reactance of the rotor phase winding laid in notches and relative to the stator, in which the film effect is manifested;  $X'_{2i}$  is the reactance of the rotor phase winding in which the film effect can be neglected;  $k_{r(INV)}$  and  $k_{x(INV)}$  are the equivalent global factors of resistance variation, of the rotor winding reactance corresponding to all the harmonics, including the fundamental, respectively;  $k_r$  and  $k_x$  are the increasing factor of rotor resistance and of the reducing factor of the rotor reactance in the sinusoidal supply conditions, respectively.

In order to determine the equivalent magnetization resistance  $R_{1m(INV)}$ , it should be noted that this is determined only by the stator ferromagnetic core losses, which are directly covered by the stator power.

By making the  $I_{01(inv)} \approx I_{\mu(CSF)}$  approximation for  $R_{1m(INV)}$ , the following results are obtained:

$$R_{1m(CSF)} = \frac{P_{z1(CSF)} + P_{j1(CSF)}}{3I_{\mu(CSF)}^2} \quad (3.91)$$

where  $P_{z1(INV)}$  and  $P_{f1(INV)}$  are the overall losses occurring in the stator teeth or in the stator yoke due to the supply of the servomotor through the converter. The determination of these losses is widely reported in [10].

When determining the total magnetization current  $I_{\mu(CSF)}$ , the effect of the superposition principle is applied (the ferromagnetic core is considered linear). Finally, the following relationship is obtained [11]:

$$I_{\mu(INV)} = \sqrt{I_{\mu(1)}^2 + \sum_{v \neq 1} I_{\mu(v)}^2} = I_{\mu} \sqrt{1 + \sum_{v \neq 1} \left( \frac{\theta_{\mu(v)}}{\theta_{\mu(1)}} \right)^2} \quad (3.92)$$

Where  $\theta_{\mu(1)}$  and  $\theta_{\mu(v)}$  represent the magnetizing windings corresponding to the fundamental and to harmonics of order  $v$ , respectively. The  $\theta_{\mu(1)}$  and  $\theta_{\mu(v)}$  computation is presented in [11].

The equivalent magnetization reactance, corresponding to all the harmonics, determined at the magnetizing base frequency  $f_{1(1)}$ , is obtained from the expression:

$$X_{1m(CSF)} \cong \sqrt{\left( \frac{U_{1(CSF)}}{I_{\mu(CSF)}} \right)^2 - (R_{1(CSF)} + R_{1m(CSF)})^2} \quad (3.93)$$

The determination of the ratio  $\frac{R'_{2(CSF)}}{S_{(CSF)}}$  is done by writing the Law of Conservation of

Active Powers: the equivalent active power corresponding to all the harmonics, including the fundamental, received by the equivalent rotor in the condition of feeding the machine through the converter is equal to the sum of the active power corresponding to the fundamental and the active powers corresponding to each harmonic  $v$  in part. After the calculations are made, the following is obtained:

$$\frac{R'_{2(INV)}}{S_{(INV)}} = \frac{R'_s}{s} \cdot \frac{1 + \sum_{v \neq 1} \frac{s_{(1)}}{s_{(v)}} \cdot \frac{R'_{2(v)}}{R'_{2(1)}} \cdot \left( \frac{I'_{2(v)}}{I'_{2(1)}} \right)^2}{1 + \sum_{v \neq 1} \left( \frac{I'_{2(v)}}{I'_{2(1)}} \right)^2} \quad (3.94)$$

where the slip corresponding to harmonics of  $v$  is:

$$s_{(v)} = 1 \mp \frac{1}{v} \pm \frac{s}{v} \quad (3.95)$$

The “- +” sign pair (located at the top) corresponds to the wave that rotates in the direction of the main wave, while the “+ -” bottom pair corresponds to the wave that

rotates in the counter sense. Thus, all the parameters of the equivalent scheme of the three-phase induction machine were determined in the condition of its feeding through a static frequency converter. For further details, bibliographies are recommended [8], [12], [13], [14].

### 3.3 Static converters fed induction machines

#### 3.3.1 Introductory elements

In the case of electric drives, the static frequency converter plays a crucial role in obtaining quick and accurate dynamic responses. The use of three-phase induction machines requires the existence of appropriate power converters generating a three-phase voltages system of variable amplitude and frequency. Most applications use static indirect frequency converters.

Static indirect frequency converters are characterized by a double conversion of the electrical energy consisting in a transformation of the alternating grid voltage (of constant amplitude and frequency) into a continuous voltage by using a rectifier with two or four quadrants, followed by the inverse transformation of the continuous voltage from the intermediate circuit into an alternating voltage, single-phase or three-phase (of variable amplitude and frequency) by using an inverter.

The static frequency converters with DC intermediate circuit consist essentially of three blocks: a rectifier, a filter and an inverter. The block diagram of such a converter is shown in Fig. 3.9.

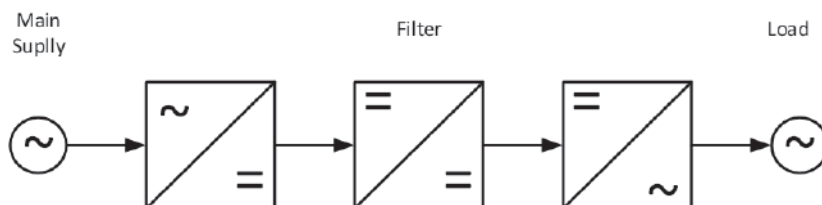


Fig. 3.9 The block diagram of a static frequency converter with DC intermediate circuit.

By the nature of the filter in the DC intermediate circuit, there are two categories of indirect converters: with intermediate continuous voltage and intermediate continuous current.

**The indirect static converters with continuous voltage in the intermediate circuit** are characterized by a DC voltage supply working in voltage generator mode - voltage source - due to the presence of a capacitor with  $C \rightarrow \infty$  in parallel with the source. This is the reason of naming the inverter a voltage inverter. In this kind of converters, the voltage is switched to the output circuit, which has a rectangular shape. The current is determined based on the load nature.

In Fig. 3.10.a and 10.b are presented two basic topologies of indirect converters with continuous voltage in the intermediate circuit, in use nowadays.

The block diagram of Fig. 3.10a corresponds to a device consisting of a voltage inverter and a passive rectifier, which is often used for low power drives applications. Since the rectifier is not controlled, for the machine generator mode, the energy cannot be passed to the grid, so, a dissipative element - the power resistance  $R$  – is connected to the intermediate circuit at the filter capacitor terminals, and if needed, it could be also connected with a static switch  $SS$  (a bipolar or IGBT transistor).

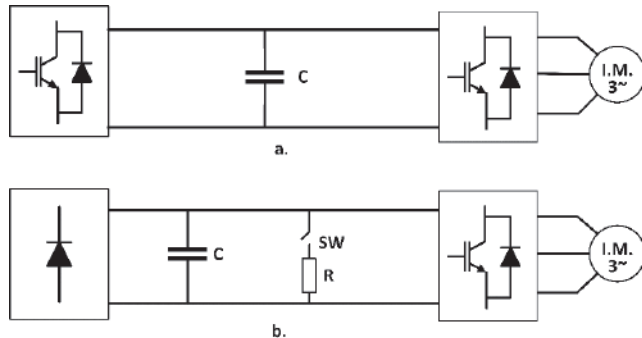


Fig. 3.10 Static indirect converter with intermediate DC voltage: a) a circuit diagram with voltage inverter and a passive rectifier; b) a scheme that allows recuperative braking.

The scheme in Fig. 3.10.b allows energy recovery back to the AC grid. In this case, the rectifier being a controlled one (uses active components in its structure), in the braking operation mode of the induction machine, it operates as an inverter. Its topology can be a two-level one or a multi-level one. The three-level inverter shows a significant reduction of harmonics, without increasing the switching frequency for this purpose. It is used in high power and voltage applications.

**The indirect static converters with continuous current in the intermediate circuit** is characterized by a DC source, which operates as a current generator mode due to the presence of a large inductance  $L$  in the source circuit. This provides the intermediate circuit with a current source nature, the inverter being known as a current inverter. The basic topologies of indirect static converters with DC current in the intermediate circuit, currently encountered in practice, are shown in Fig. 3.11.a and Fig. 3.11.b.

Currently, the scheme in Fig. 3.11.a is frequently used, where both the rectifier and the inverter are built-in using conventional thyristors in their structure. The diagram allows the power to circulate in both directions even though the current in the intermediate circuit retains the sense. For an induction machine operating in motoring mode, the grid-side converter works as a rectifier and the load-side converter works as an inverter. When the machine is operating in a recuperative braking mode, the converters change their role: the grid-side converter works as an inverter and the load-side converter works as a rectifier. For



the supply case of an induction machine, a battery of condensers is typically attached to the machine terminals, providing thus the reactive energy required for load switching off.

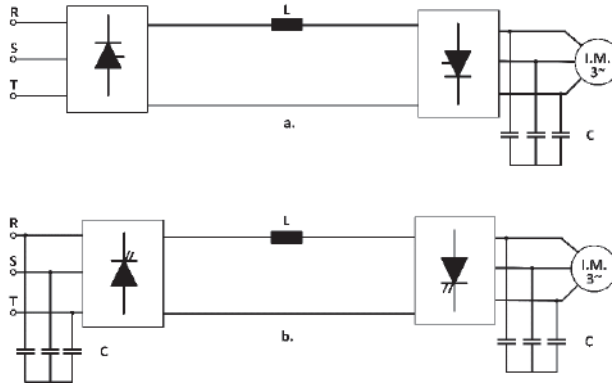


Fig. 3.11 Basic topologies of indirect converters with DC intermediate circuit: a) Rectifier - inverter operating mode with conventional thyristors; b) rectifier - inverter operating mode with GTO thyristors.

The diagram shown in Fig. 3.11.b uses GTO thyristors in the structure of the two converters.

The following is a brief overview of both voltage and current inverters topologies and, for further details, please refer to the literature [15], [16].

### 3.3.2 Three-phase voltage inverters

The three-phase voltage inverters consist of three branches R, S, T, specific to the bridge connection. Fig. 3.12 shows the principle of a voltage inverter. It can be noticed that, at the terminal points R, S, T, a symmetric three-phase voltage system is obtained, which can be described by the relationships:

$$i_R + i_S + i_T = 0; u_R + u_S + u_T = 0; u_{RS} + u_{ST} + u_{TR} = 0 \quad (3.96)$$

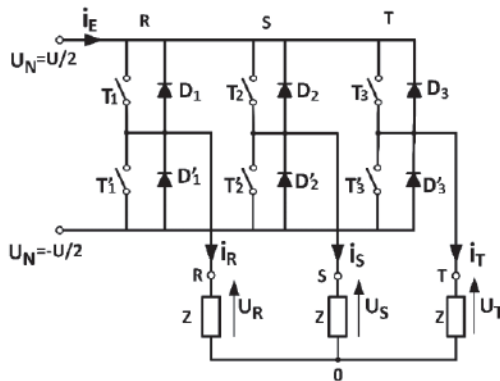


Fig. 3.12 Diagram of the voltage inverter.

In the simplest case, the valves are controlled in such way that a  $120^\circ$  phase-shift between the valves from group P to the other ones from group N is ensured, but the conduction of each valve can last only  $120^\circ$  or  $180^\circ$ . Knowing which valves are conducting at each moment, the potentials of the points R, S and T can be deduced and thus the voltages waveforms, too. In all the applications, the three-phase electric machines have an inductive-resistive character, which will result in currents phase shifting. As a result, when the current of a phase has the opposite sign of the same phase voltage, it will flow through the corresponding run-off diode. This is why the valves conduction time is actually less than  $120^\circ$  and less than  $180^\circ$ , respectively.

For an inductive-resistive load, the current waveform back phase-shifted compared with the voltage waveform; therefore, the switching between the bridge legs occurs at the same moments ( $0^\circ$ ,  $60^\circ$ ,  $120^\circ$  and so on). Within each  $60^\circ$  range, however, there is a switch between a run-off diode and the corresponding valve on the same leg. The valve will receive the priming signal as for the resistive load case, i.e. in advance, but will drive less than  $120^\circ$ . Consequently, there is a change in the voltages' waveforms ( $u_{Ri}$ ,  $u_{Si}$  and  $u_{Ti}$ ) as shown in Fig. 3.13.a. The situation is similar for the  $180^\circ$  conduction case, whose waveforms are shown in Fig. 3.13.b [3], [16].

### 3.3.2.1 Inverters with low loss transistors

For small and medium power applications, MOS and IGBT transistors are used for building these inverters. With the emergence of high-performance transistors, the three-phase inverter technique has changed substantially. Firstly, the switching frequency has increased, which has led to the improvement of converters performances in terms of dynamic response, reduction of harmonic content, reduction of acoustic noise, etc. Switching frequencies to about 15 kHz for IGBTs and 20 kHz for MOSFET transistors are very common. Under these circumstances, the only factor limiting the switching frequencies is the dynamic losses of commutation. Reducing the losses is possible by soft switching at zero voltage (ZV) or zero current (ZC), by adding to the valves resonating elements, as shown in Fig. 3.14.

The disadvantage of soft switching is the high voltage or current stresses for the valves. Adding the characteristic of the resonant elements LC to a three-phase voltage inverter, the diagram in Fig. 3.15 yields. The resonant circuit causes an oscillation in the intermediate circuit between zero and nearly double the supply voltage  $U$ . All valves in the inverter will be switched to ZV when the capacitor voltage  $C$  reaches 0. Due to the high voltage stress on the valves, it would be recommended an active circuit to fix the voltage peaks on the bridge valves to more reasonable values of  $(1.2-1.5)U$ . The diagram of such an inverter is shown in Fig. 3.16. Here, in order to precisely determine the zero crossing of the intermediate circuit voltage, the losses in the resonant circuit are compensated, resulting in a variation different from the ideal one. This is done by providing the coil  $L$  with an initial current.

A more refined version of the scheme presented in Fig. 3.15 is shown in Fig. 3.17. The two bi-directional auxiliary valves  $A_1$  and  $A_2$  allow the supply voltage of the oscillating circuit to be cancelled whenever the bridge valves have to switch. These will be switched to ZV and the two auxiliary valves at ZC. The S-valve works at the inverter switching frequency and all the available power is passed through it.

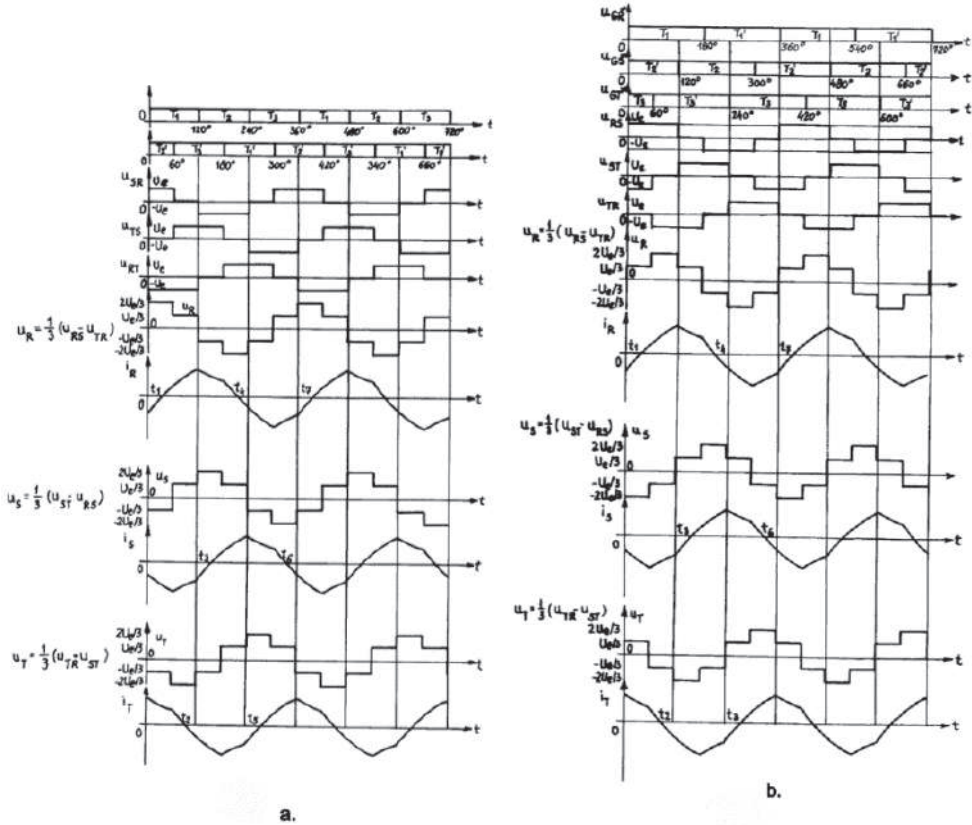


Fig.3.13 Voltages and currents produced for an inductive-resistive load: a) 120°; b) de 180°.

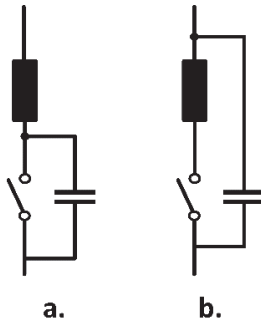


Fig. 3.14 Configurations for soft switching: a) ZV; b) ZC.

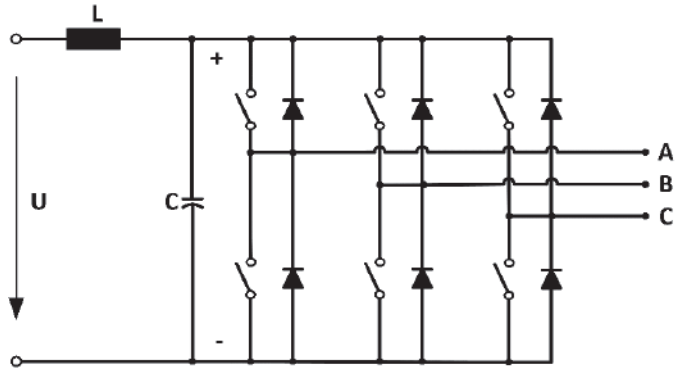


Fig. 3.15 Three-phase inverter with resonant intermediate circuit.

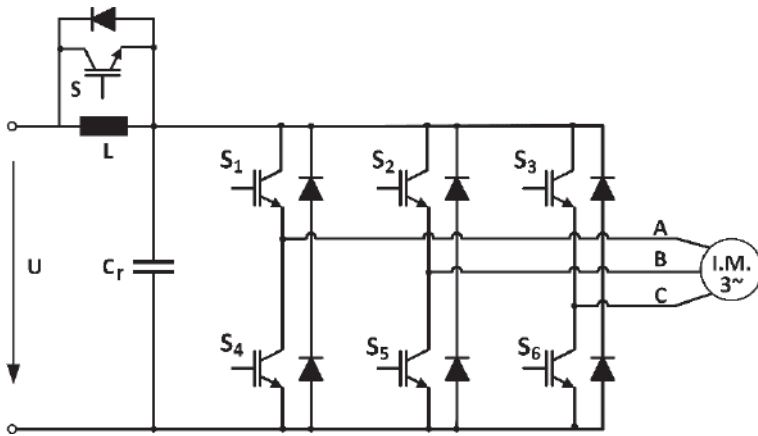


Fig. 3.16 Three-phase resonant active inverter.

Each time the voltage in the intermediate circuit becomes zero, all the inverter elements are briefly short-circuited by the S-valve, causing an initial current in the coil L. Then, a new switching cycle starts and a new resonant cycle begins. The bi-directional nature of the S-valve is emphasized.

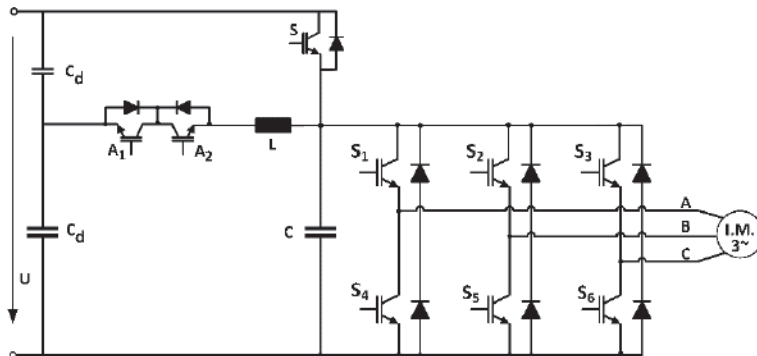


Fig. 3.17 Active resonant circuit inverter and auxiliary valves.

There are also diagrams that use a series of LC elements in the intermediate circuit, those being added to a current source converter (see Fig. 3.18). Here, all the valves are switched on when the current in the intermediate circuit passes through zero, (ZC). The disadvantage here is the current demand for the valves. Here, for an accurate determination of the current zero passing moment, an initial voltage compensates the losses across the capacitor. Each time the current becomes zero in the intermediate circuit, all the valves lock up, which yields an initial voltage on the resonant capacitor.

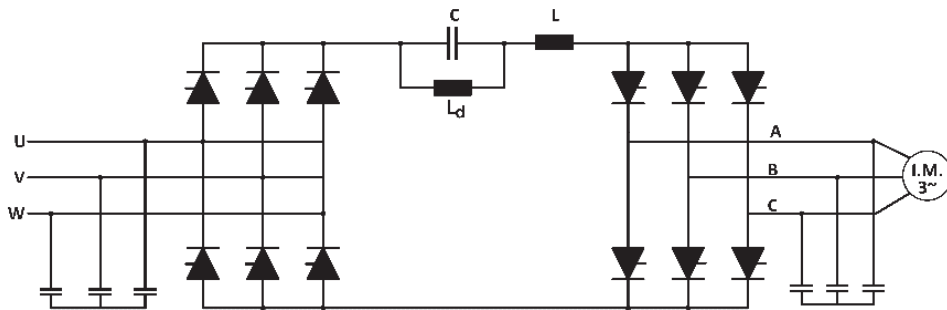


Fig. 3.18 Resonant LC series converter.

Unlike PWM-controlled inverters, soft-switching inverters are controlled based on the correct detection of voltage (current) zero passing in the intermediate circuit, using specific strategies [17].

### 3.3.2.2 Multi-level inverters

The multi-level voltage inverters generate a stairs waveform of the voltage, which provides a better approximation of the sinewave voltage, resulting in a significant increase in the fundamental and a significant reduction in the higher harmonics in the alternating voltage produced. On the alternative voltage side, three or more voltage levels are generated. For this purpose, at least two DC voltage sources are used. There is although a disadvantage, namely the large number of valves, which makes them suitable only for high power applications, where the valves used are GTO thyristors. Fig. 3.19 shows a simplified representation of a multi-level inverter: the switching element on each phase (Fig. 3.19.b), consists of four controlled valves and six diodes for three voltage levels. The generated voltage from the voltage block control is shown in Fig. 3.19.c. There are twelve transitions and each valve is turn on only once within a period of time. This is the reason why this scheme is also known as the scheme with twelve steps (switches). The potential of the neutral  $U_{np}$  contains the zero sequence voltages, which do not occur in the voltage at load terminals, thus reducing the harmonic voltage content.

The valves control mode is based on the angle  $\alpha$ , Fig. 3.19.c, or on applying the pulse width modulation technique (PWM) in case of aiming at a superior performance [3], [16].

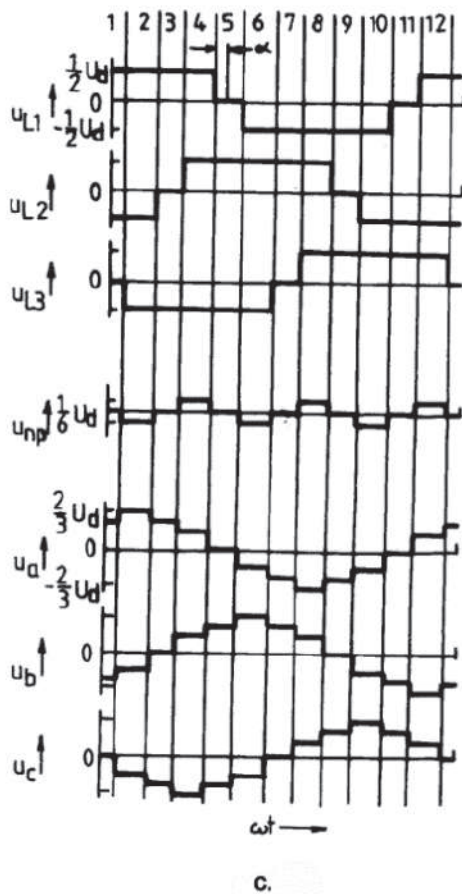
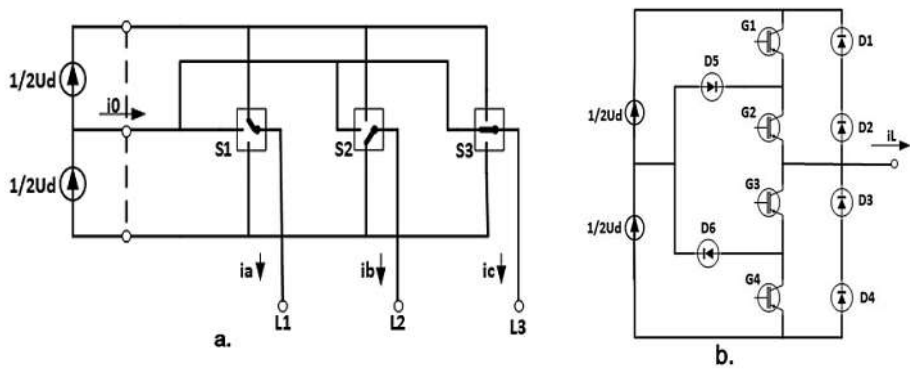


Fig. 3.19 Three-phase multi-level inverter: a) the simplified scheme; b) the switching elements in detail; c) the obtained waveforms.

### 3.3.3 Three-phase current controlled inverters

For these kind of inverters, the valves are bi-directionally used in the voltage and unidirectional in the current due to the current of the intermediate circuit. The valves used can be antiparallel diode-free thyristors.

#### 3.3.3.1 Current inverters with autonomous turning off

These inverters use an auxiliary bridge of thyristors (see Fig. 3.20).

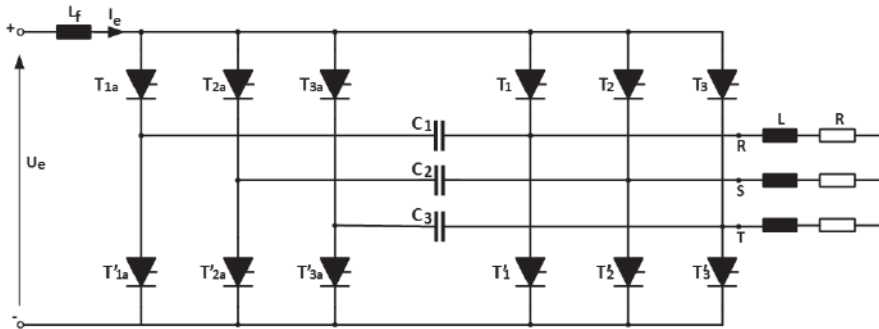


Fig. 3.20 Current inverters with autonomous turning off.

The priming of each auxiliary thyristor causes the lock of the corresponding main thyristor. The load is embedded in the switching circuit. Each extinguishing capacitor serves two valves from the same bridge leg. Thus, for example, to block  $T_2$ ,  $T_{2a}$  must be primed. The capacitor  $C_2$  is discharged between  $T_2$  and  $T_{2a}$ . Upon completion of the switching process, the capacitor  $C_2$  is recharged and ready to block the thyristor  $T_2$ . A variant of this scheme, shown in Fig. 3.21, is using a single capacitor, provided that all commutations take place at different sequences and thus avoiding overlapping.

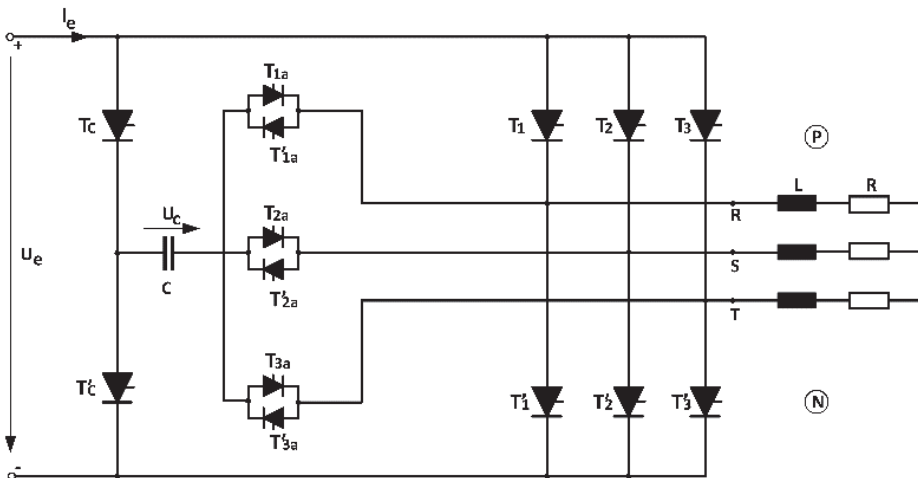


Fig. 3.21 Current inverters with autonomous turning off and only one capacitor.

Here, the auxiliary thyristors  $T_a$  lead the capacitor current to the valve that has to be blocked, and  $T_c$  and  $T_c'$  control the capacitor's polarization with the polarity required to block the thyristors of the group P or N. In this scheme, the capacitor is charged and discharged six times over a period of time [3], [16].

### 3.3.3.2 Autonomous current inverter

This inverter substantially reduces the number of valves, using only six thyristors (see Fig. 3.22). The separation diodes,  $D_s$ , placed in series with bridge thyristors, are designed to prevent the discharge of the extinguishing capacitors through the load. Assuming that the  $T_2$  and  $T_1$  valves are in the conduction mode, the capacitor  $C_2$  is charged as shown in Fig. 3.22. To lock  $T_2$ ,  $T_3$  is turned on. A discharge of the capacitor  $C_2$  between  $T_2$  and  $T_3$  immediately follows and, then,  $T_2$  is blocked. Due to the load's inductive nature, the current is switched from  $D_{s2}$  (the path that includes  $T_2$ ) to  $D_{s3}$  (the path of  $T_3$ ), only after the capacitor  $C_2$  recharges with the opposite polarity. The recharging circuit is  $T_3$ , phase S, phase R and  $T_1'$ .

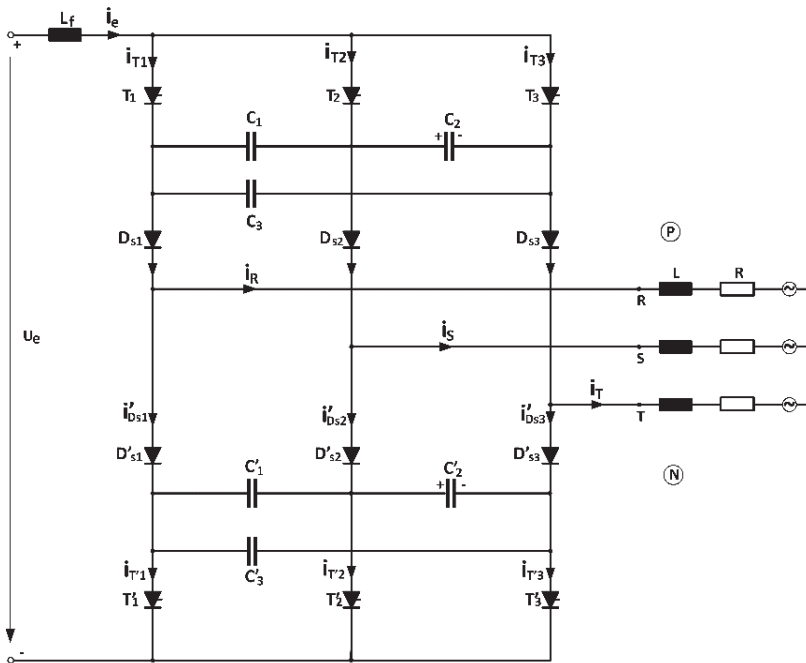


Fig. 3.22 Autonomous current inverter.

Current inverters can be controlled in pulse with width modulation, PWM, as voltage inverters, but it is important to keep in mind that short-circuiting of the load (considered as a voltage source) or unloading the power supply are forbidden. At one point, there must be a P-valve and another N-valve, not on the same phase, in conduction mode. In addition, the valves must have controlled both the priming and the locking [3], [16].



### 3.3.4 Control of the three-phase inverters

#### 3.3.4.1 Pulse width modulation (PWM) for three-phase inverters

The purpose of the modulation techniques is to determine a set of three-phase voltages of varying amplitude and frequency, starting from a constant input voltage constant. In order for the three voltages to be symmetrical, the same triangular voltage must be compared to three reference sinusoidal voltages that are offset by  $120^\circ$ , as in Fig. 3.23.a, where  $m_f$  is the **frequency modulation ratio** defined as  $m_f = f_s/f_i$ , where  $f_s =$  **the frequency of the triangular signal** and the frequency of the carrier;  $f_i$  is the frequency of the fundamental voltage generated by the inverter - **modulating frequency**.

From Fig. 3.23.b it can be seen that the same continuous component is present in the  $u_{AN}$  and  $u_{BN}$  voltages, measured at the negative voltage supply pole. In the line voltage waveform, this component disappears in the same way as in the single-phase bridge inverter. In fact, for the three-phase inverters, only the harmonics in the line voltages present interest.

Considering the harmonics of the  $m_f$  order and the harmonics of an odd multiple order, the phase difference between the harmonics of the  $m_f$  order in the  $U_{AN}$  and the  $U_{BN}$  is  $(120 \times m_f)$ . This phase difference becomes zero if  $m_f$  is an odd number and a multiple of 3. As a consequence, of the harmonics of  $m_f$  order disappear from the  $U_{AB}$  waveform. The same goes for the harmonics for the odd multiples of  $m_f$ . In fact, this is the reason for choosing  $m_f$  to be an odd number and a multiple of 3. In this way, a whole series of harmonics from the three-phase line voltage can be eliminated by choosing  $m_f$  accordingly. It can be concluded that:

- for low values of  $m_f$ , a **synchronized modulation technique** (the triangle and the command signal are synchronized) must be used in order to eliminate the harmonics.  $m_f$  must be an odd number and a multiple of 3;
- the **asynchronous modulation technique** can be practiced in the range of  $m_f > 21$  because the amplitude of the subharmonics due to this process is small. In this control mode, the frequency of the triangular signal is kept constant and only the frequency of the command signal is changed. The result is that  $m_f$  can have values that are no longer integer numbers. However, the process should be avoided if the output frequency is of a few hertz due to the subharmonics that can cause the appearance of significant currents of low frequencies;
- using **the overmodulation technique** ( $m_a > 1$ ), regardless of the value of  $m_f$ , the behavior is the same as the one for low  $m_f$  cases.

$m_a$  is **the modulation ratio in amplitude** defined as  $m_a = \frac{U_{cm}}{U_{Tm}}$ , where  $U_{cm}$  is the amplitude of the reference voltage and  $U_{Tm}$  is the amplitude of the triangular signal, that is generally constant.

In the linear region ( $m_a \leq 1$ ) the fundamental content in the output voltage varies linearly with  $m_a$ .

Seeing that the amplitude of the fundamental is given by the relationship:

$$(u_{A0m})_1 = m_a \frac{U_d}{2}, \quad m_a \leq 1 \quad (3.97)$$

where  $U_d$  is the voltage of the intermediate circuit, the fundamental content of the line voltage is:

$$u_{L1} = \frac{\sqrt{3}}{\sqrt{2}} (u_{A0m})_1 = \frac{\sqrt{3}}{\sqrt{2}} m_a U_d \approx 0.612 m_a U_d \quad (3.98)$$

The harmonic components of the line voltage are presented in Table 3.1, taking into account the fact that the harmonics are presented as effective values.

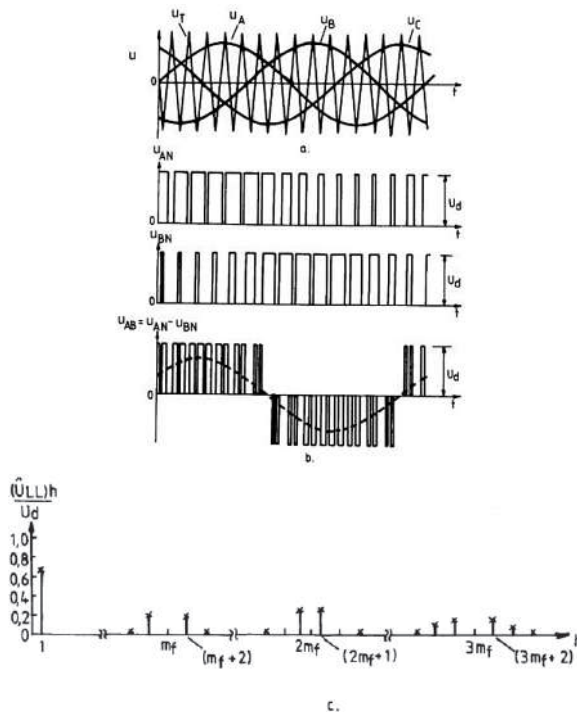


Fig. 3.23 Pulse width modulation in three-phase inverters: a) comparison between the triangular carrier and the modulating sinusoidal voltages; b) the produced line voltage; c) harmonics spectrum.

In the overmodulation zone, the spikes in the command voltages waveforms may exceed the voltage triangular waveforms. In this mode of operation, the content of the fundamental voltage waveform does not increase proportionally with  $m_a$ . This can be seen in Fig. 3.24. For large enough values, the modulation turns into a rectangular waveform.

Table 3.1. The reported value of harmonics in line voltage for a large, odd and multiple of  $3m_f$ .

$m_a$	0.2	0.4	0.6	0.8	1
<b>fundamental</b>	0.122	0.245	0.367	0.490	0.612
<b><math>m_f \pm 2</math></b>	0.010	0.037	0.080	0.135	0.195
<b><math>m_f \pm 4</math></b>				0.005	0.0011
<b><math>2m_f \pm 1</math></b>	0.116	0.2	0.227	0.192	0.111
<b><math>2m_f \pm 5</math></b>				0.008	0.020
<b><math>3m_f \pm 2</math></b>	0.027	0.085	0.124	0.108	0.038
<b><math>3m_f \pm 4</math></b>		0.007	0.029	0.064	0.096
<b><math>4m_f \pm 1</math></b>	0.100	0.096	0.005	0.064	0.042
<b><math>4m_f \pm 5</math></b>			0.021	0.051	0.073
<b><math>4m_f \pm 7</math></b>				0.010	0.030
$m_a$	0.2	0.4	0.6	0.8	1

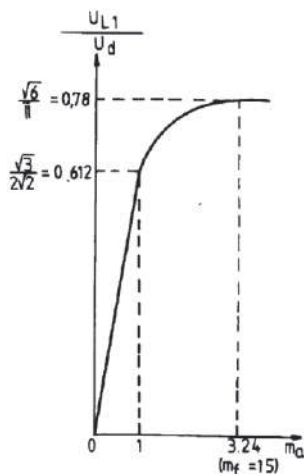


Fig. 3.24 The reported fundamental content  $U_{L1}/U_d$  as function of  $m_a$  for the three-phase inverter.

In the overmodulation zone, comparing to the linear one ( $m_a \leq 1$ ), there are several lateral harmonics centered on the harmonics of the  $m_f$  order and their multiples. However, the dominant harmonics may not have a magnitude as large as in the case of  $m_a \leq 1$ . Therefore, it is found that, depending on the charge character and the switching

frequency, the losses due to these harmonics may be smaller in the overmodulation area than in the linear zone of the PWM [3], [113].

### 3.3.4.2 Closed Loop Pulse Width Modulation (PWM)

For the three-phase converters fed AC machines, the generation of pulse width modulation occurs in a closed loop based on current or flux. In fact, the current and (or) flux are state variables that can be measured or observed in the control loop.

The block diagram of a hysteresis current controller is shown in Fig. 3.25.a. To be noted that there is one control block on each phase that causes the current error on the respective phase to be maintained within the width of the hysteresis band,  $\pm\Delta$ .

There is no correlation between the three controllers, which is a disadvantage. It is also noted that the current error is not strictly limited as situations where all the valves are blocked and the current is determined by the motion induced voltage may occur (see Fig. 3.25.b). However, the error cannot exceed  $2\Delta$ , [18]-[115]. Thus, in Fig. 3.25.b, with "1" is marked the situation in which the signal exceeds the hysteresis zone. This can happen if the zero vector is active (see Fig. 3.27.c), while the vector corresponding to the motion induced voltages opposes the previous state of conduction. The maximum exceedance is  $2\Delta$ . The high-frequency switching cycles that may occur are marked by "2". This kind of controllers work at high switching frequencies, thus, compensating for the quality of the modulation.

A carrier-based modulation brings improvements to the previous scheme. Fig. 3.26 shows a more elaborate scheme. A PI (proportional-integral) controller provides the voltage reference for the width modulator. This voltage reference is filtered and at the same time, the influence of the load motion induced voltage is compensated.

Difficulties may arise if the reference exceeds in amplitude the triangular signal (see Fig. 3.26.b), in which case the valves are blocked.

The vector control is based on the voltage vector, which can be determined from the principle scheme shown in Fig. 3.27.a, generating the voltages from Fig. 3.27.b. Based on the relationship:

$$u_s = \frac{2}{3}(u_a + a \cdot u_b + a^2 \cdot u_c) \quad (3.99)$$

where  $a = e^{2\pi/3}$  applied to the voltages in Fig. 3.27.b, the six voltage vectors ( $U_1 \dots U_6$ ) represented in Fig. 3.27.c can be determined.

When applying pulse width modulation (PWM) vector control strategies, there are two zero vectors,  $u_o$  and  $u_z$ . These zero vectors are associated with one of the two inverter states when all the valves P are closed (1),  $u_z$ , and when all the valves N are closed,  $u_o$ , respectively. The existence of the two zero vectors brings new possibilities for the PWM vector control strategies [3], [16], [18].

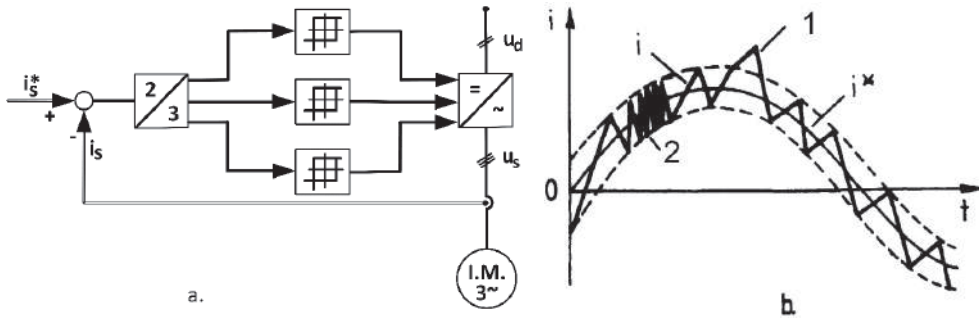


Fig. 3.25 Modulation based on current hysteresis: a) Principle scheme; b) One phase current variation.

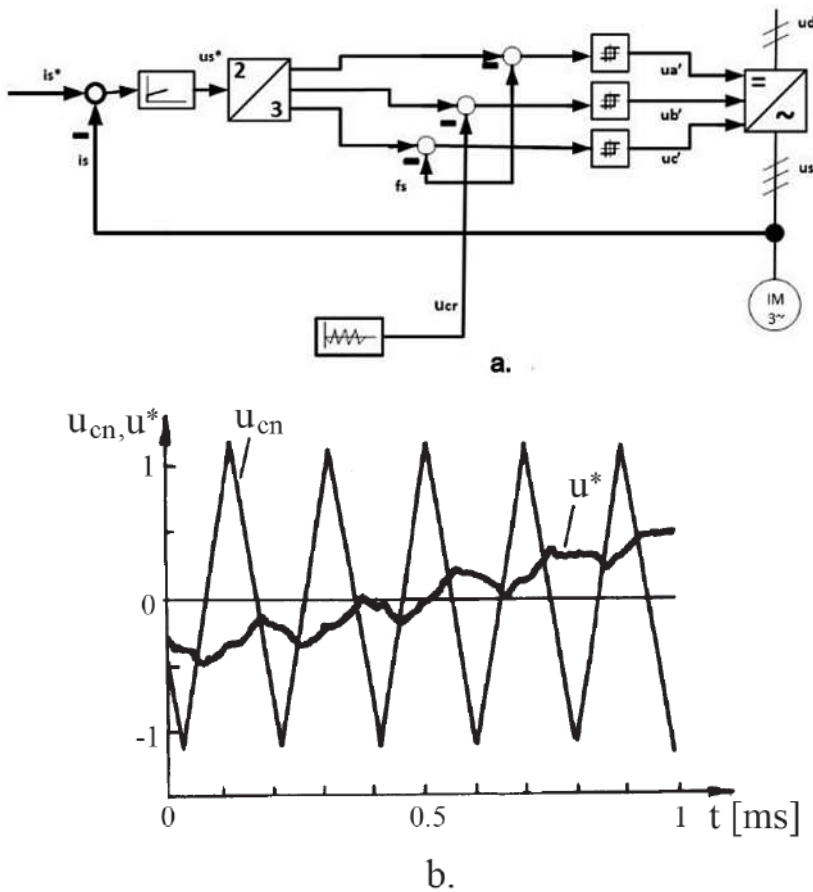


Fig. 3.26 Modulation with triangular command signal: a) principle scheme; b) the comparison between the triangular signal and the reference signal.

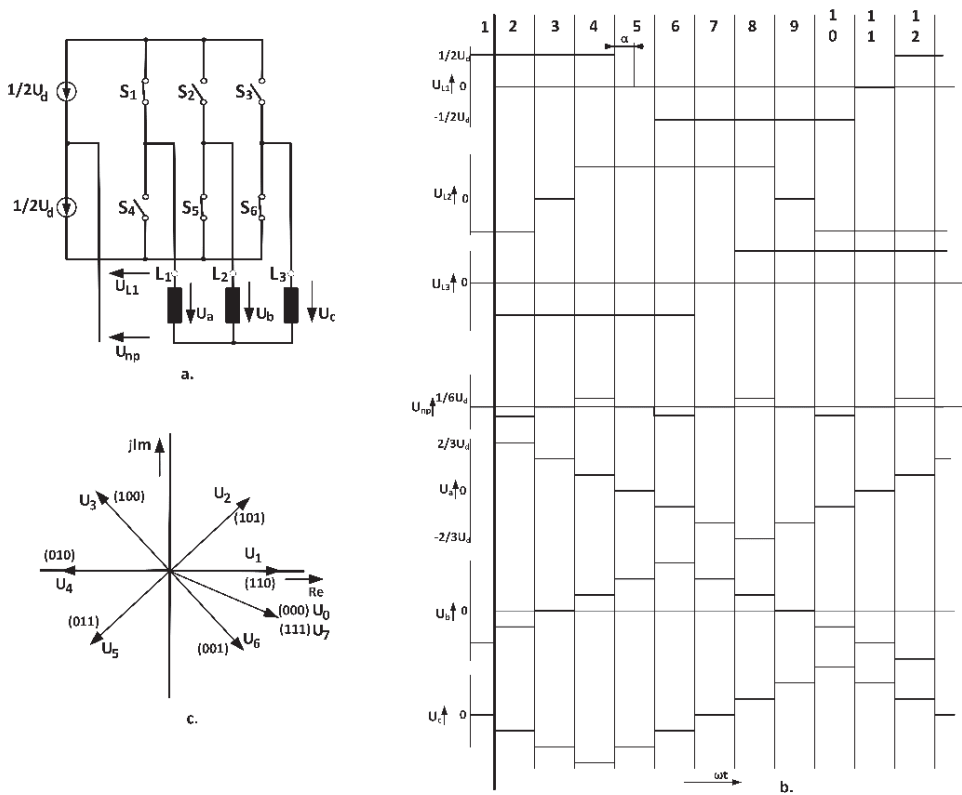


Fig. 3.27 Generation of voltage vectors: a) inverter principle scheme; b) rectangular waveforms; c) voltage vectors with equivalent code.

### 3.4 Scalar speed control of induction machines by change of voltage / current supply frequency

#### 3.4.1 General Elements

Despite its simple and robust design, the motion control of the three-phase induction motors must take into account the complexity of the non-linear dynamic and time-varying model and the fact that the physical parameters of the machine are not always known with great precision. Under these conditions, motion control involves speed control and/or position control and torque control, respectively. The faster the torque response is, the more efficient the speed control is.

Basically, there are two control strategies:

- the scalar control;
- the vector control.

**The scalar control** can be performed in an open or closed speed control loop and can be achieved with the relationships existing between voltage/current magnitudes and frequency, for example:  $u_s = f(f_1)$  or  $i_s = f(f_2)$ . It is usually necessary to keep the stator flux constant and equal to the nominal one ( $\Phi_s = \Phi_{sn} = \text{const.}$ ). This strategy is based on a simple model of the induction machine in steady-state. The advantage of the scalar control lies in the simplicity of the control circuits, but presents the disadvantage of generally obtaining variable speeds with low accuracy, the dynamic performance of the system being also low. Satisfactory results are obtained, but only when the machine is working at stationary speeds for long periods. If there are voltage fluctuations or load disturbances or if the drive system requires rapid acceleration or deceleration, the open loop control is unsatisfactory. To improve the dynamic performance of the drive systems, closed-loop control schemes with external speed response and internal responses of one or more variables, such as voltages, currents, magnetic flux, are adopted. Sometimes, algorithms are used to optimize parameters such as power factor, efficiency, distortion level, etc. The control equipment can be analogue or analogue-to-numeric in systems where the performance or the numerical performance is not required, using large-scale integrated circuits, e.g. microcontrollers. The use of dedicated microcontrollers, with microprocessors or digital signal processors (DSPs), provides complete control of the drive system by producing a large number of functions such as PWM inverter control, adjustment of control algorithms to load type, interfacing for communication with the local operator and with control systems, diagnostics, protection, etc. In conclusion, it can be stated that the implementation of the scalar control, despite its simplicity, is limited by the accuracy of the machine speed and torque responses.

**The vector control** is based on the dynamic model of the induction machine. It has been developed as a closed-loop speed / torque control method and is used when the dynamic system response and the motion control precision are important. The vector control restores one of the advantages of the DC drive systems, the separation of speed and torque loops. The promoters of vector control are K. Hasse and F. Blaschke. There are indirect and direct vector control strategies in the torque. From a practical point of view, vector control systems can be grouped into:

- analog systems, built with integrated circuits and transistors;
- digital systems, built with digital signal processors DSPs, microprocessors and computer interfaces;
- hybrid systems, where the control circuits are both analog and digital.

Another classification of the control methods can be made by the way kinematic magnitudes are measured. Thus, one can distinguish:

- motion control using transducers for the kinematic magnitudes;
- control without motion transducers.

Control methods using transducers for kinematic magnitudes (position and speed) are used for applications in an extended range of speeds (1: 1000; 1: 10000). It should be highlighted that transducers are generally expensive, sensitive to disturbances and temperature variations, while increasing the weight and gauge of an electric drive.

Driving without using motion transducers, known in the English literature as "sensorless control", requires an alternative to the first strategy, being necessary to reduce the hard part of the drive systems as well as to increase the operational safety. This applies to systems characterized by a moderate speed range (1:100). In this situation, the kinematic magnitudes are estimated and the system state observers use current and voltage measurements at terminals.

As stated above, for induction machine drive systems with low dynamics demands, the positioning of the spatial phasor of the stator voltages or of the rotor currents is dispensed. In this situation, only the frequency of the voltage generated by the converter is controlled from the outside. All these methods of controlling the voltage or current feeding of the machine form together a separate category of **scalar control methods** [19].

The scalar control of induction machines has been implemented based on their steady-state equations model. The big advantage of this strategy is given by the simplicity of the control circuits, but its drawback is the modest dynamic performance.

The scalar control method of the induction motor speed is known in the literature as the "U/f = const." control or the "V/Hz" principle. This is the only classic speed control method which is also in use nowadays. Although considered as an efficient control method only in the stationary mode, it can also be used with good results in the dynamic regimes if a scheme with magnetic flux and electromagnetic torque internal reactions is adopted or if the machine is provided with slip compensation.

In terms of losses, the process of changing the induction motor speed by modifying the frequency is the most economical one, in the sense that the extra losses occurring in the machine due to the frequency modulation system are relatively small if compared with the ones obtained for operation at the rated frequency and voltage [20].

Based on the relationships that define the induction motor mathematical model in steady-state (see paragraph 3.2.4), it results that the synchronous speed changes proportionally with the frequency and the electromagnetic torque changes proportionally with the reactances, respectively. If the supply frequency  $f_1$  is not much different from the  $f_{1n}$  nominal frequency, the expression of the critical torque in relationship (3.80) can be written in a simpler form, neglecting the stator resistance with respect to the dispersion reactances:

$$M_k = \frac{m_1 p U_s^2}{4\pi f_1 x_s + C_1 X_r'^2 C_1} = A \left( \frac{U_s}{f_1} \right)^2 \quad (3.100)$$



where  $A$  is a constant that includes all the constant elements, to highlight the critical torque dependence on the square of the ratio  $\frac{U_s}{f_1}$ , i.e. equal to  $\frac{U_{sm}}{f_{1n}}$ . If this ratio is not kept constant and, for example,  $f_1$  decreases, while  $U_s = \text{const.}$ , then, based on the relationship:

$$U_s \approx U_{es} = \frac{2\pi}{\sqrt{2}} f_1 N_1 \phi_s = c f_1 \phi_s \quad (3.101)$$

in which  $\phi_s$  is the amplitude of the total stator flux and " $c$ " is a constant, yields to a flux increase when the frequency decreases. Increasing the  $\phi_s$  flux causes the core saturation and thus the increase of the magnetization current. Increasing the frequency while  $U_s = \text{const.}$ , the machine flux decreases, which results in the decrease of the developed torque. If the stator flux can be kept constant, the behavior of the induction motor controlled in frequency is similar to that of the DC machine with separate excitation in the voltage control mode.

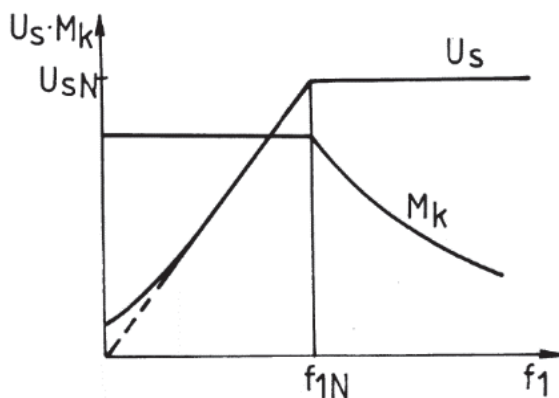


Fig. 3.28 Voltage dependence on frequency for the induction servomotor.

The expression of the critical slip (3.79) shows that  $s_k$  is inversely proportional to the frequency, which means that, with the decrease of  $f_1$ , the mechanical characteristics will be slightly more inclined or leaner.

Fig. 3.28 shows that the supply voltage  $U_s$  and the frequency  $f_1$  should be interdependent. For values less than rated frequency, the machine flux is kept constant, which determines a constant critical torque. At low frequencies, the stator resistance has high values, while the dispersion reactances have low values; therefore, it cannot be neglected as in the relationship (3.100). Thus, the critical torque decreases if the  $\frac{U_s}{f_1}$  ratio

is constant. Therefore, the variation of the  $\frac{U_s}{f_1}$  ratio will be chosen as in the Fig. 3.28 and thus the effect of the stator resistance at low frequencies is compensated. Above the rated frequency, the supply voltage remains constant,  $U_s = U_{sn}$ , and as a result, in this area, the critical torque decreases due to the flux reduction while the maximum active power remains constant.

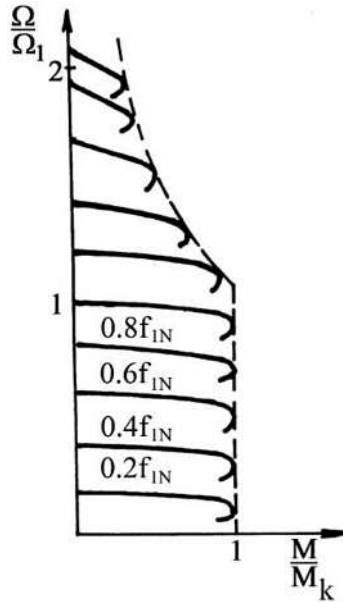


Fig. 3.29 Characteristics of induction actuator at frequency change.

The situation is similar to the DC machine control under field weakening. Mechanical characteristics in p.u. values obtained by changing the frequency are shown in Fig. 3.29. Basically, the transition from one stable point of operation to another, on the drawn characteristics, is possible in two ways: maintaining a constant flux by modifying the slip, and keeping the slip constant by modifying the flux, respectively.

For the motor, considered unsaturated, to operate providing the same efficiency, power factor and critical torque, under the conditions of frequency changes, it may be necessary to use the relationship:

$$\frac{U'_s}{U_s} = \frac{f'_1}{f_1} \sqrt{\frac{M'}{M}} \quad (3.102)$$

Where  $U'_s$  and  $M'$  correspond to the frequency, relationship which shows the same type of torque dependence on the  $\frac{U_s}{f_1}$  ratio as the relationship (3.100).

In case it is necessary to keep the overload capacity unchanged, based on the relationship (3.100), the ratio of the critical torques to two different speeds must be equal to the ratio of the resistive torques, i.e.:

$$\frac{M'_k}{M_k} = \frac{M'_R}{M_R} = \left( \frac{U'_s}{U_s} \cdot \frac{f_1}{f'_1} \right)^2 \quad (3.103)$$

or

$$\frac{U'_s}{U_s} = \frac{f'_1}{f_1} \sqrt{\frac{M'_R}{M_R}} \quad (3.104)$$

similar to (3.102). Relationship (3.104) shows that the optimal way of changing the voltage when speed modifies, by changing the frequency, is similar to the relationship expressing the torque variation mode.

The control systems used for the scalar speed control of the induction motors are divided into two categories, depending on the absence or presence of the external speed control loop in:

- **open loop control systems;**
- **closed loop control systems.**

It is generally based on the relationships existed between the scalar magnitudes:  $u_s = f(f_1)$  or  $i_s = f(f_2)$ . It is usually necessary to keep the stator flux constant and equal to the nominal one  $\Phi_s = \Phi_{sn} = const$ .

Based on these theoretical notions, there are some basic schemes for performing the induction motors' scalar control.

### 3.4.2. Open loop control systems

In the configuration of these control systems, the machine speed is not used as feedback for determining the command, but there can be internal control loops with feedback to some controlled quantities such as voltages, currents, torque, slip.

#### 3.4.2.1 Control systems without internal reactions

This control systems category, with no feedback from the controlled speed or other machine parameters, has the simplest scalar speed control structure.

In many variable speed drives in which a small variation of the machine angular speed with load is allowed, the open-loop scalar control without internal reactions uses the  $u_s = f(f_1)$  at  $\Phi_s = const$ . with a compensation of stator resistance effect at low frequencies (see Fig.30).

The diagram in Fig. 3.30 implements the linear voltage/frequency characteristic shown in Fig. 3.31. The characteristic "1" in Fig. 3.31 is nonlinear. The stator voltage  $U_s$  is proportional to the frequency  $f_1$  in the high frequency range, but in the low frequency area

a compensation of the stator resistance effect is required to keep the critical torque constant (see Fig. 3.28). The linear characteristic in Fig. 3.30, on which the control of the system is based, is defined by the following equation:

$$U_s = U_0 + kf_1 \quad (3.105)$$

where  $U_0$  represents the constant stator voltage component and  $k$  is the slope of the characteristic. The two magnitudes are chosen in such a way that the voltage required to compensate for the effect of stator resistance is applied to  $f_1 = 0$  Hz and for  $f_1 = f_{1n}$ ,  $U_s = U_{sn}$  is obtained. In other words, the  $U_s$  voltage compensation is done by injection of the voltage  $U_0$ , which can decrease as the frequency increases, or it can be set to the minimum value,  $U_0$ .

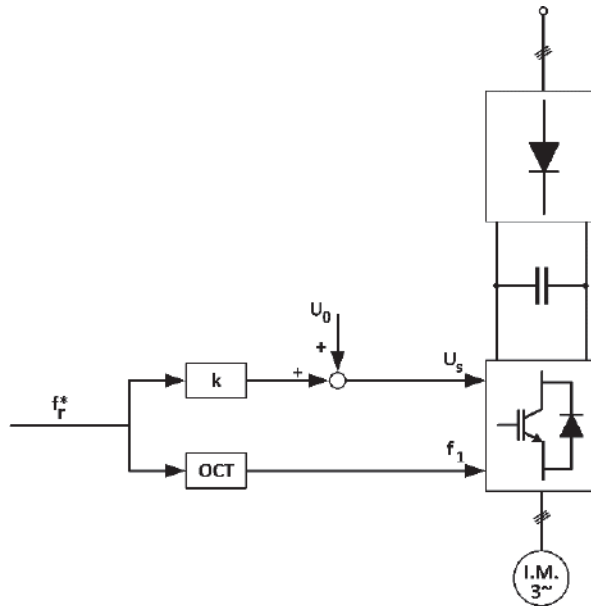


Fig. 3.30 Scalar open-loop control with  $u_s = f(f_1)$  at  $\Phi_s = const.$  and compensating the stator resistance effect at low frequencies.

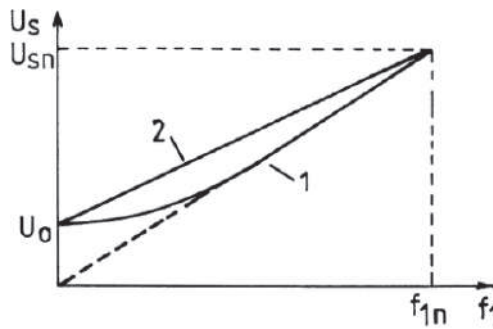


Fig. 3.31 Explanatory to the linear voltage / frequency characteristic used by the system of Fig. 3.30.

The control frequency of the inverter  $f_i$  is generated by the oscillator controlled by the OCT voltage based on the machine speed reference value,  $\Omega_r^*$  (rotation frequency  $f_r^*$ ). This magnitude directly determines the  $U_s$  control voltage.

Another possibility to implement the scalar control without internal reactions is shown in Fig. 3.32.

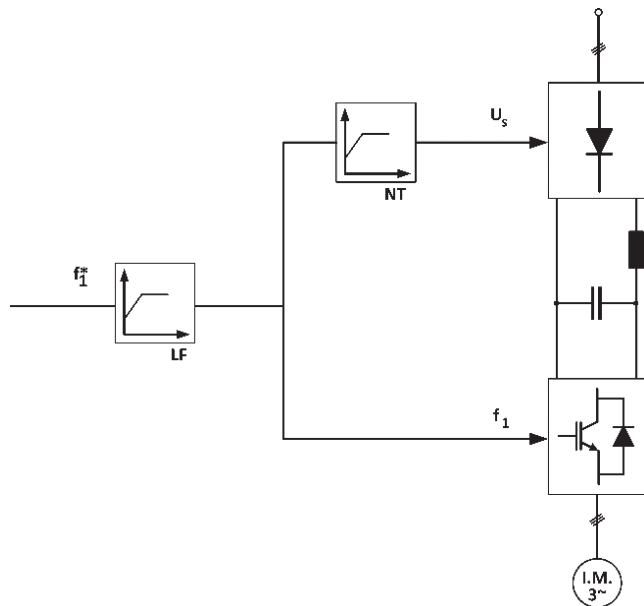


Fig. 3.32 The scheme diagram of the scalar speed control system without reactions.

The scheme allows obtaining the dependence  $u_s = f(f_i)$  at  $\Phi_s = const.$ , by implementing the previous voltage/frequency linear characteristic scheme in Fig. 3.31. The NT block, providing the voltage level can be easily implemented analogously or numerically. The ramp-limiting block on the LF control signal ensures that the acceleration-deceleration slopes are limited. In both schemes, the command being made in an open loop, protective elements of the rectifier-inverter assembly are used to protect the drive system.

### 3.4.2.2 Control systems with internal voltage and current feedbacks

To provide extra precision to speed regulation, open loop control systems use internal voltages and currents feedback loops. These internal feedback signals are especially necessary for the acceleration / deceleration of the control slope. The signal required for the voltage feedback is usually obtained by the intermediate circuit voltage and the signal required for the current feedback is obtained by the current measured at the inverter input or output. In many cases, the DC current is preferred to be set as being the feedback current signal. The advantage of its choice is that this current is no longer to be rectified and filtered, and is particularly useful for diagnosing and rapidly protecting the inverter in case of malfunction.

The principle scheme of such a drive system using a PWM inverter is shown in Fig. 3.33.

The Limitation and Protection Block (LPB) is designed to limit acceleration / deceleration slopes and to achieve efficient protection against exceeding current limit values in case of internal faults. When the machine is operating in the motor mode, if  $f_1$  rises too fast compared to machine speed, then the slip and therefore the stator current will increase rapidly. To limit the maximum acceleration slope so that the current flowing through the inverter and motor does not exceed a limit value  $I_{dcm}$ , the instantaneous current value is compared to this limit, and the error acts through a current controller  $C_i$  to reduce the acceleration rate to a maximum admissible value. The current response works similarly when the machine is in braking operating mode, limiting the deceleration rate to a permissible limit value.

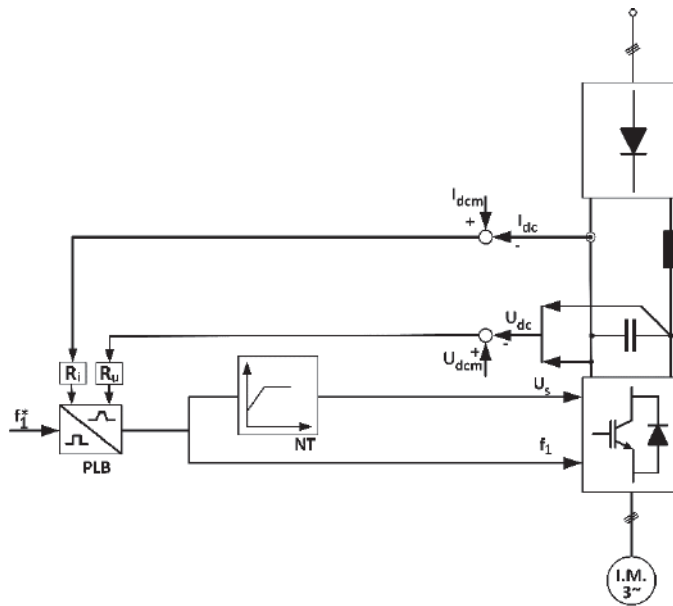


Fig. 3.33 The principle diagram of an open-loop drive system with internal voltage and current feedbacks.

In braking mode, the voltage at the capacitor terminals in the intermediate circuit must be kept below a certain limit value. For rapid deceleration, this voltage may rise above the limit  $U_{dcm}$ . The voltage response acts similarly to the current in order to limit the machine deceleration rate. In modern drives, where microprocessors are used for the implementation of controllers, in some cases, choosing the optimal acceleration / deceleration rates involves advanced control techniques or elements specific to artificial intelligence.

Current and voltage responses can also be used to compensate the machine slip. The above diagram neglects the slip variation. The imposed machine stator frequency was

considered to be approximately equal to the machine rotation speed. A torque variation at the machine shaft leads to a change in slip. Under these circumstances, in order to maintain constant speed, it is necessary to also keep the slip constant, preferably at its nominal value. The slip is proportional to the machine electromagnetic torque and, in order to determine its value, an accurate torque estimation is needed. In a first approximation, the torque can be estimated by measuring the power in the intermediate circuit (DC). Thus, the electromagnetic power  $P$  can be calculated, from which the electromagnetic torque  $M$  and the slip (slip frequency)  $f_2$  are determined according to the following relationships:

$$M = \frac{P}{\Omega_1} \approx \frac{P}{\omega_1} U_{dc} I_{dc} \quad (3.106)$$

$$f_2 = sf_1 = \frac{M}{k\Phi_s^2} \quad (3.107)$$

The principle scheme of a slip compensation actuator is shown in Fig. 3.34.

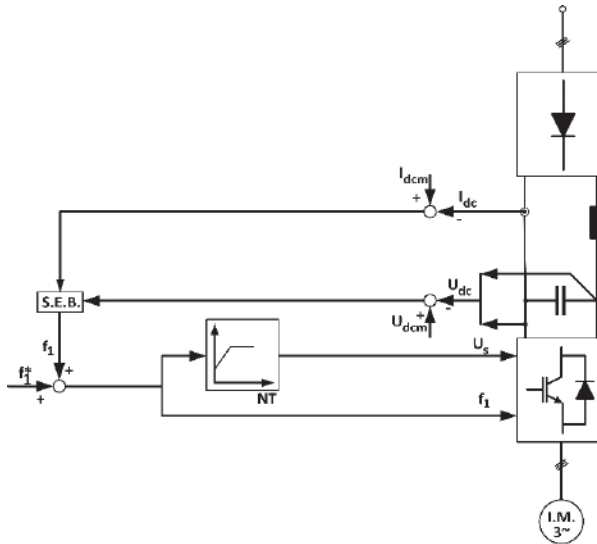


Fig. 3.34 Principle scheme of the open loop control system with slip compensation.

### 3.4.3 Closed loop control systems

In open loop control systems, the speed is dependent on the load torque unless action is taken to compensate for the slip, which is influenced by the voltage variations. Their dynamic performances are also modest. If greater speed accuracy is required, then closed loop speed control is needed.

A closed loop control scheme of the flux and torque is shown in Fig. 3.35 [20]. At the output of the torque controller, a signal proportional to the slip  $f_2$  is generated, which, in addition to the machine rotation frequency  $f_r$ , generates the control frequency  $f_i$ . The

machine flux can be kept constant, as in the DC machine with separate excitation, or programmed depending on the developed electromagnetic torque. There is also the possibility of bi-positioning the current of the machine if the parameter estimation block allows the generation of a three-phase system proportional to the currents of the machine. The diagram claims high dynamic performances because it only has a high electromechanical time constant that can be annihilated in the control process.

Fig. 3.36 shows a control scheme in which the speed control is made in a closed loop, while the slip is also controlled. The difference between the required speed  $f_r^*$  (machine rotating frequency) and its measured value supplied by the TG tacho-generator is applied at the input of the speed controller. Its output signal is the required value of the rotor frequency  $f_2$  (slip frequency). This signal is added to the tacho-generator signal, obtaining thus the required value of the stator feed frequency  $f_1$ . In addition, this signal is also applied to the input of the function generator FG -  $(\frac{U_s}{f_1})$ , which prescribes the imposed value for the stator voltage  $U_s$ , amplified at low operating frequencies so that the air gap flux is kept approximately constant. Under these conditions, the motor torque is proportional to the slip and the slip control loop operates subordinately to the torque control loop.

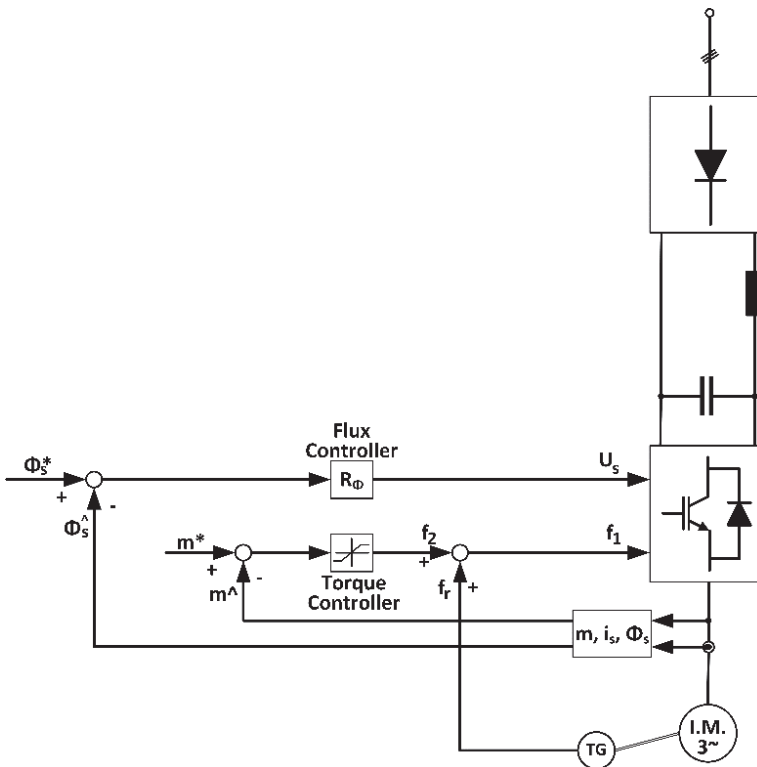


Fig. 3.35 Flux and torque scalar control.



When a sudden increase in machine speed is required, the speed controller limits the slip frequency, which leads to the development of a dynamic torque for a rapidly reach of the prescribed speed.

Machine speed control can also be done using the control scheme in which the inverter part of the static frequency converter is a current source and the rectifier part is a controlled one. The intermediate circuit has in this case a DC current source nature. The current source inverters produce a current having the waveform as shown in Fig. 3.37, which causes overvoltage peaks overlapped over the sinusoidal alternating voltage due to the current variation in the switching range.

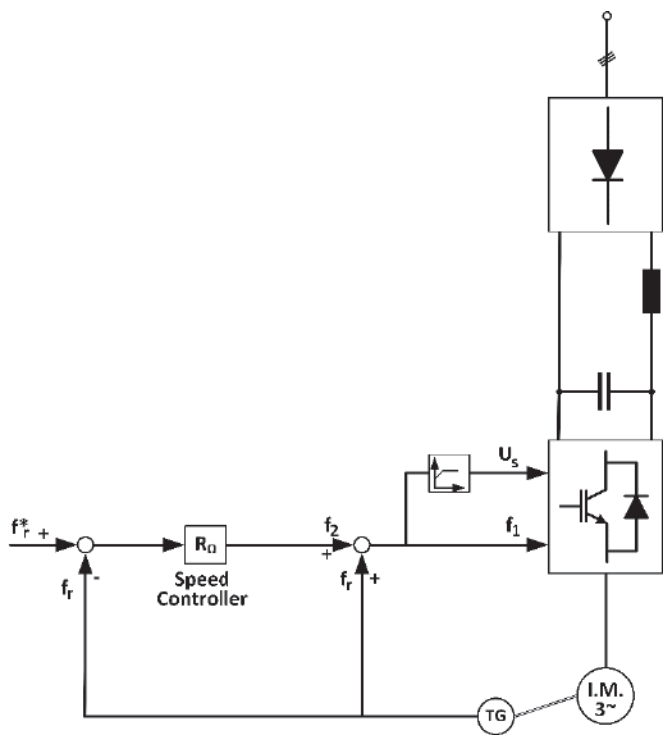


Fig. 3.36 Closed loop scalar control of speed and slip.

The current source inverter is self-extinguishing, the priming of a thyristor causing the former to lock in the conduction. Thus, a switching process takes place to transfer the current from one machine phase to another over a period, determined by the size of the current, the condensator capacitance and the motor inductance. As the machine inductance depends on saturation, the switching process could increase the machine flux above its nominal value.

For this inverter particularly, the machine flux supervision is also favorable for the inverter operation. Due to the high inductance of the coil in the intermediate circuit, for each value of the current  $I_{dc}$  in the intermediate circuit, the machine current is load

independent. The mechanical characteristics for different currents reported at the machine nominal speed, for the same feed frequency, are shown in Fig. 3.38.

If the induction motor operates at the rated current, on characteristic "1", the starting torque developed by the machine is very small, compared to the one given for the nominal voltage supply due to the reduced flux corresponding to the machine short-circuit impedance. As the speed increases, the voltage increases at the machine terminals due to the increase in impedance and thus of the machine flux and torque increase, respectively. If saturation is neglected, the torque would rapidly increase to a high value (the discontinuous line) and would quickly fall to zero at synchronous speed.

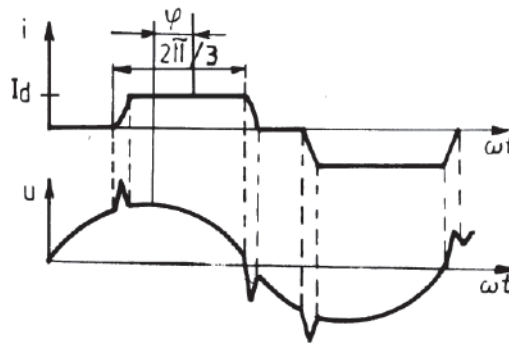


Fig. 3.37 The current and voltage of the induction servomotor fed through a current source inverter  $I_d$  becomes  $I_{dc}$ .

Under the influence of saturation, the maximum torque is reduced. For comparison, the mechanical characteristic corresponding to the nominal voltage "1" is shown. The intersection of the two mechanical characteristics determines the point A which, on the characteristic "2", is unstable. On the same characteristic "2", the machine can develop the same torque value also in the point B, which is stable. At point A, the machine flux is the nominal one because the point A is also part of characteristic "1", while in B, the flux is somewhat higher and the saturation causes additional iron losses and torque ripples. In terms of losses in copper, the stator ones are equal in A and B, and the rotor ones are slightly larger in A than in B. However, it is desirable to operate at point A on the Fig. 3.38, as this point corresponds to the nominal flux value, which can be achieved only in automatic control due to the instability existent at that point of operation A [20]. A control scheme, in which the slip is constant and the speed is modified by the prescribed current in the intermediate circuit, is shown in Fig. 3.39. The scheme recalls for the characteristics in Fig. 3.38.

The prescribed value of the slip is chosen on the unstable portion of the mechanical characteristic, as shown above. When prescribing speed  $f_r$  (rotation frequency), the machine accelerates and thus a high value for the current in the intermediate circuit results, which finally develops a proportional torque leading in the end to a process being

stabilized at the required operating point. The disadvantage of the scheme is that the machine flux varies greatly for the various operating points imposed to the machine.

A more refined scheme is shown in Fig. 3.40, where both the machine speed and the air gap flux are controlled. The electromagnetic torque is controlled by the prescribed current. As for the flux, this is provided by a functional block that ensures the dependence between the torque and the flux by means of slip with the  $f_2 = f(i_{dc})$ , for adequate machine operation.

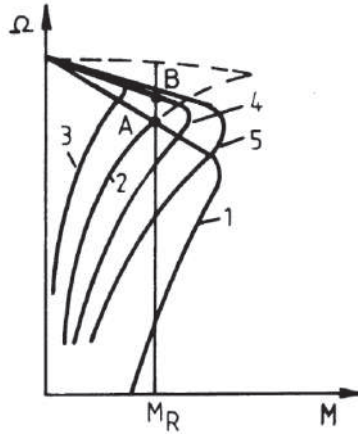


Fig. 3.38 Characteristics of induction actuator: "1"-characteristic corresponding to the nominal voltage; characteristics "2" ÷ "5" corresponding to feeding by the current source inverter. "2" – at  $I_{sn}$ ; "3" – at  $0.5 I_{sn}$ ; "4" – at  $1.5 I_{sn}$ ; "5" – at  $2 I_{sn}$ .

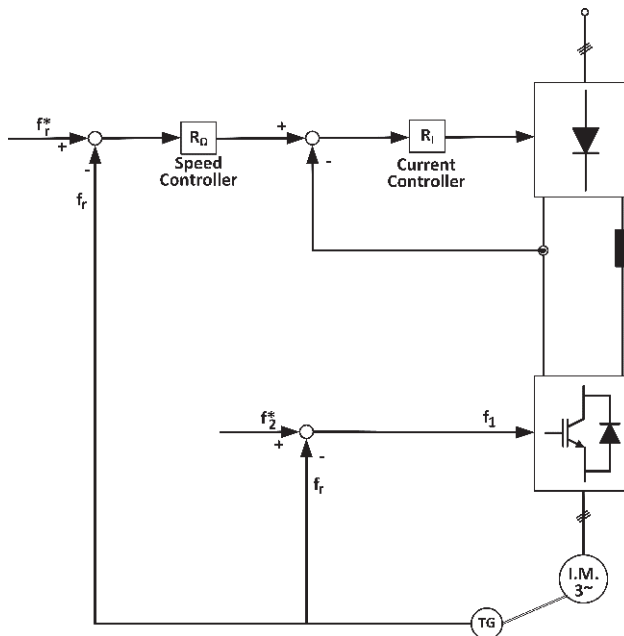


Fig. 3.39 Block diagram for constant slip speed control.

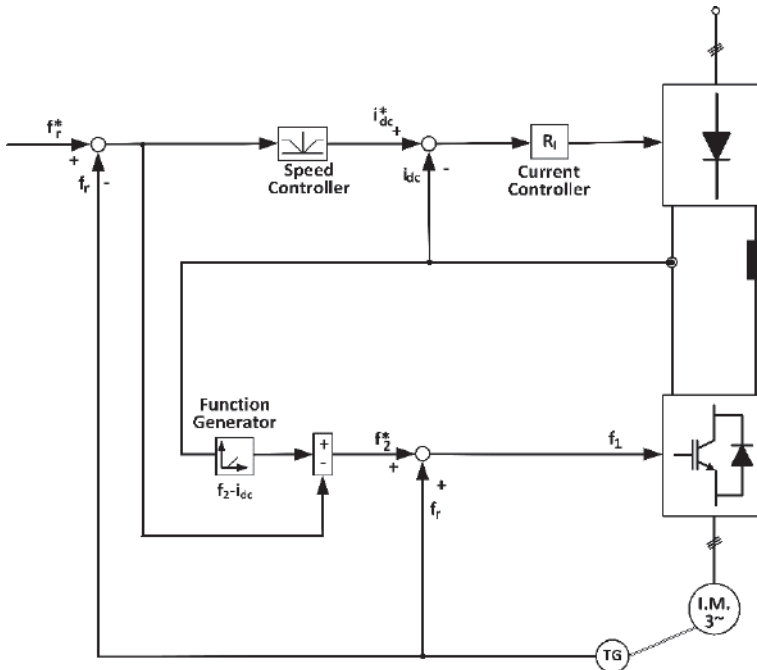


Fig. 3.40 Block diagram for the control of the induction servomotor with current source inverter.

The operation in the flux weakening area is possible only for machine speed ranges over the nominal value speed, by prescribing the speed when the active rectifier reaches its maximum voltage allowance. In this particular situation, the flux becomes inversely proportional to the speed. Neither of these control procedures, as in the case of the stand-alone inverter with voltage source, fast controlled processes can be achieved because of the inertia introduced by the inductance in the intermediate circuit [20].

Fig. 3.41 shows a very robust scalar control scheme in which the static frequency inverter is transformed into a current source by the command using hysteresis current controllers. The motor speed is set by the function  $i_s = f(f_2)$  at  $\Phi_s = \text{const}$ .

The value of the machine rotation frequency  $f_r$  (rotation speed) measured by the tachogenerator (TG) is compared to its reference value  $f_r^*$ , the difference being applied to the PI-type speed controller. At its output, the reference value of the rotor frequency  $f_2^*$ , which is applied to the input of the function generator  $i_s - f_2$ , is obtained. It prescribes the imposed amplitude of the stator current, maintaining the constant stator flux  $\Phi_s$ ;  $i_{s1}^* = i_s^*$  as long as  $U_s$  is less than or equal to  $U_{sn}$ , and  $f_i$  is less than or equal to  $f_{1n}$ .

If the stator voltage  $U_s$  measured by the voltage transducer exceeds the prescribed limit,  $U_{slim}$  at the voltage controller output the value  $i_{s2}^* < i_{s1}^*$  is applied to the min value of DFV-min. This limits the value of  $i_s^*$ , which becomes equal to  $i_{s2}^*$ . In this way, the induction machine will work with weakened stator flux.

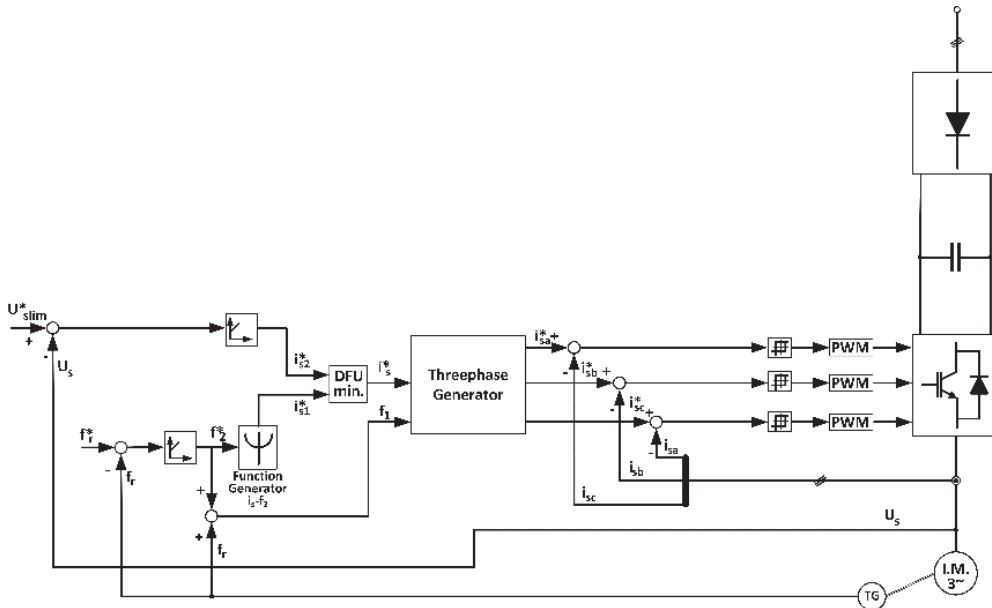


Fig.3.41 Scalar control of the induction servomotor with current-controlled inverter.

The sinusoidal stator currents obtained at the output of the three-phase generator  $i_{sa}^*$ ,  $i_{sb}^*$ ,  $i_{sc}^*$  are proportional to the prescribed value of the stator current  $i_s^*$  given by DFV-min and their frequency is  $f_2$ , the value imposed on the stator frequency obtained by measuring  $f_r$  (measured) and  $f_2'$  (imposed).

The inverter is controlled so that the inverter output current is maintained at the reference value. In the case of the presented scheme, this is done with the help of three hysteresis current controllers. The diagram illustrates the indirect control of the stator flux by controlling the stator current.

As a conclusion to this paragraph, it can be said that, due to advantages such as simplicity, high reliability, low cost of the control systems, the scalar speed control method of the induction machine is the most suitable method for general use variable electric drives, where no demanding dynamic performance is required.

### 3.5 References

- [1] Kelemen, M. Imecs, "Sisteme de reglare cu orientare după câmp ale mașinilor de curent alternativ", Editura Academiei R.S.R., București, 1989.
- [2] A. Kelemen, M. Imecs, "Acționări electrice", Editura Didactică și Pedagogică, București, 1979.
- [3] S. Mușuroi, D. Popovici, "Acționări electrice cu servomotoare", Editura Politehnica, Timișoara, 2006.
- [4] M. Biriescu, "Mașini electrice rotative. Parametri, caracteristici, încercări", Editura de Vest, Timișoara, 1997.

- [5] A. Câmpeanu, "Introducere în dinamica mașinilor electrice de curent alternativ", Editura Academiei Române, București, 1998.
- [6] I. Boldea, "Transformatoare și mașini electrice", Editura Politehnica, Timișoara, 2001.
- [7] S. Mușuroi, V. Olărescu, "The Mathematical Model for Three- Phase Cage Induction Motors Supplied by Static Frequency Converters", International Aegean Conference on Electrical Machines and Power Electronics, ACEMP 2001, Kusadasi, Turkey.
- [8] S. Mușuroi, "Mașina de inducție alimentată prin convertoare statice de frecvență", Editura Eurostampa, Timișoara, 2014.
- [9] A. Rui, S. Mușuroi, "Induction motor. Modelling and control. Chapter 2. The Behavior in Stationary Regime of an Induction Motor Powered by Static Frequency Converters", InTech Europe, Rijeka, Croația, 2012.
- [10] S. Mușuroi, M. Bogoevici, "Determinarea pierderilor din fierul rotorului al mașinilor trifazate cu rotorul în colivie în situația alimentării acestora prin convertoare statice de frecvență", Lucrările științifice ale simpozionului internațional Universitatea ROPET, Petroșani, pp. 41-44, Petroșani, 2000.
- [11] S. Mușuroi, Gh. Bogoevici, "Determinarea parametrilor echivalenți ai circuitului magnetic al mașinilor de inducție trifazate cu rotorul în scurtcircuit alimentate prin invertoare de tensiune", Sielmen –2001, vol. I, pp. 21-22, Chișinău, Moldova.
- [12] S. Mușuroi, V. Olărescu, "The Equivalent Factors Determination of Rotor Parameters Modification in Case of Cage Induction Motors Supplied by Static Frequency Converters", Applied Research Review on Technology and Automation, Pireu, 2000, Greece.
- [13] S. Mușuroi, Gh. Bogoevici, "The Determination of the Equivalent Modification Factors of the Rotoric Parameters while the Cage Induction Motors are Being Supplied by Invertors", 15th International Conference on Electrical Machines, ICEM 2001, Bruges, Belgium.
- [14] R. Schönfeld, E. Habiger, "Automatisierte Elektroantriebe", VEB Verlag Technik, Berlin, 1981.
- [15] N. Mohan, T. Underland, W. Robbins, "Power Electronics", John Wiley & Sons, Inc., New York, 1995.
- [16] D. Popovici, "Bazele convertoarelor statice", Editura Politehnica, Timișoara, 1999.
- [17] M. Dehmlow, K. Hermann, R. Sommer, "Resonant inverter systems for drive applications", EPE Journal, nr. 4, 1992.
- [18] B. Bose, "Power Electronics and Variable Frequency Drives", IEEE Press, New York, 1997.
- [19] I.F. Soran, "Sisteme de acționare electrică", Matrix Rom, București, 2010.
- [20] E. Seracin, D. Popovici, "Tehnica acționărilor electrice", Editura Tehnică, București, 1985.

## 4.1 Introduction

Modern electric drive systems use induction or synchronous machines supplied by power electronic converters that are digitally controlled by advanced microprocessors. At present, the induction machine (IM) is the predominant electric machine employed by electromechanical conversion systems in the vast majority of the industrial applications. IMs have a simple and robust construction, are reliable and easy to maintain, can be operated in difficult environments, and are inexpensive. The cage-rotor IMs cover a wide power range, from under 100 W to 10 MW, while wound-rotor IMs can handle even higher power levels. When supplied by power converters, IMs can be efficiently operated over a wide range of speed, torque, and power, and have a good overloading capability. IMs are less expensive than synchronous machines, but they have a lower power density, are less efficient, and run with a lower power factor. The IM was independently invented by Nikola Tesla and Galileo Ferraris in the late nineteenth century [1].

Conventional IM drives that are supplied from the industrial power grid at constant voltage and frequency are limited to driving loads which require nearly constant rotor speed or, at best, several discrete speeds. Operating a grid-tied IM at other speeds than the rated speed is difficult and involves a substantial degradation of its efficiency. The problem has been overcome by using variable voltage-frequency power converters that allow four-quadrant operation at variable speed and are able to adjust the motor torque in a continuous fashion. An electric system composed of an electric machine, a power electronic converter, a dedicated control system, a mechanical load, and other related equipment forms an adjustable speed drive (ASD). Historically, one of the first ASDs using DC motors was patented by Harry Ward Leonard in 1891 [2].

Modern ASDs employ two major techniques for motion control: scalar control, known as voltage-frequency control, and vector control, also known as field-oriented control. Whereas the voltage-frequency control is a simple feedforward-type open-loop scheme that delivers a relatively modest performance, the vector control is a closed-loop feedback scheme that offers fast and accurate speed and torque control. Accurate motion control (torque, speed, and position control) with IMs is a challenging theoretical problem, as the IM dynamic model is nonlinear and time-variable, rotor currents are most often non-measurable, and electrical parameters are variable or imprecisely known.

Recent research efforts have been aimed at developing high performance vector-controlled schemes that provide fast, robust, and accurate motion control without using motion sensors. To this end, advanced state observers are used as replacements for mechanical sensors in what is named motion sensorless control. Observers allow stable operation over speed ranges of above 1:100, and these drives are more reliable and less expensive. However, the very low speed operation is still a challenging problem, and only a few sensorless schemes are capable of superior performance.

This chapter is dedicated to the most advanced vector control techniques employed for ASDs with IMs. Three conventional schemes, direct vector control, indirect vector control, and direct torque control are discussed in what follows. Several modern schemes based on linear control and sliding mode control are also described. A subchapter is dedicated to IM state-space modeling, while another one describes several state-of-the-art observers. Most of the concepts are supported by experimental results performed by the author in the motion control laboratory at University Politehnica of Timisoara.

#### 4.1.1 Space-vector definition

The concept of complex space vectors is a powerful tool used for the analysis, modeling, and control of three-phase systems. A space vector provides a compact notation, allows algebraic manipulations based on the complex numbers algebra, has simple graphical interpretations, and offers a logical understanding of concepts that are more difficult to handle using real variable analysis.

Consider a three-phase electrical system represented by instantaneous values of a three-phase variable, for instance the three voltages ( $u_a, u_b, u_c$ ) of the industrial grid. This system can be uniquely described by a complex space vector  $\underline{u}$ , and a zero-sequence component  $u_0$ , defined as

$$\underline{u} = \frac{2}{3}(u_a + \underline{a}u_b + \underline{a}^2u_c) \quad (4.1)$$

$$u_0 = \frac{1}{3}(u_a + u_b + u_c) \quad (4.2)$$

where  $\underline{a} = e^{j2\pi/3}$  and  $\underline{a} = e^{-j2\pi/3}$  are unity vectors that define the three-phase axes.

In general, the space vector is a complex variable,  $\underline{u} = u_\alpha + ju_\beta$ , which represents the instantaneous three-phase variables in the two-dimensional complex plane. The real and imaginary components are defined as

$$u_\alpha = u_a - \frac{1}{3}(u_a + u_b + u_c) \quad (4.3)$$

$$u_\beta = \frac{1}{\sqrt{3}}(u_b - u_c) \quad (4.4)$$



In all practical situations when the system is symmetrical the zero component is zero,  $u_0 = 0$ , and the real component is equal to the phase-a variable,  $u_\alpha = u_a$ . It is usual for IMs to attach the reference frame of the complex plane to the physical stator, with the real axis aligned along the magnetic axis of the phase a. This frame is stationary with respect to ground and it is called the “stator reference frame”.

It is possible to define revolving reference frames that rotate with an arbitrary angular speed  $\omega_e = d\theta_e/dt$ . The space vector  $\underline{u}$  can be represented in a rotating frame as  $\underline{u}^e = u_d + ju_q$ , where superscript “e” denotes the frame name, and “d” and “q” are names of the real and imaginary axes (initials of “direct” and “quadrature”). The transformation from the stator to rotating frame is

$$\underline{u}^e = \underline{u} \cdot e^{-j\theta_e} \quad (4.5)$$

$$u_d = u_\alpha \cos(\theta_e) + u_\beta \sin(\theta_e) \quad (4.6)$$

$$u_q = -u_\alpha \sin(\theta_e) + u_\beta \cos(\theta_e) \quad (4.7)$$

The inverse transformation from the rotating to the stator frame is

$$\underline{u} = \underline{u}^e \cdot e^{j\theta_e} \quad (4.8)$$

$$u_\alpha = u_d \cos(\theta_e) - u_q \sin(\theta_e) \quad (4.9)$$

$$u_\beta = u_d \sin(\theta_e) + u_q \cos(\theta_e) \quad (4.10)$$

Equations (4.1) to (4.10) apply to all variables in an electric machine, i.e. to voltages, currents, flux linkages, and MMFs. In this case, the space vectors represent quantities that are variable in space and in time. The revolving magnetic field is sinusoidally distributed in space along the air-gap, and travels with finite speed from one phase to another when the stator currents are modified. Therefore, the MMF is a true space vector because its spatial direction and polarity can be determined at each time instant.

## 4.2 State-space models of induction machines

Although the IM has a very simple structure, it owns the most complex dynamic model when compared to other electric machines and it proves to be the most challenging in terms of control engineering and state estimation. The steady state, per-phase equivalent circuit (3.75) is inadequate when dealing with fast dynamic processes encountered in ASDs. Advanced control systems and state observers require dynamic modeling of the IM behavior in order to run at any operating point in the speed-torque plane.

IM modeling and analysis can be performed using physical three-phase quantities. By analyzing the machine structure and using Maxwell’s electromagnetic field theory, the three-phase real-variable model can be obtained, as shown section 3.2.2. In this case, the IM electromagnetic model consists of six circuits with an extensive amount of coupling

between them. In all the situations in which the fundamental polyphase symmetry is retained, the analysis can be carried out in vector form and the IM model is reduced to a compact second-order complex-variable model. The order reduction permits a considerable simplification and it is valuable in the constant speed analysis when the otherwise nonlinear IM model becomes a linear time-invariant dynamic system.

The IM modeling is based on the following simplifying assumptions [3]-[7]:

- a. The air-gap is uniform, and the machine is symmetrical from an electro-magnetic perspective. This assumption is true for all IMs.
- b. The stator and rotor windings have a sinusoidal spatial distribution along the stator inner periphery and the rotor outer periphery. This assumption implies that the magnetic flux density has a sinusoidal distribution along the air-gap.
- c. The space harmonics and other effects caused by the placement of the actual conductors in the discrete slots are neglected. The windings can be visualized as being of negligible depth and located in the air-gap.
- d. Magnetic saturation and iron losses are neglected. The permeability of the stator and rotor iron cores is assumed to be infinite
- e. The end winding effects, the magnetic anisotropy effect, and the skin effect are all neglected.

#### 4.2.1 The space-vector general model

Consider an IM supplied in the stator by a balanced voltage system ( $u_{sa}, u_{sb}, u_{sc}$ ), with short-circuited rotor. The IM electromagnetic model in the stator reference frame is

$$\underline{u}_s = R_s \underline{i}_s + \frac{d}{dt} \underline{\psi}_s \quad (4.11)$$

$$\underline{0} = R_r \underline{i}_r + \frac{d}{dt} \underline{\psi}_r - j\omega_r \underline{\psi}_r \quad (4.12)$$

$$\underline{\psi}_s = L_s \underline{i}_s + L_m \underline{i}_r \quad (4.13)$$

$$\underline{\psi}_r = L_r \underline{i}_r + L_m \underline{i}_s \quad (4.14)$$

where  $\underline{u}_s = u_{s\alpha} + ju_{s\beta}$  is the stator voltage vector,  $\underline{i}_s = i_{s\alpha} + ji_{s\beta}$  is the stator current vector,  $\underline{i}_r = i_{r\alpha} + ji_{r\beta}$  is the rotor current vector (stator referred),  $\underline{\psi}_s = \psi_{s\alpha} + j\psi_{s\beta}$  is the stator flux linkage vector,  $\underline{\psi}_r = \psi_{r\alpha} + j\psi_{r\beta}$  is the rotor flux linkage (stator referred) vector, and  $\omega_r$  is the electrical rotor speed. IM electrical parameters are: the stator and rotor (stator referred) resistances,  $R_s$ , and  $R_r$ , the magnetizing inductance,  $L_m$ , the stator inductance,  $L_s = L_m + L_{s\sigma}$ , and the rotor inductance (stator-referred),  $L_r = L_m + L_{r\sigma}$ , where  $L_{ss}$ , and  $L_{rs}$  are the stator and rotor leakage inductances. For the vast majority of practical applications it is sufficient to consider all IM parameters as constants. In reality, resistances change slowly and substantially with the temperature, while inductances change with the magnetic saturation.

The actual three-phase circuits of an IM are shown in Fig. 4.1.a. and the space-vector circuit, equivalent to the electromagnetic model (4.11)-(4.14), is illustrated in Fig. 4.1.b.

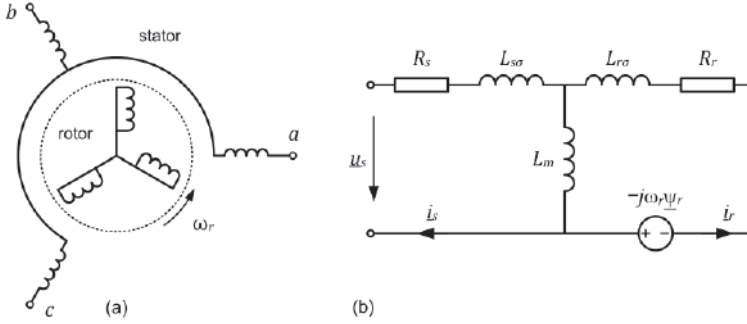


Fig. 4.1 Induction machine (a) physical three-phase stator and rotor circuits and (b) the space-vector equivalent circuit in the stator reference frame.

The electromagnetic torque produced by an IM is the output power divided by the mechanical rotor speed. It can be proven that the torque is proportional with the vector product between the stator current and stator flux vectors, as

$$T_e = \frac{3}{2} p \Im m \left( \underline{i}_s \underline{\psi}_s^* \right) = \frac{3}{2} p (\psi_{s\alpha} i_{s\beta} - \psi_{s\beta} i_{s\alpha}) \quad (4.15)$$

The torque can be expressed using other quantities, as in the following equations.

$$T_e = \frac{3}{2} p \frac{L_m}{L_r} \Im m \left( \underline{i}_s \underline{\psi}_r^* \right) = \frac{3}{2} p \frac{L_m}{L_r} (\psi_{r\alpha} i_{s\beta} - \psi_{r\beta} i_{s\alpha}) \quad (4.16)$$

$$T_e = \frac{3}{2} p \Im m \left( \underline{\psi}_r \underline{i}_r^* \right) = \frac{3}{2} p (\psi_{r\beta} i_{r\alpha} - \psi_{r\alpha} i_{r\beta}) \quad (4.17)$$

$$T_e = \frac{3}{2} p L_m \Im m \left( \underline{\psi}_s \underline{\psi}_r^* \right) = \frac{3}{2} p \frac{L_m}{L_s L_r \sigma} (\psi_{s\beta} \psi_{r\alpha} - \psi_{s\alpha} \psi_{r\beta}) \quad (4.18)$$

The mechanical subsystem that describes the motion of the rotor is

$$\frac{J}{p} \frac{d}{dt} \omega_r + \frac{B}{p} \omega_r = T_e - T_L \quad (4.19)$$

where  $T_L$  is the load torque,  $J$  is the total inertia of the system referred to the motor shaft,  $p$  is the IM number of pole pairs, and  $B$  is the damping (friction) coefficient. The mechanical rotor speed is  $\omega_m = \omega_r/p$ . Taking into account the torque and speed equations, the entire IM model is a fifth-order cross-coupled nonlinear system.

In most practical situations the electromagnetic time constants are much smaller than the mechanical time constant, and the system can be frequency-separated into two subsystems: a fast electromagnetic system (4.11)-(4.14) and a slow mechanical system (4.19). The electromagnetic system becomes linear time-variable if all parameters are assumed as being constant and the rotor speed is regarded as a slowly-variable parameter. The mechanical system is always linear and the torque equation (4.15) is the only nonlinear connection between these two subsystems.

Equations (4.13) and (4.14) are algebraic constraints relating currents to fluxes, and can be used to eliminate one or two variables. By removing the rotor current between (4.13)-(4.14) and solving for the stator and rotor fluxes, one obtains

$$\underline{\psi}_s = \frac{L_m}{L_r} \underline{\psi}_r + L_s \sigma \underline{i}_s \quad (4.20)$$

$$\underline{\psi}_r = \frac{L_r}{L_m} \underline{\psi}_s - \frac{L_s L_r}{L_m} \sigma \underline{i}_s \quad (4.21)$$

where  $\sigma = (L_s L_r - L_m^2)/(L_s L_r)$  is the leakage coefficient.

The electromagnetic model can be generalized for any reference frame, which rotates with an arbitrary speed,  $\omega_e = d\theta_e/dt$ . Using the transformation (4.8) for all variables in (4.11)-(4.14), one obtains the most general IM model

$$\underline{u}_s^e = R_s \underline{i}_s^e + \frac{d}{dt} \underline{\psi}_s^e + j\omega_e \underline{\psi}_s^e \quad (4.22)$$

$$\underline{0} = R_r \underline{i}_r^e + \frac{d}{dt} \underline{\psi}_r^e + j(\omega_e - \omega_r) \underline{\psi}_r^e \quad (4.23)$$

$$\underline{\psi}_s^e = L_s \underline{i}_s^e + L_m \underline{i}_r^e \quad (4.24)$$

$$\underline{\psi}_r^e = L_r \underline{i}_r^e + L_m \underline{i}_s^e \quad (4.25)$$

Notice that model (4.22)-(4.23) in the rotating frame can be obtained from the model in the stator frame by substituting the differentiation operator  $d/dt$  with  $d/dt + j\omega_e$ . Algebraic relations, such as the torque equations (4.15)-(4.18), are the same in all reference frames. The equivalent circuit for this model is illustrated in Fig. 4.2.

Depending on the control system requirements, the reference system can be attached to one of the complex vectors in the machine, either the stator flux, the rotor flux, or the stator current. In this case the  $d$  axis is aligned along the direction of that vector and the frame moves synchronously with it. The stator flux orientation is obtained when the frame is aligned with the stator flux and its speed is equal with the speed of the stator flux vector,  $\omega_e = \omega_{\psi_s}$ . Similarly, the rotor flux orientation is obtained when the frame is aligned with the rotor flux and its speed is equal with the speed of the rotor flux vector,  $\omega_e = \omega_{\psi_r}$ . Regardless of the reference frame, the IM model is nonlinear and contains cross-coupling between the real and imaginary equations.

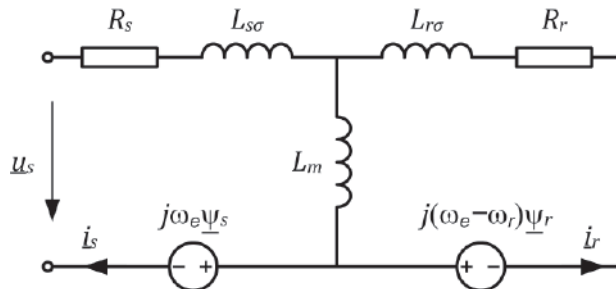


Fig. 4.2 Induction machine equivalent circuit in arbitrary reference frame.

The elimination of two complex variables using the algebraic equations (4.13)-(4.14) is a simplification that produces state-space models. For squirrel-cage IMs, the rotor current is not accessible, it is not controlled, and can be removed from all equations. The stator current is always measured and appears either as a state variable and/or as an output. In general, when stator flux control is desired, the rotor flux is eliminated, and the “stator flux model” is obtained. When rotor flux control is desired, the stator flux is eliminated, and the “rotor flux model” is obtained. If both stator and rotor fluxes are retained as state variables and the stator current is output, then the “flux model” is found. The flux model is useful when saturation effects are considered. Models including the magnetizing flux and magnetizing current may also be developed but are not further discussed.

### 4.2.2 The stator flux model

The stator flux model contains as state variables the stator current and the stator flux linkage vectors,  $x = [\underline{i}_s, \underline{\psi}_s]^T$ . The stator voltage and the rotor speed are inputs and the stator current is output,  $y = \underline{i}_s$ . This model is obtained by solving (4.24) for the rotor current and then substituting this current and the rotor flux from (4.25) into (4.23).

The IM stator flux model in an arbitrary reference frame is

$$\frac{d}{dt} \underline{i}_s^e = - \left( \frac{R_{eqs}}{L_s \sigma} + j(\omega_e - \omega_r) \right) \underline{i}_s^e + \frac{1}{L_s \sigma} \left( \frac{1}{T_r} - j\omega_r \right) \underline{\psi}_s^e + \frac{1}{L_s \sigma} \underline{u}_s^e \quad (4.26)$$

$$\frac{d}{dt} \underline{\psi}_s^e = -R_s \underline{i}_s^e - j\omega_e \underline{\psi}_s^e + \underline{u}_s^e \quad (4.27)$$

where  $T_s = L_s/R_s$  and  $T_r = L_r/R_r$  are the stator and rotor time constants, and  $R_{eqs} = R_s + R_r L_s/L_r$  is an equivalent resistance for (4.26). Equation (4.27) is the same as (4.22).

The stator flux model is a second-order time-variable nonlinear system. It becomes linear for operation at constant speed.

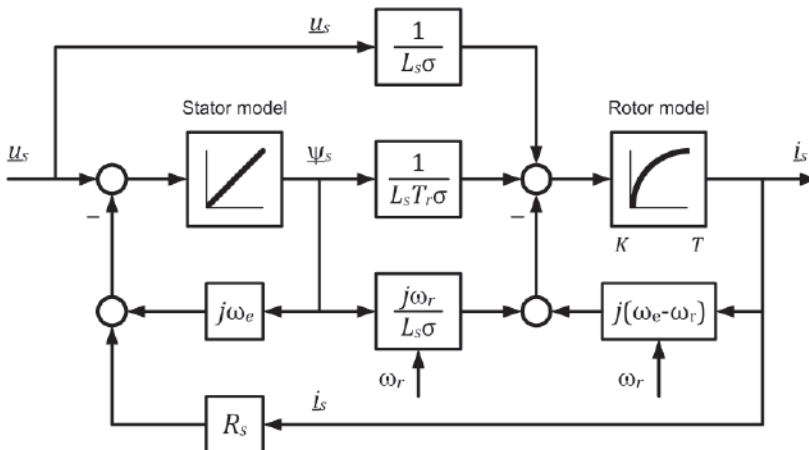


Fig. 4.3 Structural block diagram of the induction machine stator flux model.

The structural block diagram, where all variables are space-vectors, is shown in Fig. 4.3. The equation (4.26), known as the rotor model or the current model, is represented as a first-order transfer function  $H(s) = K/(Ts + 1)$  with gain  $K$  and time constant  $T$ , both specified below the block. For this model the gain and the time constant are equal,  $K = T = L_s\sigma/R_{eqs}$ . The equation (4.27), known as the stator model or the voltage model, is represented by an integrator block.

Assuming constant or slowly-variable speed, the state matrix is

$$A = \begin{bmatrix} -\left(\frac{R_{eqs}}{L_s\sigma} + j(\omega_e - \omega_r)\right) & \frac{1}{L_s\sigma}\left(\frac{1}{T_r} - j\omega_r\right) \\ -R_s & -j\omega_e \end{bmatrix} \quad (4.28)$$

The four eigenvalues of  $A$  are speed-dependent and have a remarkable property: they always add to a constant real value that is independent of the rotor speed [3].

In the stator reference frame, with  $\omega_e = 0$ , the stator flux model is

$$\frac{d}{dt}\underline{i}_s = \left(-\frac{R_{eqs}}{L_s\sigma} + j\omega_r\right)\underline{i}_s + \frac{1}{L_s\sigma}\left(\frac{1}{T_r} - j\omega_r\right)\underline{\psi}_s + \frac{1}{L_s\sigma}\underline{u}_s \quad (4.29)$$

$$\frac{d}{dt}\underline{\psi}_s = -R_s\underline{i}_s + \underline{u}_s \quad (4.30)$$

The simple voltage model (4.30) is speed-independent and forms the basis for a family of simple stator flux estimators implemented in the stator frame.

For stator flux orientation, the model is transformed to the stator flux reference frame that rotates with the stator flux speed,  $\omega_e = \omega_{\psi_s}$ . In this case the flux has real component only,  $\underline{\psi}_s^s = \psi_{sd}$  (superscript "s" denotes the stator flux frame) and the model is

$$\frac{d}{dt}\underline{i}_s^s = -\left(\frac{R_{eqs}}{L_s\sigma} + j(\omega_{\psi_s} - \omega_r)\right)\underline{i}_s^s + \frac{1}{L_s\sigma}\left(\frac{1}{T_r} - j\omega_r\right)\underline{\psi}_s^s + \frac{1}{L_s\sigma}\underline{u}_s^s \quad (4.31)$$

$$\frac{d}{dt}\underline{\psi}_s^s = -R_s\underline{i}_s^s - j\omega_{\psi_s}\underline{\psi}_s^s + \underline{u}_s^s \quad (4.32)$$

This model is mostly used for the stator flux orientation and control in direct vector control and in direct torque control schemes.

### 4.2.3 The rotor flux model

The rotor flux model contains as states the stator current and the rotor flux linkage vectors,  $x = [\underline{i}_s, \underline{\psi}_r]^T$ . The stator voltage and rotor speed are inputs and the rotor flux is output,  $y = \underline{\psi}_r$ . The IM rotor flux model in an arbitrary reference frame is

$$\frac{d}{dt}\underline{i}_s^e = -\left(\frac{R_{eqr}}{L_s\sigma} + j\omega_e\right)\underline{i}_s^e + \frac{L_m}{L_sL_r\sigma}\left(\frac{1}{T_r} - j\omega_r\right)\underline{\psi}_r^e + \frac{1}{L_s\sigma}\underline{u}_s^e \quad (4.33)$$

$$\frac{d}{dt}\underline{\psi}_r^e = \frac{L_m}{T_r}\underline{i}_s^e - \left(\frac{1}{T_r} + j(\omega_e - \omega_r)\right)\underline{\psi}_r^e \quad (4.34)$$

where  $R_{eqr} = R_s + R_rL_m^2/L_r^2$  is an equivalent resistance for the stator model (4.33).

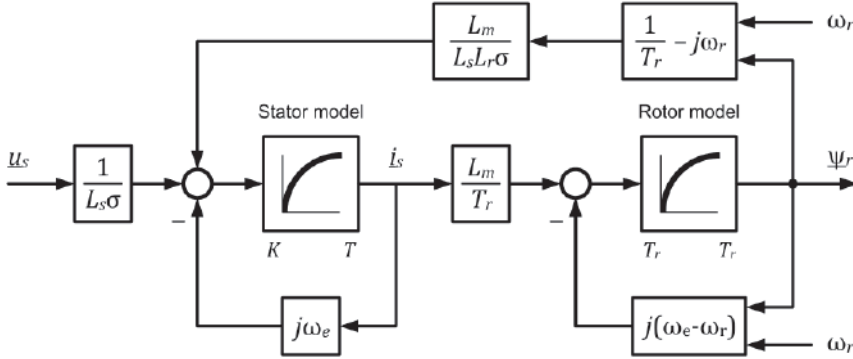


Fig. 4.4 Structural block diagram of the induction machine rotor flux model.

The rotor flux model is a second-order time-variable nonlinear system, which becomes linear for constant speed operation. The block diagram, with all space vector variables, is shown in Fig. 4.4. Both equations are represented as first-order transfer functions. The gain and time constant of the stator model are  $K = T = L_s\sigma/R_{eqr}$ . The gain and time constant of the rotor model (4.34) are  $K = T = T_r$ .

Assuming constant or slowly-variable speed, the model is linear and the state matrix is

$$A = \begin{bmatrix} -\left(\frac{R_{eqr}}{L_s\sigma} + j\omega_e\right) & \frac{L_m}{L_s L_r \sigma} \left(\frac{1}{T_r} - j\omega_r\right) \\ \frac{L_m}{T_r} & -\left(\frac{1}{T_r} + j(\omega_e - \omega_r)\right) \end{bmatrix} \quad (4.35)$$

In the stator reference frame, with  $\omega_e = 0$ , the rotor flux model is

$$\frac{d}{dt} \underline{i}_s = -\frac{1}{L_s\sigma} \left( R_s + R_r \frac{L_m^2}{L_r^2} \right) \underline{i}_s + \frac{L_m}{L_s L_r \sigma} \left( \frac{1}{T_r} - j\omega_r \right) \underline{\psi}_r + \frac{1}{L_s\sigma} \underline{u}_s \quad (4.36)$$

$$\frac{d}{dt} \underline{\psi}_r = \frac{L_m}{T_r} \underline{i}_s - \left( \frac{1}{T_r} - j\omega_r \right) \underline{\psi}_r \quad (4.37)$$

This model is mostly used to implement speed-adaptive rotor flux observers.

For rotor flux orientation, the model is represented in the rotor flux reference frame that rotates with the rotor flux speed,  $\omega_e = \omega_{\psi_r}$ . The rotor flux has real component only,  $\underline{\psi}_r^r = \psi_{rd}$  (superscript "r" denotes rotor flux frame), and the model is

$$\frac{d}{dt} \underline{i}_s^r = -\left( \frac{R_{eqr}}{L_s\sigma} + j\omega_{\psi_r} \right) \underline{i}_s^r + \frac{L_m}{L_s L_r \sigma} \left( \frac{1}{T_r} - j\omega_r \right) \underline{\psi}_r^r + \frac{1}{L_s\sigma} \underline{u}_s^r \quad (4.38)$$

$$\frac{d}{dt} \underline{\psi}_r^r = \frac{L_m}{T_r} \underline{i}_s^r - \left( \frac{1}{T_r} + j(\omega_{\psi_r} - \omega_r) \right) \underline{\psi}_r^r \quad (4.39)$$

This model is extensively used for rotor flux orientation and control in conventional direct and indirect vector control schemes. The current model (4.39) is used for rotor flux and slip speed estimation. Taking into account that  $\psi_{rq} = 0$ , the slip speed is calculated from the imaginary part of (4.39) as

$$\omega_2 = \omega_{\psi_r} - \omega_r = \frac{L_m}{T_r} \cdot \frac{i_{sq}}{\psi_{rd}} \quad (4.40)$$

#### 4.2.4 The flux model

The flux model (stator flux and rotor flux model) is obtained when both currents are solved from (4.24) and (4.25) and then substituted into (4.22) and (4.23). This model has the stator and rotor flux vectors as states,  $x = [\underline{\psi}_s, \underline{\psi}_r]^T$  (superscript  $T$  denotes matrix transposition). The stator voltage and rotor speed are inputs and the stator current is output,  $y = \underline{i}_s$ . The IM flux model in an arbitrary reference frame is

$$\frac{d}{dt} \underline{\psi}_s^e = -\left(\frac{1}{T_s\sigma} + j\omega_e\right) \underline{\psi}_s^e + \frac{L_m}{L_r T_s \sigma} \underline{\psi}_r^e + \underline{u}_s^e \quad (4.41)$$

$$\frac{d}{dt} \underline{\psi}_r^e = \frac{L_m}{L_s T_r \sigma} \underline{\psi}_s^e - \left(\frac{1}{T_r\sigma} + j(\omega_e - \omega_r)\right) \underline{\psi}_r^e \quad (4.42)$$

$$\underline{i}_s^e = \frac{1}{L_s\sigma} \underline{\psi}_s^e - \frac{L_m}{L_s L_r \sigma} \underline{\psi}_r^e \quad (4.43)$$

This model was obtained by solving (4.24)-(4.25) for currents and substituting them in (4.22)-(4.23). The output equation (4.43) was obtained by finding the current from (4.20).

Equation (4.41) is the stator model and (4.42) is the rotor model. The structural block diagram of the flux model, with space vector variables, is shown in Fig. 4.5. Dynamic parameters are  $K = T = T_s\sigma$  for the stator model and  $K = T = T_r\sigma$  for the rotor model.

The state space matrix is

$$A = \begin{bmatrix} -\left(\frac{1}{T_s\sigma} + j\omega_e\right) & \frac{L_m}{L_r T_s \sigma} \\ \frac{L_m}{L_s T_r \sigma} & -\left(\frac{1}{T_r\sigma} + j(\omega_e - \omega_r)\right) \end{bmatrix} \quad (4.44)$$

In the stator reference frame, with  $\omega_e = 0$ , the flux model is

$$\frac{d}{dt} \underline{\psi}_s = -\frac{1}{T_s\sigma} \underline{\psi}_s + \frac{L_m}{L_r T_s \sigma} \underline{\psi}_r + \underline{u}_s \quad (4.45)$$

$$\frac{d}{dt} \underline{\psi}_r = \frac{L_m}{L_s T_r \sigma} \underline{\psi}_s - \left(\frac{1}{T_r\sigma} - j\omega_r\right) \underline{\psi}_r \quad (4.46)$$

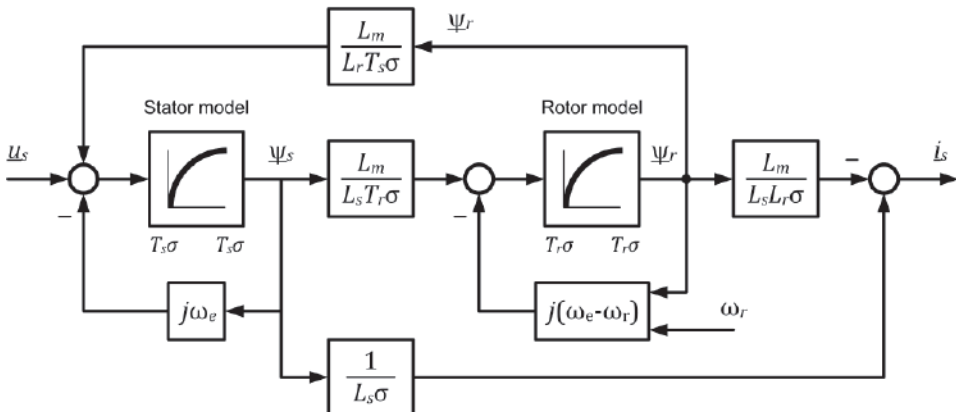


Fig. 4.5 Structural block diagram of the induction machine flux model.



For stator flux orientation, the flux model in the stator flux frame is

$$\frac{d}{dt} \underline{\psi}_s^s = -\left(\frac{1}{T_s \sigma} + j\omega_{\psi_s}\right) \underline{\psi}_s^s + \frac{L_m}{L_r T_s \sigma} \underline{\psi}_r^s + \underline{u}_s^s \quad (4.47)$$

$$\frac{d}{dt} \underline{\psi}_r^s = \frac{L_m}{L_s T_r \sigma} \underline{\psi}_s^s - \left(\frac{1}{T_r \sigma} + j(\omega_{\psi_s} - \omega_r)\right) \underline{\psi}_r^s \quad (4.48)$$

For rotor flux orientation, the flux model in the rotor flux frame is

$$\frac{d}{dt} \underline{\psi}_s^r = -\left(\frac{1}{T_s \sigma} + j\omega_{\psi_s}\right) \underline{\psi}_s^r + \frac{L_m}{L_r T_s \sigma} \underline{\psi}_r^r + \underline{u}_s^r \quad (4.49)$$

$$\frac{d}{dt} \underline{\psi}_r^r = \frac{L_m}{L_s T_r \sigma} \underline{\psi}_s^r - \left(\frac{1}{T_r \sigma} + j(\omega_{\psi_s} - \omega_r)\right) \underline{\psi}_r^r \quad (4.50)$$

In all the cases the output equation is the same as (4.43). Only the flux linkages are present in this model, which is an advantage when the saturation is taken into account.

All state-space models are time-variable and speed-dependent, regardless of the reference system. This is an inconvenience in sensorless IM drives where flux observers are needed but the rotor speed is unknown. Most of the IM state observers are speed-adaptive, i.e. they simultaneously estimate one or both fluxes and the speed.

None of the state space models described to this point contains the rotor current as a state variable, since in most cases the rotor current is not available for measurements. However, when wound rotor motors are used (for example in dual-feed wind generators), the rotor current can be measured and similar models using the rotor current as state can be developed in the same way.

#### 4.2.5 The mechanical model

The state-space dynamic model of the mechanical subsystem has as states the rotor speed  $\omega_r$  and the rotor position  $\theta_r$ , both electric,  $x = [\omega_r, \theta_r]^T$ . The electromagnetic torque is the control input and the load torque is an unknown perturbation (known as load perturbation).

$$\frac{J}{p} \frac{d}{dt} \omega_r = -\frac{B}{p} \omega_r + T_e - T_L \quad (4.51)$$

$$\frac{d}{dt} \theta_r = \omega_r \quad (4.52)$$

For a drive system composed of an IM with rotor inertia  $J_M$  and a load with mass moment of inertia  $J_L$ , connected by a gear box with gear ratio  $N$ , the total moment of inertia referred to the motor shaft is

$$J = J_M + N^2 J_L \quad (4.53)$$

The mechanical system is linear and its poles are  $s_1 = 0$  and  $s_2 = -B/J$ . The mechanical time constant  $T = J/B$  is much larger than the electrical time constants  $T_s$  and  $T_r$ . Thus, the mechanical dynamics is much slower than the electrical dynamics and the two models are separated in frequency and can be independently analyzed.

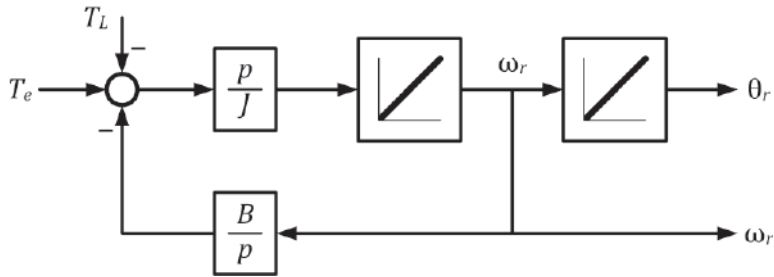


Fig. 4.6 Block diagram of the mechanical model of an induction machine.

Controllers for mechanical and electrical quantities can also be separately designed. In many situations, the friction coefficient is neglected,  $B = 0$ , and the mechanical model becomes a double integrator with two zero poles. Figure 4.6 shows a block diagram of the mechanical model with the rotor position and speed as outputs.

### 4.3 Direct vector control

Vector control or *field-oriented control (FOC)* is a modern technique that allows independent control of the electromagnetic torque and the magnetic flux of AC motors. It is intended for AC motor drives that require continuous torque (and speed) control and it involves a coordinated manipulation of the current and flux vectors. The concept of field orientation was proposed by Hasse and Blaschke in 1972 [8] and since then it has become a de-facto standard of most AC motor drives. [3]-[10].

The fundamental principle of field orientation is simple: make the IM emulate a DC machine with separate excitation, in terms of torque and flux control. The torque equation of a DC motor is of unrivaled simplicity: the torque is proportional with the product of a flux and a current. The flux is produced by the field current,  $i_f$ , is stationary, and is aligned along the direct axis of the stator. The armature current,  $i_a$ , circulates in the rotor and produces a space vector that is always orthogonal to the flux, i.e. it is aligned with the stator quadrature axis. This spatial constraint ensures that the torque production is optimal, as it gives the highest torque for a specified current. The field and armature currents flow in separate circuits and do not interact with each other. Therefore, the torque and the flux can be independently controlled by modifying these currents.

Standard IMs are supplied in the stator, and the stator current and voltage vectors are the only variables available for control. The instantaneous control of stator currents and voltages governs the spatial orientation and magnitude of the revolving magnetic field in the machine, which has led to the name of field-oriented control.

There are three requirements for any vector control scheme for AC machines:

- (a) an independently controlled current accounting for torque production;
- (b) an independently controlled or a constant value of the field flux; and

(c) an independently controlled spatial angle between the flux axis and the magnetomotive force axis.

If these requirements are met at every moment, the torque will instantaneously follow the torque current and the IM can be controlled in the same way as a separately excited DC motor. If these conditions are only met for steady-state conditions, only steady-state torque control will be achieved. It is difficult to visualize and implement separated torque and flux control in the stator frame, where all variables are sine-waves. The key for field orientation is to use a reference frame that is attached to- and rotates in synchronism with one of the flux vectors, either the rotor or the stator flux. The rotor speed control is not part of the field orientation and it is implemented separately when necessary.

### 4.3.1 Rotor flux orientation

The torque production in IMs is governed by any of the torque equations (4.15)-(4.18), which are sums of products between fluxes and currents. In the stator frame, it is difficult to identify a field current and a torque current. Consider the rotor flux orientation where the direct axis of the reference frame is positioned along the rotor flux vector and both rotate with the rotor flux speed,  $\omega_{\psi_r} = d\theta_{\psi_r}/dt$ , where  $\theta_{\psi_r}$  is the flux vector position with respect to the stator alpha axis. The torque equation (4.16) can be expressed in the rotor flux frame as

$$T_e = \frac{3}{2}p \frac{L_m}{L_r} (\psi_{rd}i_{sq} - \psi_{rq}i_{sd}) \quad (4.54)$$

In this frame, the rotor flux vector has only real component, equal with the flux magnitude,  $\underline{\psi}_r^r = \psi_{rd}$ , and has zero imaginary component,  $\psi_{rq} = 0$ . Thus, the torque equation becomes similar to that of a DC motor

$$T_e = \frac{3}{2}p \frac{L_m}{L_r} \psi_{rd}i_{sq} \quad (4.55)$$

The quadrature component of the stator current,  $i_{sq}$ , controls the torque and plays the same role as the armature current in a DC motor. This current is called the torque current. As long as the rotor flux magnitude is kept constant, the torque reacts instantly and identically to all changes in the torque current.

Consider the rotor flux model (4.38)-(4.39) in the rotor flux frame. By transforming to Laplace domain and rearranging, this model can be expressed as

$$(L_s\sigma s + R_{eqr}) \underline{i}_s^r = \underline{u}_s^r - j\omega_{\psi_r}L_s\sigma \underline{i}_s^r + \frac{L_m}{L_r T_r}(1 - j\omega_r T_r) \underline{\psi}_r^r \quad (4.56)$$

$$(T_r s + 1) \underline{\psi}_r^r = L_m \underline{i}_s^r - j(\omega_{\psi_r} - \omega_r)T_r \underline{\psi}_r^r \quad (4.57)$$

where the standalone symbol "s" is the Laplace operator and  $R_{eqr} = R_s + R_r L_m^2 / L_r^2$ .

The rotor flux magnitude can be obtained from the real part of (4.57) as

$$\psi_{rd} = \frac{L_m}{T_r s + 1} i_{sd} = H_{\psi_r}(s) i_{sd} \quad (4.58)$$

The transfer function  $H_{\psi_r}(s)$  from the stator current to the rotor flux magnitude is first-order linear with time constant  $T = T_r$ . It follows that the flux can be controlled by the direct component of the stator current,  $i_{sd}$ , which is called the flux current. This plays the role of a field current in a DC motor. Moreover, the torque current has no influence on flux, i.e. the flux is decoupled from torque.

Solving the torque current from (4.55) and substituting into the imaginary part of (4.57), one obtains the slip speed, which is proportional with the torque

$$\omega_2 = \omega_{\psi_r} - \omega_r = \frac{2R_r}{3p\psi_r^2} \cdot T_e \quad (4.59)$$

It follows that the rotor speed,  $\omega_r = \omega_1 - \omega_2$ , changes linearly with the torque, in the same way as for a DC machine. Equations (4.55) and (4.59) show that there is a substantial similarity between a separately excited DC motor and an IM in rotor flux orientation. However, the current model (4.56) and the flux model (4.58) are different than the armature and field equations of a DC motor.

The direct vector control is a feedback control system, which uses the estimated or measured rotor flux position to achieve the field orientation. The typical scheme of the direct vector control employs rotor flux orientation and rotor flux control, and it is shown in Fig. 4.7. This scheme uses closed-loop control of all important variables.

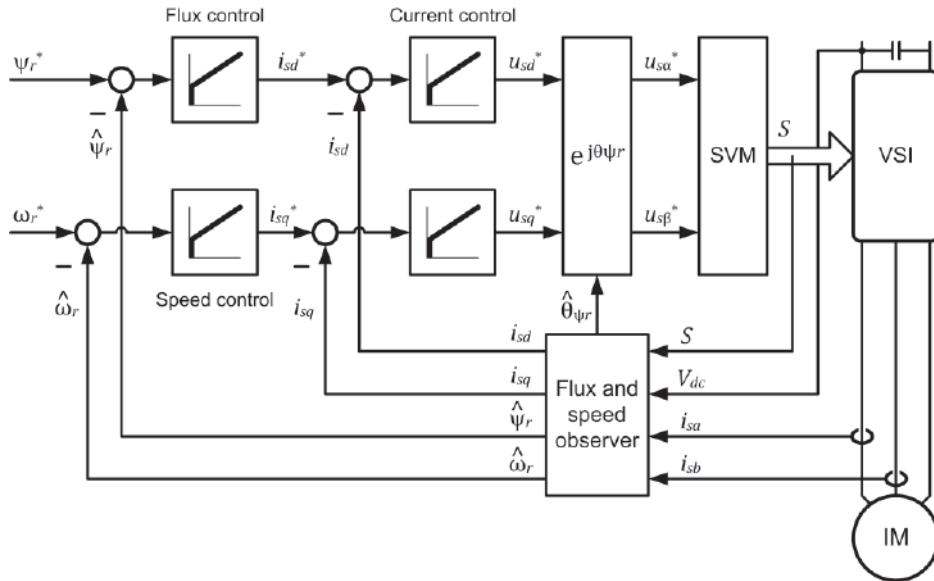


Fig. 4.7 Direct vector control with rotor flux orientation and rotor flux control.

The direct and quadrature currents are controlled by the inner loops, while the rotor flux magnitude and speed are controlled by the outer loops. The block diagram contains a state observer for estimating the rotor speed and the rotor flux (estimated variables are denoted by a hat, " $\hat{\cdot}$ "). This is the most popular control system for sensorless drives.

One of the key components in all vector control schemes is the current controller. This topic is very broad and, in time, a multitude of current regulators have been developed for this task. Figure 4.7 shows the simplest solution, realized with standard proportional-integral (PI) controllers in the rotor flux frame as

$$u_{sd}^* = (K_P + K_I \frac{1}{s}) \cdot (i_{sd}^* - i_{sd}) \quad (4.60)$$

$$u_{sq}^* = (K_P + K_I \frac{1}{s}) \cdot (i_{sq}^* - i_{sq}) \quad (4.61)$$

where  $u_{sd}^*$  and  $u_{sq}^*$  are reference voltages for the two axes,  $i_{sd}^*$  and  $i_{sq}^*$  are reference currents, and  $K_P$  and  $K_I$  are positive gains.

The reason for using PI controllers is that both  $d$  and  $q$  currents are DC in steady-state operation and the stator model of an IM is of first-order. However, the stator equation is different than the armature equation of a DC motor, which complicates the current control, to some extent. A number of advanced current control schemes are described in section 4.3.2. For now, it is sufficient to say that the current control is able to respond fast and to accurately track any practical reference. By properly tuning the PI gains, the dynamics of the current control loop (from reference to actual current) can be reduced to a first-order or second-order transfer function with very small time constants – the typical current response time is one or few milliseconds. Therefore, in order to simplify the design of the flux and speed loops, it is acceptable to neglect all time constants of the current loop and assume that the current follows its reference instantly, that is  $\underline{i}_s^r = \underline{i}_s^{r*}$ .

The rotor flux magnitude is controlled by a simple PI compensator that outputs the flux current reference

$$i_{sd}^* = (K_{P\psi} + K_{I\psi} \frac{1}{s}) \cdot (\psi_{rd}^* - \psi_{rd}) \quad (4.62)$$

where  $\psi_{rd}^*$  is the flux reference and  $K_{P\psi}$  and  $K_{I\psi}$  are positive gains.

In order to find the dynamics of the flux control loop, assume instantaneous current control and substitute  $i_{sd}^*$  for  $i_{sd}$  in the rotor equation (4.58). The closed-loop transfer function is second-order linear,

$$H_\psi(s) = \frac{\psi_{rd}}{i_{sd}^*} = \frac{L_m(K_{P\psi}s + K_{I\psi})}{T_r s^2 + (L_m K_{P\psi} + 1)s + L_m K_{I\psi}} \quad (4.63)$$

Selecting  $K_{P\psi} = K_{I\psi} T_r$  the controller zero cancels the motor pole and the transfer function becomes first-order with bandwidth  $\omega_0 = L_m K_{I\psi}$ .

$$H_\psi(s) = \frac{L_m K_{I\psi}}{s + L_m K_{I\psi}} \quad (4.64)$$

In regular operation the rotor resistance changes with temperature and perfect pole-zero compensation cannot be achieved with constant gains. The PI gains are designed by selecting a bandwidth,  $\omega_0$  and a damping factor,  $\beta$  for transfer function (4.63). Matching  $H_\psi(s)$  with a standard second-order system, the gains are

$$K_I = T_r \omega_0^2 / L_m \quad \text{and} \quad K_{P\psi} = (2\beta\omega_0 T_r - 1) / L_m \quad (4.65)$$

The rotor flux reference is set constant for operation at and below the rated speed and is modified in inverse proportion with the speed for operation above the rated speed. This way, the drive can develop the rated torque for the entire speed range below the rated speed, known as the constant torque range, and it can develop the rated power above the rated speed, a zone known as the constant power range.

A block diagram of the rotor flux control system for rotor flux orientation is shown in Fig. 4.8. The flux controller (4.62) has the transfer function  $K_{P\psi}(s) = K_{P\psi} + K_{I\psi}/s$ , while the process is modeled by the rotor flux transfer function  $H_{\psi r}(s)$  in (4.58). The current control loop is reduced to a first-order low-pass filter with a time constant  $T_i = L_s \sigma / K_p$ .

The rotor speed is controlled by a PI compensator that outputs the torque reference, in the most general case. For the vast majority of IM drives, the rotor flux is constant or changes slowly, and the torque instantly follows the torque current. Therefore, it is sufficient to design a speed controller that outputs the torque current reference as

$$i_{sq}^* = (K_{P\omega} + K_{I\omega} \frac{1}{s}) \cdot (\omega_r^* - \omega_r) \quad (4.66)$$

where  $\omega_r^*$  is the speed reference and  $K_{P\omega}$  and  $K_{I\omega}$  are positive gains.

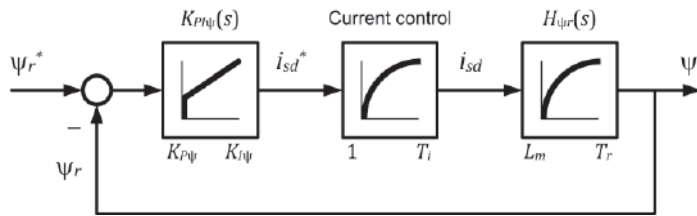


Fig. 4.8 Rotor flux control system for vector control with rotor flux orientation.

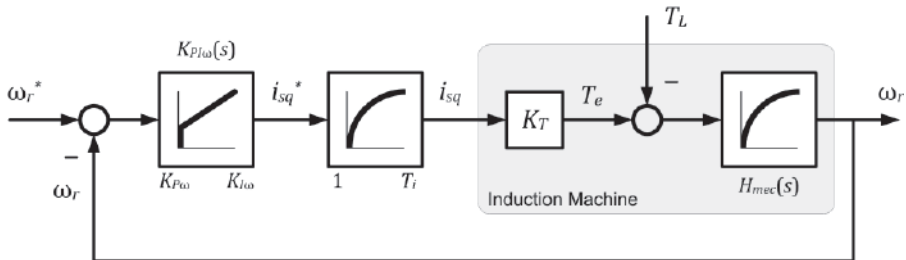


Fig. 4.9 Speed control system for vector controlled IM drives.

A block diagram of the speed control system is shown in Fig. 4.9. The speed controller is denoted by a PI transfer function,  $K_{PI}(s) = K_{P\omega} + K_{I\omega}/s$ . The speed equation (4.51) is modelled by a first-order transfer function,  $H_{mec}(s) = p/(Js + B)$ , in the rightmost block. The torque is  $T_e = K_T i_{sq}$ , where  $K_T = 1.5pL_m\psi_{rd}/L_r$  is the torque constant.

Assuming instantaneous current control ( $T_i = 0$ ), the transfer function of the speed control loop is obtained by analyzing the closed-loop system in Fig. 4.8, as

$$H_\omega(s) = \frac{K_T K_{PI}(s) H_{mec}(s)}{1 + K_T K_{PI}(s) H_{mec}(s)} = \frac{K_{P\omega_1} s + K_{I\omega_1}}{J s^2 + (K_{P\omega_1} + B) s + K_{I\omega_1}} \quad (4.67)$$

where  $K_{P\omega_1} = p K_T K_{P\omega}$  and  $K_{I\omega_1} = p K_T K_{I\omega}$  are gains scaled by  $p K_T$ .

The gains can be designed by selecting a bandwidth,  $\omega_0$  and a damping factor,  $\beta$  for this transfer function. Equating it with a standard second-order system, the gains are

$$K_{P\omega_1} = 2\beta\omega_0 J - B \quad \text{and} \quad K_{I\omega_1} = J\omega_0^2 \quad (4.68)$$

When the rotor flux is modified, all changes can be accounted for by updating  $K_T$ . In this way, the actual gains can be made flux-adaptive when calculated back from (4.68).

The load torque acts as a load disturbance for this system. The transfer function from load torque to actual speed is known as the load sensitivity function,

$$S(s) = \frac{H_{mec}(s)}{1 + K_T K_{PI}(s) H_{mec}(s)} = \frac{ps}{J s^2 + (K_{P\omega_1} + B) s + K_{I\omega_1}} \quad (4.69)$$

The sensitivity function indicates that the integral gain is a measure of disturbance rejection at frequencies lower than  $\omega_0$ . Large values of  $K_{I\omega}$  are necessary to reduce the sensitivity and to attenuate the speed transients at loading. However, too large integral gains (and too small proportional gains) cause overshoots and oscillations following step changes of the speed reference. There are three possible solutions that are able to avoid oscillatory responses: (a) increase  $K_{P\omega}$  in order to add damping, (b) use ramp or S-shaped speed references with no step changes and (b) shape the input-output response by using a feedforward control that adds to the feedback control. The simplest response shaping solution is a first-order low-pass filter applied to the speed reference  $\omega_r^*$ , before it enters the feedback loop (in series to the reference input of Fig. 4.9).

A variant of the vector control scheme in Fig. 4.7 is obtained when the flux controller is replaced by a decoupling network. A decoupling network is a feedforward function that calculates the reference currents using actual flux and torque references. The reference current vector can be obtained from (4.58) and (4.55) as

$$\underline{i}_s^* = i_{sd}^* + j i_{sq}^* = \frac{T_r s + 1}{L_m} \psi_{rd}^* + j \frac{2L_r}{3pL_m \psi_{rd}^*} T_e^* \quad (4.70)$$

Equation (4.70) describes the decoupling network for the rotor flux orientation. As this operation involves the flux derivative, the rotor flux reference is not allowed to change abruptly. The current and speed controllers are unchanged.

### 4.3.2 Current control

This section describes four practical current control schemes used by vector-controlled drives. The analysis is based on the rotor flux model for the rotor flux orientation, and it can be easily extended to stator flux orientation by using the stator flux model.

Recall the regular PI current control described by (4.60) and (4.61). In regular operation, the inverter output voltage vector is equal to its reference, i.e.  $\underline{u}_s^r = \underline{u}_s^{r*}$ . The transfer function  $H_i(s)$  of the current control loop (from reference current to actual current) can be obtained by substituting  $\underline{u}_s^{r*} = u_{sd}^* + j u_{sq}^*$  for  $\underline{u}_s^r$  into (4.56).

$$H_i(s) = \frac{\underline{i}_s^r}{\underline{i}_s^{r*}} = \frac{K_P s + K_I}{L_s \sigma s^2 + (R_{eqr} + K_P + j \omega_{\psi r} L_s \sigma) s + K_I} \quad (4.71)$$

A closer inspection of the stator model (4.56) reveals the presence of a cross-coupling between the  $d$  and  $q$  currents, caused by the EMF term  $j \omega_{\psi r} L_s \sigma \underline{i}_s^r$ . The loop transfer function (4.71) inherits the cross-coupling term and it is dependent on the synchronous speed. Even though the flux and torque are decoupled, the currents are not, and simple controllers, like those in (4.60)-(4.61), cannot eliminate or compensate this coupling. An extensive analysis in [11] shows that the real zero of a simple PI controller with constant gains is unable to cancel the motor complex pole, and the transient response of the drive is significantly degraded at high speed operation.

A better dynamic response and pole-zero cancellation can be obtained if PI controllers with cross-coupling decoupling are used. These can be described in vector form as

$$\underline{u}_s^{r*} = \left( K_P + K_I \frac{1}{s} \right) \cdot (\underline{i}_s^{r*} - \underline{i}_s^r) + j \omega_{\psi r} L_s \sigma \underline{i}_s^r \quad (4.72)$$

where the last term is the same as the cross-coupling term in (4.56)

A block diagram of the current controllers with cross-coupling decoupling is illustrated in Fig. 4.10.

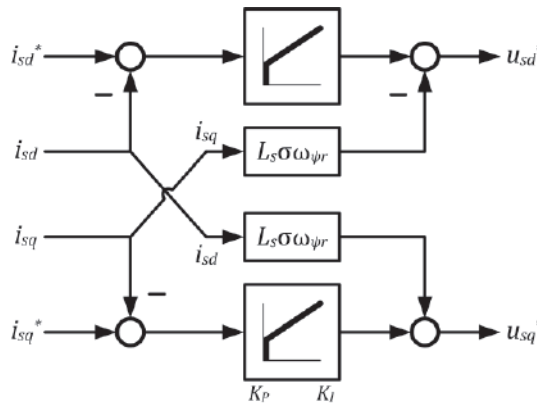


Fig. 4.10 PI current control with cross-coupling decoupling for rotor flux orientation.



Substituting again  $\underline{u}_s^{r*}$  for  $\underline{u}_s^r$  into (4.56), the coupling term vanishes and the equation of the current control loop is

$$(L_s \sigma s^2 + (R_{eqr} + K_P)s + K_I) \underline{i}_s^r = (K_P s + K_I) \underline{i}_s^{r*} + \frac{L_m}{L_r T_r} (1 - j\omega_r T_r) s \underline{\psi}_r^r \quad (4.73)$$

The closed-loop transfer function for the current control is second-order linear,

$$H_i(s) = \frac{\underline{i}_s^r}{\underline{i}_s^{r*}} = \frac{K_P s + K_I}{L_s \sigma s^2 + (R_{eqr} + K_P)s + K_I} \quad (4.74)$$

The PI gains can be designed by selecting a bandwidth,  $\omega_0$  and a damping factor,  $\beta$  for this transfer function. Equating  $H_i(s)$  with a standard second-order system, the gains are

$$K_P = 2\beta\omega_0 L_s \sigma - R_{eqr} \quad \text{and} \quad K_I = L_s \sigma \omega_0^2 \quad (4.75)$$

Moreover, if the gains are selected so as to satisfy the constraint  $K_I L_s \sigma = K_P R_{eqr}$ , then the controller zero cancels the motor pole and the closed-loop transfer function becomes a first order low-pass filter with bandwidth  $\omega_0 = K_P / (L_s \sigma)$ .

$$H_i(s) = \frac{K_P}{L_s \sigma s + K_P} \quad (4.76)$$

The last term in (4.73) can be regarded as a slowly-changing perturbation, as both the rotor flux and the speed change more slowly than the current. The current controller must be designed with a fast response, in order to compensate for this perturbation.

Assuming a constant rotor flux magnitude, the sensitivity function to speed is

$$R_i(s) = \frac{\underline{i}_s^r}{\omega_r} = \frac{s}{L_s \sigma s^2 + (R_{eqr} + K_P)s + K_I} \cdot \frac{L_m}{L_r} \underline{\psi}_{rd} \quad (4.77)$$

The integral gain influences the sensitivity at frequencies lower than  $\omega_0$ , and in order to increase the robustness during speed transients, the integral gain must be large.

An alternative way of achieving the pole-zero cancellation is by using a space-vector PI controller that has frequency-adaptive complex gains [11]. This controller has a complex zero and can be formulated in the space vector form as

$$\underline{u}_s^{r*} = \left( K_P + (K_I + j\omega_{\psi r} K_P) \frac{1}{s} \right) \cdot (\underline{i}_s^{r*} - \underline{i}_s^r) \quad (4.78)$$

Substituting  $\underline{u}_s^{r*}$  for  $\underline{u}_s^r$  into (4.56), the transfer function of the closed-loop current control is second order with complex coefficients

$$H_i(s) = \frac{\underline{i}_s^r}{\underline{i}_s^{r*}} = \frac{K_P s + K_I + j\omega_{\psi r} K_P}{L_s \sigma s^2 + (R_{eqr} + K_P + j\omega_{\psi r} L_s \sigma)s + K_I + j\omega_{\psi r} K_P} \quad (4.79)$$

If the gains are selected as to satisfy  $K_I L_s \sigma = K_P R_{eqr}$ , then an exact pole-zero cancellation happens and the closed-loop transfer function is reduced to (4.76).

A block diagram of the current controller with complex gains is shown in Fig. 4.11. Whereas both schemes deliver identical performance, the one shown in Fig. 4.10 is the most popular and it has become a de-facto standard for vector-controlled drives.

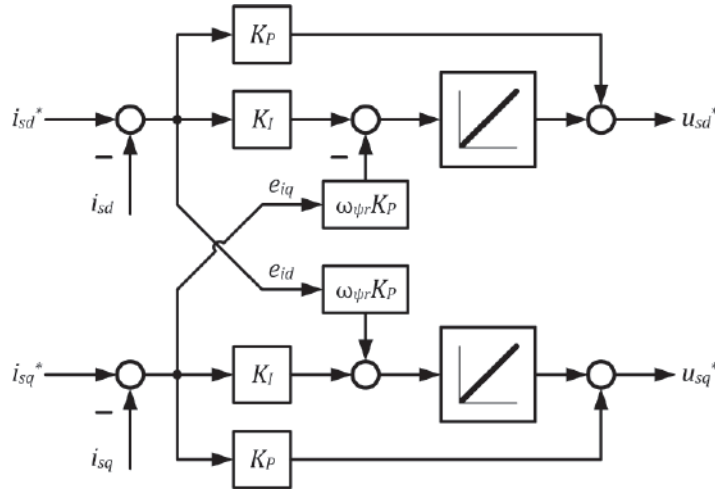


Fig. 4.11 PI current controller with complex gains for rotor flux orientation.

Sliding-mode control (SMC) is a nonlinear technique suitable for controlling systems affected by perturbations, uncertainties, variable parameters, or modelling errors [12]. SMC works with fast switching of the control quantity for achieving a robust and accurate operation of the closed loop system. It works with finite-time convergence but during steady-state operation it produces high frequency oscillations (known as chattering) of the controlled variables. Applied to AC drives, SMC provides excellent robustness and superior dynamic performance for a wide range of speeds [12].

In vector-controlled drives there are some imperfections that degrade the robustness: (a) variable or inaccurate parameters, such as the stator resistance and rotor time constant, (b) imperfect field orientation caused by estimation and measurement errors, (c) simplifying assumptions such as the constant flux operation, and (d) uncompensated cross-coupling terms. The SMC has the ability to maintain robust operation during large speed and torque transients, in the presence of all errors, if they are bounded.

A practical sliding mode current controller for rotor flux orientation is

$$\underline{u}_s^{r*} = \left( K_p + K_i \frac{1}{s} \right) \cdot \text{sign}(\underline{i}_s^{r*} - \underline{i}_s^r) + j\omega_{\psi r} L_s \sigma \underline{i}_s^r \quad (4.80)$$

where  $\text{sign}(\cdot)$  is the sign function and its argument,  $\underline{s} = \underline{i}_s^{r*} - \underline{i}_s^r$ , is the sliding function.

In order to reduce the chattering in the controlled current, the sign function may be replaced by a saturation function,  $\text{sat}(\cdot)$ , with a narrow linear zone  $h$ , defined as

$$\text{sat}(x) = \begin{cases} 1 & \text{if } x \geq h \\ x/h & \text{if } -h < x < h \\ -1 & \text{if } x \leq -h \end{cases} \quad (4.81)$$

The saturation band can be selected in the range of 2-5% the rated current. Inside this linear zone the chattering is substantially reduced but the robustness is also diminished.

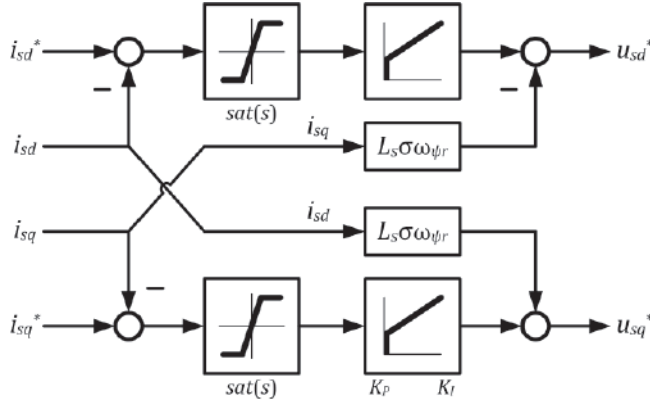


Fig. 4.12 Sliding mode current controller for rotor flux orientation.

The closed loop system is stable and reaches the current reference in finite time if the proportional gain is selected large enough, in order to compensate for perturbations and modelling errors. The decoupling term is not part of the sliding mode algorithm and can be absent. A block diagram of the sliding mode controller is shown in Fig. 4.12.

A simpler form of this controller is proposed in [12], with zero integral gain,  $K_I = 0$ , at the expense of using large proportional gains – in this case  $K_P$  must be  $K_P \geq 2V_{dc}/3$  in order to entirely use the voltage capability of the VSI. However, nonzero integral gains are beneficial as they allow using smaller  $K_P$  for reduced chattering, provide faster dynamic response, and increase the robustness at low frequencies. In general, the PI gains should be larger than the gains of a linear PI controller for the same drive.

Super-twisting sliding mode (STSM) control is a modern scheme that belongs to the family of high-order sliding modes [14]. In particular, the STSM is a second-order SMC algorithm designed for systems with relative degree one and it has two advantages: (a) provides finite-time convergence to zero of the sliding variable and its first derivative, and (b) produces a continuous control signal that ensures the sliding mode operation and reduces or eliminates the chattering.

The STSM current controller for rotor flux orientation is designed as [14]:

$$u_{sd}^* = \left( K_P \cdot |S_d|^r + K_I \frac{1}{s} \right) \cdot \text{sign}(S_d) - j\omega_{\psi r} L_s \sigma i_{sq} \quad (4.82)$$

$$u_{sq}^* = \left( K_P \cdot |S_q|^r + K_I \frac{1}{s} \right) \cdot \text{sign}(S_q) + j\omega_{\psi r} L_s \sigma i_{sd} \quad (4.83)$$

where exponent  $r$  is a positive constant,  $0 \leq r \leq 1$ , and the sliding function  $d$  and  $q$  components are the current errors,  $S_d = i_{sd}^* - i_{sd}$  and  $S_q = i_{sq}^* - i_{sq}$ .

Parameter  $r$  defines the controller behavior and shapes the closed-loop response. If  $r = 0$ , the proportional component is discontinuous and the controller becomes the same SMC described by (4.80). As  $r$  approaches zero, the sliding-mode effect is stronger and the controller behaves like an SMC, with low overshooting and increased chattering.

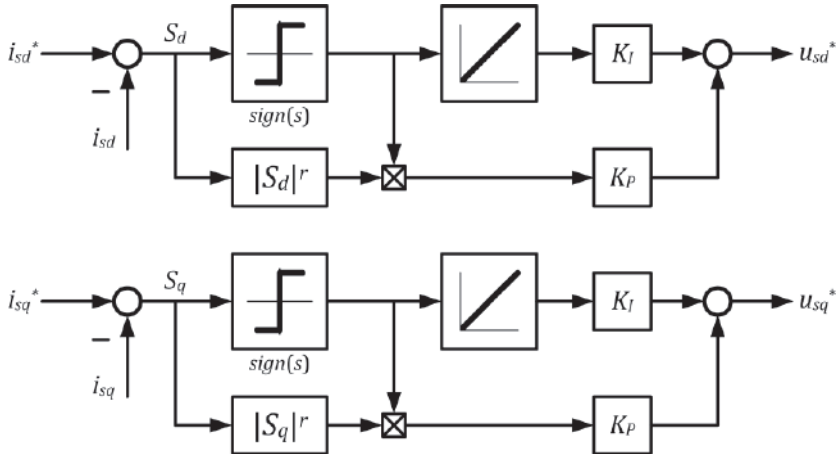


Fig. 4.13 Super-twisting sliding mode current controller for vector-controlled drives.

If  $r = 1$ , the proportional component is linear with the current error, and (4.82)-(4.83) turn into asymptotical PI controllers. When  $r$  moves towards one, the operation approaches that of a linear PI controller, the chattering vanishes and larger overshooting may occur. Practical values for STSM current controllers for low and medium power IM drives are  $r = 0.3 - 0.6$ , with a typical value  $r = 0.5$  [14]. This way the robust sliding mode operation is retained and the current ripples are very low.

The closed loop system is stable for large positive PI gains. In general, these gains can be selected equal with or larger than the gains of a linear PI controller for the same system, as specified by (4.75). Figure 4.13 shows a block diagram of the STSM current controller (without decoupling terms).

### 4.3.3 Stator flux orientation

Consider the stator flux orientation where the direct axis of the reference frame is positioned along the stator flux vector and both rotate with the stator flux speed,  $\omega_{\psi_s} = d\theta_{\psi_s}/dt$ , where  $\theta_{\psi_s}$  is the flux position with respect to the stator alpha axis. In this frame, the stator flux vector has a direct component equal to its magnitude,  $\underline{\psi}_s^s = \psi_{sd}$ , and has zero quadrature component,  $\psi_{sq} = 0$ . The torque equation (4.15) can be transformed to the stator flux frame using (4.5) as

$$T_e = \frac{3}{2}p(\psi_{sd}i_{sq} - \psi_{sq}i_{sd}) = \frac{3}{2}p\psi_{sd}i_{sq} \quad (4.84)$$

Torque control can be realized using the quadrature component of the stator current,  $i_{sq}$ , named the torque current, and the torque reacts instantly to any changes of this current. Usually, the flux magnitude is kept constant or is slowly modified.

The flux control is based on the stator equation (4.32) in the stator flux frame. Its real component gives the dynamic model for the stator flux magnitude

$$\frac{d}{dt}\psi_{sd} = u_{sd} - R_s i_{sd} \quad (4.85)$$

This equation is similar to the field equation of a DC motor and indicates that the stator flux can be controlled by the direct component of the stator voltage.

In order to obtain the transfer functions for the stator flux control, consider the stator flux model (4.31)-(4.32) expressed in the Laplace domain

$$(L_s \sigma s + R_{eqs}) \underline{i}_s^s = \underline{u}_s^s - j\omega_2 L_s \sigma \underline{i}_s^s + \left(\frac{1}{T_r} - j\omega_r\right) \underline{\psi}_s^s \quad (4.86)$$

$$s \underline{\psi}_s^s = \underline{u}_s^s - R_s \underline{i}_s^s - j\omega_{\psi s} \underline{\psi}_s^s \quad (4.87)$$

where  $\omega_2 = \omega_{\psi s} - \omega_r$  is the slip speed for the stator flux, and  $R_{eqs} = R_s + R_r L_s / L_r$ .

Substituting the stator voltage from (4.87) into (4.86), the stator flux dynamic model (4.88) is obtained, after some manipulations.

$$(T_r s + 1 + j\omega_2 T_r) \underline{\psi}_s^s = L_s (T_r \sigma s + 1 + j\omega_2 T_r \sigma) \underline{i}_s^s \quad (4.88)$$

The stator flux magnitude can be solved from the real part of (4.88) as

$$\psi_{sd} = L_s \frac{T_r \sigma s + 1}{T_r s + 1} i_{sd} - \omega_2 \frac{L_s T_r \sigma}{T_r s + 1} i_{sq} \quad (4.89)$$

The transfer function from the direct current to the flux magnitude is a lag element with minimum-phase and time constant  $T = T_r$ ,

$$H_{\psi s}(s) = \frac{\psi_{sd}}{i_{sd}} = L_s \frac{T_r \sigma s + 1}{T_r s + 1} \quad (4.90)$$

The stator flux control can be realized using the direct current,  $i_{sd}$  (flux current), and the stator flux reacts faster than the rotor flux due to the presence of a zero in (4.90). The last term in (4.89) is seen as a fast-changing disturbance and a complex decoupling network has to be applied in order to cancel the influence of the torque current. The slip speed with respect to the stator flux can be solved from the imaginary part of (4.88) as

$$\omega_2 = \frac{L_s (T_r \sigma s + 1)}{T_r (\psi_{sd} - L_s \sigma i_{sd})} i_{sq} \quad (4.91)$$

The stator flux and the slip speed depend on both currents, a notable disparity with respect to a DC motor. The stator flux orientation allows separate control of the torque and the flux magnitude by manipulating the current vector, but it requires a more involved decoupling network than that for rotor flux orientation. The advantage is that an accurate estimation of the stator flux is easier than the estimation of the rotor flux.

Direct vector control for stator flux orientation is implemented using PI controllers for all variables involved, in the same way as for rotor flux orientation. Figure 4.14 shows the block diagram of a typical sensorless IM drive with stator flux orientation and stator flux control. In this scheme, the observer estimates the stator flux and the rotor speed.

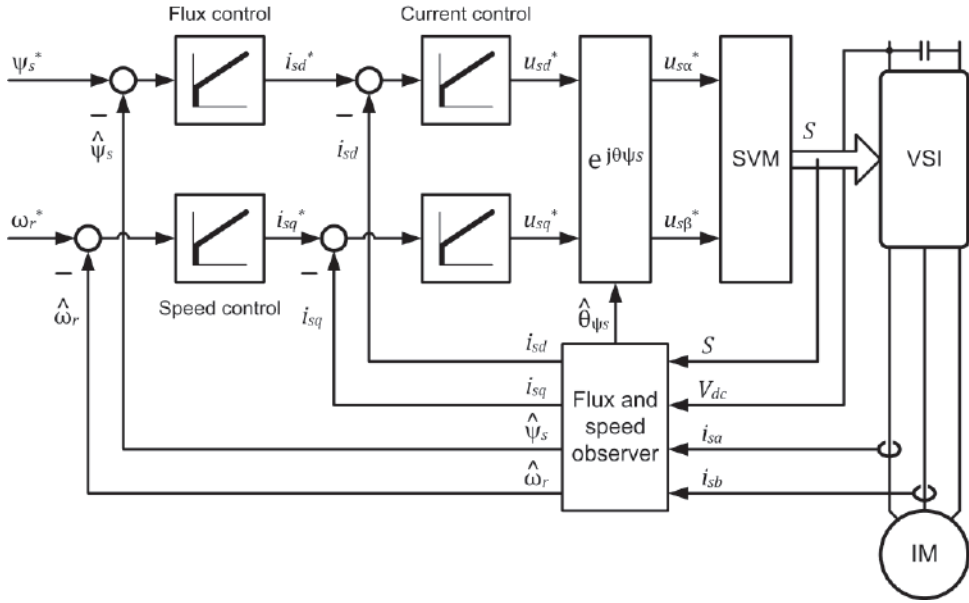


Fig. 4.14 Direct vector control with stator flux orientation and stator flux control.

The current controller with cross-coupling decoupling is expressed in vector form as

$$\underline{u}_s^{s*} = \left( K_p + K_I \frac{1}{s} \right) \cdot (\underline{i}_s^{s*} - \underline{i}_s^s) + j\omega_2 L_s \sigma \underline{i}_s^s \quad (4.92)$$

where the last term is the same as the cross coupling in (4.86),  $\underline{i}_s^{s*} = i_{sd}^* + j i_{sq}^*$  is the current reference, and  $K_p$  and  $K_I$  are positive gains.

Assuming an ideal inverter and substituting the voltage  $\underline{u}_s^{s*}$  for  $\underline{u}_s^s$  into (4.86), the coupling term vanishes and the equation of the current control loop is

$$\left( L_s \sigma s^2 + (R_{eqs} + K_p) s + K_I \right) \underline{i}_s^s = (K_p s + K_I) \underline{i}_s^{s*} + \left( \frac{1}{T_r} - j\omega_r \right) s \underline{\psi}_s^s \quad (4.93)$$

The closed-loop transfer function for the current control is similar to (4.74),

$$H_i(s) = \frac{\underline{i}_s^s}{\underline{i}_s^{s*}} = \frac{K_p s + K_I}{L_s \sigma s^2 + (R_{eqs} + K_p) s + K_I} \quad (4.94)$$

Selecting gains that satisfy  $K_I L_s \sigma = K_p R_{eqs}$ , the controller zero cancels the motor pole and the closed-loop transfer function becomes a low-pass filter identical to (4.76). The bandwidth is set by selecting a proportional gain  $K_p = \omega_0 L_s \sigma$ . The last term in (4.93) is a slowly-changing perturbation, and  $K_p$  must be large enough to compensate it.

All current controllers already described in section 4.3.2 can be used for this control scheme, and all design details and block diagrams remain the same. The single difference is in the decoupling terms: the stator flux orientation uses the slip speed, while the rotor flux orientation uses the rotor flux speed. Notably, the stator flux orientation is less sensitive to cross coupling because the slip speed (4.91) is always a small quantity.

The stator flux is controlled by a PI regulator that outputs the flux current reference

$$i_{sd}^* = (K_{P\psi} + K_{I\psi} \frac{1}{s}) \cdot (\psi_{sd}^* - \psi_{sd}) \quad (4.95)$$

where  $\psi_{sd}^*$  is the flux reference and  $K_{P\psi}$  and  $K_{I\psi}$  are positive gains.

Assuming instantaneous current control and taking into account (4.90), the closed-loop dynamic model is a lead-lag transfer function

$$H_{\psi}(s) = \frac{\psi_{sd}}{\psi_{sd}^*} = \frac{L_s(K_{P\psi}s + K_{I\psi})(T_r\sigma s + 1)}{(L_sT_r\sigma K_{P\psi} + T_r)s^2 + (L_sT_r\sigma K_{I\psi} + L_sK_{P\psi} + 1)s + L_sK_{I\psi}} \quad (4.96)$$

Selecting  $K_{P\psi} = K_{I\psi}T_r$  the controller zero cancels the motor pole and the closed-loop transfer function becomes a first-order lag compensator.

$$H_{\psi}(s) = \frac{L_sK_{I\psi}(T_r\sigma s + 1)}{(L_sT_r\sigma K_{I\psi} + 1)s + L_sK_{I\psi}} \quad (4.97)$$

The cutoff frequency is  $\omega_0 = L_sK_{I\psi}(L_sT_r\sigma K_{I\psi} + 1)^{-1}$ . For large integral gains this function approaches unity and the flux follows a reference with a very small delay.

Another practical selection is  $K_{P\psi} = 0$ , in which case the transfer function becomes second order with bandwidth defined by  $\omega_0 = L_sK_{I\psi}/T_r$ .

According to (4.89), the torque current is a perturbation input for the flux control loop. The disturbance rejection can be improved at low frequencies if large integral gains are used. However, a PI controller with reasonably large gains is not able to fully compensate this sensitivity at high frequencies and the stator flux will change each time when large torque steps occur. A better solution is extending the PI controller with a feedforward compensator, known as decoupling network.

Starting with a reference flux magnitude and a reference torque current,  $i_{sq}^*$  (produced by the speed controller), the direct current reference can be solved from (4.89) as

$$i_{sdFF}^* = \frac{T_r s + 1}{L_s(T_r\sigma s + 1)} \psi_{sd}^* + \omega_2 \frac{T_r\sigma}{T_r\sigma s + 1} i_{sq}^* \quad (4.98)$$

This equation describes the decoupling network for the stator flux orientation. Its output can be seen as the ideal operating current needed for producing the flux and torque references. The total reference current produced by the augmented flux controller is the sum of the PI controller output (4.95) and the feedforward current (4.98),  $i_{sd}^{**} = i_{sd}^* + i_{sdFF}^*$ .

The speed control for stator flux orientation is the same as for rotor flux orientation – the speed controller is (4.66) with gains selected as in (4.68). All of the design considerations, the transfer functions, and the block diagram depicted in Fig. 4.9 remain the same. There are only two minor differences: the current reference is represented in the stator flux frame and the torque constant is  $K_T = 1.5p\psi_{sd}$ .

In conclusion, both orientation schemes allow simultaneous control of the torque and flux by positioning the stator current vector with respect to either the stator or the rotor

flux vector, in such a way that its direct component controls the flux and its quadrature component controls the torque. The desired currents are imposed using current controllers, pulse width modulation, and voltage source inverters. This way the inverter becomes a controlled current source. The rotor flux orientation allows a simple implementation using PI controllers for all variables, whereas the stator flux orientation benefits from employing very simple stator flux estimators, but requires a decoupling network. The air-gap flux orientation and control can be implemented in a similar way as the stator flux orientation, since the air-gap flux is defined as  $\underline{\psi}_m = \underline{\psi}_s - L_{s\sigma}\underline{i}_s$ .

#### 4.4 Indirect vector control

The *indirect vector control* is a strategy that uses feedforward control of the flux magnitude, implemented as a decoupling network, and feedforward calculation of the slip speed. The stator currents are controlled in the same way as for the direct vector control, by one of the methods described in section 4.3.2. The rotor speed can be either measured or estimated. Figure 4.15 shows a block diagram of the indirect vector control, employed for generic field orientation.

The main rationale behind using a feedforward controller is to avoid the design and implementation of flux and speed observers, which were considered computationally intensive and less precise. In this case, the absence of an observer requires using expensive and sometimes unreliable motion sensors, such as incremental encoders or resolvers, in order to measure the rotor position, as shown in Fig. 4.15. Recently, the advent of fast and inexpensive microcontrollers enabled the development of advanced state estimators that can reliably replace motion sensors.

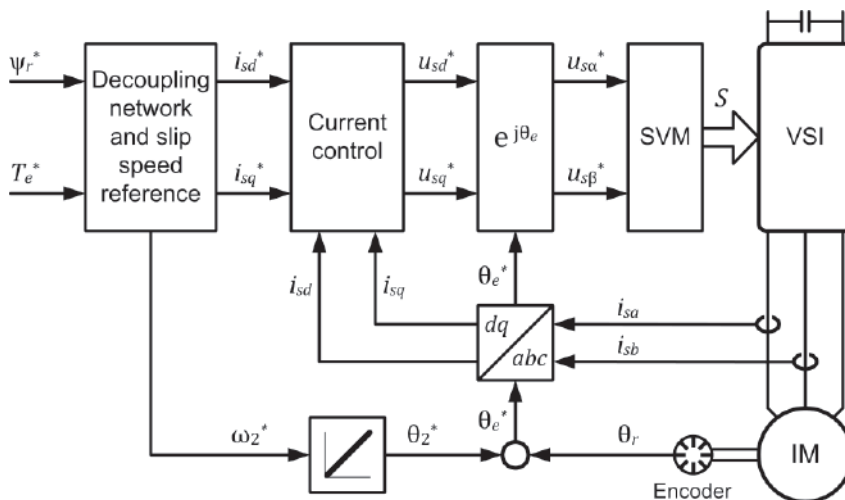


Figure 4.15 Indirect vector control for IM drives.



The decoupling network for rotor flux orientation is described by the very simple equation (4.70). This has the reference flux magnitude and torque as inputs, and requires the evaluation of a flux derivative, which can be easily calculated by finite differences. To avoid large current peaks, it is sensible to change the flux reference using ramps rather than steps. The slip speed  $\omega_2$  is calculated as in (4.59), using reference values for the flux and the torque. Then, the slip angle is obtained by integrating the slip speed. Finally, the field position  $\theta_e$  is computed by adding the slip angle  $\theta_2$  to the rotor position

$$\theta_e = \theta_r + \theta_2 \quad (4.99)$$

This way, the field position is a sum of a feedback quantity, i.e. the measured rotor position, and a feedforward one, the slip angle. This approach has the ability to maintain a stable operation of the drive in all regimes and at all speeds.

The stator flux orientation requires a more involved network – the direct current is solved from (4.89) and the quadrature current is calculated from (4.84) using references for the flux and the torque. The decoupling network is described by

$$\underline{i}_s^* = i_{sd}^* + j i_{sq}^* = \frac{T_r s + 1}{L_s (T_r \sigma s + 1)} \psi_{sd}^* + \frac{\omega_2}{K_T} \cdot \frac{T_r \sigma}{T_r \sigma s + 1} T_e^* + j \frac{1}{K_T} T_e^* \quad (4.100)$$

where  $K_T = 1.5p\psi_{sd}^*$  is the torque constant.

The slip speed  $\omega_2$  is calculated as in (4.91), using reference values for flux and current. This involves calculating the current derivative which is sensitive to noise and can be approximated by a high-pass filter. The slip angle is obtained by integrating the slip speed and then the field position is produced by (4.99).

The indirect vector control is known for its simplicity and its ability to provide stable operation in all situations, at the expense of using an encoder. However, the direct vector control is also stable when paired with a position sensor. A disadvantage of the indirect control is its dependency on motor parameters, which change with the temperature and magnetic saturation. In particular, the rotor time constant and the slip speed depend on the rotor resistance that is temperature-sensitive. The majority of IM drives uses direct vector control or direct torque control, and the indirect control became less relevant.

## 4.5 Direct torque control

The *direct torque control (DTC)* is a strategy that departs from the similarity to DC motors and achieves simultaneous flux and torque control by taking into account the IM model and the VSI operation. In particular, DTC does not divide the current vector into a flux and a torque current and it does not use current controllers or current decoupling networks. As the main objective of any motor drive is to control the flux and torque, DTC employs specific controllers for the flux and the torque. This technique was developed in 1985 as a fast and robust torque control strategy for IM drives [15]. Since then, the method

was generalized for all AC motor drives, and was recognized as a viable alternative to vector control [16].

The operating principle of the DTC may be specified as follows: a simultaneous control of the torque and the stator flux magnitude is achieved by directly adjusting the stator voltage space-vector. On the basis of the torque and flux errors, the algorithm directly computes the next voltage vector to be applied to the motor, or the next inverter state. The control methods used to achieve this objective can be freely chosen by the designer. In general, the stator flux orientation is employed for this scheme [15]-[23].

In time, DTC has evolved from a single controller to a broad concept. There are two DTC families: the classical line that directly employs the instantaneous voltage vectors available in a VSI, and the modern line that uses PWM. In conventional DTC, successive voltage vectors are selected in such a way that the torque and flux errors are maintained within predefined limits. This scheme produces a sequence of active and zero voltage vectors that drive the stator flux vector on a quasi-circular trajectory. PWM is not used, but the vector-switching operation matches well the fast-switching nature of a VSI. Modern DTC schemes use torque and flux controllers that produce space-vector voltage references, which are generated by PWM.

DTC offers several important advantages: (a) it provides a fast and robust dynamic response for the torque control, (b) it is well-matched to the discrete nature of VSI, (c) it is robust with respect to motor parameter detuning, and (d) it is an inherently sensorless control as it does not require any mechanical information from the motor shaft. The classical DTC has some disadvantages: (a) it works with a high torque and current ripple in the steady-state, (b) the VSI switching frequency is variable and it is much lower than the controller sampling frequency, (c) it produces acoustical noise and vibrations, and (d) it is not capable of directly controlling and limiting the current.

The most effective way to reduce the torque and current ripple is to increase the time density of the voltage vectors by running the algorithm at high sampling frequencies. Classical DTC should operate at frequencies four to six times higher than the sampling frequency of PWM-based controllers in order to produce comparable torque ripple. High sampling frequencies might be excessive for mainstream microcontrollers, but with the advent of hybrid FPGA-microcontroller systems, DTC drives running at high-frequencies are practical. However, the VSI switching frequency is variable as long as the classical DTC scheme is used.

Another simple way to decrease the torque ripple is to increase the time resolution of the voltage vectors by using PWM-based controllers. In a sampling period the PWM creates sequences of four or six vectors with adjustable duration for each vector, which substantially increases the control precision. Modern DTC schemes use either linear or nonlinear controllers and run with low torque and current ripple and with constant switching frequency for the VSI [18]-[24].

Compared to FOC, the DTC offers a similar performance, each scheme with advantages and drawbacks: DTC is very robust, responsive, and is adequate for applications with fast dynamics, but the robustness is obtained at the cost of a higher torque and current ripples. FOC is able to achieve fast and accurate current and torque control, but it is sensitive to motor parameter detuning and it is more complex.

#### 4.5.1 Torque and flux control principles

Direct torque control is a strategy based on the stator flux orientation and the stator flux control. The IM stator equation (4.22) and its real and imaginary components can be expressed in the stator flux frame, rotating at a speed  $\omega_e = \omega_{\psi_s}$ , as

$$\frac{d}{dt} \underline{\psi}_s^s = -R_s \underline{i}_s^s - j\omega_{\psi_s} \underline{\psi}_s^s + \underline{u}_s^s \quad (4.101)$$

$$\frac{d}{dt} \psi_{sd} = u_{sd} - R_s i_{sd} \quad (4.102)$$

$$\omega_{\psi_s} \psi_{sd} = u_{sq} - R_s i_{sq} \quad (4.103)$$

The real equation (4.102) is similar to the field equation of a DC motor and indicates that the flux magnitude can be controlled by the direct component of the stator voltage – a positive voltage increases the flux, while a negative one decreases the flux. The resistive voltage drop is a perturbation input for (4.102) and in most situations it is very small and can be neglected. It is obvious that using the voltage to control the flux is a much simpler and direct solution than using an intermediate current controller as in FOC. The vector control of the stator flux is based on the complex equation (4.88); recall that the perturbation in (4.89) cannot be neglected and a decoupling network is necessary.

The torque equation (4.15) can be expressed in the stator flux frame as

$$T_e = \frac{3}{2} p \psi_{sd} i_{sq} \quad (4.104)$$

Solving the current from (4.103) and substituting into (4.104), the torque becomes

$$T_e = \frac{3p}{2R_s} \psi_{sd} (u_{sq} - \omega_{\psi_s} \psi_{sd}) \quad (4.105)$$

This relation indicates that the torque can be controlled by the quadrature component of the stator voltage – a voltage larger than the EMF produces a positive torque, a voltage smaller than the EMF or zero produces a negative torque.

The IM torque production is understood as an interaction between the stator and the rotor flux vectors, based on the torque equation (4.18). This can be expressed as a product of magnitudes of the stator and rotor fluxes, denoted by  $|\psi_s|$  and  $|\psi_r|$ , as

$$T_e = -\frac{3}{2} p \frac{L_m}{L_s L_r \sigma} \psi_{sd} \psi_{rq} = \frac{3}{2} p \frac{L_m}{L_s L_r \sigma} |\psi_s| |\psi_r| \sin(\delta) \quad (4.106)$$

where  $\delta$  is the angle between the rotor and stator flux vectors known as the torque angle.

The torque can be modified by changing the relative position of the stator flux vector with respect to the rotor flux vector – the torque is positive when the stator flux leads the

rotor flux, and it is negative when the stator flux trails the rotor flux. According to the stator model (4.11), the stator flux is the time-integral of voltage (if the resistive drop is neglected). When a voltage vector is supplied, the stator flux is driven along the direction of that voltage vector, at a speed proportional to its amplitude.

According to the rotor flux dynamic model (4.48), the rotor flux follows the stator flux with a time constant  $T = T_r \sigma$ , implying that the stator flux is able to rotate faster than the rotor flux. Therefore, a large quadrature voltage moves the stator flux away from the rotor flux increasing the torque angle and the torque, while a small or zero voltage slows down or stops its motion, decreasing the torque angle. In this way,  $u_{sq}$  is able to control the torque, while  $u_{sd}$  controls the flux magnitude.

### 4.5.2 Conventional direct torque control

The conventional DTC exploits the fact that the stator flux vector moves in the direction of the stator voltage vector. By supplying an adequate sequence of discrete voltage vectors it is possible to drive the flux along a quasi-circular trajectory at a desired speed. To this end, DTC uses the eight voltage vectors available in two-level VSIs.

Figure 4.16 shows the trajectory of the stator flux vector when a sequence of three VSI voltage vectors is supplied –  $V_3$  for a duration  $t_1$ ,  $V_2$  for  $t_2$ , and again  $V_3$  for  $t_3$ . The flux has a zigzag trajectory – initially it was positioned at  $\underline{\psi}_s(t)$ , during time  $t_1$  it moves by  $V_3 t_1$  and reaches  $\underline{\psi}_s(t+t_1)$ , during  $t_2$  it moves by  $V_2 t_2$ , and during  $t_3$  it moves by  $V_3 t_3$ , reaching the final value  $\underline{\psi}_s(t+t_1+t_2+t_3)$ . The vector  $V_3$  has a large  $q$  component that rotates the flux faster, increasing the torque (decreasing the flux magnitude), while the vector  $V_2$  has a large  $d$  component that increases the flux and slows down the rotation.

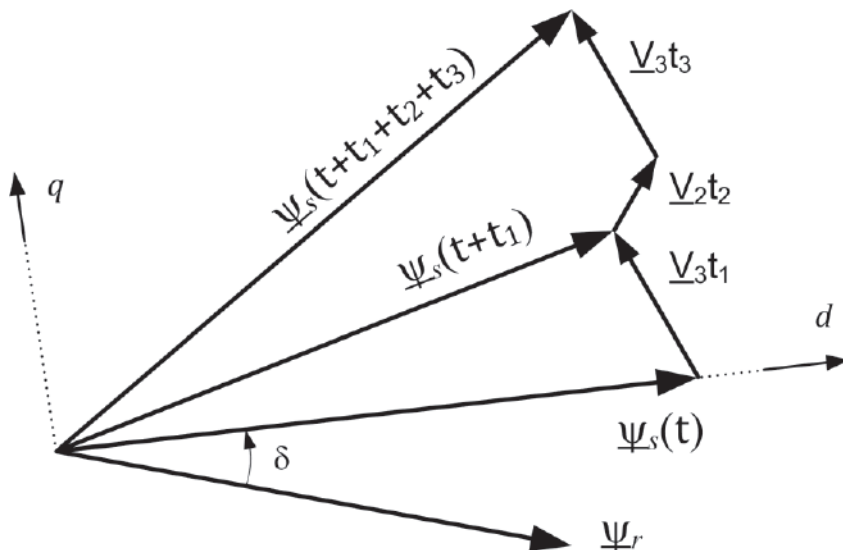


Fig. 4.16 Stator flux trajectory when three VSI voltage vectors are supplied.

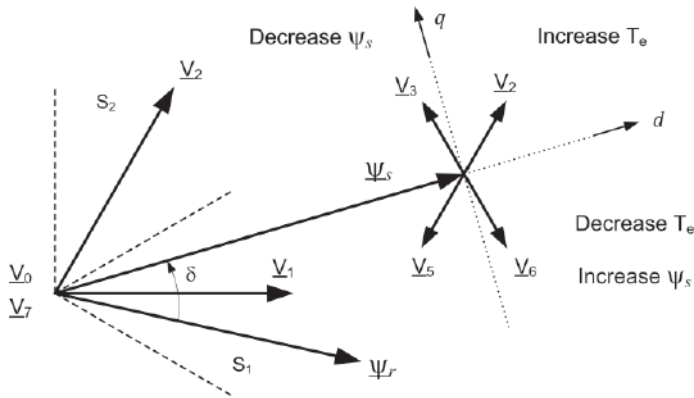


Fig. 4.17 Principle of direct torque and flux control for IM drives.

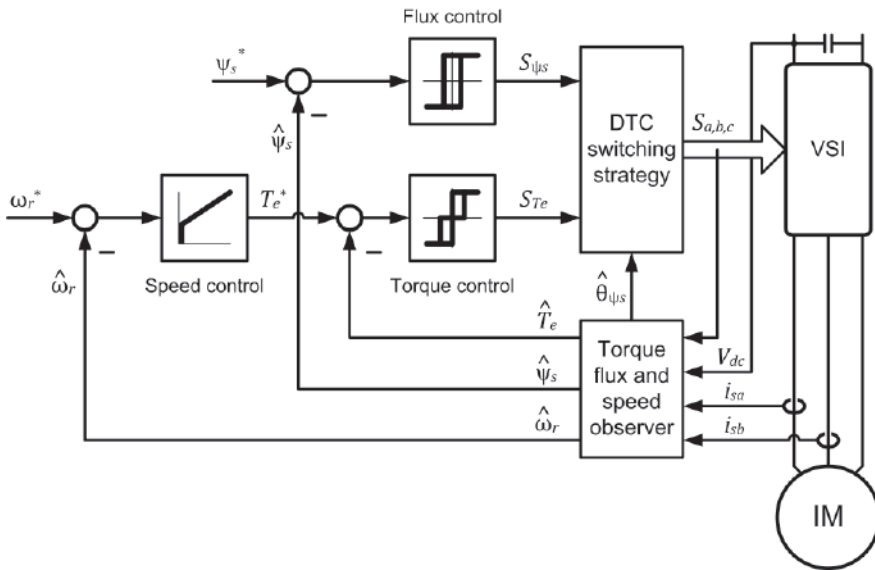


Fig. 4.18 Conventional direct torque control for IM drives.

The operating principle of classical DTC is illustrated in Figure 4.17. For this example the stator flux vector is located in the vicinity of the voltage vector  $V_1$ , in sector  $S_1$  (sectors are delimited by dashed lines and are marked  $S_1$  and  $S_2$ ). For this case it is obvious that voltage vectors  $V_1$ ,  $V_2$ , and  $V_6$  have positive real parts and are able to increase the flux, while vectors  $V_3$ ,  $V_4$ , and  $V_5$  have negative real parts and can decrease it. Moreover, vectors  $V_2$  and  $V_3$  have positive imaginary parts and are able to increase the torque, while vectors  $V_5$  and  $V_6$  have negative imaginary parts and can decrease it. For this sector there are four nonzero voltage vectors that can be employed for control:  $V_2$  increases the torque and the flux,  $V_5$  decreases both,  $V_3$  increases the torque and decreases the flux, and  $V_6$  decreases the torque and increases the flux. The two zero vectors,  $V_0$  and  $V_7$ , can be used to decrease the torque and to keep the flux almost constant, in all situations.

In order to control the flux vector during a complete rotation, the complex plane is divided into six circular sectors, each one sixty-degree wide having a VSI voltage vector as bisector – see  $S_1$  and  $S_2$  in Fig. 4.17. The same analysis that was described for  $S_1$  applies when the flux is located in any sector. For each sector there are two nonzero voltage vectors that increase the torque and other two that decrease it. There are also two vectors that increase the flux and other two that decrease it.

A block diagram of the conventional DTC for sensorless IM drives is shown in Fig. 4.18. This scheme contains two switching controllers with hysteresis, one for the torque and one for the flux, which decide when the torque and the flux are to be increased or decreased. The hysteresis bands have the role to limit the switching frequency when the controllers are implemented at a very high sampling frequency. For regular digital implementations running at moderate sampling frequencies (tenths of kHz) the hysteresis bands are not needed and the controllers are simple comparators.

The torque controller is a three-level comparator that outputs the torque signal  $S_{Te}$ .

$$S_{Te} = \begin{cases} 1 & \text{if } T_e^* - T_e \geq h_p \\ 0 & \text{if } h_n < T_e^* - T_e < h_p \\ -1 & \text{if } T_e^* - T_e \leq h_n \end{cases} \quad (4.107)$$

where  $T_e^*$  is a torque reference, and  $h_p$  and  $h_n$  are the positive and negative thresholds. The typical selection for thresholds is:  $h_p = 0$  and  $h_n < 0$  when the field speed is positive,  $\omega_{\psi_s} > 0$ , and  $h_p > 0$  and  $h_n = 0$  when the field speed is negative,  $\omega_{\psi_s} < 0$ . In order to avoid demagnetization, zero vectors should not be used at speeds lower than 5% rated speed, and these thresholds should be very small or zero,  $h_p = h_n = 0$ .

The flux controller is a two-level comparator that outputs the flux signal  $S_{\psi_s}$ .

$$S_{\psi_s} = \text{sign}(\psi_{sd}^* - \psi_{sd}) \quad (4.108)$$

The “DTC switching strategy” block in Fig. 4.18 contains the voltage vector selection strategy described in Fig. 4.17. It receives as inputs the torque and flux signals and selects the voltage vector that simultaneously decreases the flux and torque errors. This switching strategy is implemented as a table with three inputs:  $S_{Te}$  and  $S_{\psi_s}$ , and the sector  $S_n$  where the flux is located. Table 4.1 gives the typical switching strategy for the DTC. It contains the vector selection for all of the six sectors and is valid for operation at both positive and negative rotor speeds.

A zero vector, either  $V_0$  or  $V_7$ , is selected in all situations when the torque error is small and the torque absolute value must be decreased, i.e. whenever  $S_{Te} = 0$ . Zero vectors stop the stator flux motion and, as the rotor flux continues to rotate, the torque always decreases. Active vectors are selected in all other situations, when the torque must increase or decrease. Whenever an IM operates at low speeds the stator voltage is low and zero vectors are applied for long time periods. An extensive use of zero vectors causes a gradual decrease of the stator flux and eventually the loss of magnetization.

Table 4.1 Switching table for Direct Torque Control

Flux sector		S1	S2	S3	S4	S5	S6
$S_{\psi_s} = 1$	$S_{T_e} = 1$	V2	V3	V4	V5	V6	V1
	$S_{T_e} = 0$	V7	V0	V7	V0	V7	V0
	$S_{T_e} = -1$	V6	V1	V2	V3	V4	V5
$S_{\psi_s} = -1$	$S_{T_e} = 1$	V3	V4	V5	V6	V1	V2
	$S_{T_e} = 0$	V0	V7	V0	V7	V0	V7
	$S_{T_e} = -1$	V5	V6	V1	V2	V3	V4

Therefore, using zero vectors at very low speeds for long time intervals is not recommended, for two reasons: (a) to avoid decreasing the stator flux and (b) to achieve a fast torque response for falling torque steps. A simple solution that avoids using zero vectors is setting the zero-vector band (defined as  $h_0 = h_p - h_n$ ) to zero, i.e.  $h_p = h_n = 0$ , for low speed operation. In this case the torque controller is a two-level comparator,  $S_{T_e} = \text{sign}(T_e^* - T_e)$ . Practical values for  $h_0$  are from five to twenty percent the rated torque, with small values at low speeds. To accommodate all situations for a wide speed range operation, the torque thresholds can be adapted in real-time.

The torque reference is produced by a PI speed controller

$$T_e^* = (K_{P\omega} + K_{I\omega} \frac{1}{s}) \cdot (\omega_r^* - \omega_r) \tag{4.109}$$

where  $\omega_r^*$  is the speed reference and  $K_{P\omega}$  and  $K_{I\omega}$  are positive gains.

Assuming instantaneous torque control, the speed control block diagram is similar to the one shown in Fig. 4.9 for FOC, and the closed-loop transfer function is

$$H_\omega(s) = \frac{K_{P\omega}s + K_{I\omega}}{Js^2 + (K_{P\omega} + B)s + K_{I\omega}} \tag{4.110}$$

The gains are designed in the same way as explained in relation to equation (4.68).

It is remarkable that the conventional DTC scheme can be regarded as a variable structure control system designed to take advantage of the eight-state discrete nature of the VSI [12]. The stability conditions for this controller are: (a) the available quadrature voltage must be higher than the back-emf, in absolute values,  $|u_{sq}| > |\omega_{\psi_s} \psi_{sd}|$ , and (b) the load angle must be less than ninety degrees,  $|\delta| < \pi/2$ .

Figures 4.19 to 4.22 show experimental results for direct torque and flux control of a 1.1 kW sensorless drive that uses a squirrel-cage IM supplied by a 2.2 kVA VSI, with the block diagram in Fig. 4.18. The IM nameplate data is:  $P_N = 1.1$  kW,  $U_N = 380$  V,  $I_N = 2.77$  A,  $n_N = 1410$  rpm,  $f_N = 50$  Hz, and  $T_N = 7.5$  Nm. This experiment illustrates the torque step response

– with the drive running at zero speed, the torque reference is set to 12 Nm (160% rated torque) at time  $t = 10$  ms, while the flux reference is constant.

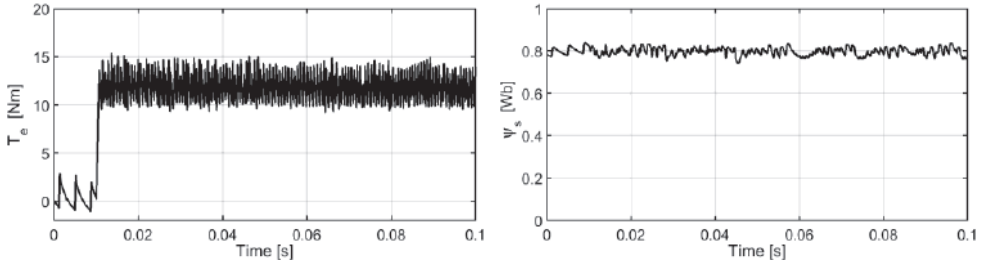


Fig. 4.19 Direct torque and flux control for 12 Nm torque step reference at constant stator flux, with 10 kHz DTC sampling frequency;  $T_e$  – torque,  $\psi_s$  – stator flux magnitude.

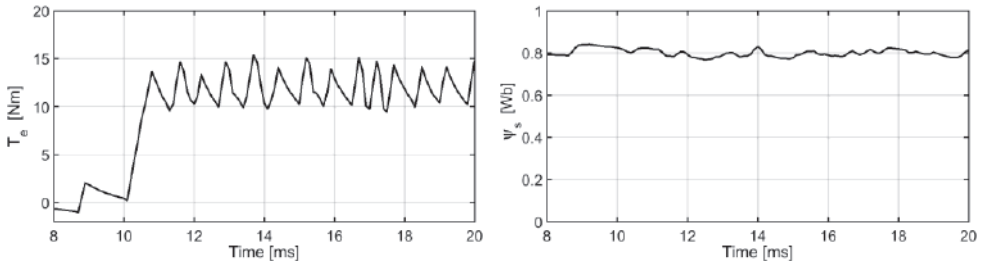


Fig. 4.20 Enlarged view of the torque and flux waveforms in Fig. 4.19.

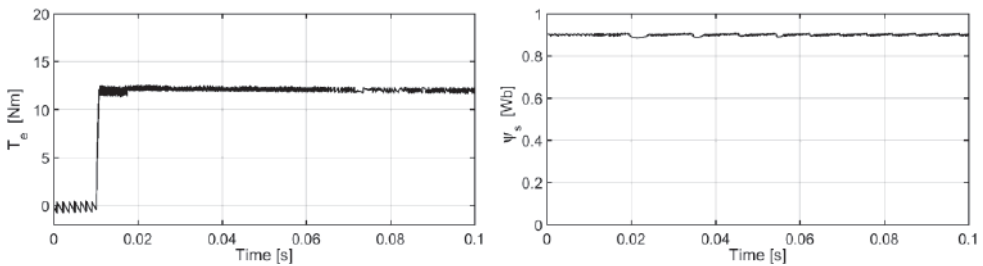


Fig. 4.21 Direct torque and flux control for 12 Nm torque step reference at constant stator flux, with 40 kHz DTC sampling frequency;  $T_e$  – torque,  $\psi_s$  – stator flux magnitude.

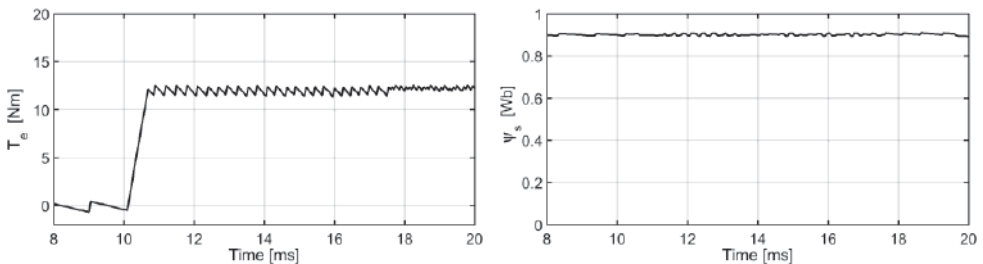


Fig. 4.22 Enlarged view of the torque and flux waveforms in Fig. 4.21.



Fig. 4.19 shows the estimated torque  $T_e$ , and stator flux magnitude  $\psi_s$ , when the DTC algorithm runs at 10 kHz sampling frequency. Fig 4.20 is a detail of the same waveforms, which zooms-in on the torque response – the torque ripple is 5 Nm and the actual vector switching frequency is 5 kHz or less. Fig. 4.21 shows the torque and stator flux magnitude when the DTC runs at 40 kHz. Fig 4.22 shows an enlarged view of the same waveforms. The benefit of running at higher frequencies is clear: both the torque and the flux ripples are significantly smaller than those for 10 kHz operation. Notably, the torque response time is less than one millisecond and the control is extremely robust, in all situations. This response time increases to three milliseconds when the drive runs at the rated speed.

The adaptation of the zero-vector band is also illustrated in Figs. 4.21 and 4.22 – at speeds below 30 rad/s the zero-vector band is zero,  $h_p = h_n = 0$ , the torque ripple is about 1 Nm, and the actual vector switching frequency is 7 kHz. As the speed increases, the algorithm switches to a nonzero band ( $h_0 = 2$  Nm at time  $t = 17.5$  ms), the ripple reduces to 0.4 Nm, and the vector switching frequency becomes 15 kHz.

### 4.5.3 Torque and flux ripple

The IM torque model can be obtained by differentiating the torque equation (4.18). After substituting the flux derivatives from (4.41) and (4.42), the torque dynamic model in the stator flux frame, with voltages  $u_{sd}$  and  $u_{sq}$  as inputs, is nonlinear,

$$\frac{d}{dt}T_e + \frac{T_s+T_r}{T_s T_r \sigma} T_e = k_T (\psi_{rd} u_{sq} - \psi_{rq} u_{sd}) - k_T \omega_r \psi_{sd} \psi_{rd} \quad (4.111)$$

where  $k_T = 3pL_m / (2L_s L_r \sigma)$ . The torque time constant,  $T_T = T_s T_r \sigma / (T_s + T_r)$ , is smaller than one millisecond, and it can be neglected for all practical purposes.

The torque response depends on the rotor speed which acts as third input for (4.111). At low speeds, the speed-dependent term in (4.111) is negligible and the voltage term is very large, whenever an active voltage vector is applied. Therefore the torque increases very fast. Conversely, when a zero-voltage vector is applied, the RHS of (4.111) becomes very small and the torque decreases slowly. This behavior is visible in Figs 4.20 and 4.22 – the torque increases fast in just one sampling period and then it slowly decreases during several subsequent periods. At high speeds, the speed-dependent term is large and the opposite behavior occurs – when an active voltage vector is applied both the RHS terms in (4.111) have large magnitudes and the torque increases slowly. When a zero vector is applied the last term alone causes a fast decrease in the torque.

The stator flux dynamic response is governed by (4.102) or by (4.47). For medium- and high-speed operation the voltage drop on the stator resistance can be neglected and the flux is an integral of the direct voltage  $u_{sd}$ . As the VSI voltage vectors are fixed and the flux rotates,  $u_{sd}$  is variable along one sector. Therefore, the flux slope changes as the flux vector

moves within a sector, a fact visible in Figs. 4.19 to 4.22. However, the flux dynamic response does not depend on speed.

In digitally-controlled systems, the DTC is implemented on a per-sample basis. During each sampling period the algorithm finds a voltage vector that is supplied to the motor in the next sampling period. Each voltage vector is activated for an entire sampling period without using PWM. This way, the vector switching frequency (frequency at which the voltage vectors are updated) is at most equal to the sampling frequency. In reality, the vector frequency is smaller than the sampling frequency for operation at low speeds, while the two tend to become equal at medium and high speeds.

A simple and very effective way to reduce the torque ripple is to increase the vector frequency by running the DTC algorithm at higher sampling frequencies. This method preserves all of the DTC advantages but due to very short sampling times involved, it requires fast microcontrollers or FPGAs for implementation. The torque ripple reduction of this approach is significant, as confirmed by Figs. 4.21-4.22, where the algorithm runs on a dual-core 32-bit floating-point microcontroller.

Another way to increase the vector density is by applying sequences of several voltage vectors in one sampling period. For this approach the sampling period is divided into three equal intervals and combinations of three voltage vectors with equal durations are applied. The DTC algorithm selects the best combination of three vectors by using the basic DTC principles outlined in section 4.5.1. This method, called discrete space vector modulation, is further described in [17]. Test results presented in [17] show that the torque ripple is reduced by half with respect to the conventional DTC and the VSI switching frequency is still variable.

## 4.6 Linear direct torque control

All DTC schemes based on the principles of the conventional DTC suffer from the fact that all voltage vectors have the same time duration regardless of the error magnitudes, and that time is predefined and uncontrolled. An additional degree of freedom can be added if the time resolution is increased, i.e. if the duration of each vector is controlled with a finer time-step. A similar reasoning as for the infinitesimal calculus applies: the classical DTC runs with large ripple as it uses only one vector in each sampling period. The torque ripple is reduced when the sampling period is divided into three intervals, and three vectors are applied. The period can be further divided into multiple of subintervals and the ripple will gradually decrease when more vectors are used. Eventually, a quasi-linear space with a high time resolution can be obtained, and the torque will exhibit an asymptotical ripple-free behavior. It follows that an asymptotical controller followed by a pulse width modulator can be designed to control this system.

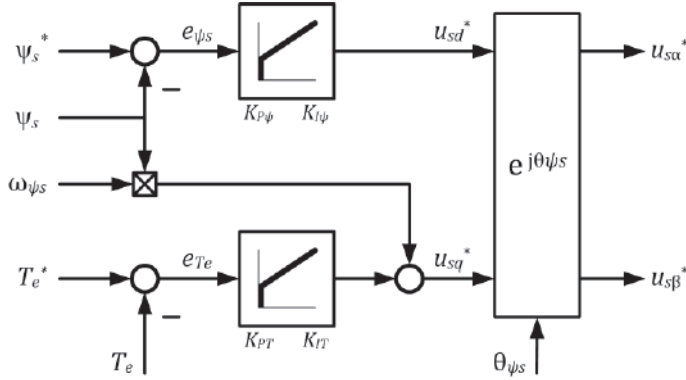


Fig. 4.23 Linear direct torque and flux controller for IM drives.

The *linear direct torque control (Linear-DTC)* approaches the DTC idea from the perspective of linear control – it replaces the hysteresis controllers with linear controllers and the switching table with a PWM that has high time-resolution. This scheme employs two PI controllers, one for the torque and one for the flux, and a simple decoupling component, all implemented in the stator flux reference frame. A block diagram of the Linear-DTC controller is shown in Fig. 4.23. This scheme was proposed in [18].

As indicated in section 4.5.1, the stator voltage components in the stator flux frame have the ability to control the flux and the torque. Therefore, the flux controller produces the direct voltage reference  $u_{sd}^*$ , while the torque controller produces the quadrature voltage reference  $u_{sq}^*$ . No current controllers are used for the Linear-DTC.

$$u_{sd}^* = (K_{P\psi} + K_{I\psi} \frac{1}{s}) \cdot (\psi_{sd}^* - \psi_{sd}) \quad (4.112)$$

$$u_{sq}^* = \left( K_{PT} + K_{IT} \frac{1}{s} \right) \cdot (T_e^* - T_e) + \omega_{\psi_s} \psi_{sd} \quad (4.113)$$

where  $K_{P\psi}$ ,  $K_{I\psi}$ ,  $K_{PT}$ , and  $K_{IT}$  are positive gains,  $\psi_{sd}^*$  is the stator flux reference, and  $T_e^*$  is the torque reference.

The last term in (4.113) is a decoupling that compensates for the similar e.m.f. term in (4.105). If the IM stator resistance is large, then another term that decouples the resistive voltage drop  $R_s i_{sd}$  can be added to (4.112). In most cases this is not necessary, as the PI controller has the ability to compensate that. The last step is to transform the reference voltage vector,  $\underline{u}_s^{S*} = u_{sd}^* + j u_{sq}^*$ , to the stator frame using the estimated stator flux position,  $\underline{u}_s^* = \underline{u}_s^{S*} e^{j\theta_{\psi_s}}$ . This reference voltage is produced by regular PWM or space vector modulation (SVM), in the same way as for vector control. A high time-resolution of the vector durations is obtained in this way [18], [19].

Assuming an ideal inverter and substituting (4.112) for the direct voltage into (4.102), and neglecting the stator resistance, the closed-loop transfer function for flux control is

$$H_{\psi}(s) = \frac{\psi_{sd}}{\psi_{sd}^*} = \frac{K_{P\psi}s + K_{I\psi}}{s^2 + K_{P\psi}s + K_{I\psi}} \quad (4.114)$$

If the desired bandwidth for the flux controller is  $\omega_0$  and the desired damping factor is  $\beta$ , then the gains can be selected as

$$K_{I\psi} = \omega_0^2 \quad \text{and} \quad K_{P\psi} = 2\beta\omega_0 \quad (4.115)$$

Practical bandwidth values for low-power IM drives are in the range of 20 to 100 rad/s, and damping factors should be larger than unity. Another design possibility is to select a small or zero integral gain (proportional controller), in which case the transfer function becomes first order with bandwidth  $\omega_0 = K_{P\psi}$ . A first-order response is convenient at flux-startup to avoid over-currents during the magnetization process.

The simplicity of the transfer function (4.114) is remarkable. It does not depend on motor parameters and it is simpler than the stator flux dynamic model (4.96) that was obtained for vector control using flux and current controllers. It can be concluded that a current controller for the direct axis is not needed when the stator flux control is desired.

Substituting (4.113) for the quadrature voltage into (4.105) and assuming a constant flux magnitude, the closed-loop transfer function for the torque control is

$$H_T(s) = \frac{T_e}{T_e^*} = k_T \frac{K_{PT}s + K_{IT}}{(1 + K_{PT})s + k_T K_{IT}} \quad (4.116)$$

where  $k_T = 1.5p\psi_{sd}/R_s$  is assumed constant.

A first-order transfer function is obtained with zero proportional gain (integral torque controller), in which case the torque bandwidth is  $\omega_0 = k_T K_{IT}$ . Conversely, an almost instantaneous response can be obtained if the proportional gain is large. In any case, the torque control loop works with zero steady state error, unlike the classical DTC.

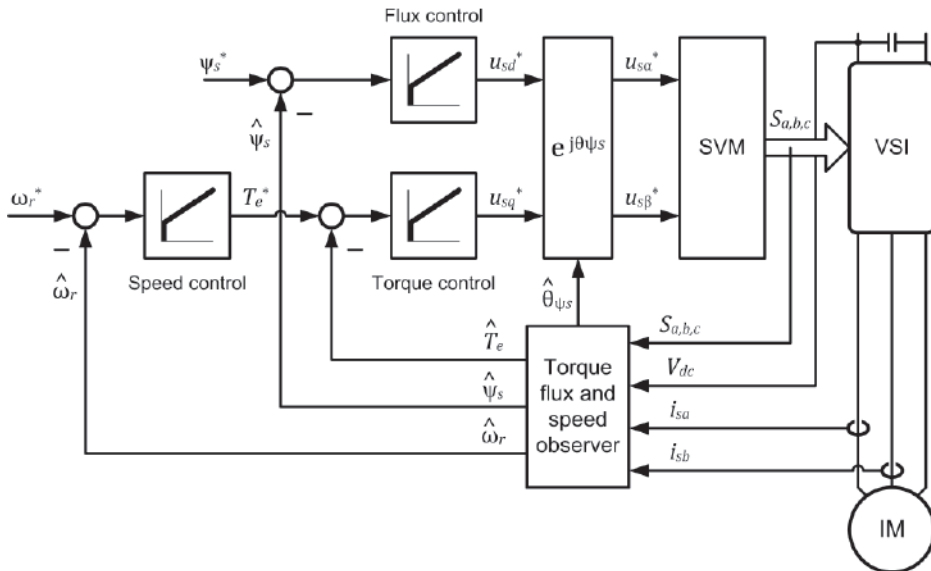


Fig. 4.24 Sensorless IM drive with linear direct torque control (Linear-DTC).

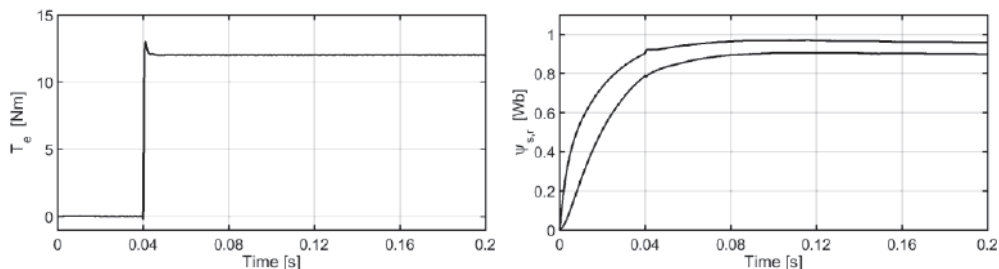


Fig. 4.25 Linear-DTC step response for 12 Nm torque step reference and 0.95 Wb stator flux step reference;  $T_e$  – torque,  $\psi_s$  and  $\psi_r$  – stator and rotor flux magnitudes.

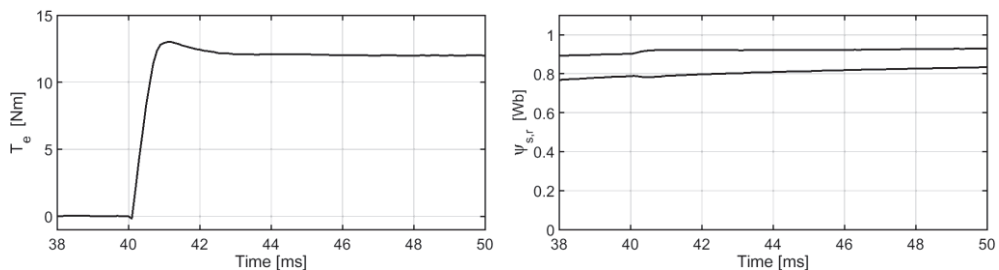


Fig. 4.26 Enlarged view of the torque and flux waveforms in Fig. 4.25.

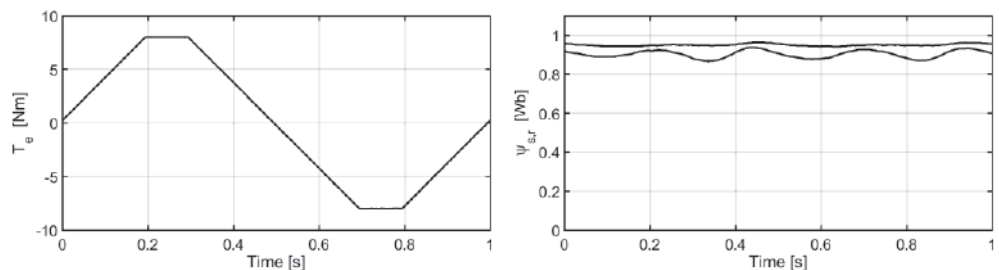


Fig. 4.27 Torque reference tracking with Linear-DTC control;  $T_e$  – torque,  $\psi_s$  and  $\psi_r$  – stator and rotor flux magnitudes.

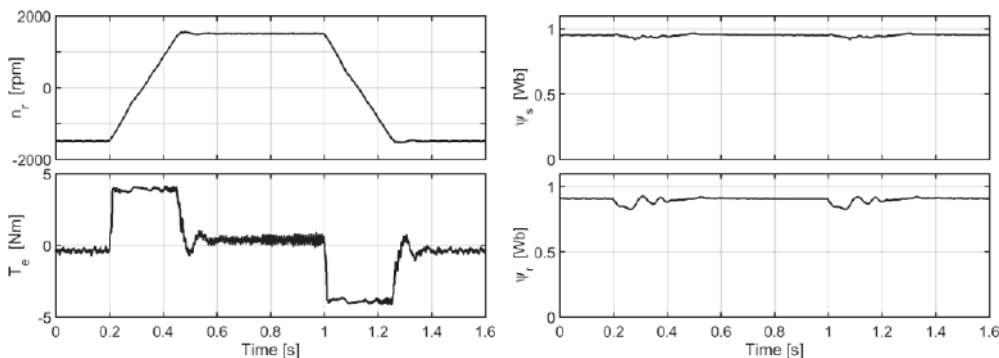


Fig. 4.28 Speed reversals at nominal speed with Linear-DTC control for a 0.5 kW drive;  $n_r$  – rotor speed,  $T_e$  – torque,  $\psi_s$  and  $\psi_r$  – stator and rotor flux magnitudes.

In order for the torque loop to operate linearly, the stator flux must be constant or slowly variable. If this condition is satisfied, then a fast and decoupled torque control can be achieved without employing current control or decoupling networks. This is the main reason for which the flux control loop must be fast and robust.

Fig. 4.24 shows the typical block diagram of a sensorless IM drive that uses Linear-DTC. Apart from the torque and flux controllers, located in the central area, this diagram contains a PI speed controller, a SVM block, and a state estimator for the flux, torque, and speed. The speed controller operates in the same way as it was described for the direct vector control. Assuming an instantaneous torque control, the closed-loop transfer function for the speed control is (4.67) with  $K_T = 1$ , and all of the design considerations remain the same.

Experimental results with Linear-DTC are presented in Figs. 4.25 to 4.28 for the same 1.1 kW IM drive used for DTC. Both, the sampling frequency and the VSI switching frequency are 10 kHz. Fig. 4.25 shows the response of the torque and flux controllers to step references during startup – first the flux reference is set to  $\psi_{sd}^* = 0.95$  Wb and then, 40 ms later, the torque reference is set to  $T_e^* = 12$  Nm (160% rated torque). Fig. 4.26 shows an enlarged view of the same waveforms – torque, stator flux, and rotor flux – at the time when a torque step is applied. The flux controller gains are  $K_{P\psi} = 140$  and  $K_{I\psi} = 1600$  for a bandwidth  $\omega_0 = 40$  rad/s and damping  $\beta = 1.75$ . The torque controller gains are  $K_{PT} = 40$  and  $K_{IT} = 60000$ , for a step-response time of one millisecond, with 0.6 Nm overshoot and 2.5 ms settling time. The response time is the same as for the classical DTC (Figs. 4.20 and 4.22), and the steady-state operation is ripple-free.

Fig. 4.27 illustrates the reference tracking performance of the torque controller. The torque reference is a trapezoidal figure with a ramp of 40 Nm/s between  $\pm 8$  Nm levels. The motor torque perfectly tracks this reference, proving a practically instantaneous control. For this test, the IM is loaded with a reactive speed-proportional load, to prevent an excessive increase of speed. Fig. 4.28 illustrates the operation at high speeds and reversals of a 0.5 kW drive. For this test the motor is reversed between  $\pm 1500$  rpm ( $\pm 50$  Hz stator frequency) once per second and the torque limit is set to 4 Nm (rated torque is 3 Nm). The flux and torque oscillations during large speed and torque transients are due to estimation errors and to imperfect decoupling between torque and flux axes. These oscillations denote a reduced robustness of the Linear-DTC.

The Linear-DTC has some specific features and advantages compared to the classical DTC: (a) the torque response time is as fast as the one produced by DTC and it is tunable, (b) it has asymptotical operation without torque, flux, and current ripples during steady-state, (c) the VSI switching frequency is constant and controllable, (d) uses PI controllers that can be easily tuned via standard procedures. The main disadvantage is that the Linear-DTC is less robust than DTC.

## 4.7 Sliding mode direct torque control

### 4.7.1 Conventional sliding mode DTC

Sliding Mode Control (SMC) or Variable Structure Control (VSC) is a nonlinear control method used for a wide range of problems and dynamic systems, including nonlinear, perturbed, and uncertain systems. VSC is able of maintaining stability and consistent performance in face of disturbances, modeling imprecisions, and unmodeled dynamics. Its most important feature is the ability to produce very robust, in many cases, invariant control systems [12]-[14].

SMC is a nonlinear controller that changes the dynamics of a system based on a set of predefined control criteria, named switching function(s). The control law contains a mechanism that switches from one dynamic structure to another and drives the system states on a specified trajectory in the state-space, called the “sliding surface”. This surface is located at the operational boundary between the two control structures. Once the sliding surface is reached, the trajectory of the system is permanently restricted on that surface. The evolution of this system as it slides along the sliding surface represents the desired system dynamics and is called “sliding mode”.

The synthesis of a sliding controller involves two steps: (a) design of a switching function that defines a desired dynamic response and (b) design of a control law that specifies the switching rules and enforces the sliding mode.

The *variable structure direct torque control* (VSC-DTC) is a scheme based on the stator flux orientation and stator flux control and it has a topology similar to Linear-DTC. It employs two sliding mode controllers, one for torque and one for flux, implemented in the stator flux frame. A block diagram of a VSC-DTC controller is shown in Fig. 4.29. This method was proposed in [20] and [21].

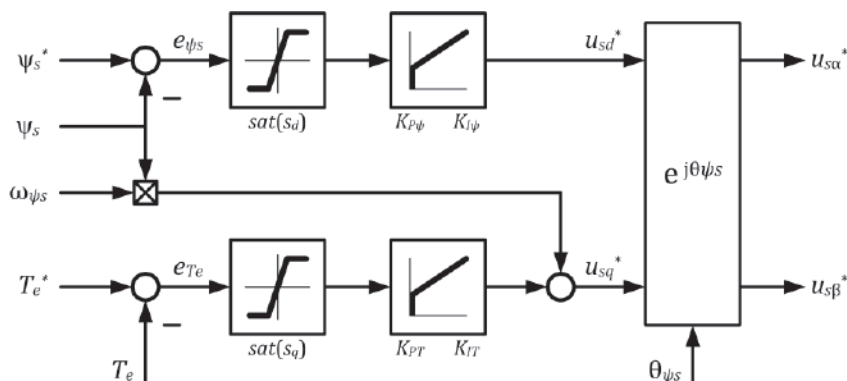


Fig. 4.29 Sliding mode direct torque and flux controller for IM drives.

The switching function contains two components equal to the torque and flux errors,

$$S = s_d + js_q = \psi_{sd}^* - \psi_{sd} + j(T_e^* - T_e) \quad (4.117)$$

This selection of this sliding function relies on the fact that both the flux model (4.47) and the torque model (4.111) have relative degree one. The sliding surface is defined by the equation  $S = 0$ , and is reduced to just two points in the state space.

The flux and torque controllers are PI compensators with discontinuous inputs. As for the Linear-DTC, the former produces the direct voltage  $u_{sd}^*$ , while the latter produces the quadrature voltage  $u_{sq}^*$ .

$$u_{sd}^* = (K_{P\psi} + K_{I\psi} \frac{1}{s}) \cdot \text{sign}(s_d) \quad (4.118)$$

$$u_{sq}^* = \left( K_{PT} + K_{IT} \frac{1}{s} \right) \cdot \text{sign}(s_q) + \omega_{\psi s} \psi_{sd} \quad (4.119)$$

where  $K_{P\psi}$ ,  $K_{I\psi}$ ,  $K_{PT}$ , and  $K_{IT}$  are positive gains.

The reference voltage vector,  $\underline{u}_s^* = u_{sd}^* + ju_{sq}^*$ , is transformed to the stator frame using the estimated stator flux position,  $\underline{u}_s^* = \underline{u}_s^{s*} e^{j\theta_{\psi s}}$ . Then, this voltage is the reference input for a space vector modulator that outputs the VSI switching signals.

The closed-loop system is stable if  $S \cdot \frac{dS}{dt} < 0$ . Assuming a constant reference for the flux controller and substituting (4.118) for the  $u_{sd}^*$  voltage in (4.102), this condition is satisfied if  $K_{P\psi} > |R_s i_{sd}|$ . The proportional gain must be larger than all disturbances ( $R_s i_{sd}$  is seen as a disturbance) and other modeling errors that may be present. A similar condition can be obtained for the torque loop taking into account (4.111). Large gains improve the dynamic performance and increase the robustness in face of perturbations and modeling errors. However, too large  $K_p$  gains cause large torque and flux ripples, and an adequate tradeoff between low ripple and high gain requirements should be found.

In order to reduce the ripple (chattering) associated to the SMC operation the sign function can be replaced by the saturation function (4.81), as shown in Fig. 4.29. A boundary layer is created in this way and inside this layer the controller becomes a Linear-DTC with high gain. The block diagram of an IM drive with VSC-DTC control is the same as the one in Fig. 4.24, where the PI flux and torque controllers are replaced by the sliding controllers (4.118) and (4.119).

Experimental results with VSC-DTC are presented in Figs. 4.30 to 4.33 for the same 1.1 kW IM drive used for DTC. The sampling frequency and the VSI switching frequency are 10 kHz. Fig. 4.30 shows the response of the torque and flux controllers to step references during startup – first the flux reference is set to 0.95 Wb and then the torque reference is set to  $T_e^* = 12$  Nm. Fig. 4.31 shows an enlarged view of the same waveforms – torque, stator flux, and rotor flux – at the time instant when a torque step is applied. The flux controller gains are  $K_{P\psi} = 40$  and  $K_{I\psi} = 600$ . The torque controller gains are  $K_{PT} = 20$  and  $K_{IT} = 12000$ , which give a step-response time of five milliseconds.



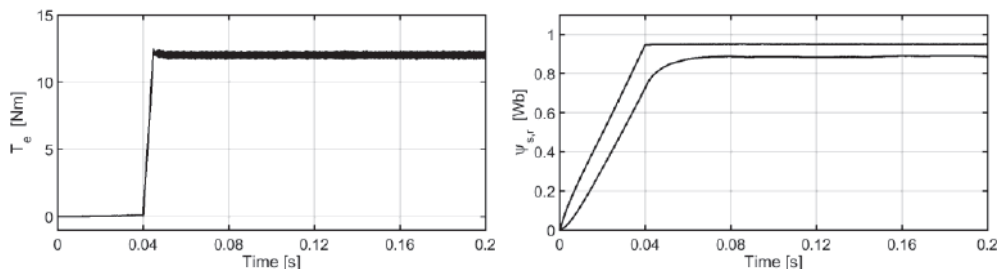


Fig. 4.30 VSC-DTC step response for 12 Nm torque step reference and 0.95 Wb stator flux step reference;  $T_e$  – torque,  $\psi_s$  and  $\psi_r$  – stator and rotor flux magnitudes.

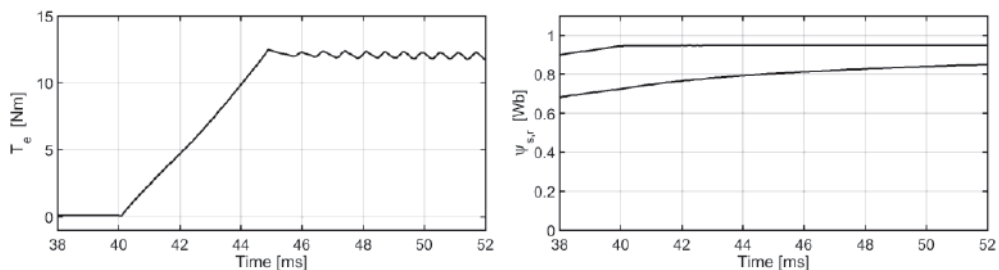


Fig. 4.31 Enlarged view of the torque and flux waveforms in Fig. 4.30.

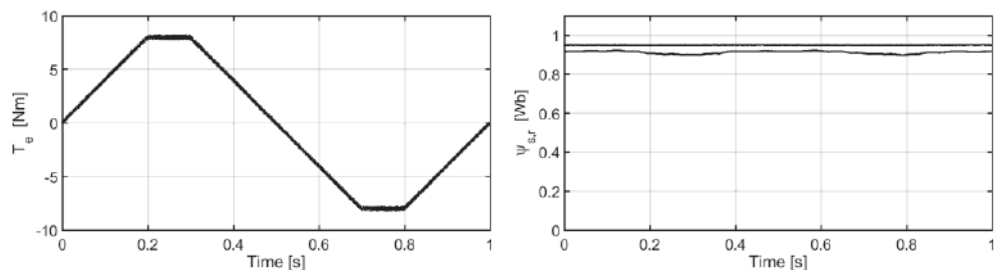


Fig. 4.32 Torque reference tracking with VSC-DTC;  $T_e$  – torque,  $\psi_s$  and  $\psi_r$  – stator and rotor flux magnitudes.

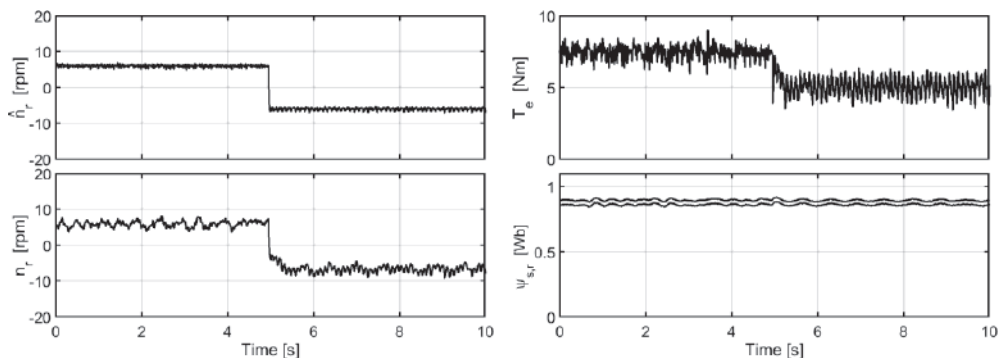


Fig. 4.33 Speed reversal at 6 rpm with VSC-DTC;  $\hat{n}_r$  – estimated speed,  $n_r$  – measured speed,  $T_e$  – estimated torque,  $\psi_s$  and  $\psi_r$  – estimated stator and rotor flux magnitudes.

Compared to Linear-DTC the response time is longer and a 0.5 Nm ripple is present. Fig. 4.32 illustrates the reference tracking performance of the torque controller. The same trapezoidal reference as for Linear-DTC was used and the motor torque perfectly tracks this reference. For this test the torque gains are smaller and the ripple is also smaller. Fig. 4.32 proves the VSC robustness – the stator flux control is stiff, without any oscillations, unlike Fig. 4.27 where the flux is sensitive to torque transients.

Fig. 4.32 demonstrates stable operation as motor and generator, at very low speeds. While running at 6 rpm (0.2 Hz stator frequency), the machine is loaded with rated torque and then it reverses to -6 rpm in the generator mode. Stable operation at zero speed is also possible. The main advantage of VSC-DTC over Linear-DTC is its strong robustness, while its disadvantage is a longer response time and the presence of the torque ripple.

### 4.7.2 Linear and sliding mode control

The *linear and variable structure direct torque control* (Linear+VSC) is a superposition of two controllers, a Linear-DTC and a VSC-DTC. This scheme was proposed in [22] and it takes advantage of the best features of the two strategies.

The switching function is  $S = s_d + js_q = \psi_{sd}^* - \psi_{sd} + j(T_e^* - T_e)$ , the same as for VSC-DTC. The Linear+VSC control law is the sum of a sliding mode controller and a linear controller, both implemented in the stator flux frame,

$$u_{sd}^* = (K_{P\psi} + K_{I\psi} \frac{1}{s}) \cdot (s_d + K_{S\psi} \cdot \text{sign}(s_d)) \quad (4.120)$$

$$u_{sq}^* = (K_{PT} + K_{IT} \frac{1}{s}) \cdot (s_q + K_{ST} \cdot \text{sign}(s_q)) + \omega_{\psi s} \psi_{sd} \quad (4.121)$$

where  $K_{P\psi}$ ,  $K_{I\psi}$ ,  $K_{PT}$ ,  $K_{IT}$ ,  $K_{S\psi}$ , and  $K_{ST}$  are positive gains.

Figure 4.34 shows the block diagram of the Linear+VSC controller.

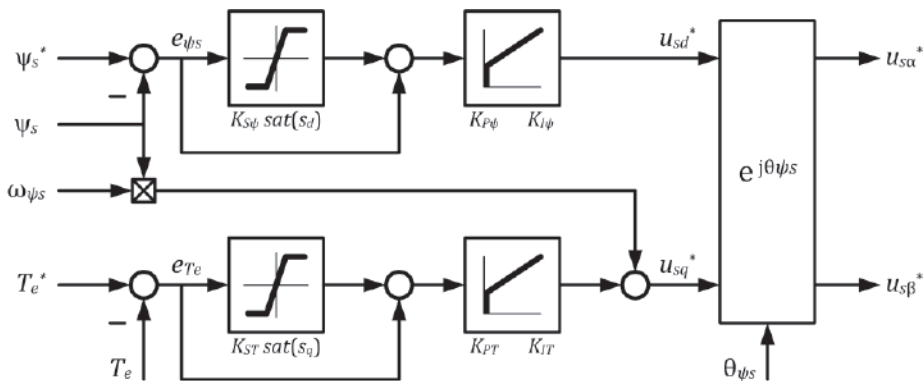


Fig. 4.34 Linear and sliding mode direct torque controller for IM drives.

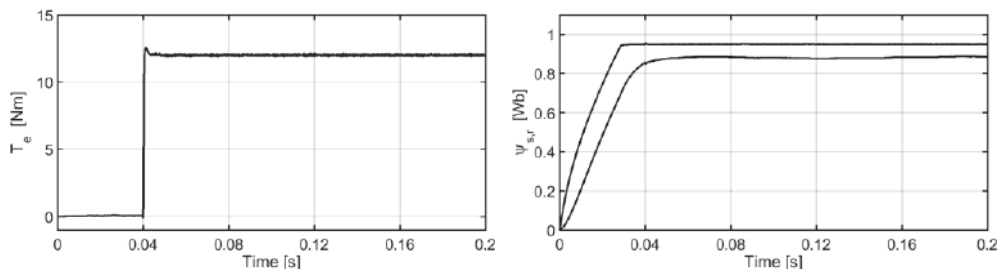


Fig. 4.35 Linear+VSC step response for 12 Nm torque step reference and 0.95 Wb stator flux step reference;  $T_e$  – torque,  $\psi_s$  and  $\psi_r$  – stator and rotor flux magnitudes.

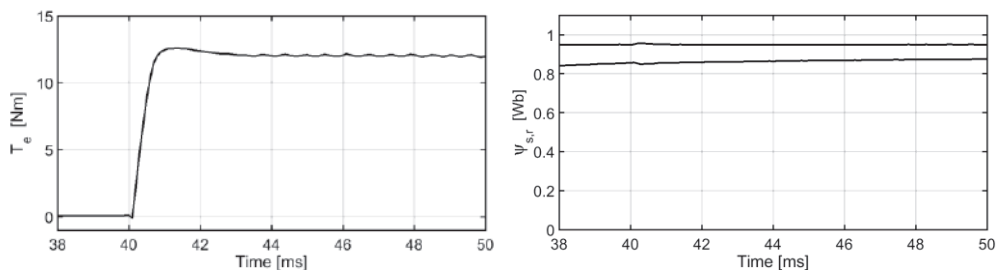


Fig. 4.36 Enlarged view of the torque and flux waveforms in Fig. 4.35.

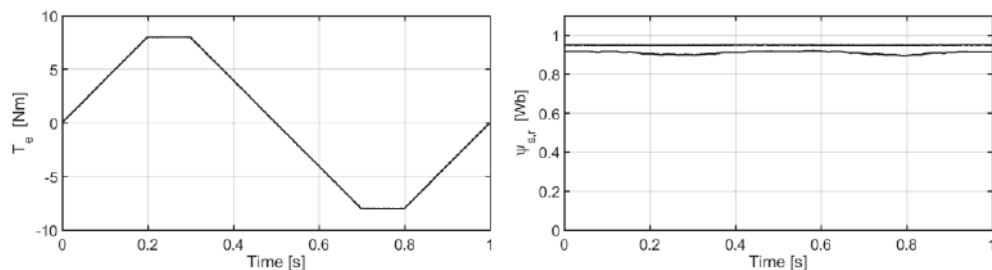


Fig. 4.37 Torque reference tracking with Linear+VSC;  $T_e$  – torque,  $\psi_s$  and  $\psi_r$  – stator and rotor flux magnitudes.

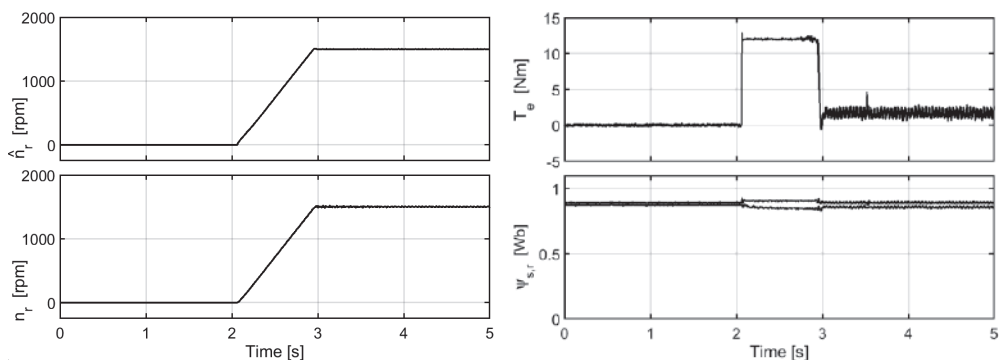


Fig. 4.38 Acceleration from zero to 1500 rpm with Linear+VSC;  $\hat{n}_r$  – estimated speed,  $n_r$  – measured speed,  $T_e$  – torque,  $\psi_s$  and  $\psi_r$  – stator and rotor flux magnitudes.

This controller is simple and versatile. It combines in a convenient way the linear and discontinuous operation. During transient operation, the torque and flux errors are large, and the control effort of the linear component is dominant. Thus, the linear component controls the transient behavior and the PI gains define the response time. During steady-state operation the errors are almost zero, the PI contribution is small, and the discontinuous mode becomes dominant. Thus, a robust switching operation and a VSC-like behavior prevail in the steady-state.

The PI gains are selected in the same way as for Linear-DTC, using (4.115) and (4.116). The sliding mode gains,  $K_{S\psi}$  and  $K_{ST}$ , provide a degree of freedom for tuning the sliding mode behavior. When these gains are large enough the system operates in sliding mode, similar to a VSC-DTC, while a small or zero  $K_S$  leads to quasi-linear operation with very low ripple. There is a separation between the two functional modes, which can be easily balanced by modifying the sliding gains.

The block diagram of an IM drive with Linear+VSC control is the same as in Fig. 4.24, where the PI flux and torque controllers are replaced by the sliding controllers (4.120) and (4.121). Experimental results with Linear+VSC are presented in Figs. 4.35 to 4.38 for the same 1.1 kW IM drive used for Linear-DTC. Fig. 4.35 shows the response of torque and flux controllers to step references during startup – first the flux reference is set to 0.95 Wb and then the torque reference is set to  $T_e^* = 12$  Nm. Fig. 4.36 shows an enlarged view of the same waveforms – torque, stator flux, and rotor flux – at the time instant when a torque step is applied. The flux controller gains are  $K_{p\psi} = 40$ ,  $K_{I\psi} = 400$ , and  $K_{S\psi} = 1$ . The torque controller gains are  $K_{pT} = 40$ ,  $K_{IT} = 40000$ , and  $K_{ST} = 0.2$ . During transients the torque exhibits linear behavior, similar to Linear-DTC. The torque reaches 12 Nm in one millisecond, the same time as for DTC. In the steady-state the torque has a typical VSC behavior with very small ripples.

Fig. 4.37 illustrates the reference tracking performance of the torque controller. The same torque reference as for Linear-DTC was used, and the motor torque perfectly tracks this reference. The flux control is insensitive to torque transients, like VSC-DTC. Fig. 4.38 shows operation at zero speed followed by acceleration to 1500 rpm. The flux magnitude is constant during large speed transients, which tells that the Linear+VSC is robust.

### 4.7.3 Super-twisting sliding mode control

The *super-twisting sliding mode* (STSM) is an algorithm developed in the context of high-order sliding modes [14]. These controllers force the switching of the higher-order time derivatives of the sliding variable, while its first derivative is continuous. STSM is a second-order sliding controller designed for dynamic systems with relative degree one. During the sliding mode, both the sliding function and its first derivative are driven to zero and the control variable converges to the equivalent control.

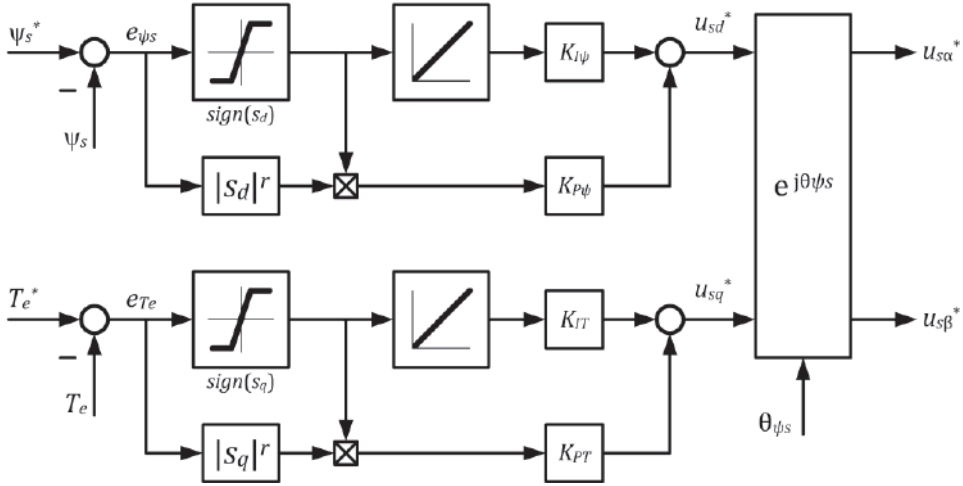


Fig. 4.39 Super twisting sliding mode direct torque controller for IM drives.

The switching function is defined based on torque and flux errors as  $S = s_d + js_q = \psi_{sd}^* - \psi_{sd} + j(T_e^* - T_e)$ .

The STSM control law computes a voltage reference in the stator flux frame

$$u_{sd}^* = \left( K_{P\psi} \cdot |S_d|^{r_d} + K_{I\psi} \frac{1}{s} \right) \cdot \text{sign}(s_d) \quad (4.122)$$

$$u_{sq}^* = \left( K_{PT} \cdot |S_q|^{r_q} + K_{IT} \frac{1}{s} \right) \cdot \text{sign}(s_q) + \omega_{\psi_s} \psi_{sd} \quad (4.123)$$

where  $K_{P\psi}$ ,  $K_{I\psi}$ ,  $K_{PT}$ , and  $K_{IT}$  are positive gains, and the exponents are  $0 < r_{d,q} < 1$ .

The reference voltage is translated to the stator frame using the estimated stator flux position,  $\underline{u}_s^* = \underline{u}_s^{s*} e^{j\theta\psi_s}$ . Then this voltage is input to a SVM module that controls the VSI. A block diagram of the STSM controller is shown in Fig. 4.39. The block diagram of an IM drive with STSM control is the same as in Fig. 4.24, where the flux and torque controllers are replaced by the STSM controllers (4.122) and (4.123).

The first term of each controller employs the magnitude of the sliding function raised at power  $r$ . These exponents modify the static and dynamic behavior of the system in a substantial way. When  $r = 0$ , the first component is discontinuous,  $K_p \text{sign}(s)$ , and the controller becomes identical to a VSC-DTC described by (4.118)-(4.119). When  $r = 1$ , the first term is proportional with the error,  $K_p s$ , and the controller becomes similar to a Linear-DTC. A mix of these situations is obtained when the exponents are changed between zero and one. The sliding mode effect is strong and the apparent gain is large as  $r$  approaches zero. The linear effect is dominant and the operation becomes asymptotical as  $r$  approaches one. A typical value recommended in [14] is  $r = 0.5$ . Practical values for low power drives are  $r_d = 0.1 - 0.3$  for the flux control and  $r_q = 0.4 - 0.5$  for the torque control. The flux has low ripple due to larger time constants, and the flux controller can be tuned more towards the sliding mode operation, with benefits in robustness.

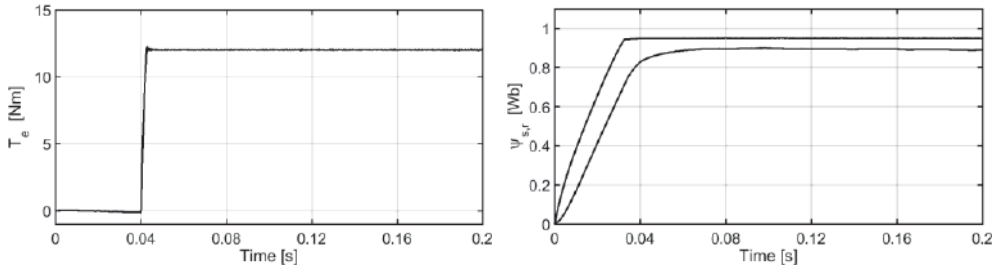


Fig. 4.40 STSM step response for 12 Nm torque step reference and 0.95 Wb stator flux step reference;  $T_e$  – torque,  $\psi_s$  and  $\psi_r$  – stator and rotor flux magnitudes.

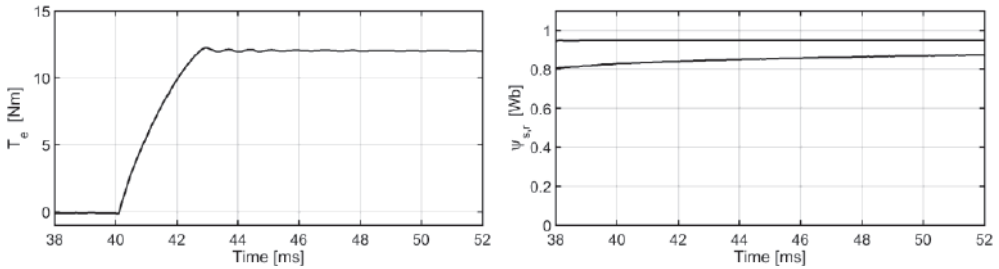


Fig. 4.41 Enlarged view of the torque and flux waveforms in Fig. 4.40.

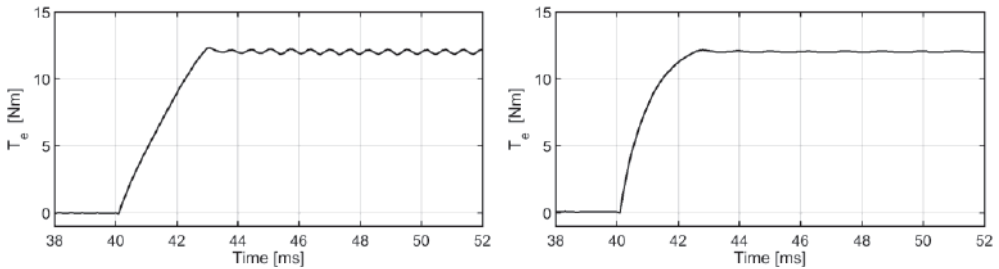


Fig. 4.42 STSM torque response for different tuning –  $r_q = 0.4$  (left) and  $r_q = 0.7$  (right).

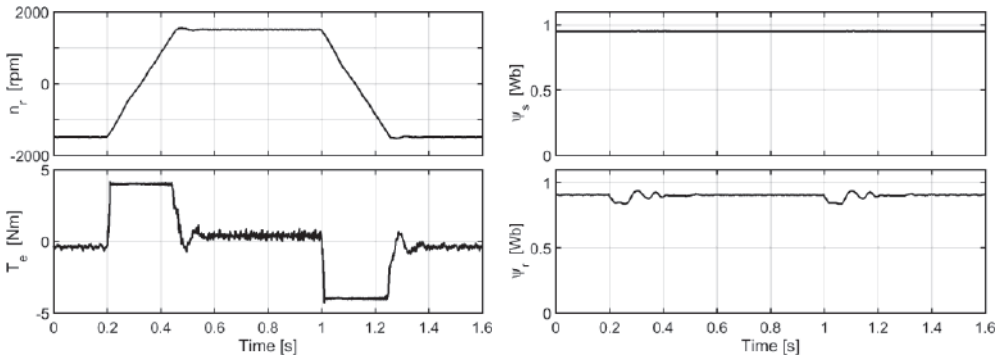


Fig. 4.43 Speed reversals at nominal speed with STSM control for a 0.5 kW drive;  $n_r$  – rotor speed,  $T_e$  – torque,  $\psi_s$  and  $\psi_r$  – stator and rotor flux magnitudes.

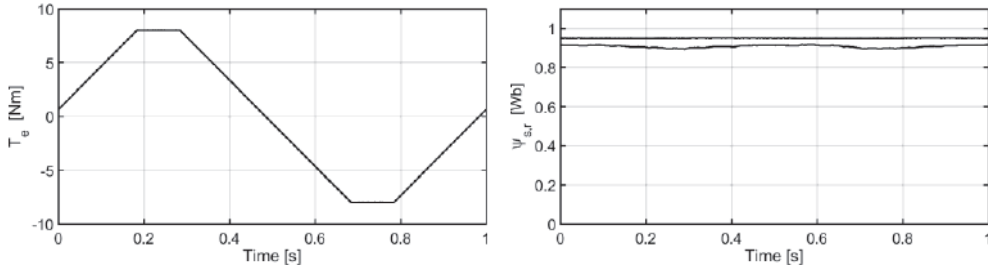


Fig. 4.44 Torque reference tracking with STSM control;  $T_e$  – torque,  $\psi_s$  and  $\psi_r$  – stator and rotor flux magnitudes.

The PI gains are designed based on the desired dynamic performance, using (4.115) and (4.116) as guidelines. Changing the  $K_P$  gain is the most effective way to control the response time for both the torque and the flux, while the  $K_I$  gain influences the control accuracy in steady-state. In general, STSM responds slightly slower than a Linear-DTC.

Experimental results with STSM control are presented in Figs. 4.40 to 4.44 for the same 1.1 kW drive and 0.5 kW drive used for Linear-DTC. Fig. 4.40 shows the response of the torque and flux controllers to step references during startup – first the flux reference is set to 0.95 Wb and then the torque reference is set to  $T_e^* = 12$  Nm. Fig. 4.41 shows an enlarged view of the same waveforms – torque, stator flux, and rotor flux – at the time instant when a torque step is applied. The flux controller gains are  $K_{P\psi} = 60$ ,  $K_{I\psi} = 400$ , and  $r_a = 0.1$ . The torque controller gains are  $K_{PT} = 30$ ,  $K_{IT} = 30000$ , and  $r_q = 0.5$ . Fig. 4.42 shows how the behavior changes when the torque exponent is  $r_q = 0.4$  and  $r_q = 0.7$ . The sliding mode behavior and chattering appear in the former case, and quasi-asymptotical operation in the latter. The step response time is 2.5 ms for all the tests.

Fig. 4.43 illustrates the operation at  $\pm 1500$  rpm and fast reversals of the 0.5 kW drive. Compared to Linear-DTC in Fig. 4.28, no oscillations are present in the flux and torque waveforms during speed transients. This proves the excellent robustness of the STSM controller. Fig. 4.44 shows the torque reference tracking performance for the 1.1 kW drive. As for other sliding controllers, the tracking is perfect and the flux control is insensitive to torque transients.

The STSM DTC was proposed in [23] and has two advantages for IM drives: (a) delivers a sliding mode operation which is very robust and runs with low torque, flux, and current ripples and (b) provides finite-time convergence and the response time is tunable. Of the four controllers presented in this section, the STSM and Linear+VSC provide the best performance and are practical for sensorless IM drives.

## 4.8 State observers for induction motor drives

Modern control strategies for AC drives require accurate knowledge of the motor state variables, at each moment. In mainstream sensorless drives only the stator currents are measured, while the stator or rotor flux, the electromagnetic torque, and the rotor speed are estimated by state observers. High-performance or mission-critical drives use motion sensors to measure the speed, while the flux and torque are estimated.

A state observer is a real-time model of a real process or dynamic system, which produces an approximation of the state vector of that system, and whose characteristics are somewhat free to be determined by the designer [25]. The observer inputs are the inputs and the available outputs of the real process whose state is to be estimated. The observer state vector is composed of all quantities that have to be estimated. In motor drives, state observers are employed as sensor replacements and are more reliable and more affordable than the sensors they replace.

There are two classes of observers in AC drives: (a) observers based on fundamental excitation, which assume a sinusoidal distribution of the flux density along the air-gap, and estimate the fundamental or the low-frequency harmonic components of the flux; (b) observers that use high-frequency signals injected into the machine in order to detect magnetic anisotropic properties and/or the magnetic saturation of that machine. As IMs are magnetically symmetric, the first type is practical for IM drives. In terms of complexity, IM observers can be full-order or reduced-order, and adaptive or inherently sensorless.

### 4.8.1 Speed-adaptive observers

Speed-adaptive observers are full-order Luenberger observers designed using the IM state-space models described in section 4.2. A Luenberger observer has the same model and structure as the observed system, and has an additional input that accounts for the mismatch between the measured and estimated output of the system. Such an observer can have arbitrary dynamics and it is stable if the process is completely observable [25].

The rotor speed appears in all IM models in section 4.2 as a time-variable parameter. If the speed is constant or slowly-variable then all models become linear time-invariant. The adaptive observer design involves two steps: (a) design a linear observer for the flux and the current, assuming a linear IM model where the speed is known and constant, and (b) design a speed observer and then update the speed value for the flux observer. The speed update forms a so-called adaptation loop. In some cases, the stator resistance or the rotor time constant may be estimated and adapted by another loop.

Consider first the rotor flux model in the stationary reference frame (4.36)-(4.37), where the stator voltage is a known input and the stator current is a measured output. If the stator current is estimated, then an observer can use the error between measured and estimated currents in order to correct the estimation. An adaptive observer for the rotor flux and the stator current, implemented in the stator frame, is [26], [27]



$$\frac{d}{dt} \hat{\underline{i}}_s = -\frac{R_{eqr}}{L_s \sigma} \hat{\underline{i}}_s + \frac{L_m}{L_s L_r \sigma} \left( \frac{1}{T_r} - j \hat{\omega}_r \right) \hat{\underline{\psi}}_r + \frac{1}{L_s \sigma} \underline{u}_s + K_1 (\underline{i}_s - \hat{\underline{i}}_s) \quad (4.124)$$

$$\frac{d}{dt} \hat{\underline{\psi}}_r = \frac{L_m}{T_r} \hat{\underline{i}}_s - \left( \frac{1}{T_r} - j \hat{\omega}_r \right) \hat{\underline{\psi}}_r + K_2 (\underline{i}_s - \hat{\underline{i}}_s) \quad (4.125)$$

where  $K_1$  and  $K_2$  are the observer gains, and symbol hat " $\hat{\cdot}$ " denotes estimated variables.

Figure 4.45 shows a block diagram of the adaptive rotor flux observer, where the gain and time constant of the current estimator are  $K = T = L_s \sigma / R_{eqr}$ . The estimated speed is shown as an input, but the measured speed, if available, can also be used. The last terms in (4.124) and (4.125) are functions of the current errors and represent the corrective feedback, shown on the bottom side of Fig. 4.45.

It is possible to design a sliding mode observer, in which case the correction terms are proportional with the sign of the current error [12]

$$\frac{d}{dt} \hat{\underline{i}}_s = -\frac{R_{eqr}}{L_s \sigma} \hat{\underline{i}}_s + \frac{L_m}{L_s L_r \sigma} \left( \frac{1}{T_r} - j \hat{\omega}_r \right) \hat{\underline{\psi}}_r + \frac{1}{L_s \sigma} \underline{u}_s + K_1 \cdot \text{sign}(\underline{i}_s - \hat{\underline{i}}_s) \quad (4.126)$$

$$\frac{d}{dt} \hat{\underline{\psi}}_r = \frac{L_m}{T_r} \hat{\underline{i}}_s - \left( \frac{1}{T_r} - j \hat{\omega}_r \right) \hat{\underline{\psi}}_r + K_2 \cdot \text{sign}(\underline{i}_s - \hat{\underline{i}}_s) \quad (4.127)$$

The observer gains are designed so that the observer is stable. If the speed is assumed constant, then (4.124)-(4.125) is a linear system and the classical stability analysis for linear systems can be used. By subtracting (4.124)-(4.125) from (4.36)-(4.37), the observer state matrix can be found as  $E = A - KC$ , where  $A$  is the IM state matrix in (4.35),  $K = [K_1 \ K_2]^T$ , and  $C = [1 \ 0]$  is the output matrix. The observer poles are eigenvalues of  $E$  and they must be selected with negative real parts in order to ensure stability.

A possible choice is to make the observer poles,  $p_{1,2}$ , proportional to motor poles,  $m_{1,2}$  (the motor is always stable), that is,  $p_{1,2} = km_{1,2}$ , where  $k > 1$  is a constant [26].

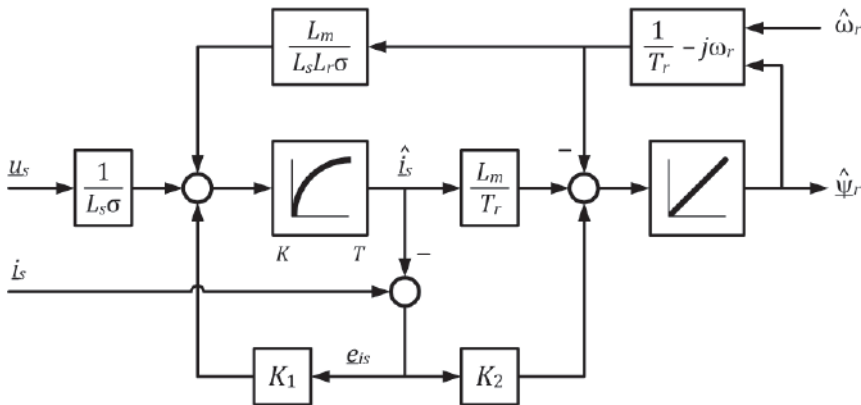


Fig. 4.45 Adaptive rotor flux observer using the rotor flux model in the stator frame.

With this selection, the observer gains are

$$K_1 = (k - 1) \left( \frac{1}{T_s \sigma} + \frac{1}{T_r \sigma} - j \hat{\omega}_r \right) \quad (4.128)$$

$$K_2 = (k^2 - 1) \frac{R_s L_r}{L_m} - (k - 1) \frac{L_s L_r}{L_m} \left( \frac{1}{T_s} + \frac{1}{T_r} \right) + (k - 1) \frac{L_s L_r \sigma}{L_m} j \hat{\omega}_r \quad (4.129)$$

At high speeds, the pole imaginary parts become too large and oscillations may occur. Therefore,  $K_1$  and  $K_2$  must be kept constant for high speed operation.

A better choice is to select the observer poles with the same imaginary parts as the motor poles and with smaller real components (left-shifted in the complex plane), that is,  $p_{1,2} = m_{1,2} - k$ , where  $k$  is a real positive constant [28]. In this case, the gains are

$$K_1 = 2k \quad \text{and} \quad K_2 = k(a_{22} - a_{11} + k)/a_{12} \quad (4.130)$$

where  $a_{11}$ ,  $a_{12}$ , and  $a_{22}$  are elements of the matrix  $A$  from (4.35), with  $\omega_e = 0$ .

This method produces a fast and well damped response at all speeds, including very low, at the cost that  $K_2$  must be calculated in real time. Another practical selection is to make the observer gains speed-adaptive using a scheduling function [29], [30]

$$K_1 = (k_{1r} + jk_{1i} \cdot \text{sign}(\omega_r)) \cdot z(\omega_r) \quad (4.131)$$

$$K_2 = (k_{2r} + jk_{2i} \cdot \text{sign}(\omega_r)) \cdot z(\omega_r) \quad (4.132)$$

where  $z(\omega_r) = \min(|\omega_r|/\omega_0, 1)$  is the scheduling function, and  $k_{1r}$ ,  $k_{1i}$ ,  $k_{2r}$ , and  $k_{2i}$  are positive constants. A simple and effective choice is  $k_{1r} = k_{2r}$  and  $k_{1i} = k_{2i}$ .

At speeds below a threshold speed  $\omega_0$  the gains change in proportion with the speed, while they are constant at speeds above  $\omega_0$ . This speed is selected  $\omega_0 = (0.3 - 1)\omega_{rated}$ . Another practical possibility is to keep  $z$  constant for all speeds. All these choices produce well damped observer dynamics with low computational effort.

The speed estimation and adaptation are designed as a PI compensator with constant gains, driven by an input proportional with the torque error

$$\hat{\omega}_r = \left( K_{P\omega} + K_{I\omega} \frac{1}{s} \right) \cdot (\hat{\psi}_{r\alpha} e_{i\beta} - \hat{\psi}_{r\beta} e_{i\alpha}) \quad (4.133)$$

where  $e_i = e_{i\alpha} + je_{i\beta} = \underline{i}_s - \hat{\underline{i}}_s$  is the current error, and  $K_{P\omega}$  and  $K_{I\omega}$  are positive gains.

This PI estimator can be seen as a PLL observer, where the PI input is a phase error proportional with the imaginary current error in the rotor flux frame.

The stator resistance changes with temperature and it can be estimated and adapted by an integrator with very slow action (a PI can also be used)

$$\hat{R}_s = R_{s0} + K_{Rs} \frac{1}{s} \cdot (\hat{i}_{s\alpha} i_{s\beta} - \hat{i}_{s\beta} i_{s\alpha}) \quad (4.134)$$

where  $R_{s0}$  is the cold-state resistance and  $K_{Rs}$  is a small positive constant.

The error variable that is driven to zero by (4.134) is proportional with the estimated imaginary current, in the current reference frame,  $\hat{i}_{s\alpha} i_{s\beta} - \hat{i}_{s\beta} i_{s\alpha} = \hat{i}_{sq} |\underline{i}_s|$ .

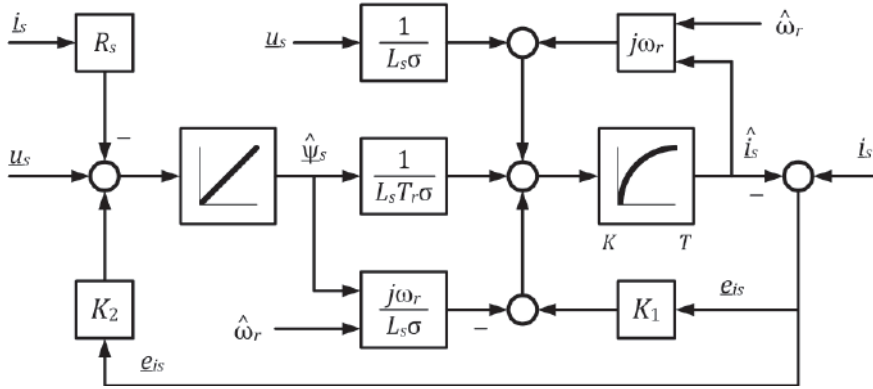


Fig. 4.46 Adaptive stator flux observer using the stator flux model in the stator frame.

Consider now the stator flux model in a stationary reference frame (4.29)-(4.30), where the stator voltage is a known input and the stator current is a measured output. An adaptive observer for the stator flux and the stator current, in the stator frame, is

$$\frac{d}{dt} \hat{i}_s = \left( -\frac{R_{eqs}}{L_s\sigma} + j\hat{\omega}_r \right) \hat{i}_s + \frac{1}{L_s\sigma} \left( \frac{1}{T_r} - j\hat{\omega}_r \right) \hat{\psi}_s + \frac{1}{L_s\sigma} u_s + K_1 (i_s - \hat{i}_s) \quad (4.135)$$

$$\frac{d}{dt} \hat{\psi}_s = -R_s \hat{i}_s + u_s + K_2 (i_s - \hat{i}_s) \quad (4.136)$$

where  $K_1$  and  $K_2$  are the observer gains to be determined so that it is stable.

Figure 4.46 shows a block diagram of the stator flux observer, where the gain and the time constant of the current estimator are  $K = T = L_s\sigma/R_{eqs}$ . The last terms in (4.135)-(4.136) are proportional with current errors and represent the corrective feedback.

As for the rotor flux observer, a sliding mode stator flux observer is [32]

$$\frac{d}{dt} \hat{i}_s = \left( -\frac{R_{eqs}}{L_s\sigma} + j\hat{\omega}_r \right) \hat{i}_s + \frac{1}{L_s\sigma} \left( \frac{1}{T_r} - j\hat{\omega}_r \right) \hat{\psi}_s + \frac{1}{L_s\sigma} u_s + K_1 \cdot \text{sign}(i_s - \hat{i}_s) \quad (4.137)$$

$$\frac{d}{dt} \hat{\psi}_s = -R_s \hat{i}_s + u_s + K_2 \cdot \text{sign}(i_s - \hat{i}_s) \quad (4.138)$$

The gains are selected in the same way, using equations (4.130) to (4.132), with the remark that  $a_{11}$ ,  $a_{12}$ , and  $a_{22}$  are elements of the matrix  $A$  from (4.28), with  $\omega_e = 0$ .

Speed estimation and adaptation are designed as a PI compensator with constant gains, driven by the torque error

$$\hat{\omega}_r = \left( K_{P\omega} + K_{I\omega} \frac{1}{s} \right) \cdot (\hat{\psi}_{s\alpha} e_{i\beta} - \hat{\psi}_{s\beta} e_{i\alpha}) \quad (4.139)$$

where  $K_{P\omega}$  and  $K_{I\omega}$ , are positive gains.

The stator resistance is estimated by (4.134) or (4.140), both producing similar results.

$$\hat{R}_s = R_{s0} + K_{RS} \frac{1}{s} \cdot (\hat{i}_{s\alpha} e_{i\alpha} - \hat{i}_{s\beta} e_{i\beta}) \quad (4.140)$$

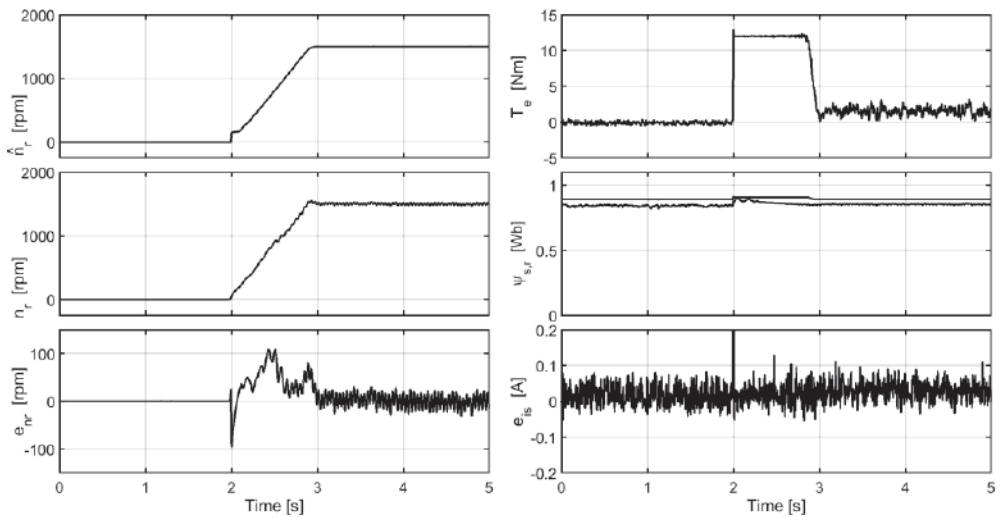


Fig. 4.47 Acceleration from zero to 1500 rpm with Linear+VSC and rotor flux adaptive observer;  $\hat{n}_r$  – estimated speed,  $n_r$  – measured speed,  $e_{nr}$  – speed estimation error,  $T_e$  – torque,  $\psi_s$  and  $\psi_r$  – stator and rotor flux magnitudes,  $e_{is}$  – current estimation error.

Another possibility is to design an adaptive observer by using the flux model in the stator frame, or in the rotor frame [28]-[30]. The speed is estimated by either (4.133) or (4.139). Kalman filter observers can also be designed using the same models [31].

Figure 4.47 shows experimental results with the 1.1 kW IM drive using the rotor flux adaptive observer and Linear+VSC control. The drive runs at zero speed for two seconds and then it accelerates to rated speed with a 12 Nm torque. The bottommost waveforms are the speed error  $e_{nr} = n_r - \hat{n}_r$  and current magnitude error  $e_{is} = |\hat{i}_s| - |i_s|$ . It is apparent that the PI speed estimator works well during constant-speed operation, but provides modest results and errors during fast speed transients.

#### 4.8.2 Inherently sensorless observers

An inherently sensorless observer is a flux and current observer that avoids using the estimated speed or the estimated rotor position, in any way. The lack of an adaptation feedback is seen as an advantage because the estimated speed is affected by errors that can propagate back into the flux estimation.

In digital systems that operate sequentially, the speed is estimated in the last step of the algorithm, after the flux is estimated. Usually, an estimated speed contains a certain amount of noise and other errors, and it is time delayed. This erroneous estimate is fed back to the flux observer in subsequent sampling periods and its errors affect the flux estimation. Although adaptive observers are stable, undesirable effects, such as limit cycles, high sensitivity to noise, and phase delays, may occur and may deteriorate the

overall performance of a drive system. An example is Fig. 4.47, where the estimated speed is delayed with respect to the actual speed during startup.

The idea that facilitates the design of sensorless observers is to use two reference frames instead of a single frame [18]-[22]. A close inspection of the state-space models in section 4.2 reveals that neither the stator equation in the stator frame, nor the rotor equation in the rotor frame contains the rotor speed. Moreover, the rotor equation in the rotor flux frame contains only the slip speed, which is related to the torque.

Consider the flux model (4.41)-(4.43). A dual reference frame observer can be designed with the stator equation in the stator frame, as (4.45), and the rotor equation in the rotor flux frame, as (4.50). A sensorless observer based on (4.45) and (4.50) is

$$\frac{d}{dt} \underline{\hat{\psi}}_s = -\frac{1}{T_s \sigma} \underline{\hat{\psi}}_s + \frac{L_m}{L_r T_s \sigma} \underline{\hat{\psi}}_r + \underline{u}_s + K_1 (\underline{i}_s - \underline{\hat{i}}_s) \quad (4.141)$$

$$\frac{d}{dt} \underline{\hat{\psi}}_r^r = \frac{L_m}{L_s T_r \sigma} \underline{\hat{\psi}}_s^r - \left( \frac{1}{T_r \sigma} + j\omega_2 \right) \underline{\hat{\psi}}_r^r + K_2 (\underline{i}_s^r - \underline{\hat{i}}_s^r) \quad (4.142)$$

$$\underline{\hat{i}}_s = \frac{1}{L_s \sigma} \underline{\hat{\psi}}_s - \frac{L_m}{L_s L_r \sigma} \underline{\hat{\psi}}_r \quad (4.143)$$

where  $\omega_2$  is the slip speed given by (4.40), and  $K_1$  and  $K_2$  are observer gains.

Assuming a correct orientation of the rotor flux frame, the rotor flux has only real component,  $\underline{\psi}_r^r = \psi_{rd}$ , and (4.142) separates into

$$\frac{d}{dt} \psi_{rd} = \frac{L_m}{L_s T_r \sigma} \psi_{sd} - \frac{1}{T_r \sigma} \psi_{rd} + \mathcal{Re} \left( K_2 (\underline{i}_s^r - \underline{\hat{i}}_s^r) \right) \quad (4.144)$$

$$\frac{d}{dt} \psi_{rq} = \mathcal{Im} \left( K_2 (\underline{i}_s^r - \underline{\hat{i}}_s^r) \right) \quad (4.145)$$

None of these equations contains the rotor speed and the observer is sensorless. The rotor flux position needed to implement (4.142) is evaluated as  $\hat{\theta}_{\psi r} = \arctan(\hat{\psi}_{r\beta}^s / \hat{\psi}_{r\alpha}^s)$ , where  $\hat{\psi}_r^s$  is a separate rotor flux value estimated with (4.146) in the stator frame.

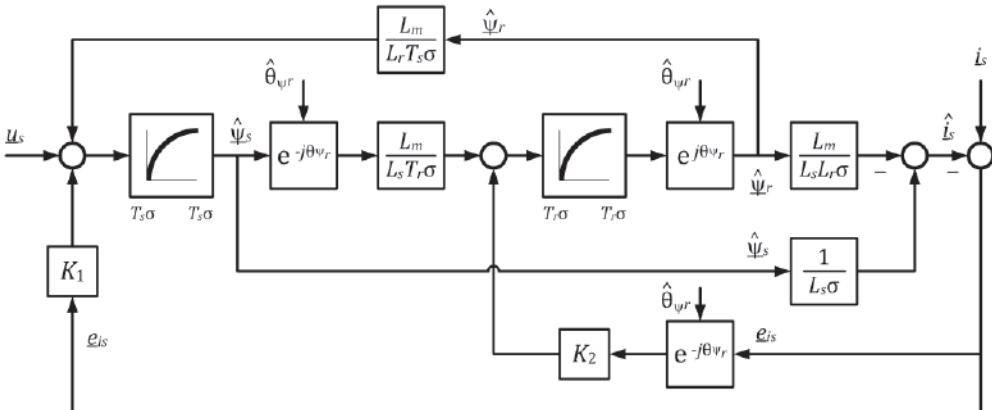


Fig. 4.48 Inherently sensorless observer (1.141)-(1.143) using two reference frames.

$$\underline{\hat{\psi}}_r^s = \frac{L_r}{L_m} \underline{\hat{\psi}}_s - \frac{L_s L_r}{L_m} \sigma \underline{\dot{i}}_s \quad (4.146)$$

Figure 4.48 shows a block diagram of a sensorless observer implemented with (1.141)-(1.146). The gains can be calculated by any design method described in section 4.8.1. For example, equations (4.131)-(4.132), with constant or variable  $z$  and with  $k_{2r} < 0$ , are a practical and effective choice.

A slightly improved scheme can be obtained if the stator equation (4.30) is used to estimate the stator flux, while the rotor flux is estimated in the same way as before, from (4.50). The sensorless observer based on (4.30) and (4.50) is [19]

$$\frac{d}{dt} \underline{\hat{\psi}}_s = -R_s \underline{\dot{i}}_s + \underline{u}_s + K_1 (\underline{\dot{i}}_s - \underline{\hat{i}}_s) \quad (4.147)$$

$$\frac{d}{dt} \underline{\hat{\psi}}_r^r = \frac{L_m}{L_s T_r \sigma} \underline{\hat{\psi}}_s^r - \left( \frac{1}{T_r \sigma} + j\omega_2 \right) \underline{\hat{\psi}}_r^r + K_2 (\underline{\dot{i}}_s^r - \underline{\hat{i}}_s^r) \quad (4.148)$$

$$\underline{\hat{i}}_s = \frac{1}{L_s \sigma} \underline{\hat{\psi}}_s - \frac{L_m}{L_s L_r \sigma} \underline{\hat{\psi}}_r \quad (4.149)$$

The rotor flux equation (4.148) is implemented in the rotor flux frame with (4.144)-(4.145), while all other equations are in the stator frame. In order to improve the accuracy, the measured current is used in (4.147) to calculate the voltage drop on  $R_s$ . The gains are designed using equations (4.131)-(4.132), with  $k_{2r} < 0$  and, possibly,  $k_{1i} = 0$ .

Figure 4.49 shows a block diagram of the sensorless observer described by (4.147)-(4.149). The rotor flux position is estimated as  $\hat{\theta}_{\psi r} = \arctan(\hat{\psi}_{r\beta}^s / \hat{\psi}_{r\alpha}^s)$ , where  $\hat{\psi}_r^s$  is an additional rotor flux evaluated with (4.146), as shown in the upper part of Fig. 4.49. In order to avoid a transformation, the compensation term in (4.148) is implemented in the stator frame, i.e. it is added to the stator flux term before transforming to  $d$ - $q$  frame.

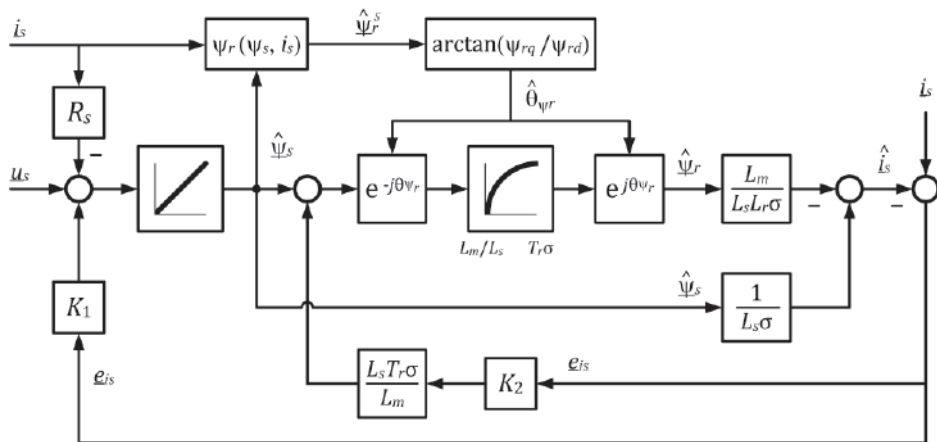


Fig. 4.49 Inherently sensorless observer (1.146)-(1.148) with dual reference frame.

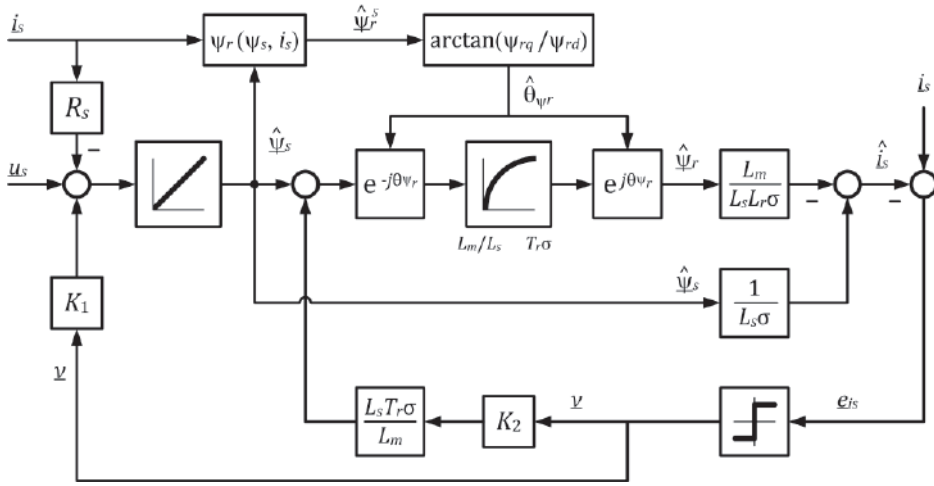


Fig. 4.50 Inherently sensorless sliding mode observer with dual reference frame.

At low speed operation all observers are sensitive to measurement errors, in particular to low-frequency and DC errors, known as offset. In order to reduce this sensitivity, a small integral compensation can be added to the stator equation,

$$\frac{d}{dt} \hat{\underline{\psi}}_s = -R_s \hat{\underline{i}}_s + \underline{u}_s + K_1 (\hat{\underline{i}}_s - \underline{i}_s) + K_1 \int (\hat{\underline{i}}_s - \underline{i}_s) dt \quad (4.150)$$

where  $K_1$  is a small positive gain, usually  $K_1 \leq 25$ .

A major source of errors is the variation of the IM parameters due to temperature and saturation. Detuning of the stator resistance causes large errors at low and medium speeds, and  $R_s$  should be estimated with (4.134) or (4.140).

Both of the sensorless schemes can be redesigned as sliding observers [20]-[22]. To this end, the linear compensation terms,  $K_{1,2}(\hat{\underline{i}}_s - \underline{i}_s)$ , are replaced by terms proportional with the error sign,  $K_{1,2} \cdot \text{sign}(\hat{\underline{i}}_s - \underline{i}_s)$ . A block diagram of a sliding mode sensorless observer that uses the stator equation is shown in Fig. 4.50, where  $\underline{v} = \text{sign}(\hat{\underline{i}}_s - \underline{i}_s)$ .

In general, sliding mode observers are more accurate and robust than similar linear observers. A sliding observer with large enough gains can compensate, to some extent, for parameter errors and measurement offsets [32]. However, sliding mode observers are sensitive to stator resistance detuning and the resistance adaptation is recommended at low and medium speeds, whenever the motor is loaded [33]. All the experimental results reported in sections 4.5 to 4.7 have been obtained using either the sensorless observer in Fig. 4.49, or the sliding observer in Fig. 4.50.

Another approach to design sensorless observers is to consider the rotor speed as an unknown perturbation. Recall that both equations of the rotor flux model (4.36)-(4.37) contain the back-EMF term  $j\omega_r \underline{\psi}_r$ . A sliding mode sensorless observer in the stator frame is constructed ignoring the back-EMF terms [33],

$$\frac{d}{dt} \hat{i}_s = -\frac{R_{eqr}}{L_s \sigma} \hat{i}_s + \frac{L_m}{T_r L_s L_r \sigma} \hat{\psi}_r + \frac{1}{L_s \sigma} \underline{u}_s - \frac{L_m}{L_s L_r \sigma} \underline{v} \quad (4.151)$$

$$\frac{d}{dt} \hat{\psi}_r = \frac{L_m}{T_r} \hat{i}_s - \frac{1}{T_r} \hat{\psi}_r + \underline{v} \quad (4.152)$$

where the correction term is implemented as a PI compensator with gains  $K_P$  and  $K_I$ .

$$\underline{v} = \left( K_P + K_I \frac{1}{s} \right) \cdot \text{sign}(\dot{i}_s - \hat{i}_s) \quad (4.153)$$

Sliding mode operation enforces the equality of currents,  $\dot{i}_s = \hat{i}_s$ . Comparing (4.151)-(4.152) with the rotor flux model it follows that the equivalent component (equivalent control) of the correction term approximates the back-EMF,  $\underline{v}_{eq} = j\omega_r \underline{\psi}_r$ .

Another possibility is to design the compensation using integral sliding modes,

$$\underline{v} = K \cdot \text{sign} \left[ \left( 1 + K_I \frac{1}{s} \right) (\dot{i}_s - \hat{i}_s) \right] \quad (4.154)$$

where  $K$  and  $K_I$  are large positive gains.

All gains in (4.153) and (4.154) must be large in order to enforce sliding modes at all speeds and load conditions. In particular, the sliding gain  $K$  in (4.154) must be larger than the rated voltage magnitude. Such large gains cause severe chattering and the estimated rotor flux tends to be noisy. The saturation function (4.81) can be used instead of the sign function to attenuate the chattering.

### 4.8.3 Reduced-order observers

Reduced-order observers estimate only the stator or rotor flux and do not estimate the current. As the stator current is always measured, it is not necessary to calculate it and the observer can be designed with first-order (complex) dynamics.

A family of simple first-order observers can be constructed using the IM stator model as the main vehicle for the stator flux estimation. This approach is very practical for vector control schemes that use stator flux orientation and control, and for all DTC methods.

The stator flux vector can be found by integrating the stator equation (4.30). However, the pure integrator is marginally stable and it amplifies the DC offsets. A practical solution that provides stability and has finite DC gain is to substitute the integrator with a low pass filter (LPF) with a small cutoff frequency

$$\frac{d}{dt} \hat{\underline{\psi}}_s + \omega_0 \hat{\underline{\psi}}_s = \underline{u}_s - R_s \dot{i}_s \quad (4.155)$$

where  $\omega_0 = 2\pi f_0$  is the LPF cutoff frequency.

This estimator provides an approximation of the integral when the stator frequency is several times larger than  $f_0$ . At stator frequencies equal and lower than  $f_0$  the LPF causes severe phase and amplitude errors. Therefore, the cutoff frequency should be very small, usually  $f_0 = 0.5 - 2$  Hz, and the drive operation is restricted to frequencies above 3-5 Hz.



An improvement is to correct the LPF phase and gain errors at the fundamental stator frequency,  $\omega_s = 2\pi f_s$ . The compensated LPF is

$$\frac{d}{dt} \underline{\hat{\psi}}_s + \omega_0 \underline{\hat{\psi}}_s = (\underline{u}_s - R_s \underline{i}_s) \sqrt{\omega_s^2 + \omega_0^2} \frac{1}{|\omega_s|} e^{-j\varphi} \quad (4.156)$$

where the phase correction is  $\varphi = \pi/2 - \arctan(\omega_s/\omega_0)$ .

An LPF reduces the offset problem but it does not eliminate it. In order to totally cancel all offsets a band-pass filter (BPF) topology can be used. The stator flux observer is constructed as an integrator with PI feedback

$$\frac{d}{dt} \underline{\hat{\psi}}_s = \underline{u}_s - R_s \underline{i}_s - K_P \underline{\hat{\psi}}_s - K_I \int \underline{\hat{\psi}}_s dt \quad (4.157)$$

If the BPF central frequency is  $f_0 = 0.5 - 2$  Hz and  $\omega_0 = 2\pi f_0$ , then the gains are

$$K_P = 2\omega_0 \quad \text{and} \quad K_I = \omega_0^2 \quad (4.158)$$

As for the LPF estimators, the drive must operate at frequencies several times larger than  $f_0$ . Phase and magnitude corrections can be applied as in (4.156). An improved scheme is obtained if an additional compensation proportional to the flux reference (from an existing flux controller) is added to (4.157) [34].

LPF and BPF estimators are simple and relatively robust, as they depend on the stator resistance only. They are practical for low-cost drives that run at speeds above 10% the rated speed and for drives that do not require the rotor flux estimation.

Reduced-order observers can also be designed using the rotor flux model (4.36)-(4.37). First, the stator voltage is estimated from (4.36) using the measured current and then the voltage error is used to estimate the rotor flux from (4.37) [27]

$$\underline{\hat{u}}_s = L_s \sigma \frac{d}{dt} \underline{i}_s + R_{eqr} \underline{i}_s - \frac{L_m}{L_r} \left( \frac{1}{T_r} - j\hat{\omega}_r \right) \underline{\hat{\psi}}_r \quad (4.159)$$

$$\frac{d}{dt} \underline{\hat{\psi}}_r = \frac{L_m}{T_r} \underline{i}_s - \left( \frac{1}{T_r} - j\hat{\omega}_r \right) \underline{\hat{\psi}}_r + K \frac{1}{L_s \sigma} (\underline{u}_s - \underline{\hat{u}}_s) \quad (4.160)$$

Substituting (4.159) into (4.160), the reduced-order observer with gain  $K$  is

$$\frac{d}{dt} \underline{\hat{\psi}}_r + K \frac{d}{dt} \underline{i}_s = \left( \frac{1}{T_r} - j\hat{\omega}_r \right) \left( K \frac{L_m}{L_s L_r \sigma} - 1 \right) \underline{\hat{\psi}}_r + \left( \frac{L_m}{T_r} - K \frac{R_{eqr}}{L_s \sigma} \right) \underline{i}_s + K \frac{1}{L_s \sigma} \underline{u}_s \quad (4.161)$$

The variable  $\underline{x} = \underline{\hat{\psi}}_r + K \underline{i}_s$  is obtained by integrating (4.161), and then the flux can be solved knowing the current. In this way a calculation of the current derivative is avoided.

The gain is designed as a speed-dependent function that changes from zero to  $k_0$

$$K = jk_0 \cdot \text{sign}(\omega_r) \cdot \min(|\omega_r|/\omega_0, 1) \quad (4.162)$$

where  $k_0$  is positive and  $\omega_0$  is the transition band, usually 5-20% of the rated speed.

This is a first-order speed-adaptive observer. It is somewhat simpler than a full-order observer, but it produces less accurate results at low speeds.

#### 4.8.4 Speed observers

Accurate speed estimation is the most difficult task in AC drives and the quality of the speed estimation is decisive for the overall performance of the entire drive system. The classical approach is to estimate the speed from measured voltages and currents, that is, to use the machine itself as a speed sensor. This is a challenging task due to the presence of variable parameters and the nonlinearity of the IM dynamic model.

The rotor speed of an IM is a difference between the revolving field speed and the slip speed. In most situations, these are estimated separately: the field speed as the angular velocity of the rotor flux vector,  $\omega_{\psi_r} = d\theta_{\psi_r}/dt$ , and the slip speed from the torque and flux magnitude, using (4.59). This approach works well at medium and high speeds, while at low speeds the estimation accuracy is lower due to the rotor resistance detuning and unaccounted inverter nonlinearities.

A particular situation occurs at zero stator frequency (DC supply) where the back-EMF is zero and the stator flux becomes DC. It follows from (4.11) that  $\underline{u}_s = R_s \dot{i}_s$  and the stator current is exclusively governed by the stator voltage. The current is the main variable used for state estimation but in this case there is no feedback from the rotor side, and the speed does not influence the current in any way. Therefore, the speed is unobservable at zero frequency and persistent sensorless operation is not possible [35].

A very simple and effective way to estimate the speed is by an open-loop computation of the field speed. The derivative of the flux position is evaluated as

$$\hat{\omega}_{\psi_r} = \frac{d}{dt} \text{actan} \left( \frac{\psi_{r\beta}}{\psi_{r\alpha}} \right) = \frac{1}{\psi_{rd}^2} \left( \psi_{r\alpha} \frac{d}{dt} \psi_{r\beta} - \psi_{r\beta} \frac{d}{dt} \psi_{r\alpha} \right) \quad (4.163)$$

where  $\psi_{rd}^2 = \psi_{r\alpha}^2 + \psi_{r\beta}^2$  is the squared flux amplitude.

The flux derivatives in one sampling period can be approximated by finite differences as  $\frac{d}{dt} \psi_{r(k)} = (\psi_{r(k)} - \psi_{r(k-1)})/T_s$ , where  $\psi_{r(k-1)}$  and  $\psi_{r(k)}$  are values from consecutive sampling periods,  $k-1$  and  $k$ , and  $T_s$  is the sampling time. The rotor flux can be estimated by any method described in the previous sections (for simplicity, hat symbols are omitted here). The estimated flux speed becomes

$$\hat{\omega}_{\psi_r} = \frac{1}{T_s \psi_{rd}^2} (\psi_{r\alpha(k-1)} \psi_{r\beta(k)} - \psi_{r\beta(k-1)} \psi_{r\alpha(k)}) \quad (4.164)$$

The slip speed is estimated by (4.40) or (4.59) and then the rotor speed is

$$\hat{\omega}_r = \hat{\omega}_{\psi_r} - \hat{\omega}_2 \quad (4.165)$$

This method produces accurate and noisy results because the flux derivatives amplify the noise. In practice, the flux should be filtered before being used in (4.164), while the speed produced by (4.165) can also be filtered by a second-order LPF. All LPFs introduce phase delays that reduce the speed controller bandwidth and a tradeoff between noise and dynamic response must be found.

An advanced method for speed estimation is based on closed-loop observers that behave similarly with phase locked loop (PLL) systems. PLLs are nonlinear observers used for phase and frequency detection in various grid-connected systems.

Consider the mechanical model (4.51)-(4.52) with  $B = 0$ . A simplified second-order observer for the rotor speed and position, with gains  $K_1$  and  $K_2$ , is [32]

$$\frac{d}{dt} \hat{\theta}_r = \hat{\omega}_r + K_1 \varepsilon \quad (4.166)$$

$$\frac{d}{dt} \hat{\omega}_r = K_2 \varepsilon \quad (4.167)$$

where  $\varepsilon$  is the phase error, to be specified.

While the speed can be obtained by integrating (4.167), a better estimate is the right-hand side of (4.166), which produces the speed at the output of a PI controller

$$\hat{\omega}_{rpi} = \hat{\omega}_r + K_1 \varepsilon = \left( K_1 + K_2 \frac{1}{s} \right) \varepsilon \quad (4.168)$$

This equation is the typical formulation for a PLL frequency estimator and (4.166)-(4.167) describe a PLL loop filter. The PLL phase detector produces the phase error

$$\varepsilon = \sin(\theta_r) \cos(\hat{\theta}_r) - \cos(\theta_r) \sin(\hat{\theta}_r) = \sin(\theta_r - \hat{\theta}_r) \quad (4.169)$$

where  $\theta_r$  is the actual rotor position, measured or estimated by another method. Moreover, the phase error can be  $\varepsilon = \theta_r - \hat{\theta}_r$ , which makes a linear observer.

In sensorless drives, the phase error is defined in relation to the flux observer. The speed estimation for adaptive observers is performed by (4.133) or (4.139), which have the same form as (4.168) and can be seen as PLL estimators. In this case the flux observer plays the role of a phase detector and produces the phase error.

Speed estimation for systems with sensorless observers is based on (4.165) and is executed as a separate process. In this case the flux observer provides the flux, and the position observer (4.166) is modified to estimate the rotor flux position

$$\frac{d}{dt} \hat{\theta}_{\psi r} = \hat{\omega}_r + \hat{\omega}_2 + K_1 \varepsilon \quad (4.170)$$

The PLL phase error is defined as the rotor flux position error

$$\varepsilon = \sin(\theta_{\psi r}) \cos(\hat{\theta}_{\psi r}) - \cos(\theta_{\psi r}) \sin(\hat{\theta}_{\psi r}) \quad (4.171)$$

As most of the time the rotor fluxes are sine waves, this can be reformulated as

$$\varepsilon = \frac{1}{\psi_{rd}^2} (\psi_{r\beta} \cos(\hat{\theta}_{\psi r}) - \psi_{r\alpha} \sin(\hat{\theta}_{\psi r})) \quad (4.172)$$

where  $\underline{\psi}_r = \psi_{r\beta} + j\psi_{r\alpha}$  is a rotor flux vector estimated by any flux observer.

It is also possible to define a linear phase error,  $\varepsilon = \theta_{\psi r} - \hat{\theta}_{\psi r}$ , where the flux position is calculated as  $\theta_{\psi r} = \text{actan}(\psi_{r\beta}/\psi_{r\alpha})$ . Obviously, the two solutions are equivalent for small errors and they produce similar results.

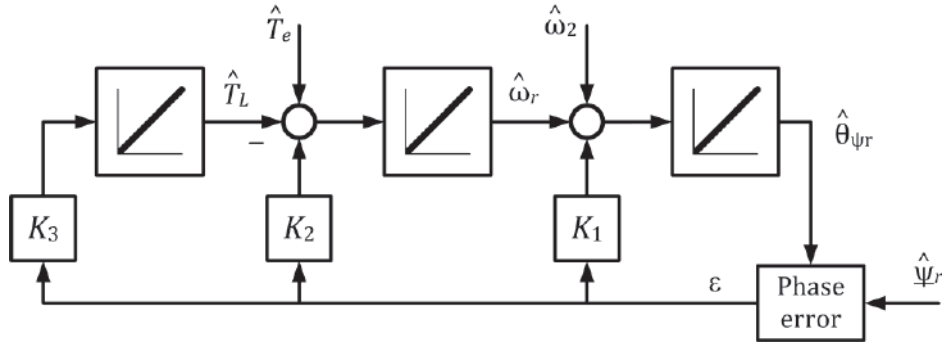


Fig. 4.51 Third-order PLL speed observer for IM drives.

The rotor speed can be estimated either from (4.167), as  $\hat{\omega}_r$ , or from (4.168), as  $\hat{\omega}_{rpi}$ . The latter provides a better dynamic performance, but it is noisier.

Considering a linear phase error, the transfer function from the actual position to the estimated position is obtained from (4.167) and (4.170) as

$$H_{\theta}(s) = \frac{\hat{\theta}}{\theta} = \frac{K_1 s + K_2}{s^2 + K_1 s + K_2} \quad (4.173)$$

Selecting two stable poles,  $p_1$  and  $p_2$ , the gains are  $K_1 = -p_1 - p_2$  and  $K_2 = p_1 p_2$ .

Second-order PLL observers provide modest results during speed transients (as shown in Fig. 4.47). Comparing equations (4.167) and (4.51), it is evident that the torque was ignored and the speed observer was designed on the assumption of a constant speed, i.e. equation (4.167) is based on a “constant speed model”,  $d\omega_r/dt = 0$ .

A third-order PLL observer for the rotor speed and position can be designed with the (estimated) slip speed and torque as inputs

$$\frac{d}{dt} \hat{\theta}_{\psi r} = \hat{\omega}_r + \hat{\omega}_2 + K_1 \varepsilon \quad (4.174)$$

$$\frac{d}{dt} \hat{\omega}_r = \frac{p}{J} (\hat{T}_e - \hat{T}_L) + K_2 \varepsilon \quad (4.175)$$

$$\frac{d}{dt} \hat{T}_L = K_3 \varepsilon \quad (4.176)$$

The phase error is either nonlinear, as in (4.172), or linear,  $\varepsilon = \theta_{\psi r} - \hat{\theta}_{\psi r}$ . The torque is estimated with (4.15) or (4.16) and the slip speed is (4.59). The last equation provides an approximation of the load torque,  $\hat{T}_L$ , assuming a constant load torque. It is also possible to estimate the speed by adding to  $\hat{\omega}_r$  the last term of (4.174),  $\hat{\omega}_{rpi} = \hat{\omega}_r + K_1 \varepsilon$ .

The characteristic equation of this observer is  $s^3 + K_1 s^2 + K_2 s - p K_3 / J = 0$  and the gains can be designed using the pole placement method. Selecting three stable poles,  $p_1$ ,  $p_2$  and  $p_3$ , the gains are ( $K_1$  and  $K_2$  are positive,  $K_3$  is negative)

$$K_1 = -p_1 - p_2 - p_3, \quad K_2 = p_1 p_2 + p_2 p_3 + p_3 p_1, \quad K_3 = p_1 p_2 p_3 \frac{J}{p} \quad (4.177)$$

Figure 4.51 shows the block diagram of the third-order PLL observer.

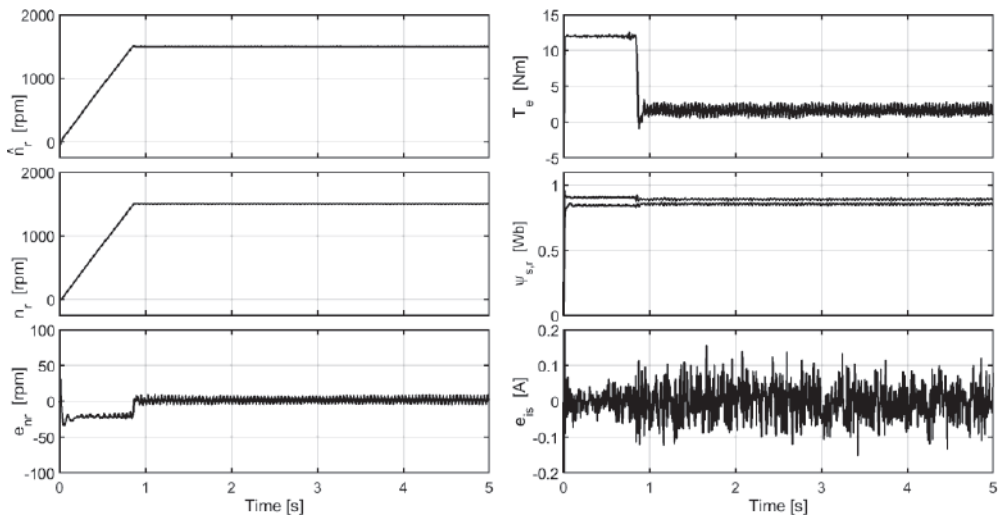


Fig. 4.52 Startup to 1500 rpm with third-order PLL speed observer;  $\hat{n}_r$  – estimated speed,  $n_r$  – measured speed,  $e_{nr}$  – speed estimation error,  $T_e$  – estimated torque,  $\psi_s$  and  $\psi_r$  – stator and rotor flux magnitudes,  $e_{s}$  – current estimation error.

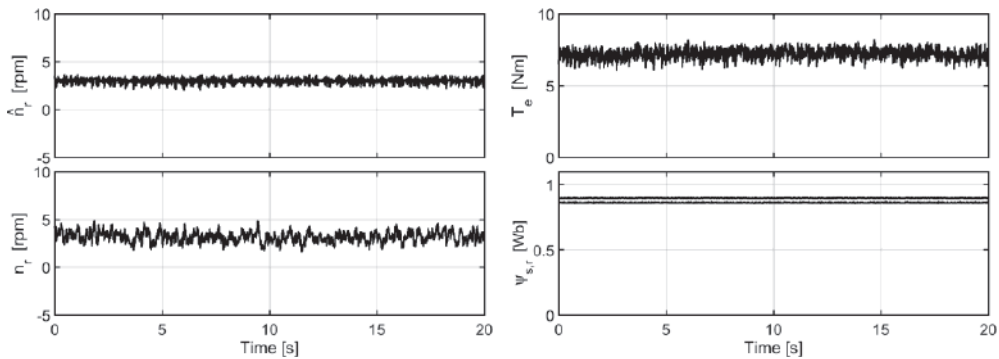


Fig. 4.53 Very low speed operation with PLL speed observer;  $\hat{n}_r$  – estimated speed,  $n_r$  – measured speed,  $T_e$  – estimated torque,  $\psi_s$  and  $\psi_r$  – stator and rotor flux magnitudes.

This scheme was proposed in [32] and it provides excellent results for the steady-state and for the transient operation. A similar third-order observer can be designed for speed adaptive observers [28].

Experimental results with the third-order PLL observer are presented in Figs. 4.52 and 4.53 for the 1.1 kW IM drive controlled by the Linear+VSC DTC (Fig. 4.34). Figure 4.52 shows the startup transients and operation at 1500 rpm (50 Hz). During startup the speed error,  $e_{nr} = n_r - \hat{n}_r$ , is negative, meaning that the estimated speed is slightly anticipated with respect to the actual speed. Compared to an adaptive observer which uses a PI speed estimator (results are shown in Fig. 4.47), the speed errors are smaller, despite of the fact

that the current estimation is noisier in Fig. 4.52. Figure 4.53 shows persistent operation at 3 rpm (0.1 Hz) with full load (7 Nm). A sliding mode sensorless observer (Fig. 4.50) that employs the offset compensation (4.150), the stator resistance estimation (4.140), and a rotor resistance estimator was used for this test.

## 4.9 References

- [1] Nikola Tesla, "A new system of alternate current motors and transformers," *Trans. American Institute of Electrical Engineers*, vol. V, no. 10, May 1888, pp. 308-327.
- [2] Harry Ward Leonard, "Volts vs. Ohms. Speed regulation of electric motors," *Trans. American Institute of Electrical Engineers*, vol. XIII, Nov. 1896, pp. 373-386.
- [3] Donald W. Novotny, Thomas A. Lipo, "Vector Control and Dynamics of AC Drives," Clarendon Press, Oxford, Oxford University Press, New York, 1996.
- [4] Andrzej M. Trzynadlowski, "The Field Orientation Principle in Control of Induction Motors," Kluwer Academic Press, Boston, 1994.
- [5] Werner Leonhard "Control of Electrical Drives, third ed." Springer-Verlag, Berlin, Heidelberg, New York, 2001.
- [6] Seung-Ki Sul, "Control of Electric Machine Drive Systems," IEEE Press, John Wiley and Sons, Hoboken, 2011.
- [7] Rik de Doncker, Duco W.J. Pulle, Andre Veltman, "Advanced Electrical Drives. Analysis, Modeling, Control," Springer, Dordrecht, Heidelberg, London, New York, 2011.
- [8] F. Blaschke, "The principle of field-orientation as applied to the new 'transvector' closed-loop control system for rotating field machines," *Siemens Review*, vol. 35, no. 5, 1972, pp. 217-220.
- [9] Joachim Holtz, "Sensorless control of induction motor drives," *Proceedings IEEE*, vol. 90, no. 8, Aug. 2002, pp. 1359-1394.
- [10] Joachim Holtz, "Sensorless control of induction machines – with or without signal injection?," *IEEE Trans Industrial Electronics*, vol. 53, no. 1, Feb. 2006, pp. 7-30.
- [11] F. Briz, M.W. Degner, and R.D. Lorenz, "Analysis and design of current regulators using complex vectors," *IEEE Trans. Industry Applications*, vol. 36, no. 3, May/June 2000, pp. 817-825.
- [12] V. Utkin, J. Guldner, and J. Shi, "Sliding Mode Control in Electromechanical Systems," Second Edition, CRC Press Taylor & Francis Group, Boca Raton, 2009.
- [13] Y. Shtessel, C. Edwards, L. Fridman, and A. Levant, "Sliding Mode Control and Observation," Springer, New York, USA, 2014.
- [14] Arie Levant, "Principles of 2-sliding mode design," *Automatica*, vol. 43, no. 4, Apr. 2007, pp. 576-586.
- [15] I. Takahashi and T. Noguchi, "A new quick response and high efficiency control strategy of an induction motor," *IEEE Trans. Industry Applications*, vol. IA-22, no. 5, Sep./Oct. 1986, pp. 820-827.
- [16] D. Casadei, F. Profumo, G. Serra, A. Tani, "FOC and DTC: two viable schemes for induction motors torque control," *IEEE Trans. Power Electronics*, vol. 17, no. 5, Sept. 2002, pp. 779-787.
- [17] D. Casadei, G. Serra, and A. Tani, "Implementation of a direct torque control algorithm for induction motors based on discrete space vector modulation," *IEEE Trans. Power Electronics*, vol. 15, no. 4, July 2000, pp. 769-777.

- [18] Cristian Lascu, Ion Boldea, Frede Blaabjerg, "A modified direct torque control for induction motor sensorless drive," *IEEE Trans. Industry Applications*, vol. 36, no. 1, Jan./Feb. 2000, pp. 122-130.
- [19] Cristian Lascu and Andrzej M. Trzynadlowski, "A sensorless hybrid DTC drive for high-volume low-cost applications," *IEEE Trans. Industrial Electronics*, vol. 51, no. 5, Oct 2004, pp. 1048-1055.
- [20] C. Lascu, I. Boldea, F. Blaabjerg, "Direct torque control of sensorless induction motor drives: A sliding mode approach," *IEEE Trans. Industry Applicat.*, vol. 40, no. 2, Mar./Apr. 2004, pp. 582-590.
- [21] Cristian Lascu, Ion Boldea, and Frede Blaabjerg, "Variable-structure direct torque control – a class of fast and robust controllers for induction machine drives," *IEEE Trans. Industrial Electronics*, vol. 51, no. 4, Aug. 2004, pp. 785-792.
- [22] Cristian Lascu, Ion Boldea, and Frede Blaabjerg, "Very-low-speed variable structure control of sensorless induction machine drives without signal injection," *IEEE Trans. Industry Applications*, vol. 41, no. 2, Mar./Apr. 2005, pp. 591-598.
- [23] Cristian Lascu, Alin Argeseanu, Frede Blaabjerg, "Super-twisting sliding-mode direct torque and flux control of IM drives," *IEEE Trans. Power Electronics*, vol. 35, no. 5, May 2020, pp. 5057-5065.
- [24] C. Lascu, S. Jafarzadeh, S.M. Fadali, and F. Blaabjerg, "Direct torque control with feedback linearization for IM drives," *IEEE Trans. Power Electronics*, vol. 32, no. 3, Mar. 2017, pp. 2072-2080.
- [25] D.G. Luenberger, "An introduction to observers," *IEEE Trans. Automatic Control*, vol. AC-16, no. 6, Dec. 1971, pp. 596-602.
- [26] H. Kubota, K. Matsuse, and T. Nakano, "DSP based speed adaptive flux observer for induction motor applications," *IEEE Trans. Industry Applications*, vol. 29, no. 2, Mar./Apr. 1993, pp. 344-348.
- [27] L. Harnefors and M. Hinkkanen "Complete stability of reduced-order and full-order observers for sensorless IM drives," *IEEE Trans. Industrial Electronics*, vol. 55, no. 3, March 2008, pp. 1319-1329.
- [28] J. Maes, J. Melkebeek, "Speed sensorless direct torque control of induction motors using an adaptive flux observer," *IEEE Trans. Industry Applications*, vol. 36, no. 3, May/June. 2000, pp. 778-785.
- [29] Marko Hinkkanen, "Analysis and design of full-order observers for sensorless induction motors," *IEEE Trans. Industrial Electronics*. vol. 51 no. 5 Oct. 2004, pp. 1033-1040.
- [30] Z. Qu, M. Hinkkanen, L. Harnefors, "Gain scheduling of a full-order observer for sensorless induction-motor drives," *IEEE Trans. Ind. Applications*, vol. 50, no. 6, Nov./Dec. 2014, pp. 3834-3845.
- [31] S. Jafarzadeh, C. Lascu, S.M. Fadali, "State estimation of induction motor drives using the unscented Kalman filter," *IEEE Transactions on Ind. Electr.*, vol. 59, no. 11, Nov. 2012, pp. 4207-4216.
- [32] Cristian Lascu, Ion Boldea, and Frede Blaabjerg, "Comparative study of adaptive and inherently sensorless observers for variable-speed induction-motor drives," *IEEE Trans. Industrial Electronics*, vol. 53, no. 1, Jan. 2006, pp. 57-65.
- [33] Cristian Lascu, Ion Boldea, and Frede Blaabjerg, "A class of speed-sensorless sliding-mode observers for high-performance induction motor drives," *IEEE Trans. Industrial Electronics*, vol. 56, no. 9, Sep. 2009, pp. 3394-3403.
- [34] Cristian Lascu and Gheorghe-Daniel Andreescu, "Sliding-mode observer and improved integrator with dc-offset compensation for flux estimation in sensorless-controlled induction motors," *IEEE Trans. Industrial Electronics*, vol. 53, no. 3, June 2006, pp. 785-794.
- [35] L. Harnefors and M. Hinkkanen, "Stabilization methods for sensorless induction motor drives – a survey," *IEEE Jour. Emerg. Selected Topics Power Electronics*, vol. 2, no. 2, June 2014, pp. 132-142.

## 5.1 Introductory elements

The permanent magnet synchronous motors (PMSMs) have recently experienced increased dynamics, especially due to the superior energy performance of the new magnetic materials, becoming thus a more attractive variant than the induction motors.

The first permanent magnet excited machines were built in the nineteenth century. Thus, the achievements of T. Davenport and M. H. Jacobi [1], [2] have to be highlighted. The first prototypes used tough, poor quality magnetic materials that led to discouraging results. The idea of permanent magnet excitation was resumed in the early 1930s, with the invention of magnets made of AlNiCo. The dynamic performance of permanent magnet machines has been substantially improved by the occurrence of rare earth magnets.

The use of permanent magnets for the excitation of synchronous motors has a number of advantages:

- PMs allow for a simple construction to be obtained by eliminating the excitation winding and the sliding contacts and, thus, for a reduction of the machine gauge (under the same loading conditions on the machine shaft, the volume of a SPMSM can be reduced by up to 40% of a DC engine [3]);
- eliminating the electrical losses from the excitation winding and, at the same time, the additional power sources, yields to an increased machine efficiency;
- a higher value of the electromagnetic torque reported to the volume unit is achieved and higher dynamic performances are obtained compared to the electromagnetic excitation synchronous machines (greater magnetic induction in the air gap);
- a simplified maintenance, an increased reliability and a relatively low-cost price for some machine types are achieved.

The PMSMs can operate at rated load at unitary or even capacitive power factor, being characterized by superior power factor and efficiency compared to other AC motors. By associating them with static converters, these machines are used in high-speed variable speed drives with a maximum speed ratio of more than 1:10000 and an acceleration of more than 20,000 rad/s<sup>2</sup> [4].

From a constructive point of view, the PMSMs' stator is similar to that of asynchronous machines having in the slots a bi, three or poly-phase winding system. For low power



machines, windings can be concentrated and, depending on the chosen construction solution, they can be arranged in various geometries.

The construction of the machine's rotor, using permanent magnets, presents two solutions:

- cylindrical rotor and radial air gap;
- disc rotor and axial air gap.

The PMSMs can present different rotor configurations, yielding to machines characterized only by an excitation electromagnetic torque (the fundamental torque), at which the longitudinal and transversal synchronous inductances are equal  $L_d = L_q$  (machines with prominent poles) or to machines with a reluctance torque (reactive), at which  $L_d \neq L_q$  (machines with hidden poles).

From the construction point of view, the rotor has two parts: the permanent magnets, arranged in a certain geometry, creating a certain number of poles and the rotor cage.

The permanent magnets must generate the machine exciting magnetic field and must ensure the stability of this field in the case of disturbing action of various factors: demagnetization fluxes, shocks, temperatures, etc.

The rotor cage must perform the following functions:

- to ensure an asynchronous starting when supplying the machine at a constant frequency;
- to damp certain rotor oscillations when disturbances occur;
- to ensure the shielding of permanent magnets from the occurrence of demagnetizing transient magnetic fields.

If the PMSMs are powered through inverters, the starting cage is generally not necessary, because the source frequency is synchronized with the rotor frequency. The presence of the cage in this situation might be imposed by the need of the other performing functions.

For the development of the mathematical model of these machines, the following simplifying hypotheses are adopted [5]:

- the case of the synchronous machine will be treated with permanent magnets located in the rotor (with prominent poles), IPMSM (interior permanent magnet synchronous motor). The mathematical model of the machine with full poles, SPMSM, is considered to be a particular case of this model [6];
- it is considered that the stator windings have a sinusoidal distribution, i.e. the number of notches on the pole and phase  $q \geq 2$ . In this situation, the magnetic field in the machine's interior has a sinusoidal spatial distribution. It is also assumed that the stator windings are identical, having a spatial phase gap of  $120^\circ$  between them [7];

- the temperature variation of the stator resistance and the permanent magnet is not taken into account [8];
- the effect of the magnetic saturation, which introduces harmonics into the flux, is neglected [9];
- the case of permanent magnets (AlNiCo or Ferrites) is considered. In this case, the machines require the presence of a damping cage and shielding [10].

In what follows, different mathematical models for the permanent magnet synchronous motors will be presented. Then, the scalar control methods will be stated. They are divided into two main categories: the open-loop and the closed-loop ones. The difference between the two categories is the fact that, for the closed-loop control case, it is necessary for the speed to be measured and used as a feedback in the control. The main concerns regarding the V/f control are the system instability and the speed oscillations. In order to remove them and, thus, to improve the V/f control, one or two stabilizing loops can be added [11] ÷ [17].

The simulation and experimental results were obtained by the research team at the Department of Electrical Engineering of Politehnica University of Timișoara [18] ÷ [23].

## 5.2 General equations of PMSM. The dynamic model

### 5.2.1 The model in phases coordinates

For the development of the mathematical model in the stator reference phases coordinates, an IPMSM, represented in Fig. 5.1, is considered. The magnetic axes of the stator phases  $A, B, C$  are denoted by  $A_m, B_m, C_m$  and the rotor is considered as a magnetic barrier so that two different magnetic circuits can be considered after the two perpendicular axes denoted by  $d$  and  $q$ , respectively. The equations of the stator voltages are:

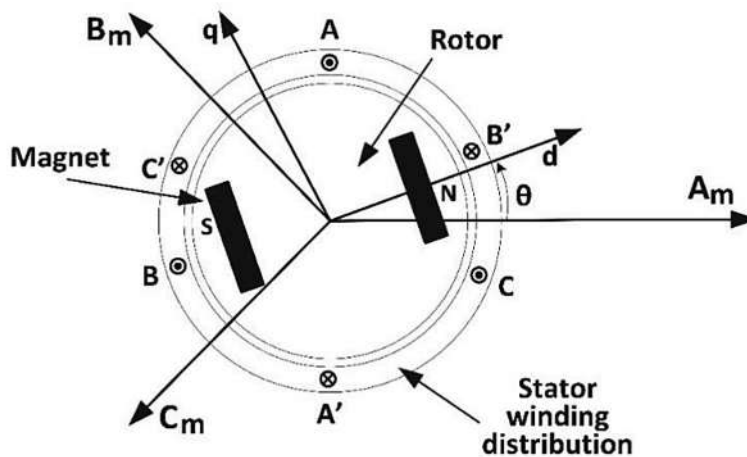


Fig. 5.1 The PMSM model in phases coordinates.

$$\begin{aligned}
u_A &= R_s i_A + \frac{d\psi_A}{dt}, \\
u_B &= R_s i_B + \frac{d\psi_B}{dt}, \\
u_C &= R_s i_C + \frac{d\psi_C}{dt}.
\end{aligned}
\tag{5.1}$$

where:  $u_A, u_B, u_C$  - represent the stator phase voltages,  $i_A, i_B, i_C$  - are the stator phase currents,  $R_s$  - is the stator phase resistance (considered  $R_A = R_B = R_C = R_s$ ) and  $\psi_A, \psi_B, \psi_C$  - are the total fluxes of the stator phases.

The magnetic fluxes corresponding to the three magnetic axes can be determined considering the connection between the stator currents and the flux generated by the permanent magnet in the rotor as follows:

$$\begin{aligned}
\psi_A &= L_{AA}i_A + L_{AB}i_B + L_{AC}i_C + \psi_E \cos\theta, \\
\psi_B &= L_{BA}i_A + L_{BB}i_B + L_{BC}i_C + \psi_E \cos\left(\theta - \frac{2\pi}{3}\right), \\
\psi_C &= L_{CA}i_A + L_{CB}i_B + L_{CC}i_C + \psi_E \cos\left(\theta + \frac{2\pi}{3}\right).
\end{aligned}
\tag{5.2}$$

where:  $L_{AA}, L_{BB}, L_{CC}$  - are the inductances of the stator (armature) phases;  $L_{AB}, L_{AC}, L_{BC}, L_{BA}, L_{CA}, L_{CB}$  - are the mutual inductances between two stator phases;  $\psi_E$  - represents the amplitude of the permanent magnet flux seen from the stator referencer;  $\theta$  - the electric angle between the rotor and the stator phase A.

In case the magnetic saturation is neglected, between the inductances with permuted indices, the following equality is valid:

$$L_{AB} = L_{BA}; \quad L_{AC} = L_{CA}; \quad L_{BC} = L_{CB}, \tag{5.3}$$

As for the determination of the permanent magnet synchronous machine's mathematical model, an IPMSM (interior permanent magnet synchronous motor) was considered, i.e. a machine with prominent poles, its air gap is not uniform and, thus, its own and mutual inductances are dependent on the rotor position and then, the following relationships can be written (it is considered that the three phases of the machine are identical):

$$\begin{aligned}
L_{AA} &= L_{\sigma s} + L_{hs0} + L_{hsp} \cos 2\theta, \\
L_{BB} &= L_{\sigma s} + L_{hs0} + L_{hsp} \cos\left(2\theta + \frac{2\pi}{3}\right), \\
L_{CC} &= L_{\sigma s} + L_{hs0} + L_{hsp} \cos\left(2\theta - \frac{2\pi}{3}\right), \\
L_{AB} &= -\frac{1}{2}L_{hs0} + L_{hsp} \cos\left(2\theta - \frac{2\pi}{3}\right), \\
L_{AC} &= -\frac{1}{2}L_{hs0} + L_{hsp} \cos\left(2\theta + \frac{2\pi}{3}\right), \\
L_{CA} &= -\frac{1}{2}L_{hs0} + L_{hsp} \cos\left(2\theta + \frac{2\pi}{3}\right), \\
L_{BC} &= -\frac{1}{2}L_{hs0} + L_{hsp} \cos 2\theta.
\end{aligned} \tag{5.4}$$

- is the dispersion inductance and  $L_{hs0}$  and  $L_{hsp}$  – are the inherent inductances These can also be calculated according to the geometrical dimensions of the machine as follows:

$$\begin{aligned}
L_{hs0} &= \frac{1}{2}L_o \left( \frac{1}{g_{\min}} + \frac{1}{g_{\max}} \right) = \frac{1}{4}L_o \left( \frac{1}{g_{\min}} - \frac{1}{g_{\max}} \right); \\
L_o &= \frac{1}{8} \mu_0 N_s^2 \pi d l.
\end{aligned} \tag{5.5}$$

where:  $\mu_0$  - is the magnetic permeability of the air,  $d$  - is the inside diameter of the machine,  $l$  - represents the stator length,  $N_s$  - is the number of stator windings,  $g_{\min}$  - is the minimum value of the machine's air gap, while  $g_{\max}$  represents its maximum value.

The IPMSM voltages equation in the phases coordinates can also be written in the matrix form:

$$\left[ u_{ABC} \right] = \left[ R_{ABC} \right] \cdot \left[ i_{ABC} \right] + \frac{d}{dt} \left[ \psi_{ABC} \right], \tag{5.6}$$

where, the magnetic flux is:

$$\left[ \psi_{ABC} \right] = \left[ L_{ABC} \right] \left[ i_{ABC} \right] + \left[ \psi_E \right] \left[ \cos_{ABC} \right]. \tag{5.7}$$

In the above relationships:

$$\begin{aligned} \begin{bmatrix} u_{ABC} \end{bmatrix} &= \begin{bmatrix} u_A \\ u_B \\ u_C \end{bmatrix}; \begin{bmatrix} i_{ABC} \end{bmatrix} = \begin{bmatrix} i_A \\ i_B \\ i_C \end{bmatrix}; \begin{bmatrix} \psi_{ABC} \end{bmatrix} = \begin{bmatrix} \psi_A \\ \psi_B \\ \psi_C \end{bmatrix}; \begin{bmatrix} \cos_{ABC} \end{bmatrix} = \begin{bmatrix} \cos \theta \\ \cos \left( \theta - \frac{2\pi}{3} \right) \\ \cos \left( \theta + \frac{2\pi}{3} \right) \end{bmatrix}, \\ L_{ABC} &= \begin{bmatrix} L_{\sigma s} + L_{hs0} + L_{hsp} \cos(2\theta) & -\frac{1}{2}L_{hs0} + L_{hsp} \cos(2\theta - \frac{2\pi}{3}) & -\frac{1}{2}L_{hs0} + L_{hsp} \cos(2\theta + \frac{2\pi}{3}) \\ -\frac{1}{2}L_{hs0} + L_{hsp} \cos(2\theta - \frac{2\pi}{3}) & L_{\sigma s} + L_{hs0} + L_{hsp} \cos(2\theta + \frac{2\pi}{3}) & -\frac{1}{2}L_{hs0} + L_{hsp} \cos(2\theta) \\ -\frac{1}{2}L_{hs0} + L_{hsp} \cos(2\theta + \frac{2\pi}{3}) & -\frac{1}{2}L_{hs0} + L_{hsp} \cos(2\theta) & L_{\sigma s} + L_{hs0} + L_{hsp} \cos(2\theta - \frac{2\pi}{3}) \end{bmatrix} \quad (5.8) \end{aligned}$$

### 5.2.2 The model of spatial phasors

A simple mathematical model of the PMSM, easy to manipulate algebraically and frequently used for the analysis of the control systems, is represented by the spatial phasors model. Using this model, the machine's instantaneous values of the currents, voltages and fluxes can be represented by the spatial phasor. Firstly, a fixed orthogonal system relative to the stator that has as its real axis the axis of phase A is considered. In these conditions, the following relationships for the spatial phasors of the stator voltages, currents, and magnetic fluxes can be written in the phases' coordinates:

$$\begin{bmatrix} \underline{u}_{ABC} \\ \underline{i}_{ABC} \\ \underline{\psi}_{ABC} \end{bmatrix} = \frac{2}{3} \begin{bmatrix} u_A + a u_B + a^2 u_C \\ i_A + a i_B + a^2 i_C \\ \psi_A + a \psi_B + a^2 \psi_C \end{bmatrix}, \quad (5.9)$$

where:

$$\begin{aligned} a &= e^{j\frac{2\pi}{3}} = \cos\left(\frac{2\pi}{3}\right) + j \sin\left(\frac{2\pi}{3}\right); \\ a^2 &= e^{j\frac{4\pi}{3}} = \cos\left(\frac{4\pi}{3}\right) + j \sin\left(\frac{4\pi}{3}\right). \end{aligned} \quad (5.10)$$

Thus, the following mathematical relationships can be written:

$$ae^{j\theta} = \cos\left(\theta + \frac{2\pi}{3}\right) + j \sin\left(\theta + \frac{2\pi}{3}\right), \quad (5.11)$$

$$a^2e^{j\theta} = \cos\left(\theta + \frac{4\pi}{3}\right) + j \sin\left(\theta + \frac{4\pi}{3}\right).$$

The conjugate of the voltage, current and magnetic flux phasors in the phases coordinates are expressed as:

$$\begin{bmatrix} \underline{u}_{ABC}^* \\ \underline{i}_{ABC}^* \\ \underline{\psi}_{ABC}^* \end{bmatrix} = \frac{2}{3} \begin{bmatrix} u_A + a^2u_B + au_C \\ i_A + a^2i_B + ai_C \\ \psi_A + a^2\psi_B + a\psi_C \end{bmatrix} \quad (5.12)$$

Considering the relationships (5.7), (5.8) and (5.9), the magnetic flux phasor can be written as:

$$\underline{\psi}_{ABC} = \left(L_{\sigma s} + \frac{3}{2}L_{hs0}\right)\underline{i}_{ABC} + \frac{3}{2}L_{hsp}\underline{i}_{ABC}^*e^{j2\theta} + \underline{\psi}_E e^{j\theta}. \quad (5.13)$$

From the relationships (5.1) and (5.10), the equation of the stator voltages phasors results:

$$\underline{u}_{ABC} = R_s \underline{i}_{ABC} + \frac{d\underline{\psi}_{ABC}}{dt}. \quad (5.14)$$

The relationships (5.13) and (5.14) represent the IPMSM mathematical model written using the spatial phasors in the phases' coordinates.

**Note:** The coefficient used in the relationships (5.9) guarantees that the amplitude of the spatial phasor is equal to the amplitude of the symmetrical three-phase model (see [5]).

### 5.2.3 The generalised orthogonal mathematical model of the machine

The IPMSM mathematical model in the phases' coordinates has the disadvantage of the dependence of the magnetic flux on the rotor position. The implementation of such a model for a control system point of view is quite difficult, so that the existence of a machine mathematical model in an orthogonal reference system that rotates towards the stator is imposed. For its implementation, the machine mathematical model in the phases' coordinates, presented in the previous paragraph, represents the starting point.

Fig. 5.2 shows both the three-phase stator system  $A_m, B_m, C_m$  and the orthogonal  $xy$  system, which rotates at an arbitrary angular electrical speed  $\omega_{xy}$ . There are two particular cases of the generalised orthogonal model, as presented below:

- the situation in which the rotation angular speed of the orthogonal system  $xy$  is  $\omega_{xy} = 0$  ( $\theta_x = 0$ ), the orthogonal system being noted with  $a\beta$ ;
- the situation in which the orthogonal system  $xy$  rotates in solidarity with the machine rotor  $\omega_{xy} = \omega_r$  ( $\theta_x = \theta$ ), the orthogonal system being noted with  $dq$ .

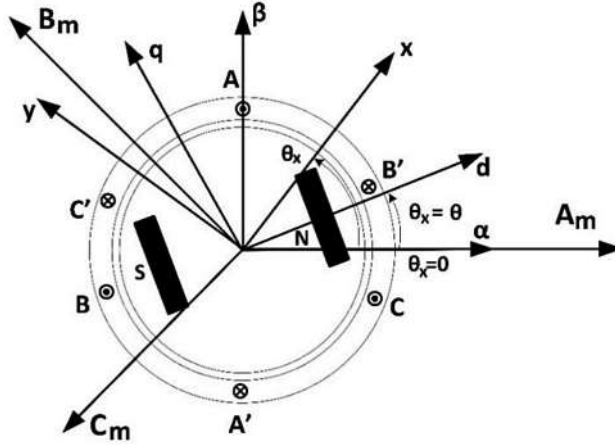


Fig. 5.2 The three-phase stator axes  $A_m, B_m, C_m$ , the orthogonal  $xy$  axes, the orthogonal  $dq$  axes and the orthogonal  $a\beta$  axes, respectively.

If it is wished to represent the quantities of the three axes  $A_m, B_m, C_m$  into a generalised orthogonal system  $xy$ , which rotates with an arbitrary angular speed, the following relationships can be written:

$$d_x = \frac{2}{3} \left( a_s \cos(-\theta_x) + b_s \cos\left(-\theta_x + \frac{2\pi}{3}\right) + c_s \cos\left(-\theta_x + \frac{4\pi}{3}\right) \right), \quad (5.15)$$

$$d_y = \frac{2}{3} \left( a_s \sin(-\theta_x) + b_s \sin\left(-\theta_x + \frac{2\pi}{3}\right) + c_s \sin\left(-\theta_x + \frac{4\pi}{3}\right) \right). \quad (5.16)$$

In the above relationships, the sign  $(-\theta_x)$  appears because the magnetic axis  $A_m$  is behind the  $x$ -axis of the orthogonal system. The quantities  $a_s, b_s, c_s$  can be any of the three-phase stator quantities (voltage, current or flux).

To achieve the complete transformation from the three-phase model into the orthogonal model  $xy$ , a homopolar component given by the below relationship is defined:

$$d_0 = \frac{1}{3} (a_s + b_s + c_s). \quad (5.17)$$

From (5.15) and (5.16) relationships, the spatial phasor “ $f$ ” in the generalised coordinates can be written as:

$$\underline{f}_{-xy} = d_x + jd_y = \frac{2}{3} \left( a_s e^{-j\theta x} + b_s e^{j\left(-\theta x + \frac{2\pi}{3}\right)} + c_s e^{j\left(-\theta x + \frac{4\pi}{3}\right)} \right). \quad (5.18)$$

The above relationship can be rewritten by taking into account the relationship (5.10), as being:

$$\underline{f}_{-xy} = \frac{2}{3} e^{-j\theta x} (a_s + ab_s + a^2 c_s) = e^{-j\theta x} \underline{f}_{ABC}. \quad (5.19)$$

The relation (5.19) describes the transformation of the spatial phasors into a generalised rotational system.

Multiplying the relationship (5.24) by  $e^{j\theta x}$ , it results that:

$$\underline{u}_{ABC} e^{-j\theta x} = R_s \underline{i}_{ABC} e^{-j\theta x} + e^{-j\theta x} \frac{d\psi_{ABC}}{dt}. \quad (5.20)$$

or

$$\underline{u}_{ABC} e^{-j\theta x} = R_s \underline{i}_{ABC} e^{-j\theta x} + \frac{d(\psi_{ABC} e^{-j\theta x})}{dt} + j\omega_{xy} \psi_{ABC} e^{-j\theta x}. \quad (5.21)$$

Considering the relationships (5.19) and (5.21), the machine’s volt-amp equations in the generalised orthogonal model can be written as being:

$$\underline{u}_{xy} = R_s \underline{i}_{xy} + \frac{d\psi_{xy}}{dt} + j\omega_{xy} \psi_{xy}. \quad (5.22)$$

The magnetic flux in the generalised orthogonal model is written as being:

$$\underline{\psi}_{xy} = e^{-j\theta x} \underline{\psi}_{ABC} = \left( L_{\sigma s} + \frac{3}{2} L_{hs0} \right) \underline{i}_{ABC} e^{-j\theta x} + \frac{3}{2} L_{hsp} \underline{i}_{ABC}^* e^{j2(\theta-\theta x)} + \psi_E e^{j(\theta-\theta x)}. \quad (5.23)$$

Therefore, the below relationship gives the magnetic flux in the generalised coordinates:

$$\underline{\psi}_{xy} = \left( L_{\sigma s} + \frac{3}{2} L_{hs0} \right) \underline{i}_{xy} + \frac{3}{2} L_{hsp} \underline{i}_{xy}^* e^{j2(\theta-\theta x)} + \psi_E e^{j(\theta-\theta x)}. \quad (5.24)$$

In complex, the relationships of the voltage, the current and the flux, respectively, in the generalised orthogonal model can be written as:



$$\underline{u}_{xy} = u_x + j u_y, \quad (5.25)$$

$$\underline{i}_{xy} = i_x + j i_y, \quad (5.26)$$

$$\underline{\psi}_{xy} = \psi_x + j \psi_y. \quad (5.27)$$

In the above relationships  $u_x, i_x, \psi_x$  represent the stator voltage, the stator current and the magnetic flux along the  $x$  – axis, while  $u_y, i_y, \psi_y$  represent the stator voltage, the stator current, and the magnetic flux along the  $y$  – axis, respectively.

Thus, the IPMSM volt-ampere equations on the two axes, the real and the imaginary one, in the generalised coordinates system, are given by the relationships:

$$u_x = R_s i_x + \frac{d\psi_x}{dt} - \omega_{xy} \psi_y, \quad (5.28)$$

$$u_y = R_s i_y + \frac{d\psi_y}{dt} + \omega_{xy} \psi_x. \quad (5.29)$$

The magnetic flux along the real and the imaginary axes, in the generalised coordinates system, can be written considering the relationship (5.22):

$$\begin{aligned} \psi_x = & \left( L_{\sigma s} + \frac{3}{2} (L_{hs0} + L_{hsp} \cos(2(\theta - \theta_x))) \right) i_x \\ & + \frac{3}{2} L_{hsp} \sin(2(\theta - \theta_x)) i_y + \psi_E \cos(\theta - \theta_x) \end{aligned} \quad (5.30)$$

$$\begin{aligned} \psi_y = & \left( L_{\sigma s} + \frac{3}{2} (L_{hs0} - L_{hsp} \cos(2(\theta - \theta_x))) \right) i_y \\ & + \frac{3}{2} L_{hsp} \sin(2(\theta - \theta_x)) i_x + \psi_E \sin(\theta - \theta_x) \end{aligned} \quad (5.31)$$

Also, the relationships (5.15), (5.16) and (5.17) can be written in the matrix form:

$$\begin{pmatrix} d_x \\ d_y \\ d_0 \end{pmatrix} = \frac{2}{3} \begin{pmatrix} \cos(-\theta_x) & \cos\left(-\theta_x + \frac{2\pi}{3}\right) & \cos\left(-\theta_x + \frac{4\pi}{3}\right) \\ \sin(-\theta_x) & \sin\left(-\theta_x + \frac{2\pi}{3}\right) & \sin\left(-\theta_x + \frac{4\pi}{3}\right) \\ \frac{1}{2} & \frac{1}{2} & \frac{1}{2} \end{pmatrix} \begin{pmatrix} a_s \\ b_s \\ c_s \end{pmatrix}, \quad (5.32)$$

respectively:

$$\begin{pmatrix} a_s \\ b_s \\ c_s \end{pmatrix} = \frac{2}{3} \begin{pmatrix} \cos(-\theta_x) & \sin(-\theta_x) & \frac{1}{2} \\ \cos\left(-\theta_x + \frac{2\pi}{3}\right) & \sin\left(-\theta_x + \frac{2\pi}{3}\right) & \frac{1}{2} \\ \cos\left(-\theta_x + \frac{4\pi}{3}\right) & \sin\left(-\theta_x + \frac{4\pi}{3}\right) & \frac{1}{2} \end{pmatrix} \begin{pmatrix} d_x \\ d_y \\ d_0 \end{pmatrix}. \quad (5.33)$$

The generalised mathematical model of the machine being given, the complex instantaneous apparent power can be written as:

$$\underline{s} = \frac{3}{2} \underline{u}_{xy} \underline{i}_{xy}^* = \frac{3}{2} (u_x i_x + u_y i_y) + j \frac{3}{2} (u_y i_x - u_x i_y) = p + jq. \quad (5.34)$$

From (5.34), the relationships for the instantaneous active power  $p$  and the instantaneous reactive power  $q$ , respectively:

$$p = \frac{3}{2} (u_x i_x + u_y i_y), \quad (5.35)$$

$$q = \frac{3}{2} (u_y i_x - u_x i_y). \quad (5.36)$$

### 5.2.3.1 The orthogonal mathematical model in the stator reference frame

From Fig. 5.2, presented in the previous paragraph, it is observed that if the rotation angular speed of the orthogonal system  $xy$  is  $\omega_{xy} = 0$  ( $\theta_x = 0$ ), the particular case of the orthogonal system in the stator reference frame, noted with  $\alpha\beta$ , is obtained. In this case, the  $\alpha$ -axis of the orthogonal system coincides with the magnetic  $A_m$ -axis of the three-phase stator system.

Under these conditions, the volt-ampere equation (5.22) can be written in the matrix form, in the stator reference frame, as follows:

$$\underline{u}_{\alpha\beta} = R_s \underline{i}_{\alpha\beta} + \frac{d\underline{\psi}_{\alpha\beta}}{dt}, \quad (5.37)$$

where (see the relation (5.24)):

$$\underline{\psi}_{\alpha\beta} = \left( L_{\sigma s} + \frac{3}{2} L_{hs0} \right) \underline{i}_{\alpha\beta} + \frac{3}{2} L_{hsp} \underline{i}_{\alpha\beta}^* e^{j2\theta} + \psi_E e^{j\theta}. \quad (5.38)$$

Next, the equations for voltage, current or flux relationships in the stator reference frame can be written as being:

$$\underline{u}_{\alpha\beta} = \underline{u}_\alpha + j\underline{u}_\beta, \quad (5.39)$$

$$\underline{i}_{\alpha\beta} = \underline{i}_\alpha + j\underline{i}_\beta, \quad (5.40)$$

$$\underline{\psi}_{\alpha\beta} = \underline{\psi}_\alpha + j\underline{\psi}_\beta. \quad (5.41)$$

Under these conditions, the machine volt-ampere equations, in stator reference frame, along the two  $\alpha$  and  $\beta$  - axes (the real and the imaginary axes), are given by the relationships (see (5.28) and (5.29)):

$$u_\alpha = R_s i_\alpha + \frac{d\psi_\alpha}{dt}, \quad (5.42)$$

$$u_\beta = R_s i_\beta + \frac{d\psi_\beta}{dt}. \quad (5.43)$$

The magnetic fluxes along the real and imaginary axes can be written considering the relationships (5.29) and (5.30) in the form:

$$\psi_\alpha = \left( L_{\sigma s} + \frac{3}{2} (L_{hs0} + L_{hsp} \cos(2\theta)) \right) i_\alpha + \frac{3}{2} L_{hsp} \sin(2\theta) i_\beta + \psi_E \cos(\theta), \quad (5.44)$$

$$\psi_\beta = \left( L_{\sigma s} + \frac{3}{2} (L_{hs0} - L_{hsp} \cos(2\theta)) \right) i_\beta + \frac{3}{2} L_{hsp} \sin(2\theta) i_\alpha + \psi_E \sin(\theta). \quad (5.45)$$

In the case of the orthogonal model in the stator reference frame,  $\omega_{xy} = 0$  ( $\theta_x = 0$ ), the relationships (5.32), (5.33) are written as being:

$$\begin{pmatrix} d_\alpha \\ d_\beta \\ d_0 \end{pmatrix} = \frac{2}{3} \begin{pmatrix} 1 & -\frac{1}{2} & -\frac{1}{2} \\ 0 & \frac{\sqrt{3}}{2} & -\frac{\sqrt{3}}{2} \\ \frac{1}{2} & \frac{1}{2} & \frac{1}{2} \end{pmatrix} \begin{pmatrix} a_s \\ b_s \\ c_s \end{pmatrix}, \quad (5.46)$$

$$\begin{pmatrix} a_s \\ b_s \\ c_s \end{pmatrix} = \frac{2}{3} \begin{pmatrix} 1 & 0 & \frac{1}{2} \\ -\frac{1}{2} & \frac{\sqrt{3}}{2} & \frac{1}{2} \\ -\frac{1}{2} & -\frac{\sqrt{3}}{2} & \frac{1}{2} \end{pmatrix} \begin{pmatrix} d_\alpha \\ d_\beta \\ d_0 \end{pmatrix} \quad (5.47)$$

The matrix:

$$[T_{\alpha\beta 0}] = \frac{2}{3} \begin{pmatrix} 1 & -\frac{1}{2} & -\frac{1}{2} \\ 0 & \frac{\sqrt{3}}{2} & -\frac{\sqrt{3}}{2} \\ \frac{1}{2} & \frac{1}{2} & \frac{1}{2} \end{pmatrix}; [T_{\alpha\beta 0}]^{-1} = \frac{2}{3} \begin{pmatrix} 1 & 0 & \frac{1}{2} \\ -\frac{1}{2} & \frac{\sqrt{3}}{2} & \frac{1}{2} \\ -\frac{1}{2} & -\frac{\sqrt{3}}{2} & \frac{1}{2} \end{pmatrix}. \quad (5.48)$$

is also known as **the direct Clarke transformation** or **the inverse Clarke transformation**.

With its help, the transition from the three-phase model in the stator phases' coordinates to the orthogonal model in the machine stator reference frame is possible, and the inverse transition from the orthogonal model in the stator reference frame to the three-phase model in the stator phases' coordinates, respectively, is also possible.

In the situation of the orthogonal mathematical model in the stator reference frame  $\alpha\beta$  and taking into account the relationships (5.44), (5.45), (5.46), the instantaneous apparent power, the instantaneous active power and the instantaneous reactive power, respectively, are written as follows:

$$\underline{s}_{\alpha\beta} = \frac{3}{2} \underline{u}_{\alpha\beta} \underline{i}_{\alpha\beta}^* = \frac{3}{2} (u_\alpha i_\alpha + u_\beta i_\beta) + j \frac{3}{2} (u_\beta i_\alpha - u_\alpha i_\beta) = p_{\alpha\beta} + j q_{\alpha\beta}, \quad (5.49)$$

$$p_{\alpha\beta} = \frac{3}{2} (u_\alpha i_\alpha + u_\beta i_\beta), \quad (5.50)$$

$$q_{\alpha\beta} = \frac{3}{2} (u_\beta i_\alpha - u_\alpha i_\beta). \quad (5.51)$$

Considering the relationships (5.42) and (5.43), the expression of the instantaneous active power can be written as being:

$$p_{\alpha\beta} = \frac{3}{2} \left( R_s (i_\alpha^2 + i_\beta^2) + i_\alpha \frac{d\psi_\alpha}{dt} + i_\beta \frac{d\psi_\beta}{dt} \right). \quad (5.52)$$

By substituting the relationships (5.44) and (5.45) in the relationship (5.52), it results that:

$$\begin{aligned}
 p_{\alpha\beta} = & \frac{3}{2} R_s \left( i_{\alpha}^2 + i_{\beta}^2 \right) + \frac{3}{2} \left[ \left( L_{\sigma s} + \frac{3}{2} \left( L_{hs0} + L_{hsp} \cos(2\theta) \right) \right) i_{\alpha} \left( \frac{di_{\alpha}}{dt} + \omega_r i_{\beta} \right) \right. \\
 & + \frac{3}{2} L_{hsp} \sin(2\theta) i_{\alpha} \left( \frac{di_{\beta}}{dt} - \omega_r i_{\alpha} \right) + \left. \left( L_{\sigma s} + \frac{3}{2} \left( L_{hs0} - L_{hsp} \cos(2\theta) \right) \right) \right. \\
 & \left. i_{\beta} \left( \frac{di_{\beta}}{dt} - \omega_r i_{\alpha} \right) + \frac{3}{2} L_{hsp} \sin(2\theta) i_{\beta} \left( \frac{di_{\alpha}}{dt} + \omega_r i_{\beta} \right) \right] + \frac{3}{2} \omega_r \left( \psi_{\alpha} i_{\beta} - \psi_{\beta} i_{\alpha} \right)
 \end{aligned} \quad (5.53)$$

Analysing the relationship (5.53), the following can be determined:

- **the copper losses,  $p_{\alpha\beta Cu}$ :**

$$P_{\alpha\beta Cu} = \frac{3}{2} R_s \left( i_{\alpha}^2 + i_{\beta}^2 \right). \quad (5.54)$$

- **the electromagnetic power,  $p_{\alpha\beta elm}$ :**

$$P_{\alpha\beta elm} = \frac{3}{2} \omega_r \left( \psi_s i_{\beta} - \psi_{\beta} i_{\alpha} \right). \quad (5.55)$$

- **the increase of the stored magnetic power,  $p_{\alpha\beta m}$ :**

$$\begin{aligned}
 p_{\alpha\beta m} = & \frac{3}{2} \left[ \left( L_{\sigma s} + \frac{3}{2} \left( L_{hs0} + L_{hsp} \cos(2\theta) \right) \right) i_{\alpha} \left( \frac{di_{\alpha}}{dt} + \omega_r i_{\beta} \right) \right. \\
 & + \frac{3}{2} L_{hsp} \sin(2\theta) i_{\alpha} \left( \frac{di_{\beta}}{dt} - \omega_r i_{\alpha} \right) \\
 & + \left( L_{\sigma s} + \frac{3}{2} \left( L_{hs0} - L_{hsp} \cos(2\theta) \right) \right) i_{\beta} \left( \frac{di_{\beta}}{dt} - \omega_r i_{\alpha} \right) \\
 & \left. + \frac{3}{2} L_{hsp} \sin(2\theta) i_{\beta} \left( \frac{di_{\alpha}}{dt} + \omega_r i_{\beta} \right) \right].
 \end{aligned} \quad (5.56)$$

From the electromagnetic power equation, the expression of the electromagnetic torque in the machine stator reference frame can be determined as follows:

$$m_{\alpha\beta} = \frac{p_{elm} p}{\omega_r} = \frac{3}{2} p \left( \psi_{\alpha} i_{\beta} - \psi_{\beta} i_{\alpha} \right). \quad (5.57)$$

where:  $p$  - represents the number of the machine pole pairs.

### 5.2.3.2 The orthogonal mathematical model in the rotor reference frame

Another particular case can be obtained from the generalised orthogonal mathematical model, in which the orthogonal system rotates solidarity with the machine rotor  $\theta_x = \theta$ ,  $\omega_{xy} = \omega_{xr}$  (see Fig. 5.2). In this case, the  $xy$ - axes of the generalised orthogonal system are noted by  $dq$ .

For this particular case, the volt-ampere equation is written as follows:

$$\underline{u}_{dq} = R_s \underline{i}_{dq} + \frac{d\underline{\psi}_{dq}}{dt} + j\omega_r \underline{\psi}_{dq}. \quad (5.58)$$

The magnetic flux in the orthogonal model in the rotor reference frame is:

$$\underline{\psi}_{dq} = \left( L_{\sigma s} + \frac{3}{2} L_{hs0} \right) \underline{i}_{dq} + \frac{3}{2} L_{hsp} \underline{i}_{dq}^* e^{j0} + \underline{\psi}_E e^{j0}. \quad (5.59)$$

The relationships for the voltage, current, and flux phases, respectively, in the rotor reference frame  $dq$ , are as follows:

$$\underline{u}_{dq} = u_d + j u_q, \quad (5.60)$$

$$\underline{i}_{dq} = i_d + j i_q, \quad (5.61)$$

$$\underline{\psi}_{dq} = \psi_d + j \psi_q. \quad (5.62)$$

Thus, the machine volt-ampere equations along the two axes (real and imaginary) in the rotor reference frame  $dq$ , are given by the relationships:

$$u_d = R_s i_d + \frac{d\psi_d}{dt} - \omega_r \psi_q, \quad (5.63)$$

$$u_q = R_s i_q + \frac{d\psi_q}{dt} + \omega_r \psi_d. \quad (5.64)$$

Similarly, the magnetic fluxes along the real and imaginary axes can be written considering the relationship (5.62), as being:

$$\psi_d = \left( L_{\sigma s} + \frac{3}{2} (L_{hs0} + L_{hsp}) \right) i_d + \psi_E, \quad (5.65)$$

$$\psi_q = \left( L_{\sigma s} + \frac{3}{2} (L_{hs0} - L_{hsp}) \right) i_q. \quad (5.66)$$

In the case of the IPMSM model in the rotor reference frame, the relationships (5.32) and (5.33) can be rewritten as:

$$\begin{pmatrix} d_d \\ d_q \\ d_0 \end{pmatrix} = \frac{2}{3} \begin{pmatrix} \cos(-\theta) & \cos\left(-\theta + \frac{2\pi}{3}\right) & \cos\left(-\theta + \frac{4\pi}{3}\right) \\ \sin(-\theta) & \sin\left(-\theta + \frac{2\pi}{3}\right) & \sin\left(-\theta + \frac{4\pi}{3}\right) \\ \frac{1}{2} & \frac{1}{2} & \frac{1}{2} \end{pmatrix} \begin{pmatrix} a_s \\ b_s \\ c_s \end{pmatrix}, \quad (5.67)$$

respectively:

$$\begin{pmatrix} a_s \\ b_s \\ c_s \end{pmatrix} = \frac{2}{3} \begin{pmatrix} \cos(-\theta) & \sin(-\theta) & \frac{1}{2} \\ \cos\left(-\theta + \frac{2\pi}{3}\right) & \sin\left(-\theta + \frac{2\pi}{3}\right) & \frac{1}{2} \\ \cos\left(-\theta + \frac{4\pi}{3}\right) & \sin\left(-\theta + \frac{4\pi}{3}\right) & \frac{1}{2} \end{pmatrix} \begin{pmatrix} d_d \\ d_q \\ d_0 \end{pmatrix}. \quad (5.68)$$

It is noted that:

$$[T_{dq0}] = \frac{2}{3} \begin{pmatrix} \cos(-\theta) & \cos\left(-\theta + \frac{2\pi}{3}\right) & \cos\left(-\theta + \frac{4\pi}{3}\right) \\ \sin(-\theta) & \sin\left(-\theta + \frac{2\pi}{3}\right) & \sin\left(-\theta + \frac{4\pi}{3}\right) \\ \frac{1}{2} & \frac{1}{2} & \frac{1}{2} \end{pmatrix}. \quad (5.69)$$

$$[T_{dq0}]^{-1} = \frac{2}{3} \begin{pmatrix} \cos(-\theta) & \sin(-\theta) & \frac{1}{2} \\ \cos\left(-\theta + \frac{2\pi}{3}\right) & \sin\left(-\theta + \frac{2\pi}{3}\right) & \frac{1}{2} \\ \cos\left(-\theta + \frac{4\pi}{3}\right) & \sin\left(-\theta + \frac{4\pi}{3}\right) & \frac{1}{2} \end{pmatrix}. \quad (5.70)$$

The matrices from the above relationships are known in the specialised literature as **the direct and the inverse Park transformations**. By using them, the transition from the three-phase model in the phases' coordinates to the orthogonal model in the rotor reference frame or the inverse transition from the orthogonal model in the rotor reference frame to the three-phase model in the phases' coordinates (the natural model), respectively, can be achieved.

If noted:

$$L_{ad} = \frac{3}{2}(L_{hs0} + L_{hsp}); L_{aq} = \frac{3}{2}(L_{hs0} - L_{hsp}). \quad (5.71)$$

the inductances according to the  $d$ -axis and  $q$ -axis, respectively, in the rotor reference frame, can be written as follows:

$$L_d = L_{\sigma s} + L_{ad}; L_q = L_{\sigma s} + L_{aq}. \quad (5.72)$$

In this case, the relationships (5.65) and (5.66), can be written as follows:

$$\psi_d = L_d i_d + \psi_E, \quad (5.73)$$

$$\psi_q = L_q i_q. \quad (5.74)$$

Considering the relationships (5.73) and (5.74), the machine volt-ampere equations in the rotor reference frame become as follows:

$$u_d = R_s i_d + L_d \frac{di_d}{dt} - \omega_r L_q i_q, \quad (5.75)$$

$$u_q = R_s i_q + L_q \frac{di_q}{dt} + \omega_r (L_d i_d + \psi_E). \quad (5.76)$$

or

$$u_d = R_s i_d + L_d \frac{di_d}{dt} - \omega_r \psi_q, \quad (5.77)$$

$$u_q = R_s i_q + L_q \frac{di_q}{dt} + \omega_r \psi_d. \quad (5.78)$$

In the steady state, the currents  $i_d = I_d = \text{const.}$ ,  $i_q = I_q = \text{const.}$  and the derivatives of the currents in time is zero. Under these conditions, the volt-ampere equations in the rotor reference frame receive the form:

$$U_d = R_s I_d - \omega_r L_q I_q, \quad (5.79)$$

$$U_q = R_s I_q + \omega_r (L_d I_d + \psi_E). \quad (5.80)$$

where:  $U_d$ ,  $U_q$  and  $I_d$ ,  $I_q$  represent the voltage and the currents, respectively, along the  $d$  and  $q$ -axes, in the steady state, and  $\omega_r$  is the electric angular speed or the rotor electric pulsation.



Considering the relationships (5.34), (5.35) and (5.36), the expressions of the apparent, active and reactive instantaneous power in the rotor reference frame can be determined as follows:

$$\underline{s}_{dq} = \frac{3}{2} \underline{u}_{dq} \underline{i}_{dq}^* = \frac{3}{2} (u_d i_d + u_q i_q) + j \frac{3}{2} (u_q i_d - u_d i_q) = p_{dq} + j q_{dq}, \quad (5.81)$$

$$p_{dq} = \frac{3}{2} (u_d i_d + u_q i_q), \quad (5.82)$$

$$q_{dq} = \frac{3}{2} (u_q i_d - u_d i_q). \quad (5.83)$$

If the expressions (5.77) and (5.78) are used, the instantaneous power equation results:

$$p_{dq} = \frac{3}{2} \left( R_s (i_d^2 + i_q^2) + \frac{L_d}{2} \frac{di_d^2}{dt} + \frac{L_q}{2} \frac{di_q^2}{dt} + \omega_r (\psi_d i_q - \psi_q i_d) \right). \quad (5.84)$$

Analysing the relationship (5.84), it results that:

- **the copper losses,  $p_{dqCu}$ ,** are:

$$p_{dqCu} = \frac{3}{2} R_s (i_d^2 + i_q^2). \quad (5.85)$$

- **the increased magnetic power stored,  $p_{dqm}$ ,** is:

$$p_{dqm} = \frac{3}{2} \left( \frac{L_d}{2} \frac{di_d^2}{dt} + \frac{L_q}{2} \frac{di_q^2}{dt} \right). \quad (5.86)$$

- **the electromagnetic power,  $p_{dqelm}$ ,** is

$$p_{dqelm} = \frac{3}{2} (\omega_r (\psi_d i_q - \psi_q i_d)). \quad (5.87)$$

From the electromagnetic power, the expression of the electromagnetic torque in the machine rotor reference frame can be determined:

$$m_{dq} = \frac{p_{dqelm} p}{\omega_r} = \frac{3}{2} p (\psi_d i_q - \psi_q i_d). \quad (5.88)$$

where,  $p$  - is the number of the machine pole pairs.

**Note:** When determining the electromagnetic torque from the electromagnetic power, the connection between the mechanical angular speed and the electric angular speed was considered:

$$\omega_r = p\Omega_r. \quad (5.89)$$

where  $\omega_{r\_este}$  – is the rotor electrical angular speed and  $\Omega_r$ – is the rotor mechanical angular speed.

Within the orthogonal mathematical model in the rotor reference frame, the expression of the electromagnetic torque of the IPMSM can be written according to the inductances, based on the relationships (5.73) and (5.74):

$$m_{dq} = \frac{3}{2} p \left( \psi_E i_q + (L_d - L_q) i_d i_q \right). \quad (5.90)$$

**Note:** In the steady state, the expression of the electromagnetic torque (5.90) becomes:

$$M_{dq} = \frac{3}{2} p \left( \psi_E I_q + (L_d - L_q) I_d I_q \right). \quad (5.91)$$

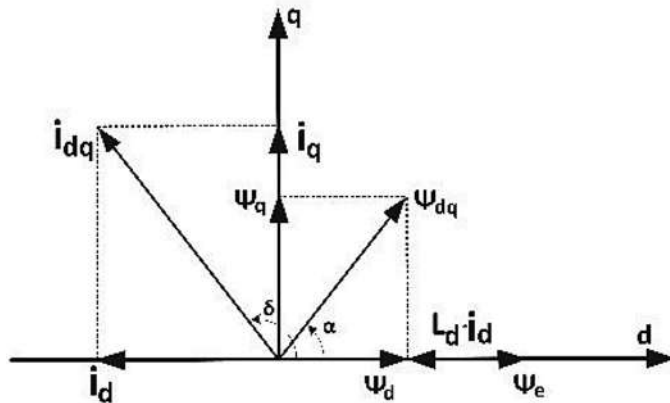


Fig. 5.3 The resulting flux and the resulting current in the case of an orthogonal model in the rotor reference frame.

From the analysis of the relationship (5.90), it can be observed that, in the expression of the electromagnetic torque, there are two terms, namely:

- $m_{dqE} = \frac{3}{2} p \psi_E i_q$ , which represents the component of the electromagnetic torque produced by the permanent magnet flux;
- $m_{dqrel} = \frac{3}{2} p (L_d - L_q) i_d i_q$ , which is the component of the reluctant electromagnetic torque, given by the inductances difference.

In general,  $i_d \leq 0$ , such that the reluctant torque is positive only if  $L_d \leq L_q$ .

The current components along the  $d$ -axis and the  $q$ -axis can be written according to the amplitude of the resulting current and the angle  $\delta$  (see Fig. 5.3):

$$i_d = i_{dq} \cos \delta, \quad (5.92)$$

$$i_q = i_{dq} \sin \delta. \quad (5.93)$$

Thus, the electromagnetic couple given by the relation (5.90) can be rewritten as:

$$m_{dq} = \frac{3}{2} p \left( \psi_E i_{dq} \sin \delta + \frac{1}{2} (L_d - L_q) i_{dq}^2 \sin(2\delta) \right). \quad (5.94)$$

Considering the relationship (5.94), the variation of the electromagnetic torque can be graphically represented according to the angle  $\delta$ , for a given value of the current amplitude. Fig. 5.4 shows the variation of the electromagnetic torque ( $m_{dqE}$ ), of the torque provided by the permanent magnet flux ( $m_{dqE}$ ) and of the reluctant torque ( $m_{dqrel}$ ), respectively, according to the angle  $\delta$ , for a given value of the current amplitude.

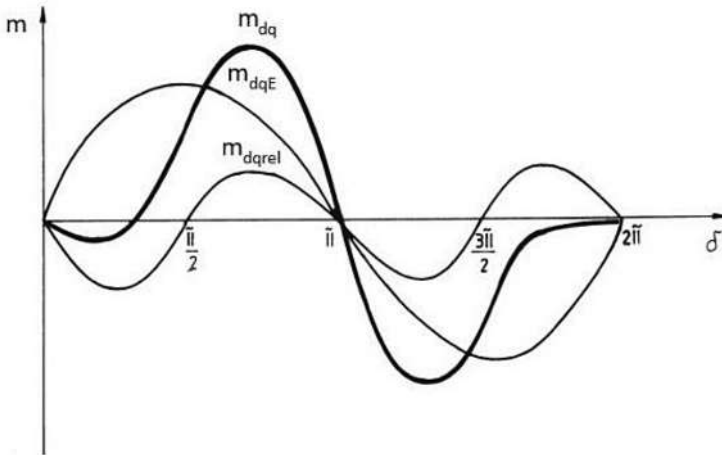


Fig. 5.4 The variation of  $m_{dq}$ ,  $m_{dqE}$  and  $m_{dqrel}$ , depending on the angle  $\delta$  for a given value of the current amplitude.

The fluxes along the  $d$ -axis and  $q$ -axis, respectively, can be rewritten considering the relationships (5.73) and (5.74) as well as the amplitude of the resulting flux  $\psi_{dq}$  (see Fig. 5.3):

$$\psi_d = \psi_{dq} \cos \alpha = L_d i_d + \psi_E, \quad (5.95)$$

$$\psi_q = \psi_{dq} \sin \alpha = L_q i_q. \quad (5.96)$$

In the case of the orthogonal model in the rotor reference frame, the electromagnetic torque can also be written depending on the amplitude of the fluxes, the inductance along the  $d$ -axis, the inductance along the  $q$ -axis and the angle  $\alpha$ , respectively:

$$m_{dq} = \frac{3}{2} p \left( \frac{\psi_E \psi_{dq} \sin \alpha}{L_d} + \frac{\psi_{dq}^2 (L_d - L_q) \sin(2\alpha)}{2L_d L_q} \right). \quad (5.97)$$

### 5.2.3.3 The connection between the orthogonal model in the rotor reference frame and the orthogonal model in the stator reference frame

Considering the relations (5.71) and (5.72), the following relationships can be written:

$$\begin{aligned} L_{hs0} &= \frac{1}{3} (L_{ad} + L_{aq}) = \frac{1}{3} (L_d + L_q - 2L_{\sigma s}); \\ L_{hsp} &= \frac{1}{3} (L_{ad} - L_{aq}) = \frac{1}{3} (L_d - L_q). \end{aligned} \quad (5.98)$$

The magnetic fluxes of the orthogonal model in the stator reference frame (see relationships (5.44) and (5.45)) are written according to the inductivities  $L_d$  and  $L_q$ , as follows:

$$\psi_\alpha = \left( \frac{(L_d + L_q)}{2} + \frac{(L_d - L_q)}{2} \cos(2\theta) \right) i_\alpha + \frac{(L_d - L_q)}{2} \sin(2\theta) i_\beta + \psi_E \cos(\theta), \quad (5.99)$$

$$\psi_\beta = \left( \frac{(L_d + L_q)}{2} - \frac{(L_d - L_q)}{2} \cos(2\theta) \right) i_\beta + \frac{(L_d - L_q)}{2} \sin(2\theta) i_\alpha + \psi_E \sin(\theta). \quad (5.100)$$

The relationship (5.69) can be rewritten as:

$$\begin{pmatrix} d_d \\ d_q \\ d_0 \end{pmatrix} = \begin{pmatrix} \cos \theta & \sin \theta \\ -\sin \theta & \cos \theta \\ 1 & 0 \end{pmatrix} \frac{2}{3} \begin{pmatrix} 1 & -\frac{1}{2} & -\frac{1}{2} \\ 0 & \frac{\sqrt{3}}{2} & -\frac{\sqrt{3}}{2} \\ \frac{1}{2} & \frac{1}{2} & \frac{1}{2} \end{pmatrix} \begin{pmatrix} a_s \\ b_s \\ c_s \end{pmatrix}. \quad (5.101)$$

Considering the relationship (5.48), the relationship, which makes possible the transition from the orthogonal model in the stator reference frame into the orthogonal model in a rotor reference frame, has the following matrix expression:

$$\begin{pmatrix} d_d \\ d_q \\ d_0 \end{pmatrix} = \begin{pmatrix} \cos \theta & \sin \theta \\ -\sin \theta & \cos \theta \\ 1 & 0 \end{pmatrix} \begin{pmatrix} d_\alpha \\ d_\beta \\ d_0 \end{pmatrix}. \quad (5.102)$$

From (5.102), the inverse transformation that does the transition from the orthogonal model in the rotor reference frame into the orthogonal model in the stator reference frame has the following matrix expression:

$$\begin{pmatrix} d_\alpha \\ d_\beta \\ d_0 \end{pmatrix} = \begin{pmatrix} \cos \theta & -\sin \theta \\ \sin \theta & \cos \theta \\ 1 & 0 \end{pmatrix} \begin{pmatrix} d_d \\ d_q \\ d_0 \end{pmatrix}. \quad (5.103)$$

It is noted that:

$$[T_\theta] = \begin{pmatrix} \cos \theta & \sin \theta \\ -\sin \theta & \cos \theta \\ 1 & 0 \end{pmatrix}; [T_\theta]^{-1} = \begin{pmatrix} \cos \theta & -\sin \theta \\ \sin \theta & \cos \theta \\ 1 & 0 \end{pmatrix}. \quad (5.104)$$

The transformation from the orthogonal model in the machine's stator reference frame into the orthogonal model in the machine's rotor reference frame, respectively, the inverse transformation from the orthogonal model in the machine's rotor reference frame into the orthogonal model in the machine's stator reference frame is possible by using the two matrices. Considering the relationship (5.103) and the relationships (5.99) and (5.100), respectively, the magnetic fluxes of the orthogonal model in the stator reference frame can also be written as:

$$\psi_\alpha = L_d i_d \cos \theta - L_q i_q \sin \theta + \psi_E \cos \theta, \quad (5.105)$$

$$\psi_\beta = L_d i_d \sin \theta + L_q i_q \cos \theta + \psi_E \sin \theta. \quad (5.106)$$

#### 5.2.3.4 The motion equation

The motion equation can be written according to the IPMSM mechanical angular speed as below:

$$J \frac{d\Omega_r}{dt} = m - K_{fr} \Omega_r - m_r. \quad (5.107)$$

where:  $J$  - represents the inertia moment of the rotor together with the driven load and related to the machine shaft,  $m$  - is the electromagnetic torque developed by the IPMSM,  $m_r$  - represents the resistant torque component, which is independent of the speed,  $K_{fr}$  - is the viscous friction coefficient and  $\Omega_r$  - is the machine's mechanical angular speed.

### 5.2.4 The mathematical model in p.u.

When analysing the steady state and the dynamic regimes of the IPMSM as well as its control strategies, the equations in p.u. are frequently used in order to obtain results with a higher degree of generality, independent of the machine's power. Therefore, a dimensionless model is obtained. The advantages of using the equations in p.u. are:

- obtaining a higher degree of generality,
- simplifying some mathematical relationships,
- easily implementing the model in the digital signal processors (DSPs) or digital signal microcontrollers (DSCs).

All the sizes will be related to the values of the nominal operating point, which will be noted below with the index "n". The basic sizes are:

- **the base current**,  $I_b = \sqrt{2}I_n$ , where  $I_n$  - represents the nominal value of the machine phase current;

**Note:** If the p.u. representation in values smaller than one is desired, the maximum value of the current allowed by the frequency inverter is chosen to be  $I_b$ .

- **the base voltage**,  $U_b = \sqrt{2}U_n$ , where  $U_n$  - represents the nominal value of the motor's phase voltage;

**Note:** If the p.u. representation in values smaller than one is desired, the maximum value of the voltage that can be provided by the frequency inverter is chosen to be  $U_b$ . If the motor operates in the field weakening area, it must also be taken into account that the base voltage is greater than the induced voltage or, in other words, the flux produced by the permanent magnet in p.u. or the machine inductances in p.u. will be less than one.

- **the base electrical speed**,  $\omega_b = 2\pi f_b$ ,  $\omega_b$  - is the base electrical speed;  $f_b$  - represents the nominal electric frequency or the maximum electric frequency of the motor;

- **the base mechanical speed**,  $\Omega_b = \frac{\omega_b}{p}$  ;

- **the base flux**,  $\psi_b = \frac{U_b}{\omega_b}$  ;

- **the base impedance**,  $Z_b = \frac{U_b}{I_b}$  ;

- **the base inductance**,  $L_b = \frac{Z_b}{\omega_b}$  ;

- the base electromagnetic torque,  $m_b = \frac{3}{2} p \psi_b I_b$ ;
- the apparent base power,  $S_b = \frac{3}{2} U_b I_b$ ;
- the base time,  $t_b = \omega_b t$ ;
- the inertia constant,  $H = \frac{J}{S_b} \left( \frac{\omega_b}{p} \right)^2$ .

With the help of the basic definitions from the above, IPMSM, the orthogonal model in the stator or rotor reference frames in p.u., is introduced below.

#### 5.2.4.1 The orthogonal model in the stator reference frame in p.u.

The volt-ampere equations, (5.42) and (5.43), in p.u., can be written as:

$$u_{\alpha pu} = r_{pu} i_{\alpha pu} + \frac{d\psi_{\alpha pu}}{dt_b}, \quad (5.108)$$

$$u_{\beta pu} = r_{pu} i_{\beta pu} + \frac{d\psi_{\beta pu}}{dt_b}. \quad (5.109)$$

where:

$$u_{\alpha, \beta pu} = \frac{u_{\alpha, \beta}}{U_b}; i_{\alpha, \beta pu} = \frac{i_{\alpha, \beta}}{I_b}; \psi_{\alpha, \beta pu} = \frac{\psi_{\alpha, \beta}}{\psi_b}; r_{pu} = \frac{R_s}{Z_b}. \quad (5.110)$$

The magnetic fluxes along the real and imaginary axes (see relationships (5.44), (5.45)), in p.u., have the following expressions:

$$\begin{aligned} \psi_{\alpha pu} = & \left( l_{\sigma spu} + \frac{3}{2} (l_{hs0 pu} + l_{hsppu} \cos(2\theta)) \right) i_{\alpha pu} \\ & + \frac{3}{2} l_{hsppu} \sin(2\theta) i_{\beta pu} + \psi_{Epu} \cos(\theta), \end{aligned} \quad (5.111)$$

$$\begin{aligned} \psi_{\beta pu} = & \left( l_{\sigma spu} + \frac{3}{2} (l_{hs0 pu} - l_{hsppu} \cos(2\theta)) \right) i_{\beta pu} \\ & + \frac{3}{2} l_{hsppu} \sin(2\theta) i_{\alpha pu} + \psi_{Epu} \sin(\theta). \end{aligned} \quad (5.112)$$

where:

$$l_{\sigma s, hs0, hsppu} = \frac{L_{\sigma s, hs0, hsp}}{L_b}; \psi_{Epu} = \frac{\psi_E}{\psi_b}. \quad (5.113)$$

In p.u., the instantaneous apparent power, the instantaneous active power and the instantaneous reactive power (see relationships (5.49), (5.50) and (5.51)) are rewritten as:

$$\begin{aligned} \underline{s}_{\alpha\beta pu} &= \left( u_{\alpha pu} i_{\alpha pu} + u_{\beta pu} i_{\beta pu} \right) + j \left( u_{\beta pu} i_{\alpha pu} - u_{\alpha pu} i_{\beta pu} \right) \\ &= P_{\alpha\beta pu} + j Q_{\alpha\beta pu}, \end{aligned} \quad (5.114)$$

$$P_{\alpha\beta pu} = \left( u_{\alpha pu} i_{\alpha pu} + u_{\beta pu} i_{\beta pu} \right), \quad (5.115)$$

$$Q_{\alpha\beta pu} = \left( u_{\beta pu} i_{\alpha pu} - u_{\alpha pu} i_{\beta pu} \right). \quad (5.116)$$

where:

$$\underline{s}_{\alpha\beta pu} = \frac{\underline{s}_{\alpha\beta}}{S_b}, P_{\alpha\beta pu} = \frac{P_{\alpha\beta}}{S_b}; Q_{\alpha\beta pu} = \frac{Q_{\alpha\beta}}{S_b}. \quad (5.117)$$

**The copper losses in p.u.,  $p_{\alpha\beta Cupu}$**  (see relationship (5.54)), are given by the relationship:

$$P_{\alpha\beta Cupu} = r_{pu} \left( i_{\alpha pu}^2 + i_{\beta pu}^2 \right). \quad (5.118)$$

**The increase of the magnetic power stored in p.u.,  $p_{\alpha\beta mpu}$**  (see relationship (5.55)), is:

$$\begin{aligned} P_{\alpha\beta mpu} &= \left( l_{\sigma spu} + \frac{3}{2} (l_{hs0pu} + l_{hsppu} \cos(2\theta)) \right) i_{\alpha pu} \left( \frac{di_{\alpha pu}}{dt_b} + \omega_{rpm} i_{\beta pu} \right) + \\ &+ \frac{3}{2} l_{hsppu} \sin(2\theta) i_{\alpha pu} \left( \frac{di_{\beta pu}}{dt_b} - \omega_{rpm} i_{\alpha pu} \right) + \\ &+ \left( l_{\sigma spu} + \frac{3}{2} (l_{hs0pu} - l_{hsppu} \cos(2\theta)) \right) i_{\beta pu} \left( \frac{di_{\beta pu}}{dt_b} - \omega_{rpm} i_{\alpha pu} \right) + \\ &+ \frac{3}{2} l_{hsppu} \sin(2\theta) i_{\beta pu} \left( \frac{di_{\alpha pu}}{dt_b} + \omega_{rpm} i_{\beta pu} \right) \end{aligned} \quad (5.119)$$

**The electromagnetic power in p.u.,  $p_{\alpha\beta elmpu}$**  (see relationship (5.56)), is written as follows:

$$P_{\alpha\beta elmpu} = \omega_{rpm} \left( \psi_{\alpha pu} i_{\beta pu} - \psi_{\beta pu} i_{\alpha pu} \right), \quad (5.120)$$

where:



$$P_{\alpha\beta C_{pu}} = \frac{P_{\alpha\beta C_u}}{S_b}; P_{\alpha\beta m_{pu}} = \frac{P_{\alpha\beta m}}{S_b}; P_{\alpha\beta elm_{pu}} = \frac{P_{\alpha\beta elm}}{S_b}; \omega_{rpu} = \frac{\omega_r}{\omega_b}. \quad (5.121)$$

The electromagnetic torque in p.u.,  $m_{\alpha\beta}$  (see relationship (5.57)), is:

$$m_{\alpha\beta pu} = \Psi_{\alpha pu} i_{\beta pu} - \Psi_{\beta pu} i_{\alpha pu}, \quad (5.122)$$

where:

$$m_{\alpha\beta pu} = \frac{T_{\alpha\beta}}{T_b}. \quad (5.123)$$

#### 5.2.4.2 The orthogonal model in the rotor reference frame in p.u.

The volt-ampere equations in the rotor reference frame in p.u. (see relationships (5.63), (5.64)) are written as:

$$u_{dpu} = r_{pu} i_{dpu} + \frac{d\psi_{dpu}}{dt_b} - \omega_{rpu} \Psi_{qpu}, \quad (5.124)$$

$$u_{qpu} = r_{pu} i_{qpu} + \frac{d\psi_{qpu}}{dt_b} + \omega_{rpu} \Psi_{dpu}. \quad (5.125)$$

The fluxes along the  $d$ -axis and  $q$ -axis, respectively, in p.u. (see relationships (5.84), (5.85)), have the expressions:

$$\Psi_{dpu} = l_{dpu} i_{dpu} + \Psi_{Epu}, \quad (5.126)$$

$$\Psi_{qpu} = l_{qpu} i_{qpu}. \quad (5.127)$$

where,

$$u_{d,qpu} = \frac{u_{d,q}}{U_b}; i_{d,qpu} = \frac{i_{d,q}}{I_b}; \Psi_{d,q,Epu} = \frac{\Psi_{d,q,E}}{\Psi_b}; l_{d,qpu} = \frac{L_{d,q}}{L_b}. \quad (5.128)$$

Taking into consideration the relationships (5.124), (5.125), (5.126) and (5.127), the phase diagram of the orthogonal mathematical model in the rotor reference frame in p.u. is represented in Fig. 5.5. below:

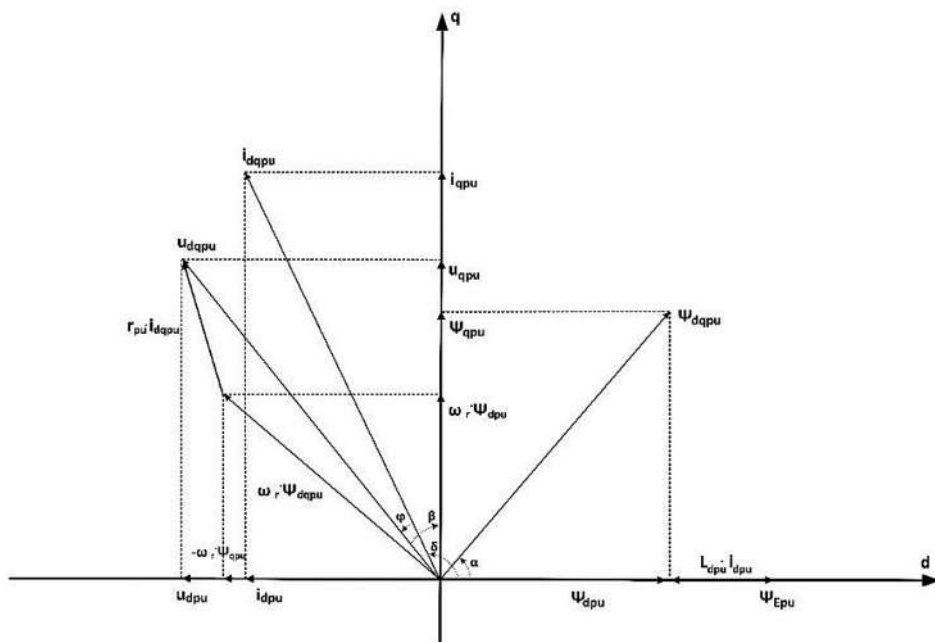


Fig. 5.5 Phase diagram of the orthogonal mathematical model in the rotor reference frame in p.u.

In the case of the orthogonal model in the stator reference frame, the instantaneous apparent power, the instantaneous active power and the reactive instantaneous power in p.u. (see relationships (5.81), (5.82), (5.83)) have the following expressions:

$$\underline{s}_{dqpu} = \left( u_{dpu} i_{dpu} + u_{qpu} i_{qpu} \right) + j \left( u_{qpu} i_{dpu} - u_{dpu} i_{qpu} \right) = P_{dqpu} + jQ_{dqpu}, \quad (5.129)$$

$$P_{dqpu} = \left( u_{dpu} i_{dpu} + u_{qpu} i_{qpu} \right), \quad (5.130)$$

$$Q_{dqpu} = \left( u_{qpu} i_{dpu} - u_{dpu} i_{qpu} \right). \quad (5.131)$$

where:

$$\begin{aligned} \underline{s}_{dqpu} &= \frac{S_{dq}}{S_b}, \\ P_{dqpu} &= \frac{P_{dq}}{S_b}, \\ Q_{dqpu} &= \frac{Q_{dq}}{S_b}. \end{aligned} \quad (5.132)$$

**The copper losses in p.u.,  $P_{dqCupu}$**  (see relationship (5.85)), have the expression:

$$P_{dqCupu} = r_{pu} \left( i_{dpu}^2 + i_{qpu}^2 \right). \quad (5.133)$$

**The increase of the magnetic power stored in p.u.,  $P_{dqmpu}$**  (see relationship (5.86)), is:

$$P_{dqmpu} = \left( \frac{l_{dpu}}{2} \frac{di_{dpu}^2}{dt_b} + \frac{l_{qpu}}{2} \frac{di_{qpu}^2}{dt_b} \right). \quad (5.134)$$

**The electromagnetic power in p.u.,  $P_{dqelpu}$**  (see relationship (5.87)), is written as:

$$P_{dqelpu} = \omega_{rpu} \left( \psi_{dpu} i_{qpu} - \psi_{qpu} i_{dpu} \right), \quad (5.135)$$

where:

$$P_{dqCupu} = \frac{P_{dqCu}}{S_b}; P_{dqmpu} = \frac{P_{dqm}}{S_b}; P_{dqelpu} = \frac{P_{dqelm}}{S_b}. \quad (5.136)$$

**The electromagnetic torque in p.u.,  $m_{dqpu}$**  (see relationship (5.88)), corresponds to the expression:

$$m_{dqpu} = \psi_{dpu} i_{qpu} - \psi_{qpu} i_{dpu}. \quad (5.137)$$

The connection between the mechanical angular speed and the electric angular speed in the p.u. is given by the relationship:

$$\omega_{rpu} = \Omega_{rpu}. \quad (5.138)$$

where,

$$m_{dqpu} = \frac{m_{dq}}{m_b}; \omega_{rpu} = \frac{\omega_r}{\omega_b}; \Omega_{rpu} = \frac{\Omega_r}{\Omega_b}. \quad (5.139)$$

The relationship (5.90) of the electromagnetic torque, in the rotor reference of the permanent magnet synchronous motor with apparent poles, has in p.u. the expression:

$$m_{dqpu} = \psi_{Epu} i_{qpu} + (l_{dpu} - l_{qpu}) i_{qpu} i_{dpu}. \quad (5.140)$$

The relationships of the current along the  $d$ -axis and  $q$ -axis, respectively, depending on the amplitude of the resulting current and on the angle  $\delta$  (see relationships (5.92) and (5.93)) are written in p.u., as follows:

$$i_{dpu} = i_{dqpu} \cos \delta, \quad (5.141)$$

$$i_{qpu} = i_{dqpu} \sin \delta. \quad (5.142)$$

Considering these conditions, the electromagnetic torque, given by the relationship (5.104), becomes in p.u.:

$$m_{dqpu} = \psi_{Epu} i_{dqpu} \sin \delta + \frac{1}{2} (l_{dpu} - l_{qpu}) i_{dqpu}^2 \sin (2\delta). \quad (5.143)$$

The relationships (5.95) and (5.96), which express the flux along the  $d$ -axis and  $q$ -axis, respectively, depending on the amplitude of the resulting flux and on the  $\alpha$  angle are written in p.u., as follows:

written in p.u., as follows:

$$\psi_{dpu} = \psi_{dqpu} \cos \alpha = l_{dpu} i_{dpu} + \psi_{Epu}, \quad (5.144)$$

$$\psi_{qpu} = \psi_{dq} \sin \alpha = l_{qpu} i_{qpu}. \quad (5.145)$$

where,

$$\psi_{dqpu} = \frac{\psi_{dq}}{\psi_b}; i_{dqpu} = \frac{i_{dq}}{\psi_b}. \quad (5.146)$$

The electromagnetic torque given by the relationship (5.97) is rewritten in p.u., as follows:

$$m_{dqpu} = \left( \frac{\psi_{Epu} \psi_{dqpu} \sin \alpha}{l_{dpu}} + \frac{\psi_{dqpu}^2 (l_{dpu} - l_{qpu}) \sin (2\alpha)}{2l_{dpu} l_{qpu}} \right). \quad (5.147)$$

The two components of the magnetic flux on the  $\alpha\beta$  axes of the orthogonal stator referencer (see relationships (5.99) and (5.100)) are written in p.u. depending on the inductivities  $l_d$  and  $l_q$ , respectively, as follows:

$$\begin{aligned} \psi_{\alpha pu} = & \left( \frac{(l_{dpu} + l_{qpu})}{2} + \frac{(l_{dpu} - l_{qpu})}{2} \cos(2\theta) \right) i_{\alpha pu} \\ & + \frac{(l_{dpu} - l_{qpu})}{2} \sin(2\theta) i_{\beta pu} + \psi_{Epu} \cos(\theta). \end{aligned} \quad (5.148)$$

$$\begin{aligned} \psi_{\beta pu} = & \left( \frac{(l_{dpu} + l_{qpu})}{2} - \frac{(l_{dpu} - l_{qpu})}{2} \cos(2\theta) \right) i_{\beta pu} \\ & + \frac{(l_{dpu} - l_{qpu})}{2} \sin(2\theta) i_{\alpha pu} + \psi_{Epu} \sin(\theta). \end{aligned} \quad (5.149)$$

The relationships (5.105) and (5.106) in p.u. become:

$$\psi_{\alpha pu} = l_{dpu} i_{dpu} \cos \theta - l_{qpu} i_{qpu} \sin \theta + \psi_{Epu} \cos \theta. \quad (5.150)$$

$$\psi_{\beta pu} = l_{dpu} i_{dpu} \sin \theta + l_{qpu} i_{qpu} \cos \theta + \psi_{Epu} \sin \theta. \quad (5.151)$$

### 5.2.4.3 Motion equation in p.u.

In the case of the mathematical model in p.u., the motion equation (5.117) is written as:

$$H \frac{d\Omega_{rpu}}{dt} = m_{pu} - \frac{K_{fr}}{J} H \Omega_{rpu} - t_{rpu}, \quad (5.152)$$

or

$$H \omega_b \frac{d\Omega_{rpu}}{dt_b} = m_{pu} - \frac{K_{fr}}{J} H \Omega_{rpu} - t_{rpu}, \quad (5.153)$$

where:

$$m_{pu} = \frac{m}{T_b}; t_{rpu} = \frac{m_r}{T_b}. \quad (5.154)$$

### 5.3 V/f control methods

Fig. 5.6 shows the V/f control approach for a PMSM. An important advantage of the PMSM drive is that the rotor speed is dependent only on the machine excitation frequency and it does not require slip compensation as does the induction machine drive. Controlling the PMSMs in open loop is quite a difficult job due to the fact that the machine does not guarantee the synchronization between the AC excitation frequency and the rotor frequency. Furthermore, the system can oscillate or it cannot even be driven. Thus, the instability, the oscillatory power and the difficulty of achieving fast dynamic responses, associated with the open loop schemes, represent their most important disadvantages. The control system from Fig. 5.6 does not allow the damping of the torque and speed ripples, which represents an important deficiency. These inconveniences can be withdrawn if the PMSMs have a rotor with cage windings, but this supposes supplementary costs and losses [13].

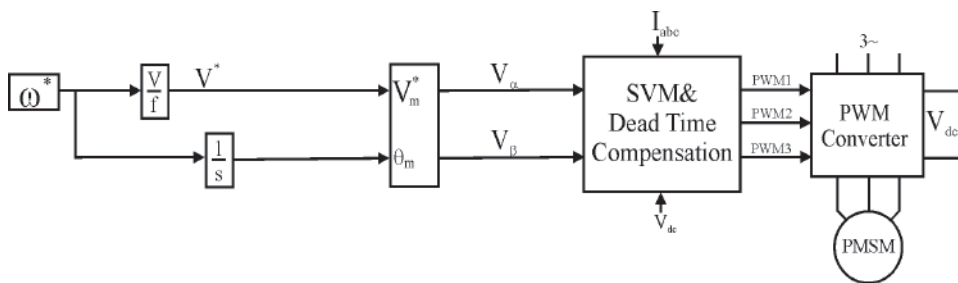


Fig. 5.6 The standard open loop V/f control.

So, the standard V/f control is mainly used in applications such as pumps or fans that do not require fast dynamic responses. Alternatively, a closed-loop control scheme could be developed in order to withdraw this disadvantage and to allow the achievement of a more accurate machine control.

Furthermore, in the specialized literature, there are control methods based on the standard closed loop V/f control, but at which stabilizing loops are attached [17]. Fig. 5.5 presents a control system that uses a stabilizing loop added to the frequency prescription. The correction is performed by analyzing the variation of the inverter DC-link current or the active power variation.

The control systems using either one of the stabilizing loops or even two of them can be proposed. However, there is an important difference on how the stabilizing loops are designed. Depending on the chosen strategy, in some cases, these corrections lead to small improvements by reducing the pulsations in the speed waveform specific to the standard V/f control or, in other cases, they could even improve the results achieved with the vector control.

This paragraph introduces a stabilizing loop to correct the reference frequency in order to improve the standard V/f control of the SPMSMs.

At a super high speed (above 30,000 rpm), the SPMSMs drives control is hampered by the shortness of the online computation cycle and by the limited switching frequency in the IGBT power converters. This is the reason why the V/f and the I-f control with a stabilizing loop has been proposed ([14] to [16]) instead of the vector control, which implies a starting sequence in the rotor coordinates [13].

The  $dq$  model of the surface permanent magnet synchronous motor (SPMSM) in the rotor reference frame is based on the one presented in the previous paragraph for the IPMSM, with the mention that now  $L_d=L_q$ .

The solution shown in Fig. 7 [15] uses a stabilizing loop, which depends on the DC-link current or power perturbations. The correction is performed by analyzing the variation of the inverter DC-link current or of the active power variation. This solution claims to operate up to 200 rad/s.

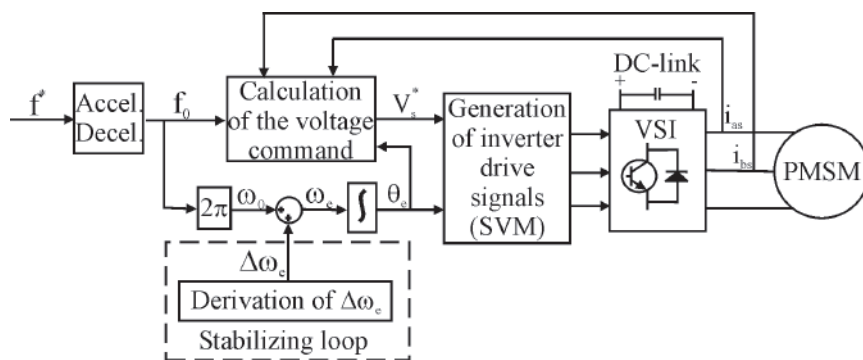


Fig. 5.7 The V/f control with one stabilising loop [15].

### 5.3.1 The digital simulations results

The digital system simulations have been processed in Matlab/Simulink for an easy translation into the dSpace 1103 platform. The motor data are given in Table 5.1.

Fig. 5.8 and Fig. 5.9 illustrate the performances of the standard (or classical) V/f control and the V/f control with DC-link power oscillations correction loop, respectively. While for the standard V/f control, the speed oscillations increase with the load as no damping is provided, in the case of the V/f control with one stabilizing loop, the speed oscillations decrease under similar circumstances.

In the first case, the speed is ramped to 80,000 rpm and the standard V/f open-loop control was applied (Fig. 5.8), with a step load torque applied at  $t=12$  sec. The machine remains in synchronism, meaning that it oscillates around the prescribed speed with 100 rpm at 0.1 Nm torque load and with 300 rpm at 0.4 Nm load torque.

The compensation loops work on limiting the oscillations under loading conditions, as it can be seen in Fig. 5.9.

Both solutions have high speed and torque oscillations at 80,000 rpm, which can be unacceptable for some applications. The future work will concentrate on developing a control system which can damp the oscillations almost completely. This can be achieved by introducing additional stabilizing loops.

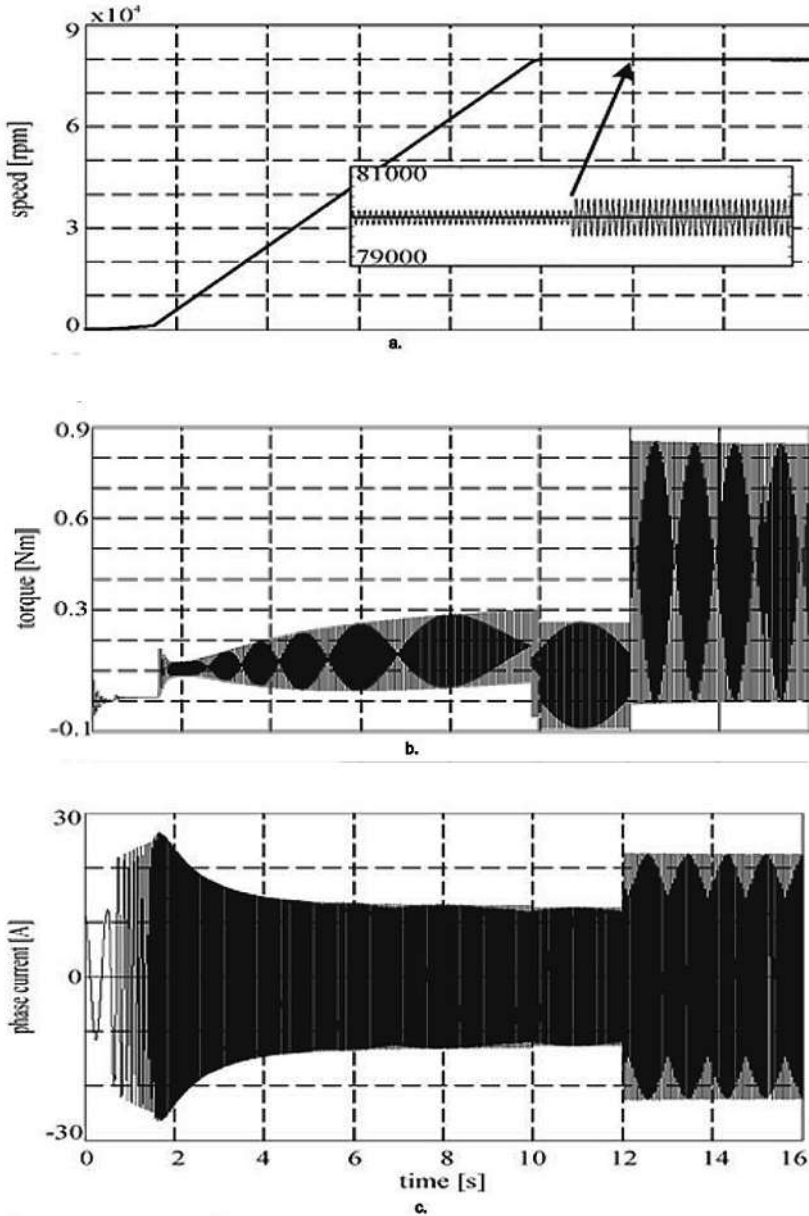


Fig. 5.8 The standard V/f control without any stabilization loop: the speed, the torque and the phase current.



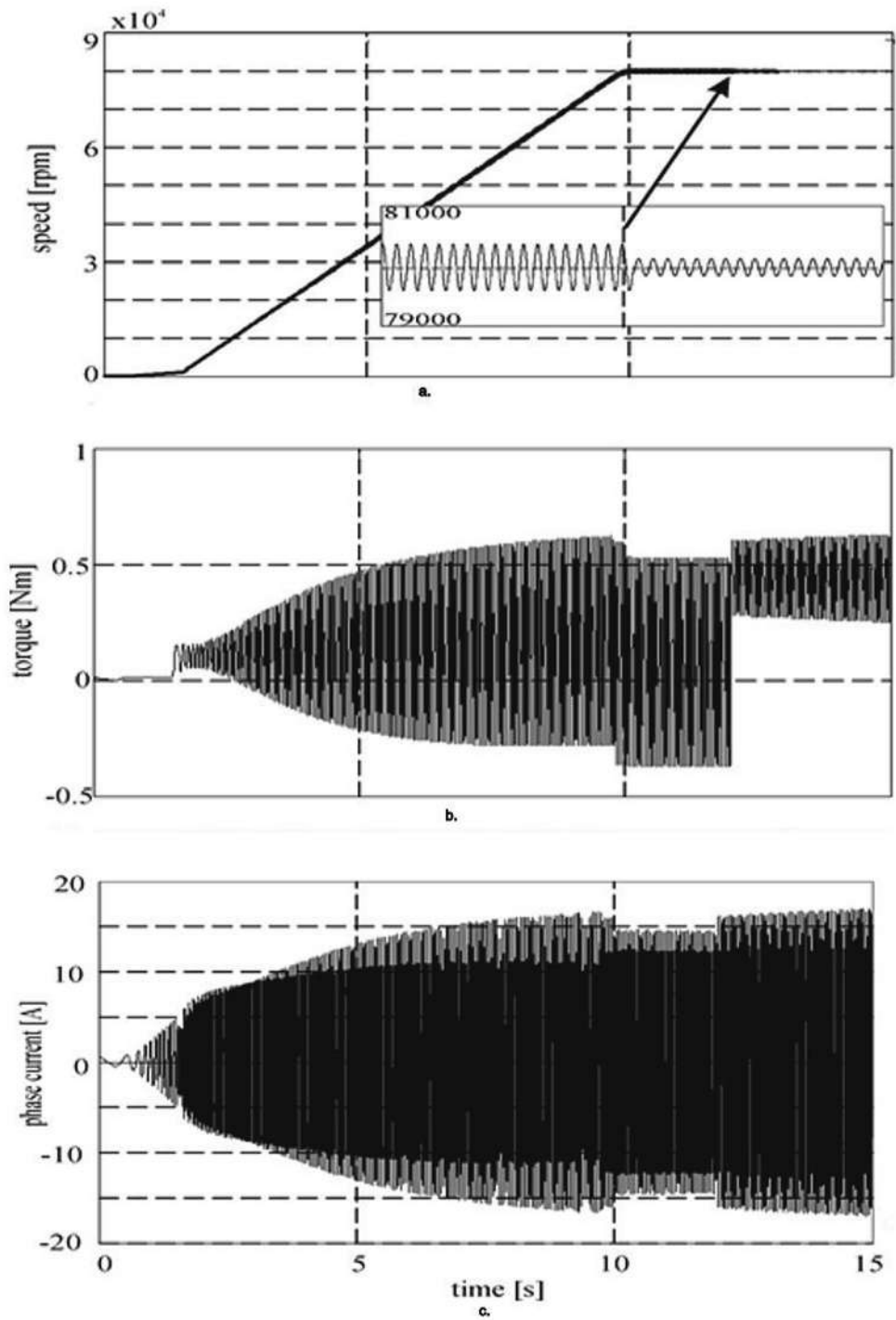


Fig. 5.9 The V/f control with DC-link power oscillations correction loop (e.g. the V/f control with one stabilizing loop): the speed, the torque and the phase current.

Table 5.1. The specifications of the SPMSM used in simulation

Number of pole pairs (p)	1
Rated power	3 kW
Rated speed	80,000 rpm
Rated frequency	1,333 Hz
Rated torque	0.358 Nm
Rated phase to phase voltage	380 V(rms)
Rated phase current	20 A(rms)
Stator resistance per phase ( $R_s$ )	$0.6 \Omega$
d-axis inductance ( $L_d$ )	1 mH
q-axis inductance ( $L_q$ )	1 mH
Rotor permanent - magnet ( $\lambda_{PM}$ )	$0.031 \text{ V s rad}^{-1}$
Inertia of the rotating system (J)	$10^{-4} \text{ kgm}^2$
Viscous friction coefficient ( $B_m$ )	$10^{-5} \text{ Nms/rad}$

### 5.3.2 Experimental results

The experimental setup was built-up in the Intelligent Motion Control Lab at the Department of Electrical Engineering of UPT, with the intended purpose of proving that the high speed PMSM-simulated control methods previously presented are really working.

The schematic principle of the test bench setup is presented in Fig.10.

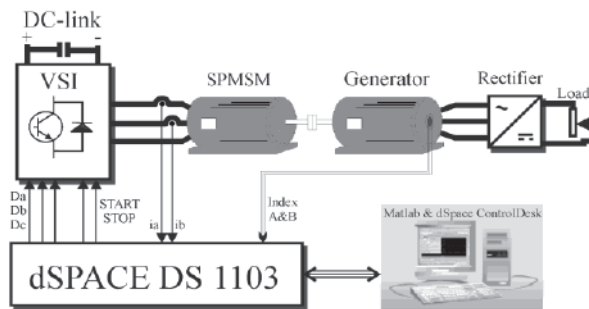


Fig. 5.10 The scheme of the experimental system setup for the high speed SPMSM.

The setup consists of two identical 0.8 kW, 20,000 rpm, 4 pole SPMSMs with sinusoidal back-emf, which are mechanically coupled (see Fig. 5.11).

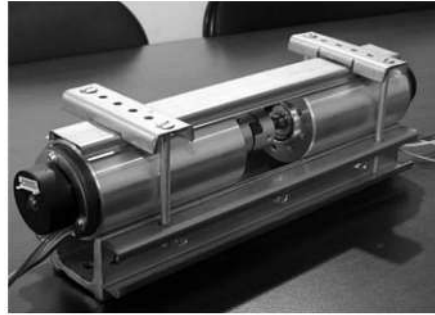


Fig. 5.11 The high speed SPMSM used in experiments.

The motor data are presented in Fig. 5.12. A 50V / 300A MOSFET inverter feeds the motor with 20 kHz switching frequency.

The encoder has 500 pulses-per-revolution and provides the actual rotor position and speed.

The control algorithms, using 10 KHz sampling frequency, are developed in Matlab-Simulink and implemented on a dSpace platform.

Table 5.2. The real SPMSM specifications

Number of pole pairs ( $p_1$ )	2
Rated speed	20,000 rpm
Rated frequency	667 Hz
Rated torque	0.4 Nm (at 20,000 rpm)
Rated phase to phase voltage	39 V(rms)
Rated phase current	29.5 A(rms) (at 20,000 rpm)
Stator resistance per phase ( $R_s$ )	0.083 $\Omega$
Inductance ( $L_s$ )	0.0425 mH
Rotor permanent-magnet ( $\lambda_{PM}$ )	0.00635 Vsrad <sup>-1</sup>
Inertia of rotating system ( $J$ )	40*10 <sup>-6</sup> kgm <sup>2</sup>
Viscous friction coefficient ( $B_m$ )	10 <sup>-6</sup> Nms/rad

The experiments using the V/f control with a stabilizing loop for a high speed SPMSM were performed for different loads and at various speeds

- no load start-up at 10,000 rpm (see Fig. 5.12);
- no load start-up at 10,000 rpm followed by loading at 80% of rated torque (see Fig. 5.13);

- no load start-up at 15,000 rpm and loading at 80% of rated torque at 0.8 s (see Fig. 5.14);
- no load start-up at 2,000 rpm, loading at 80% of rated torque at 0.6 s, reverse speed from 2,000 rpm to -2,000 rpm at 1.2 s rpm and loading at 80% of rated torque (see Fig. 5.15).

The results are depicted in the Fig. 5. 12 ÷ Fig. 5. 15 below and it can be concluded that they are as expected, proving the results obtained by simulation.

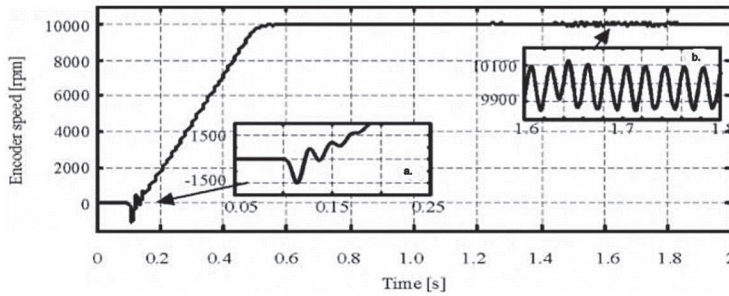


Fig. 5.12 No load start-up at 10,000 rpm using the V/f control with a stabilizing loop: a). zoom on the encoder speed waveform during transients (on the startup); b). zoom on encoder speed waveform during steady-state operation; c). three phase currents.

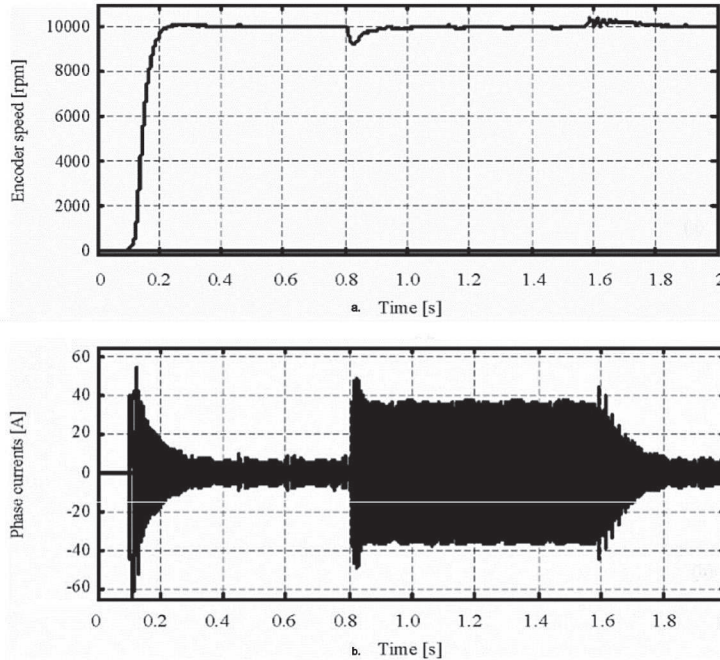


Fig. 5.13 No load start-up at 10,000 rpm followed by loading at 80% of rated torque at 0.8 s and unloading at 1.6 s in the case of the V/f control with a stabilizing loop: a) encoder speed; b) three phase currents.

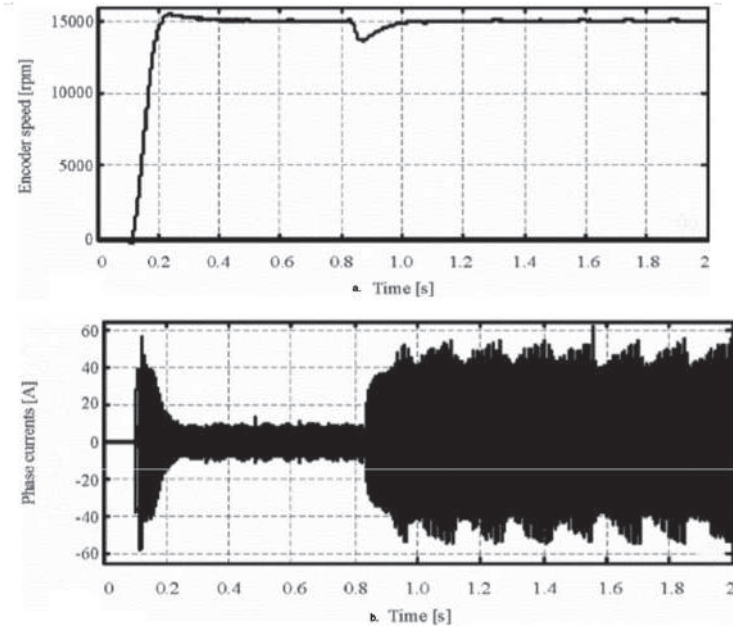


Fig. 5.14 No load start-up at 15,000 rpm and loading at 80% of rated torque at 0.8 s using the V/f control with a stabilizing loop: a) encoder speed; b) three phase currents.

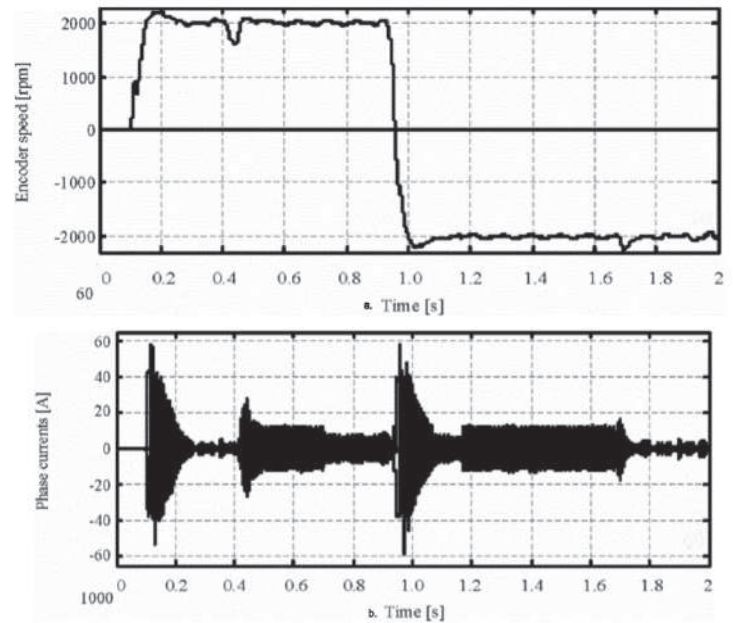


Fig. 5.15 No load start-up at 2,000 rpm, loading at 80% of rated torque at 0.6 s, reverse speed from 2,000 rpm to -2,000 rpm at 1.2 s using the V/f control with a stabilizing loop: a) encoder speed; b) three phase currents.

## 5.4 Conclusion

The approach of this chapter was the scalar control of the permanent magnet synchronous motors (PMSMs).

Firstly, different mathematical models for the permanent magnet synchronous motors were presented and, particularly, for the interior permanent magnet synchronous motors (IPMSMs), for which  $L_d \neq L_q$ .

Then the scalar control methods were stated. They are divided into two main categories: the open-loop and the closed-loop ones. The main concerns regarding the V/f control are the system instability and the speed oscillations. In order to remove them and, thus, to improve the V/f control, one or two stabilizing loops can be added.

It was demonstrated through simulations results done in Matlab/Simulink environment that the V/f with one stabilizing loop has better results than the standard V/f control, both of them operating in open-loop.

The digital simulations were then compared with the experimental results, obtained by using the dSpace real-time hardware in the loop tool and thus proving the simulation results.

All the results, provided either by simulation or by experiments, have demonstrated acceptable performances, taking into account that they are operating in open-loop.

The online computation effort it is believed to be less intensive than for the vector control, especially due to the missing part of the PI regulators' cascade.

The future work will concentrate on developing a control system which can damp the oscillations almost completely. This can be achieved by introducing additional stabilising loops.

The results were obtained by the research team at the Department of Electrical Engineering of the University Politehnica Timisoara [18] ÷ [23].

## 5.5 References

- [1] Gieras, J., Wing, M. Permanent Magnet Motor Technology. Design and Applications. Second Edition, Marcel Dekker, Inc., New-York, 2002.
- [2] Bowers, B. Philips Techn. Review 35(4): 77-95, 1975.
- [3] Cremer, R. Current status of rare-earth permanent magnets. Int. Conf. on Maglev and Linear Drives, Hamburg, Germany, pp.391-398, 1988.
- [4] Boldea, I. Transformatoare și mașini electrice. Editura Politehnica, Timișoara, 2001.
- [5] S. Musuroi, D. Popovici, "Actionari electrice cu servomotoare", Editura Politehnica, Timisoara, 2006, ISBN 978-973-625-352-2
- [6] C. Grabner, "Variable Speed Induction Drive System in V/f Control Mode - Numerical Calculation Versus Practical Measurement", Electrical and Computer Engineering, CCECE 2007, 22-26 April, pp. 550 – 555.

- [7] J. Itoh, T. Hoshino, T. Kaneko, "A Performance Improvement of V/f Control Using a Disturbance Observer", Power Electronics and Motion Control Conference, EPE-PEMC 2006. Aug. 2006 pp. 1167 – 1172.
- [8] K. Suzuki, S. Saito, T. Kudor, A. Tanaka, and Y. Andoh, "Stability improvement of V/f controlled large capacity voltage-source inverter fed induction motor", in Conf. Record IEEE-IAS 2006, vol. 1, pp. 90–95, Oct. 2006.
- [9] Voicu, M. Tehnici de analiză a stabilității sistemelor automate. Editura Tehnică, București, 1986.
- [10] L. Zhao, C. H. Ham, Q. Han, T. X. Wu, L. Zheng, K. B. Sundaram, J. Kapat, and L. Chow, "Design of an optimal V/f control for a super high speed permanent magnet synchronous motor", in Proc. IEEE-IECON 2004, Nov. 2004, vol. 3, pp. 2260–2263.
- [11] Q. Yu, Q. Song, W. Liu, Y. Li, "DSP LF2407 in NPC three-level inverter using constant V/f principle and SHE-PWM method", Signal Processing, International Conference, Aug. 2002 vol.2, pp. 1723 – 1726.
- [12] J.-I. Itoh, N. Nomura, and H. Ohsawa, "A comparison between V/f control and position-sensorless vector control for the permanent magnet synchronous motor", in Proc. Power Conversion Conf. PCC Osaka 2002, April 2002, vol. 3, pp. 1310–1315.
- [13] Y. Kumsuwan, S. Premrudeepreechacharn, K. Oranpiroj, T. Boonsai, A. Toliyat, "A Direct Torque Control of Induction Motor Using V/f PWM Technique", Power Electronics and Drives Systems, PEDS 2005, Jan. 2006 pp. 751 – 755.
- [14] J.-G. Kim, Y.-G. Jung, S.-H. Na, Y.-C. Lim, "A new random PWM (SRP-PWM) technique for decreasing acoustic noise radiated from v/f controlled motor drives", IEEE, IECON 2004. 2-6 Nov, vol. 1, pp. 832 – 837.
- [15] K. Jezernik, A. Kapun, M. Curkovic, "Robust sensorless Control of PMSM", ISIE 2008.
- [16] B.-H. Bae, S.-K. Sul, J.-H. Kwon, J.-S. Byeon, "Implementation of Sensorless Vector Control for Super-High-Speed PMSM of Turbo-Compressor", IEEE Trans. on Ind. Applicat., Vol.39, No. 3, May/June 2003.
- [17] L. Xu, C. Wang "Implementation and experimental implementation of sensorless control schemes for PMSM drives", IEEE Trans. on Ind. Applicat., vol 39, no3, 2003, pp. 783-791.
- [18] P. D. Chandana Perera, Frede Blaabjerg, John K. Pedersen and Paul Thogersen "A Sensorless, Stable V/f Control Method for Permanent-Magnet Synchronous Motor Drives", APEC 2002.
- [19] J. Oyama, T. Higuchi, T. Abe, K. Shigematsu, X. Yang, E. Matsuo "A Trial Production of Small Size Ultra-High Speed Drive System", IEMDC 2003.
- [20] J.-H. Jung, G.-Y. Jeong, B.-H. Kwon, "Stability Improvement of V/f-Controlled Induction Motor Drive Systems by Dynamic Current Compensator", IEEE Trans. on Ind. Vol. 51, no. 4, 2004, pp. 930-933.
- [21] R. Ancuti, I. Boldea, "V/f control of PM-SM super high speed drives with flux and power angle stabilizing loops," in Proc. OPTIM 2006, Brasov, May 2006, CD-ROM.
- [22] V. Olarescu, S. Mușuroi, "Enhanced simplified control algorithm for surface-mounted permanent magnet with sinusoidal excitation", IPERC 2004 China, Vol. 2, pag. 1049-1053
- [23] V. Olarescu, S. Mușuroi, "The Simplified Control Algorithm for Permanent Synchronous Motors with Sinusoidal Current Control (BLAC)", ICEM 2004 Cracow.

## 6.1 Introduction

In the last two decades, the permanent magnet synchronous motors (PMSMs) became the preferential motors for the drive systems over the induction motors, due to their high efficiency, high torque to inertia ratio and high - power density. Applications like traction, spindles and home appliances require wide speed range drives, where all the features mentioned before are needed. As the price of the permanent magnet tends to decrease and the price of iron and the price of copper tend to increase, the choice of PMSM for electric drive systems becomes imminent. Also, the use of PMSM may further eliminate the need of a gearbox. Meanwhile, the price for digital signal processors (DSP) for motor control applications has been decreased, thus, the choice of vector control of PMSM drive system became more attractive, especially for low power applications. Therefore, the use of variable speed PMSM drives for low power applications increases the energy efficiency and the performance of the system and may further eliminate the need of a gearbox.

The IPMSM (interior permanent magnets synchronous motors) and the surface permanent magnets synchronous motors (SPMSMs) belong to the permanent magnets synchronous motors (PMSMs) category. Therefore, they are machines with permanent magnets that have distributed or concentrated stator windings, for which the number of slots per pole per phase is fractional, so that the motion induced voltage has a sinusoidal or quasi-sine waveform. The permanent magnets are located on the periphery of the rotor, thus resulting the SPMSMs (or full-pole PMSMs), for which  $L_d = L_q$ , or inside the rotor, resulting the IPMSMs (or prominent-pole PMSMs), for which  $L_d \neq L_q$ . As already mentioned, from the point of view of the electromagnetic torque production, the SPMSMs require static sinusoidal currents, so that at any given time all the three stator phases of the SPMSM are active, resulting in a more complex control system than in the case of trapezoidal PMSMs control systems. The higher pulses in the electromagnetic torque produced by the trapezoidal PMSMs and the reduced performance in the field weakening area, as well as the acoustic noise produced make SPMSMs to be preferred over trapezoidal PMSMs in most applications where a wide speed range is required. In general, the control system of the SPMSMs is more complicated than that of the trapezoidal PMSMs, a more accurate knowledge of the rotor position being required. The SPMSMs are a good choice in competition with the induction machines. The SPMSM control systems appeared in the 70's and, due to the possibility of achieving



efficient control systems they are increasingly used in different applications, nowadays representing a good alternative for the home appliances.

PMSM control systems can be classified as: open loop control system, scalar control system, field-oriented vector control system, direct torque and flux control system.

The field-oriented vector control system is an efficient method in variable speed PMSM applications where the torque varies rapidly in a wide speed range, including in the field weakening area. The basic principle of the field-oriented vector control system consists of decoupling the drive in two parallel control loops, one for the electromagnetic (fast) torque control, represented by the reference current  $i_q^*$ , and the other one for the flux control (slower), represented by the reference current  $i_d^*$ . When using this control system, it is necessary to use the mathematical model of the PMSM in the rotor reference frame. The components of the stator current of the mathematical model of PMSM in rotor reference frame are aligned with the rotor flux.

For the calculation of the currents on the "d" or "q" axis, knowing the phase currents  $i_{as}, i_{bs}, i_{cs}$ , it is necessary to know the position of the rotor. Due to the use of the PMSM mathematical model in the rotor reference, the control system is relatively simple and is similar to that of the DC machines. A schematic diagram of a field-oriented vector control system is shown in Fig. 6.1. In there, it can be observed that the output of the speed controller is the reference torque  $T^*$  (it is the driver for the control of  $\theta_r$ , respectively  $\omega_r$ ). Depending on the value of the reference torque, and on the rotor speed, respectively, the reference currents values  $i_d^*, i_q^*$  can be determined. For example, if the rotational speed is lower than the base speed (not in the area field weakening), the following control strategies can be used: the control strategy maintaining  $i_d=0$ , the maximum torque control strategy for a given current, the unity power factor control strategy, the constant resultant flux control strategy. In the field weakening area, for determining the reference current values  $i_d^*, i_q^*$ , the control strategies specific to the field weakening are used. These control strategies will be presented in the next paragraph.

In the shown control system, applying to the measured currents  $i_a, i_b, i_c$  the Clarke transformation and the Park transformation, respectively, the real values of the currents  $i_d$  and  $i_q$  can be obtained. The errors of the currents along the two axes are processed using the current regulators resulting in the reference voltages  $v_d^*, v_q^*$ . Then, using the inverse Park transformation, the reference voltage values in the stator reference frame  $v_\alpha^*, v_\beta^*$  can be obtained. These voltages are then used as input values for the SVM generation module. The field-oriented vector control system of Fig. 6.1 has as reference the rotational speed of the motor  $\omega_r^*$ , and as feedback the measured rotor position  $\theta_r$ , the measured rotor speed  $\omega_r$ , and the currents of the motor respectively,  $i_a, i_b, i_c$  and as output quantities the reference value of the voltage in the stator coordinates  $v_\alpha^*, v_\beta^*$ . The disturbance quantities are the load torque, the inverter supply voltage, the motor temperature, the magnetic saturation and the moment of inertia.

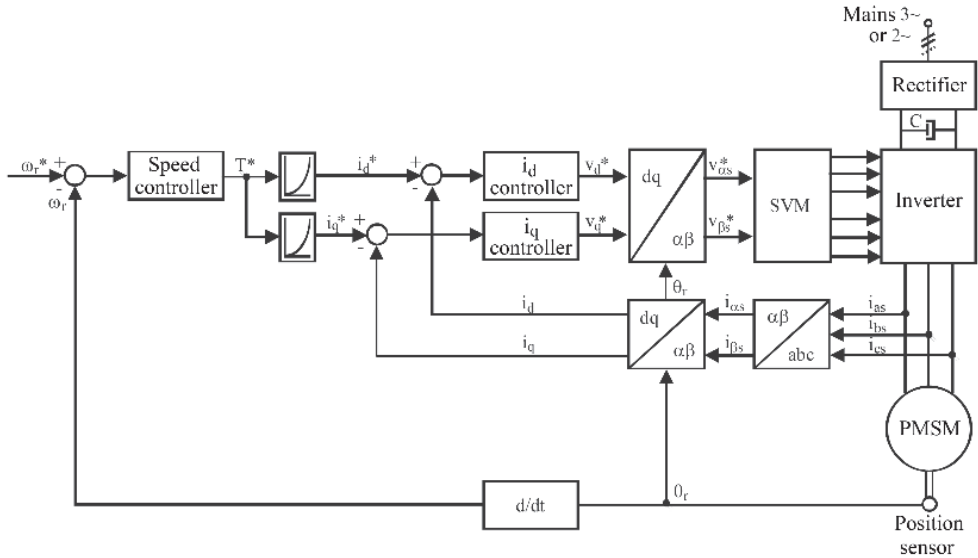


Fig. 6.1 General block diagram of a PMSM field-oriented vector control system.

In the proposed control system, all the three motor phase currents are measured. Another variants would be to measure only two currents or the reconstruction of the motor currents from the value of the current in the DC voltage circuit. In general, in the case of field-oriented vector control systems, for applications within powers ranges up to 1.2 kW, a position transducer with high resolution is needed, even in the case of using two sensors. Hall type sensors are providing good performances, in general.

For the field-oriented vector control system implementation, a relatively high volume of computation is required, therefore, the use of the 16 [bit] microcontrollers or digital signal processors is required. This adjustment method is applied in industry to a large number of electric drives, ensuring a fast dynamic response.

In general, the tendency for the PMSMs control systems, in applications within a power range up to 1.2 kW, is to eliminate the motion sensors, so that the rotor position and speed are estimated from the measured electrical quantities (currents and stator voltage).

The advantages of eliminating the motion sensors would be:

- the costs reduction of the control system (in the case of household applications, in general, only the current sensors are used, the voltage being calculated using the continuous voltage in the intermediate circuit of the inverter, and the use of a mathematical model for modeling non-linearities of the inverter and the dead-time);
- the reduction of the control system weight, eliminating the necessary wiring between the control system and the motion sensors;
- the elimination of the electromagnetic disturbances that may appear in the case of motion sensors;

- the elimination of the mechanical problems that may arise in positioning the sensors of absolute position value;
- the elimination of the economic problems that may occur in the chain of procurement-storage-assembly-maintenance of motion sensors as an additional benchmark that intervenes in bad analysis of the control systems with PMSMs.

The problems that may arise when estimating the rotor position and the speed, respectively, from the measured electrical quantities (the stator currents and voltages) are the following:

- the determination of the initial position of the rotor when starting;
- the estimation of the rotor position and speed at low speeds;
- the influence of the PMSM parameters in determining the respective position of the speed.

The methods based on [1] are generally used to estimate the rotor position and speed from the stator currents and voltages of the PMSMs:

- calculation of the motion induced voltage;
- calculation of the total magnetic flux;
- calculation of the stator inductance;
- injection of high frequency signals.

In general, to determine the rotor position and the speed, respectively, from the measured currents stator voltages, respectively, estimators are used. By using the mathematical model in the stator coordinates or the orthogonal mathematical model in the stator or rotor reference frame, they can estimate the following:

- the induced electric voltage - which is dependent on the rotor position and the rotational speed;
- the total magnetic flux - dependent on the rotor position;
- the stator inductance - dependent on the rotor position;
- the rotor position by injecting high frequency signals.

It can be seen from the above that the estimated electrical quantities are, in general, difficult to be measured and require additional costs.

In general, the estimators can be classified in [2]:

- estimators without reaction, that later will be called estimators and which for the determination of the aforementioned quantities are using only the mathematical model of the PMSM;
- asymptotic or reaction estimators, that will later be called observers; in the case of observers, the mathematical model of the PMSM has the same inputs (e.g. voltages) as the physical system, and the outputs (e.g. currents) of the system are compared with the measured quantities of the physical system, resulting thus resulting in an

estimation error that is used as a reaction in the mathematical model to correct the estimated quantities. Using this method, a faster convergence and greater robustness in parameter estimation can be achieved.

A classification of the methods for estimating the rotor position and speed using observers would be as follows [2]:

- the classical method of using the observers;
- the predictive observers;
- the Kalman filter;
- the phase mounted observers;
- the observers using the extended model of the motion induced voltage;
- the sliding mode observers;
- the adaptive observers.

Finally, it can be said that, for the control systems using PMSMs, there are different solutions to estimate the rotor position and the rotor speed. Unfortunately, these solutions are not widely applied in practice. Currently, there is a growing interest in the development of PMSM control systems without motion sensors, due to the evolution of prices for the microcontrollers and digital signal processors.

This study **proposes two novel control methods, developed by the team within the Electrical Engineering Department from UPT, which are next presented.**

## 6.2 Novel Method for Flux Weakening Control of PMSMs

### 6.2.1 Introduction

Many PMSM control methods able to **generate the d and q axes reference currents** in the constant torque area and in the flux-weakening area have been investigated so far in the literature (e.g. [3], [4], [5], [6], [7], [8], [9], [10], [11], [12], [13]). In [4] and [5], the mathematical model of the PMSM is used to generate the  $d$ -axis reference current, which is sensitive to the motor parameters variation (due to the temperature and the saturation effect). On the other hand, the flux-weakening methods proposed in [6], [7], [8], [9] are not parameters sensitive. In [6], the  $d$ -axis current is adjusted according to the current error in the  $q$ -axis. In [7], the  $q$ -axis voltage error is used to adjust the  $d$ -axis current and in [8] the voltage error is used to adjust the  $d$ -axis and  $q$ -axis currents. A voltage control method is proposed in [9], providing the  $d$ -axis current. In [10], [11], [12], [13] a look-up table method is presented, but it is motor parameters dependent. Different methods of carrier-based pulse width modulation (PWM) in overmodulation region are investigated in [14] and [15].

The method proposed in this paragraph (see Fig. 6.2), starting with the mathematical model of the PMSM (with salient-pole or nonsalient-pole) in pu, is used to compute the optimal reference currents on the  $d$  and  $q$ -axes, in the constant torque region and in the

field weakening region. The existing constraints for the operation in the field weakening region are the VSI maximum output voltage and current or the maximum permitted current of the PMSM [16], [17].

By using the overmodulation method, the capacity of the VSI is used efficiently and the dynamic and steady-state control system performances would be improved because of the lower order harmonics and of the reduced switching losses.

The proposed control method presents the following advantages:

- the control of the motor is simple; it does not need any look-up tables for the  $d$ - and  $q$ -axis reference currents;
- the direct limitation of the maximum  $q$ -axis current for the whole OM speed range;
- the flux-weakening area is well exploited;
- the control stability in the overmodulation region.

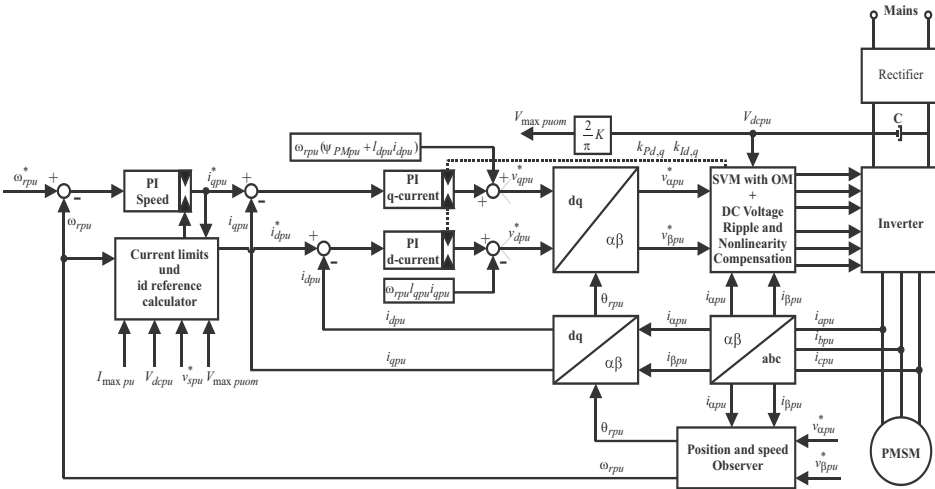


Fig. 6.2 Block diagram of the proposed vector control.

## 6.2.2 System Limitation

### 6.2.2.1 Dynamic model of PMSM

The PMSM mathematical model in p.u., in  $d$ - $q$  rotor reference frame, can be written as follows (see chapter 5):

$$\begin{bmatrix} v_{dpu} \\ v_{qpu} \end{bmatrix} = \begin{bmatrix} r_{pu} + sl_{dpu} & -\omega_{rpm}l_{qpu} \\ \omega_{rpm}l_{dpu} & r_{pu} + sl_{qpu} \end{bmatrix} \begin{bmatrix} i_{dpu} \\ i_{qpu} \end{bmatrix} + \begin{bmatrix} 0 \\ \omega_{rpm}\Psi_{PMpu} \end{bmatrix} \quad (6.1)$$

$$t_{dqelmpu} = \Psi_{PMpu}i_{qpu} + (l_{dpu} - l_{qpu})i_{qpu}i_{dpu} \quad (6.2)$$

where:  $\omega_{rpu}$  is the electrical angular velocity in p.u.,  $i_{dpu}, i_{qpu}$  are the armature currents in p.u. on the  $d$  and  $q$  axes,  $v_{dpu}, v_{qpu}$  are the terminal voltages in p.u. on the  $d$  and  $q$  axes,  $r_{pu}$  is the armature resistance in p.u.,  $l_{dpu}, l_{qpu}$  are the  $d$  and  $q$  axes inductances in p.u. on the  $d$  and  $q$  axes,  $\psi_{pmpu}$  is the permanent magnet flux linkage,  $t_{dqelmpu}$  is the developed electric torque in p.u. and  $s$  is the differential operator in p.u..

In the case of **nonsalient-pole PMSM**, the relationship between the inductances on the  $d$  and  $q$  axes is  $l_{dpu} = l_{qpu}$ , while in the case of **salient-pole PMSM**, the relationship is  $l_{dpu} \neq l_{qpu}$ .

### 6.2.2.2 Voltage and current limitation

In this study, all variables are in p.u..

In order to do not exceed the inverter maximum current, the PMSM maximum current must be restricted by limiting the  $q$ -axis current, which is the torque producing component, while the  $d$ -axis current must be unaffected. Regarding the maximum voltage, this is dependent on the inverter DC-link voltage. Thus, the limitation conditions for the maximum current and voltage are:

$$i_{qpu} \leq \sqrt{I_{\max pu}^2 - i_{dpu}^2} \quad (6.3)$$

$$\sqrt{v_{dpu}^2 + v_{qpu}^2} \leq V_{\max pu} \quad (6.4)$$

where:  $V_{\max pu}$  is the maximum voltage magnitude in p.u.,  $I_{\max pu}$  is the maximum current magnitude in p.u.,  $i_{dpu}, i_{qpu}$  are the armature currents in p.u. on the  $d$  and  $q$  axes and  $v_{dpu}, v_{qpu}$  are the terminal voltages in p.u. on the  $d$  and  $q$  axes.

### 6.2.2.3 Operating conditions of PMSM

The analysis of the PMSM in different operation regions could be done using the circle diagram in the  $I_d$ - $I_q$  plane. Assuming that the stator resistance of the PMSM is neglected, the current limit in the  $I_d$ - $I_q$  plane is represented by a circle, with its center in the origin, while the voltage limit in the  $I_d$ - $I_q$  plane is an ellipse, with the center in the point of  $(-i_{carpu}$  (F, or U), 0) coordinates (see Fig. 6.3).

In the constant torque region, the  $d$ -axis reference current in p.u. is generated using the maximum torque-per-ampere control method (MTPA) (see relationship (6.5)). In this case, the operating points are on the curve AOJ or on the curve MOT (see Fig. 6.3).

In the flux-weakening there are two operating regions [3] (see Fig. 6.3):

- **the flux-weakening region I**, where the operation is limited by  $V_{\max pu}$  and  $I_{\max pu}$ , (area OACFHI in Fig. 6.3.a, or OMQT in Fig. 6.3.b);

- the flux-weakening region II, where the operation is limited by  $V_{maxpu}$  (CFH area in Fig. 6.3.a)

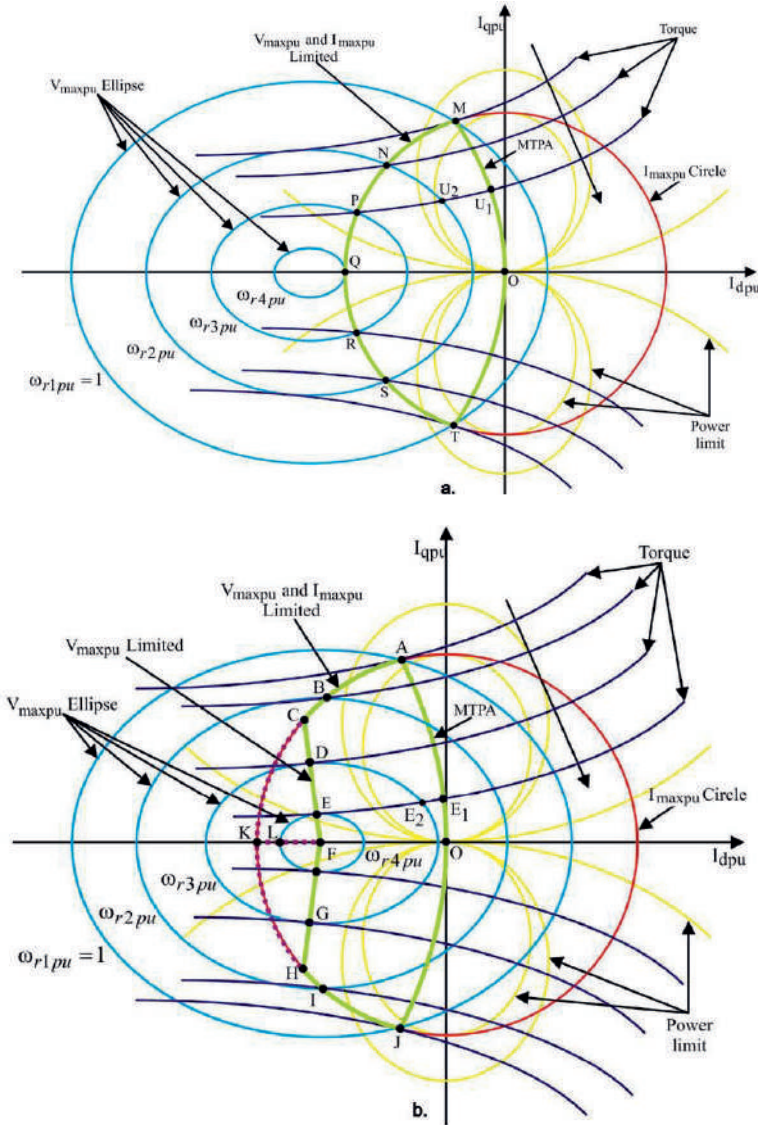


Fig. 6.3 Cycle diagrams of PMSM drive system.

The operation of the PMSM drive system in the flux-weakening region II is possible only if the current characteristic  $i_{carpu} = (\psi_{PMpu}/I_{dpu})$  is less than  $I_{maxpu}$  (the center of the voltage ellipse (F in Fig. 6.3.a) is inside of the current limit). In this case, theoretically, there is no speed limit and the control needs a maximum torque per voltage control strategy. An example of flux-weakening control trajectory in region II is presented in Fig. 6.3.a, line CFH.

### 6.2.2.4 Current reference calculator

The proposed current reference calculator is presented in Fig. 6.4 and, as it can be seen, the output of the PI speed controller is the amplitude of the  $q$ -axis current in p.u. ( $i_{qpu}^*$ ). Based on the speed region (e.g. on either the constant-torque region or the flux-weakening region) and on ( $i_{qpu}^*$ ), the  $d$ -axis current and the limit for the  $q$ -axis current can be determined.

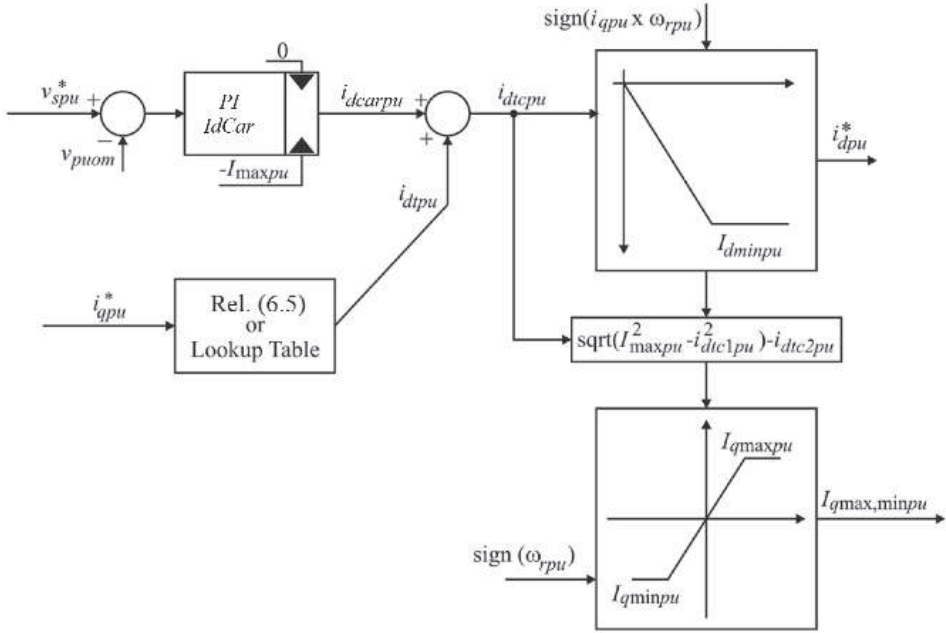


Fig. 6.4 Block diagram of the proposed control method.

In the constant-torque region, the maximum torque-per-ampere (MTPA) control method is used and, thus, the  $d$ -axis reference current in p.u. can be computed as following:

$$i_{dpu}^* = -\frac{\Psi_{PMpu}}{2(l_{dpu} - l_{qpu})} - \sqrt{\left(\frac{\Psi_{PMpu}}{2(l_{dpu} - l_{qpu})}\right)^2 + i_{qpu}^{*2}} \quad (6.5)$$

In the case of nonsalient-pole PMSM, the  $d$ -axis reference current is:

$$i_{dpu}^* = 0 \quad (6.6)$$

The limit for the  $q$ -axis reference current is:

$$i_{qpu}^* = \sqrt{I_{maxpu}^{*2} - i_{dpu}^{*2}} \quad (6.7)$$



The MTPA control trajectory is implemented by a lookup table or it can be calculated using the relationship (6.8) or (6.9).

In the flux-weakening region I, the  $d$ -axis reference current in p.u. is computed either by using the relationship ( $r_{pu} = 0$ ):

$$i_{dpu}^* = -\frac{\psi_{PMpu}}{l_{dpu}} + \frac{1}{l_{dpu}} \sqrt{\left(\frac{V_{\max pu}}{\omega_{rpu}}\right)^2 - l_{qpu}^2 i_{qpu}^{*2}} \quad (6.8)$$

or, in the case of nonsalient-pole PMSM, by using the following relationship ( $r_{pu} = 0$ ):

$$i_{dpu}^* = -\frac{\psi_{PMpu}}{l_{dpu}} + \sqrt{\left(\frac{V_{\max pu}}{l_{dpu} \omega_{rpu}}\right)^2 - i_{qpu}^{*2}} \quad (6.9)$$

while, the limit for the  $q$ -axis reference current, in the flux-weakening region I, is using the same relationship (6.7).

In the flux-weakening region II, the  $d$ -axis current reference in p.u. is computed either by using the relationship ( $r_{pu} = 0$ ):

$$i_{dpu}^* = -\frac{\psi_{PMpu}}{4(l_{dpu} - l_{qpu})l_{dpu}} \left( 4l_{dpu} - 3l_{qpu} - \sqrt{l_{qpu}^2 + \frac{8V_{\max pu}^2 (l_{dpu} - l_{qpu})^2}{\omega_{rpu}^2 \psi_{PMpu}^2}} \right) \quad (6.10)$$

or, in the case of nonsalient-pole PMSM, by using the following relationship:

$$i_{dpu}^* = -\frac{\psi_{PMpu}}{l_{dpu}} \quad (6.11)$$

The  $q$ -axis reference current in flux-weakening region II is provided by the relationship ( $r_{pu}=0$ ):

$$i_{qpu}^* = \pm \frac{1}{l_{qpu}} \sqrt{\left(\frac{V_{\max pu}}{\omega_{rpu}}\right)^2 - (l_{dpu} i_{dpu}^* + \psi_{PMpu})^2} \quad (6.12)$$

**For even more accurate relationships of the reference currents on the  $d$  and  $q$ -axes, the saturation and the cross-saturation must be also considered.**

### 6.2.3 Description of the proposed control method

The proposed control method, for wide speed range PMSM drives, can be easily integrated in a well-known vector control (see Fig. 6.3), where the currents on the  $d$ -axis and the  $q$ -axis are the main control variables.

The block named “**Current limit and  $i_d$  reference calculator**” (see Fig. 6.3 and Fig. 6.4) is providing the limits of the speed controller and the optimum value for the  $d$ -axis reference current in a wide speed range. This control method is suitable for the PWM-VSI working in overmodulation region. For the constant torque region, the “**PIIdCor**” controller is not active (the positive limit of the controller is zero) and the  $d$ -axis reference current is calculated using the relation (6.8) or (6.9) (see Fig. 6.3), by taking into account the required value for the  $q$ -axis current. In the flux-weakening area, the  $d$ -axis reference current is provided by the PI voltage controller, named “**PIIdCor**”, whose limits being  $(0, -I_{\max pu})$ . In conclusion, with the proposed control method, a fast dynamic response and a smooth transition between the two operating regions can be achieved. Thus, the minimum  $d$ -axis reference current can be calculated using the following relationship:

$$i_{d \min pu} = \begin{cases} -I_{\max pu}, & \text{if } i_{qpu} \omega_{rpu} < 0 \\ -I_{\max pu}, & \text{if } i_{qpu} \omega_{rpu} \geq 0 \text{ and } I_{carpu} \geq I_{\max pu} \\ (6.10) \text{ or } (6.11), & \text{if } i_{qpu} \omega_{rpu} \geq 0 \text{ and } I_{carpu} < I_{\max pu} \end{cases} \quad (6.13)$$

If  $I_{carpu} = \Psi_{PMpu} / I_{dpu} > I_{\max pu}$ , the PMSM operates in the flux-weakening region I (see Fig. 6.3.b) and the maximum  $d$ -axis current and the maximum  $q$ -axis current can be computed in the motor mode and generator mode. But, if  $I_{\max pu} > I_{carpu}$ , the PMSM operates in the flux-weakening region I and the flux-weakening region II (see Fig. 6.3.a) and the limit for the  $d$ -axis current can be computed using the relationship (6.10) or (6.11) or using a look-up table that associates the maximum  $d$ -axis current with the actual motor speed. The values of the look-up table can be evaluated either analytically (6.13) or experimentally, when the model is not accurately known.

If  $i_{dtcpu} < I_{d \min pu}$ , the  $d$ -axis current is limited at this value, and the  $q$ -axis current will be reduced using the relationship:

$$I_{q \min, \max pu} = \text{sign}(\omega_{rpu}) \cdot \left( \pm \sqrt{I_{\max pu}^2 - i_{dtc1pu}^2} - i_{dtc2pu} \right) \quad (6.14)$$

where  $i_{dtc1pu}$  and  $i_{dtc2pu}$  can be computed using the following relationship:

$$i_{dtc1pu} = \begin{cases} |i_{dtcpu}|, & \text{if } i_{dtcpu} \geq I_{d \min pu} \text{ - region I} \\ I_{d \min pu}, & \text{if } i_{dtcpu} < I_{d \min pu} \text{ - region II} \end{cases} \quad (6.15)$$

$$i_{dtc2pu} = \begin{cases} 0, & \text{if } i_{dtcpu} \geq I_{d \min pu} \text{ - region I} \\ |i_{dtcpu}| - I_{d \min pu}, & \text{if } i_{dtcpu} < I_{d \min pu} \text{ - region II} \end{cases}$$

The degree of the overmodulation can be determined by the relationship:

$$V_{\max puom} = \frac{2}{\pi} K V_{dcpu} \quad (6.16)$$

It can be concluded that the d-axis reference current and the q-axis current limit are influenced by the modulation index and that the proposed control method is relatively simple to be implemented.

### 6.2.4 Carrier-based PWM-VSI Overmodulation Strategy

The PWM-VSI goes into the overmodulation region when the reference voltage is located outside the inner circle. The overmodulation region is subdivided into two regions: the overmodulation region I, where the overmodulation factor  $K$  is between  $0.907 \leq K < 0.952$  (see Fig. 6.5.a) and the overmodulation region II, where the overmodulation factor  $K$  is between  $0.951 \leq K \leq 1.00$  (see Fig. 6.5.b) [14]. In the overmodulation region I, the magnitude of the reference voltage vector changes, while the angle of the reference voltage vector does not change. In the overmodulation region II, both the magnitude and the angle of the reference voltage vector are manipulated by the preprocessor.

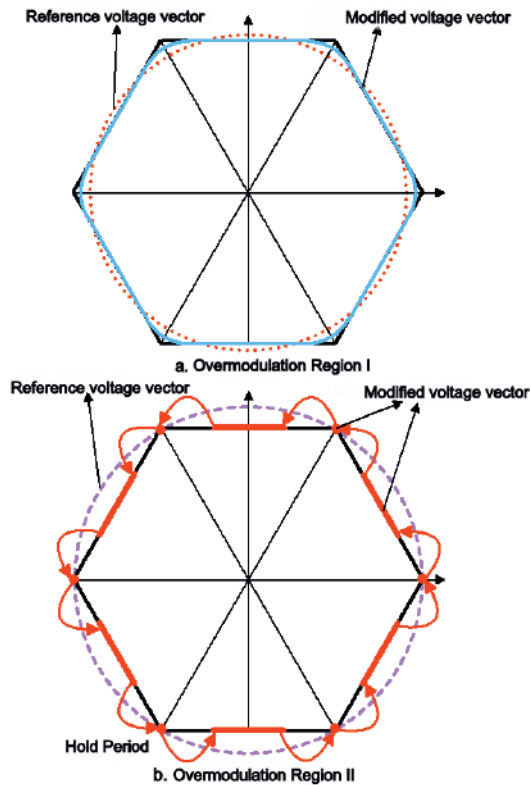


Fig. 6.5 Trajectory of the voltage vector in: a) Overmodulation Region I; b) Overmodulation Region II.

### 6.2.5 Experimental results obtained by implementing the proposed control method

The experimental test results of the sensorless variant of the proposed control method on a PMSM drive is presented in Fig. 6.3. The motor control method was implemented using a 16 [bit] microcontroller on a 1 kW PMSM and the performance of the system was tested with a dynamometer. To simulate the same inertia as for the real application of the drive system an additional weight is added to the motor shaft. To verify the advantages of the proposed control method using a PWM-VSI operating in the overmodulation region, different acceleration, braking and steady-state tests were performed. The experimental results both in constant-torque region and flux-weakening region, are shown in Fig. 6.6, Fig. 6.7, Fig. 6.8 and Fig. 6.9.

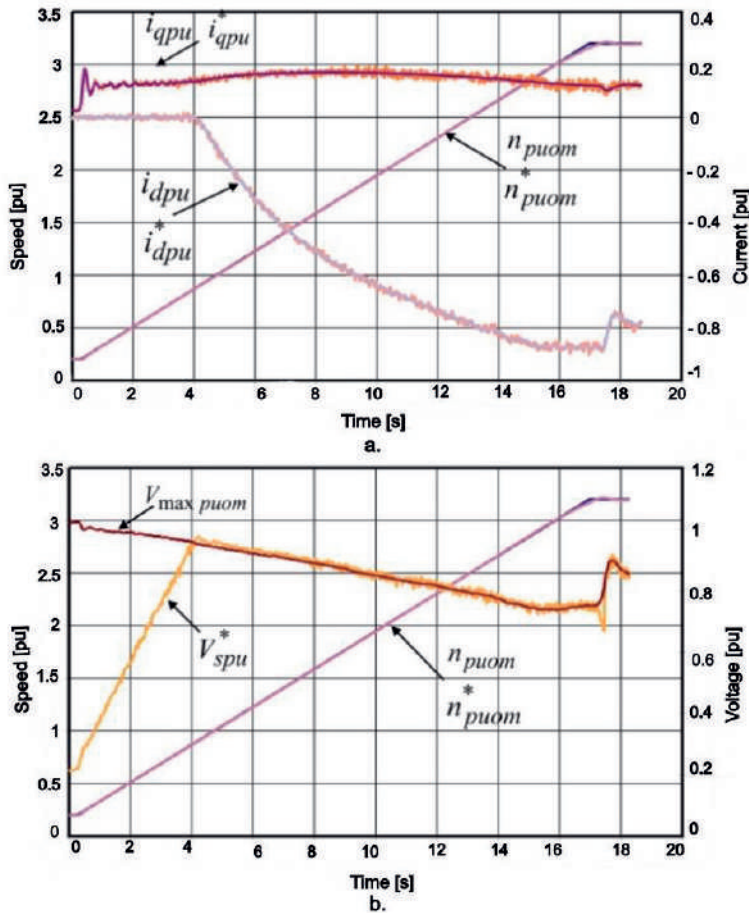


Fig. 6.6 Acceleration with 0.03 p.u. gradient: a) the reference and actual speed ( $n_{puom}^*$ ,  $n_{puom}$ ), the reference and actual  $d$ -axis current ( $i_{dpu}^*$ ,  $i_{dpu}$ ) and the reference and actual  $q$ -axis current ( $i_{qpu}^*$ ,  $i_{qpu}$ ), b) the reference and actual speed ( $n_{puom}^*$ ,  $n_{puom}$ ), the regulated stator voltage ( $V_{spu}^*$ ) and the maximum terminal voltage ( $V_{max\ puom}$ ).

**Acceleration performances** are shown in the Fig. 6.6. Fig. 6.6.a shows the reference currents on the  $d$  and  $q$ -axes, generated by the proposed control method, with 0.03 p.u. acceleration gradient, in the constant-torque region and also in the field weakening region I and II. Fig. 6.6.b shows the armature voltage reference  $V_{spu}^*$  and the inverter maximum terminal voltage ( $V_{maxpu}$ ).

Because the inverter has no regenerative unit, in the case of regenerative braking, the DC-link voltage is limited by using the proposed control method, if the regenerative energy is supposed to be dissipated in the PMSM.

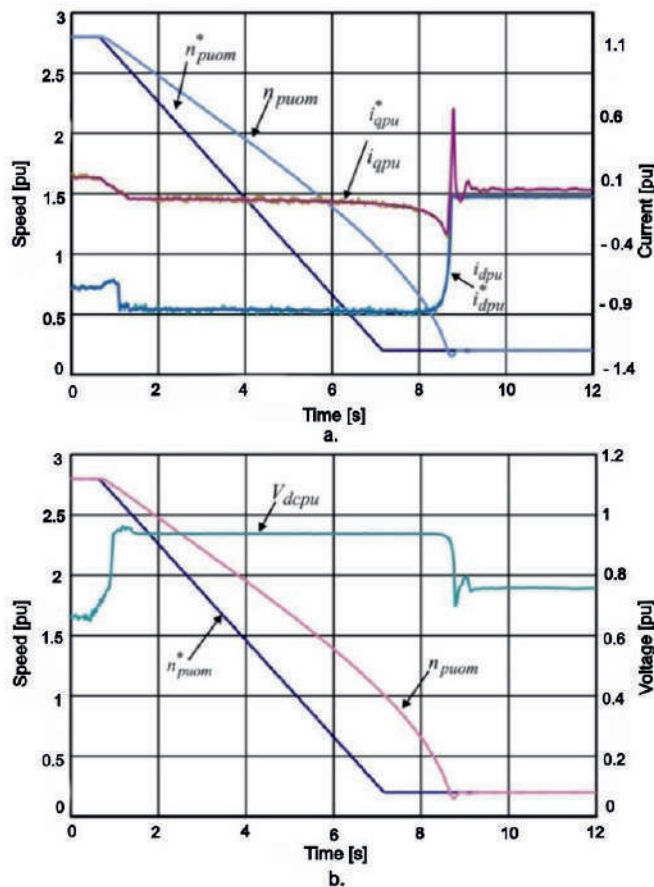


Fig. 6.7 Braking operation gradient 0.02 p.u.: a) the reference and actual speed ( $n_{puom}^*$ ,  $n_{puom}$ ), the reference and actual d-axis current ( $i_{dpu}^*$ ,  $i_{dpu}$ ) and the reference and actual q-axis current ( $i_{apu}^*$ ,  $i_{apu}$ ), b) the reference and actual speed ( $n_{puom}^*$ ,  $n_{puom}$ ), the regulated DC link voltage ( $V_{dcpu}$ ).

If the deceleration gradient is too big, the rotor speed of the PMSM is not capable of following the reference speed. In this case, **the deceleration performance** of the proposed control method is shown in Fig. 6.7.

**The regenerative braking performance** is limited by the storage capability of the PMSMS stator resistance where the regenerative energy is dissipated. Fig. 6.7.a shows the generated reference current on the  $d$  and  $q$ -axes in the regenerative mode. While the  $d$ -axis reference current is kept at its maximum value, the  $q$ -axis reference current is reduced, due to the DC - link voltage limitation ( $V_{dcpu}$ ).

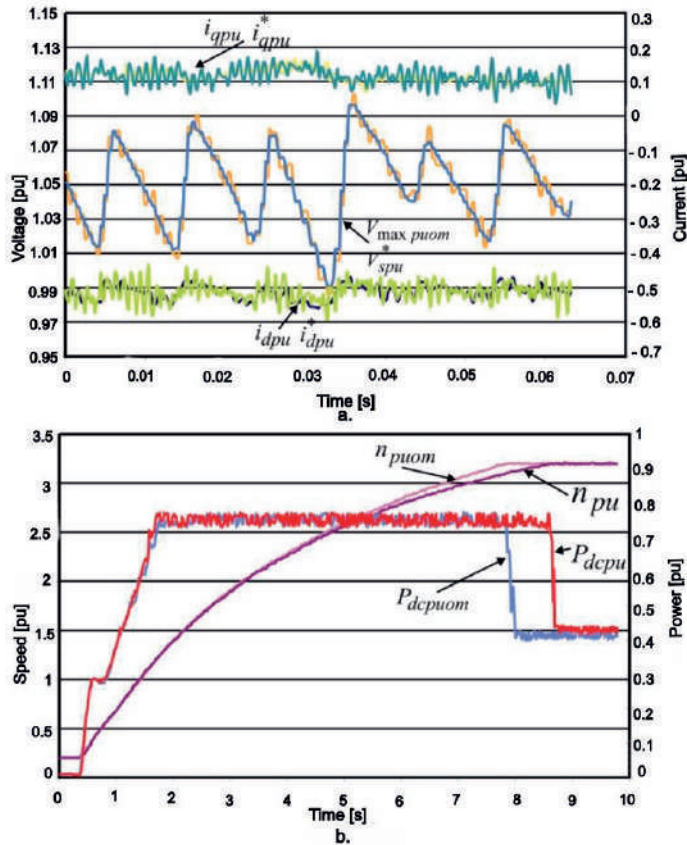


Fig. 6.8 Motor overmodulation performances: a) the  $V_{max, puom}$  and  $V_{spu}$ , the reference and actual  $d$ -axis current ( $i_{dpu}^*$ ,  $i_{dpu}$ ) and the reference and actual  $q$ -axis current ( $i_{qpu}^*$ ,  $i_{qpu}$ ), b) the reference and actual motor speed ( $n_{puom}$ ,  $n_{pu}$ ) and the regulated DC link power ( $P_{dcpuom}$ ,  $P_{dcpu}$ ).

The Fig. 6.8.a shows **the performances of the current controllers in the overmodulation region and the maximum generated voltage according to the DC-link voltage in the case of using the proposed control method. The benefits of operation in overmodulation region** are shown in Fig. 6.8.b. In this case, the motor is accelerated using the VSI in overmodulation region ( $n_{puom}$ ,  $P_{dcpuom}$ ) and then using the VSI in the linear region ( $n_{pu}$ ,  $P_{dcpu}$ ) under the same power limitation (see Fig. 6.8.b). A better acceleration performance in the case of the VSI with the overmodulation region is observed.

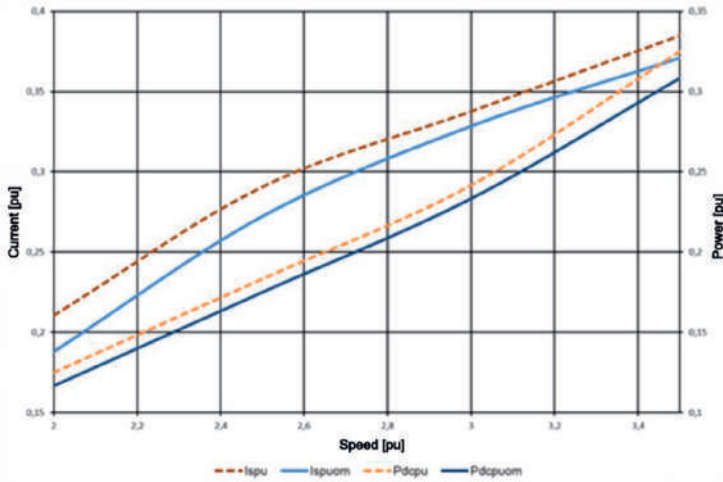


Fig. 6.9 With or without overmodulation motor performances in steady-state: the ( $i_{spuom}$ ,  $i_{spu}$ ) and the DC link power ( $P_{dcpuom}$ ,  $P_{dcpu}$ ) versus motor speed.

**The advantages of the operating in the overmodulation region in steady-state** are presented in Fig. 6.9. The experimental results show that the required motor current ( $i_{spuom}$ ) and the power consumption ( $P_{dcpuom}$ ) in overmodulation region are lower than the required motor current ( $i_{spu}$ ) and the power consumption ( $P_{dcpu}$ ) in linear modulation region for the same load value. It is, therefore, confirmed that the operation in overmodulation region is more effective. **Moreover, by using the proposed control method in the overmodulation region, the stability of the system is not compromised.**

The carrier-based PWM voltage during overmodulation is shown in Fig. 6.10, for the case of  $K = 0.98$  (see (6.19)).

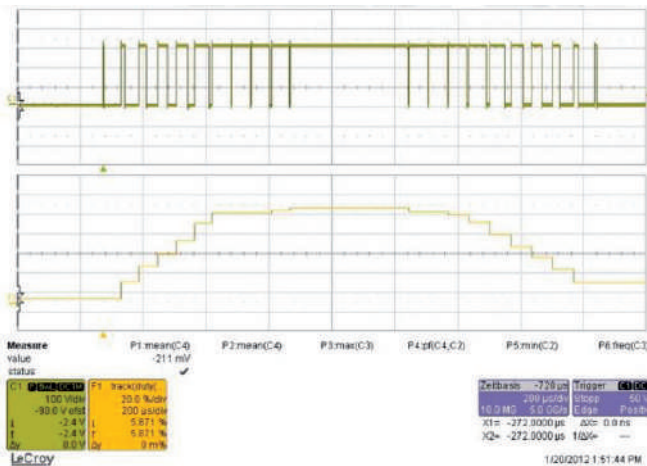


Fig. 6.10 Carrier-based PWM voltage operating in the overmodulation region.

## 6.3 Optimal Current Referencers for Four-Quadrant Operation of PMSM Drive Systems

### 6.3.1 Introduction

An accurate field-oriented vector control is considered to be that control appropriate for the operating conditions and the type of the PMSM used. The control supposes the presence of current sensors and of the high-resolution position sensor such as a rotary encoder or a resolver, which has a lot of disadvantages, such as cost, machine size, reliability and noise immunity. Therefore, an intense effort has been made in discovering new techniques for the rotor position sensor elimination to improve thus the reliability and to reduce the cost of the drive.

There are many position sensorless drive systems for synchronous motors applications in the today literature, mentioning in here only few [18] ÷ [47]. The need of the current sensors, in order to estimate the rotor position and speed, is crucial for a position sensorless drive system. In [18] ÷ [31], the proposed sensorless drive system uses high-resolution position sensors. In [32] ÷ [47], the currents are estimated using the motor mathematical model and, thus, become inaccurate with parameter drifts due to temperature and saturation effects.

In this paragraph, an improved field-oriented control for the PMSM drives, where the classical current sensors are eliminated and only two Hall-effect position sensors are used instead of a high-resolution position sensor, is presented. The high performant current control is achieved by use of a state observer for the currents' estimation. Moreover, a novel control method to generate the optimal d- and q-axes current references in different operating regions and the limits of the speed controller ( $I_{spu\ max}$ ,  $I_{spu\ min}$ ) are proposed in here.

The proposed control scheme may be used for traction applications and home appliances.

### 6.3.2 Drive system design

#### 6.3.2.1 Speed control system description

The block diagram of the proposed speed control PMSM drive is presented in Fig. 6.11. This novel control method uses the PMSM mathematical model in p.u.. A 16 [bit] microcontroller was used for its implementation. The speed control uses a PI controller, whose output represents the armature current ( $i_{spu}^*$ ).





where:  $\omega_{rpu}$  is the electrical angular velocity in p.u.,  $i_{dpu}$ ,  $i_{qpu}$ , are the armature currents on the  $d$ - and  $q$ -axes in p.u.,  $u_{dpu}$ ,  $u_{qpu}$ , are the  $d$ - and  $q$ -axes terminal voltages in p.u.,  $r_{pu}$  is the armature resistance in p.u.,  $l_{dpu}$ , are the  $d$ - and  $q$ -axes inductances in p.u. and  $\psi_{PMpu}$  is the permanent magnet flux linkage. In the case of the nonsalient-pole PMSM, the relationship between the  $d$ - and  $q$ -axes inductances is  $l_{dpu} = l_{qpu}$ , while in the case of salient-pole PMSM, the relationship between the  $d$ - and  $q$ -axes inductances is  $l_{dpu} \neq l_{qpu}$ .

### 6.3.2.3 Current observer

Assuming an ideal inverter, i.e. the output power of the inverter is equal with the input power of the inverter, the following relationship can be written:

$$P_{dcpu} = V_{dcpu} I_{dcpu} \approx \frac{3}{2} P_{dqpu} = \frac{3}{2} (v_{dpu} i_{dpu} + v_{qpu} i_{qpu}) \quad (6.18)$$

where  $V_{dcpu}$  is the DC-link voltage in pu and  $I_{dcpu}$  is the DC - link current in pu. Thus, the relationship (6.18) can be rewritten as:

$$I_{dcpu} = C i_{pu} \quad (6.19)$$

where:

$$C = \frac{2}{3} \begin{bmatrix} v_{dpu} & v_{qpu} \\ V_{dcpu} & V_{qcpu} \end{bmatrix} \quad (6.20)$$

Considering the relationships (6.17), (6.18), **a typical Luenberger state observer** can be built:

$$\frac{d\hat{i}_{pu}}{dt_b} = A\hat{i}_{pu} + Bv_{pu} + K_{PMpu} + L(I_{dcpu} - \hat{I}_{dcpu}) \quad (6.21)$$

where:  $\hat{i}_{pu}$  is the matrix of the estimated armature currents in p.u. on the  $d$ - and  $q$ -axes,  $\hat{I}_{dcpu}$  is the estimated DC-link current and  $L$  is the observer gain matrix. The unknown observer gains of the matrix  $L$  ( $l_1$ ,  $l_2$ ) can be calculated using the relationship:

$$\left| sI - (A - LC^T) \right| = 0 \quad (6.22)$$

where:  $I$  is the identity matrix.

The characteristic equation (6.22) can be expressed as:

$$(s - p_1) \cdot (s - p_2) = s^2 + \alpha_1 s + \alpha_2 \quad (6.23)$$

where:  $p_{1,2}$  are the poles of characteristic equation.

The desired pole location are given by the relationship:

$$p_{1,2} = \sigma \pm j\omega_d = \xi\omega_n + j\omega_n\sqrt{1-\xi^2} \quad (6.24)$$

where:  $\xi$  is the damping ratio, and  $\omega_n$  is the natural frequency.

For determining the values for  $\xi$  and  $\omega_n$ , the desired values for the rise time, settling time and maximum overshoot to be chosen as following:

$$t_r = \frac{1.8}{\omega_n} \approx 0.6 \text{ s} \quad t_s = \frac{4.6}{\xi\omega_n} \approx 2.6 \text{ s} \quad M_p = e^{-\frac{\xi\pi}{\sqrt{1-\xi^2}}} \approx 10 \% \quad (6.25)$$

The coefficients of the gain matrix can be determined from the relationships (6.22) and (6.23). Finally, the estimated currents in p.u. on the  $d$ - and  $q$ -axes, using the state observer, can be calculated using the following discrete equations:

$$\begin{aligned} \hat{i}_{dpuk} = & \left(1 - \frac{r_{pu}}{l_{dpu}}t_b\right)\hat{i}_{dpuk-1} + \frac{l_{qpu}}{l_{dpu}}t_b\omega_{rpuk}\hat{i}_{qpuk-1} \\ & + \frac{t_b}{l_{dpu}}v_{dpuk} + l_1t_b\left(I_{dcpuk} - \hat{I}_{dcpuk}\right) \end{aligned} \quad (6.26)$$

$$\begin{aligned} \hat{i}_{qpuk} = & \left(1 - \frac{r_{pu}}{l_{qpu}}t_b\right)\hat{i}_{qpuk-1} - \frac{l_{dpu}}{l_{qpu}}t_b\omega_{rpuk}\hat{i}_{dpuk-1} \\ & - \frac{\psi_{PMpu}}{l_{qpu}}\omega_{rpuk} + \frac{t_b}{l_{qpu}}v_{qpuk} + l_1t_b\left(I_{dcpuk} - \hat{I}_{dcpuk}\right) \end{aligned} \quad (6.27)$$

where:  $t_b$  is the base time.

The DC-link current  $\hat{I}_{dcpu}$  is deduced from the estimated values of the armature currents on the  $d$ - and  $q$ -axes using the relation (6.18).

#### 6.3.2.4 Current reference calculator

In the block diagram from Fig. 6.11, the PI speed controller output represents the amplitude of the armature current in p.u. ( $i_{spu}^*$ ). Based on this value ( $i_{spu}^*$ ) and on the speed region (constant-torque or flux-weakening region), the current references on the  $d$ - and  $q$ -axes can be computed. In the constant-torque operating region, the  $d$ - and  $q$ -axes current references in p.u. are computed using the maximum torque-per-ampere control method and thus, yielding to:

$$i_{dpu}^* = -\frac{\psi_{PMpu}}{4(l_{dpu} - l_{qpu})} - \sqrt{\left(\frac{\psi_{PMpu}}{4(l_{dpu} - l_{qpu})}\right)^2 + \frac{i_{spu}^{*2}}{2}} \quad (6.28)$$

or, if

$$l_{dpu} = l_{qpu} : i_{dpu}^* = 0 \quad (6.29)$$

$$i_{qpu}^* = \sqrt{i_{spu}^{*2} - i_{dpu}^{*2}} \quad (6.30)$$

In the field-weakening operating region, the armature voltage and current in p.u. are limited by the inverter:

$$V_{spu} = \sqrt{V_{dpu}^2 + V_{qpu}^2} \leq V_{\max pu} \quad (6.31)$$

$$I_{spu} = \sqrt{I_{dpu}^2 + I_{qpu}^2} \leq I_{\max pu} \quad (6.32)$$

where:  $V_{\max pu}$  is the maximum voltage magnitude in p.u. and  $I_{\max pu}$  is the maximum current magnitude in p.u..

In the flux-weakening region, there are two operating regions [17]:

- **the flux-weakening region I**, where the operation is limited by  $V_{\max pu}$  and  $I_{\max pu}$ .
- **the flux-weakening region II**, where the operation is limited by the  $V_{\max pu}$ .

The operation of the PMSM drive system, in the flux-weakening operating region II, is possible only if  $l_{carpu} = \psi_{PMpu} / l_{dpu} < I_{\max pu}$ , meaning that the center of the voltage ellipse is inside of the current limit. In the flux-weakening operating region I, the  $d$ - and  $q$ -axes current references in p.u. can be calculated as follows:

$$i_{dpu}^* = -\frac{\psi_{PMpu} I_{dpu}}{4(l_{dpu}^2 - l_{qpu}^2)} - \sqrt{\left(\frac{\psi_{PMpu} I_{dpu}}{(l_{dpu}^2 - l_{qpu}^2)}\right)^2 - \frac{\psi_{PMpu}^2 - \left(\frac{V'_{\max pu}}{\omega_{rpu}}\right) + l_{qpu}^2 i_{spu}^{*2}}{(l_{dpu}^2 - l_{qpu}^2)}} \quad (6.33)$$

or, if ( $l_{dpu} = l_{qpu}$ ):

$$i_{dpu}^* = \frac{\psi_{PMpu}^2 - \left(\frac{V'_{\max pu}}{\omega_{rpu}}\right) + l_{qpu}^2 i_{spu}^{*2}}{2\psi_{PMpu} l_{dpu}} \quad (6.34)$$

$$i_{qpu}^* = \sqrt{i_{spu}^{*2} - i_{dpu}^{*2}} \quad (6.35)$$

In the flux-weakening operating region II, the current references in p.u., on the  $d$ - and  $q$ -axes, can be calculated using the following relationships:

$$i_{dpu}^* = -\frac{\psi_{PMpu}}{4(l_{dpu} - l_{qpu})l_{dpu}} \left( 4l_{dpu} - 3l_{qpu} - \sqrt{l_{qpu}^2 + \frac{8V_{\max pu}^2 (l_{dpu} - l_{qpu})^2}{\omega_{rpu}^2 \psi_{PMpu}^2}} \right) \quad (6.36)$$

or, if ( $l_{dpu} = l_{qpu}$ ):

$$i_{dpu}^* = -\frac{\psi_{PMpu}}{l_{dpu}} \quad (6.37)$$

$$i_{qpu}^* = \pm \frac{1}{l_{qpu}} \sqrt{\left( \frac{V'_{\max pu}}{\omega_{rpu}} \right)^2 - \left( l_{dpu} i_{dpu}^* + \psi_{PMpu} \right)^2} \quad (6.38)$$

In (6.33), (6.35), (6.36) and (6.38), the  $V'_{\max pu}$  can be computed as follows:

$$V'_{\max pu} = V_{\max pu} - r_{pu} I_{spu} \quad (6.39)$$

$$V_{\max pu}^2 = V_{\max pu}^2 - 2r_{pu} P_{dqpu} + r_{pu}^2 I_{spu}^2 \quad (6.40)$$

where:  $P_{dqpu}$  is the electrical output power of the inverter in p.u.

Taking into account the above considerations, many methods to generate the current references on the  $d$ - and  $q$ -axes in the different operating regions could be found [16], [17]. In here, the proposed control method, is capable to generate the current references on the  $d$ - and  $q$ -axes in the different operating regions and also the limits of the speed controller ( $I_{spu \max}$ ,  $I_{spu \min}$ ), for electric drive operation in all four quadrants (see Fig. 6.12). In the constant-torque operating region, the  $d$ -axis current reference is calculated using eq. (6.28), and the output of the **voltage PI controller, called "PI\_IdCor"**, is zero. In the flux-weakening operating region, the output of the **voltage PI controller, called "PI\_IdCor"**, is added to the  $d$ -axis current reference calculated using (6.28).

The inputs of the **voltage PI controller, called "PI\_IdCor"**, are  $V_{\max pu}$  and  $V_{spu}^*$ .

There are power converters that do not have any regenerative unit due to cost reasons. In this case, in the proposed control method, the voltage PI controller, called "PI\_SVCor", is designed to increase the  $d$ -axis current reference and decrease the  $q$ -axis reference current, only if  $V'_{dcipu} < V_{dcipu}$  (regenerative braking).  $V'_{dcipu}$  is the maximum allowed DC-link voltage.

### 6.3.2.5 Voltage reference calculator

In the rotor reference frame, the currents on the  $d$ - and  $q$ -axes become DC values in steady state and, therefore, two PI controllers can be used. **These PI controllers control the  $d$ - and  $q$ -axes independently, by decoupling the rotor cross coupling.** The block for

the voltage reference calculator is presented in Fig. 6.13, the values of  $I_{dpu}$ ,  $I_{qpu}$  inductances are experimentally established, considering the saturation effect. These values are then, implemented in a table as function of  $d$ - and  $q$ -axes current.

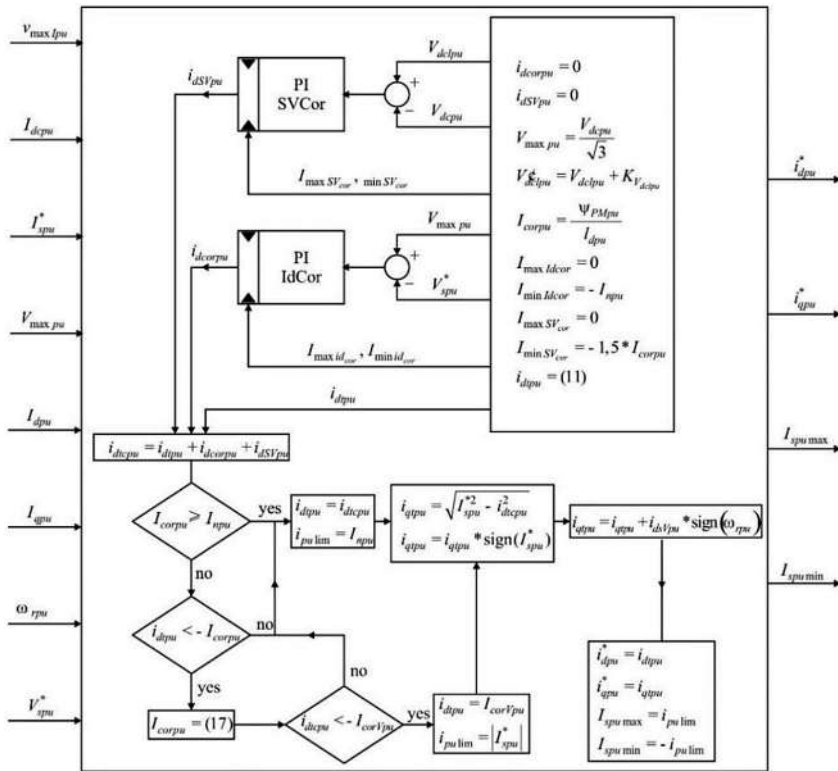


Fig. 6.12 Block diagram of the proposed current reference calculator.

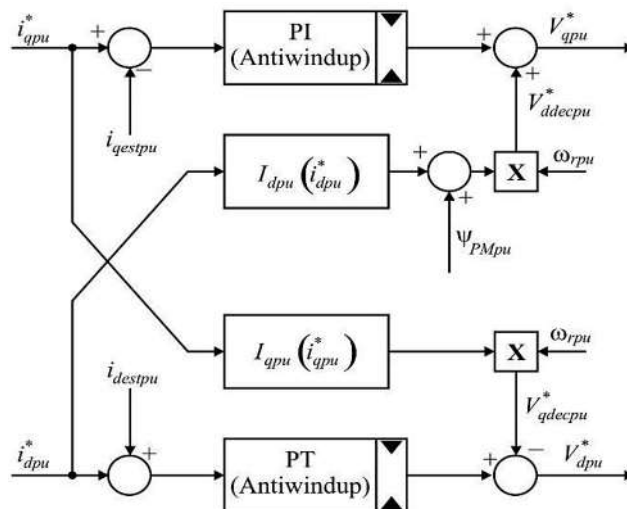


Fig. 6.13 Block diagram of the voltage reference calculator in rotor reference frame.

### 6.3.2.6 Compensation of the DC voltage ripples and of the inverter nonlinearities

The DC-link voltage is not constant. Its variation will cause variations in the stator voltage. A control method (in stator reference frame) to solve this issue is proposed in Fig. 6.14.

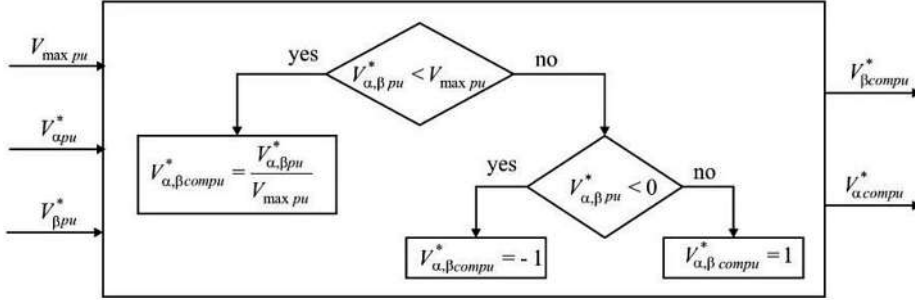


Fig. 6.14 DC-link voltage ripples compensation.

The inverter nonlinearities are caused by the dead-time and by the voltage drops on diodes and IGBTs. The voltage drops are compensated using the following relationships [22]:

$$\Delta u_{cna,b,cpu}^* = \begin{cases} -\frac{1}{T_c} \left( V_{dcpu} t_m - \frac{V_{dcpu}^2 C_T Z_b}{2i_{a,b,cpu}} \right), & i_{a,b,cpu} < -\frac{V_{dcpu} C_T Z_b}{t_m} \\ \frac{t_m^2}{2C_T Z_b T_c} i_{a,b,cpu}, & |i_{a,b,cpu}| < -\frac{V_{dcpu} C_T Z_b}{t_m} \\ \frac{1}{T_c} \left( V_{dcpu} t_m - \frac{V_{dcpu}^2 C_T Z_b}{2i_{a,b,cpu}} \right), & i_{a,b,cpu} > -\frac{V_{dcpu} C_T Z_b}{t_m} \end{cases} \quad (6.41)$$

where:  $\Delta u_{cna,b,cpu}^*$  is the corrected voltage for the phase  $a, b, c$  in p.u.,  $t_m$  is the dead-time,  $C_T$  is the capacity of IGBT and  $T_c$  is the SVM period.

### 6.3.2.7 Rotor position and speed estimation

For the PMSM drive system position and speed estimation, two Hall-effect sensors are used. Their resolution is only 90 electrical degrees. The signals measured by them are shown in Fig. 6.15.

The average speed between two Hall-effect sensor signals can be calculated with the following relationship:

$$\omega_{ravpu} = \omega_{rpu} = \omega_{rmpu} = \frac{f_{timer}}{2f_b V_{ctimer}} \quad (6.42)$$

where:  $f_{timer}$  is the timer frequency,  $V_{ctimer}$  is the counted value.

The rotor position can be estimated using the following relationship:

$$\theta_{rpuk} = \theta_{rpuk-1} + \omega_{rpm} t_s \quad (6.43)$$

where:  $t_s$  is the sampling time.

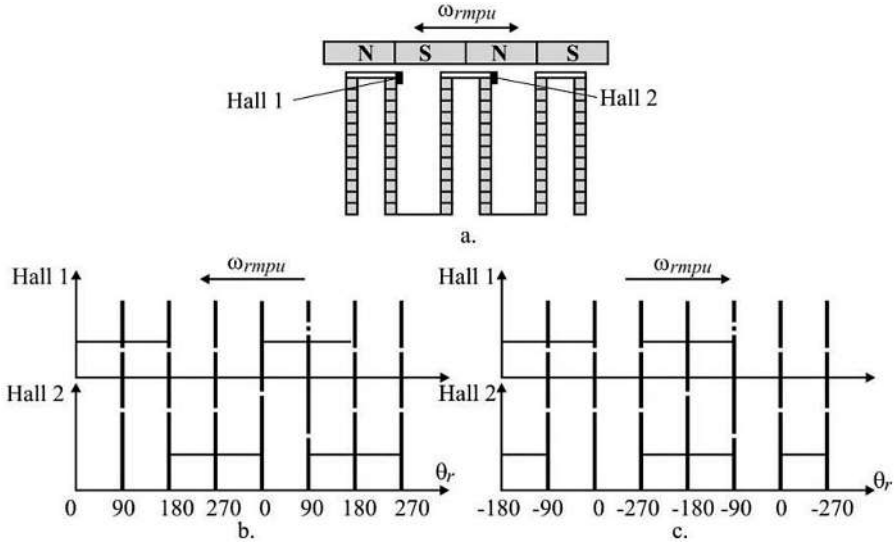


Fig. 6.15 Hall-effect position sensor signals.

Relationship (6.42) is valid only if the rotor speed is constant. In order to improve the estimated rotor position between the signals of two Hall-effect sensors, the rotor speed can be calculated with the following relation:

$$\omega_{rpmk} = \omega_{rpmk-1} + K_{cu} I_{spu} t_s \quad (6.44)$$

where:  $K_{cu}$  is a test value.

### 6.3.3 Experimental results of the proposed drive system of PMSMS

The proposed speed control drive system was implemented using a 16 [bit] microcontroller and a 2 kW PMSM motor. For the experimental tests, a dynamometer was used. Performances of the proposed control method in both the constant-torque and the flux-weakening regions are shown next.

The control system performances analysis in the field-weakening area is done by accelerating the motor from 560 rpm to 16400 rpm with a gradient of 460 rpm/s, while the torque load from the motor shaft is  $T_s = 0$  or  $T_s \neq 0$ .

For the control system performances presented in Fig. 6.16, the generation of the reference currents is done firstly from the PMSM parameters, while for the ones presented in Fig. 6.17 and Fig. 6.18, the reference currents are obtained from the variation of the reference voltage when the output of the speed controller is  $I_s^*$  and  $i_q^*$ , respectively.



As it can be observed, the speed dynamics are very good. The inverter used has no regenerative unit, but, despite this, the current references provided by the proposed control method are limiting the DC-link voltage in the case of regenerative braking.

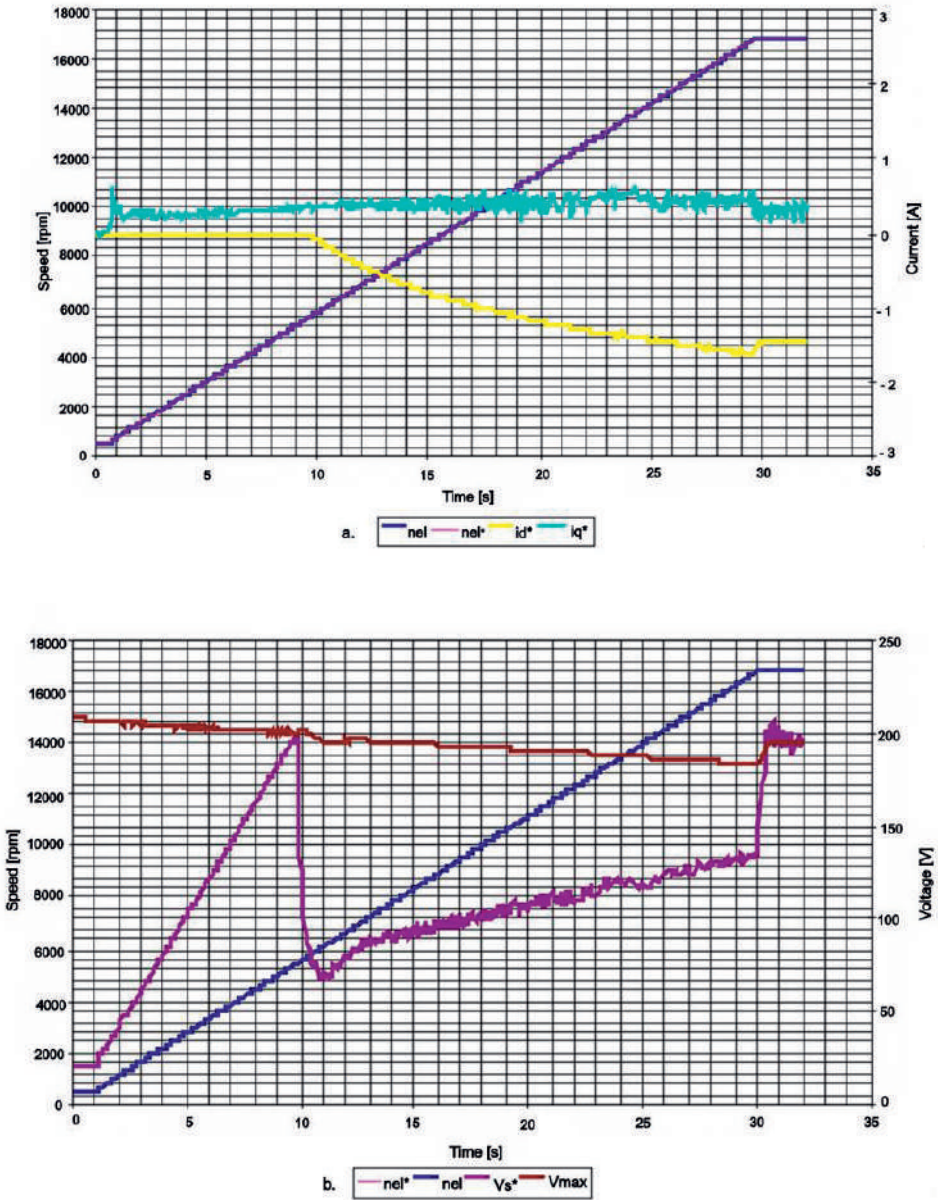


Fig. 6.16 Performances of the proposed speed control for the PMSM drive systems during acceleration when for generating the reference currents the PMSM parameters are used: a)  $n_{el}$ ,  $n_{el}^*$ ,  $i_d^*$ ,  $i_q^*$ , b)  $n_{el}^*$ ,  $n_{el}$ ,  $V_s^*$ ,  $V_{max}$ .

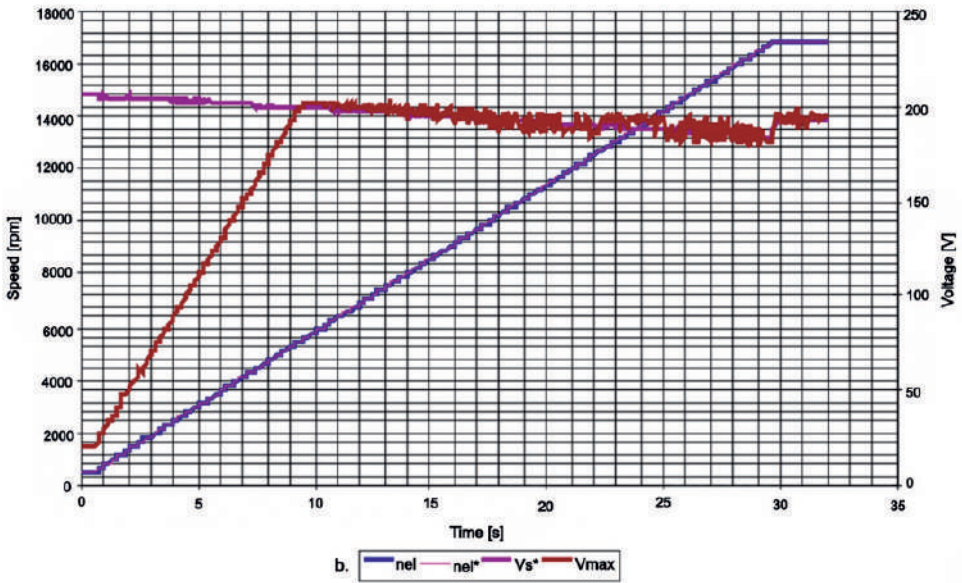
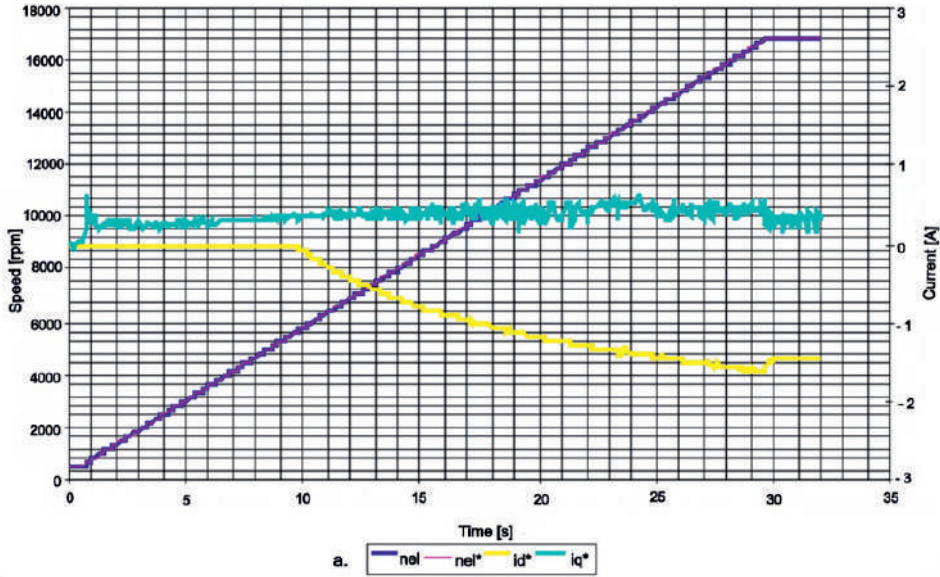


Fig. 6.17 Performances of the proposed speed control for the PMSM drive systems during acceleration when the voltage reaction  $V_{max}$  is used to generate the reference currents and the output of the speed controller is  $I_s^*$ : a)  $n_{el}$ ,  $n_{el}^*$ ,  $i_d^*$ ,  $i_q^*$ , b)  $n_{el}$ ,  $n_{el}^*$ ,  $V_s^*$ ,  $V_{max}$ .

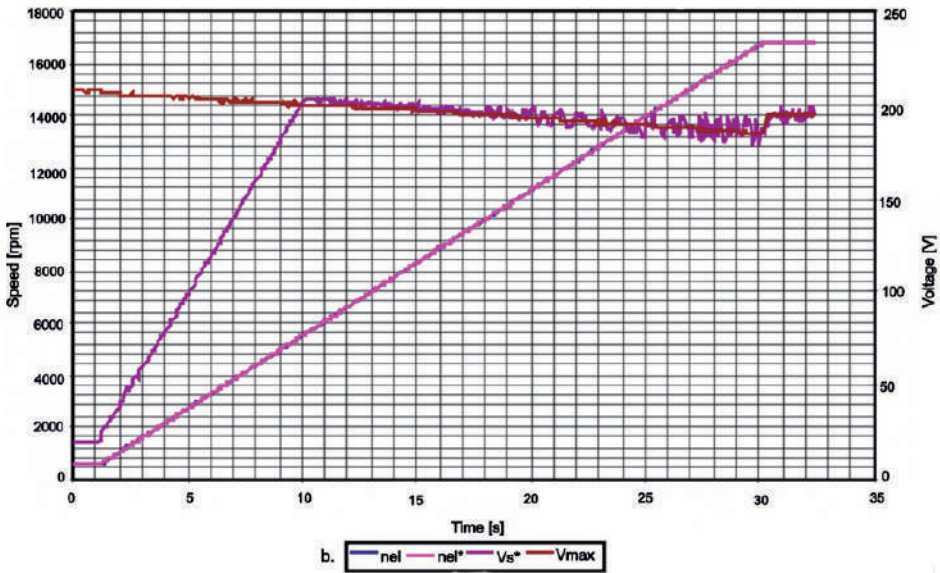
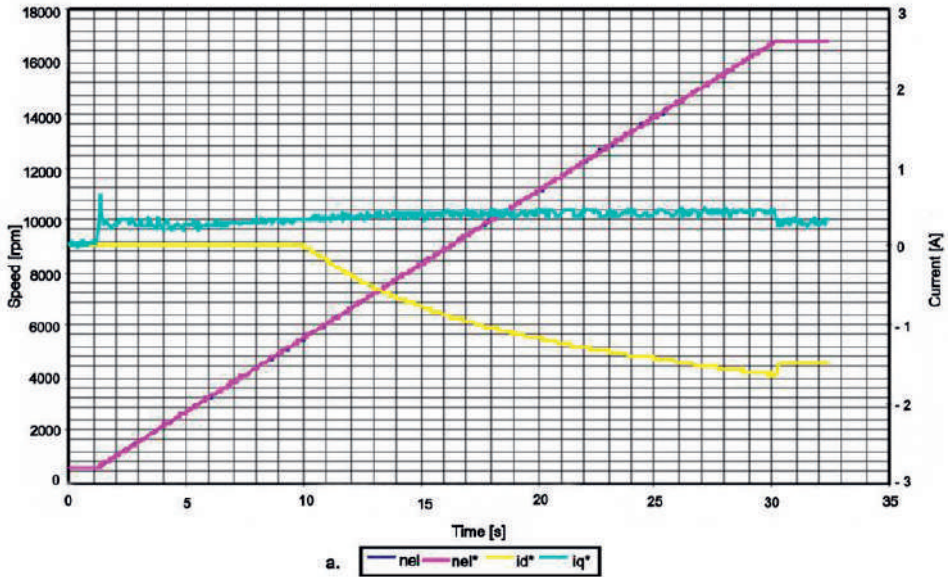
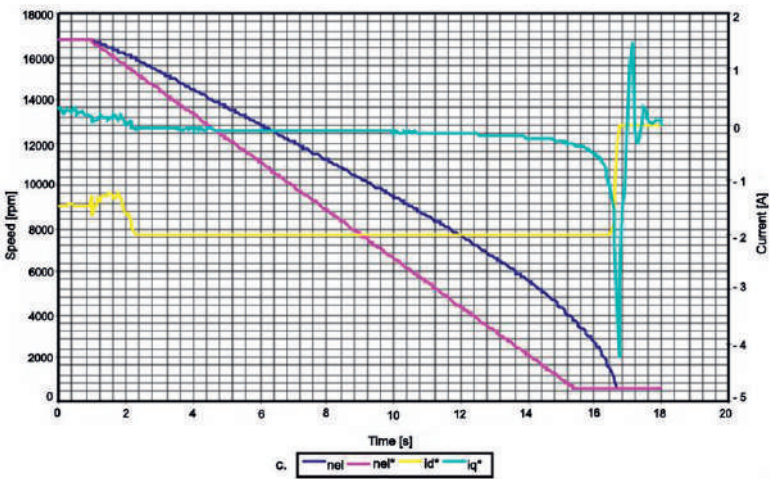
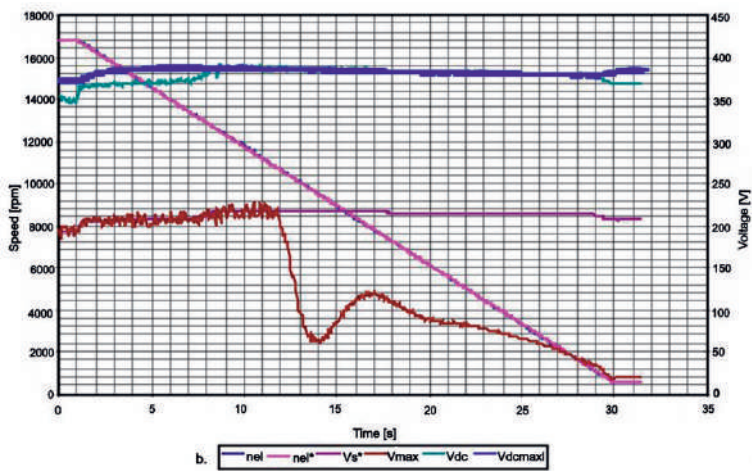
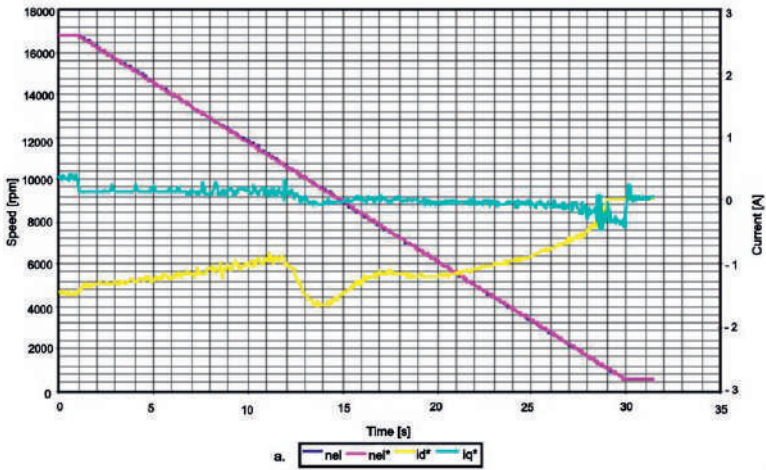


Fig. 6.18 Performances of the proposed speed control for the PMSM drive systems during acceleration when the voltage reaction  $V_{max}$  is used to generate the reference currents and the output of the speed controller is  $i_q^*$ : a)  $n_{el}$ ,  $n_{el}^*$ ,  $i_d^*$ ,  $i_q^*$ , b)  $n_{el}$ ,  $n_{el}^*$ ,  $V_s^*$ ,  $V_{max}$ .



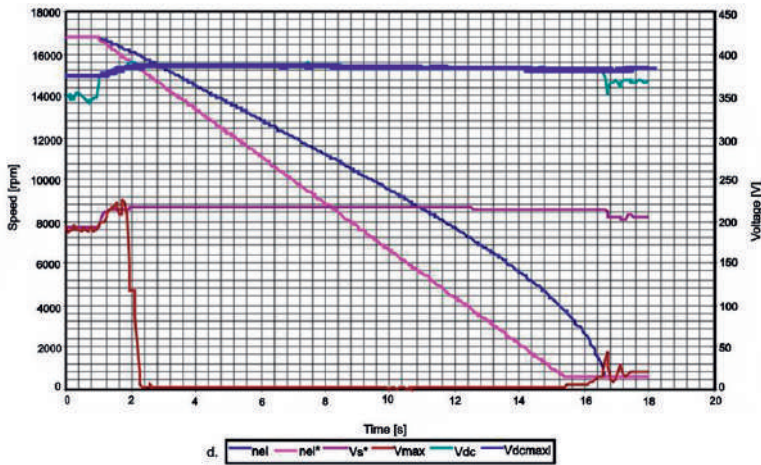
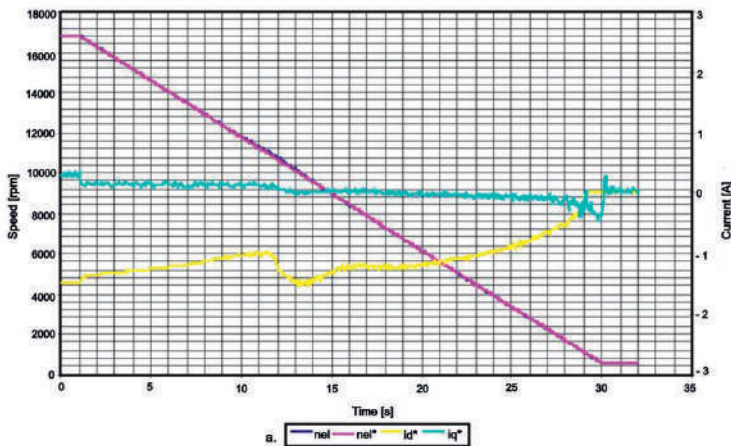


Fig. 6.19 Performances of the proposed speed control for the PMSM drive systems during deceleration when the voltage reaction  $V_{max}$  is used to generate the reference currents and the output of the speed controller is  $I_s^*$ : a)  $n_{el}, n_{el}^*, i_d^*, i_q^*$ , for a gradient of 560 rpm/s, b)  $n_{el}, n_{el}^*, V_s^*, V_{max}$  for a gradient of 560 rpm/s, c)  $n_{el}, n_{el}^*, i_d^*, i_q^*$ , for a gradient of 1120 rpm/s, d)  $n_{el}, n_{el}^*, V_s^*, V_{max}$  for a gradient of 1120 rpm/s.

The deceleration performances of the PMSM drive system are depicted in Fig. 6.19 and Fig. 6.20, for two cases: when the voltage reaction is used to generate the reference currents and the output of the speed controller is and, respectively, in for two gradients: one of 560 rpm/s and the second, of 1120 rpm/s.

It can be noticed that, if the deceleration gradient is too high, the PMSM speed will not be capable of following the reference speed (see Fig. 6.19). Generally, the regenerative braking performance is limited due to the DC-link voltage limitation. Particullary, by using the proposed control method, the DC - link voltage will be limited at the maximum value  $V_{dcmx}$ .



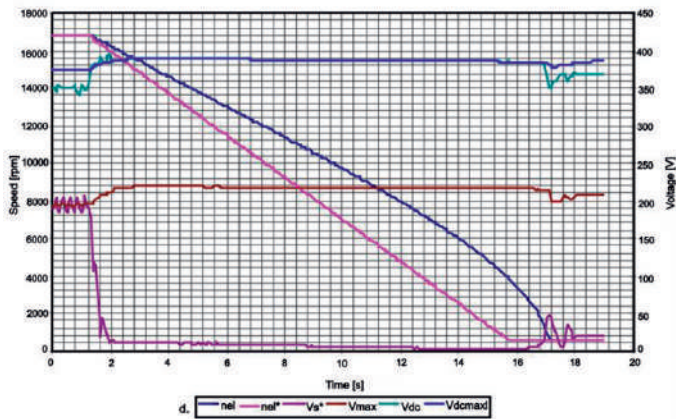
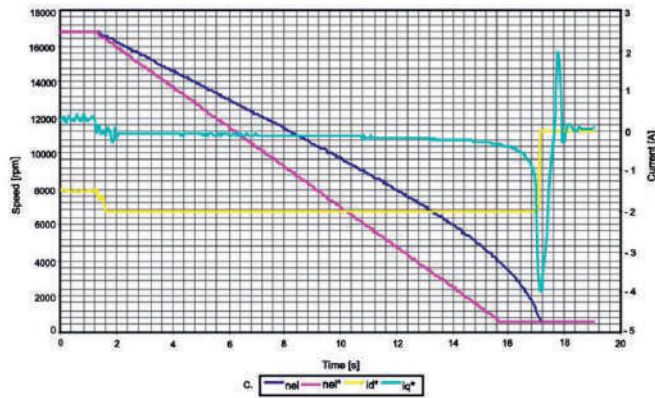
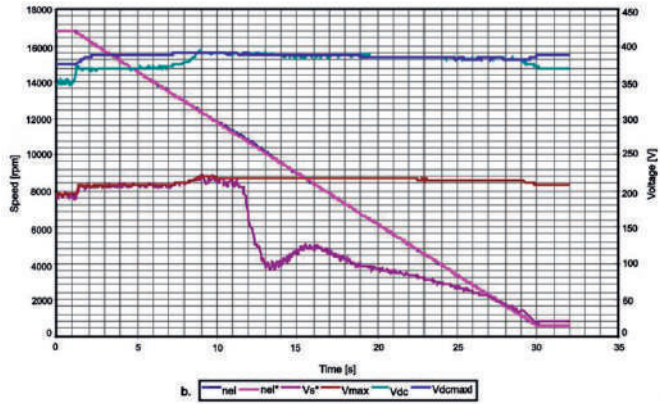
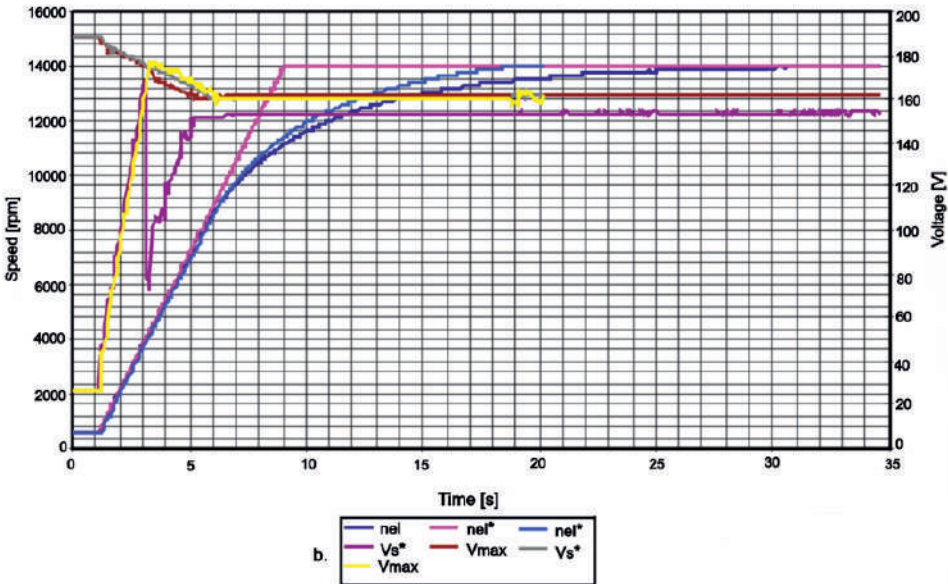
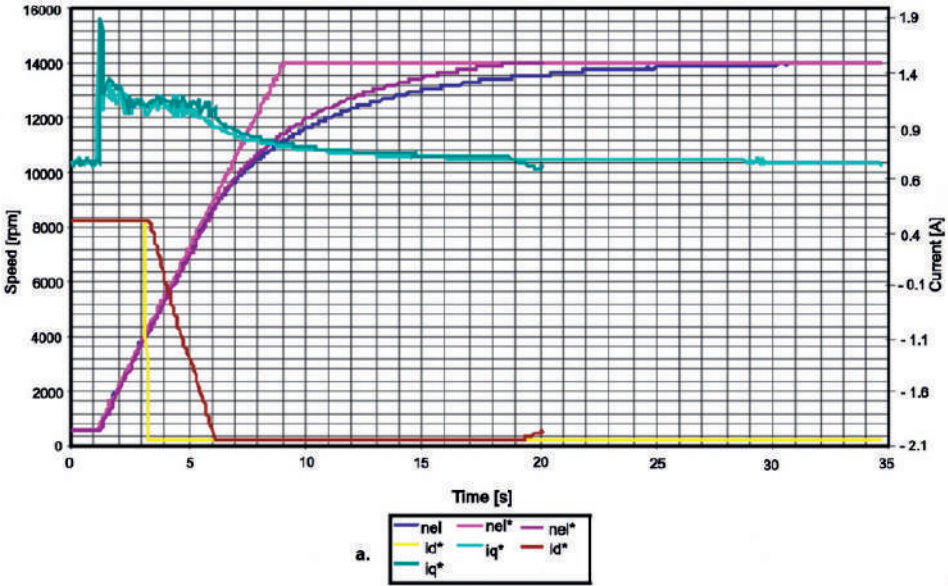


Fig. 6.20 Performances of the proposed speed control for the PMSM drive systems during deceleration when the voltage reaction  $V_{max}$  is used to generate the reference currents and the output of the speed controller is  $i_q^*$ : a)  $n_{el}$ ,  $n_{el}^*$ ,  $i_d^*$ ,  $i_q^*$  for a gradient of 560 rpm/s, b)  $n_{el}$ ,  $n_{el}^*$ ,  $V_s^*$ ,  $V_{max}$  for a gradient of 560 rpm/s, c)  $n_{el}$ ,  $n_{el}^*$ ,  $i_d^*$ ,  $i_q^*$  for a gradient of 1120 rpm/s, d)  $n_{el}$ ,  $n_{el}^*$ ,  $V_s^*$ ,  $V_{max}$  for a gradient of 1120 rpm/s.

In order to further prove the superiority of the proposed control system performances, another test has been performed in the case of accelerating the PMSM from 0 rpm to 14000 rpm, with a 1680 rpm/s gradient, when the load torque is  $T_s = 3.2 \text{ Nm}$  (see Fig. 6.21.a, b), and in the case of accelerating the PMSM from 0 rpm to 16400 rpm, with a 1680 rpm/s gradient, when the load torque is  $T_s = 2.2 \text{ Nm}$  (see Fig. 6.21.c, d), respectively.



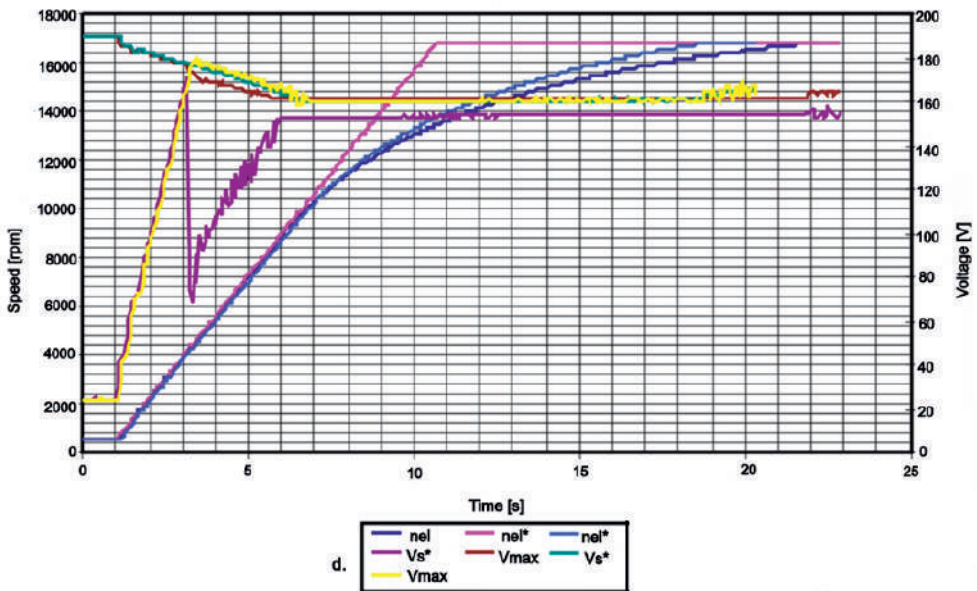
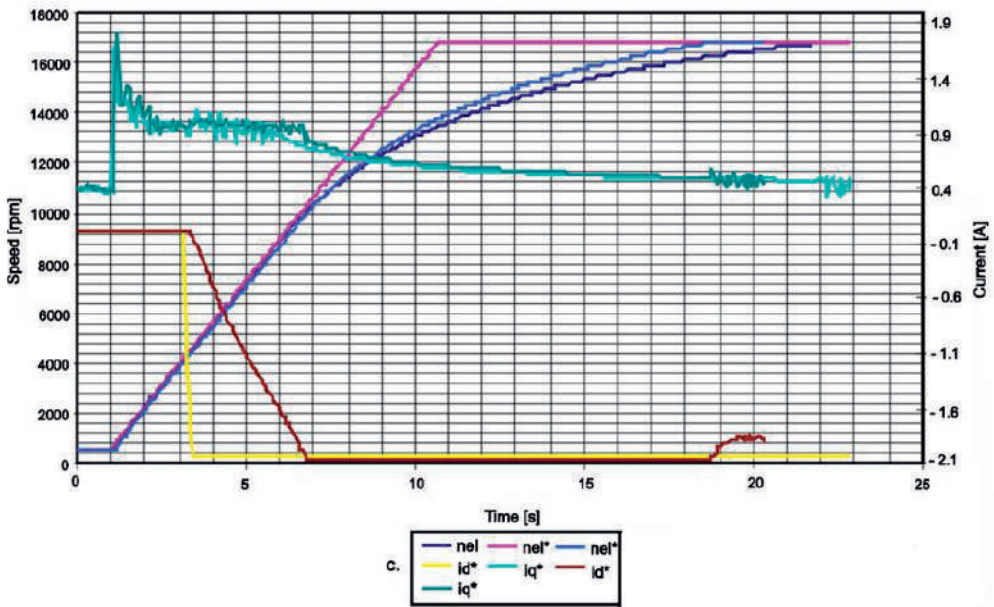


Fig. 6.21 Control system performances during acceleration for the three control strategies for currents determination  $i_d^*$ ,  $i_q^*$ , : a) and b) performances during acceleration from 0 to 14000 rpm with a 1680 rpm/s gradient, and the resistive torque of  $T_s = 3.2 Nm$ ; c) and d) performances during acceleration from 0 to 16 400 rpm with a 1680 rpm/s gradient, and the resistive torque of  $T_s = 2.2 Nm$ .



In what follows, the control system analysis will be performed in the constant torque area, where the speed of the motor is tried to be maintained constant at 560 rpm, while the load torque varies from 0 Nm to 28 Nm for one second. In Fig. 6.22 the variation of the speed (the speed varies  $n_{el} = 560 \pm 60$ ) in the case of changing the load torque can be observed.

In Fig. 6.23, the measured and estimated variations of the DC current and of the d- and q-axes currents are presented for the load torque variation from 0 Nm to 28 Nm for one second  $I_{dc}$  and  $I_{dcest}$ , respectively  $i_d^*$ ,  $i_d$ ,  $i_{dcest}$ ,  $i_q^*$ ,  $i_q$ ,  $i_{qest}$ .

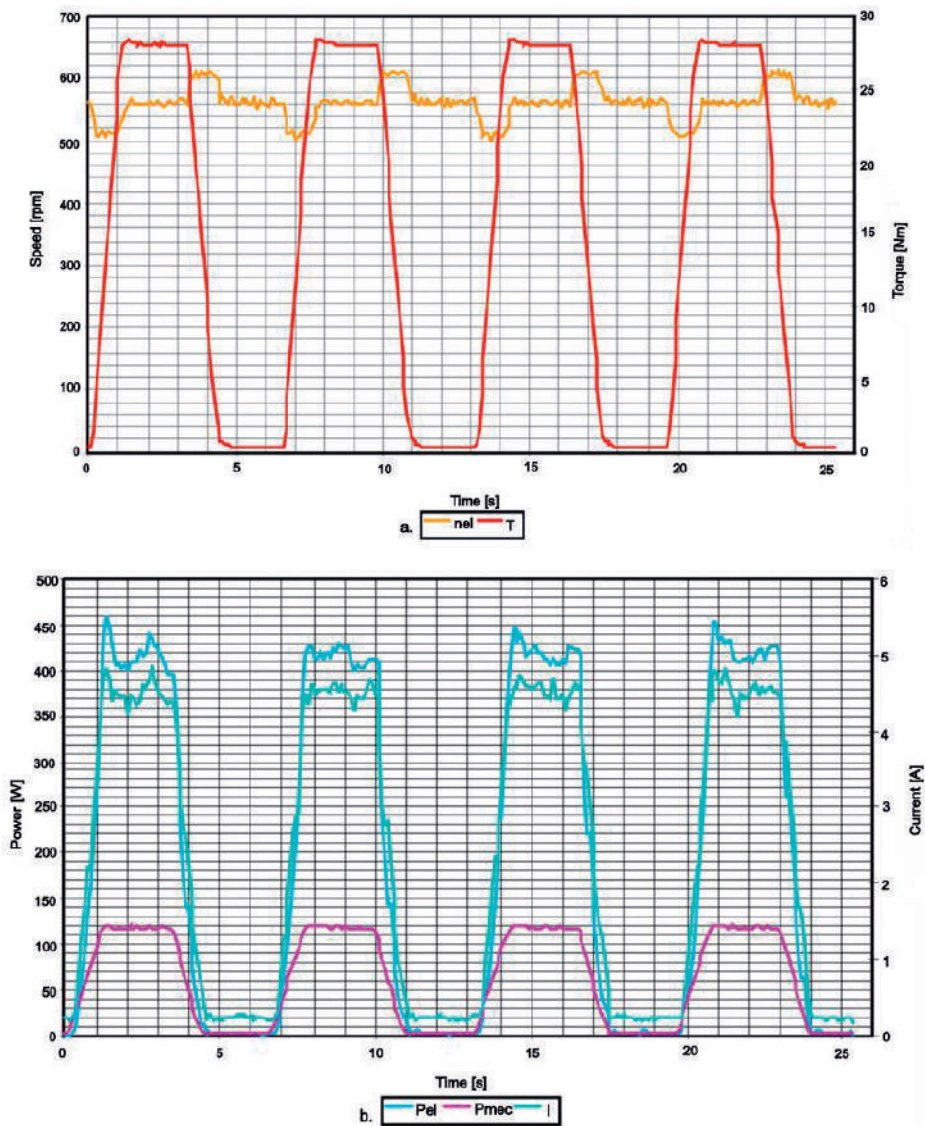


Fig. 6.22 Speed control performances in the constant-torque operating region when the torque varies  $T_s = 0 \rightarrow 28 \text{ Nm}$  in 1 s: a)  $n_{el}$ ,  $T$ ; b)  $P_{el}$ ,  $P_{mec}$ .

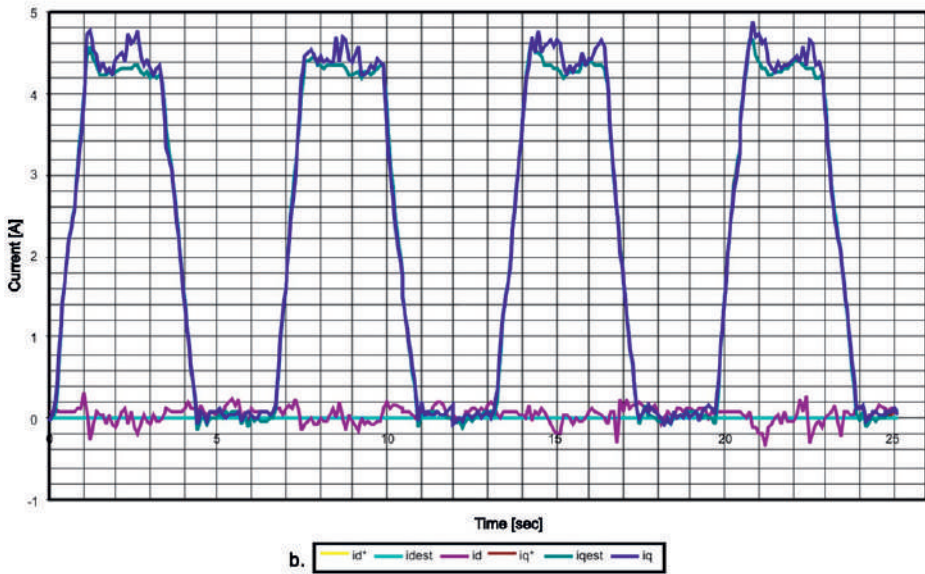
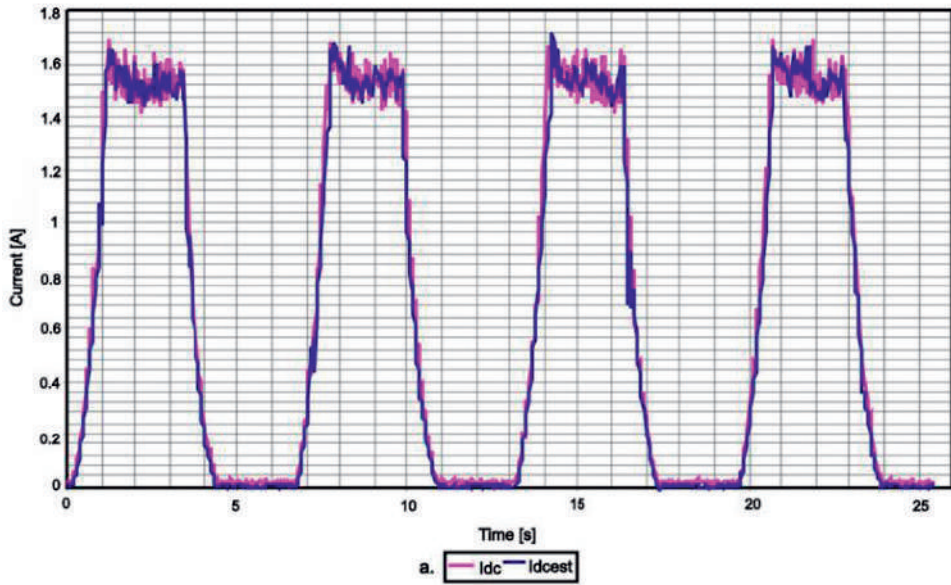


Fig. 6.23 Control system performances in the constant-torque operating region when the torque varies  $T_s = 0 \rightarrow 28 \text{ Nm}$  in 1 s: a)  $I_{dc}$ ,  $I_{dcest}$ ; b)  $i_d^*$ ,  $i_d$ ,  $i_{dest}$ , and  $i_q^*$ ,  $i_{qest}$ ,  $i_q$ , respectively.

## 6.4 Conclusions

This study, carried out by the research team within the Electrical Engineering Department from UPT, in the first paragraph, has presented a novel control method for PMSM drives fed by PWM-VSI operating in the overmodulation region in a wide speed range. The PMSM drive system is operating in generator mode, using the proposed control method. The PWM-VSI is equipped with a regenerative unit to supply the ac power from the mains. If the PWM-VSI wasn't equipped with a regenerative unit, the generator mode operation of the PMSM would be avoided, by limiting the maximum  $q$ -axis current. The proposed control method provides a smooth transition into and out of the field-weakening region over a wide speed range. Moreover, the method is not sensitive to the motor parameters and it is relatively simple to implement using a 16 [bit] microcontroller. The PMSM drive dynamic and steady state performances are improved by using the VSI in the overmodulation region, while the switching losses in the power module will be reduced. The control is stable in the overmodulation region and it is capable of following the DC-link variations. The experimental results have shown the benefits of using the proposed control method.

The experimental results obtained with the second proposed control for a PMSM drive system, have also shown good dynamic performance of the proposed current observer and also a good dynamic speed response. In general, in order to estimate the  $d$ - and  $q$ -axes armature currents, the DC-link voltage and current need to be measured. For that, a fast analogue to digital converter can be used. The proposed control method could be implemented using a 16 [bit] microcontroller. For the proposed speed regulation drive system, the current sensors are eliminated and only two Hall-effect sensors for position and speed estimation are used. Therefore, the cost of the drive is reduced. In the proposed drive system, the influences of the inverter nonlinearities, the DC-link voltage and the saturation effect are eliminated. Moreover, this second novel control method is capable of calculating the current references on the  $d$ - and  $q$ -axes, in a wide speed range, for a drive operating in all four quadrants, even if the power converter is not provided with a regenerative unit.

## 6.5 References

- [1] P.P. Acarnley, J.F. Watson, "Review of Position-Sensorless Operation of Brushless Permanent-Magnet Machines", IEEE Trans. on Ind. Electronics, vol. 53, Nr. 2, Aprilie, 2006.
- [2] Gh. D. Andreescu, "Estimatoare în sisteme de conducere a acțiunilor electrice", Editura Orizonturi Universitare, Timișoara, 1999.
- [3] N. Bianchi, S. Bolognani, "Parameters and Volt-Ampere Ratings of a Synchronous Motor Drive for Flux-Weakening Applications", IEEE Trans. On Power Electron. vol. 12 no. 5 pp. 895–903, September, 1997.

- [4] S. Morimoto, M. Sanada, Y. Takeda, "Effects and Compensation of Magnetic Saturation in Flux-Weakening Controlled Permanent Magnet Synchronous Motor Drives", *IEEE Trans. On Ind. Appl.*, vol. 30, no. 6, November/December 1994.
- [5] S. Morimoto, M. Sanada, Y. Takeda, "Wide-Speed Operation of Interior Permanent Magnet Synchronous Motors with High-Performance Current Regulator", *IEEE Trans. On Ind. Appl.*, Vol. 30, No. 4, pp. 920-926, July/August 1994.
- [6] J.M. Kim, S.K. Sul, "Speed Control of Interior Permanent Magnet Synchronous Motor Drive for the Flux Weakening Operation", *IEEE Trans. On Ind. Appl.*, Vol. 33, No. 1, pp. 43-48, January/February, 1997.
- [7] T.S. Kwon, S.K. Sul, "Novel Antiwindup of a Current Regulator of a Surface-Mounted Permanent-Magnet Motor for Flux-Weakening Control", *IEEE Trans. On Ind. Appl.*, vol. 42, no. 5, pp. 1293-1300, September/October 2006.
- [8] Y.D. Yoon, S.K. Sul, "New Flux Weakening Control for Surface Mounted Permanent Magnet Synchronous Machine Using Gradient Descent Method", *The 7th International Conference on Power Electronics*, pp. 1208-1212, October 2007.
- [9] G. Gallegos-Lopez, F.S. Gunawan, J.E. Walters, "Optimum Torque Control of Permanent-Magnet AC Machines in the field-Weakened Region", *IEEE Trans. On Ind. Appl.* vol. 41, no. 4 pp. 1020-1028, July/August 2005.
- [10] R.U. Lenke, R.W. De Doncker, M.S. Kwak, S.K. Sul, "Field Weakening Control of Interior Permanent Magnet Machine using Improved Current Interpolation", *IEEE PESC*, pp. 1-5, June 2006.
- [11] B.H. Bae, N. Patel, S. Schulz, S.K. Sul, "New Field Weakening Technique for High Saliency Interior Permanent Magnet Motor", *IEEE 38th IAS Annual Meeting*, vol. 2, pp. 898-905, October 2003.
- [12] G.Y. Choi, M.S. Kwak, T.S. Kwon, S.K. Sul, "Novel Flux-Weakening Control of an PMSM for Quasi Six-Step Operation", *IEEE IAS Annual Meeting*, pp. 1315-1321, September 2007.
- [13] R. Nalepa, T. Orłowska-Kowalska, "Optimum Trajectory Control of the Current Vector of a Nonsalient-Pole PMSM in the Field Weakening Region", *IEEE Trans. On Ind. Electronics*, vol. 59, no. 7 pp. 2867-2876, July 2012.
- [14] A.M. Hava, R.J. Kerkman, T.A. Lipo, "Carrier-Based PWM-VSI Overmodulation Strategies: Analysis, Comparison, and Design", *IEEE Trans. On Power Electronics* vol. 13, no. 4 pp. 647-689, July 1998.
- [15] M. Khambadkone, R. and J. Holtz, "Compensated Synchronous PI Controller in Overmodulation Range and Six-Step Operation of Space-Vector-Modulation-Based Vector-Controlled Drives", *IEEE Trans. On Ind. Electronics*, vol. 49, no. 3 pp. 574-580, July 2002.
- [16] N. V. Olărescu, S. Muşuroi, C. Şorândaru, M. Weinmann, St. Zeh, "Optimum Current Control for Wide Speed Range operation of PMSM Drive Without regenerative Unit Utilizing PWM-VSI Overmodulation", *Proceedings of 13th International Conference on Optimization of Electrical and Electronic Equipment OPTIM 2012, Braşov, 24-26 Mai*, pp. 612-617, ISBN 978-1-4673-1652-1, 2012.
- [17] N. V. Olărescu, M. Weinmann, S. Muşuroi, C. Şorândaru, "Novel flux-weakening control algorithm for PMSM with large DC-link variations utilizing PWM-VSI overmodulation", *Electromotion*, Vol. 20, No. 1-4, pp. 53-59, ISSN 1223-057X, 2013.
- [18] T. Matsuo, T.A. Lipo, "Current sensorless field oriented control of synchronous reluctance motor", *Conf. Rec. IEEE-IAS Annual Meeting*, pp. 672-678, 1993.
- [19] K. Ohishi, Y. Nakamura, "High Performance Current Sensor-less Speed Servo System of PM Motor Based on Current Estimation", *Trans. on Ind. Appl.*, vol. 37, pp. 1240-1246, September/October, 2001.
- [20] S. Morimoto, M. Sanada, Y. Takeda, "Optimum efficiency operation of synchronous reluctance motor without current sensor", in *Proc. 8th Int. Conf. Power Electronics and Variable Speed Drives*, pp. 506-511, 2000.

- [21]. S. Morimoto, M. Sanada, Y. Takeda, "High-Performance Current-Sensorless Drive for PMSM and SynRM with Only Low-Resolution Position Sensor", *Trans. on Ind. Appl.* vol. 39, no 3, pp. 792–801, May/June 2003.
- [22]. H. Schmirgel, J.O. Krah, "Compensation of Nonlinearities in the IGBT Power Stage of Servo Amplifiers through Feed Forward Control in the Current Loop", *PCIM Europe*, pp. 94–99, June 2005.
- [23]. N.V. Olărescu, S. Muşuroi, "Enhanced Simplified Control Algorithm for Surface-Mounted Permanent Magnet with Sinusoidal Excitation", *IPEMC China*, vol. 2, pp. 1049–1053, August 2004.
- [24]. N. V. Olărescu, S. Muşuroi, C. Şorândaru, F. M. Frigură-Iliasa, „Scalar control systems with permanent magnet synchronous motors with sinusoidal current control. Calculatin of speed controller parameters”, *Revue Roumaine des Sciences Techniques. Serie Electrotechnique et Energetique*, Tome 57, Issue 1, pp. 70-79, ISSN 0035-4066, 2012.
- [25]. N. V. Olărescu, M. Weinmann, St. Zeh, S. Muşuroi, C. Şorândaru, „Control of Wide Speed Range PMSM Drives with Large DC-Link Variations without Regenerative Unit utilizing PWM-VSI overmodulation”, *Proceedings of 4th Annual IEEE Energy Conversion Congress&Exposition ECCE 2012*, Raleigh, North Carolina, 15-20 Septembrie, pp. 831-837, ISBN 978-1-4673-0801-42012, 2012.
- [26]. N. V. Olărescu, M. Weinmann, St. Zeh, S. Muşuroi, C. Şorândaru, „Optimum Current Reference Generation Algorithm for Four Quadrant Operation of PMSMS Drive System without Regenerative Unit”, *IEEE International Symposium On Industrial Electronics (ISIE 2010)*, Conference Proceeding, Bari, Italia, 4-7 Iulie, pp. 1408-1413, ISBN 978-1-4244-6391-6, 2010.
- [27]. N. V. Olărescu, M. Weinmann, St. Zeh, S. Muşuroi, C. Şorândaru, „Optimum Current Reference Generation Algorithm for PMSMS Drive System for Wide Speed Range”, *MELECON 2010*, The 15th IEEE Mediterranean Electrotechnical Conference, Conference Proceeding, Malta, 25-28 Aprilie, pp. 1073-1077, ISBN 978-1-4244-5795-3, 2010.
- [28]. N. V. Olărescu, S. Muşuroi, C. Şorândaru, M. Weinmann, St. Zeh, "Optimum Current Command Algorithm for Wide Speed Range and Four Quadrant Operation of PMSMS Drive without Regenerative Unit", *Proceedings of the International Conference on Optimisation of Electrical and Electronic Equipment, OPTIM 2010*, 20 - 22 Mai, pp. 704-709, ISSN 18420133, ISBN 978-142447019-8, 2010.
- [29]. N. V. Olărescu, M. Weinmann, St. Zeh, S. Muşuroi, "Novel Flux Weakening Control Algorithm for PMSMS", *Proceedings of 2009 International Conference on power Engineering Energy and Electrical Drives*, Lisbon, IEEE Ind. Elect. Soc., 18-20 Martie, pp. 123-127, ISBN 978-1-4244-4611-7, 2009.
- [30]. N. V. Olărescu, S. Muşuroi, C. Şorândaru, Gh. Atanasiu, "Enhanced Current-Sensorless Drive System for PMSMS Using Two Hall-Effect Sensors for Wide Speed Range", *Proceedings of the 11th International Conference on Optimization of Electrical and Electronic Equipment, OPTIM 2008*, Braşov 22-23 Mai, pp. 87-92, ISBN 978-973-131-030-5, Library of the Congress: 2007905111, 2008.
- [31]. N. V. Olărescu, S. Muşuroi, "The Simplify Control Algorithm for Permanent Synchronous Motors with Sinusoidal Current Control (BLAC)", *Conference Proceedings, 16th International Conference on Electrical Machines IECM 2004*, Cracow-Poland, 5-8 Septembrie, nr. 401, 4 pagini, ISBN 12-345678-90, 2004.
- [32]. J. Holtz, J. Quan, "Drift and parameter compensated flux estimator for persistent zero stator frequency operation of sensorless controlled induction motor", in *IEEE Transaction on Industry Applications*, vol. 39, No. 4, July/Aug. 2003, pp. 1052-1060.
- [33]. X. Xu, R. De Doncker, D.W. Novotny, "A stator flux oriented induction machine drive", *Conf. Rec. IEEE PESC 1988*, vol. 5, pp. 870-876.
- [34]. X. Xu, R. De Doncker, D.W. Novotny, "Stator flux orientation control of induction machines in the field weakening region", *IEEE IAS Annual Meeting*, 1988, vol. 1, pp.437-443.

- [35]. X. Xu, D.W. Novotny, "Selection of the flux reference for induction machine drive in the field weakening region", *IEEE Transactions on Industry Applications*, vol. 28, no. 6, pp. 1353-1358, Nov./Dec. 1992.
- [36]. S.H. Kim, S.K. Sul, "Maximum torque control of an induction machine in the field weakening region", *IEEE Transactions on Industry Applications*, vol. 31, no. 4, pp. 787-794, Jul./Aug. 1995.
- [37]. M.H. Shin, D.S. Hyun, S.B. Cho, "Maximum torque control of stator-flux-oriented induction machine drive in the field-weakening region", *IEEE Transactions on Industry Applications*, vol. 38, no. 1, pp. 117-121, Jan./Feb. 2002.
- [38]. R. Bojoi, P. Guglielmi, G. Pellegrino, "Sensorless stator field - oriented control for low cost induction motor drives with wide field weakening range", *IEEE IAS Annual Meeting*, 2008, pp.1-7.
- [39]. F. Britz, A. Diez, M.W. Degner, R.D. Lorenz, "Current and flux regulation in field weakening operation of induction motors", *IEEE Transactions on Industry Applications*, vol. 37, no. 1, pp. 42-50, Jan./Feb. 2001.
- [40]. A. Bunte, H. Grotstollen, P. Krafska, "Field weakening of induction motors in a very wide range region with regard to parameter uncertainties", *Conf. Rec. IEEE PESC*, 1996, vol. 1, pp. 944-950.
- [41]. H. Grotstollen, J. Wiesing, "Torque capability and control of a saturated induction motor over a wide range of flux weakening", *IEEE Transaction on Industrial Electronics*, vol. 42, no. 4, pp. 374-380, August 1995.
- [42]. H. Abu-Rub, H. Schmirgel, J. Holtz, "Sensorless control of induction motors for maximum steady-state torque and fast dynamics at field weakening", in *IEEE IAS Annual Meeting*, Tampa, FL, Oct. 8-12, pp. 96-103, 2006.
- [43]. V. Blasko, "Power conditions and control of a regenerative Brake", *IEEE IAS Annual Meeting*, vol. 2, pp. 1504-1510, 1998.
- [44]. J. Jiang, J. Holtz, "An efficient braking method for controlled AC drives with a diode rectifier front end", *IEEE Transactions on Industry Applications*, vol. 37, no. 5, pp. 1299-1307, September/October 2001.
- [45]. M. Hinkkanen, J. Luomi, "Braking scheme for vector-controlled induction motor drives equipped with diode rectifier without braking resistor", *IEEE Transactions on Industry Applications*, vol. 42, no. 5, pp. 1257-1263, September/October 2006.
- [46]. O. Wasynczuk, S. D. Sudhoff, K. A. Corzine, J. L. Tichenor, P. C. Krause, I. G. Hansen, L. M. Taylor, "A maximum torque per ampere control strategy for induction motor drives", *IEEE Transaction*.
- [47]. N. V. Olărescu, M. Weinmann, St. Zeh, S. Muşuroi, C. Şorândaru, "Optimum torque control algorithm for wide speed range and four quadrant operation of stator flux oriented induction machine drive without regenerative unit", *Proceedings of 3rd Annual IEEE Energy Conversion Congress and Exposition, ECCE 2011, Conference Proceeding*, Phoenix, AZ; Code 87357, 17 Septembrie, pp. 1773-1777, ISBN 978-145770542-7, 2011.

# SENSORLESS - VECTOR CONTROL OF PM - ASSISTED RELUCTANCE SYNCHRONOUS MOTOR DRIVES

## 7.1 Introduction

Nowadays, there is continuous demand for better performance, lower emissions and improved fuel economy in today's vehicles. Therefore, the manufacturers are investigating all kinds of features (electric power steering, electromechanical valves, etc.) for this purpose.

In order to meet this need for power, a practical idea is taken into consideration – the replacement of the starter and of the alternator in a vehicle with an electronically-controlled and very competitive electrical machine. Such a machine, mounted on the crankshaft, offers a very compact package and a very fast response regarding the transmission of the torque to the shaft.

The PM-assisted Reluctance Synchronous Machine can be used for this purpose. The need for a good efficiency in a very wide power-speed range of 6:1 in a hybrid electric vehicle can be accomplished by using this kind of machine when it operates at high flux densities [18].

The variable speed permanent magnet synchronous motors' (PMSMs) drives lead to the following advantages: a high efficiency, the elimination of an additional power supply, the high values of the electromagnetic torque per volume unit, the possibility of high performance control system achievement, the possibility to obtain application-specific drives [19] ÷ [22].

The PMSMs are characterised by a superior power factor and efficiency if compared to other AC machines. The PMSM manufacturers choose to use a particular type of permanent magnet (PM), depending on the parameters imposed on the machine, on the PM performances, on the procurement conditions, and, particularly, on the PM cost [1]. Now, the rare-earth permanent magnets and Ferrites are the mostly used types. Rare-earth permanent magnets (PM) are the best technical solution for the PMSM. The Samarium-Cobalt PM has the advantage of a high residual magnetic induction, high-energy density, linear demagnetisation curve and a very good thermal stability. The lower maximum operating temperature ( $\sim 250^{\circ}\text{C}$ ) and the high price can be presented as a drawback. The PM of neodymium-iron-boron have the highest residual magnetic induction, the highest energy density and a high coercive field strength. The drawback is the low value for the

maximum working temperature ( $\sim 150^{\circ}\text{C}$ ) and the oxidation possibility. Due to their characteristics, a PMSM with low weight due to the high energy density [6], [1], [5] could be built.

In conclusion, rare-earth magnets (SmCo, NdFeB) are a good alternative to the PMSM, but they claim a rapidly rising price trend in the last years; therefore, in the literature, during the past decade, different design solutions for the PMSM using Ferrites to overcome this problem were presented. Ferrite PM is an alternative to the PMSM built, due to their low price and the fact that they are easy to be produced. Ferrites have a linear magnetisation curve, a moderate maximum operating temperature ( $\sim 350^{\circ}\text{C}$ ), but the residual magnetic flux density is low [6]. The result is a high volume and weight machine.

Synchronous reluctance motors (SynRM) are apparent-pole synchronous machines with large saliency ratio. They are referred to in the literature as the reactive synchronous machines or the variable reluctance synchronous machines with a passive rotor. A large saliency ratio can be achieved by both the axially and the transversally laminated rotor structures. The process of the electromagnetic torque production in a SynRM is based on the anisotropy shape, which characterises the machine. In the last decade, the transversally laminated rotor structure is preferred, since the axially laminated rotor structure has some drawbacks, from the mechanical point of view. The rotor has different construction variants [6], [17]. Generally, all these types aim at obtaining different magnetic permeances on the  $d$ - and  $q$ -axes, necessary to produce the reluctance torque (reactive). The advantages of these machines are:

- the simplicity of the technological process,
- the low-cost,
- the low noise and the robustness [1], [6], [7], [8], [17].

The main disadvantages are related to the low value of the developed electromagnetic torque, the low value of the power factor and the low efficiency.

SynRM electromagnetic characteristics can be improved by creating a rotor having both the permanent magnets and the variable reluctance, obtaining thus the permanent magnet assisted synchronous reluctance motor (PM-RSM). In Fig. 7.1 and Fig. 7.2, the two types of permanent magnet assisted synchronous reluctance motor (PM-RSM) are presented. Fig. 7.1 shows a transversally laminated PM-RSM. Fig. 7.2 shows a four-pole PM-RSM. Such a construction achieves an improvement of the magnetic characteristics such as power versus internal torque angle, power factor versus mechanical power and efficiency versus mechanical power [9]. To achieve superior performances with this new topology, a PM-RSM optimisation procedure is required. Many valuable papers are dealing with this subject, such as [10] ÷ [16].





Fig. 7.1 Transversally laminated PM-RSM.

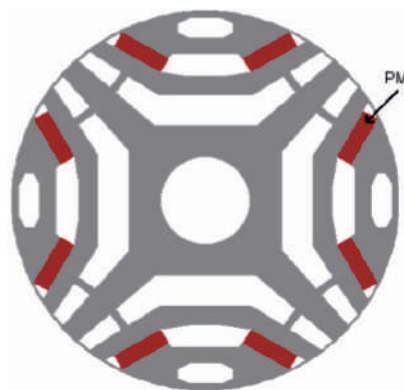


Fig. 7.2 A four-pole PM-RSM.

SynRM under closed-loop control can easily be controlled and operated, due to the completely new possibilities through the development of power electronics-based drives. Thus, the drawback of this machine under direct operation and supply, especially stability and start-up torque, can be overcome. Both field-oriented control and DTC and similar methods have been presented in the literature for the SynRM operation. It has been shown that the SynRM under closed-loop control has some advantages compared to the induction motor, which is the powerful industrial competitor of the SynRM, when variable speed operation with high efficiency is demanded. The simplicity and adaptability in production and operation, the higher efficiency and torque density, the higher overload capacity and the lower temperature are some of the SynRM advantages in comparison to the induction machine. The main advantages of the SynRM are the following:

- the possibility of starting by the direct connection to the grid, due to the squirrel cage in a rotor;
- the very simple construction and manufacturing technology;
- the low manufacturing costs.

On the other hand, the construction of the SynRM has many disadvantages:

- the low value of the developed electromagnetic torque;
- the low value of the power factor and the low efficiency;
- the rated output is lower than the rated power of the induction machine.

As far as the motion control of the PM synchronous machine is concerned, it requires accurate position and velocity signals to realise the field orientation. In general, these feedback signals come from devices mechanically coupled to the rotor, to electromagnetic resolvers, resolvers or optical encoders. However, these additional sensors, connectors and wiring increase the cost of the system and decrease its reliability [19].

The reduction in the mechanical robustness and the cost of the sensors makes the elimination of these devices very desirable.

In the last decades, there have been numerous publications or methods to eliminate the position sensors on electrical machines. Most of these techniques are based on tracking the back-EMF, which limits the machine's low speed operation and its sensitivity to the machine parameters' estimation, such as the stator inductance or resistance.

It has been found that PMSM reacts in different ways to the high frequency (400-1,000Hz) phase voltage injection depending on its rotor speed and position. The irregularities in the rotor structure generate oscillations in the current amplitude due to the high frequency carrier, which are proportional to the rotor position. At the same time, the frequency of these amplitude modulations is proportional to the machine's speed. This is due to the change in the magnetic path when the stator slots appear in different positions with respect to the rotor iron structure or to the PM position. A fast Fourier transform (FFT) analysis of the phase currents reveals spectral components at the frequency related to both the rotor speed and the number of slots. Therefore, the motor is employed as a kind of resolver, due to the change in the magnetic reluctance that can be advantageously considered for the position estimation.

Two basic methods for the initial position are used - the pulse signal injection or the sinusoidal carrier signal injection. The pulse signal injection methods are often based on estimating the minimum inductance location using a calculated  $di/dt$  obtained during some form of iterative square wave voltage injection to arbitrary axis such as that in [20]-[24] and can be applied to both the surface [20, 21, 22-24] and the interior permanent synchronous machine [23]-[24].

The motion-sensorless control methods of PMSM fall into two main categories: 1) emf tracking based on the fundamental model, that fails at zero and very low speed, and 2) signal injection methods, which work from standstill but should be dropped at a certain low speed in favour of the emf tracking methods.

The PMSM is blessed with the  $d$ - $q$  saliency, which is tracked for the rotor position estimation. Persistent high-frequency carrier-voltage ( $f_c = 300$ -1,000 Hz,  $V_c = 1$ -10 V)

[19]–[24], or discrete voltage pulses [20] can be injected in the machine for the rotor position tracking. The resulting carrier-current harmonics contain the rotor position information. While a low pass filter (LPF) separates the fundamental current, a band pass filter (BPF) in a specific reference selects the targeted carrier-current harmonic. The BPF is complemented by a phase-locked loop (PLL) tracking observer that extracts the rotor speed and position.

In this research study, the team at the Department of Electrical Engineering of UPT has proposed, firstly, two new low-cost ferrite V permanent magnets assisted synchronous reluctance rotor geometries (VPM-RSM). The first proposed rotor geometry has one V flux barrier (1V), while the second one has two V flux barriers (2V). The flux barriers used are made from Ferrites in order to improve the motor performances. For the extreme cases (which is also the case presented here), these flux barriers will be completely filled with Ferrites, so that the rotor configuration is also known in the literature as the interior inclined V permanent magnet synchronous motor. Secondly, the research team has proposed a new rotor topology with flux concentration (PM-RSM-FC) made of ferrite magnets, as an alternative to the PMSM made of rare-earth magnets, too. All the studied solutions aim at a much cheaper alternative to the rare-earth permanent magnet synchronous motors.

In the second part of this chapter, the vector control is used for the motion sensorless implementation of a transversally laminated PM-RSM (PM-assisted reluctance synchronous motor). The space vector modulation (SVM) is applied to it.

After having reviewed the saliency-tracking estimators [20]–[22], [24] and the mirror-phase estimator [5], a simplified estimator with only one D-module vector filter (compared with two in mirror-phase) is used to estimate the rotor position & speed [19].

A hybrid voltage-current model closed-loop flux observer takes the rotor position into its current model at low speed, and uses only the voltage model at medium-high speed.

A detailed presentation of the proposed drive, including the experimental results, is also presented here.

## 7.2 PM-RSM design aspects

Mainly, the purpose of this research is to study the performances of the motor having a novel geometry, obtained by combining the stator of an inserted tangential NdFeB permanent magnet synchronous motor with the proposed rotor geometries. The proposed rotor geometries must be optimally designed in order to achieve the same torque per current ratio in the constant torque area and the same torque capability in the field weakening region as for the PMSM with NdFeB having the initial rotor geometry. The main challenge of the rotor design using Ferrites is the small space available for the PM and the flux barriers.

The proposed rotor design is based on the existing 12 stator slots with concentrated windings, having an inner diameter of 50 mm. The stator length is 37 mm. The winding scheme is presented in Fig. 7.3.

The new rotor has the same number of poles and the same outer diameter of 49.3 mm, the same as for the initial rotor. The permanent magnet used for the new proposed rotors is a strontium ferrite FS-4 with the following magnetic properties:  $B_{min} = 0.4$  T,  $H_c \geq 223$  kA/m and  $(BH)_{max} = 27.2$  kJ/m<sup>3</sup>.

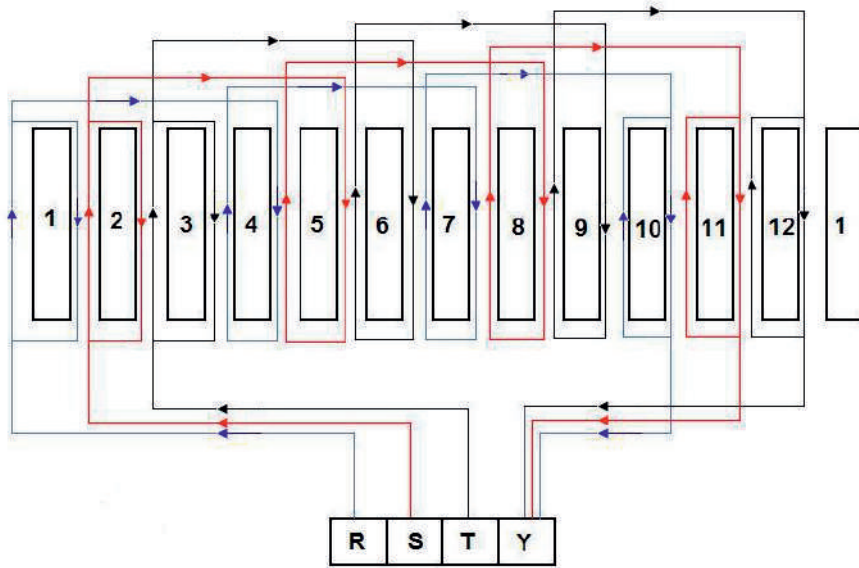


Fig. 7.3 The machine stator-winding scheme.

### 7.2.1 The design method for the PM volume

For the calculation of the required permanent magnet volume, the below equation was used:

$$V_{PM} = \frac{2}{\pi^2} \cdot \frac{k_\phi \cdot k_{ad} (1 + \varepsilon)}{f_s \cdot k_{um} \cdot k_{lm} \cdot B_r \cdot H_c \cdot \eta_m \cdot \cos \phi_m} \cdot k_m \cdot T_{mN} \cdot \Omega_N \quad (7.1)$$

where:  $k_\phi$  - is the shape coefficient of the permanent magnet field,  $k_{ad,q}$  - is the air gap magnetic reaction coefficient,  $\varepsilon$  - is the motor excitation degree,  $f_s$  - is the stator frequency,  $k_{um}$  - is the coefficient of permanent magnets use,  $\eta_m$  - is the efficiency and  $\cos \phi_m$  - is the motor power factor,  $T_{mN}$  - is the rated torque,  $\Omega_N$  - is the mechanical speed and  $k_m$  - is the motor overload factor, and it can be calculated by using the below relationship:

$$k_m = \sqrt{1 + \frac{1}{\varepsilon^2} \cdot \left( \frac{k_{ad}}{k_{aq}} \right)^2} \quad (7.2)$$

### 7.2.2 The design method for the inductances $L_d$ and $L_q$

The design of the proposed rotors was carried out using the two-dimensional finite element software Vector Fields OPERA, which takes into consideration the magnetic nonlinear behaviour of the materials, which plays a key role in the motor performance prediction. The back EMF, the cogging torque and the torque ripples caused by the permeance variations are considered by the movement of the rotor over the stator slot pitch. For the simulation of the  $d$ - and  $q$ -axes inductances, a standstill method using the FEM software is proposed here. For a nonlinear magnetic material, the inductance depends on the current level.

Fig. 7.4 shows the variation of the  $d$ - and  $q$ -axes magnetic flux versus the current on the  $d$ - and  $q$ -axes. The inductance in a certain point “ $k$ ” can be calculated using the following relationships:

$$L_{d,qk}(I_{d,qk}) = \frac{d\Psi_{sd,qk}}{dI_{d,qk}} \quad (7.3)$$

The  $d$ - and  $q$ -axes stator flux linkages can be calculated using the following relationship:

$$\Psi_{sd,qk} = \int_0^{t_k} (U_{sd,q} - R^* i_{d,q}(t)) dt \quad (7.4)$$

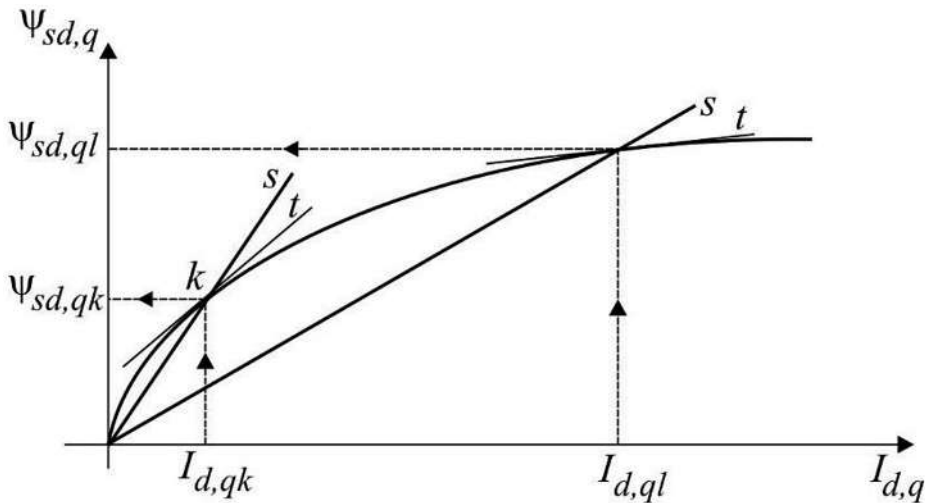


Fig. 7.4 Nonlinearity of the  $d$ - and  $q$ -axes inductances.

### 7.2.3 The design method for the rotor's different geometries

In order to obtain the desired rotor geometry, many patented rotor geometries, existing already in production, were studied. From the beginning, the desired geometry was a new transversal rotor geometry that can be implemented by a series production. There were 8 variants proposed, as illustrated in Fig. 7.5 [17].

As it can be seen in Fig. 7.5, there are 7 variants of variable reluctance rotors assisted by permanent magnets (numbered as 2, 4, 5, 6, 7, 8) and one variant with rotor flux concentration (number 3).

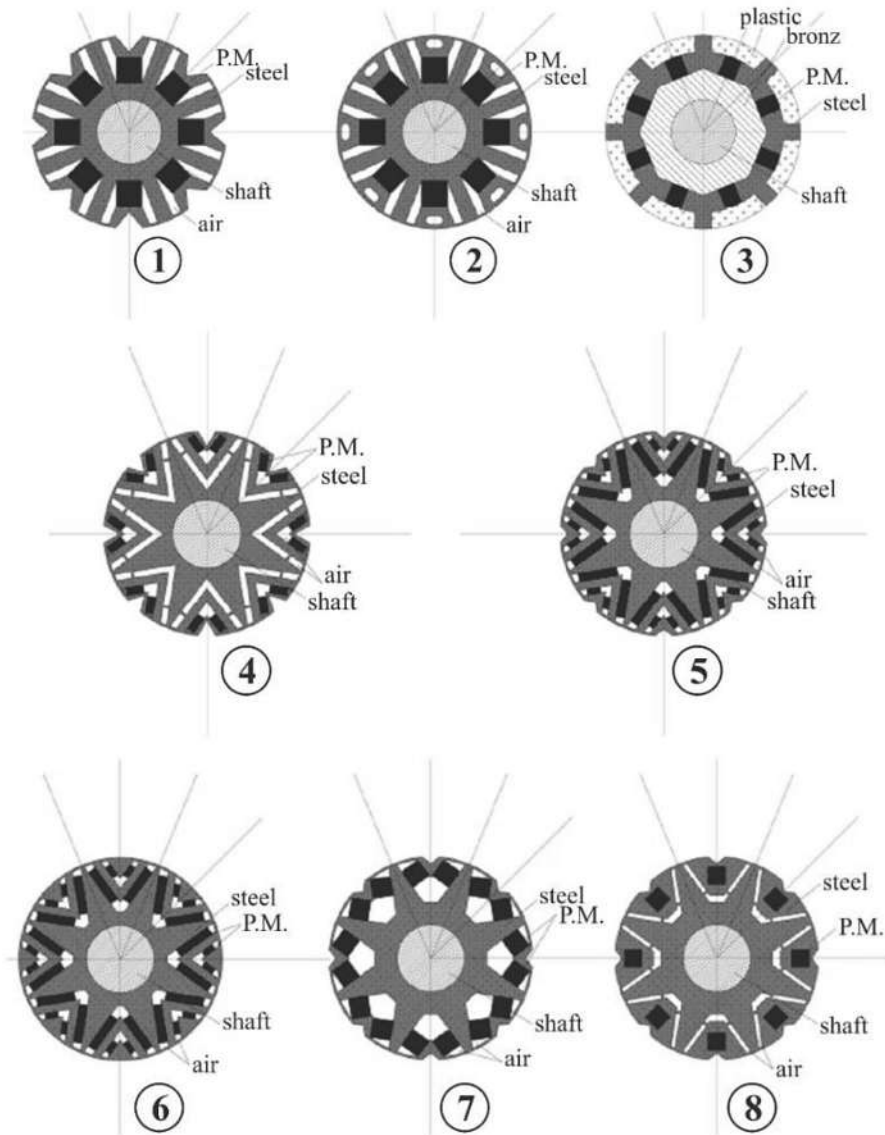


Fig. 7.5 The proposed rotor type variants for the PM-RSM.

In conclusion, the scope of this research was to design all the rotor geometries presented in Fig. 7.5, from which three variants: the variant with one V flux barrier (1V), with two V flux barriers (2V) and a variant with flux concentration (PM-RSM-FC) made of Ferrites, as an alternative to the rare-earth magnets, were extracted for a deeper analysis.

### 7.3 PM-RSM rotor's geometry variants

In what follows, three types of rotor geometries for the PM-RSM case are presented. They were all developed by the research team at the Department of Electrical Engineering of UPT.

#### 7.3.1 The VPM-RSM with One V Flux Barrier - 1 V

The first variant proposed here is the VPM-RSM-1V rotor geometry, as shown in Fig. 7.6. The permanent magnet volume value  $V_{PM} = 39587.37 \text{ mm}^3$  was determined using the equations (7.42) and (7.43).

As Fig. 7.6 shows, the ferrite required volume is high, yielding to a flux barrier adjustment according to the magnet volume; in which case, there are not so many possibilities to optimise the shape of the flux barrier. The width of the flux barrier is 5.7 mm. In Fig. 7.6, the permanent magnet flux plots on the  $d$ - and  $q$ -axes are depicted. The PM flux density distribution in the air gap, obtained by simulation, is shown in Fig. 7.7.

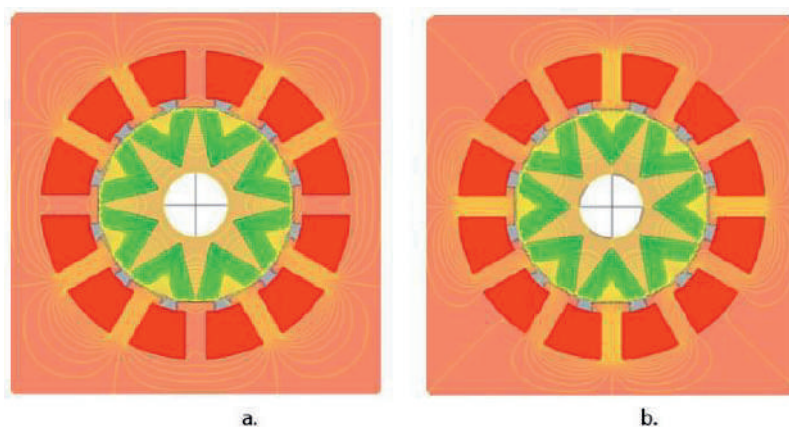
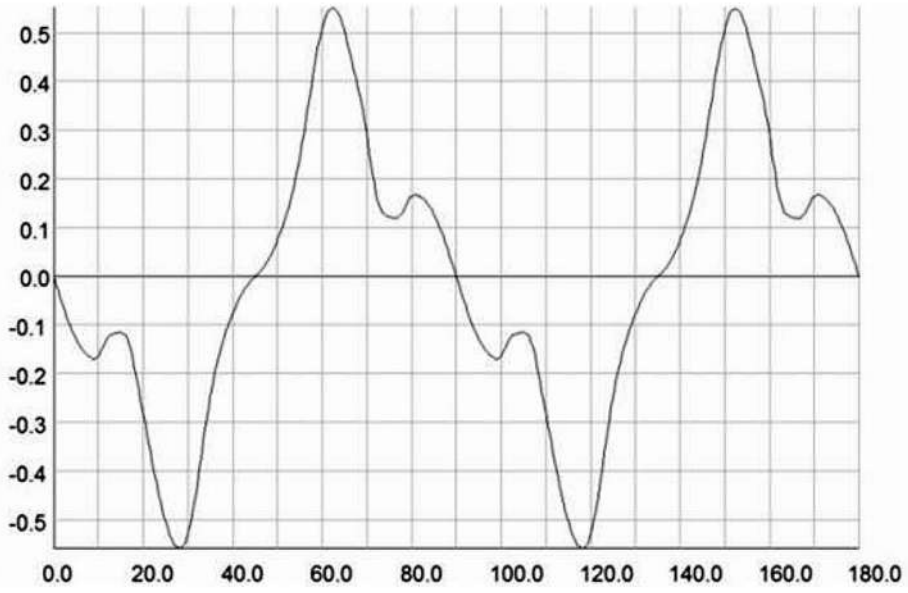
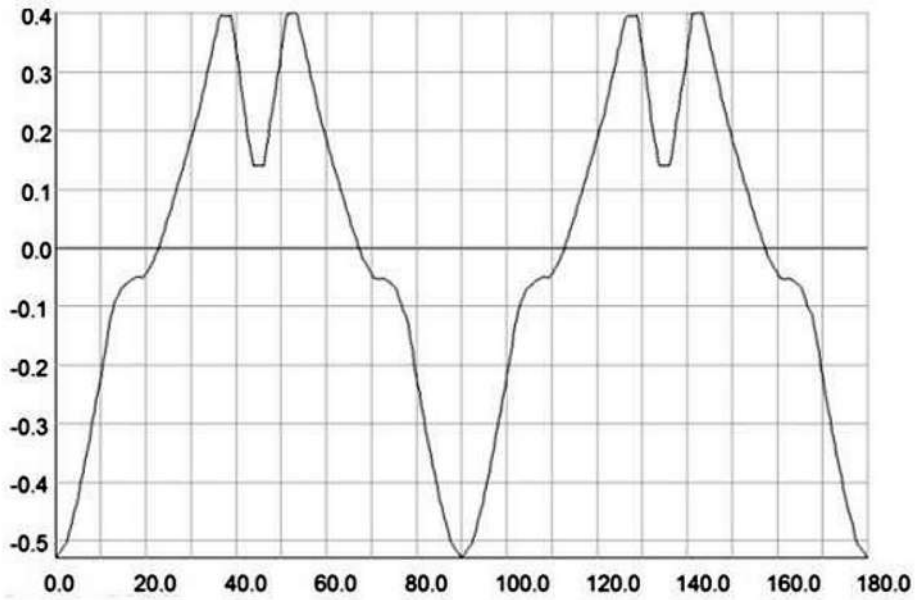


Fig. 7.6 One V flux barrier rotor geometry: a) the PM flux plots on the  $d$ -axis, b) the PM flux plots on the  $q$ -axis.

The peak values of the PM flux density distribution in the air gap are 0.55 T and 0.4 T, respectively. Fig. 7.8 shows the shape of the back-EMF and the shape of the cogging torque at 750 rpm. This figure allows the determination of the back-EMF peak value ( $E_{pk} = 16 \text{ V}$ ) and of the cogging torque peak value ( $T_{cogg} = 0.045 \text{ Nm}$ ). The permanent magnet flux linkage value is  $\psi_{PM} = 0.051 \text{ Wb}$ . The inductances  $L_d$  and  $L_q$  curves versus the  $I_d$  and  $I_q$  currents, resulted from simulation, are shown in the Fig. 7.9. They were obtained using the FEM and the method described above by the relationships (7.44) and (7.45). For the inductances on the  $d$ - and  $q$ -axes, the next values were obtained:  $L_d(4A) = 23.80 \text{ mH}$ ,  $L_q(4A) = 17.1 \text{ mH}$ , which means that the saliency ratio is  $L_d/L_q = 1.39$ . Fig. 7.10 presents the torque variation caused by the permeance variations at 5 A, in the constant torque area. In this case, for the proposed VPM-RSM-1V rotor geometry, at 5 A, the average torque is  $T_{av} = 7.3 \text{ Nm}$  and the torque ripple is  $T_{ripple} = 26 \%$ .



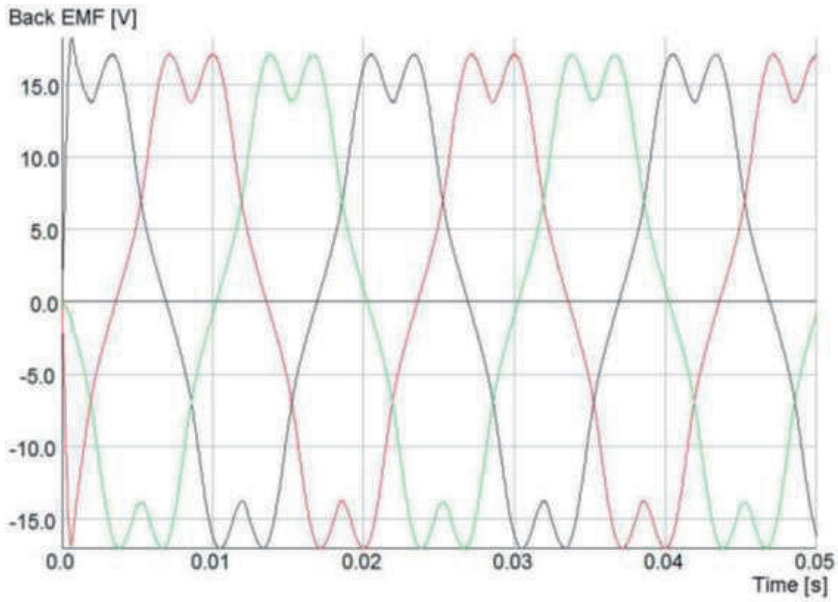
a.



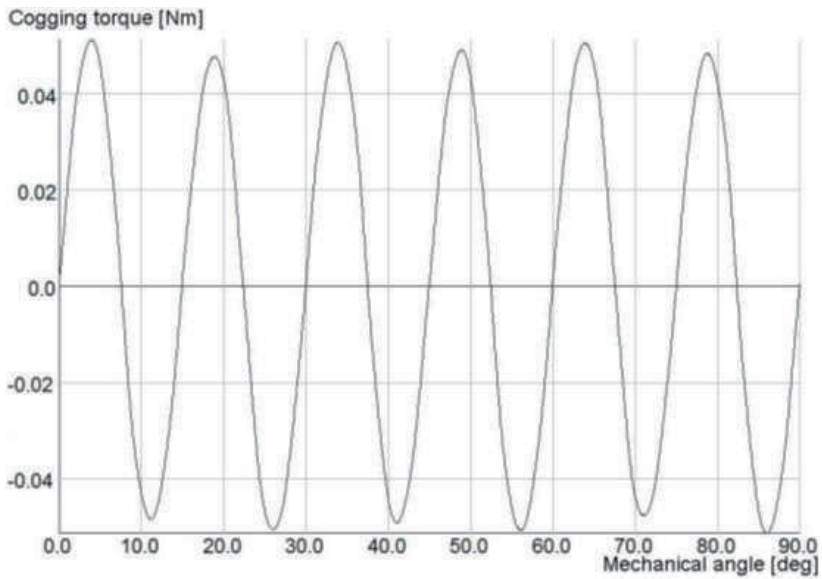
b.

Fig. 7.7 The PM flux density distribution: a) on the  $d$ -axis, b) on the  $q$ -axis.



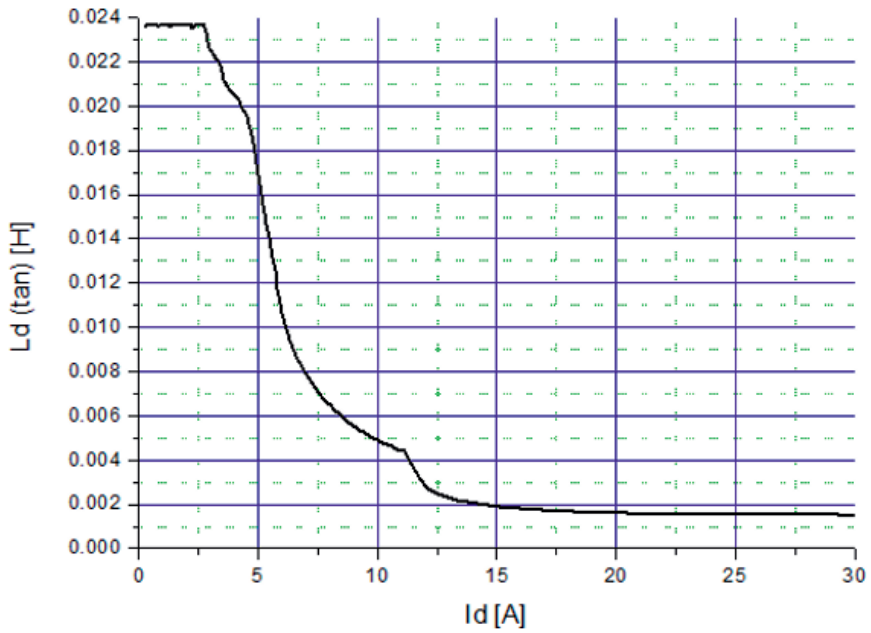


a.

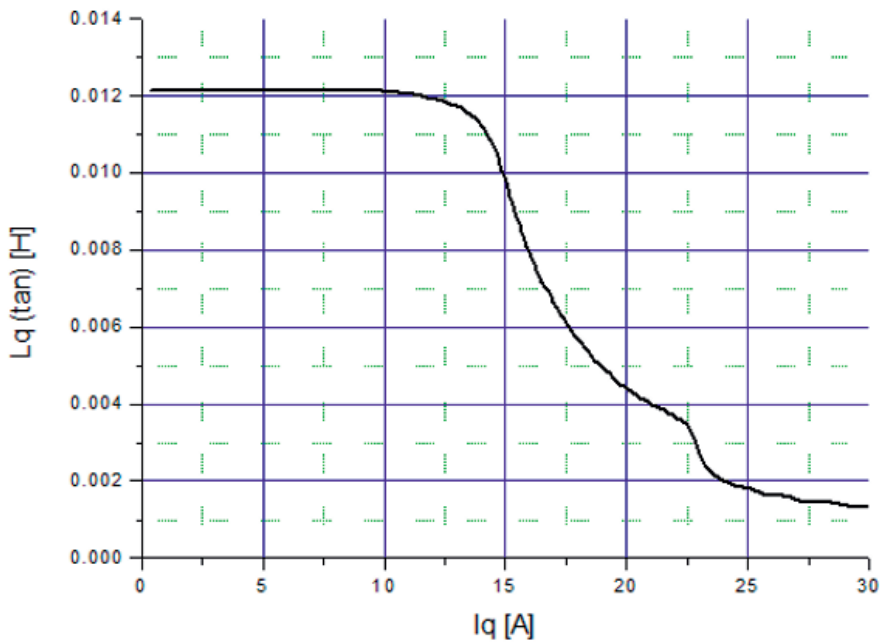


b.

Fig. 7.8 a) The back-EMF, b) The cogging torque.



a.



b.

Fig. 7.9 a) The  $L_d$  inductivity curve versus the  $I_d$  current and b) The  $L_q$  inductivity curve versus the  $I_d$  current.

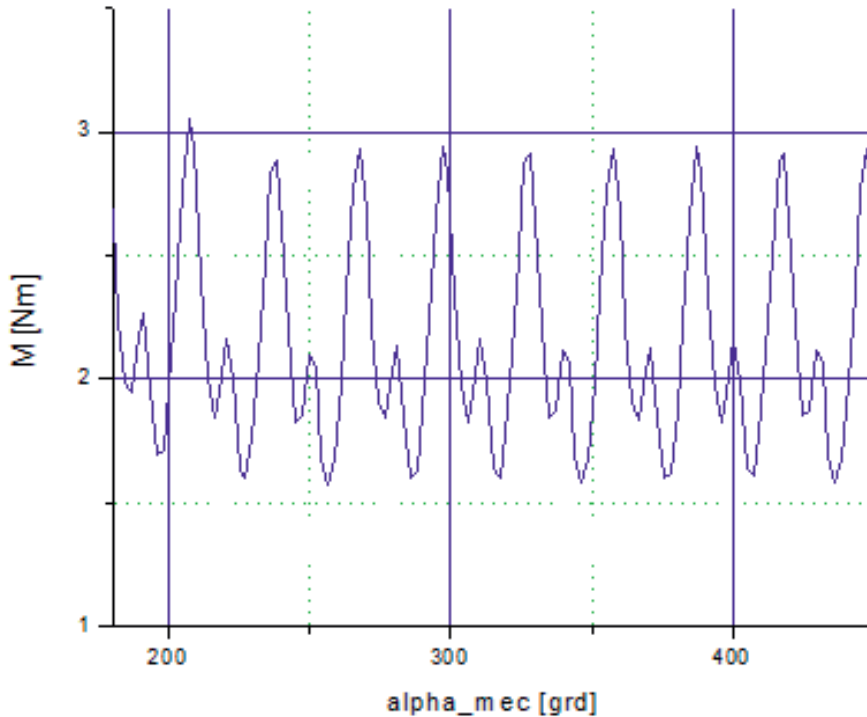


Fig. 7.10 The torque variation at 5 A.

### 7.3.2 The VPM-RSM with Two V Flux Barriers - 2V

In this paragraph, the second proposed rotor geometry (VPM-RSM-2V), with two flux barriers, filled with Ferrites is presented. From the point of view of the topology and of the material characteristics, the stator remains unchanged comparing with the first proposed variant. In this case, for the rotor geometry with two flux barriers, actually two different variants are proposed here (see Fig. 7.11.a. and b.):

- the first variant (2V) has two flux barriers with the same width (2 mm) and the permanent magnet volume is  $V_{PM} = 29,325.04 \text{ mm}^3$ ;
- the second variant (2VU) has also two flux barriers, but the width of these two flux barriers is different (7.2 mm and 1.27 mm), and the permanent magnet volume is  $V_{PM} = 24,339.78 \text{ mm}^3$  (17 % less volume than in the first variant).

For both variants with 2 flux barriers, at least 26 % less permanent magnet volume is used, by comparison with the previous variant 1V. In this case, the simulation of the PM magnetic flux density distribution (on the  $d$ -axis and  $q$ -axis), in air gap, demonstrates the same shape as for the variant 1V. The peak values of the magnetic flux density in the air gap, on the  $d$ - and  $q$ -axes, resulted from simulation, are in this case higher with about 25 % than in the case of 1V rotor geometry variant.

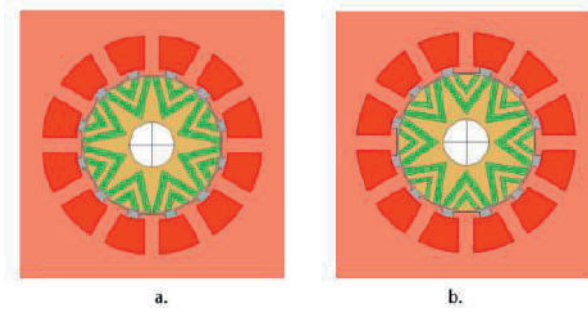


Fig. 7.11 The Two V flux barriers rotor geometry: a) with same width of flux barriers 2V; b) with different widths of the flux barriers 2VU.

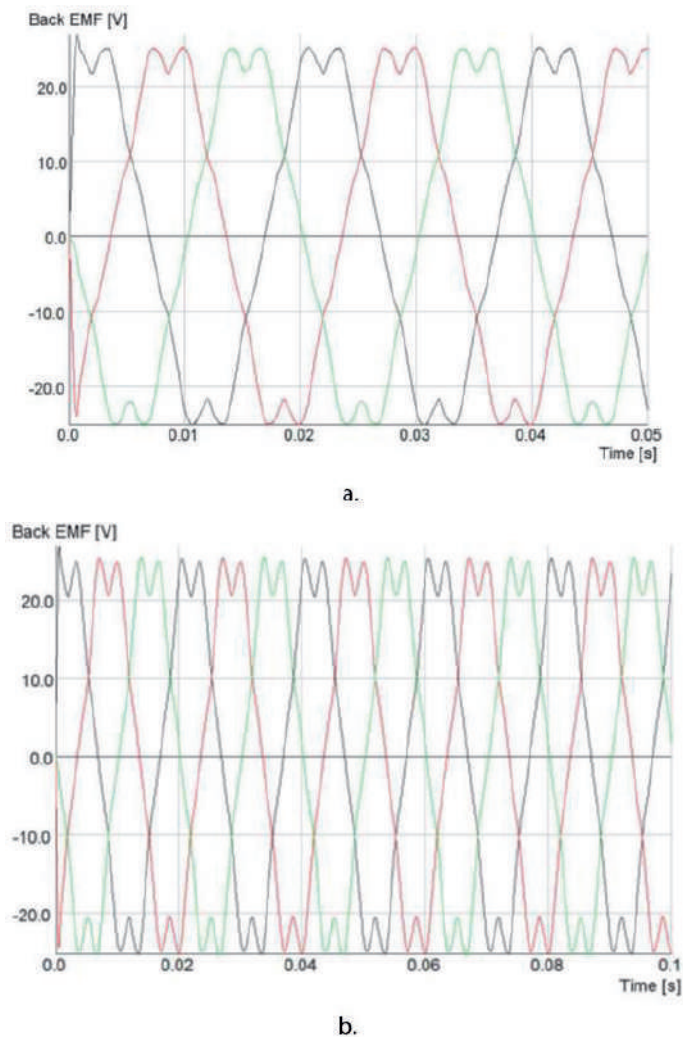
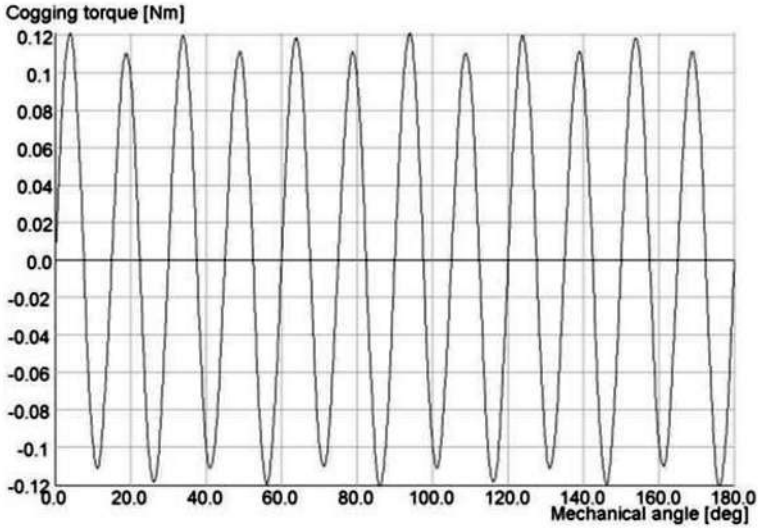
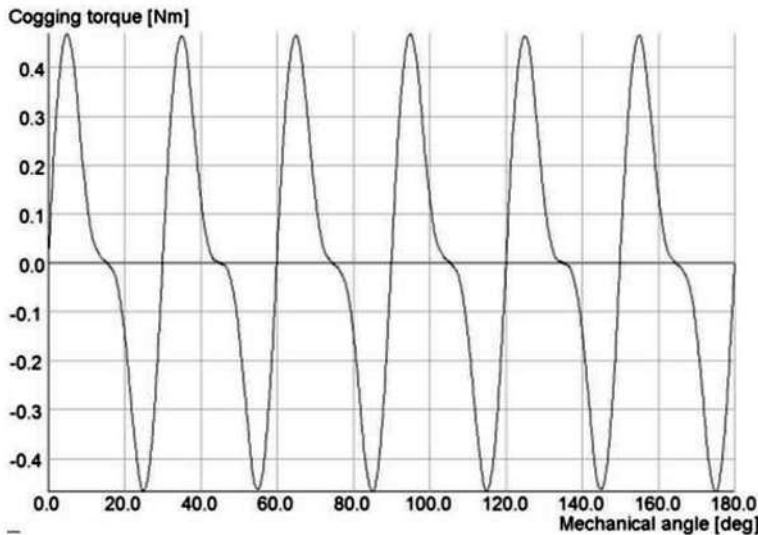


Fig. 7.12 The back-EMF a) for the 2V variant; b) for the 2VU variant.



a.



b.

Fig. 7.13 The cogging torque: a) for the 2V variant; b) for the 2VU variant.

The curves for the back-EMF and the cogging torque, obtained through simulation, shown in Fig. 7.12 and Fig. 7.13, will be further analysed. The 2V rotor geometry variant, with two equal width barriers, is characterised by a back-EMF peak value of  $E_{pk2v} = 24$  V; thus, an increase of 33 % comparing it with the 1V rotor geometry variant, while the 2VU rotor geometry variant has the peak value of the back-EMF  $E_{pk2vu} = 22$  V. The permanent magnet flux linkage has the following values  $\psi_{PM2v} = 0.076$  Wb and  $\psi_{PM2vu} = 0.070$  Wb,

respectively. The cogging torque peak value for the two proposed variants, with two flux barriers, are  $T_{cogq2v} = 0.012$  Nm and  $T_{cogq2vu} = 0.045$  Nm, respectively.

Fig. 7.14 presents the  $L_d$  and  $L_q$  inductances curves versus  $I_d$  and  $I_q$  currents for the 2 flux barriers 2V rotor geometry variant, being very close to the ones for the 2VU rotor geometry variant, not presented in this section. For the  $d$ - and  $q$ -axes inductances, the next values were obtained:  $L_d(4A) = 23.75$  mH,  $L_q(4A) = 15.8$  mH, resulting in a saliency ratio of  $L_d/L_q = 1.50$ .

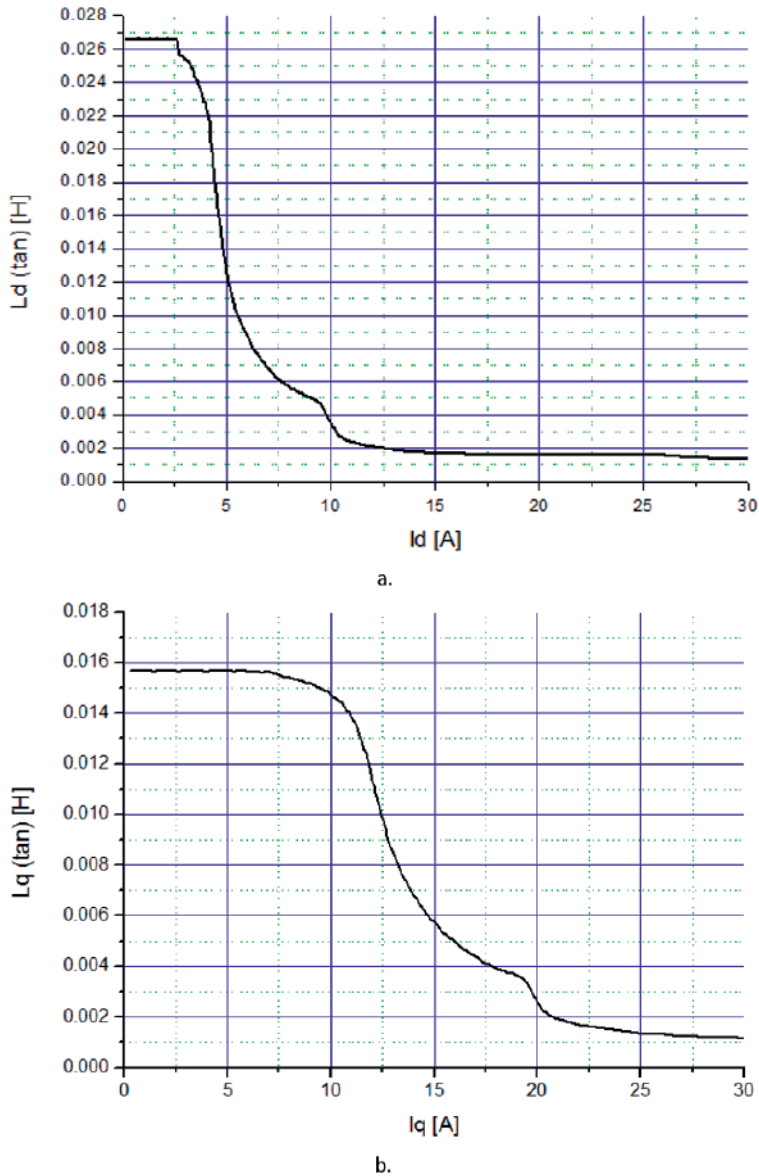


Fig. 7.14 a) The  $L_d$  inductivity curve versus  $I_d$  current and b) The  $L_q$  inductivity curve versus  $I_d$  current in the case of the VPM-RSM-2V.

Fig. 7.15 presents the torque variation caused by the permeance variations at 3.6 A, in the constant torque area, for the proposed VPM-RSM-2V rotor variant at 3.45 A, the average torque being  $T_{av2v} = 1.9$  Nm and the torque ripple being  $T_{ripple2v} = 26.3$  %.

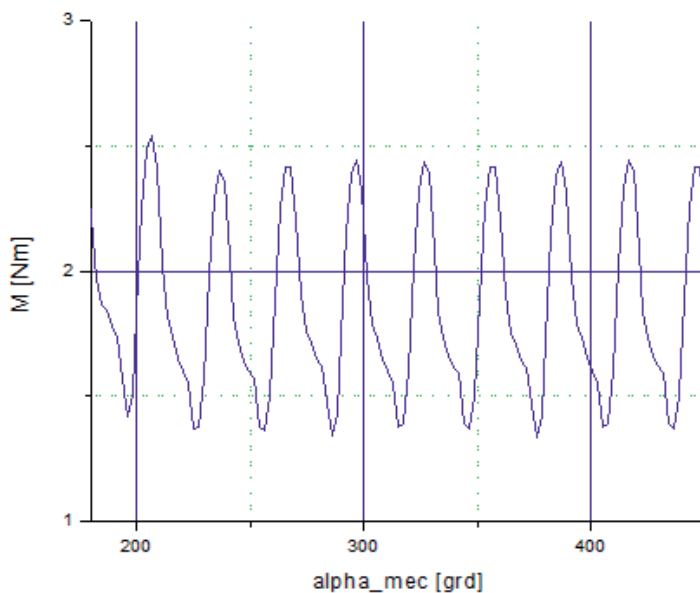


Fig. 7.15 Torque variation at 3.45 A.

### 7.3.3 The PM-RSM with the Flux Concentration Rotor (PMSM-FC)

The third new optimised variant, introduced by the research team at the Department of Electrical Engineering of UPT, is the permanent magnet synchronous motor with flux concentration (PMSM-FC). This variant (presented in Fig. 7.16), using also Ferrites, represents an alternate solution to the PMSM built with rare-earth PMs, in which case, the stator remains unchanged. The volume of the permanent magnet  $V_{PM} = 26,481.72$  mm<sup>3</sup> has been calculated using the equations (7.42) and (7.43). A volume reduction of 9.7 % in comparison with the VPM-RSM-2V variant and an increase of 8 [%] in comparison with the variant VPM-RSM-2VU, can be noticed. The simulation result of the PM flux density distribution in the air gap is shown in Fig. 7.17. The peak values of the simulation results of the  $d$ - and  $q$ -axes magnetic flux density in the air gap are greater than 0.6 T. Fig. 7.18 shows the shapes of the back-EMF and of the cogging torque at 750 rpm. From Fig. 7.18 a., the peak value of the back-EMF ( $E_{pk} = 22$  V) and the peak value of the cogging torque ( $T_{cogg} = 0.021$  Nm) can be determined. By analysing the results, it can be concluded that a decrease of the back-EMF of 8.33 % in comparison with the VPM-RSM-2V variant and the VPM-RSM-2VU variant is achieved. In the case of peak values for the cogging torque, the variant with the flux concentration rotor (PM-RSM-FC) has an increased value of 75 % in comparison with the VPM-RSM-2V variant and a diminution of 114 % in comparison with the VPM-RSM-2VU variant.

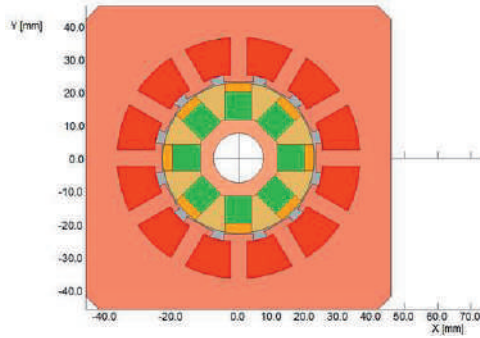
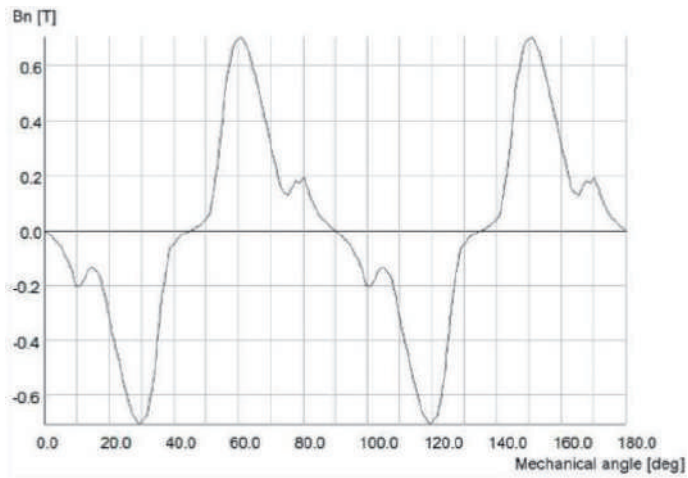
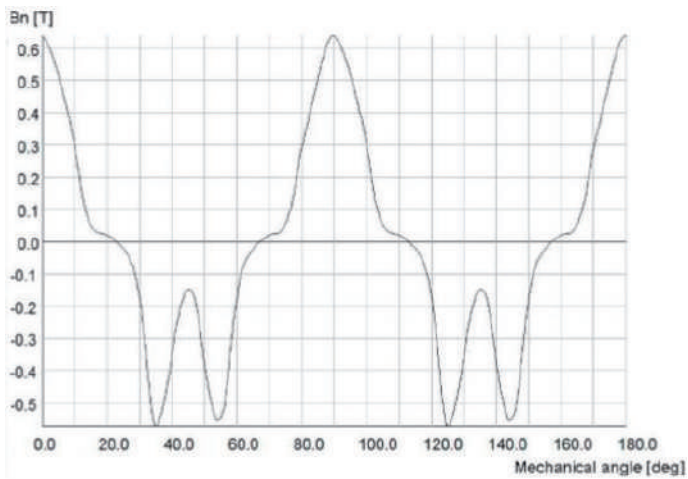


Fig. 7.16 The PM-RSM with the flux concentration (PM-RSM-FC).



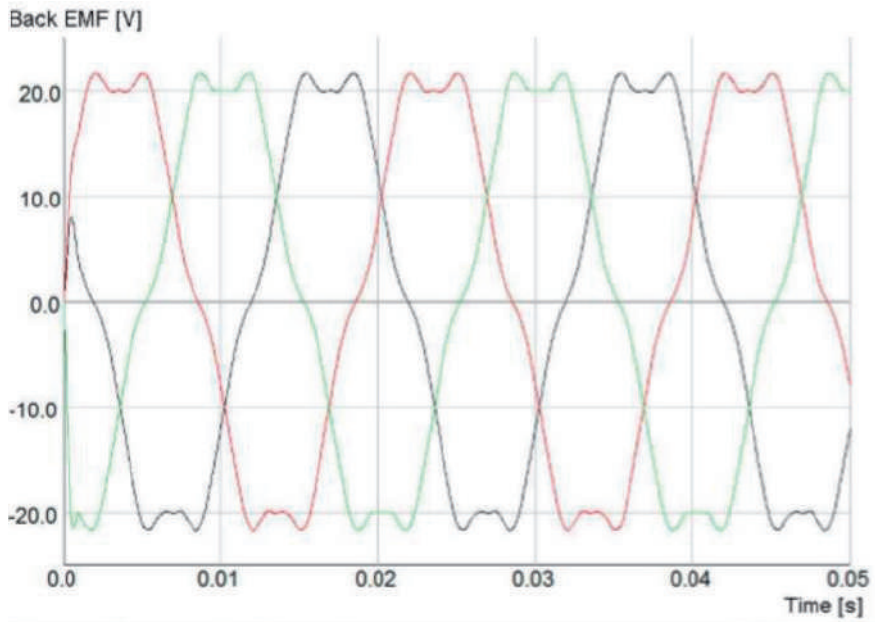
a.



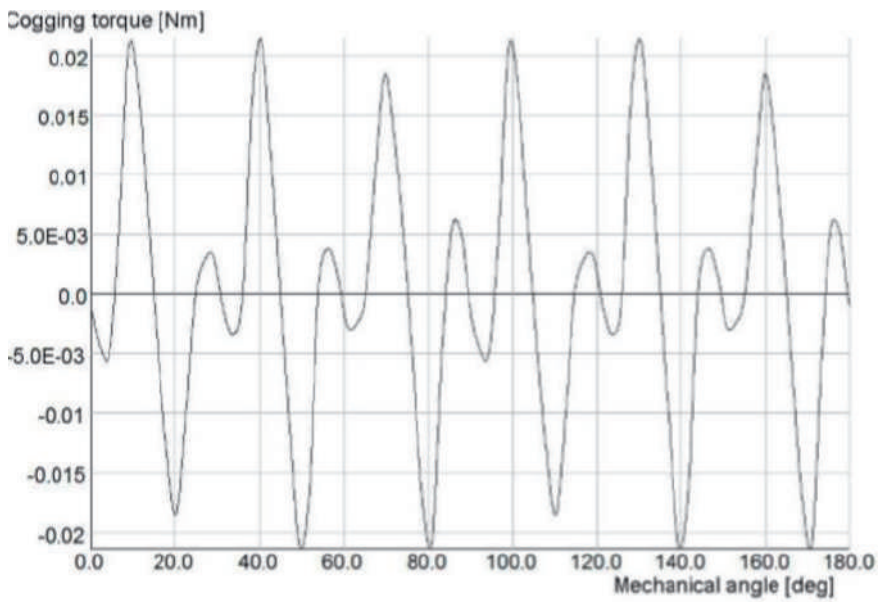
b.

Fig. 7.17 Flux density distribution: a) on the  $d$ -axis, b) on the  $q$ -axis.





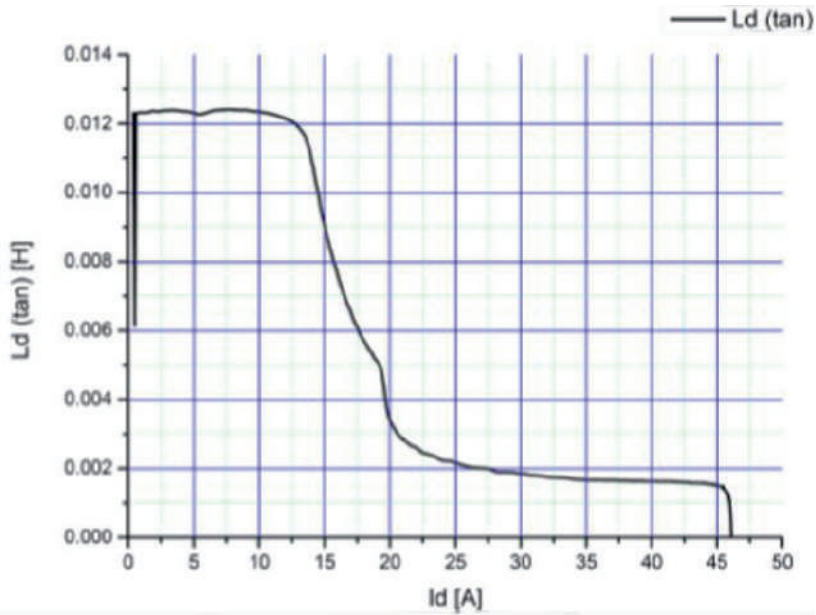
a.



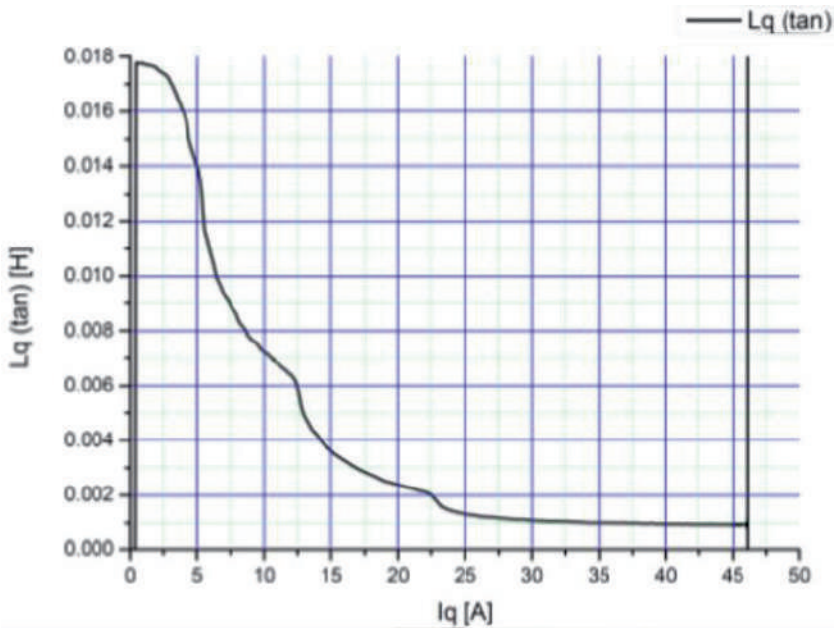
b.

Fig. 7.18 a) Back-EMF, b) Cogging torque.

The simulation curves of the  $L_d$  and  $L_q$  inductances versus the  $I_d$  and  $I_q$  currents are shown in Fig. 7.19.



a.



b.

Fig. 7.19 a)  $L_d$  inductivity curve versus  $I_d$  current and b)  $L_q$  inductivity curve versus  $I_d$  current

The inductances curves on the d- and q-axes were simulated using the FEM and the method described by the relationships (7.44) and (7.45). For the inductances on the d- and q-axes, the following values were obtained:  $L_d(4A) = 17.76$  mH,  $L_q(4A) = 15.91$  mH. Fig. 7.20 presents the torque variation caused by the permeance variations at 5 A, in the constant torque area. In this case, for the proposed PM-RSM with the rotor flux concentration at 5 A, the average torque is  $T_{av\ PMSM-FC} = 7.2$  Nm and the torque ripple is  $T_{ripple\ PMSM-FC} = 26.3$  %.

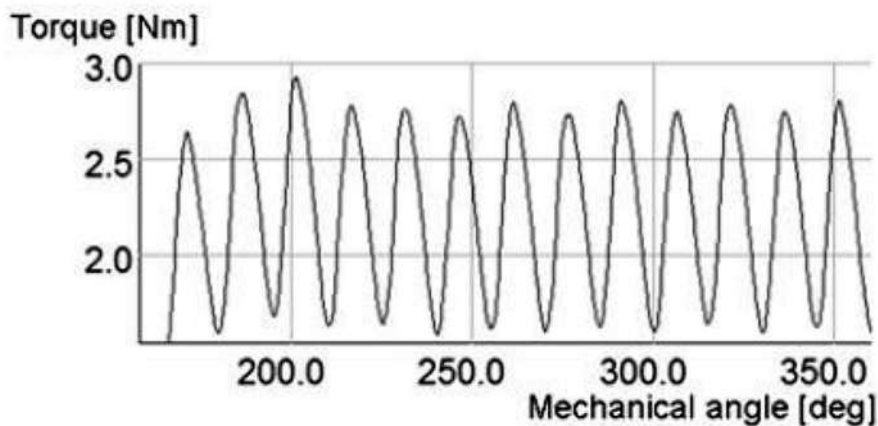


Fig. 7.20 Torque variation at 5.0 A.

The simulation results of the proposed rotor geometry solutions are listed in Table 7.1.

Tabel 7.1. Simulation results

	Rotor Type			
	Concentrated flux	2V	2VU	1V
$V_{PM}[\text{mm}^3]$	26,481.72	29,325.04	24,339.78	39,587.37
$L_d(4A)$ [mH]	17.76	23.75	~23.75	23.80
$L_q(4A)$ [mH]	15.91	15.8	~15.8	17.1
$L_q/L_d$	0.8	1.50	~1.50	1.96
$\psi_{PM}$ [Wb]	0.070	0.076	0.070	0,051
$T_{av}/I$ [Nm/Apk]	7.2/4.5	1.9/3,45	~1.9/3.45	2,3/5
$T_{ripple}$ [%]	26.3	26.3	~26.3	26

### 7.3.4 The experimental results

The PM-RSM-FC rotor, shown in Fig. 7.21, was manufactured by the Electromotor Company, in Timișoara. The experimental results were compared with the simulation results.

The measured values of the PM-RSM-FC motor parameters are listed in Table 7.2.

Tabel 7.2. The measured PM-RSM-FC motor parameters

$R_s$ [ $\Omega$ ]	$L_d$ [mH]	$L_q$ [mH]	$\Phi_{PM}$ [mWb]
7.65	19.12	14.98	68.0



Fig. 7.21 The PM-RSM with the flux concentration rotor (PM-RSM-FC).

The measured values of the inductances on the  $d$ - and  $q$ -axes are different from the simulation values and the  $L_q/L_d$  ratio is better for the measured values case. This difference can be explained by the fact that the pole geometry was modified for a better fixation of the magnets. The difference between the simulation values and the measurements is that the PM flux linkage is small and, thus, the simulation results have been validated by the experimental ones. The obtained prototype was also tested on the dynamometer. The PM-RSM-FC electromechanical performance (the motor current versus the torque and the efficiency versus the torque) are presented in Fig. 7.22 and Fig. 7.23.

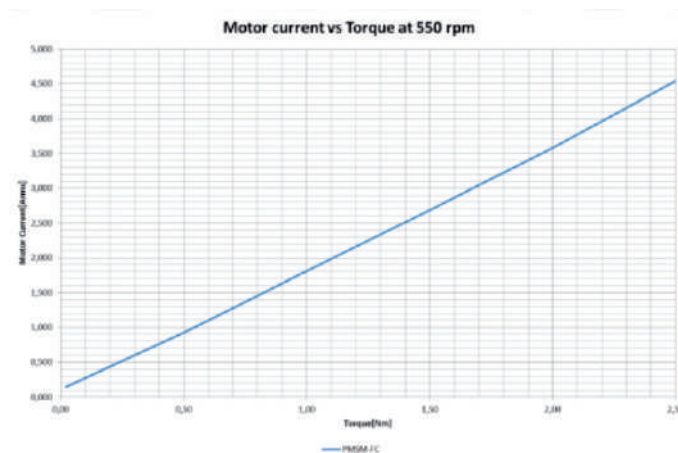


Fig. 7.22 Motor performances: the motor current versus the torque.

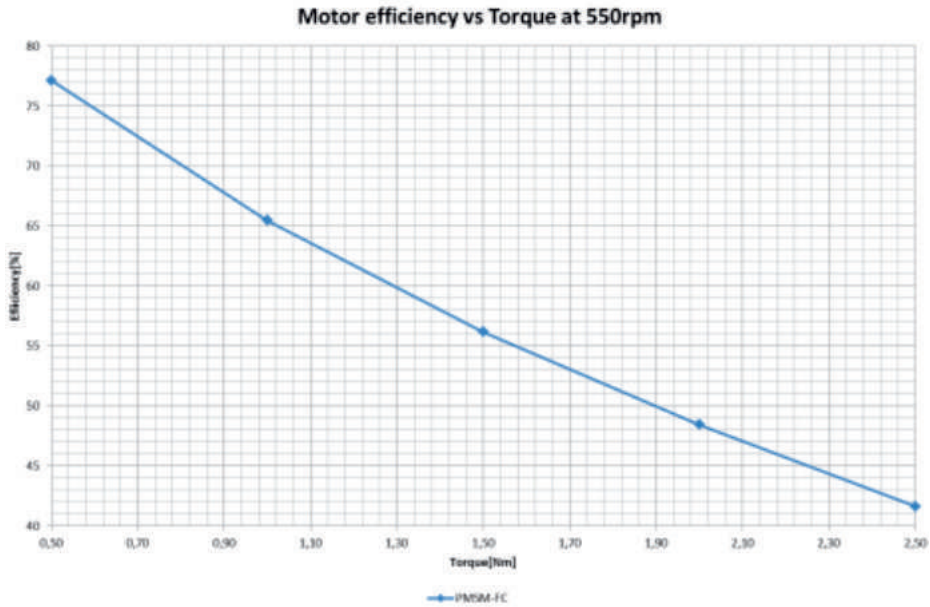


Fig. 7.23 Motor performances: the motor efficiency versus the torque.

## 7.4 Implementation of a PM – RSM motion sensorless vector control

### 7.4.1 The PM-RSM experimental setup

A photograph of the PM - RSM prototype used for the motion sensorless vector control implementation is presented in Fig. 7.24.a, together with its rotor lamination configuration (see Fig. 24.b), [18].

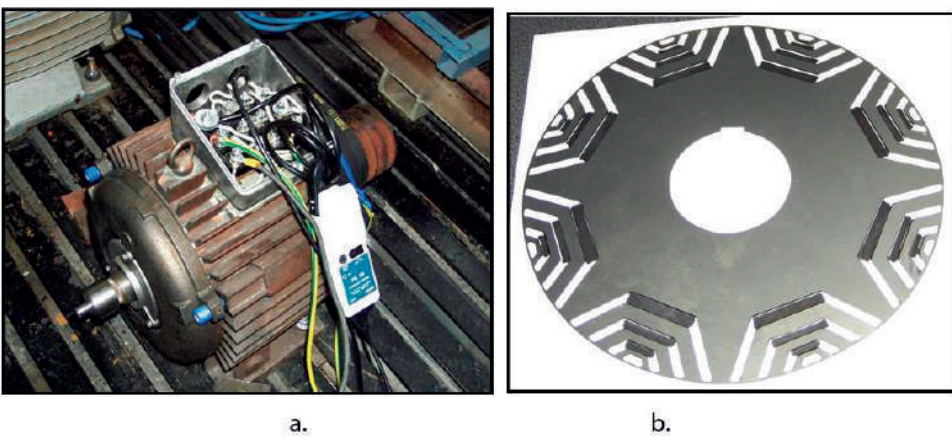


Fig. 7.24 a) The PM-RSM prototype used in the experimental setup of the motion sensorless control; b) the rotor lamination configuration of the PM-RSM.

The prototype's main specifications are presented in Table 7.3.

Tabel 7.3. Pm-Rsm Specifications

Rated power	750 W
Rated speed	1,500 rpm
Rated frequency	50 Hz
Rated torque	6.3 Nm
Rated phase to phase voltage	22 V (rms)
Rated phase current	50 A (rms)
Number of pole pairs ( $p_1$ )	2
Stator resistance per phase ( $R_s$ )	0.037 $\Omega$
Stator resistance per phase including wires resistance ( $R_s$ )	0.065 $\Omega$
$d$ -axis inductance ( $L_d(i_d)$ )	2.5 mH (saturated value)
$q$ -axis inductance ( $L_q$ )	0.5 mH
Permanent magnet flux ( $\psi_{PM}$ )	0.011 Vs/rad
Total inertia ( $J$ )	1x10 <sup>-3</sup> kgm <sup>2</sup>
Viscous friction coefficient ( $B$ )	1x10 <sup>-4</sup> Nm s/rad

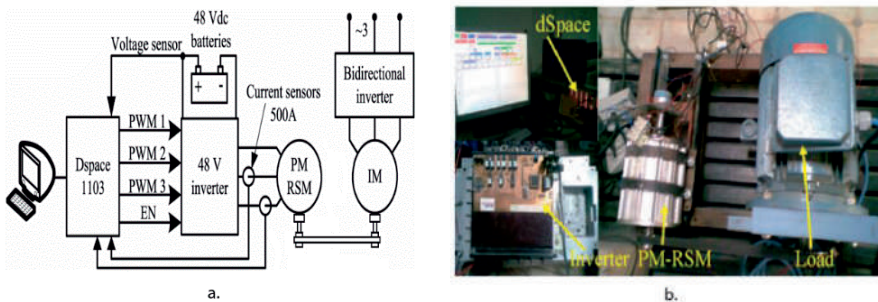


Fig. 7.15 The overview of the experimental setup: a) the control block scheme; b) the control real implementation.

The experimental setup contains a belt transmission 10 / 13 kW (1,500 / 3,000 rpm) and an induction motor driven by an ACS 600 inverter (see Fig. 7.25). This experimental setup was carried out in the Intelligent Motion Control Lab, Faculty of Electrical Engineering, Timisoara, Romania.

### 7.4.2 The mathematical model of the PM-RSM including magnetic saturation effects

The PM-RSM is rather a good saliency interior PM rotor synchronous machine. The PMs are placed on the  $q$ -axis, while the  $d$ -axis shows higher magnetic permeance ( $L_d > L_q$ ).

In general, in the synchronous machine model, the flux-current relationship is linear with the constant inductance. But, because of the magnetic saturation, the flux cannot be expressed as a function of the inductance.

So, the magnetisation function represents the flux-current function  $\psi_d(i_d) = L_d(i_d)i_d$ . Therefore, the general PM-assisted reluctance synchronous machine model, including the magnetic saturation effects, is comprised of the following expressions:

$$\bar{V}_s = R_s \cdot \bar{i}_s + \frac{d\bar{\psi}_s}{dt} + j\omega_r \cdot \bar{\psi}_s \quad (7.5)$$

$$\bar{\psi}_s = L_d(i_d) \cdot i_d + j(L_q \cdot i_q - \psi_{PMq}) \quad (7.6)$$

$$T_e = \frac{3}{2} \cdot p_1 \cdot [\psi_{PMq} + (L_d(i_d) - L_q) \cdot i_q] \cdot i_d = \frac{3}{2} \cdot p_1 \cdot \text{Re}(j \cdot \bar{\psi}_s \cdot \bar{i}_s^*) \quad (7.7)$$

Where  $V_s$  is the stator voltage,  $i_s$  is the stator current,  $R_s$  is the stator resistance,  $L_d$ ,  $L_q$  are the  $dq$  axes inductances,  $\psi_s$  is the stator flux,  $\psi_{PMq}$  is the PM flux linkage,  $T_e$  is the electromagnetic torque,  $\omega_r$  is the electrical rotor speed and  $p_1$  is the number of pole pairs. The magnetic saturation is considered only in the  $d$ -axis  $L_d(i_d)$  as depicted in fig. 7.26, with  $L_q$  constant.

In practice, a memorised look-up table with linear interpolation between points was used.

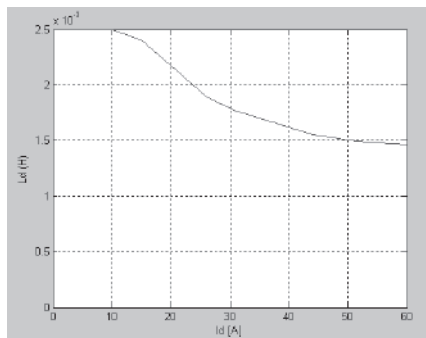


Fig. 7.26 The magnetic saturation curve  $L_d(i_d)$ .





### 7.4.3.1 The speed and position observers using the signal injection method

**For low speed operation,** a speed observer using the signal injection has been implemented as shown in Fig. 7.28. A rotating carrier-voltage  $\underline{V}_c = V_c \exp(j\omega_c t)$  with  $V_c = 1V$  and  $\omega_c = 500$  Hz is injected in the stator superimposing on top of driving fundamental stator-voltage  $\underline{V}_s$ . The resulting stator current  $\underline{I}_s$ , modulated by the position dependent inductances with magnetic saliency, contains carrier-current harmonics with the rotor position information  $\theta_r$ . Usually, the negative 1<sup>st</sup> order sequence carrier harmonic  $\underline{I}_{cn1} = I_{cn1} \exp\{j(-\theta_c + 2\theta_r + \pi/2)\}$  with  $\theta_c = \omega_c t$  [25] is selected from the measured stator current.

Two schemes have been tested: 1) Observer with synchronous low-pass filter (LPF) in carrier reference (upper part of Fig. 7.28.a) [27]. 2) Novel observer with vector filter in D-module in stator reference as band-pass filter (BPF) with central frequency  $\omega_c$  and phase-sign discrimination (lower part of Fig. 7.28.a). Both observers select the  $\underline{I}_{cn1}$  harmonic. A phase-locked loop (PLL) tracking observer shown in Fig. 7.28.b extracts the estimation of the rotor speed  $\hat{\omega}_r$  and the position  $\hat{\theta}_r$  from the phase of  $\underline{I}_{cn1}^c$  harmonic in the carrier reference, with PLL error  $\sigma \sim 2I_{cn1}(\theta_r - \hat{\theta}_r - \hat{\theta}_{r0})$ . During the experiments, it was noticed that both observers in Fig. 7.28.a have similar behaviour, with very robust estimation, almost independent of the machine parameters.

The initial rotor position  $\hat{\theta}_{r0}$  is correctly identified at standstill by both observers in the range of  $(-\pi/2, \pi/2)$  radians. For full angle range, an uncertainty of  $\pi$  radians appears, and this is discriminated by the magnet polarity detection using the 2<sup>nd</sup> order harmonics [25], [26].

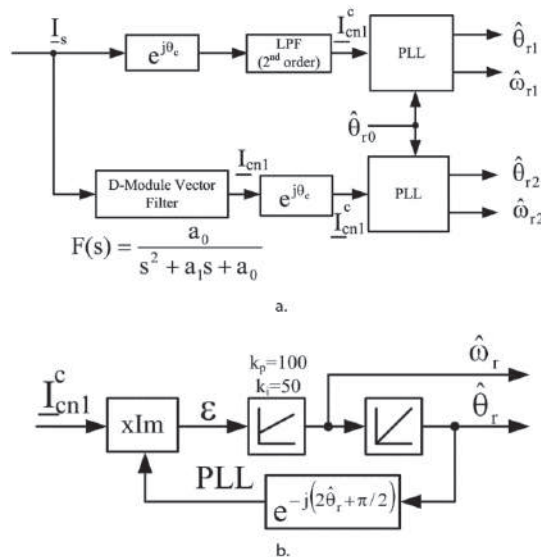


Fig. 7.28 Speed and position observers with signal injection: a) Observers with synchronous low-pass filter and with vector filter in D-module; b) PLL used in a.

### 7.4.3.2 The speed estimation from the stator flux observer

**For the medium-high speed operation**, above 50 rpm, the signal injection is disabled to reduce losses, and thus the associated speed and position observer from Fig. 7.28 is also inhibited. Now, additional speed estimation is required, with a smooth transition between the two of them. The proposed solution estimates the rotor speed  $\hat{\omega}_r$  from the estimated stator flux vector  $\hat{\underline{\Psi}}_s$ :

$$\hat{\omega}_r = \hat{\omega}_{\psi_s} + \frac{d\hat{\theta}_{\psi_{dq}}}{dt}; \hat{\omega}_{\psi_s} = \frac{d\hat{\theta}_{\psi_s}}{dt}. \quad (7.9)$$

where  $\hat{\omega}_{\psi_s}$   $\hat{\theta}_{\psi_s}$  are the estimated speed and position of  $\hat{\underline{\Psi}}_s$  in  $\alpha\beta$ -stator reference, which is given by the stator flux observer presented in the Fig. 7.29 below;  $\hat{\theta}_{\psi_{dq}}$  is the estimated position of  $\hat{\underline{\Psi}}_s$  in  $dq$ -rotor reference (Fig. 7.29).

The stator flux observers combine voltage-current models (Fig. 7.29): the current model, including the magnetic saturation, prevails at low speed, while the voltage model prevails at medium-high speed with a smooth transition between them depending on the speed. It contains the voltage model in the stator reference connected in parallel with the current model in the rotor reference frame, using a PI compensator driven by the flux estimation error. Both models are enclosed within the correction loop. The PI correction loop encloses only the voltage model, while the current model is open loop operated.

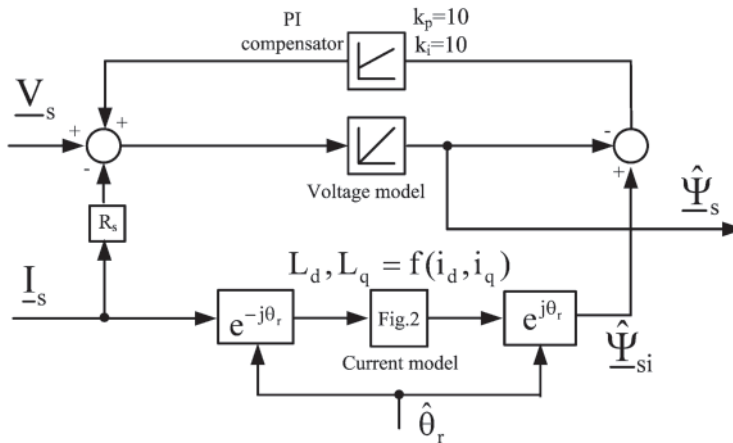


Fig. 7.29 Stator flux observer with combined voltage-current models.

With an accurate stator flux estimation and measured currents, the torque estimation is simply calculated in the  $\alpha\beta$ -stator reference as:

$$\hat{T}_e = 3 / 2 p_1 (\hat{\Psi}_\alpha I_\beta - \hat{\Psi}_\beta I_\alpha). \quad (7.10)$$

The rotor position estimation  $\hat{\theta}_r$  is required in the current model within the flux observer – but only at low speed, below 50rpm, because at medium-high speed the voltage model becomes dominant and the signal injection (which gives  $\hat{\theta}_r$ ) discontinuation does not produce a notable influence on the flux observer. The rotor speed estimation  $\hat{\omega}_r$  in the whole speed range is required in the flux (and torque) referencer, and accurately – in the speed controller.

The 1<sup>st</sup> main component of the rotor speed in (7.9), i.e.,  $\hat{\omega}_{\psi_s}$  is extracted together with  $\hat{\theta}_{\psi_s}$  from the  $\hat{\Psi}_s$  phase by a PLL observer similarly as in Fig. 7.28.b. The 2<sup>nd</sup> component, living only in transient regimes, is obtained from the electric torque expression that can be derived as:

$$\hat{T}_e = \frac{3}{2} p_1 \frac{\hat{\Psi}_s \Psi_{PMq}}{L_q} \cos \hat{\theta}_{\psi_{dq}} + \frac{3}{2} p_1 \frac{\hat{\Psi}_s^2}{2} \left( \frac{1}{L_q} - \frac{1}{L_d} \right) \sin 2\hat{\theta}_{\psi_{dq}} \cdot \quad (7.11)$$

The angle  $\hat{\theta}_{\psi_{dq}}(\hat{T}_e, \hat{\Psi}_s)$  is extracted from a look-up table with linear interpolation based on (7.11) using  $\hat{T}_e$  (7.10) and  $\hat{\Psi}_s$  from Fig. 7.29, with an average value for  $L_d$ , because the magnetic saturation is not so important. Then,  $d\hat{\theta}_{\psi_{dq}}/dt$  is calculated to finally decide  $\hat{\omega}_r$  in (7.9).

#### 7.4.4 The motion sensorless vector control experimental results

The results obtained by the real implementation of the PM-RSM motion sensorless vector control are presented in what follows [27].

Fig. 7.30 presents the 50 rpm speed reversal and back to 50 rpm using the sensorless vector control system.

As it can be observed in the estimated speed waveform (see Fig. 7.30.a), with the exception of a single spike during start up, the dynamics are very good (less than 0.25 s) during the speed reversal. As in the previous case, here again the encoder speed is not as good as the estimated speed is. In Fig. 7.30.b, the error between the encoder and the estimated speed is 120 pm during the speed reversal.

In this case, the position error (see Fig. 7.30.c) is better than in the 30 rpm case (0.1 rad for 50 rpm and 0.25 rad for -50 rpm during the steady state).

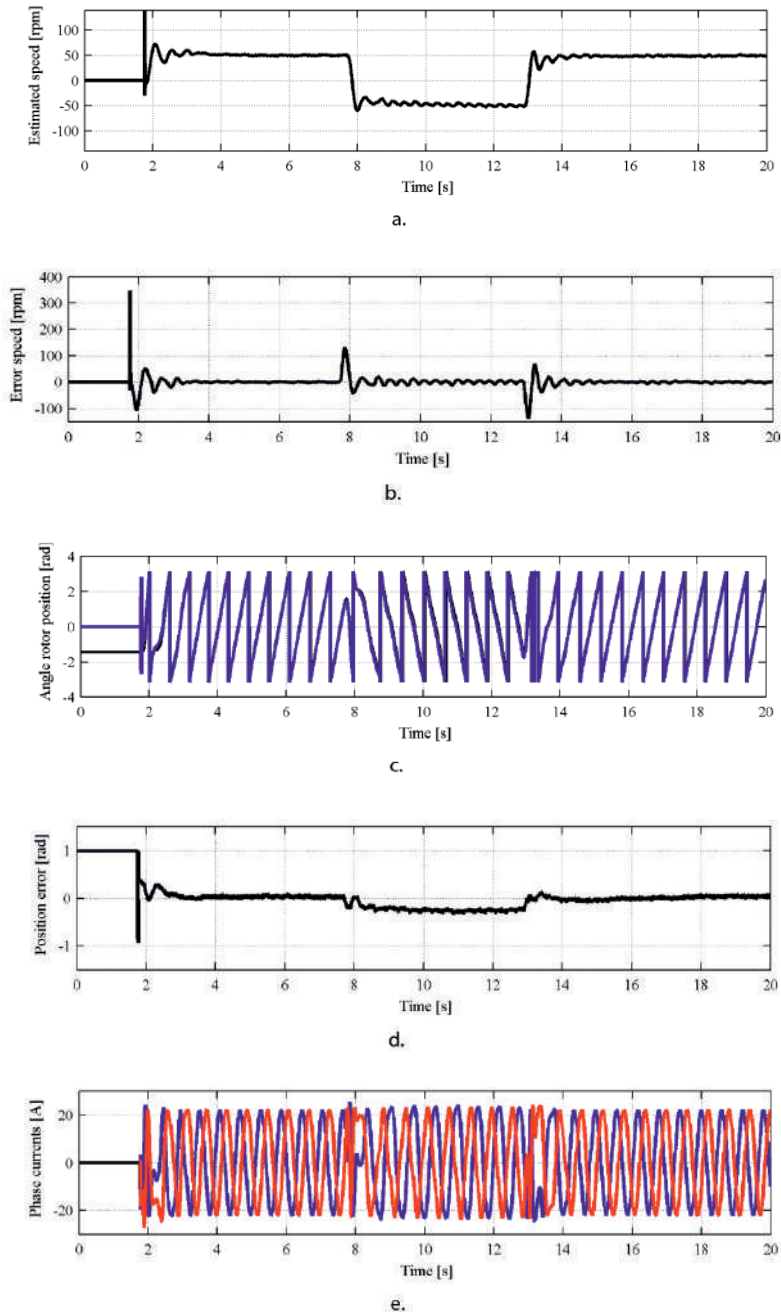


Fig.7.30  $\pm 50$  rpm speed reversal using **the sensorless vector control system**; from top to bottom: a) encoder speed; b) error between the encoder and the estimated speed; c) angle rotor position (actual and estimated (blue)); d) error between the actual and the estimated angle rotor position; e) phase currents.

The second experiment was performed at 1,000 rpm, as depicted in the below Fig. 7.31.

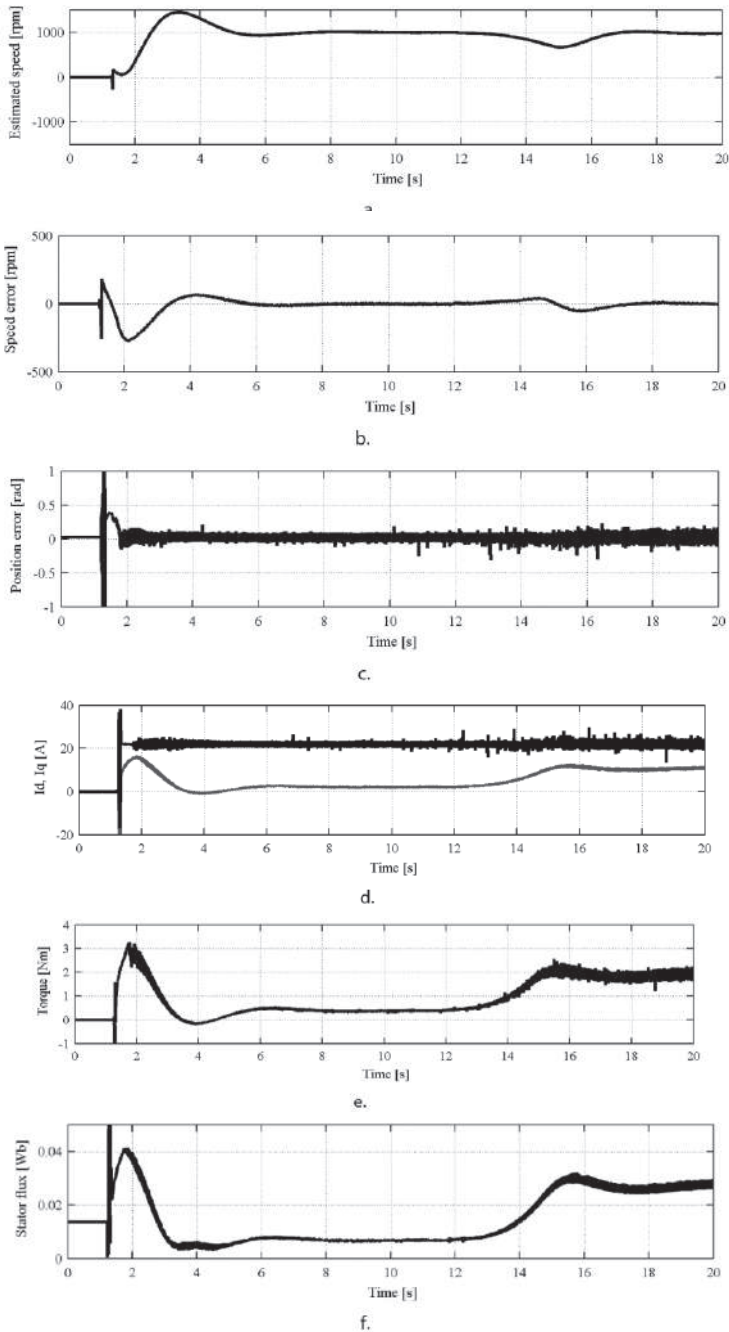


Fig. 7.31 Start up at 1,000 rpm followed by a step torque load at 5 s using the sensorless vector control system; from top to bottom: a) estimated speed; b) error between the encoder and the estimated speed; c) error between the actual and estimated angle rotor position; d)  $I_d$ ,  $I_q$  currents; e) estimated torque; f) estimated stator flux.

The speed response is indeed quite slow and with a large overshoot, but, since the purpose of this research was not to obtain high machine dynamics, it is considered satisfactory. Also, the estimated speed has a negative spike at startup, but this is favourable because the reference torque will be a bit higher (Fig. 7.31.a). However, the position error is very good, below 0.25 rad (see Fig. 7.31.c).

As it was prescribed, the  $I_q$  current is kept constant, while the  $I_d$  current increases only during loading when the necessary torque has to be developed (see Fig. 7.31.d).

This is also the case of the estimated stator flux, which at steady state is maintained at a low value (almost permanent magnet flux) and then, during loading, it increases (see Fig. 7.31.f).

It has to be noticed that significant loading operation (up to the maximum available torque) was not possible for speeds below 400 rpm due to the low performance of the bidirectional inverter driving the load machine at low speeds.

Note: The PM-RSM prototype has rather high magnetic saliency and four flux barriers/pole, which is known to make the rotor position tracking more difficult than for the inset IPMSM.

## 7.5 Conclusion

Throughout this research study, the team at the Department of Electrical Engineering of UPT proposes three different low-cost ferrite solutions: the first one is the one V permanent magnet assisted synchronous reluctance rotor (VPM-RSM), the second one is the two permanent magnet assisted synchronous reluctance rotor and the third one is a permanent magnet synchronous motor with a flux concentration rotor (PM-RSM-FC), all built as an alternative solution to the tangential inserted rare-earth permanent magnets synchronous motor (IPMSM).

The finite element (FEM) approach has been used to highlight the performances of the suggested rotor geometries. The PMSM-FC rotor was manufactured and the simulation results have been validated through experimental results. All the rotor geometries suggested here, with flux barriers or flux concentration and Ferrites, are attractive alternative solutions to reduce the cost of the rotor by changing the type of the PM.

In the second part of this chapter, a vector control system was developed for the motion sensorless implementation of a transversally laminated PM-RSM (PM-assisted reluctance synchronous motor). Its operation and its rated speed have been studied while using it.

A detailed presentation of the suggested drive as well as the experimental results related to it were also discussed here.

## 7.6 References

- [1] S. Muşuroi, C. Şorândaru, M. Greconici, N.V. Olărescu, M. Weinman, "Low-cost ferrite permanent magnet assisted synchronous reluctance rotor an alternative for rare earth permanent synchronous motors", *Industrial Electronics Society, IECON 2013- 39th Annual Conference of the IEEE*, 10-13 Nov. 2013, Vienna, pp. 2966-2970.
- [2] S. Morimoto, M. Sanada, Z. Takeda, K. Taniguchi, "Optimum machine parameters and design of inverter driven synchronous motors for wide constant power operation", in *Conf. Rec. IEEE-IAS Annual Meeting*, 1994, pp. 177–187.
- [3] J. Cross, P. Viarouge, "Synthesis of High Performance PM Motors with Concentrated Windings", *IEEE Transactions on Energy Conversion*, vol. 17, no. 2, June 2007.
- [4] A. Vagati, A. Fratta, G. Franceschini, P.M. Rosso, "AC motor for high performance drives: a design-based comparison", *IEEE Trans. On Industry Applications*, Sept.-Oct. 1996, vol. 32, n. 4, pp. 1211-1219.
- [5] H. Akita, Y. Nakahara, N. Miyake, T. Oikawa, "New Core Structure and Manufacturing Method for High Efficiency of Permanent Magnet Motors", *Rec. of 2003 IEEE Industry Applications Society Annual Meeting*, vol. 1, Salt Lake City, UT, October 2003, pp. 367-377.
- [6] Y. Takeda, N. Matsui, J. Oyama, H. Domeki, "Classification and technical term of reluctance motors from the viewpoint of control strategy and motor construction", in *Proc. JIASC'02*, vol. 2, 2002, pp. 759–767.
- [7] T.A. Lipo, A. Vagati, L. Malesani, T. Fukao, "Synchronous reluctance motors and drives-a new alternative", *IEEE-IAS Annual Meeting Tutorial*, October 1997.
- [8] A. Vagati, M. Pastorelli, G. Franceschini, S.C. Petrache, "Design of low-torque-ripple synchronous reluctance motors", *IEEE Trans. Ind. Appl.*, vol. 34, no. 4, pp. 758–765, Jul./Aug. 1998.
- [9] P. Niazi, H.A. Toliyat, D.H. Cheong, J.C. Kim, "A Low-Cost and Efficient Permanent-Magnet-Assisted Synchronous Reluctance Motor Drive", *IEEE Transactions on Industry Applications*, Vol.43, no2, (2007).
- [10] S. Talebi, P. Niazi, H.A. Toliyat, "Design of Permanent Magnet-Assisted Synchronous Reluctance Motors Made Easy", *Industry Applications Conference, 2007, 42nd IAS Annual Meeting. Conference Record of the 2007 IEEE*, 23-27 Sept. 2007, pp. 2242 – 2248.
- [11] T. Matsuo, T.A. Lipo, "Rotor design optimization of synchronous reluctance machine", *IEEE Trans. Energy Conversion*, vol. 9, pp. 359–356, June 1994.
- [12] S.A. Long, N. Schofield, D. Hawe, M. Piron, M. McClelland, "Design of a switched reluctance machine for extended speed operation", *IEEE Proc. of IEMDC03*, pp235-240.
- [13] E. Armando, P. Guglielmi, M. Pastorelli, G. Pellegrino, A. Vagati, "Accurate Magnetic Modelling and Performance Analysis of IPMPMASR Motors", *IEEE-IAS Annual Meeting*, 23-27 Sept. 2007, New Orleans (USA), pp. 133 – 140.
- [14] N. Bianchi, *Electrical Machine Analysis Using Finite Elements*, ser. Power Electronics and Applications Series. Boca Raton, FL: CRC Press, 2005.
- [15] E.E. Montalvo-Ortiz, S.N. Foster, J.G. Cintron-Rivera, E.G. Strangas, "Comparison between a spoke-type PMSM and a PMASynRM using ferrite magnets", *Electric Machines & Drives Conference IEMDC 2013*, 12-15 May, 2013, Chicago IL, pp.1080-1087.
- [16] P. Guglielmi, B. Boazzo, E. Armando, G. Pellegrino, A. Vagati, "Permanent-Magnet Minimization in PM-Assisted Synchronous Reluctance Motors for Wide Speed Range", *IEEE Transactions on Industry Applications*, vol. 49, no. 1, pp. 31-41, January/February 2013.

- [17] S. Muşuroi, D. Popovici, C. Şorândaru, M. Greconici, M. Svoboda, Contract for research-development and consultancy, Protocol contract 9228/6.07.2010.
- [18] I. Boldea, L. Tutelea, C.I. Pitic, "PM – assisted Reluctance Synchronous motor/generator (PM-RSM) for mild hybrid vehicle", OPTIM 2002, Brasov, Romania.
- [19] S. Bolognani, M. Zigliotto, M. Zordan, "Rotor position detection for sensorless pm synchronous motor drives", in Proc. 8 Int. Power Electron. Motion Contr. Conf, 1998.
- [20] P.B. Schmidt, M.L. Gaspary, G. Ray, and A.H. Wijenayake "Initial Rotor angle detection of a Non-salient Pole Permanent Magnet Synchronous Machine", Proc IEEE IAS Annual Meeting, Vol 1, 1997 pp 459-463.
- [21] S. Nakashima, Y. Ianaki, I. Miki, "Sensorless initial rotor position estimation of surface permanent magnet synchronous motor ", IEEE Trans on Ind Appl. vol.36, no.6, Nov.2000, pp1598-1603.
- [22] K. Tanaka, T. Yuzawa, R. Moriyama, I. Miki, "Initial rotor position estimation for surface magnet synchronous motor", Proc. IEEE IAS Annual Meeting, Chicago, Illinois, Sept-Oct. 2001, pp. 2592-2597.
- [23] T. Takeshita, N. Matsui, "Sensorless control and initial position estimation of salient-pole brushless DC motor", Proc. Adv. Motion Control Workshop, 1996, pp 18-23.
- [24] M. Schroedl, "Sensorless control of ac machine at low speed and standstill based on the "INFORM" method", Proc. IEEE IAS Annual Meeting, October 6-10, 1996, pp. 270-277.
- [25] H. Kim, K.K. Huh, R.D. Lorenz, T.M. Jahns, "A novel method for initial rotor position estimation for IPM synchronous machine drives", IEEE Trans, vol. IA-40, no. 5, 2004, pp. 1369-1378.
- [26] Y. Jeong, R.D. Lorenz, T.M. Jahns, S. Sul, "Initial rotor position estimation of an IPM motor", Record of IEEE-IEMDC-2003, pp. 1218-1223.
- [27] M.C. Paicu, "'Active Flux' Based Wide Speed Range Motion Sensorless Control of Permanent Magnet Synchronous Machines", PhD. Thesis, Politehnica Timisoara Press, 2009.



### 8.1 The switching reluctance motor. General presentation

This introductory chapter [37] is intended as an overview of the switching reluctance machines (SRM), highlighting in the same time their place within the drive motors used today.

Electric drives with current variable speed electric motors are built with the most varied types. They comprise classic DC motors, induction motors and single-phase electric motors with permanent magnets, DC and synchronous as well as synchronous reluctance motors (with prominent poles or flux barriers).

As it is well-known, the first electric drives were made with variable speed DC motors with series excitation due to their mechanical characteristic and the easily adjustment of speed by changing the induced voltage. However, these motors have some disadvantages linked to the presence of a mechanical collector, which limits the peripheral speed of the rotor and decreases the reliability due to the brush-collector contacts.

Thus, over time, DC motors with series excitation were replaced by AC motors, which are more reliable.

In the competition between DC motors and AC motors, AC are encouraged by the progress in the electronic control devices and in the command and control strategies. The quality of power electronic components with the possibility of gate control, the microprocessors with simple technology and dedicated peripherals, the introduction in the industrial applicability of field-oriented control and superior dynamic performances leans increasingly the balance in favour of the AC motors.

The AC drives are of two types: induction motors and synchronous motors.

Induction motors, compared to classical synchronous motors (electromagnetic excitation or permanent magnet) have only one advantage: they are more robust, having a short-circuited rotor. Instead, the electrical performance, especially the efficiency, is weaker. The reactivation of the reactive synchronous motors, both of those with distributed stator winding and with concentrated stator windings, eliminates this drawback of the induction motors.

Also, for permanent magnet synchronous motors, the time during nominal torque that is reached is much lower because the magnetic flux is inherit. This makes the permanent magnet synchronous motors to be used where a very fast torque response is required.

The SRM, known for more than 100 years, entered in the variable speed electric drives due to the modern technology of semiconductors. It can be observed that, without a well-

designed and devised control strategy, SRMs cannot be used properly. An electric drive that contains an SRM must be considered together with the control system.

Synchronous servomotors with electromagnetic excitation powered by power converters are, in fact, DC motors with static switching, thus having an electronic switch that replaces mechanical switch.

These types of synchronous motors are known in the literature under various names (self-controlled synchronous motor; Stromrichtermotor; moteur synchrone a commutation électronique).

At the beginning of his book [26], Prof. T.J.E. Miller makes a brief analysis of the terms used to designate this type of motor. Thus, in the USA, it is preferred as the "Variable reluctance motor" (variable reluctance motor), which has the disadvantage that it may be confused with a stepping motor type. The name "Switched reluctance motor" was first used by Prof. S.A. Nasar to describe a rudimentary motor with variable reluctance in 1969. The widespread use of the name "Switched reluctance motor" (switched reluctance motor) is undoubtedly due to Prof. P.J. Lawrenson and his colleagues from Switched Reluctance Drives Ltd. It is understood that it is not the reluctance that is switched, but the currents flowing through the motor phase windings [22]. Another name that is used is the "Brushless Reluctance Motor" to emphasise the fact that the motor in question has no brushes. One of the most accurate names is the "Electronically Commutated Reluctance Motor", but this can also create confusion with the permanent magnet motors. However, the name that was imposed in English and is now used in most scientific articles is the "Switched Reluctance Motor" (SRM).

The SRM is actually a high-power reactive stepper motor with parameters optimised by the controlling torque and current in the windings according to the rotor position relative to the stator. Both the stator and the rotor have prominent poles, the number of the stator poles is different than the number of the rotor poles. Fig. 8.1 represents schematically a cross-section through a conventional 3-phase SRM, with 6 stator poles and 4 rotor poles. Thus, in the stator, the concentrated excitation windings are placed on the salient poles and the rotor is without windings or permanent magnets. The number of the stator and rotor poles has a key role in optimising the machine performance. It is necessary to excite a single phase to obtain a torque in the direction of the rotation, regardless of the initial position of the rotor relative to the stator. The torque produced by the machine is obtained by the sequential supply of the phases of the stator with a DC voltage by a power converter. It should be noted that, through the windings, the current flows in the same direction, which simplifies the static power converter used to power the motor.

The SRM has a number of notable performances, among which:

- the possibility of overload without additional ventilation;
- the high efficiency (75-85%);

- maintaining a constant torque over a wide speed range;
- the rotational speed may reach high values (up to 100,000 rpm), being limited only by the bearings and the iron losses;
- the coverage of a successful low rpm range, resulting in the elimination of mechanical gearboxes.

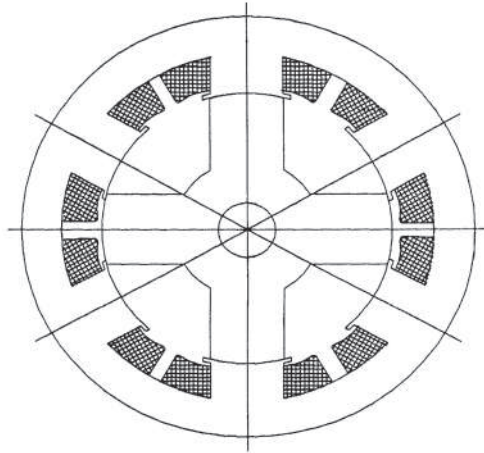


Fig. 8.1 Diagram of a cross-section of an 6/4 SRM.

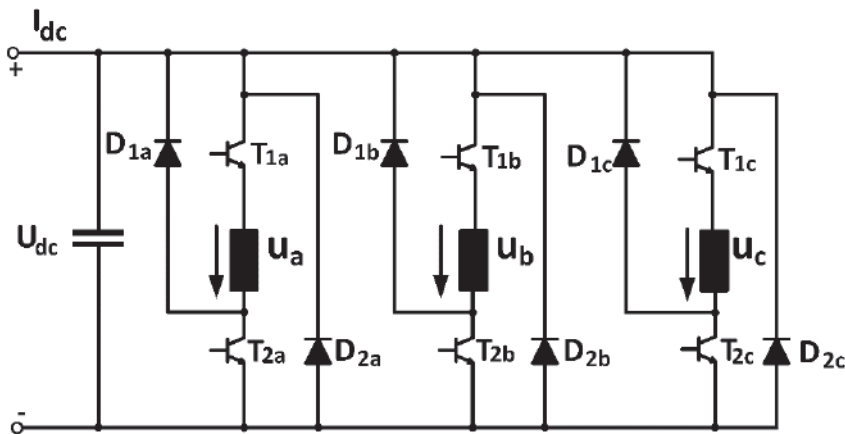


Fig. 8.2 Static power converter for a three-phase SRM.

The stator phases are powered through power devices conveniently arranged and connected to a DC power source. A type of the power converter used for controlling the SRM is shown in fig. 8.2. Although other types of SRMs and appropriate power converters have been proposed, those shown in fig. 8.1 and 8.2, respectively, are the most used.

The electromagnetic torque is of a magnetic type, corresponding to the reluctant electromagnetic torque of the synchronous machine with salient poles. When feeding a phase of the machine, the rotor is oriented in such a way that the nearest rotor poles to the stator poles of the phase fed to the stator poles lie in the extension of the powered phase. This is the principle of the minimum reluctance.

The sequential control of the power devices is performed by the control system, which takes the information received from a position encoder mounted on the motor shaft.

Fig. 8.3 and 8.4 [32] show the variation of the current flowing through one phase of the power converter of the SRM at a rotation speed of 5,000 rpm and 300 rpm, respectively.

Fig. 8.5 and 8.6 [32] show the total electromagnetic torque chart of such a motor, under the same conditions.

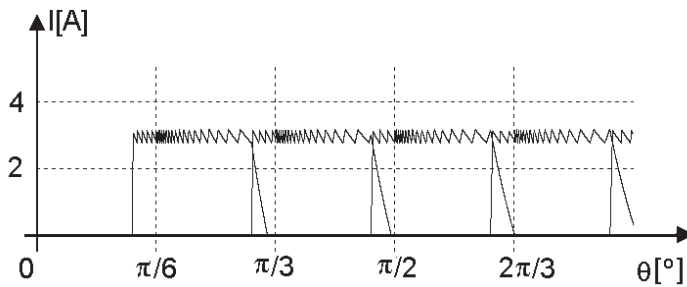


Fig. 8.3 Load current of the SRM at low speed.

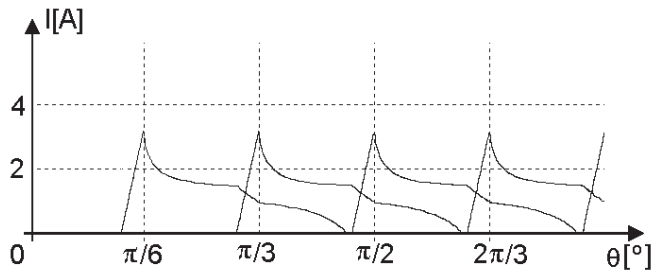


Fig. 8.4 Load current of the SRM at high speed.

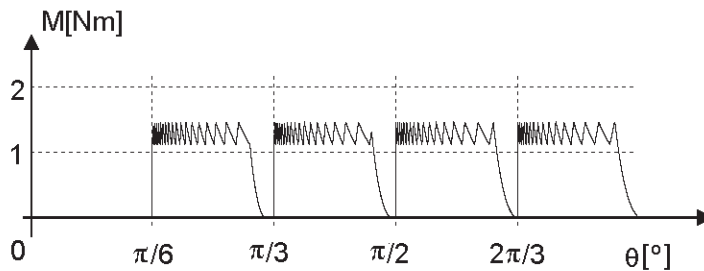


Fig. 8.5 SRM torque at low speed.

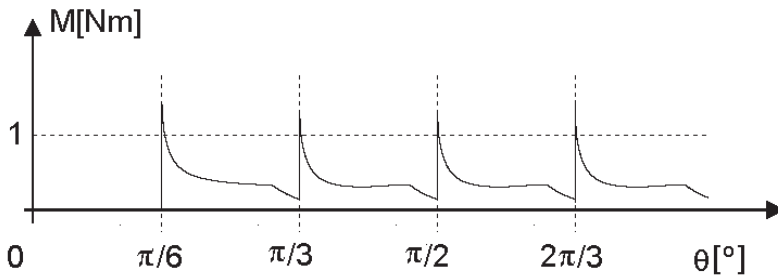


Fig. 8.6 SRM torque at high speed.

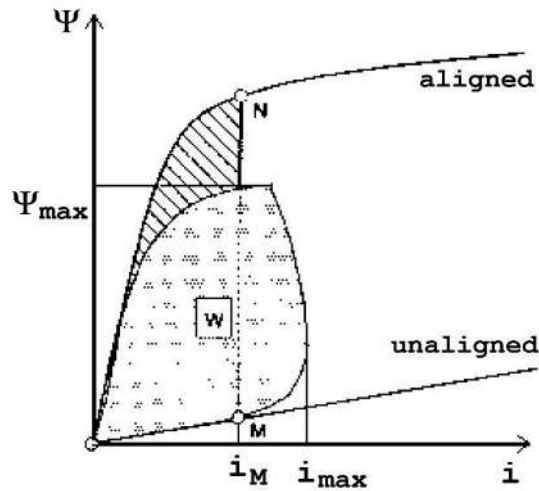


Fig. 8.7 The magnetic co-energy of the SRM.

It is noted that these four charts are the simulation results of the behaviour of an SRM existing in the *Special Electric Machines Laboratory* at Politehnica University of Timisoara.

Fig. 8.7 shows the variation of the magnetic co-energy of the SRM.

In fig. 8.8 - 8.11 [33], the average torque, the flux, the torque ripples and the m.m.f. voltage for seven types of motors are compared. The notations are as follows:

- IM            Induction Motor (IM);
- SREL        Synchronous Reluctance Motor;
- SRM         Switched Reluctance Motor;
- SPMAC      Surface Permanent Magnet AC Motor;
- SPMDC     Surface Permanent Magnet Brushless DC Motor;
- IPM         Interior Permanent Magnet Motor;
- PMDC      Permanent Magnet DC Commutator Motor.

To synchronous motors with excitation windings, electromagnetic or permanent magnet, these types of motors have clear benefits, which do not require any arguments.

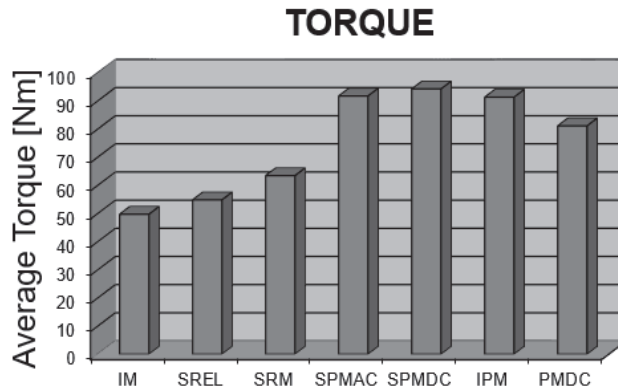


Fig. 8.8 Comparison of the average torque for 7 types of motors [33].

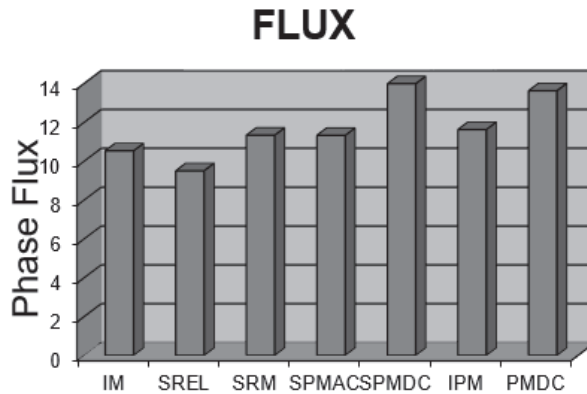


Fig. 8.9 Comparison of the flux for 7 types of motors [33].

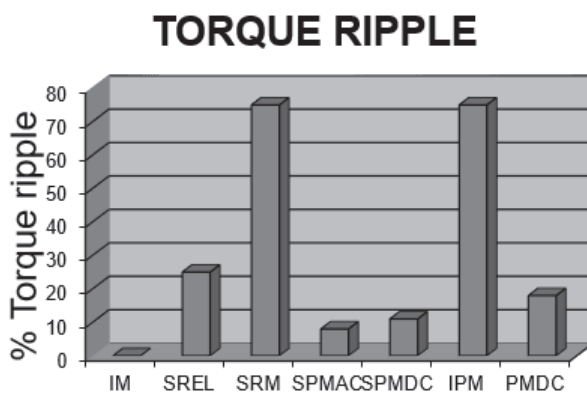


Fig. 8.10 Comparison of the torque ripple for 7 types of motors [33].

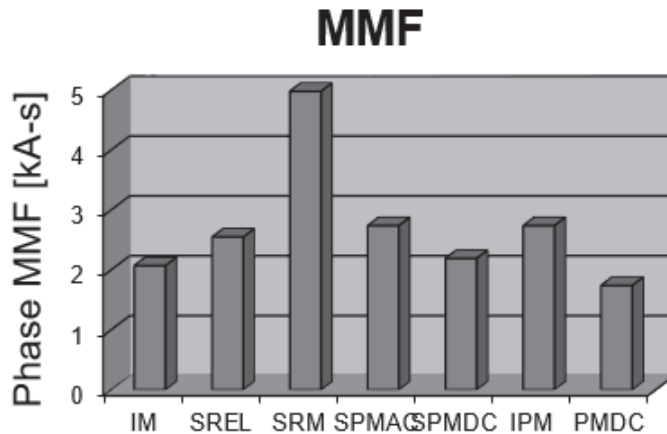


Fig. 8.11 Comparison of the magnetomotive voltage for 7 types of motors [33].

As compared to the induction motors, the following advantages are provided: increased specific power ( $P / G, W / kg$ ) and high ratio of the torque at the moment of inertia.

Other advantages of the SRM are:

- a low failure rate;
- operating at high speeds;
- an effective speed change;
- a reduced cost.

The main applications of the SRM cover:

- the aerospace industry;
- the automotive industry;
- the machines industry.

The SRM has limited functionality without external current control, which is not possible without appropriate power electronics and automatic control.

Many papers describe the various aspects of the SRM design [9]. These approaches refer to a detailed analysis from finite elements to complex nonlinear models for magnetic circuits.

## 8.2 Design considerations of the SRM

Electric motors (synchronous, induction, DC) have been extensively studied in recent decades. The design is well-known and well-documented. The design methods of the conventional machines cannot be applied in the systems with variable reluctance, due to the complications arising from the different number of phases and poles. The power converter, which is the power supply of the switched reluctance motor, is the most important element that introduces complications into the design.

For the design of this type of machine, one must distinguish between the calculation of a constant speed motor powered by a sinusoidal voltage and the computation of a variable speed motor, powered by an electronic converter. In the later case, it will be considered that the motor operates in a wide torque and speed ranges, which involves other kind of issues, such as cooling.

### **8.2.1 Classification of the design methods [15]**

If the focus is on the motor construction, it can be on:

- one or more teeth per pole;
- one or more packages;
- the cylindrical rotor or the disc rotor and the radial gap and axial gap;
- the internal or external rotor;
- the rotation or linear movement;

A deficiency of the constructive design methods is that they do not highlight the inherent design of the machine.

More useful would be the classification:

- linear methods;
- non-linear methods;
- the finite element method applied to the magnetic field, a method that leads to a direct estimation of the performance and parameters computation.

#### **8.2.1.1 The linear design method**

W.H. Koch is one of the first researchers who used this method on a three-phase machine with 6 stator poles and 4 rotor poles. He considered that the remaining flux had high values at every disconnection. A coefficient is used in the design process based on the remaining flux to show how the machine geometry must be chosen for different load characteristics. Since iron was considered as an ideal environment ( $\mu \rightarrow \infty$ ) and the analysis was made without mentioning the effects of the current conduction during the period when the inductance decreases, the results were not conclusive.

The design difficulties encountered by Koch were overcome by W.F. Ray and R.M. Davis by using a simple approximation for the derivative of the current waveform in the motor. This may lead to the values of the converter components. The calculations depend on the inductance linearisation, but allow the voltage to switch at any point during one cycle. In this case, the method was intended mainly for the converter sizing.

T.J.E. Miller took into consideration the phase current with the top landing in developing the design method. R. Krishnan has also used this method. Although useful for some given conditions, this analysis can be applied only with restrictions, taking into account the fact that the variation of the phase current waveform is one of the SRM characteristics.



### 8.2.1.2 The nonlinear method [37]

The saturation phenomenon in the SRM is important and inevitable. Both local and total saturation effects highlight the phenomenon's complexity. It cannot be compensated just by using a saturation factor as in the case of the induction motor.

Most researchers dealing with the SRM design use various types of nonlinear methods. In this regard, we can mention the contributions of L.E. Unnewehn - design of a rotor disk motor, F.J. Vallese – design of a three-phase motor with two-wire winding, R. Thornton – design of hoisting motors, E. Amina – design of traction motor and C. Polleck - analysis of a large phase number system.

E.M.H. Kamerbeek compares the SRMs with other types of electric motors of different dimensions and powers, concluding that they are superior to all motor types within the relatively large powers.

The saturation in the magnetic circuit, originally proposed by J. Jarrett, was the argument of JV Byrne in his work. They made a special contribution to the field of modelling, the simulation in designing saturated regimes from the motor and the determination of the relationship between the torque and the angle. The air gap must be as small as possible to ensure an optimal motor operation in saturated regimes.

A.J.K. Bakhnisen shows that the consideration of the iron saturation, isolated from the rest of the machine, leads to favorable results. P.J. Lawrenson [23], on the contrary, concludes that introducing magnetic restrictions is not helpful.

There is a superficial similarity between the SRM and the stepper motor, many researchers having considered the motor with more teeth per pole. In this case, design techniques are based on the ratio between the length of the airgap and the width of the tooth. In this theoretical work, the papers of M.R. Harris and H.B. Ertan are distinguished as well as the completed practical works of H. Bänsch, R. Welburn and J.W. Finch. The latter applied a valid method for the system with more teeth per pole.

There is a group of authors who describe some less used configurations and methods for the SRM modelling. For example, H.R. Bolton and C.C. Chan [10] approach the method of minimum power - minimum cost for a single-phase motor with massive iron external rotor. G. Franceschini approaches the method based on determined angles and J.H. Lang by servo applications.

The emergence of the new generation of computers made it possible to solve difficult problems related to design. You can write programmes that solve sets of equations imposed by any design. The question is what equation one should use.

N.N. Fulton and T.J.E. Miller have different approaches of the design method, although based on the same analytical method of calculating the motor's performance. Fulton uses a classic rigorous approach, which leads to a detailed but complicated results, taking into account both the machine geometry and the parameters of the power converter. The accuracy of the method was checked over the years on a great number of different sized powers, speeds and voltages.

Miller introduced an editor-based interactive programme, which uses several default parameters to determine the motor's performance.

The analysis method must be chosen before starting the design. I.E.D. Pickup and P.T. Blenkinsop use nonlinear differential equations that require the evaluation of the differential coefficients and limit the accuracy of the computation. J.M. Stephenson published a method that does not use differential coefficients; although it requires fewer inputs, it is more accurate.

J. Faiz proposes, for the preliminary calculation of the SRM performances, a method based on the use of the magnetisation characteristic in the case of aligned and non-aligned poles. The establishment of a formula for the phase flux linkage of the motor based on the excitation current and the angular position of the rotor is essential. In an existing motor flux, values can be obtained by a static test and a whole set of characteristics can be evaluated by simulation.

In order to obtain a family of excitation flux/current characteristics, Faiz proposes the use of two methods: the interpolation method and the permeances method.

In the interpolation method, the following formula (8.1) is used for the excitation current:

$$i = i_a + (i_u - i_a) \cdot \frac{1 - \cos(\theta)}{2} \tag{8.1}$$

The dependence on rotor position is given by the angle  $\theta$  and the dependence on the flux by the current values  $i_a$  (corresponding to the aligned poles) and  $i_u$  (corresponding to the non-aligned poles). In the case of an excitation current variation between 1 and 10 A, a family of characteristics is obtained as shown in Figures 8.12 a and b.

In the case of permeances method, it calculates the permeances values related to a straight air gap and a deeper notch, for different rotor angle values for a 12/10 poles SRM. Finally, it evaluates the error between the calculation and the measurement, thus resulting the superiority of the permeances method. For the saturated values of the current, astatic torque is obtained, as shown in Fig. 8.13.

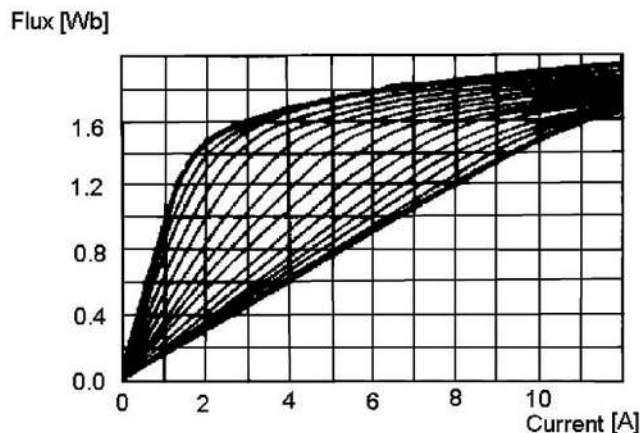


Fig. 8.12.a Flux variation versus current for the SRM case.

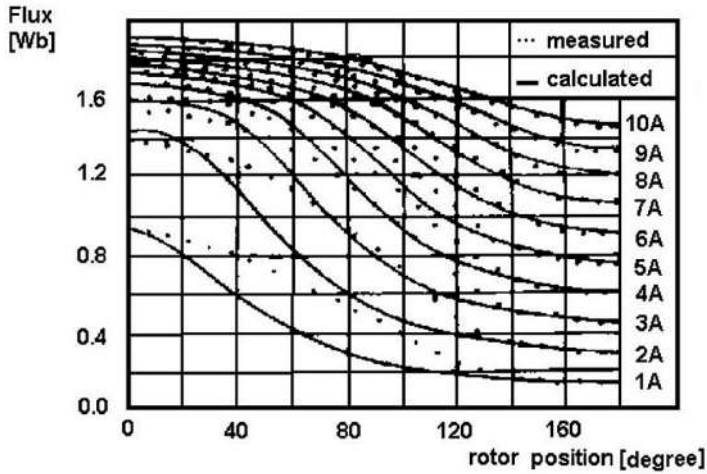


Fig. 8.12.b Flux variation depending on the rotor position for the SRM case.

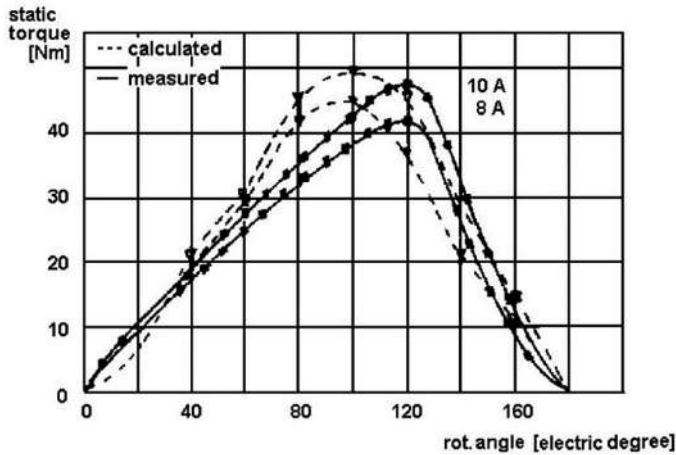


Fig. 8.13 Static torque variation of the SRM for different current values.

### 8.2.1.3 The Finite element analysis method [31]

Given the increase in computing power and the accessibility in the use of computer technology, the analysing method using a finite element became reality for designing a SRM. H. Bausch, R. Arumugan and G.E. Dawson have the most important contributions in this field.

Currently, there are industrial business units using finite element software packages to investigate performances of the SRM they produce.

Arumugan used the finite element software package to design a three-phase SRM with one tooth per pole; more precisely, Dawson used it to design a three-phase SRM with two teeth per pole. They also calculated the electromagnetic torque developed by the motor using this method.

J. Simkin applied the finite element method to a typical SRM structure, as a planar problem (two-dimensional) and spatial problem (three-dimensional).

Although the use of the finite element method brings significant progress, there are also many difficulties that might be overcome, determining the rotor angle, which introduces field unbalances, etc. The need to provide space solutions (three-dimensional) leads to a substantial complication regarding the computing requirements.

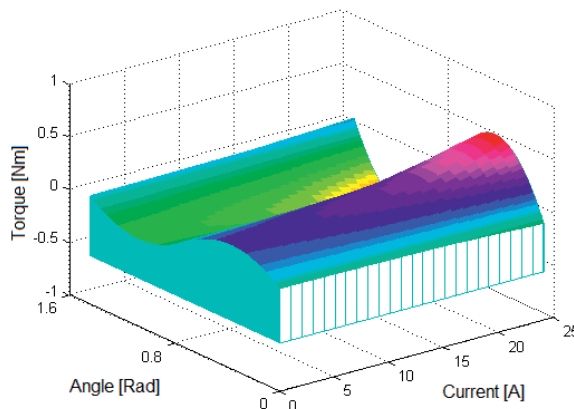


Fig. 8.14 Spatial distribution of the current and torque according to the rotor position.

To study the electromagnetic field in electric motors [13], the finite element software packages designed for this purpose, such as Flux 2D (MulticadSistemas e Computadores), magnets (Infolytica), Ansys - PC / Magnetic (Swanson Analysis Systems) Ansoft, PC Opera (Vector Fields), Cosmos / M (Structural Research and Analysis), can be used. A common two-dimensional problem involves the solving of an approximately 5,000 equations when a space problem reaches 30,000 - 200,000 nonlinear equations. Therefore, to solve the problem in a plane is over 10 times faster than in the space. Space programmes are effective in complicated geometries. Using such a programme, a distribution of the torque, as shown in Fig. 8.14, is obtained. Within the Electrical Engineering department, the behavior of an SRM with the help of finite element was studied. The areas to be specified are the following:

1. parts that are made of ferromagnetic material, the stator and the rotor of the machine.

They are constructed using sheet metal, having the magnetization curve specified in Fig.8.18;

2. free zones, where air has been defined as material, and comprising the air gap and the rest of the space between the stator and the rotor, obviously excluding the space occupied by the stator coils, including the space outside the motor;

3. stator windings, on which copper was defined as material. These were supposed to be constructed of solid copper, which has an area equivalent to the sum of all section areas

of all the conductors that form a coil. In this case, the density of the direct current passing through the copper section was also specified;

4. the machine shaft, which is made of solid steel. For simplicity, it can be assumed that the machine stator and rotor are long enough so that the end effect can be neglected.

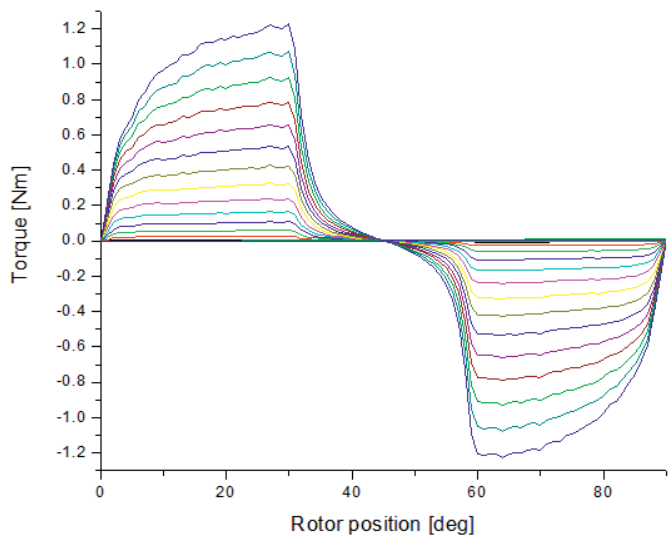


Fig. 8.15 Torque [Nm] =  $f(\text{rotor position [deg]})$  for different currents (0.5A, 1.0A, 1.5A, 2.0A, 2.5A, 3.0A, 3.5A, 4.0A, 4.5A, 5.0A, 5.5A, 6.0A, 6.5A, 7.0A).

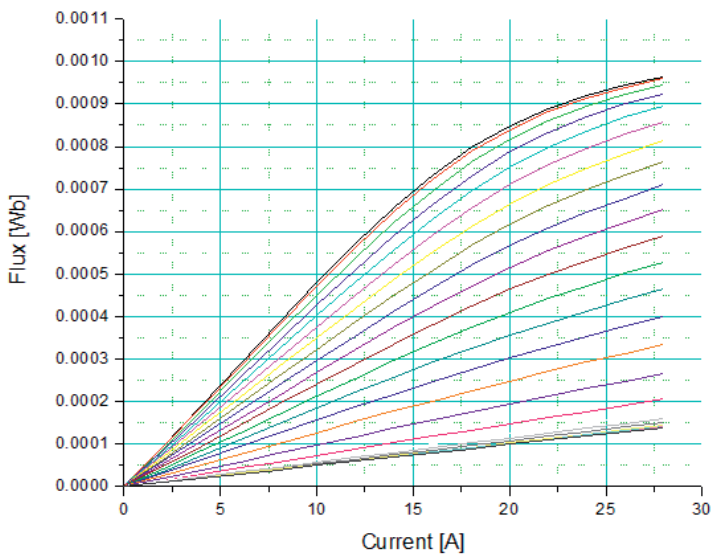


Fig. 8.16 Flux [Wb] =  $f(\text{current [A]})$  for different rotor positions (0-45 deg).

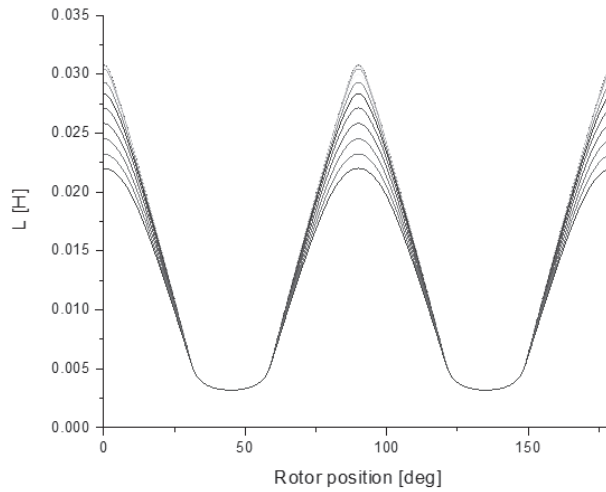


Fig. 8.17  $L$  [H] =  $f$ (rotor position [deg]) for different currents (0.5A, 1.0A, 1.5A, 2.0A, 2.5A, 3.0A, 3.5A, 4.0A, 4.5A, 5.0A, 5.5A, 6.0A, 6.5A, 7.0A).

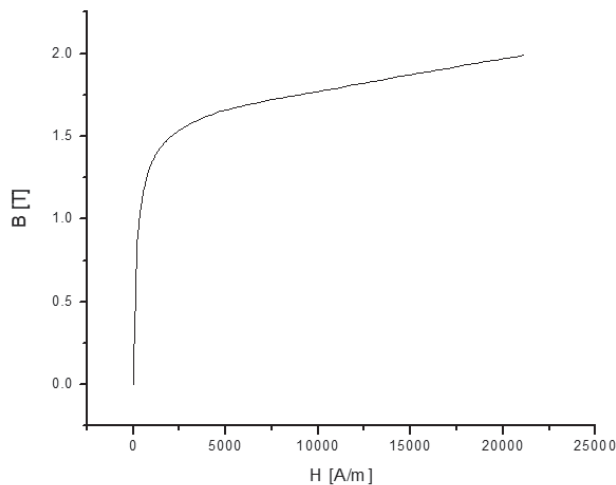


Fig. 8.18 Magnetizing curve for an accepted romanian material  $B$ [T] =  $f$ ( $H$  [A/m]).

### 8.2.2 Design considerations of the analytical methods [20]

M. Jufer, M. Crivii and P. Poffet have used a calculation model, which takes into account the saturation, the hysteresis losses and the eddy current losses to determine the static and dynamic characteristics of the SRM. On the basis of this model, a CAO programme has been developed to be used to optimize the geometric dimensions of the motor in order to obtain the maximum torque and efficiency. The programme also allows the calculation of the motor characteristics during the self-switching regime.

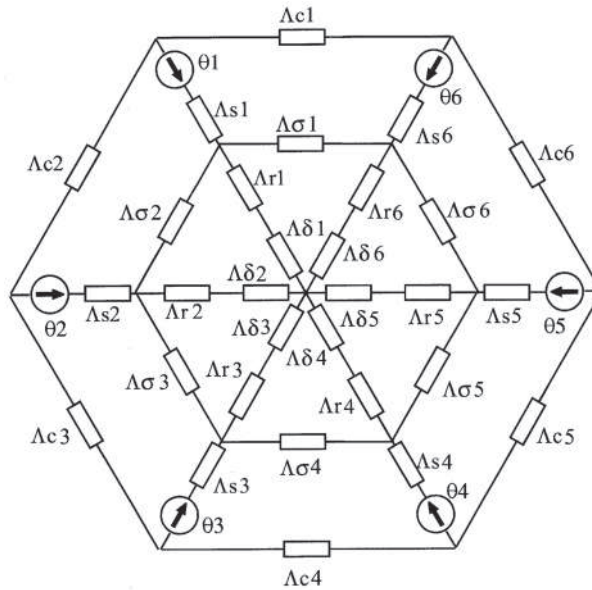


Fig. 8.19 MSPP- magnetic equivalent scheme of power converter.

The model is based on the magnetic equivalent scheme of the motor that allows the flux distribution throughout the whole motor. Fig. 8.19 presents the equivalent circuit for calculating a three-phase motor with 6/8 pole.

The scheme was established with the following assumptions:

- the magnetic material is homogeneous in all directions;
- the magnetic circuit is divided into small areas so that the magnetic flux density is homogeneous in every element;
- the airgap is divided into constant surface flux tubes so that the magnetic flux density could be uniform in each tube.

The described assumptions allowed the division of the motor geometry into saturable elements (iron) and unsaturated elements (air).

The air-gap permeance was determined by approximating the field lines with straight lines and arcs. From the harmonic analysis of the permeance, the permeance curve and the first 10 harmonics have been calculated, considering a 1000 points per teeth step.

The permeance of a saturated element was calculated taking into account the magnetisation curve of the iron approximated by analytical relationships:

$$B = \frac{a \cdot H^3 + b \cdot H^2 + c \cdot H}{H^2 + d \cdot H + e}; \quad H \leq H_{lim} \quad (8.2)$$

$$B = B_{lim} + P \cdot (H + H_{lim}); \quad H \geq H_{lim} \quad (8.3)$$

where  $(B_{lim}, H_{lim})$  is the saturation limit point. The coefficients  $a, b, c, d$  and  $e$  and the slope  $P$  are determined using the magnetization curve of the material.

The assessment of the iron losses in the SRM is very important for the calculation of heating, especially at high speeds. The iron loss can be calculated more accurately knowing the induction of each of the saturated elements.

The hysteresis losses are determined by calculating the inner surface of a hysteresis cycle obtained by powering using unipolar pulses. The analysis of the effects of the eddy currents shows that the sheet plate flux is not uniform at a high frequency. Thus, it can be considered that the permeability of the iron decreases with frequency as a result of the induced currents.

Y. Kwon and K. Reichert [21] consider the saturation of the magnetic field in the SRM using polynomial and exponential functions, partly linear interpolations in tabular form, spline polynomial and exponential functions with coefficients given by the Fourier series. The latter were checked and it was found that they modelled the real phenomenon by comparing the measured data with simulated ones.

The flux linkage in the SRM was analytically modelled based on experimental results with the relationship:

$$\Psi(i, \theta) = a_1(\theta) \cdot (1 - e^{a_2(\theta) \cdot i}) + a_3(\theta) \cdot i \quad (8.4)$$

The paper [19] presents three types of synchronous motors with electronic commutation: the DC brushless motor, the stepper motor and the SRM. For each motor type, many different geometries are possible. In these circumstances, in order to make the best choice for an electric drive can be a difficult task. The Swiss Federal Institute of Technology in Lausanne has developed a complete package of design methods and programmes, all based on the same procedure and using the same material resources. The main programmes for each motor type are: the design programme, the determination of static characteristics (torque and inductors) and a dynamic programme (including the operation and the control). The paper [19] presents the typical results, the design methodology and the modelling methods.

A not insignificant fact for the SRM design is represented by the desired output power or torque. Somehow, when it comes to a small motor case of power up to 1kW the issues might occur regarding its design appear to be otherwise for a large motor case of power up to hundreds of kW. This can be seen from the comparative study of two motors of different power ranges.

The first one [35] was published in 1991 and deals with the design of variable reluctance machines with power below 1 kW. The authors, A. Weller and P. Trawiński, provide simple formulas for the calculation of the main parameters for a motor with 6 stator poles and 4 rotor poles. One thing to note is that, although the formulas used for the calculation are



semiempirical, as the authors themselves call them, they take into account the saturation of the magnetic core relative permeability  $\mu_r$  using (B). Due to their simplicity, the formulas are not very accurate, but they can be used for the quick calculation of the performance of such a machine. Finally, an optimised motor can be achieved by experimental determinations and by using more advanced computer programmes. Also, using finite element modelling programmes, the static torque on the rotor position and phase current can be calculated. The dynamic behaviour of the motor requires more complex simulation programmes.

For motors with powers of hundreds of kW, the problems arise in a different way. A significant work in this respect is the one published by Ferreira and Richter in 1993 [14].

A detailed design of a motor / generator SRM with an output power of 250 kW for aircraft motors has been conducted under the coordination of General Electric Corporation and Sunstrand Aerospace. The ultimate goal was to demonstrate the feasibility of such a machine.

The detailed design of such a machine lies on the following stages:

- the definition of requirements and constants imposed from the outside;
- the electromagnetic analysis;
- the thermal analysis;
- the mechanical calculation and the control analysis;
- the mechanical design and the final classification.

The purpose of the electromagnetic analysis is to select the optimal topology and configuration resulting in a minimal weight for a maximum efficiency. This refers to the number of stator and rotor poles, the number of turns per pole in the stator winding, the type of material for the magnetic core, the power losses and the stator winding configuration. The machine design is simple.

Stator windings are independent of each other, both physically and magnetically. The simplicity of the construction gives to this type of motor a greater reliability. As far as the design is concerned, the attention should be given to the cooling of stator winding and to the rotor geometry. The losses in the stator winding are composed by the continuous component  $I^2R$  and the eddy current component, which is proportional to the electrical operation frequency.

As an example, the total losses in the windings for a 250-kW motor vary between 12 kW and 13.8 kW, depending on the motor speed. In addition, the magnetic field distribution in the stator windings is irregular. The conductors near the air gap are exposed to a higher magnetic flux density. In this case, the conductor closest to stator pole has the highest power loss.

The solution adopted for high and very high-powered motors is a fluid cooling system for the stator winding using a tubular copper conductor for these coils.

Attention should also be paid to the rotor geometry design. The rotor consists only of rolled sheet plates, resulting in a robust configuration, suitable for high speed motors. A key part of a robust mechanical design of the rotor is a correct calculation of the electromagnetic losses in the rotor.

The SRM has leakage losses due to the non-sinusoidal rotor flux. The hysteresis losses and the eddy currents reach approximately 6.5 kW at full load operation.

These losses are obtained in the rotor laminations at high temperatures. The mechanical strength of the material from which the laminations are made decreases with temperature. This problem can be solved by using a sheet with a minimum waste of the material, e.g. cobalt-vanadium steel.

The thermal analysis was conducted to determine the temperature distribution of the stator and rotor laminations (made from magnetic material) and the one in the stator windings. The first step is to estimate the temperature of the hollow copper conductors from the stator winding. The temperature for the hottest wire may reach 250 degrees. The second step is the calculation of the thermal distribution in rotor and in stator magnetic materials.

For these kinds of motors, an important place is occupied by the mechanical computation, developed using finite element analysis. The shaft and bearing calculation must be carefully done.

### **8.2.3 Estimated losses of the SRM**

The calculation of the motor losses plays a very important role in the design process of a SRM.

Losses consist of core losses  $P_m$  and losses in the stator windings  $P_s$ .  $P_s$  are proportional to the square of the effective current value, and  $P_m$  are based on the excitation frequency and on the flux density.

The current waveform is not sinusoidal and depends on the operation conditions. This motor usually operates at varying degrees of saturation and this complicates the core losses estimation.

Thus, the paper [25] describes a method of determining the losses in a machine operating under saturation conditions. General expressions are presented for the flow rate in different parts of the machine core. It is shown that the number of frequencies (fundamental) in the motor at the same time is according to the number of motor phases; therefore, losses in the core of the machine are a function of the excitation current and speed.

The paper shows that most losses occur in the rotor core. The Fourier analysis is applied separately to the fundamental components losses and harmonics. This analysis was used to determine the spectrum of the flux harmonics in different parts of the core. It shows that

there are harmonics of all orders, which have a significant influence, especially on the rotor core losses.

The iron loss increases with the increase of excitation and speed. For low excitations, the core losses are greater than the copper losses.

### 8.2.4 Design example of the SRM

In what follows, an example of a switched reluctance motor design conducted in the Special Electrical Machines Laboratory of the Faculty of Electrical Engineering in Timisoara [4], [5] is briefly presented.

The design was done using a computer programme written in Turbo Pascal 6.0.

After analysing the topologies of the SRM, a three-phase, 4-pole rotor and 6 stator pole-motor was chosen. Two reversible speeds for the motor have been selected : 390 rpm and 2,800 rpm.

The average power required by the electric drive is about 300 W at a rotation speed of 2,800 rpm. An air gap of 0.4 mm has been chosen for the design considerations. The motor has been designed for an uninterrupted operation mode.

Since the design programme has as input the machine nominal torque value and the machine is designed for variable torque and power according to the speed, the nominal torque is calculated such as the motor has an output power of about 300 W at a speed of 2,800 rpm:

$$P_n = M_n \cdot \Omega_n \Rightarrow M_n = \frac{P_n}{\Omega_n} \quad (8.5)$$

$$M_n = \frac{300}{\frac{2 \cdot \pi \cdot 2800}{60}} = 1.02 \text{ Nm}$$

It is, therefore, considered that the machine nominal torque was  $M_n = 1 \text{ Nm}$ .

The equivalent torque was chosen to be equal to the imposed load torque  $M_{ech} = M_n = 1 \text{ Nm}$ .

A nominal machine operating current of  $I_n = 2.2 \text{ A}$  is required. The equivalent current is also considered equal to the rated current  $I_{ech} = I_n = 2.2 \text{ A}$ .

Following some optimisation tests for the efficiency, weight and cost of active materials, respectively, the following results were obtained [6]:

1. At 2,800-rpm rotation speed:
  - in case of efficiency optimisation, the airgap induction of  $B_\delta = 1.140 \text{ T}$  is obtained;
  - in the case of weight optimisation, the airgap induction of  $B_\delta = 1.498 \text{ T}$  is obtained;
2. At 390-rpm rotation speed

- in the case of efficiency optimisation, the airgap induction of  $B_\delta = 0.890$  T is obtained;
- in the case of weight optimisation, the airgap induction of  $B_\delta = 1.498$  T is obtained;

Since the motor operates mostly on a speed of 2,800 rpm and the motor operates optimally in the saturated regime, it is considered that the air gap induction of  $B_\delta = 1.5$  T is the input value.

With these considerations in mind, the input quantities list is the following:

- $M_n = 1$  Nm nominal torque;
- the rated current = 2.2 A;
- the induction in the air gap  $B_\delta = 1.5$  T;
- the air gap  $\delta = 0.4$  mm;
- the current density  $J = 3.5$  A / mm<sup>2</sup>;
- the ratio  $\lambda = l / D = 1.2$ ;
- the number of stator phases:  $m = 3$ ;
- the number of rotor poles:  $p_r = 4$ ;

The equations characterising the behaviour of the SRM are:

$$U = R \cdot I + \frac{d\Psi}{dt} \quad (8.6)$$

And

$$\Psi = L \cdot I \quad (8.7)$$

from which the following differential equation is obtained:

$$\frac{di}{dt} = \frac{1}{L \cdot \Omega} \cdot \left( U - R \cdot i - \Omega \cdot i \cdot \frac{dL}{d\theta} \right) \quad (8.8)$$

The electrical magnetization curve of the electric steel sheet was given from point to point with a step of  $B = 0.01$  T. Considering that there are quite a lot of points, the approximation between two successive points has been done by a straight line.

Taking into consideration the induction in the air gap  $B_\delta$  as a parameter that can vary between certain limits imposed in the initial data by the designer, various variants can be obtained for the optimal machine.

The optimisation loop with  $B_\delta$  as a parameter starts with the computation of the equivalent torque equal to the nominal torque. The equivalent current of the machine will be equal to the rated current and the duty cycle of the continuous operation is required. Next, the number of turns will be calculated and the geometrical sizes of the machine will be determined. Depending on the required current density needed to calculate the diameter of the conductor section used for the winding, the standardised size immediately above them will be taken into consideration.

It will further determine the total ampere-turns, calculating the voltage drop on each magnetic portion. The equivalent current is recalculated based on the results obtained.

In determining the permeance expressions of the stator and rotor poles, two situations were considered: the misaligned poles (Fig. 8.20) and the aligned poles (Fig. 8.21).

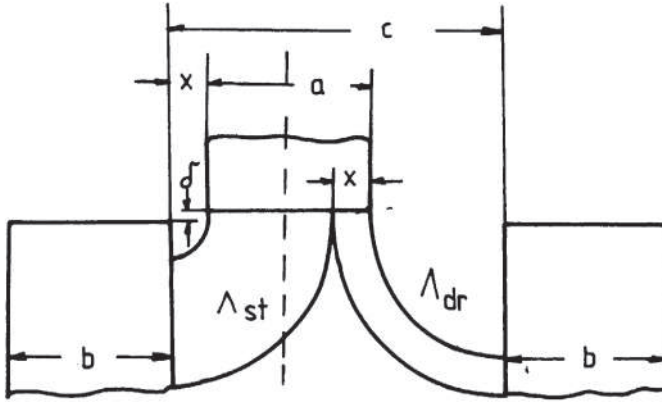


Fig. 8.20 Misaligned poles.

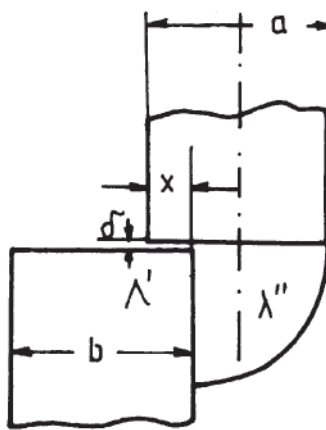


Fig. 8.21 Aligned poles.

For the case of misaligned poles, the following expression is obtained:

$$\Lambda = \frac{\mu_0}{\alpha} \cdot l_m \cdot \left[ \ln \frac{\delta + \alpha \cdot a}{\delta + \alpha \cdot (a - x)} + \ln \frac{\delta + \alpha \cdot a}{\delta + \alpha \cdot x} \right] \quad (8.9)$$

And for the aligned poles:

$$\Lambda = \mu_0 \cdot l_m \cdot \left[ \frac{x}{\delta} + \frac{1}{\alpha} \cdot \ln \frac{\delta + \alpha \cdot (a - x)}{\delta} \right] \quad (8.10)$$

where:

$$\mu_0 = 4\pi 10^{-7}$$

$\delta$  = the machine air gap

$l_m$  = the machine length

$a$  = the width of the stator pole

$b$  = the width of the rotor pole

$\alpha$  = coefficient dependent on the rotor position

$x = R\theta$ , where:

$R$  = radius of the rotor machine

$\theta$  = angle that takes into account the relative position of the poles.

The variation of the inductance is approximated by a Fourier series as follows:

$$L = L_{ct} + \frac{a_0}{2} + \sum_{j=1}^{50} a_j \cdot \cos(4 \cdot j \cdot \theta) \quad (8.11)$$

The machine torque was calculated with the formula:

$$M = \frac{1}{2} \cdot i^2 \cdot \frac{dL}{d\theta} \quad (8.12)$$

and the average torque:

$$M_{med} = \int M_t(\theta) \cdot d\theta \quad (8.13)$$

Finally, the losses, the weight of the active materials and the machine efficiency will be calculated.

The optimization design software has three possibilities:

- the optimization of machine's performance;
- the optimization of active materials' weight;
- the optimization of active materials' costs.

The Figures 8.22 – 8.25 present the SRM prototype designed at the Faculty of Electrical Engineering in 1994 and built by the Electromotor company in Timisoara.

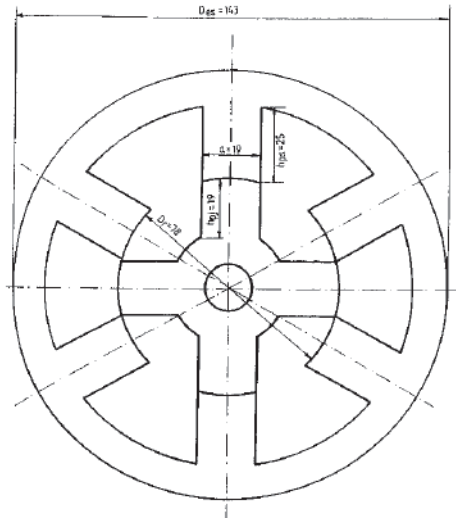


Fig. 8.22 The drawing of the 6/4 SRM designed at UPT.

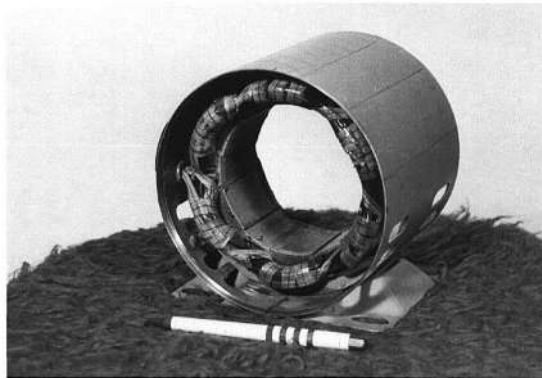


Fig. 8.23 The stator of the 6/4 SRM designed at UPT.

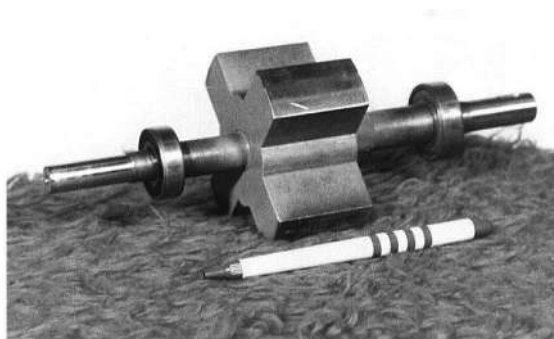


Fig. 8.24 The rotor of the 6/4 SRM designed at UPT.

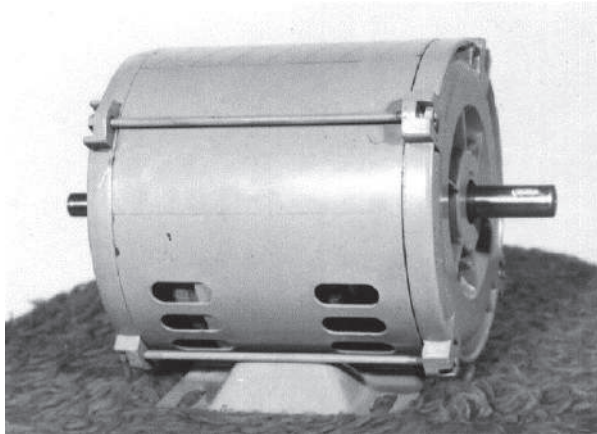


Fig. 8.25 General view of the 6/4 SRM designed at UPT.

### 8.3 Power converters for switched reluctance machines

Since the stator windings are energised with unidirectional currents, the power converters used in the SRM are simple compared to those used in induction and synchronous machines.

The main difference between the SRM power converter and the induction machine power converter is when the converter has independent circuits for each stator phase; the inverters use a bridge configuration, normally biphasic.

The most convenient power source is a battery or an AC source rectifier.

The most common type of power converters used for the SRM is with two switches per phase (fig. 8.26).

According to Prof. T.J.E. Miller [26], this circuit allows maximum flexibility with minimum components.

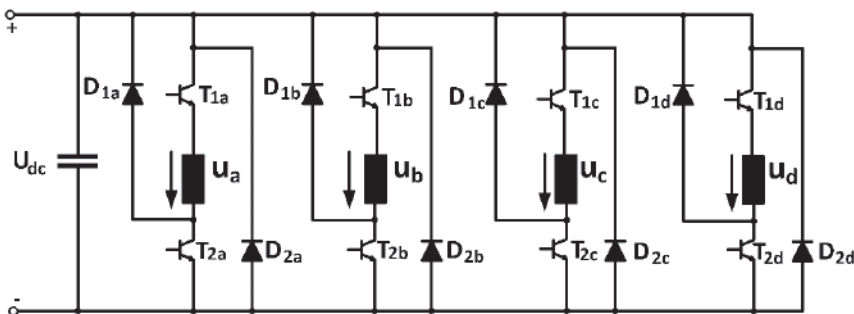


Fig. 8.26 Power converter with two power switches per phase for the SRM.

Indeed, the current regulation can be done with a single transistor (soft chopping) or with both transistors (hard chopping). The disconnection of the phase is always done by blocking both transistors of the respective phase. That means that the reverse voltage from the power



supply is applied to the respective phase. Also, the transistors can enter in the conduction state and can be locked at any angle. The scheme can be completed to power n-phases, but its main disadvantage is that it has higher costs since it uses two transistors for each phase.

Due to the unipolar current, the possibility to use power converters with more than two switches per phase might occur. For single-phase motors, it is necessary at least one switch, but for two-phase motors, two switches per phase are necessary. The two-phase motors can work with a single switch per phase if the second stage is connected in series with a diode. A motor with three or more phases requires a power converter with a single switch per phase to ensure a full flexibility of the control.

If power is supplied from a DC source, the switch must be fully controlled (bipolar transistor, MOS, IGBT or GTO thyristor) due to the requirements of voltage reversing at precise rotor position and flux decreasing at each switching on and off. Therefore, for the motors with the number of phases  $m \leq 3$ , the number of switches per phase oscillates between 1 and 2.

The Oulton scheme is shown in fig. 8.27. This circuit has been used in the well-known four-phase motor drives, with IGBT and GTO thyristors. The scheme has the advantage of allowing the voltage reversal to decrease the flow. Another advantage is that of working with a single switch on a phase without adding other passive components or sacrificing any of the control's flexibility or order. The DC voltage provided by the power supply is divided using capacitors. The main disadvantage of the scheme is that it does not allow you to soft chop and the balance between phases must be maintained carefully. Any failure increases the voltage on the capacitors. Another disadvantage of the scheme is that it uses only half of the supply voltage, because the phases are powered with  $\frac{V_s}{2}$ .

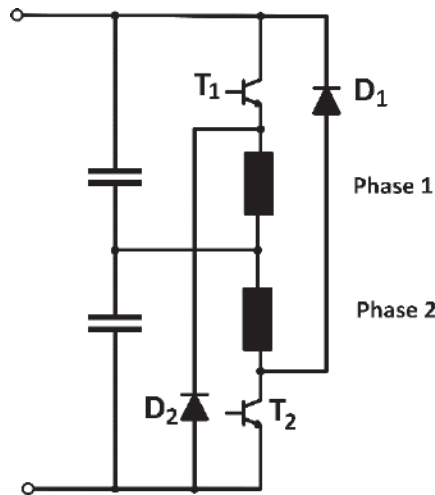


Fig. 8.27 Oulton type power converter.

In Fig. 8.28, the types of power converters used to supply the SRM, using only one switch per stage, are presented. The diagram shows a single phase, but it may be generalised to  $n$ -phases.

The circuit from fig. 8.28 a [24] does not allow the voltage reversal across the windings. The decrease of the flux thus depends on the voltage across the diode and on the winding resistance. The switching is only possible for a high resistance, which is inefficient. Another method for switching is the early blocking of the switch, which leads to poor energy conversion.

The circuit in Fig. 8.28 b uses an external resistance to lead to a decrease (reversal) of the windings voltage. This is again inefficient because the voltage decrease implies a current decrease, a decrease of the falling slope of the linkage flux and an increase of the the switching angle, which may lead to a lower efficiency.

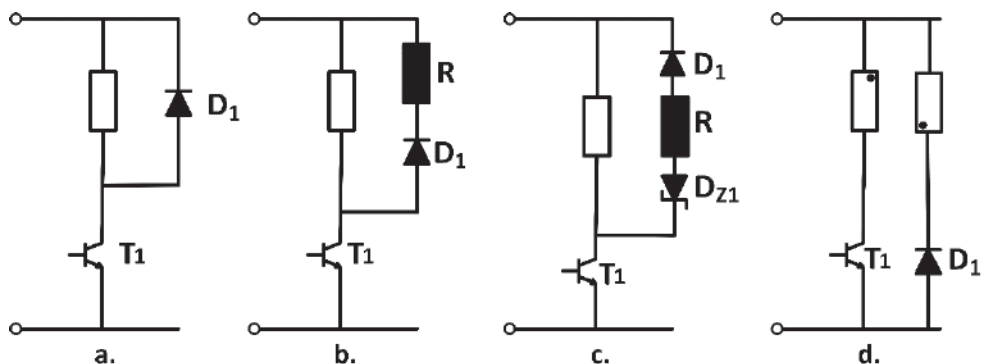


Fig. 8.28 Other converters for powering the SRM.

The circuit in Fig. 8.28 c uses a Zener diode to maintain the voltage at a high value during the return of energy.

The circuit of Fig. 8.28 d [17], [29] is used in a bifilar-wound motor. When the transistor is blocked, the current is transferred to the secondary winding and returns through the diode. This circuit allows the reverse of the whole voltage, but does not allow the soft switching because the zero-volt condition does not exist. The peak voltage on the transistor is twice the supply voltage plus a transient voltage value due to the imperfect coupling between the primary and secondary windings of the power supply.

Fig. 8.29 shows another diagram for the schme, with the mention that the switching elements represented by the contacts are power electronic devices: bipolar transistors, MOS, IGBT, thyristors or GTO thyristors.

This pattern is a specific variant for four (or multiples of four) phases of the SRM, all using only one switching element per phase. The midpoint of the power supply is not accessible, but a wound uses the entire voltage  $V_s$ .

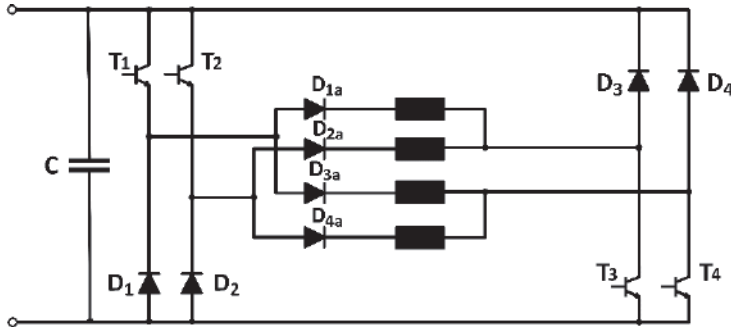


Fig. 8.29 SRM-power converter for 4 or a multiple of 4 phases.

Fig. 8.30 a [18] shows a power converter for a three-phase SRM, using four switching elements. This power converter requires a further switching element, working permanently, in addition to the  $n$  power devices dedicated to the  $n$  phases, and therefore, the phases energization is done using an unique pulse in an additional switching period. This circuit may obviously be used for motors with two or four phases.

A commonly used scheme is shown in Fig. 8.30 b, which uses one extra transistor per stages pair in the case of machines with an even number of phases.

If the common transistor is connected to phases 1 and 3 or 2 and 4, all phases may benefit from the maximum reverse voltage during blocking.

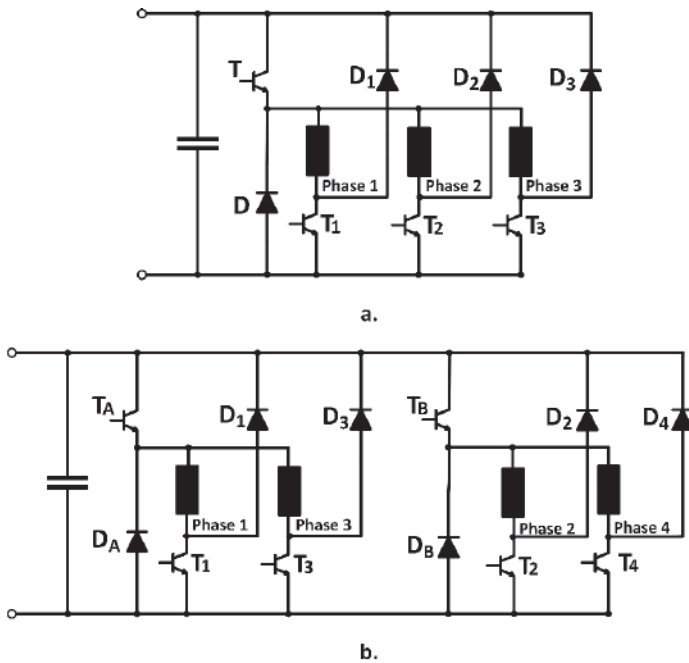


Fig. 8.30 Power converter with additional switching element a) common to all motor phases; b) common to two phases of the motor.

Fig. 8.31 shows an H diagram, obtained by removing the diodes connected in series.

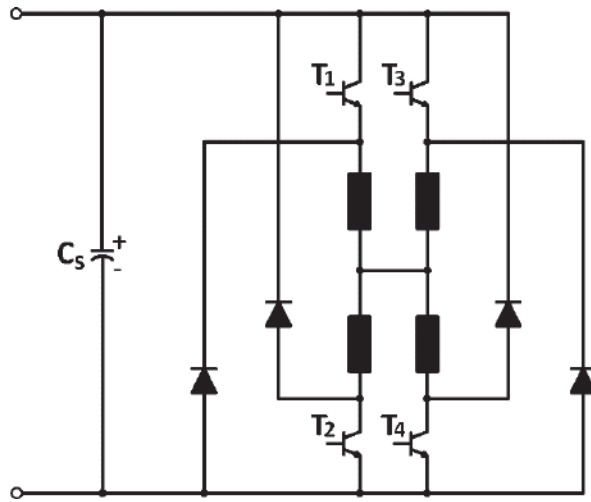


Fig. 8.31 H power converter.

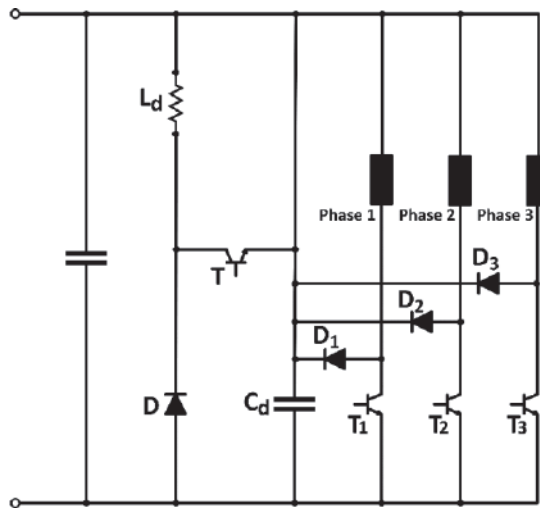


Fig. 8.32 Power converter with an additional switching element [17].

The common transistor  $Q$  is operating all the time, while the phases switching transistors is operating only for a third of time (in the case of a three-phase motor). Consequently, the switching and the conduction losses, the current average and effective values through the common transistor will be greater than in the switching transistors. The use of a common transistor destroys the main advantages of the machine, namely the failure tolerance. In this case, the phases are not independent of each other.

A free-wheeling circuit can be used instead of a common power transistor, as it can be seen in Figure 8.32. All three phases use the same dump capacitor  $C_d$ . The load charges the

$C_d$  capacitor and the voltage is controlled to an average value of about  $2V_s$  by a step-down converter consisting of  $Q$ ,  $L_d$  and  $D$ . In general, the converter components, including the capacitor, do not have small values. Moreover, the failure of the dump circuit allows the charging of the capacitor up to an uncontrollable value, which may lead to catastrophic results. Generally, there are difficulties regarding the torque ripple issue, which have made this converter to be adapted for the sinusoidal current modulation. The shapes of the torque waveforms versus their position are approximately sinusoidal and, by using the relationship:

$$\sin^2(\theta) + \cos^2(\theta) = 1$$

they are able to reduce the torque pulsations to a level of  $\pm 5\%$  of the mean value, using an open loop.

The disadvantages of this scheme are represented by the stresses of the switching devices ( $2V_s$ ), the additional circuit elements and, therefore, by a greater complexity of the system and of the control circuits.

By analysing all of these schemes, it is noted that these power converters are distinguished by the number of phase switching devices used and their configuration, i.e. the possibility of the energy recovery from the switching phases by various processes.

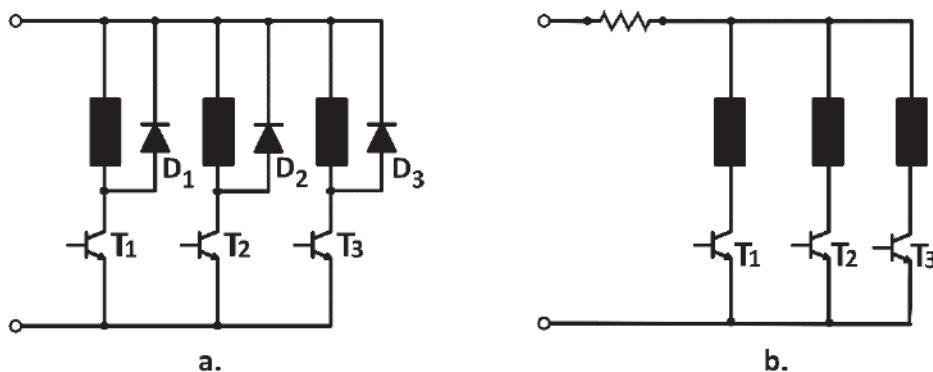


Fig. 8.33 The SRM power supply unit a) voltage; b) current.

All the schemes discussed so far have been supplied by the voltage source (Fig. 8.33). It is possible, however, to use a current power source (Fig. 8.33 b). The current power supply source is favourable to motors operating at very low speeds when the torque ripple must be very low. The voltage power supply is preferred for operation at high rotational speeds, the electric e.m.f. voltage is important and it is difficult to maintain a constant current.

In any case - power from a voltage source or a current source - it is necessary to have a compromise between the switching time and the switches' surge stresses.

The SRM is able to work continuously and as a generator. This is possible with all the above circuits, which may feed each phase winding to the inverse of the power supply. It should also be possible for the power supply circuit to be able to take or dissipate power.

The SRM can operate as a generator by retarding the turn-on angle so that the conduction period starts when the poles are aligned.

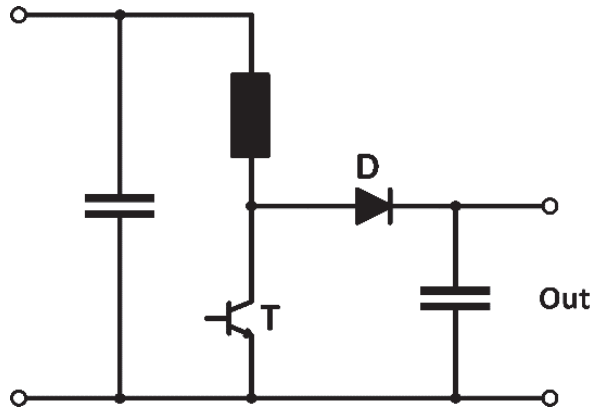


Fig. 8.34 Boost converter.

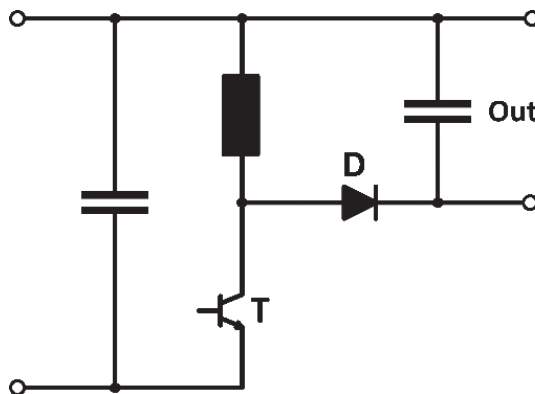


Fig. 8.35 Buck converter.

It is possible to separate the excitation circuit of the output circuit as shown in Fig. 8.34.

The scheme shows a boost converter in a well-known operation mode. The only essential difference is that the inductance is not constant but varies with the rotor position. The output voltage exceeds the input voltage. The problem occurs here if the machine operates at low speeds when the flux flows through a phase too quickly, thus reducing the energy conversion loop.

This disadvantage is eliminated by using the circuit shown in Fig. 8.35. It is based on a Buck-type converter. The output voltage is lower than the input voltage and the energy conversion loop is reduced.

## 8.4 Control structures and strategies for SRM drives

The aspects regarding the SRM control systems were limited during 1980 - 1985 in order to apply the efficient control scheme on the four quadrants, but all of them used the classical elements common to other control structures or sensors mounted on the motor shaft ([27] and [12]).

The classical control system is shown in Fig. 8.36, where the control elements are set up in an analogic manner or with a dedicated hardware, implemented with discrete components.

The goals of the performances achieved with the topology described in Fig. 8.36 were to obtain a low torque ripple and a low level noise. But the use of direct control methods, especially in low power applications, increases the price beyond acceptable limits, and further reduces the reliability of the system, making it sensitive to an environment with a more pronounced degree of vibration.

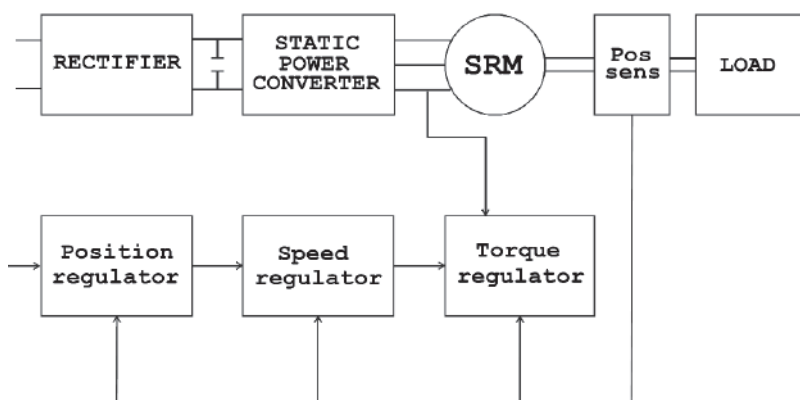


Fig. 8.36 Classic control scheme of the SRM.

The combination of these deficiencies with some limits on both volume and weight imposed by the applications in aerospace and other areas where the development of critical mass parameters and the abandon of the classic structure have become necessary for most classes of applications that required SRMs and certainly in the case of low power and low cost ones.

The control techniques trying to eliminate the mentioned drawbacks, mainly gave up. The position sensor mounted on the machine shaft has the following roles:

- to determine the rotor position by using sensors placed on the machine stator poles [8];
- to indirectly determine the rotor position by observing a phase inductance variation;
- to monitor the current waveform for rotor position detection (similar to the method applied for stepper motors with variable reluctance).

Also, the appearance of power semiconductor devices with integrated current sensors, developed structures that made possible the elimination of discrete current transducers, resistive type or based on the Hall effect, compacting the control scheme to a higher level.

### 8.4.1. The SRM experimental setup

Fig. 8.37 shows a block diagram of an electrical SRM drive using the three position sensors and a speed sensor.

In the scheme below, the SRM is presented as a block whose inputs are the each phase current and the output is represented by the torque. An example of a controller is shown in Fig. 8.38. This is called LMB1008IC and is an experimental circuit manufactured by the National Semi-conductor in collaboration with the SPEED Laboratory.

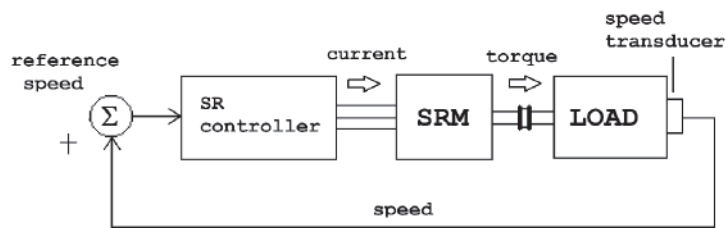


Fig. 8.37 A control block diagram using the SRM's speed and position sensors.

The speed error amplifier produces a train of pulses whose period is proportional to the speed error, and this is used to lock the power transistors at a fixed frequency. The adjustment is on the voltage rather than the current, but the current limit is still required and is compared with the signal from an external sensor in order to block the transistor when the current exceeds the prescribed value.

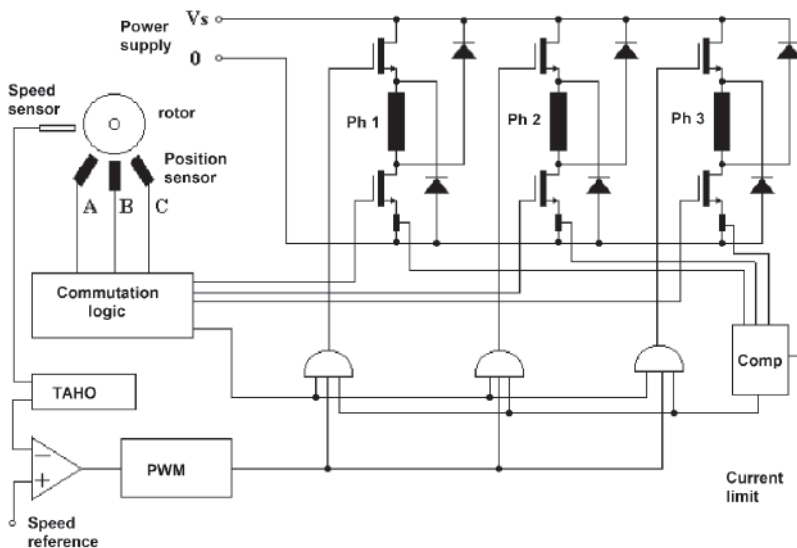


Fig. 8.38 Scheme controller 1008 LMB.



### 8.4.2 The control of a four-phase SRM with position sensors mounted on the stator poles

Fig. 8.39 [8] shows the control diagram and the placement of the optical position sensors for a SRM geometry with 4 stator poles pairs and 3 rotor poles pairs.

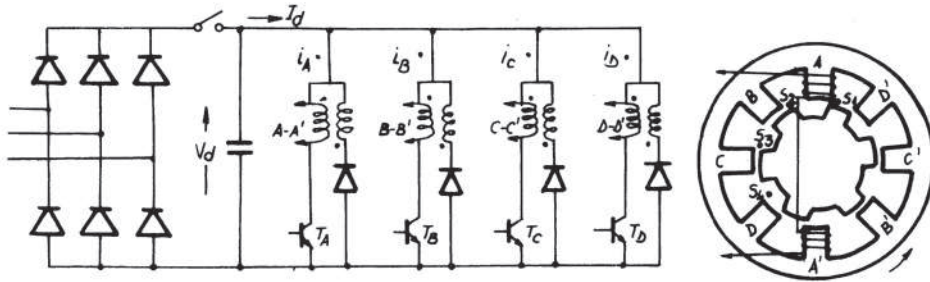


Fig. 8.39 Converter and placement of the optical position sensors for a four-phase SRM.

The control system needs to perform the following tasks:

- controlling the speed and torque in a closed loop;
- initializing the system;
- controlling the connecting sequence to ensure the desired direction of rotation;
- controlling the motor's operation mode (motor, generator, brake).
- ensuring the energy recovery stored in the inductances on each phase.

There are four optical sensors for the rotor position identification, the control sequence and the discrete current sensors for the closed loop torque control.

The optical sensors are mounted on the right corner of each pair of stator poles providing the signals, whose waveforms are shown in Fig. 8.40.

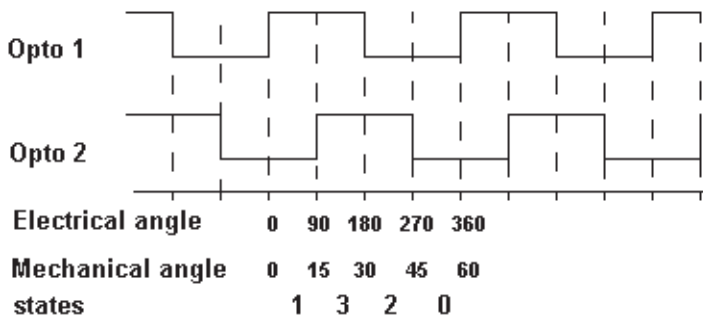


Fig. 8.40 Signals from the optical position sensors.

The signals that are 15° out of phase from each other (this angle depends on the number of stator and rotor poles pairs) are cumulated into a pulse train then generated, by dividing

another set of signals  $0.25^\circ$  through a dedicated hard scheme. In order to achieve a command of connecting the necessary phase to create the required direction of rotation on the slope corresponding to the increase of the phase inductance (positive slope) with an advance angle  $\theta_0$ , and the disconnection at the moment  $\theta_p$  so that the angle of the interrupted current  $\theta_q$  does not extend more on the negative inductance slope, an angle controller is required by four counters, one for each phase, working as down counting. They are programmed with the numerical sequences  $\theta_{pw} = \theta_0 + \theta_p$  and  $\theta_0 = 60^\circ - \theta_q$  contained by the two buffers (the pulse width control and the delay control).

Both counters have the clock corresponding to  $0.25^\circ$  that for the delay generation is validated at the transition  $1 \rightarrow 0$ . Each counter is independent and can be programmed with sequences between  $0^\circ$  and  $60^\circ$ , which is essential to control the drive in all four quadrants.

A synchronisation procedure is essential to ensure the motor starting up from any position. For the forward rotation, the phase current should be set in the range  $0^\circ - 18^\circ$  and for the turn in the opposite direction, the current pulse should be on the negative slope of the inductance, in area  $33^\circ - 60^\circ$ , generated by the coupling of signals from adjacent sensors. The result is a power dissipation, corresponding to the area  $9^\circ$ , which expresses the difference between the delimited zone and the desired zone  $42^\circ - 60^\circ$ , but the energetic phenomenon is negligible.

The torque and speed control loops are created together, with the aim of improving the speed response of the motor. A high gain loop linearizes the system, makes it robust and allows large gains within the speed loop, limited by the stability.

All the control and command functions that are critical in terms of time should be performed by the software written in the assembly language, while the passing from one state to another (switching) can be done in other languages.

Fig. 8.41 shows an example block diagram of a control system for an SRM using position sensors. The speed and current loops are implemented numerically on a microcontroller or DSP.

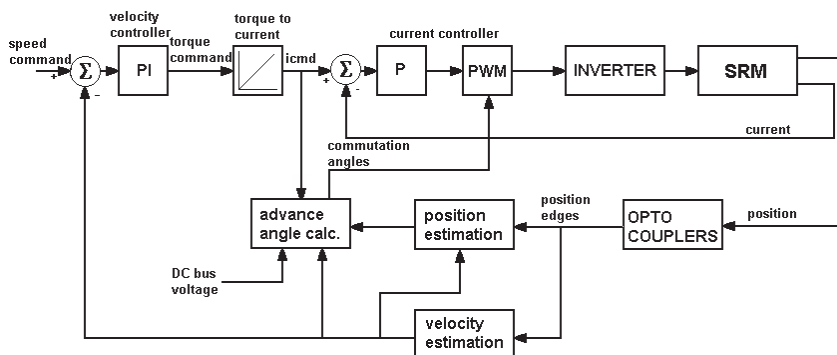


Fig. 8.41 The block diagram of the control system using position sensors.

### 8.4.3 Determination of the rotor position indirectly by observing the variation of a phase inductance. Elimination of the current sensors

The complexity of the hardware solutions containing discrete components, noise and delays introduced by the analogue to digital converters in comparison with the simplicity of the SRM, eliminates the general options for the inductance calculation in real time conditions.

The paper in [28] describes a control solution that avoids the calculation of the inductance estimator as presented by W.D. Harris and J.H. Lang or the one resulted by applying the method imposed by P.P. Acarnly [3]. This control solution has the following performances:

- the speed can be estimated and adjusted;
- a torque control loop and a phase current controller can be implemented;
- there might be a switching phases and a system initialisation;
- a four quadrants operation is viable;
- the discrete current and position sensors could be removed.

The main advantage of this method is the highly degree of magnetic independence for the phases and the strong variation in the phase inductance depending on the rotor position (Fig. 8.42).

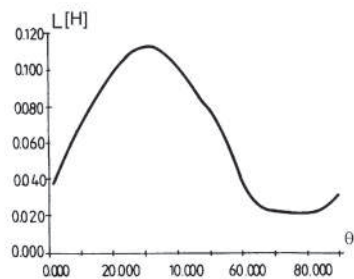


Fig. 8.42 Inductance variation with rotor position for the SRM.

The amount of torque is controlled by changing the phase current and the direction of the torque by the right placement of the active phase with respect to the rotor position (Fig. 8.43).

If the current remains constant, the torque developed by the SRM is:

$$M_e = \frac{1}{2} \cdot I^2 \cdot \frac{d}{d\theta} L(\theta) \quad (8.14)$$

where:

I - phase current;

θ - rotor position angle;

L (θ) - one phase inductance.

Fig. 8.43 shows an ideal inductance variation depending on the angle  $\theta$ . The following aspects can be distinguished:

- the SRM operates as motor - when the phase currents through the area  $\frac{dL}{d\theta} \geq 0$  and the rotor poles - stator poles are approaching the aligned position;
- the SRM operates as generator (braking torque) – when the activation of the phase is on the area  $\frac{dL}{d\theta} \leq 0$  and the stator – the rotor poles move away from the aligned position.

At high rotational speeds, the e.m.f. induced voltages opposing the change in phase current (increase, decrease), are requiring the phase connection in advance, in order to keep the maximum torque value. The earlier disconnection of the phase, before the rotor's alignment, prevents the generation of the braking torque during the desired motor operation period.

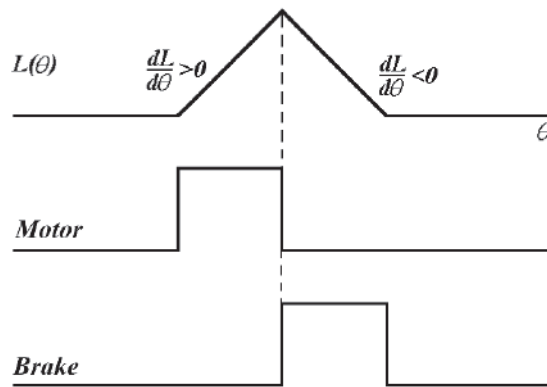


Fig. 8.43 SRM operation as motor and as brake.

In the Fig. 8.43, it can be observed that there is an interval when the phase is not supplied in order to produce the torque corresponding to the required operating regime. This time it is used by the controller to determine the rotor position.

The rotor position determination is done by obtaining the stator phase inductance variation depending on the rotor poles position relative to the stator poles one.

For a stator phase, the equation is:

$$V = I \cdot r + L(\theta) \frac{dI}{dt} + \omega \cdot I \cdot \frac{d}{d\theta} L(\theta) \quad (8.15)$$

The inductance value is obtained by applying short DC voltage pulses and it can be approximated by:

$$V \approx L(\theta) \cdot \frac{\Delta I}{\Delta t} \quad (8.16)$$

So, the current resulted by applying the voltage pulses is inversely proportional to that phase inductance. Since only the rotor's position needs to be detected, the obtained  $\Delta I$  is compared to a threshold value (Fig. 8.44). It is important to note that the voltage pulses are equally applied to the energised phase, only the application period is different. Therefore, there is no need for an additional power source.

When the phase C produces the torque, the phase B is fed with short measuring pulses to detect the moment of the phase A feeding. The phase supplied in order to produce torque can be advanced or delayed by increasing its threshold value. The phase switch in order to achieve the desired operation mode, i.e. the rotation direction, is performed by treating the system as a finite state controller whose states diagram is shown in Fig. 8.45.

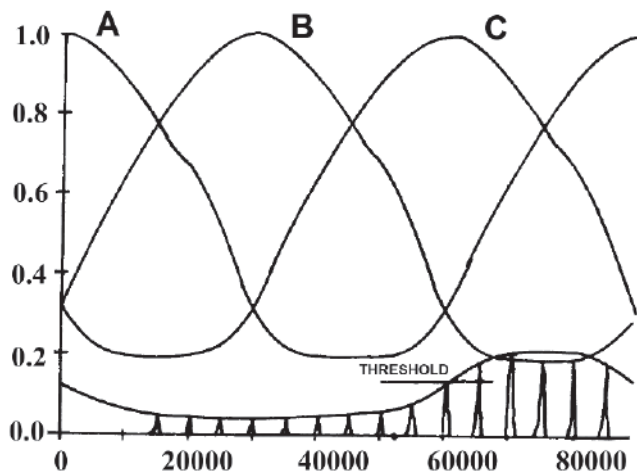


Fig. 8.44 The SRM rotor position determination [28].

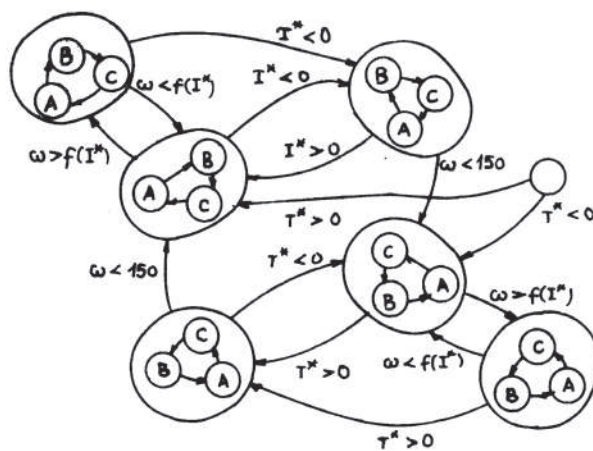


Fig. 8.45 The states chart of the SRM [28].

There are 19 possible states that can be described. The algorithm provides a different state for each switching period (three for the three-phase SRM) for each elementary switching algorithm (3) for forward and backward (2), plus a state for the start-up.

The finite controller is synchronised by a clock of 5 kHz generated by a chip-timer, thus providing a resolution angle of  $1.2^\circ$  at a rotation speed of 1,000 rev / min. The 5 KHz clock is processed to generate a 5 ms interval required to resume the controller's software functions, which determines the controller's structure. The control algorithm is implemented by the software executed in a standard Intel 8751 microcontroller.

The hardware of the power control also ensures the elimination of discrete current sensors (resistive or inductive), because power switches (MOSFET) are used with integrated current sensors. Each current sensor is an isolated structure from the power semiconductor element, having a separate power source and providing an output current proportional to the current through the switch. The usual proportional factor is 1: 1000.

If the switch is blocked, there is no current through the integrated sensor. For this reason, control strategies or the hysteresis-type current controller by comparison with the ramp signal, can no longer be achieved. The control strategy in Fig. 8.46 is recommended; the switch is off for a time period given by the "OFF" trimmer as soon as the comparator has reached a prescribed current value. The controller switches to "ON" after the "OFF" period and the process is repeated. Since the switching noise is introduced on the integrated current transducer, the elimination of the false signals is provided by the "ON" trimmer circuit.

Among the two switches feeding one phase, only one of them must be of the type described, having an integrated current sensor.

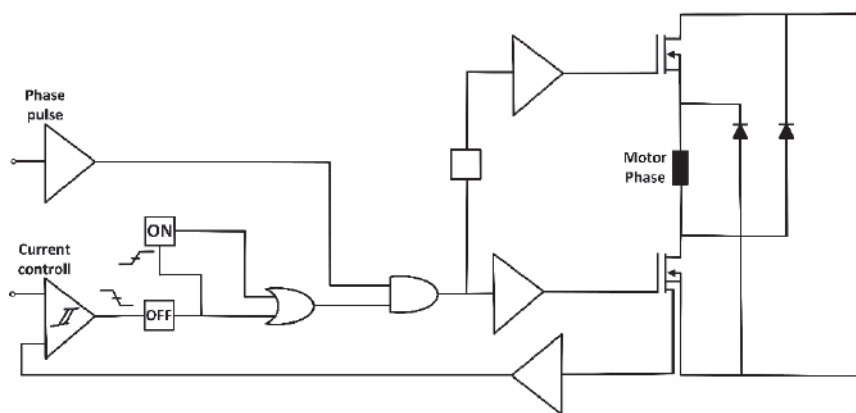


Fig. 8.46 Control strategy of the SRM [28].

The practical results obtained using the SRM scheme and the control strategy presented were very good at high speed levels (speed reversal of  $\pm 2000$  rev / min), but the minimum speed that has been controlled was only 150 rev / min.

The wide-spread variety of current sensors and switches (IGBT) and their availability for an approximately 1 HP application establishes the entire range of applications where the parameters size over weight ratios are important.

#### 8.4.4 The sensorless control method using the Kalman filter

The structure of an observer is shown in Figure 8.47. To achieve this, it is necessary to determine the discrete machine model in the time domain. The input variables of the motor are the measured voltages and the outputs are the currents, calculated on the basis of the machine model matrices A, B and C.

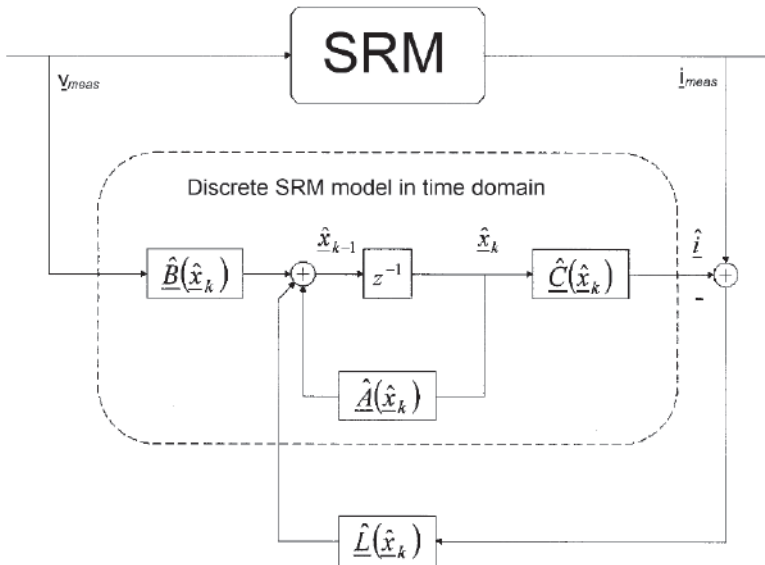


Fig. 8.47 The structure of an observer for the SRM control.

The calculated current is compared with the measured currents, the errors being reintroduced into the control system by the matrix  $\hat{L}$ . The rotor position is included as being an element in the vector  $\hat{x}_k$  and it will be estimated by the observer.

In this case, in order to simplify the solutions, the inductance is considered to be independent of current.

#### 8.4.5 The presentation of a sensorless control method based on the estimated flux [36]

The control system is designed on the structure of a sensorless algorithm, which is based on the flux control in the motor. As shown in Fig. 8.48, the control system consists of five main modules: a sensorless commutation algorithm, an outer loop to control the rotation speed, an inner loop to control the machine's phase current, a serial control block and a slope controller.

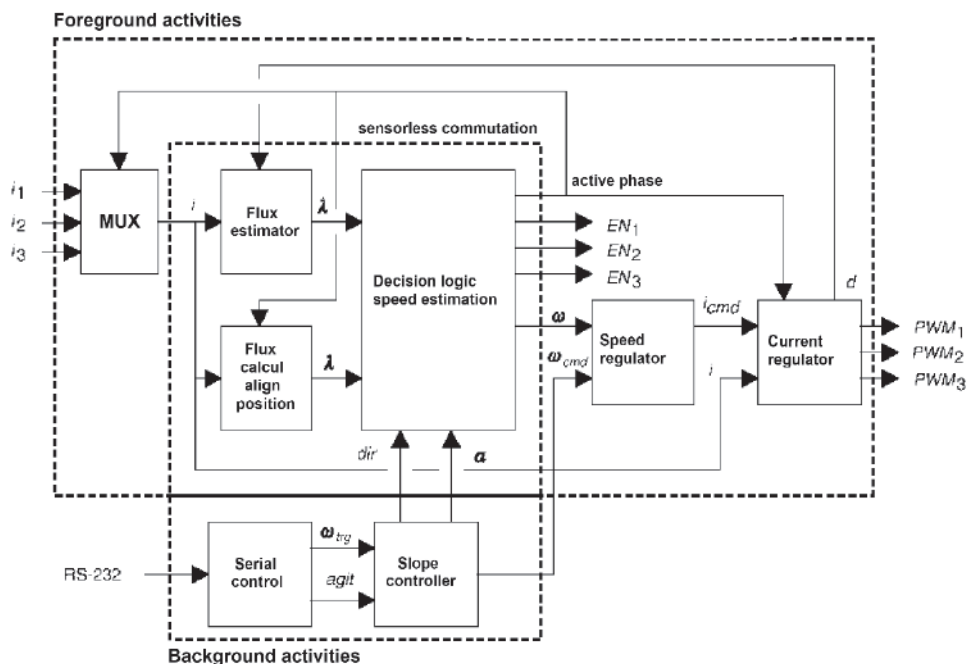


Fig. 8.48 The SRM algorithm for the SRM's sensorless control.

### The sensorless switching algorithm and the speed update

The essence of the sensorless control algorithm is the switching regulator, which contains a flux estimator, a reference flux generator and a logical decision block. Ideally, the logical decision block should execute the motor phases switching when the rotor poles and the stator poles are nearly aligned in position. In this algorithm, the flux in the active phase winding is compared with a reference flux, which is a scaled flux value in the aligned position. The logical decision block will decide on the active motor phase switching when the flux through this phase will exceed the reference flux. More specifically, the motor will be switched when:

$$\hat{\lambda} > \alpha_c \lambda_a, \quad (8.17)$$

Where  $\hat{\lambda}$  is the estimated flux in the active phase winding;  $\alpha_c$  is a scalar between 0 and 1 that is corresponding to the conduction angle;  $\lambda_a$  is the flux in the aligned position. The switching condition is shown schematically in Fig. 8.49. As it can be seen in Eq. 8.17, the correct calculation of the moment for phase switching depends on the best estimation of the flux in the active phase winding, as better knowledge of the magnetisation curve for the aligned position and the careful selection of the turn-on angle.



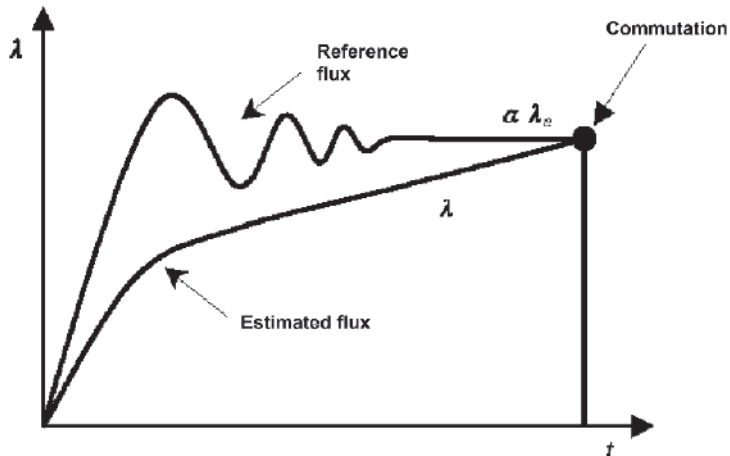


Fig. 8.49 Provided switching stages for the SRM.

### The Flux Estimator

As it can be seen in the block diagram presented in Fig. 8.48,  $\lambda$  is generated by the flux estimation block, which calculates the flux based on the duty cycle of the pulse width modulation and the current in the active phase winding. Its principle of operation is similar to that of a classic flux estimator and uses the following law of recurrence:

$$\lambda_{n+1} = \lambda_n + \underbrace{v_n - i_n r_w}_{V_{EMF}} \quad (8.18)$$

to integrate the e.m.f. voltage induced in the active phase winding. In equation 8.18,  $v_n$  is the voltage across the motor,  $i_n$  is the current flowing through the coil,  $r_w$  is the resistance of a phase winding. However, unlike a classical flux estimator, which requires the measurement of the terminal voltage and the current through the coil, this modified estimator requires only the current measurement. Instead of being measured, the terminal voltage is approximated by the relationship:

$$v_n \approx V_{bus} d_n - v_{trans}(i_n) - v_{diode}(i_n) \quad (8.19)$$

that takes into account the voltage drop along the active switch of the voltage inverter. In the equation 8.19,  $V_{bus}$  is the supply voltage,  $d_n$  is the fill factor,  $v_{trans}$  is the voltage drop across the power transistor and  $v_{diode}$  is the voltage drop across the diode. It should be noted that, in equation 8.19, it is assumed that the power supply is strong and stable and that also the power switches characteristics  $v-i$  are known. Substituting the equation 8.19 to the original recurrence formula, the relationship for the calculation of the new flux becomes:

$$\lambda_{n+1} = \lambda_n + \underbrace{V_{bus} d_n - v_{trans}(i_n) - v_{diode}(i_n) - i_n r_w}_{V_{EMF}} \quad (8.20)$$

For simplicity, the voltage drop across the power transistors, the diode and winding resistance are combined into a single term called voltage drop, thereby allowing the equation 8.20 to be written in the following form:

$$\lambda_{n+1} = \lambda_n + \underbrace{V_{\text{bus}}d_n - v_{\text{loss}}(i_n)}_{V_{\text{EMF}}}$$

where

$$v_{\text{loss}} = v_{\text{trans}}(i_n) + v_{\text{diode}}(i_n) + i_n r_w \quad (8.21)$$

With the voltage loss table according to the current, the update may be performed by two add operations, a scalar multiplication and a reading of the table.

### The operation at low speed

As the rotational speed of the rotor decreases, the update rate is made to decrease the frequency and, as a result, the bandwidth of the speed loop suffers. If the motor is suddenly loaded at a low speed (<400 rpm), the speed loop integrator may not be able to respond in a small enough time, that is, before the rotational speed of the shaft to fall below the value where the stop detector acts. To help improve the bandwidth of the loop in these conditions of speed operating below 400 rpm, the switching algorithm introduces a special low-speed operation. Thus, the speed update rate is doubled by estimating the speed twice during each switching cycle. As shown in Fig. 8.50, this is done by adding a second flux threshold, which gives an interrupted signal only if a speed update has been performed.

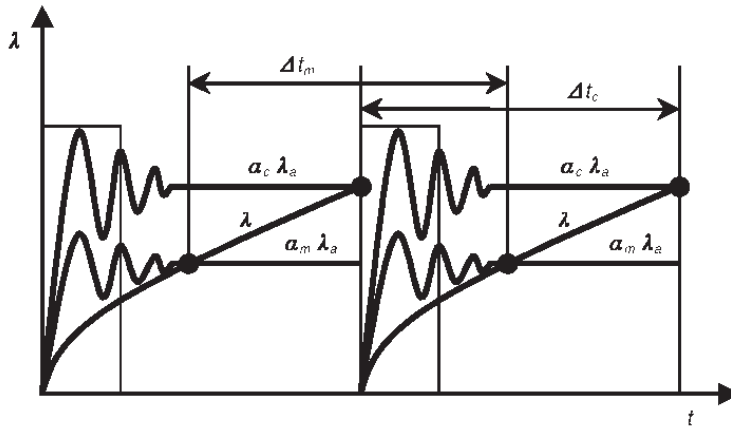


Fig. 8.50 Provided switching stages for the SRM at low speed.

Just as before, this second threshold is a scaled value of the rotor flux in the aligned position. Due to the shape of the flux waveform, by setting a scaling coefficient  $\alpha_m = \alpha_c / 2$ , the second update will be made about the middle of the switching period. To implement the update speed and medium time of the switching period, a second timer needs to be

set up to count the number of sampling periods between two consecutive intersections. This overlapping of measurement intervals allows a double update rate. Using this method of computing, the low speed range of the motor can be controlled and can be lowered from 300 to 150 rpm. It is also necessary that the exclusion zone could prevent that noise from the current waveform to lead to an update of the rotation speed of the machine shaft at an unwanted moment.

### 8.4.6 Other methods for determining the rotor position without the use of discrete sensors

From the above presented result, the tendency to eliminate the position sensors placed on the shaft or on the SRM poles and the rotor position estimation of the phase inductance variation analysis during the alignment of the poles was clear. P. Acarlay indicated the first similarity between the SRM and the stepper motor with variable reluctance in this regard and recommended the use of control techniques that have been successfully applied to stepper motors (monitoring the current variations through the fed phases or real-time calculation of the inductance of a non-energised phase) [3], [16].

The phase equation using instantaneous values is:

$$V = R \cdot i + L \cdot \frac{di}{dt} + i \cdot \frac{dL}{dt} \tag{8.22}$$

where  $L$  = the inductance instantaneous value.

Solving the above equation, the following results:

$$L = \frac{(-B + A \cdot L_0) \cdot e^{-A \cdot t} + B}{A} \tag{8.23}$$

where:

$$A = \left( \frac{di}{dt} \right) \cdot i^{-1} \text{ and}$$

$$B = \frac{V}{i} - R$$

$L_0$  = the inductance value during the measurement interval.

The biggest problems these strategies raise are the following:

- the long time for computing (which reduces the dynamic performances of the control system);
- the sensitivity to noise;
- the analogue-to-digital conversion delay.

A new concept has been developed by the University of Texas Power Electronics Laboratory using a modulated frequency converter (FM), which generates a voltage whose amplitude is proportional to the instantaneous inductance. This analogue signal contains the information on the rotor position and is subsequently processed to obtain the switching times [11].

The basic concept of FM is generating a pulse train whose frequency is proportional to the instantaneous inductance of a phase. The block diagram of the circuit is shown in Fig. 8.51. A special thing about this solution is that an FM converter is able to operate in the range of 0-100 KHz.

The frequency modulated signal of the phase inductance can be demodulated by applying it to a controller and measuring the frequency or using an inverse frequency-voltage converter which provides a linear relationship between the input and the output.

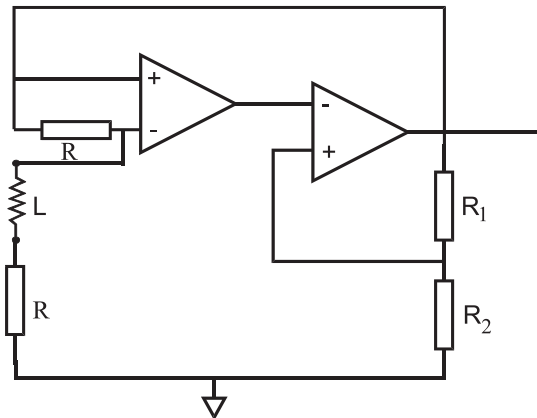


Fig. 8.51 The block diagram of a control circuit.

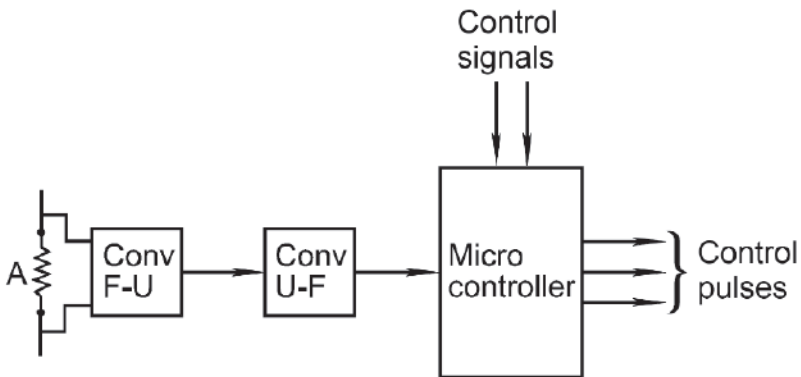


Fig. 8.52 The control system using a microcontroller.

A special thing about this solution is that an FM converter is able to operate in the range of 0-100 KHz. Throughout this field, the rotor position can be determined with high

accuracy, eliminating thus the shortcoming of the previous scheme, i.e. the inability of operating below 150 rev / min.

The scheme of such a command structure is presented in Fig. 8.52.

The phases testing and states algorithm is similar to previous cases, the only difference consisting in the perception of the phase inductance value.

### 8.4.7 Advanced control structures of the SRM

#### 8.4.7.1 The automated control system using the sliding mode

In systems with variable structure theory, the greatest attention was paid to a specific type of control law, causing a sliding mode in the system. In the sliding mode, the system structure changes / commutes with a theoretically infinite frequency (in practice, this frequency is limited by the dynamic characteristics of the switching elements).

The clearly sliding adjustment mode was entered in the field of the SRM drives.

In this sense, a work of the Italian researchers [7] is worth mentioning, who have applied the sliding mode control of the energy recovery in the C-dump converter for the switched reluctance motor drive.

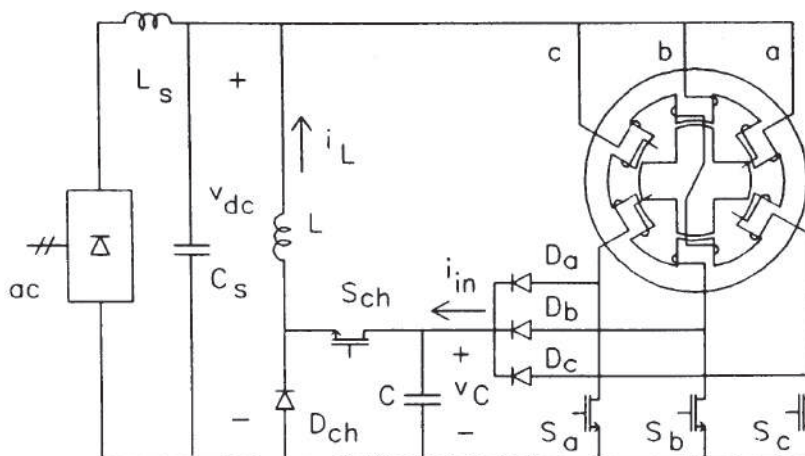


Fig. 8.53 Scheme of the SRM powered by a power converter with a C-dump capacitor.

The non-rigorous control of the energy recovery converter can cause the resonance between the elements of the converter and the motor windings. Fig. 8.53 shows the schematic of an SRM fed through a converter with a dump capacitor.

This paper proposes a new control strategy for the energy recovery converter based on the sliding mode. This allows the achievement of a continuous converter output current, with small peaks of current through the semiconductor devices and small fluctuations in the capacitor voltage.

Fig. 8.54 is the block diagram of the sliding regulator voltage on the capacitor.

The fluctuations occurring in the low frequency current  $i_L$  and the voltage on the capacitor are due to the variations in the mean value of the converter input current, caused by overlapping of conducting phase ranges. These fluctuations have an amplitude that changes with the speed and torque, but is still limited in each case. They disappear completely if the motor works with the rotor blocked.

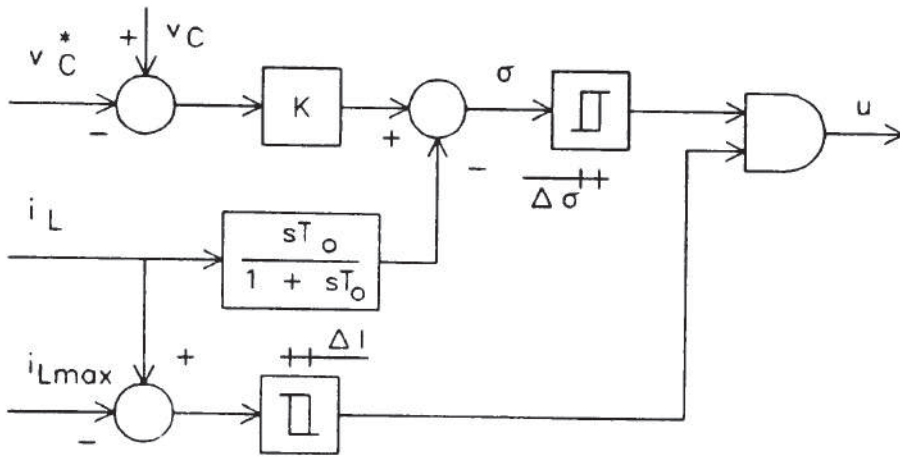


Fig. 8.54 The block diagram of the sliding mode regulator.

#### 8.4.7.2 The fuzzy logic control in the SRM

A conventional control system corrects the system parameters based on a set of differential equations that represent the dynamics of the process model.

In a fuzzy controller, these corrections are made through an expert system based on some rules, which is a logical model of human behaviour. The advantages brought by the introduction of a fuzzy controller are important [30]. Among them, are mentioned the following:

1. Designing a fuzzy logic controller does not require an exact model of the system. It is very appreciated in applications with an electric motor drive system with or without load, whose behaviour is described by a system of linear or partially unknown equations.
2. A fuzzy logic-based controller usually proves best results in comparison with a conventional controller, especially in terms of the response time, the settling time and the robustness.
3. A fuzzy controller can be designed based on the linguistic information received from the expert process or can be designed by the expert process itself. This is an important advantage especially for the speed and position loops, which are quite significantly influenced by the load behaviour.

Returning to the specific case of the SRM, the main advantage of using a fuzzy logic controller is that, by proper design, it can optimize the current shape supplied to the machine in order to minimize the torque pulsations.

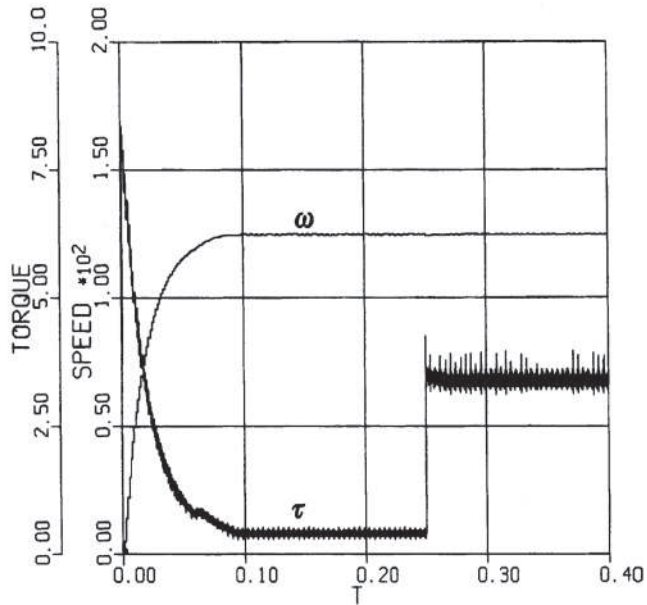


Fig. 8.55 The shape of the torque and the speed obtained with the fuzzy controller.

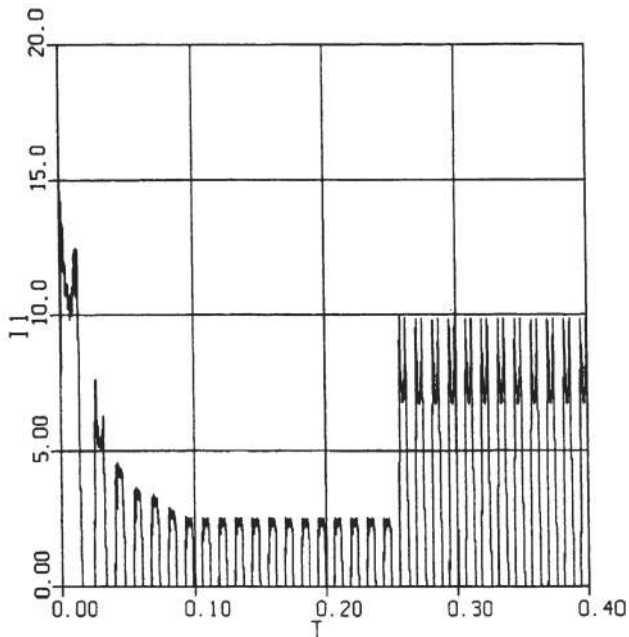


Fig. 8.56 The current waveform obtained with the fuzzy controller.

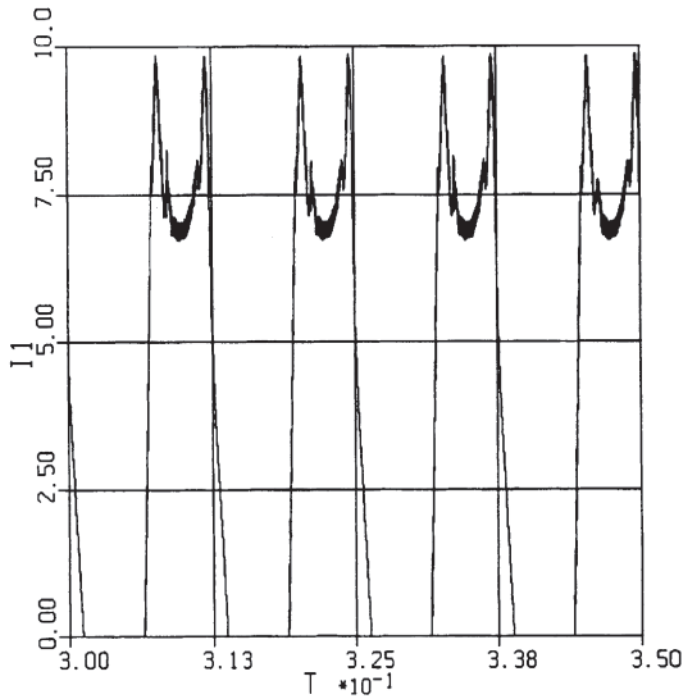


Fig. 8.57 The current waveform obtained with the fuzzy controller (detail).

In this sense, Figure 8.55 shows the shape of the speed and the torque variation of such a machine is exemplified by a no-load starting and then by machine loading. Fig. 8.56 shows the variation of the current shape for this case. Fig. 8.57 provides a detailed form for the change in the current in order to obtain the minimum torque ripple.

The representations shown in the above figures have been made taking into account a motor with 6 stator poles and 4 rotor poles, with a rated current of 18 A and a rated speed  $\omega = 200$  rad / sec

#### 8.4.7.3 The implementation of the neural network to a fuzzy logic controller [34]

The performance of a control system based on a fuzzy logic controller can be improved by setting the appropriate parameters. In most cases, this is a pretty complicated thing to accomplish. The objective of the algorithm is to set parameters of variation to reformulate the functions of the control variables in order to obtain the best response from the system.

In order to do this, you can use a neural network. One of the most important properties of neural networks, for the purpose of designing a command system, is the ability to provide an unknown arbitrary map output only by collecting the data set and the appropriate learning strategies.



# 8.5 SRM control systems developed at the Faculty of Electrical Engineering of Timisoara

## 8.5.1 The Sensor-based control system

This paragraph deals with a current control method of an 8/6 Switched Reluctance Motor using a DSP TMS320C24x. The power converter used in the experiments was a classic one, with two transistors per phase. In the scheme from Fig. 8.58. the current is sensed using two sensor resistances, one for each phases pair. The current is measured only if the two transistors of the same phase are on. The current control loop is performed using a PWM with a fixed frequency and a variable duty-ratio. A proportional controller has been used to regulate the phase current. A PI controller has been used to regulate the motor speed.

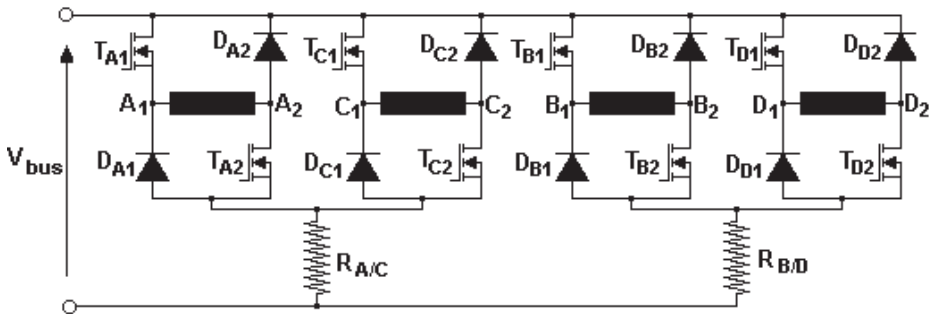


Fig. 8.58 Power converter for an 8/6 SRM.

A disadvantage of this type of power converter is that the current can be measured only if both transistors corresponding to the same phase are conducting. If one of the two transistors is off the current through the sensor resistance flows in the other sense, which means that the measured value cannot be taken into account. This problem can be solved through an appropriate software, which allows the measurement only if both transistors are on.

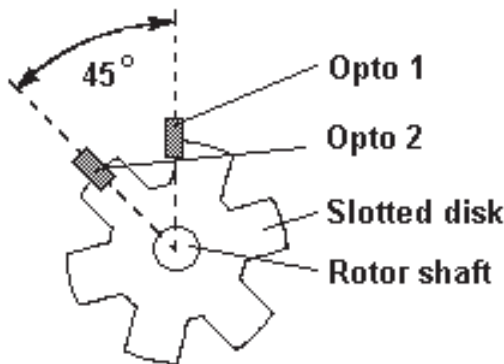


Fig. 8.59 The placement of the position sensors.

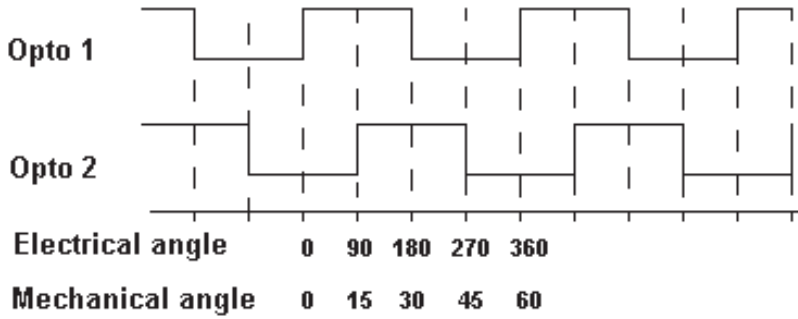
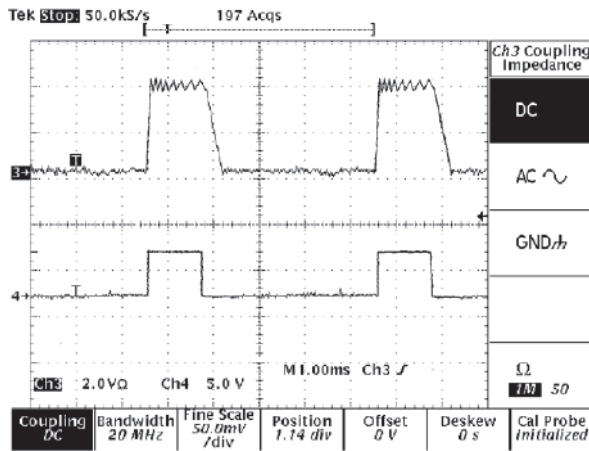
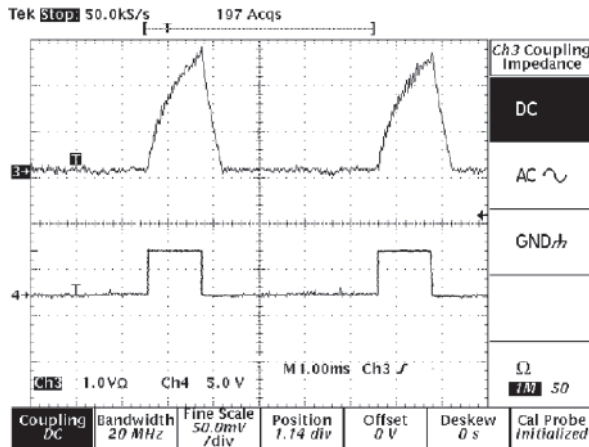


Fig. 8.60 Electrical signals from sensors.

The experimental results at high speed and low speed are presented in fig. 8.61 a and b:



a.



b.

Fig. 8.61 a) Current waveform and position signal at low speed, b) Current waveform and position signal at high speed.



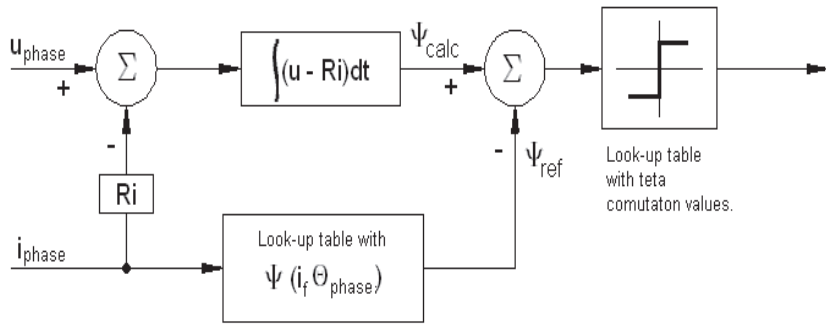
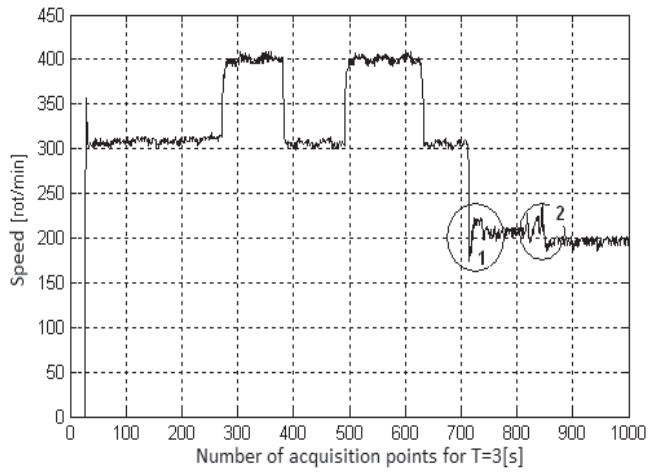
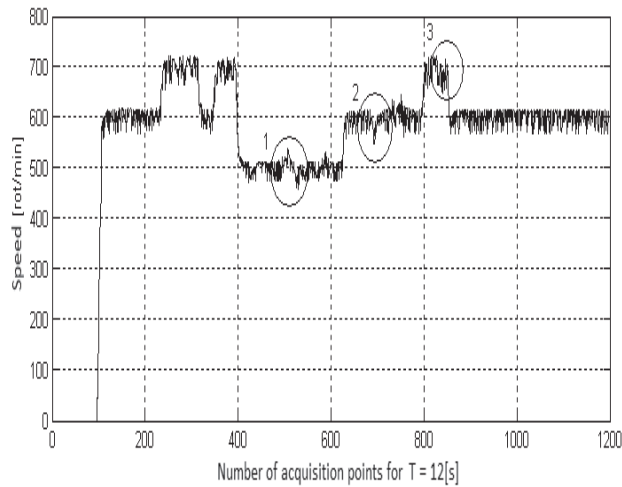


Fig. 8.63 Angle control method.



a.



b.

Fig. 8.64 Dynamic behaviour of the SRM.

The dynamic motor speed at sensorless operation has been studied by rapid changes in speed and load torque. Figure 8.64 a shows the dynamic behavior of SRM. When switching from 300rot / min to 200rot / min the load torque changed rapidly from its maximum value to zero, (point 1). In point 2, a new torque change was made from zero to its maximum value. The motor continued to run at full load

The signal applied to the engine control was of the step type. In the two graphs there are three marked areas where:

In the Figure 8.64 b the motor starts with no load at 600rot / min, after a time  $t = 0.6s$  the speed changes to 700rot / min, for a very short time  $t = 0.3s$ , the speed drops to 600rot / min and rises again to 700rot / min. At  $t = 1s$  the motor speed reaches 500rpm and at the marked area 1 the maximum load torque is applied. The motor continues to run and at  $t = 1.3s$  it rises to a speed of 600 rpm. In zone 2 the load torque decreases to 0, the motor continues to run and rises to 700 rpm where it loads with maximum torque value. During loading, its speed shifts to a new speed of 600 rpm.

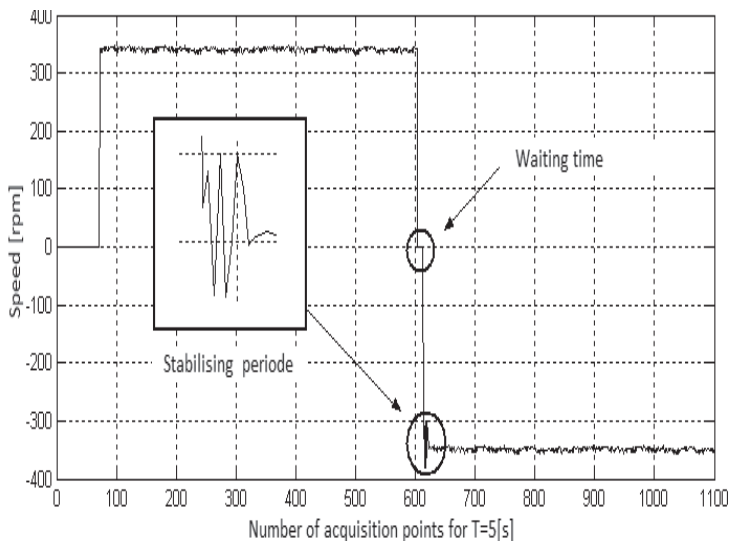


Fig. 8.65 The speed trajectory in both directions.

The figure 8.65 shows the speed trajectory in both directions. During this test, the SRM drive operating as a motor, starts in a clockwise direction and, after a certain number of revolutions, it stops for 0.2 ms and then starts in the opposite direction. This test has been performed at 350 rpm to highlight the performance of the system at low speeds. The delay time is necessary for the rotor to establish its position. The speed information was collected using an external speed sensor on the DC motor load and NI6009 for data acquisition. The SRM drive system has performed this action with a high reliability and consistency. Figure 8.66 presents the SRM test stand from the Department of Electrical Engineering, University Politehnica Timisoara.

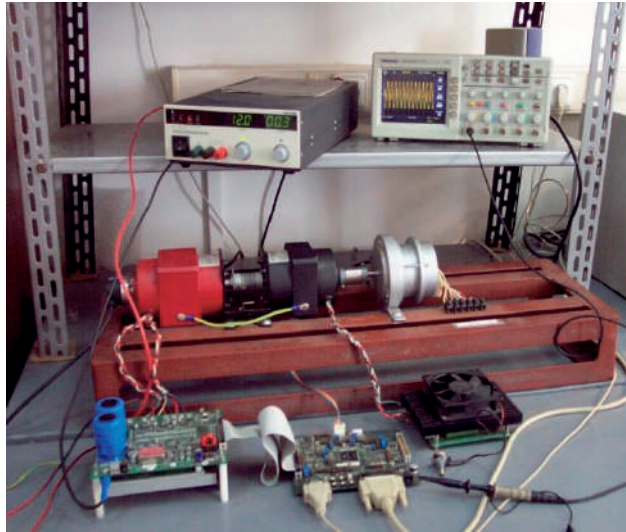


Fig. 8.66 General overview of the test stand.

## 8.6 Perspectives on using the SRM in electric drive systems

The general trend in the electric motor control is to design control systems with the lowest possible cost and the highest energy efficiency and reliability. Obviously, it relates to motors with a low production cost and a high efficiency as an example SRM can be. It also created the need to implement more effective control strategies in order to increase the performance and to reduce the overall size of the drives.

The digital signal processor (DSP) TMS320C240 equipped with an advanced control algorithm fully meet these requirements.

Having this in mind, the SRM is a natural choice for the electric drives systems, taking into account the fact that currently it is one of the cheapest electromechanical energy conversion systems.

### Control using digital signal processors [1], [2]

As far as the electric drives are concerned, the SRM has significant advantages. Due to its simple mechanical construction, high efficiency, torque / speed characteristic and low maintenance cost, the SRM is becoming one of the most used electromechanical energy converters.

Traditionally, SRM control systems were designed with quite cheap analogue components. The first disadvantage is inherent in any analogue components: aging and temperature changes make the system need regular adjustments; moreover, the system reliability decreases while the number of its components increases, and finally, any improvements to be made to the system are more difficult to achieve. A second

disadvantage lies in the limitation of the effectiveness of the analogue control structures, such as, for example, the impossibility to implement adaptive control algorithms.

All these problems are solved by using digital control structures. In fact, digital systems offer many more advantages than the analogue systems. Deviations are eliminated primarily because the functions are solved numerically, the improvements can be made easily by making changes in the programme and the number of components is reduced because the digital systems may perform several functions by integrating them in a single capsule.

The performance of the SRM depends largely on its control. Digital signal processors allow the use of real-time algorithms and sensorless control. All these advantages combined lead ultimately to the cost reduction of the whole system.

A digital signal processor has the following advantages:

- it reduces the cost of the entire system through efficient control over the entire speed range, allowing a correct sizing of the power circuits;
- it has the ability to execute performant algorithms to reduce the torque ripple, resulting in the reduction of the vibration and the increase of its life time;
- it allows the reduction of the harmonics content by using performant algorithms; this leads to the reduction of the cost of the filters;
- it allows the elimination of the position or speed sensors by implementing algorithms without sensors (sensorless algorithms);
- it reduces the number of lookup tables; this leads to the reduction of the required memory;
- it has the ability to generate optimal profiles in real-time, resulting in an improved performance;
- it can generate pulse width modulated outputs (PWM) with a high resolution;
- the entire control system is incorporated in a single capsule.

For advanced control systems, the digital signal processor can perform the following:

- it allows the control of complex multi-variable systems using filtering methods such as neural networks and fuzzy logic;
- it allows adaptive controls. Digital signal processors have a high enough speed needed at the same time to monitor the system status and to control it. A dynamic control algorithm adjusts itself in real time to the changes in the system's behaviour;
- by observing the frequency spectrum of the mechanical vibration, error modes of the behaviour can be avoided.

Fig. 8.67 presents a control system using a digital signal processor.

Given the facts presented so far, creating an SRM efficient drive can be achieved only by using a digital signal processor.

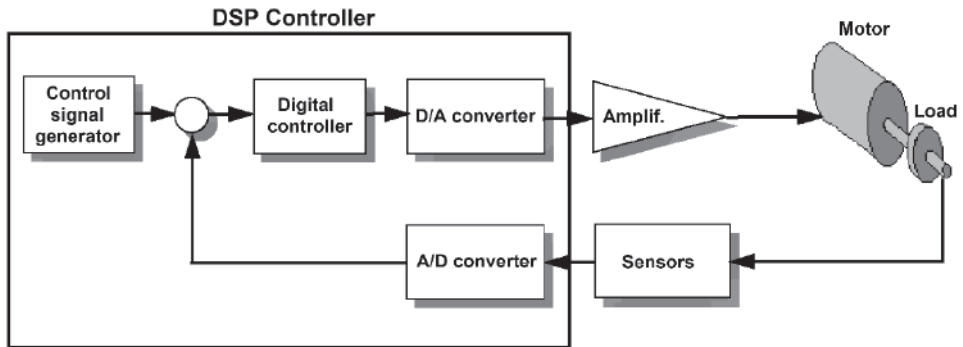


Fig. 8.67 Control system using a digital signal processor.

Following, we will take into consideration the TMS320C240 processor manufactured by Texas Instruments. It is a processor that is specifically designed and optimised for use in control drives with electric motors. Among its features, we can mention: working in fixed point, allowing the generation of pulse width modulated signals (PWM) and consisting of an analogue to digital converter.

The dedicated digital signal processors allow the SRM control both in a position and speed sensor-based control and sensorless control. In order to avoid the torque ripple, which is one of the main disadvantages of this type of machine, the implementation of an advanced control structure using fuzzy logic should be taken into consideration.

## 8.7 References

- [1] \* - Digital Signal Processing Solutions for the switched reluctance motor - Texas Instruments Literature, July 1997
- [2] \* - Using Family TMS320 DSPs in Motion Control Systems - Texas Instruments Literature, September 1996
- [3] P.P. Acarnley, R.J. Hill - Detection of rotor position in stepping motors and switched reluctance by monitoring of current waves - IEEE Trans. IE on May 1987;
- [4] Gh. Atanasiu (Coordinator) - New technical solutions on electric drive systems with variable reluctance synchronous motors and concentrated stator winding - Research contract with the Ministry of Industry, phase I, March 1993
- [5] Gh. Atanasiu (Coordinator) - New technical solutions on electric drive systems with variable reluctance synchronous motors and concentrated stator winding - Research contract with Ministry of Industry, Phase II in June 1993.
- [6] Gh. Atanasiu, C. Șorândaru - The Optimal Design of Switched reluctance Motors - Proceedings of the International Conference OPTIM '94, Brasov, Romania
- [7] S. Bolognani, E. Ognibeni, M. Zigliotto - Sliding Mode Control of the Energy Recovery in the C-dump Chopper Switched reluctance Motor Drive - IEEE Trans. on IA Jan./Feb. 1993, pp.181-186;
- [8] B.K. Bose, T.J.E. Miller, P.N. Szczesny - Microcomputer Control of SRM - IEEE Trans. IA on July - Aug. 1986;



- [9] J. Chai, R. Yao P. Chen - Principles for switched reluctance Motors Design - Proceedings, Part 2 International Conference on the Evolution and Modern Aspects of Synchronous Machines; 27 to 29 August 1991, Zurich, Switzerland, pp.445 - 448;
- [10] S. Chan, H.R. Bolton - Development of sub-KW single phase switched - reluctance motor drives, in Proc. Int. Conf. on Electrical Machines, Vol. 2, Sept. 1992;
- [11] M. Ehsani, I. Husain, A. Kulkarni - Elimination of discrete position sensor and the current sensor in the SRM drives - IEEE Trans. IA on Jan. - Feb. 1992;
- [12] M. Ehsani, J.T. Bass, T.J.E. Miller - Development of a unipolar converter for SRM drives - IEEE Trans. on May-June 1987 IA;
- [13] J. Faiz - Prediction of State Magnetisation Characteristics of Switched Reluctance Motors for general rotor position - EPE - Firenze, vol.1, 1991, pp.355 - 359;
- [14] C.A. Ferreira, E. Richter - Detailed Design of a 250-kW switched reluctance starter / generator for year Aircraft Engine - 1993 SAE Aerospace Atlantic Conference & Exposition, Dayton, Ohio, April 20-23, 1993;
- [15] N.N. Fulton, J.M. Stephenson - A Review of Switched reluctance Machine Design - ICEM '88 Proceedings, Sept. 12-14, Pisa, Italy, pp.423 - 428;
- [16] D. Harr, J. Larry - A simple motion estimator for VRM - IEEE IAS Conf. Oct. 1988;
- [17] M.R. Harris, J.W. Finch, J.A. Mallick, T.J.E. Miller - A Review of the Integral - Switched reluctance drive Horsepower - IEEE Transactions on Industry Applications, vol. IA-22, No. 4, July - August 1986, pp. 716-721;
- [18] A.M. Hava, V. Blasko, T.A Lipo - A modified C-dump Converter for Variable - reluctance Machines - IEEE Transactions on Industry Applications, vol.28, no. 5 sept./oct. 1992;
- [19] M. Jufer, M. Crivii, K. Hatefi, P. Poffet, R. Ossen - Synchronous motors Electronically comutated - design and comparison - Proceedings of ICEM 90;
- [20] M. Jufer, M. Crivii, P. Poffet - Conception du moteur à reluctance comutation ELECTRONIQUE - Proceedings MOP - 1990;
- [21] Y.A. Kwon, K. Reichert - Choppingless Operation of a Nonlinear Switched reluctance motor - Proceedings, Part 2 International Conference on the Evolution and Modern Aspects of Synchronous Machines; 27 to 29 August 1991, Zurich, Switzerland, pp.465 - 468;
- [22] P.J. Lawrenson - A brief review of switched reluctance drives status - EPE, Volume 2, No. 3, October 1992;
- [23] P.J. Lawrenson - Switched reluctance drives: A Perspective - Proceedings ICEM'92, Manchester UK, pp.12-21
- [24] H. Le-Huy, K. Slimane, P. Viaronge - A current - controlled Quasi - resonant converter for Switched - Reluctance Motor - IEEE Trans. on IE, vol.38, No.5, oct.1992;
- [25] P. Materu, R. Krishnan - Estimation of Switched reluctance motor loses - Proceedings IEEE-IAS, Pittsburgh, PA, October 1988, pp.176-186.
- [26] T.J.E. Miller - Switched Reluctance Motors and Their Control - Magna Physics Publishing and Clarendon Press, Oxford, 1993;
- [27] T.J.E. Miller, P.G. Bower, R. Becerra, M. Ehsani - Four-quadrant brushless reluctance motor drives - Proceedings of the IEEE, July 1988, pp. 273-276;
- [28] S.R. MacMinn, W.J. Rzesos, P.N. Szczesny, T.M. Jahns - Application of Sensor Integration Techniques to SRM drives - IEEE Trans. IA on Nov. - Dec. 1992;

- [29] W.F. Ray, P.J. Lawrenson, R.M Davis, J.M. Stephenson, N.N. Fulton, R. Blake - High Performance Switched reluctance Brushless Drives - IEEE Transactions on Industry Applications, Vol IA-22, No. 4, July - August 1986, pp.722 - 729 ;
- [30] S. Bolognani, M. Zigliotto - Fuzzy Logic Control of Switched reluctance motor to drive - IEEE Trans. on IA Sept./Oct. 1996, pp.1063-1068;
- [31] J.C. Sabonnadiere, A. Konrad - Computing EM Fields - IEEE Spectrum, November 1992, pp. 52-56;
- [32] C. Șorândaru, Gh. Atanasiu - Method for the simulation of variable reluctance synchronous machine – Proceedings of the jubilee communications session "ELECTRO-TECHNOLOGY, PRESENT AND FUTURE "-ICPE '95 p. SM30 Bucharest, Romania.
- [33] D.A. Staton, R.P. Deodhar, T.J.E. Soong, W.L Miller - Torque prediction Diagram Using the Flow-MMF in AC, DC, and reluctance Motors - IEEE Transactions on IA, vol.32, no.1, January / February 1996, pp.180-188
- [34] V.Trifa, E. Bore, L. Moldovan, C. Baciuc - Design and Simulation of a neuro-fuzzy controller for switched reluctance motor drives - 97 electromotion Symposium Proceedings, Cluj, Romania, pp.35-39.
- [35] A. Weller, P. Trawinski - Design and Control of a Low Power Switched reluctance Motors - Firenze Proceedings EPE 1991 pp.4-001 - 4-006;
- [36] T. Koblara - Contributions to the performant control of Switched Reluctance Motors (in Romanian), Ph.D. Thesis, Politehnica Publishing House, Serie 6: Electrical Engineering, 2009
- [37] Gh.Atanasiu (coord.) – Synchronous servomotors for electric drives, Mirton Publishing House, Timisoara, 2003 (in romanian)

# POWER FACTOR CORRECTION IN SINGLE-PHASE SWITCHING POWER SOURCES USED IN ELECTRICAL DRIVES

## 9.1 Introduction

This chapter deals with the analysis and evaluation of the main topologies and solutions for the single-phase power factor correction (PFC) converters for the 230V mains voltage existent in the literature. The research team within the Department of Electrical Engineering of the University Politehnica of Timisoara carried out the study. The research team signed in 2013 an international contract for research-development and consultancy with Diehl Company from Germany. The contract name is "Analysis and Evaluation of Current Topologies and Solutions for the Single- Phase Power Factor Correction (PFC) for Grid Tied Inverters". The goal was to analyse all the relevant single-phase power factor correction (PFC) topologies existing in the literature up to that moment. The power range of the investigated circuits ranges from 1 kW to 4 kW.

In particular, the following topologies are the subject of this analysis: the passive PFCs, the low-frequency active PFCs, the high-frequency active PFCs – known as the classical topologies, the interleaved ones, the bridgeless ones, the ones based on the soft-switching techniques (Zero Voltage/Current Switching ZVS/ZCS, Zero Voltage/Current Transition ZVT/ZCT). For all these topologies, their specific advantages and disadvantages are highlighted in this chapter.

Their evaluation has been done with regard to the electromagnetic compatibility (EMC) requirements, including radio frequency interference (RFI), which is very important in the residential ambient. Only the inverters with capacitive intermediate DC bus are considered; that means that the PFC rectifier has to feed a DC bus capacitor of about 380-400 V nominal voltage.

The criteria of selecting the relevant topologies are low component costs, high energy efficiency, easy to scale power levels (1.5 kW, 2.2 kW, 4 kW) with the same platform (PCB), high quality, high reliability, compact design (kW/dm<sup>2</sup>).

Thus, in conclusion, the target was a low cost and a high-efficient design.

A decisional matrix has been prepared for different topologies based on the above-mentioned criteria. As the power density has a low priority, the passive and low frequency active PFC topologies (100 Hz) were also taken into account within the decisional matrix.

For the four most promising topologies, the efficiency versus the output power calculation and filter requirement analysis (RFI (radio frequency interference) and THD (total harmonic distortion) (EN 61000-3-2)) has been done in order to obtain an accurate decision base. For these four topologies, the semiconductors losses (conduction and switching losses) and the passive components losses (of the inductors losses, the capacitors losses and the EMI filter components losses) have been calculated.

## 9.2 The Power Factor definition

The power factor ( $PF$ ) gives a measure of the distortion of the line voltage and current and the phase shift between these two waveforms. Poor power factors are typically due to the effect of inductive or capacitive loads. The power factor can be leading or lagging depending on whether the load is predominantly capacitive or inductive in nature. In general, a power factor ranges from zero (0) to unity (1), usually being between 0.8 and 0.95.

The power factor is defined as the ratio between the active power  $P$  and the apparent power  $S$ :

$$PF = \frac{P[W]}{S[VA]} \quad (9.1)$$

For sinusoidal voltage and current waveforms, the classical definition is obtained:

$$PF = \cos \phi \quad (9.2)$$

where  $\cos \phi$  is the displacement factor of the voltage and current. Thus, in the classical way, the PFC method represents a compensation method for the "displacement factor".

Generally, the line current is non-sinusoidal due to the load non-linearity. For the sinusoidal voltage and the non-sinusoidal current, the  $PF$  can be expressed as:

$$PF = \frac{V_{rms} \cdot I_{1,rms}}{V_{rms} \cdot I_{rms}} \cdot \cos \phi = \frac{I_{1,rms}}{I_{rms}} \cdot \cos \phi = K_D \cdot \cos \phi \quad (9.3)$$

$$K_D = \frac{I_{1,rms}}{I_{rms}}, K_D \in [0,1]$$

Where  $K_D$  is the distortion factor and it describes the harmonic content of the current with respect to the fundamental. Hence, the power factor depends on both the harmonic content and the displacement factor.

The total harmonic distortion factor  $K_{D\ THD}$  is defined as:

$$THD_i = \frac{\sqrt{\sum_{n=2}^{\infty} I_{n,rms}^2}}{I_{1,rms}} \quad (9.4)$$

Hence, the relation between  $K_D$  and  $THD_i$  is:

$$K_D = \frac{1}{\sqrt{1 + THD_i^2}} \quad (9.5)$$

The IEC 1000-3-2 standard sets limits on the harmonic content of the current, but does not specifically regulate the distortion factor  $K_D$  or the total harmonic distortion of the line current. The values of  $K_D$  and  $K_{THD}$  for which compliance with IEC 1000-3-2 is achieved depend on the power level. For low power level, even a relatively distorted line current may comply with the standard, but it does not guarantee a high- power factor ( $K_D$  close to unity, but low  $\cos\phi$ ). And, on the other hand, a high-power factor can be achieved even with a substantial harmonic content.

The advantages of using power factor correction circuits are the electricity tariff savings, the avoidance of penalties for low power factor, the reduced losses, the reduced power drawn from distribution systems and, thus optimising the sizing of the electrical infrastructure, the stabilised site voltage levels by reducing the inductive effect of the connected load.

The disadvantages of low  $PF$  are the increased KVA rating of the electrical equipments yielding an increased size and cost of the equipment, the increased size of the conductor due to the higher current in order to transmit the same amount of power at low power factor at constant voltage, the increase of copper losses of the equipment, the poor voltage regulation due to the greater voltage drop in alternators, transformers and transmission lines, caused by the current at low lagging power factor.

## 9.3 Actual publications for single - phase PFC

### 9.3.1 General aspects

In order to maximise the real power available from the mains, the power factor correction shapes the input current of various non-linear loads. Ideally, the load emulates a pure resistor, in which case the reactive power drawn by the device is zero and the current is a perfect replica of the input voltage (usually a sine wave) and is in phase with it. In this case, the current drawn from the mains has an optimum (minimum) value for the

real power required to perform the needed work, and this minimises losses and costs associated not only with the distribution of the power, but also with the generation of the power and all the equipment involved in the process.

The harmonics absence also minimises the electromagnetic interference (EMI) with other devices being powered from the same supply source. Another reason to employ PFC in many of today's power supplies is to comply with regulatory requirements. Nowadays, electrical equipment in Europe must comply with the European EN 61000-3-2, or EN 61000-3-4 standards. These requirements apply mostly to the electrical appliances with input power of 75 W or greater, and it specifies the maximum amplitude of the line-frequency harmonics up to the 39<sup>th</sup> harmonic [1], [2], [3], [4].

In the last decades, a great deal of research in the power electronics field has been devoted to finding more sophisticated ways of improving the input current waveform while simultaneously avoiding phase displacement.

There are several solutions to achieve the Power Factor Correction (PFC). Depending on whether the active switches (controllable by an external control input) are used or not, PFC solutions can be categorised as passive or active, [1], [2], [3], [4]:

- Passive PFC: only passive elements are used in addition to the diode bridge converter, to improve the shape of the line current. Obviously, the output voltage is not controllable.
- Active PFC: active switches are used in conjunction with reactive elements in order to increase the effectiveness of the line current shaping and to obtain controllable output voltage.

The switching frequency further differentiates the active PFC solutions into two classes:

- In low-frequency active PFC, the switching takes place at low-order harmonics of the line-frequency and is synchronised with the line voltage.
- In high-frequency active PFC, the switching frequency is much higher than the line frequency.

The main drawbacks, related to the PFC circuits, are:

- additional losses, thus reducing the overall efficiency;
- the increase of the EMI, due to the high-frequency content of the input current;
- the increased complexity of the circuit, with negative effects on the reliability of the equipment as well as on its size, weight and cost.

The general aim of this study is to investigate the PFC topologies and their control methods, which would annul some of the aforementioned drawbacks.

A general classification of small power single-phase PFC circuits is done in Fig. 9.1, [1], [2], [3].

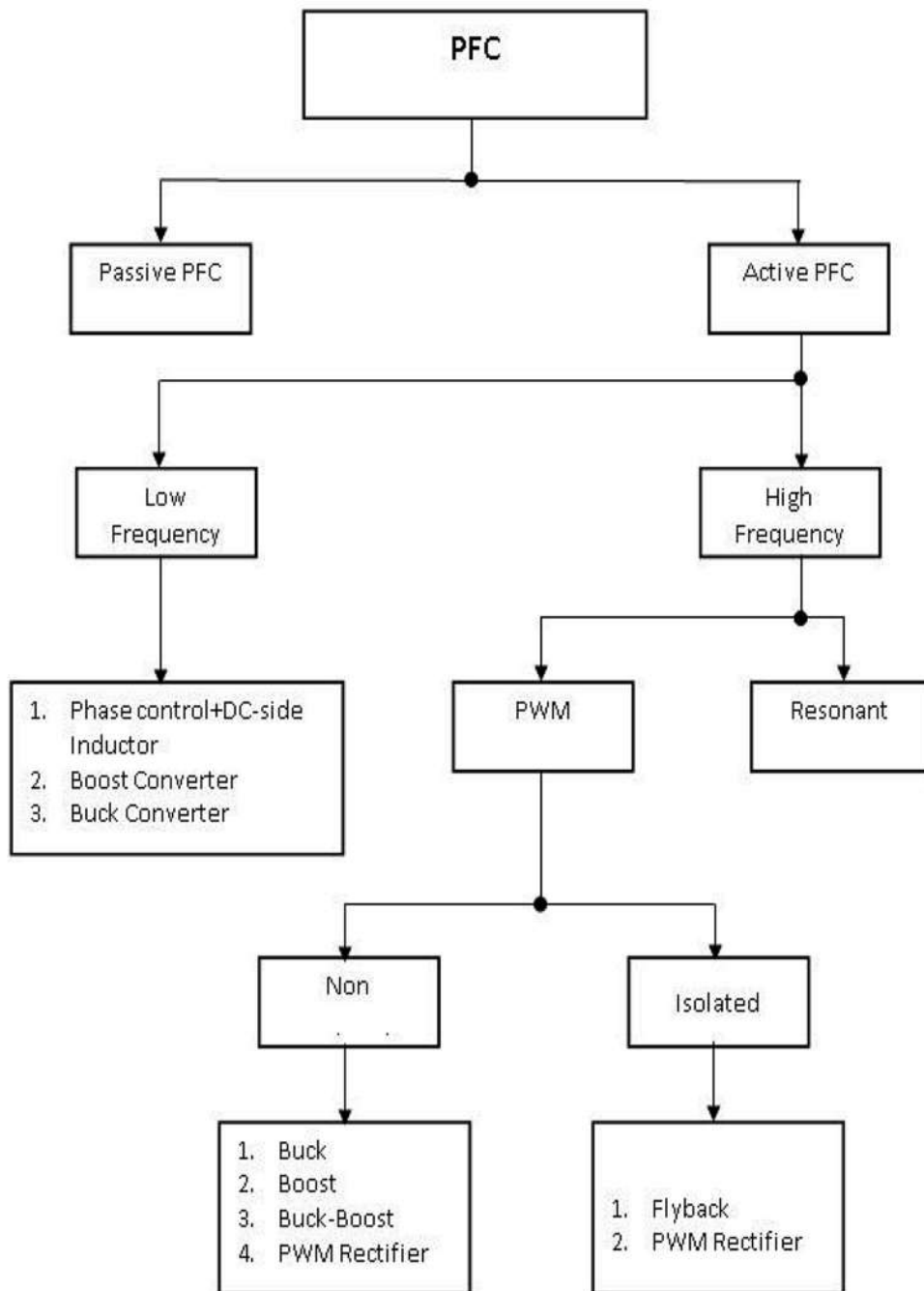


Fig. 9.1 General classification of the PFC circuits.

### 9.3.2 Passive PFC circuits

The passive PFC converters use additional passive components to the diode bridge converter topology. The schematic diagrams and their corresponding line voltages and currents are presented in Fig. 9.2- Fig. 9.9, [1]-[4]. An overall presentation of the passive PFC converters is given in Table 9.1, [1].

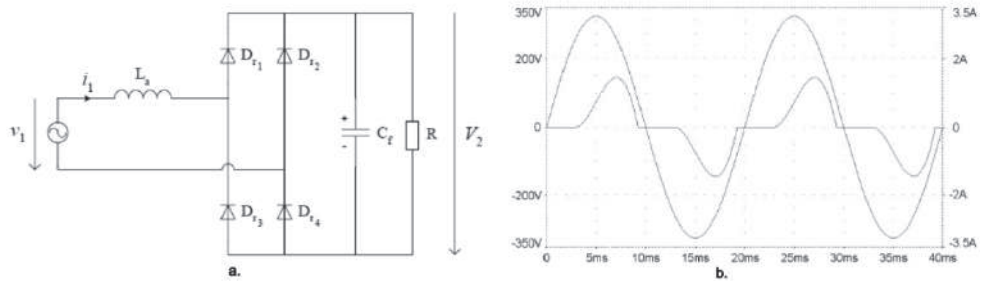


Fig. 9.2 Converter with AC-side inductor: a) schematic; b) line voltage and line current.

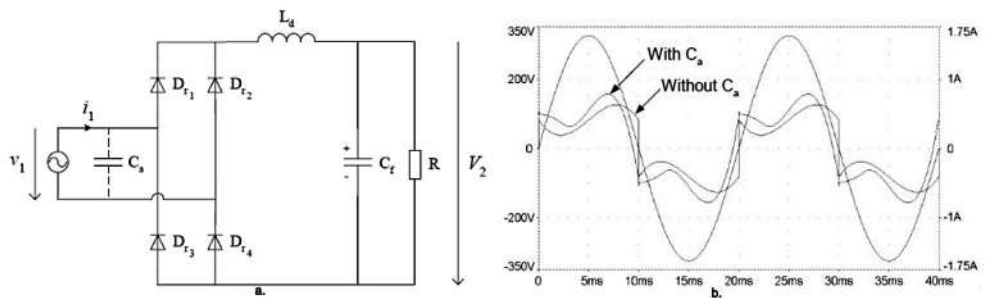


Fig. 9.3 Converter with DC-side inductor: a) schematic; b) line voltage and line current.

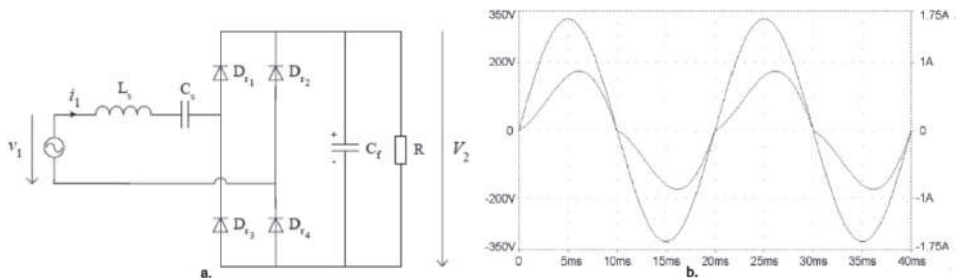


Fig. 9.4 Converter with series-resonant band-pass filter: a) schematic; b) line voltage and line current.



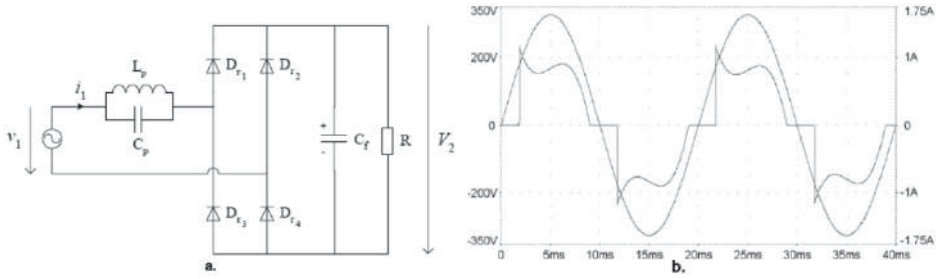


Fig. 9.5 Converter with parallel-resonant band-pass filter: a) schematic; b) line voltage and line current.

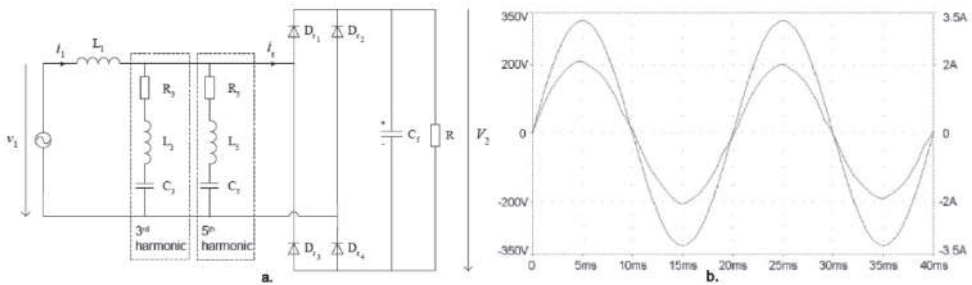


Fig. 9.6 Converter with harmonic trap filter: a) schematic; b) line voltage and line current.

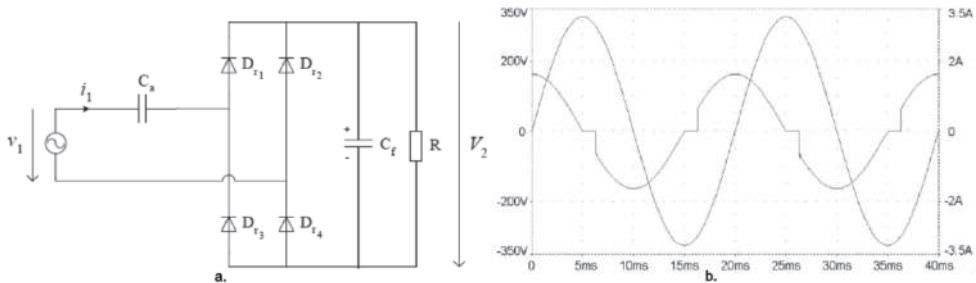


Fig. 9.7 Capacitor-fed converter: a) schematic; b) line voltage and line current.

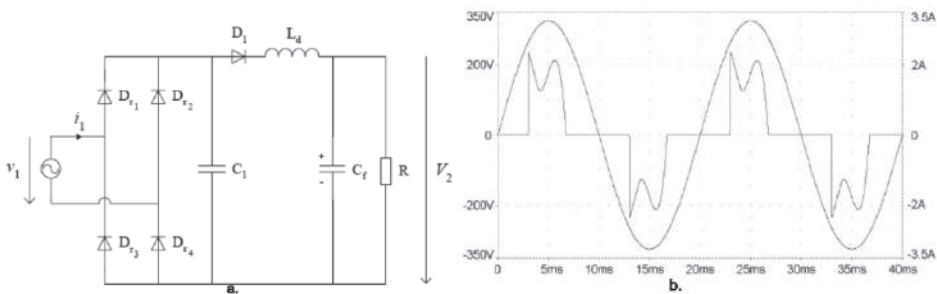


Fig. 9.8 Converter with additional inductor, capacitor and diode (LCD) a) schematic; b) line voltage and line current.

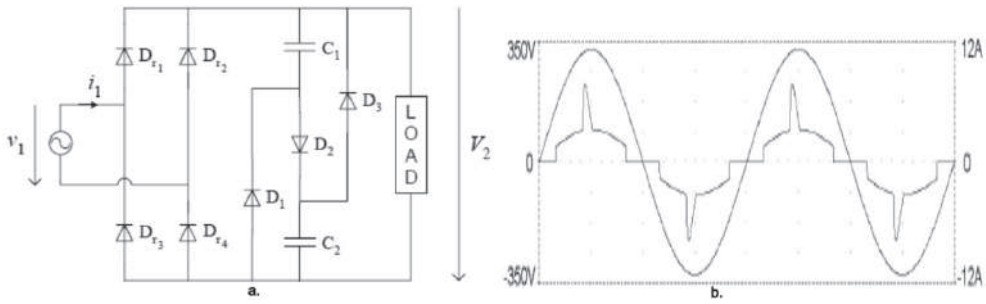


Fig. 9.9. Valley-fill converter: a) schematic; b) line voltage and line current.

Table 9.1. Overall presentation of the passive PFC methods

Crt. No.	Method	Advantages	Drawbacks	Comment
1	AC-side series inductor ( $L_a$ ), Fig. 9.2		$PF_{max}=0,76$	
2	DC-side series inductor ( $L_d$ ), Fig. 9.3	$PF_{max}=0,9$	$L_d$ – very large	
3	DC-side series inductor ( $L_d$ ) + AC-side parallel compensating capacitor ( $C_a$ ), Fig. 9.3		$L_d$ , and $C_a$ , are large, for 50Hz	
4	Series resonant band-pass filter AC-side ( $L_s, C_s$ ), Fig. 9.4		sensitive at the line frequency	tuned at the line frequency
5	Parallel-resonant band-stop filter ( $L_p, C_p$ ), Fig. 9.5	$\{L_s, C_s\} < \{L_p, C_p\}$	sensitive at the line frequency	tuned at 3 <sup>rd</sup> harmonic
6	Harmonic trap filter, Fig. 9.6	very good line current improvement	circuit complexity; expensive	tuned at a harmonic that must be attenuated

Crt. No.	Method	Advantages	Drawbacks	Comment
7	AC-side series capacitor ( $C_a$ ), Fig. 9.7	very simple circuit; line harmonic current reduction	PF – very low; $P_{max}=250\text{ W}$	
8	LCD Converter (converter with additional LCD), Fig. 9.8	relatively low values of reactive components	$PF_{max}=0.79$ ; limited reduction of current harmonics	
9	Valley-fill Converter, Fig. 9.9	$PF=0.92$ ; reduction of current harmonic content	large variations in DC output voltage; circuit complexity	

Table 9.2. The advantages and disadvantages of passive PFC circuits

Advantages	Disadvantages
<ul style="list-style-type: none"> <li>- simplicity;</li> <li>- reliability;</li> <li>- ruggedness;</li> <li>- insensitive to noises and surges;</li> <li>- no generation of HF-EMI;</li> <li>- no HF switching losses</li> </ul>	<ul style="list-style-type: none"> <li>- reactive components are heavy and bulky due to line frequency operation;</li> <li>- poor dynamic response;</li> <li>- lack voltage regulation;</li> <li>- the shape of the input current depends on the load;</li> <li>- even if the line current harmonics are reduced, the fundamental component may show an excessive phase shift that reduces the power factor;</li> <li>- possibility of parallel-resonance at different frequencies, which can amplify other harmonics</li> </ul>

### 9.3.3 Active PFC converters

An active PFC converter represents a power electronic circuit controlling the amount of power drawn by a load in order to obtain a power factor as close as possible to the unity. In most applications, the active PFC converter controls the input current of the load so that the current waveform is proportional to the mains voltage waveform (a sine wave, in general). Active switches are used together with the reactive elements in order to increase the effectiveness of the line current shaping and also to obtain controllable output voltage.

The switching frequency further differentiates the active PFC converters into two classes:

- the low frequency active PFC converters – the switching takes place at low-order harmonics of the line-frequency and is synchronised with the line voltage.
- the high frequency active PFC converters: - the switching frequency is much higher than the line frequency.

The preferable type of PFC is the active PFC since it provides a theoretical power factor of over 95 %, up to 99 %. The Active Power Factor Correction also diminishes the total harmonics distortion (THD), automatically corrects the AC input voltage and is capable of a full range of input voltage.

### 9.3.4 Low-frequency active PFC circuits

An active low frequency PFC can be implemented up to about 1.0 kW [1].

Three representative solutions are reported and presented in Fig. 9.10- Fig. 9.12 [1], [2], [3], [10]. The phase-controlled converter is shown in Fig. 9.10. It is derived from the converter with a DC side inductor, where diodes are replaced with thyristors. This solution offers controllable output voltage, is simple, reliable, and uses low-cost thyristors. On the negative side, the output voltage regulation is slow and a relatively large inductance  $L_d$  is still required.

Even if the second-order switching converter is mainly used at high switching frequencies, it is also possible to use it at low switching frequencies, too. The second low-frequency switching solution, namely the Conventional PFC Boost Converter is shown in Fig. 9.11. The active switch  $S$  is turned ON for the duration  $T_{ON}$ , as illustrated in Fig. 9.11, so as to enlarge the conduction interval of the converter diodes. It is also possible to have multiple switchings per half line-cycle, at low switching frequency, in order to improve the shape of the line current. Nevertheless, the line current has a considerable ripple. The third low-frequency switching solution, i.e. the Buck Converter, is shown in Fig. 9.12. Theoretically, the inductor current is constant for a near-infinite inductance  $L_d$ . The switch is turned ON for the duration  $T_{ON}$  and the ON-time intervals are symmetrical with respect to the zero-crossings of the line voltage. The line current is square with adjustable duty-cycle. For a 35 lower harmonic content of the line current, multiple switchings per line-cycle can be used. However, the required inductance  $L_d$  is large and impractical.

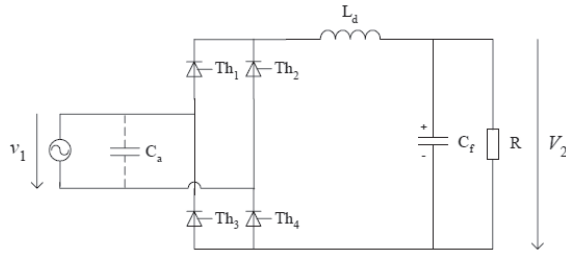


Fig. 9.10 Controlled converter with DC-side inductor.

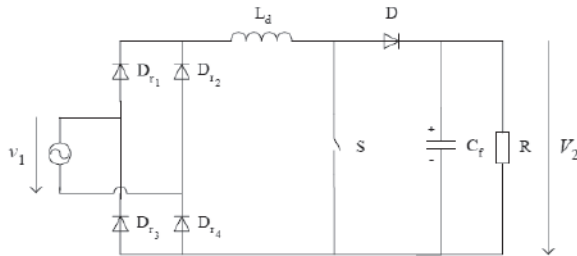


Fig. 9.11 Conventional PFC Boost Converter.

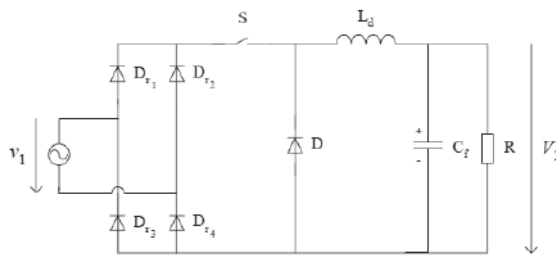


Fig. 9.12 Buck Converter.

In conclusion, the low-frequency switching PFC offers the possibility to control the output voltage in certain limits. In such circuits, switching losses and high-frequency EMI are negligible. However, the reactive elements are large and the regulation of the output voltage is slow [1], [2], [3], [9], [10], [11].

### 9.3.5 High-Frequency Active Buck-Boost PFC Converters

In the next step, a review of the high-performance, state-of-the-art, active power-factor-correction (PFC) techniques for high-power, single-phase applications is presented. At higher power levels, the continuous-current-mode (CCM) Boost Converter is the preferred topology for implementing a front end with power-factor correction (PFC).

As a result, in recent years, significant efforts have been made to improve the performance of high-power Boost converters. The majority of these development efforts have been focused on reducing the adverse effects of the reverse-recovery characteristic

of the Boost Converter on the conversion efficiency and electromagnetic compatibility (EMC). Generally, the reduction of the reverse-recovery-related losses and EMC problems requires that the Boost converter should be “softly” switched off by controlling the turn-off rate of its current.

So far, a number of soft-switched Boost converters and their variations have been proposed. All of them use additional components to form a passive snubber or an active snubber circuit that controls the turn-off  $di/dt$  rate of the Boost converter. Generally, the passive snubber approaches use only passive components such as resistors, capacitors, inductors and converters, whereas active snubber approaches also employ active switch(es). The main feature of the active approaches is that they either offer zero-voltage switching (ZVS) or zero-current switching (ZCS) of the Boost switch besides the soft switching of the Boost Converter.

The nearly unity power factor can be obtained with the “high-frequency switching active PFC” if a suitable control method is used to shape its input current or if it has inherent PFC properties.

The converters can operate in Continuous Current Mode – CCM, where the inductor current never reaches zero during one switching cycle or Discontinuous Current Mode - DCM, where the inductor current is zero during intervals of the switching cycle.

The basic types of DC-DC converters, when operating in discontinuous current mode DCM, have self power factor correction (PFC) property, i.e., if these converters are connected to the rectified AC line, they have the capability to give a higher power factor by the nature of their topologies. The input current feedback is unnecessary when these converters are employed to improve the power factor. In this chapter, the basic types of DC-DC converter topologies are studied to investigate their self-PFC capabilities [1].

The Conventional PFC Boost Converter has an imperfect “inherent” PFC property. Its input resistance changes throughout the line-cycle, but the variation decreases and the inherent PFC property improves when the ratio  $V_2/V_1$  is increased. Taking into account the fact that the line current does not have crossover distortions, the compliance with the standard is achieved comfortably. Because of the above reasons, the Conventional PFC Boost Converter is comparably superior to most of the other converters when applied to do the PFC [1], [2]. However, it should be noted that the Conventional PFC Boost Converter can operate properly only when the output voltage is higher than its input voltage. When low voltage output is needed, a step-down DC-DC converter must be cascaded.

There are many reasons why the Conventional PFC Boost Converter has become the topology of choice for a PFC front-end in many applications. Its many advantages include the following [12], [13]:

- It achieves very low THD, offering probably the best possible  $PF$ ;
- High output voltage—volumetrically efficient energy-storage capacitors, good hold-up;

- The low-side boost switch allows easy gate drive and switch current sense;
- The direct forward path from the AC input to bulk storage capacitor eases the lightning surge management;

The Conventional PFC Boost Converter also has some limitations and drawbacks, some of which are simply the corollary of its advantages:

- The output voltage must always be higher than the instantaneous AC input voltage—for the universal or high-line AC input (up to 264 V<sub>ac</sub>), the bus voltage must be set at about 400 V<sub>dc</sub>.
- It requires a subsequent high-voltage primary regulation/isolation stage to step down to practical voltage levels required by most electronic loads.
- The high bus voltage causes a higher level of common mode (CM) EMC noise;
- No inrush limitation at start-up (this is the flipside of the surge advantage listed earlier), so a potentially dissipative or costly inrush limiting mechanism is required.
- A considerable drop in efficiency at low line because of the high voltage differential between the AC input voltage and the bus voltage and the consequent effect on the PFC choke design.

The Buck-Boost Converter, shown in Fig. 9.13, can operate either as a step-down or as a step-up converter. This means that the output voltage  $V_2$  can be higher or lower than the amplitude  $V_1$  of the input voltage, which gives freedom in specifying the output voltage. The operation is possible throughout the line-cycle and a sinusoidal line current can be obtained. However, the output voltage is inverted, which translates into a higher voltage stress for the switch. Moreover, similarly to the Buck Converter, the input current is discontinuous with significant high-frequency content, as illustrated in Fig. 9.13 [2].

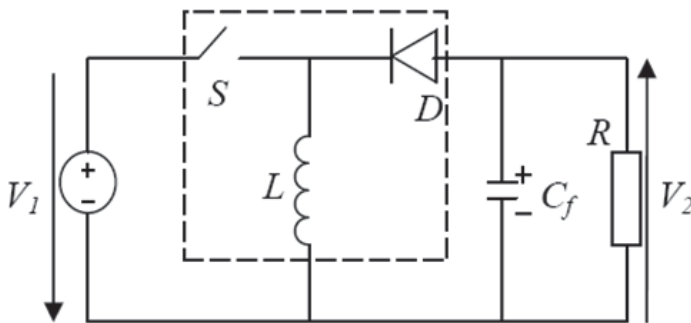


Fig. 9.13 The scheme of the high-frequency switching Buck-Boost Converter.

Because the output voltage of the the Buck-Boost Converter can be either larger or smaller than the input voltage, it demonstrates strong availability for the DCM input technique to achieve power factor correction. Therefore, theoretically, the Buck-Boost Converter is a perfect candidate. Unfortunately, this topology has two limitations:

- The polarity of its output voltage is reversed, i.e., the input voltage and the output voltage do not have a common ground; and
- It needs a floating drive for the power switch. The first limitation circumscribes this circuit into a very narrow scope of applications. As a result, the Buck-Boost Converter is not widely used.

The main advantage of using switching converters operating in DCM for PFC applications is the simplicity of the control method. Since there is no need to continuously adjust the duty-cycle  $d$  to perform the PFC, only a voltage loop is needed to regulate the voltage across the storage capacitor. The bandwidth of the voltage loop has to be low (e.g. 10-15Hz), in order to filter out the output voltage ripple at twice the line-frequency.

The simple control of converters with inherent PFC makes them attractive for low-cost applications. But the main disadvantage of using switching converters operating in DCM for a PFC application is that the input current is normally a train of triangle pulse with a nearly constant duty ratio. As a result, the high-frequency EMI is very high. In this case, an input filter is necessary for smoothing the pulsating input current into a continuous one.

The high-power quality achievement is increasingly required for the power supply systems in order to comply with the international standards such as, IEC 61000-3-2 or EN 61000-3-2. For this purpose, and especially for the single-phase low power applications, the Power Factor Correction (PFC) circuits are designed in order to ensure a high-power factor at the mains side and to emulate a purely resistive operation of the diode bridge-based front-end converter. Among the conventionally used PFC converters, we can find the Boost and the Boost-Buck topologies.

The basic Boost-type topology is shown in Fig. 9.14.a. It presents a smoothly varying input current (due to the presence of a filtering inductor at the input port), but a relatively high DC-bus voltage (at least the peak value of the source voltage) that may cause high voltage stresses on the devices. In addition, the front-end diode bridge operates in continuous current mode at the mains frequency (50 or 60 Hz) and, therefore, the presence of a high-frequency filter at the AC-side is not necessary anymore. In order to avoid the control detuning problem that occurs at zero crossings of the source voltage, the asymmetric half-bridge Boost PFC is presented in Fig. 9.14.b.

The Boost-Buck PFCs can provide non-pulsating currents at the input and output stages, with a reduced level of the output voltage, which make them highly suitable for such applications. Several single-stage topologies of Boost-Buck combinations have been introduced in the literature. In the two-stage topology depicted in Fig. 9.14.c, which consists of a series connection of Buck and Boost converters, a smooth input current is obtained at the expense of a twice number of switches.

More convenient and efficient solutions that ensure a smooth input current by using a single switch are the cascaded Boost-Buck Converter Fig. 9.14.d, the Cùk Converter Fig 9.14.e and the Single Ended Primary Inductance Converter (SEPIC) Fig. 9.14.f. The Cùk and SEPIC



topologies have similar characteristics in the PFC applications and suffer both from the control detuning phenomenon that appears at very low values of the input voltage (which would correspond to the zero-crossings of the AC source voltage); they differ, however, from each other at the output stage, where the free-wheel diode and the output inductor are permuted, and the polarity of the output voltage is inverted (which, in practice, may cause some problems if the output stage is not isolated from the input one).

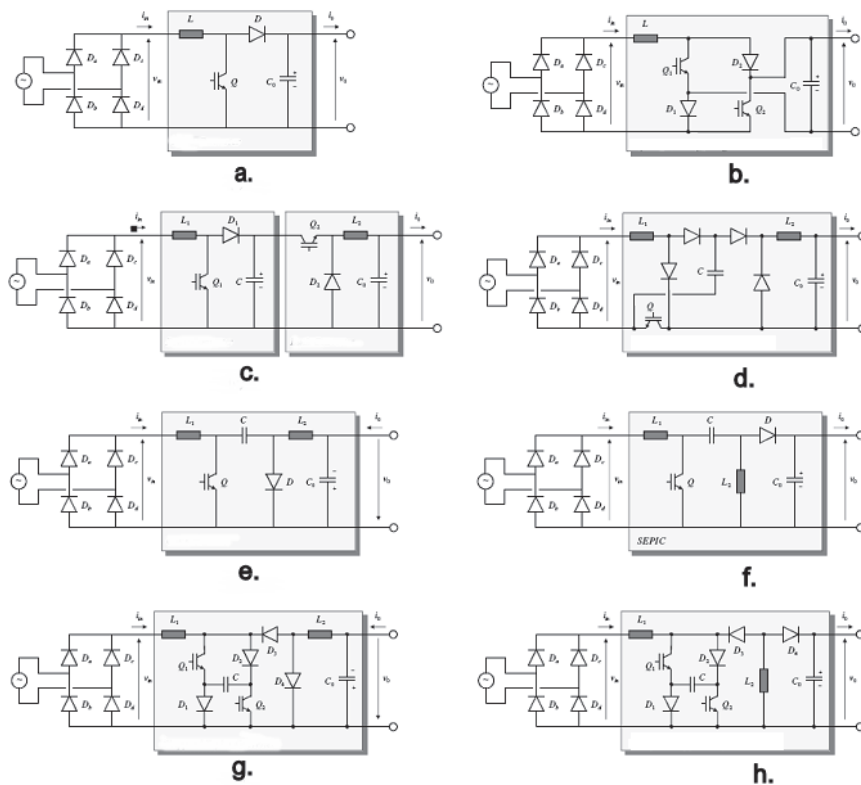


Fig. 9.14 PFC topologies: a) Basic Conventional PFC Boost Converter, b) asymmetric half-bridge Boost Converter, c) two-stage Boost-Buck Converter, d) cascaded Boost-Buck Converter, e) Cuk Converter, f) SEPIC, g) conventional Sheppard-Taylor Converter, and h) modified Sheppard-Taylor Converter [14], [15], [16].

The detuning problem in these latter PFCs is avoided by the use of the Sheppard-Taylor topology presented in Fig. 9.14.g, where the single active switch is replaced by two synchronised ones. However, the reversed polarity feature between the input stage and the output stage still exists (as in the Cuk topology).

In order to avoid this latter problem, a modified Sheppard-Taylor converter that uses the SEPIC output stage, as depicted in Fig. 9.14.h, is proposed, where two technical benefits of this newly developed topology over the former one were highlighted: first, for a same operating point, the voltage stress across the intermediate capacitor is lower and, second,

for a same operating zone, the output voltage can reach higher values and, thus, lies within a larger range loped and presented [14], [15], [16].

The advantages of the high frequency PFC circuit are as follows:

- This circuit has only two on-switches; at any instant, losses can be reduced. And it is appropriate for medium and high-power applications;
- Since switches  $S_1$  and  $S_2$  are referenced to the same ground, the gate driving circuit is very simple and the isolation is not needed.
- The location of the BOOST inductor L on the AC side contributes to the reduction in the EMI interface.

### 9.3.6 The Bridgeless PFC

#### 9.3.6.1 The Bridgeless PFC Boost Converter Topology

As mentioned before, the conventional Boost topology is the most efficient for PFC applications. It uses a dedicated diode bridge to rectify the AC input voltage to DC, which is then followed by the Boost section.

This approach is good for a low to medium power range. As the power level increases, the diode bridge becomes an important part of the application and it is necessary for the designer to deal with the problem of how to dissipate the heat in a limited surface area. The dissipated power is important from an efficiency point of view.

The Bridgeless configuration topology avoids the need for the converter input bridge, yet maintains the classic Boost topology. This is easily done by making use of the intrinsic body diode connected between the drain and the source of power MOSFET switches. A simplified schematic of the Bridgeless PFC Boost Converter configuration is shown in Fig. 9.15 [17].

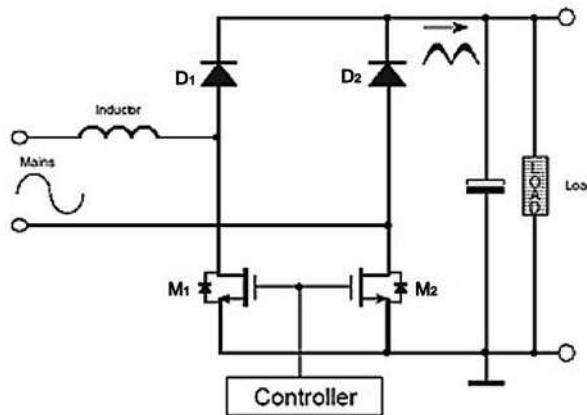


Fig. 9.15 A simplified schematic of a Bridgeless configuration [17].

In the traditional PFC topology, the current flows through two of the bridge diodes in series. In the Bridgeless PFC Boost Converter configuration, the current flows through only one diode with the power MOSFET providing the return path. To analyse the circuit operation, it is necessary to separate it into two sections. The first section operates as the Boost stage and the second section operates as the return path for the AC input signal.

Compared to a conventional Boost PFC topology, the losses due to the bridge Converter are eliminated, but the body diode conduction of the inactive MOSFET is conveyed to the coil current. Overall, there is only one diode conduction loss for a Bridgeless PFC Boost Converter compared to the conduction loss from two diodes in a conventional Boost PFC, which can improve the efficiency to eliminate the voltage drop of one diode in the line-current path, Fig. 9.16, [18].

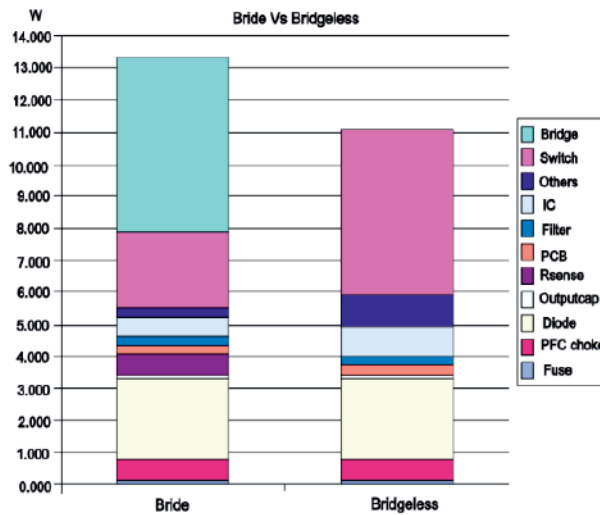


Fig. 9.16 Power Loss Comparison Between Conventional PFC and Bridgeless PFC Boost Converter, [19].

Despite many advantages of a Bridgeless PFC Boost Converter, there are some obstacles that need to be overcome [19]:

- Because the line is floating compared to the PFC stage ground, simple circuitry is not able of sensing the input voltage. Normally a low-frequency transformer or optical coupler is used to perform the input voltage sensing.
- For the conventional PFC, the current sensing is easy to monitor by simply inserting a shunt sensing resistor at the return path of the inductor current. However, for a Bridgeless PFC Boost Converter, the current path does not share the same ground at each half-line cycle. A sensing-power MOSFET and diode current are needed, which make the Bridgeless PFC Boost Converter's current sensing complicated and difficult to monitor.

- The EMI noise is another issue. For a Bridgeless PFC Boost Converter, the output voltage ground is always floating relative to the AC line input. Thus, all the parasitic capacitance including the MOSFET drain to earth and the output terminals to the earth ground contribute to the common mode (CM) noise. This large  $dv/dt$  at each phase's switching node leads to an increased common mode noise that is difficult to filter, Fig. 9.17, [6], [7], [8].

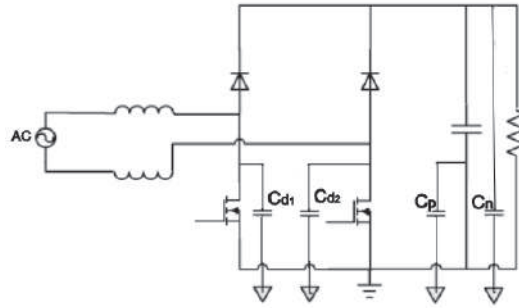


Fig. 9.17 Parasitic capacitances that contribute to common mode noise [20].

### 9.3.6.2 EMI and CM Noise Reduction

To solve the EMI noise issue, a new EMI noise reduction circuit for the Bridgeless PFC circuit is introduced. The circuit schematic is shown in Fig. 9.18. Comparing with the original Bridgeless PFC Boost Converter circuit, the circuit adds two capacitors in the circuit to create a high frequency path between the output voltage to the input AC line.

In [21], two approaches to minimise the CM noise in Bridgeless PFC Boost converters are proposed and compared. One approach is to modify the topology to achieve total symmetry.

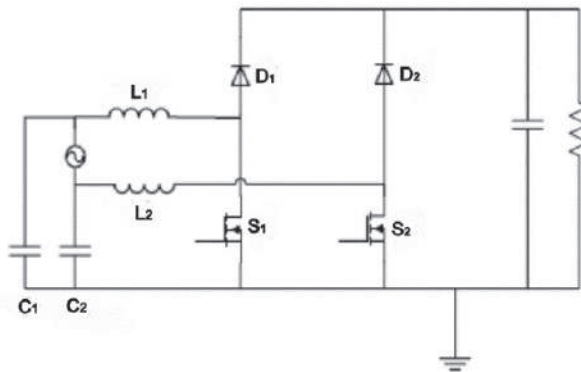


Fig. 9.18. An improved EMI performance Bridgeless PFC Boost Converter's circuit [20]

The CM noise model is derived to model the symmetric topology and important parasitic that affect topological symmetry are studied. By achieving symmetry in topology, the CM noise can be minimised.

The other approach is to implement the balance technique in the Bridgeless PFC Boost Converter. In order to apply the balance technique, a modification in topology is needed to reduce the CM noise for the whole line cycle. Experiments are done to validate the two approaches and it is shown that both can effectively reduce the CM noise to a very low level.

To implement the balance technique in the Bridgeless PFC Boost Converter to minimise the CM noise, the balance condition should be satisfied in both half-line cycles. A small inductor and two diodes are introduced to help balancing both half-line cycles, as shown in Fig. 9.19. In the positive half-line cycle,  $L_a$  is in parallel with  $L_2$ , while in the negative half-line cycle  $L_a$  is in parallel with  $L_1$  [21].

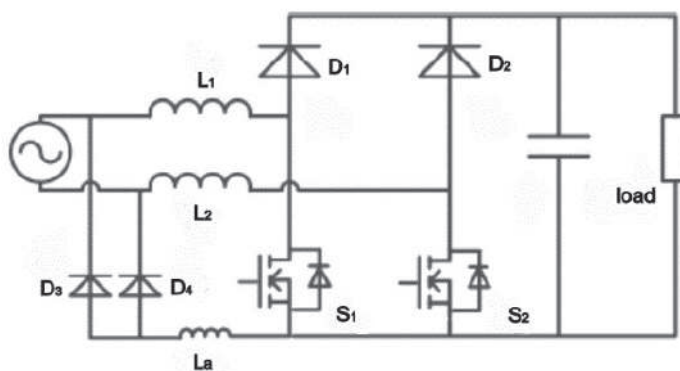


Fig. 9.19 Bridgeless PFC Boost Converter using the balance technique [21].

### 9.3.6.3 Soft Switching Techniques

The Bridgeless PFC Boost Converter can reduce the conduction loss, but it has no contribution to reduce switching losses. In order to reduce switching losses and device stress, restrict  $dv/dt$  and  $di/dt$  during switching turn-ON and turn-OFF, several soft switching circuits have been proposed in a Bridgeless PFC Boost Converter. There are two main methods to implement soft switching: the active mode and the passive mode. The active mode realises the soft switching by adding an auxiliary switch and a corresponding control circuit. The passive mode uses the resonance of the inductor and a capacitor to decrease an overlap area of switch voltage and current and realise the soft switching. The passive lossless snubber circuit is one type of passive soft switching method. The inductor and the capacitor have no energy consumption; therefore, the passive soft switching is a good method to realise a high efficiency in the Bridgeless PFC Boost Converter [17], [22], [23].

There are many soft switching Bridgeless PFC Boost converters reported. These PFC converters use an extra switch to prepare the soft switching condition for the main switches. Therefore, the complexity of the control circuit and switching losses are increased, [24], [25], [26].

### 9.3.6.4 Advanced Types

#### 9.3.6.4.1 The SiC Technology

The recent advancements in the development of the silicon carbide (SiC) technology that have made SiC converters commercially available are completely redefining the Boost-Converter design optimisation priorities. Since SiC converters virtually have no reverse-recovery charge, active snubbers to control the turn-off rate of the converter are unnecessary, which greatly simplifies the circuit design. However, as the switching frequency of the PFC boost circuit with the SiC converter is increased to minimise the size of the Boost choke, some additional circuitry for creating soft switching conditions of the Boost switch may be required, [25].

The Bridgeless PFC Boost Converter implemented with SiC converters and DSP control may become the mainstream PFC technology for the next generation of high-performance front-end converters [27].

Silicon Carbide (SiC) based power devices exhibit superior properties such as very low switching losses, fast switching behaviour, improved reliability and high temperature operation capabilities. These properties contribute toward the ability to increase the switching frequency, to decrease the size of passive components and switches and to reduce the need for cooling, making thus the devices an excellent candidate for the AC/DC power supplies [18].

#### 9.3.6.4.2 The Bridgeless SEPIC

In [19], the new Bridgeless PFC Boost Converter's circuit, based on the SEPIC topology, is introduced. Unlike the Conventional PFC Boost Converter, the SEPIC and Cuk converters offer several advantages in PFC applications, such as the easy implementation of the transformer isolation, the inherent inrush current limitation during startup and overload conditions, the lower input current ripple and the less electromagnetic interference (EMI) associated with the DCM topology.

The proposed Bridgeless SEPIC Converter is shown in Fig. 9.20. The proposed converter utilises a bidirectional switch and two fast diodes. However, the two power switches, namely, S1 and S2, can be driven with the same PWM signal, which significantly simplifies the implementation of the control circuit. Note that during each switching cycle, there is either one or two semiconductors in the flowing current path; hence, the conduction losses as well as the thermal stresses on the semiconductor devices are further reduced and the circuit efficiency is improved compared with that of the Bridgeless PFC Boost Converter. Another advantage of the proposed converter is a reduction in the semiconductor voltage stress as compared with that of the conventional SEPIC PFC Converter. The voltage stress is reduced to a level that is comparable with that of the Conventional PFC Boost Converter. On the other hand, the components' current stresses are comparable with their counterparts in the conventional SEPIC.

The proposed converter structure utilises three inductors, which are often described as a disadvantage. However, the three inductors can be coupled on the same magnetic core, allowing considerable size and cost reduction, and additionally, the “near-zero-ripple-current” condition at the input port of the converter can be achieved without compromising performance.

The measured THD was 2.5% with power conversion efficiency close to 92 %.

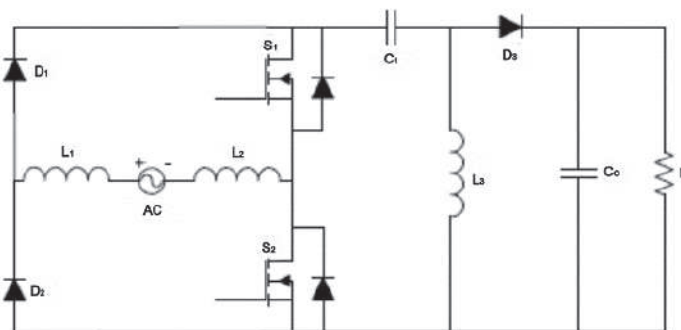


Fig. 9.20 Proposed Bridgeless SEPIC PFC [29].

### 9.3.6.5 Performance Evaluation

The Bridgeless PFC Boost converters, also called the dual-Boost PFC converters, compared to the Conventional PFC Boost converter, generally, improve the efficiency of the front-end PFC stage by eliminating one diode forward-voltage drop in the line-current path. Today, two topologies can be considered as attractive for the practical implementation: Bridgeless PFC Boost Converter with the bidirectional switch [27] and the Semi-Bridgeless PFC (Conventional PFC Boost Converter with two DC/DC boost circuits) [25].

In [28], a systematic review of the Bridgeless PFC Boost Converter implementations that have received the most attention is presented. The performance comparison between the Conventional PFC Boost Converter and a representative member of the Bridgeless PFC Boost Converter family is performed. The loss analysis and the experimental efficiency evaluation for both continuous- conduction mode (CCM) and discontinuous-conduction mode (DCM)/CCM boundary operations are provided, Table 9.3.

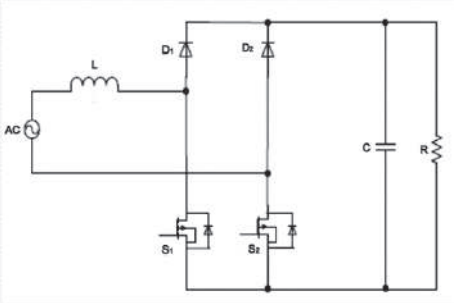
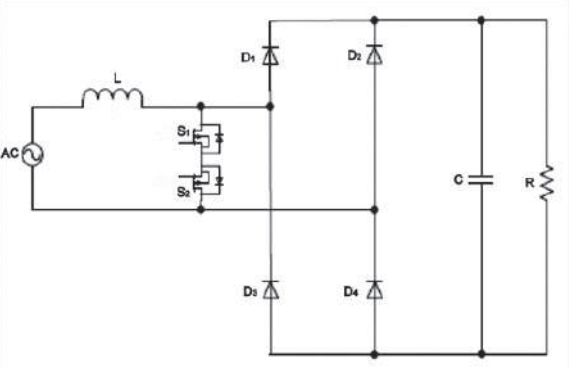
It can be concluded that only two Bridgeless PFC Boost Converter topologies are suitable for the practical implementation: Bridgeless PFC Boost Converter with the bidirectional switch (position 2) and Semi-Bridgeless PFC Converter, with two DC/DC Boost circuits (position 3).

In [25], another systematic review of Bridgeless PFC Boost Converter family is presented; conduction losses and common mode (CM) EMI performances are analysed comparing with the conventional Boost PFC.

Table 9.4 gives the semiconductor numbers in the current flow path of each PFC topology during the line positive AC period. Where, ON/OFF means ON time and OFF time

of MOSFET; DF symbolises fast diode; DL symbolises line frequency diode; M is for MOSFET and DM is the body diode of MOSFET. It shows that the Bridgeless PFC Boost converters respectively have lower semiconductor numbers comparing with the conventional Boost PFC, which will bring benefits on decreasing the conduction losses of the whole systems.

Table 9.3. Comparative evaluation of the Bridgeless PFC Boost Converter configurations [28].

Crt. No.	Denomination	Scheme
1	<p><b>Basic Bridgeless PFC</b></p> <p>The basic Bridgeless PFC Boost Converter is not a practical solution because it has significantly larger common mode noise than Conventional PFC Boost Converter.</p>	
2	<p><b>Bidirectional Switches Boost PFC</b></p> <p>The common-source node of switches is disconnected from the output ground. The diodes <math>D_1</math> and <math>D_3</math> are fast-recovery diodes, whereas diodes <math>D_2</math> and <math>D_4</math> are slow-recovery diodes. During a positive half-line cycle, the AC source is connected to the output ground through slow-recovery diode <math>D_4</math>, and during a negative half-line cycle, the AC source is connected to the positive terminal of the output through slow-recovery diode <math>D_2</math>.</p>	



Crt.  
No.

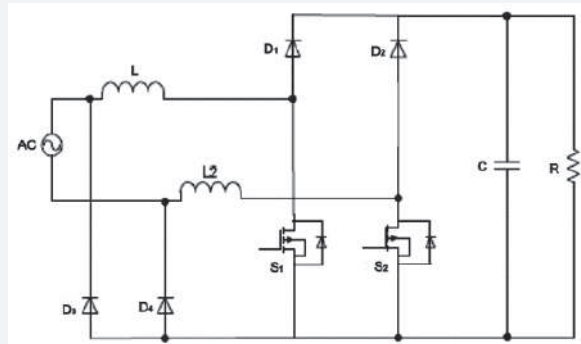
Denomination

Scheme

### Semi-Bridgeless (Two-Boost) circuit PFC

In addition to diodes  $D_3$  and  $D_4$ , which are slow recovery diodes, a second inductor is also added, resulting in two DC/DC Boost circuits, one for each half-line cycle. The drawback of this circuit is that it requires two inductors. It should also be noted that two inductors compared to a single inductor have a better thermal performance.

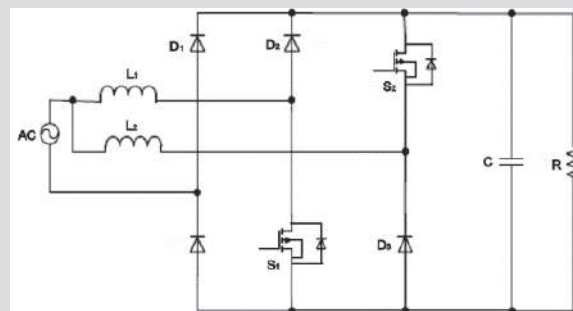
3



### Pseudo Totem-pole PFC

Because of the position of switches, this topology is called pseudo totem-pole Bridgeless PFC Boost Converter. It requires a more complex control and drive circuit and, consequently, it is less attractive for the practical implementation than its counterpart in pos. 3.

4



Crt. No.	Denomination	Scheme
----------	--------------	--------

5	<p><b>Totem-pole PFC</b></p> <p>Is obtained from the basic Bridgeless PFC Boost Converter, by exchanging the position of diode <math>D_1</math> and switch <math>S_2</math>. Because of the position of the two switches, this topology is called the totem-pole Bridgeless PFC Boost Converter.</p> <p>It can only work in DCM and at DCM/CCM boundary, and requires a complex control and drive circuit.</p>	
---	--	--

Fig. 9.21 shows the efficiency columns of six PFC topologies based on simulation results when only the conduction losses are taken into account. The Totem-pole PFC, the Two-Boostcircuit PFC and the Pseudo Totem-pole have better efficiency comparing with other topologies.

Table 9.5 gives the CM EMC and efficiency comparison among conventional Boost PFC and five BLPFCs. From this table, it comes to a conclusion that the Two-Boost-circuit PFC shows higher efficiency and lower EMI performances, which is worth for industrial application and further improvement.

Table 9.4. Semiconductor numbers in current flow path in the six PFC topologies [25]

PFC topology	On/Off	$D_F$	$D_L$	M	$D_M$	Total number
Boost PFC	On	0	2	1	0	3
	Off	1		0		
Dual Boost PFC	On	0	0	1	1	2
	Off	1		0		
Bidirectional Switches PFC	On	0	0	1	1	2
	Off	2		0	0	

Two –Boost– circuit PFC	On	0	1	1	0	2
	Off	1		0		
Pseudo Totem - pole PFC	On	0	1	1	0	2
	Off	1		0		
Totem – pole	On	0	1	1	0	2
	Off			0	1	

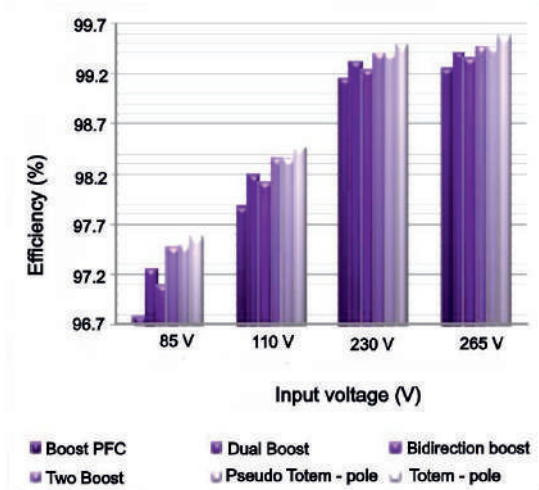


Fig. 9.21 Efficiency comparison only for conduction losses among six PFC topologies based on simulation, [25].

Table 9.5. EMC and efficiency comparison among six PFC [25]

PFC topology	Efficiency Rank	CM Voltage Rank	CM Current Rank
Boost PFC	6	1	1
Dual Boost PFC	4	5	5
Bidirectional Switches PFC	5	5	5
Two – Boost – circuit PFC	2	1	1
Pseudo Totem – circuit PFC		3	3
Totem – pole	1	3	3

### 9.3.7 Interleaved active PFC circuits

In higher power applications, to fully utilise the line, the power factor correction (PFC) is a necessity. Passive solutions were developed first, which required bulky inductors and capacitors. To reduce the volume of these bulky solutions, an active PFC using a Boost topology was developed. The active solutions had higher power densities than the passive solutions.

Interleaving PFC solutions is the next step in increasing PFC converter power densities, reducing the overall volume of the design. Interleaving will reduce the magnetic volume and has the added benefit of reducing the RMS current in the Boost capacitor.

The interleaved Boost PFC Converter has many advantages in increasing the power density, reducing the input current ripple and the RMS current of the Boost capacitor, reducing the filter volume and cutting down the cost of materials.

The single-phase two-channel interleaved PFC control system in [27] uses a PWM module set in the independent output mode, permitting the generation of two 180° phase-shifted PWM signals in center-aligned configuration for all power switches of the power stage.

The inductor ripple current cancellation allows the designer to reduce the Boost inductor magnetic volume. This is due to the energy storage requirement of the two interleaved inductors being half that of the single stage pre-regulator designed for the same power level, switching frequency and inductance. The reduction in the energy storage does not directly translate into magnetic volume reduction. A designer could expect to see up to a 25 % reduction in the magnetic volume going from a single-phase PFC pre-regulator to a dual phase interleaved PFC. Interleaving PFC pre-regulators, if done in this fashion, will not increase the size of the EMI filter. A common design practice is to select the switching frequency of the power converter below the EMI lower limit of 150 kHz. The second harmonic of the switching frequency would be twice the fundamental and will most likely be in the EMI band and would need to be filtered to meet the specifications. Interleaving two pre-regulators will cause the input to see a switching frequency that is twice the switching frequency of a single phase. This means that the fundamental switching frequency of the converter will most likely be pushed into the EMI band and will be at the second harmonic of an individual stage's switching frequency. However, the input ripple current at this frequency will be reduced by a factor of two. This should not put any additional constraints on the EMI filter. The designer also has the option of running the interleaved pre-regulator at a lower switching frequency and increase the Boost inductance slightly to reduce the input ripple current. If this is done correctly, the designer could decrease the size of the EMI filter without increasing the size of the Boost inductor volume compared to a single stage pre-regulator approach. The designer may be able to reduce both the EMI filter as well as the Boost inductor if the converter's switching frequency is not reduced too much. This reduction in the RMS current will reduce the electrical stress in the output capacitor and improve the converter's reliability.

Compared to a single-phase converter, a three-phase system would reduce the size of the EMI filter. This is because the inductor ripple current in a universal design is at its maximum at the peak of the low line, which has a duty cycle of around 69 %. At this point, the input ripple current would be 10 % of the inductor ripple current. The reduction in the input ripple current should result in a reduction of the size of the EMI filter. The four-phase system has almost no ripple current when the converter is operating at 25 %, 50 %, 75 % of the duty cycle.

Each individually added phase will continue to reduce the RMS current in the Boost capacitor. However, the amount of the reduction decreases with each additional phase.

Interleaving and paralleling power converters can increase the efficiency of the power converter as long as the inductor ripple currents are kept within reason. The semiconductor switching losses will remain roughly the same. The losses should be reduced with each additional phase. However, if the inductor currents have excessive inductor ripple, the higher RMS currents will cause greater conduction losses driving down efficiency. Also, at lower power levels, where the switching losses dominate, the interleaving will not show a drastic improvement in efficiency.

Table 9.6 summarises the advantages and disadvantages of the four topologies: Conventional PFC Boost Converter, Bridgeless PFC Boost Converter, Interleaved PFC boost converter and Bridgeless Interleaved PFC Boost Converter (BLIL).

Table 9.7 provides a summary of the component current stresses for the Conventional PFC Boost Converter and the Bridgeless PFC Boost Converter.

Table 9.8 provides a summary of the component current stresses for the Boost interleaved Converter and the Bridgeless Interleaved Boost Converter.

Table 9.6. Comparison of the four AC–DC PFC converter topologies: Conventional PFC Boost Converter, Bridgeless PFC Boost Converter, Interleaved PFC Boost Converter and Bridgeless Interleaved PFC Boost Converter.

Topology Power Rating	Conventional PFC Boost Converter < 1000 W	Bridgeless PFC Boost Converter < 2000 W	Interleaved PFC Boost Converter < 3000 W	Bridgeless Interleaved PFC Boost Converter >3000 W
EMI / Noise	Fair	Poor	<b>Best</b>	Fair
Capacitor Ripple	High	High	<b>Low</b>	<b>Low</b>
Input Main Ripple	High	High	<b>Low</b>	<b>Low</b>

Magnetic Size	Large	Medium	<b>Small</b>	<b>Small</b>
Efficiency	Poor	Fair	Fair	<b>Best</b>
Cost	<b>Low</b>	Medium	Medium	High

Table 9.7. Comparison between Conventional PFC Boost Converter and Bridgeless PFC Boost Converter

Topology	Conventional PFC Boost Converter	Bridgeless PFC Boost Converter
Inductor RMS Current	$\sqrt{\frac{97 P_{in}}{48 V_{PK}}}$	$\sqrt{\frac{97 P_{in}}{48 V_{PK}}}$
Input Bridge Diode Average Current	$\frac{2 P_{in}}{\pi V_{PK}}$	Not Applicable
Fast Diode Average Current	$\frac{P_{in}}{V_o}$	$\frac{1 P_{in}}{2 V_o}$
MOSFET RMS Current	$\frac{P_{in}}{\sqrt{6} V_{PK} V_o} \sqrt{\frac{3\pi(3V_{PK}^2 + 4V_o^2) - 64V_{PK}V_o}{\pi}}$	$\frac{P_{in}}{\sqrt{6} V_{PK} V_o} \sqrt{\frac{3\pi(3V_{PK}^2 + 4V_o^2) - 64V_{PK}V_o}{\pi}}$
MOSFET Intrinsic Body Diode Average Current	Not Applicable	$\frac{1 P_{in}}{2 V_o}$
Output Capacitor RMS Ripple Current (Low Frequency)	$\frac{\sqrt{2} P_o}{2 V_o}$	$\frac{\sqrt{2} P_o}{2 V_o}$
Output Capacitor RMS Ripple Current	$\frac{\sqrt{2}}{2V_o} \sqrt{3P_{in}^2 - 2P_o^2}$	$\frac{\sqrt{2}}{2V_o} \sqrt{3P_{in}^2 - 2P_o^2}$

Topology	Conventional PFC Boost Converter	Bridgeless PFC Boost Converter
(High Frequency)		

Table 9.8. Comparison between Interleaved PFC Boost Converter and the Bridgeless Interleaved PFC Boost Converter

Topology	Interleaved PFC Boost Converter	Bridgeless Interleaved PFC Boost Converter
Inductor RMS Current	$\frac{5 P_{in}}{4\sqrt{3} V_{PK}}$	$\frac{5 P_{in}}{4\sqrt{3} V_{PK}}$
Input Bridge Diode Average Current	$\frac{2 P_{in}}{\pi V_{PK}}$	Not Applicable
Fast Diode Average Current	$\frac{P_{in}}{2 V_o}$	$\frac{1 P_{in}}{4 V_o}$
MOSFET RMS Current	$\frac{P_{in}}{2\sqrt{6}V_{PK}V_o} \sqrt{\frac{3\pi(3V_{PK}^2 + 4V_o^2) - 64V_{PK}V_o}{\pi}}$	$\frac{P_{in}}{2\sqrt{6}V_{PK}V_o} \sqrt{\frac{3\pi(3V_{PK}^2 + 4V_o^2) - 64V_{PK}V_o}{\pi}}$
MOSFET Intrinsic Body Diode Average Current	Not Applicable	$\frac{1 P_{in}}{4 V_o}$
Output Capacitor RMS Ripple Current (Low Frequency)	$\frac{\sqrt{2} P_o}{2 V_o}$	$\frac{\sqrt{2} P_o}{2 V_o}$
Output Capacitor RMS Ripple Current (High Frequency)	$\frac{P_{in}}{V_o} \sqrt{\frac{16 V_o}{6\pi V_{PK}} - \frac{P_o^2}{P_{in}^2}}$	$\frac{P_{in}}{V_o} \sqrt{\frac{16 V_o}{6\pi V_{PK}} - \frac{P_o^2}{P_{in}^2}}$

As it can be noticed, in both the Bridgeless topology and the Bridgeless Interleaved PFC Boost Converter topology, a new loss has been introduced in the intrinsic body diodes of the MOSFETs, but since input bridge converters were eliminated, there is some efficiency gain for these topologies. In addition, the low frequency RMS ripple current through the output capacitors is constant—independent of interleaving. However, the high frequency ripple current is reduced significantly. Finally, it is observed that for the constant output power, as the input voltage increases, the high frequency ripple reduces.

### 9.3.8 Methods for the EMI reduction

As is presented in [5], the high-frequency ripple of the input current in the switching converters generates the differential-mode EMI while the common-mode EMI is a result of secondary, usually parasitic effects. Typically, the differential-mode EMI is dominant below 2 MHz, while the common-mode EMI is dominant above 2 MHz [1], [2]. The high-frequency noise must be filtered out in order to comply with the EMI standards.

The differential-mode EMI can be eliminated by introducing an EMI filter between the AC supply and the diode bridge converter. The additional losses will be reduced by using soft switching techniques such as “ZVS”, “ZCS” and “ZVT”.

A high-frequency active PFC stage significantly increases the differential-mode EMI, typically by 30 dB to 60 dB, and an EMI filter must be used to comply with the EMI standards. There are three main requirements concerning the design of the EMI filter for a PFC stage, [1], [2]:

- First requirement:

The first requirement for the EMI filter is to provide the required attenuation in order to ensure compliance with the EMC standards.

- Second requirement:

Assuming that the voltage drop across the filter inductor is very small at the mains frequency, then, only the filter capacitor introduces a displacement angle  $\Phi$  between the mains input current and voltage, which degrades the power factor. This leads to the second requirement for the EMI filter: the displacement angle  $\Phi$  must be kept low. Hence, the filter capacitor is upper limited.

- Third requirement:

The third requirement is related to the overall stability of the system. When the EMI filter is added, instabilities can arise in the system due to the interaction between the filter and the converter [2].

In [6], the design of a 600 W Boost PFC, complying with the EMC standards for the conducted EMI in the 150 kHz ÷ 30 MHz range, is presented. Different circuit design and layout solutions are taken into account and their effect on the conducted EMI behaviour of the converter is experimentally evaluated. Common-mode and differential-mode



switching noise, together with the input filters design and topology and with the printed circuit board (PCB) layout design (in terms of track length and spacing, ground and shielding planes, etc.) are the key aspects which have been considered. In particular, the paper reports the conducted EMI measurements for different filter capacitor placements and values, different power switch drive circuits, together with several other provisions: the reduction of the wire lengths for the current return paths and for the high circuit branches, together with the reduction of the areas embraced by high loops, which have turned out to be decisive in reducing the conducted EMI level of the converter. The paper also shows that the application of the theoretically derivable EMC basic design rules, which, in principle, should guarantee the limitation of the EMI in a switching power converter, may, in some cases, become partially ineffective because of second-order effects (e.g., resonances, component parasitics, connections).

The DM noise is usually overlapped with the input current waveform. The DM noise is dependent on the way the Boost inductor is made, thus, on the inductor impedance. Considering an ideal inductor, it represents the high impedance for the noise; however, the real inductor presents parasitic capacitances, which represent a low impedance path to the DM noise.

Another problem that has direct influence on the DM noise is the reverse recovery current from the Boost diode. This current circulates through the switch during the diode turn-off, causing high frequency oscillations, thus, acting directly on the DM conducted noise.

In [31], a solution to reduce the EMI generated by PFC converters is proposed and it is based on combinations between various IGBTs and new hyper-fast stealth diodes, rated at 600 V, with fast and soft recovery characteristics.

In [32], a straightforward guideline for a simplified differential mode (DM) EMI input filter design has been given. In the first step, a law to calculate the design frequency, which is needed for the input filter design, is introduced. In a second step, a volume optimisation of the DM EMI filter based on volumetric parameters of the filter inductances and capacitors is given. The resulting filter volume mainly depends on the attenuation, the design frequency, the delivered power, and finally, the number of filter stages. The optimum number of filter stages has been evaluated exemplarily for different power levels (100 W, 300 W, and 500 W) and design frequencies (200 and 400 kHz) in dependence on the required attenuation in the range of 0–150 dB.

In [30], the effects of the Boost inductors on the DM noise have been investigated. Both the theoretical analysis and the experimental results showed that the impedance of the Boost inductor significantly affects the DM noise of the Boost PFC converter. Theoretically, the main switch can be modelled as a noise voltage source. The higher the impedance, the lower the DM noise is. As a result, the impedance of the Boost inductor is determined by the converter design at low frequencies. At high frequencies, the parasitic, such as the winding capacitance of the inductor, determines the impedance of the inductor. Reducing

the effects of the parasitic so as to increase the impedance of the inductor is a key to reduce the HF DM noise. It is verified that a higher HF impedance, which is due to the smaller parasitic and higher loss, leads to a lower HF DM noise.

[31] has proposed a balance technique to reduce the common mode (CM) noise of the PFC converters. It is simple and effective compared to other CM noise reduction techniques. The high frequency model is proposed for the balance technique to predict its CM noise emission. Guidelines are provided to achieve a CM noise reduction up to 10 MHz. With the balance technique, the CM choke size can be reduced by 88 % and the total EMI filter size (including both CM and DM filter) can be reduced by 20 %.

The Bridgeless PFC Boost Converter is one of the most attractive PFC topologies, which achieves high efficiency by eliminating the line-voltage bridge converter. However, this topology emits much higher conducted common mode (CM) EMI noise than the Conventional Boost PFC converters. Significantly, larger CM chokes are needed in order to meet the EMC standards. [32] proposed two methods to reduce its CM noise, while maintain its high efficiency benefit.

One method is to make the topology totally symmetric so that the CM noise is cancelled inside the converter. The other method is to apply the balance technique to the topology. The first method can achieve better CM noise reduction while the second method is simpler in implementation.

[32] has investigated the benefit of interleaved multi-phase PFC on the EMI noise reduction. With the proper interleaving phase angle, both the differential mode (DM) and the common mode (CM) EMI noise can be reduced. The CM noise of the interleaved multi-phase PFC converter can be further reduced with the balance technique. By adding one turn on each Boost inductor and by adjusting the parasitic capacitance, the CM noise of the multi-phase PFC converter can be minimised. The EMI filter for the converter can be reduced. One extra benefit of the interleaved multi-phase PFC converter is its phase shedding ability. At light load condition, one or more phases can be shut down to achieve a higher light load efficiency. However, the converter will lose the benefit of the EMI noise reduction. With the balance technique, the CM noise of the converter remains low with phase shedding.

In [33] and [34], a comparative analysis of the EMI produced by high-frequency single-phase PFC converters is done. Three topologies were considered and investigated: Conventional Boost PFC, Interleaved PFC Boost and Bridgeless PFC Boost converters.

On the other hand, the CM noise circulates through the grounding conductor and it uses as path the parasitic elements present between the circuit and the equipment grounded chassis.

The Semi-Bridgeless PFC Converter has a source of CM conducted noise higher than the Boost and the interleaved Boost converters. This happens because the output ground of

this converter is connected to the AC source only in the positive half cycle, while, during the negative half cycle, the output ground is pulsed in relation to the AC source, with a high frequency and with an amplitude equal to the output voltage. As an alternative to reduce its conducted CM noise source and to make it similar to the CM noise of the conventional Boost, it is necessary to change the topology, in order to provide a path of low impedance between the AC source and the positive or negative output terminals. This is done through the insertion of two other diodes connected between the output ground and the input source. This leads to a higher complexity and cost.

The conducted EMI control is made through the blockage of the existing noise through the use of filters. The topology of the most used filter to control the conducted EMI is known as the  $\pi$  filter. It is compact, because it only uses one magnetic core, and efficient, because it has action on both noise types, the DM and CM conducted noises. The inductors are coupled on a single core in order to provide low impedance to the DM noise, but high impedance to the CM noise.

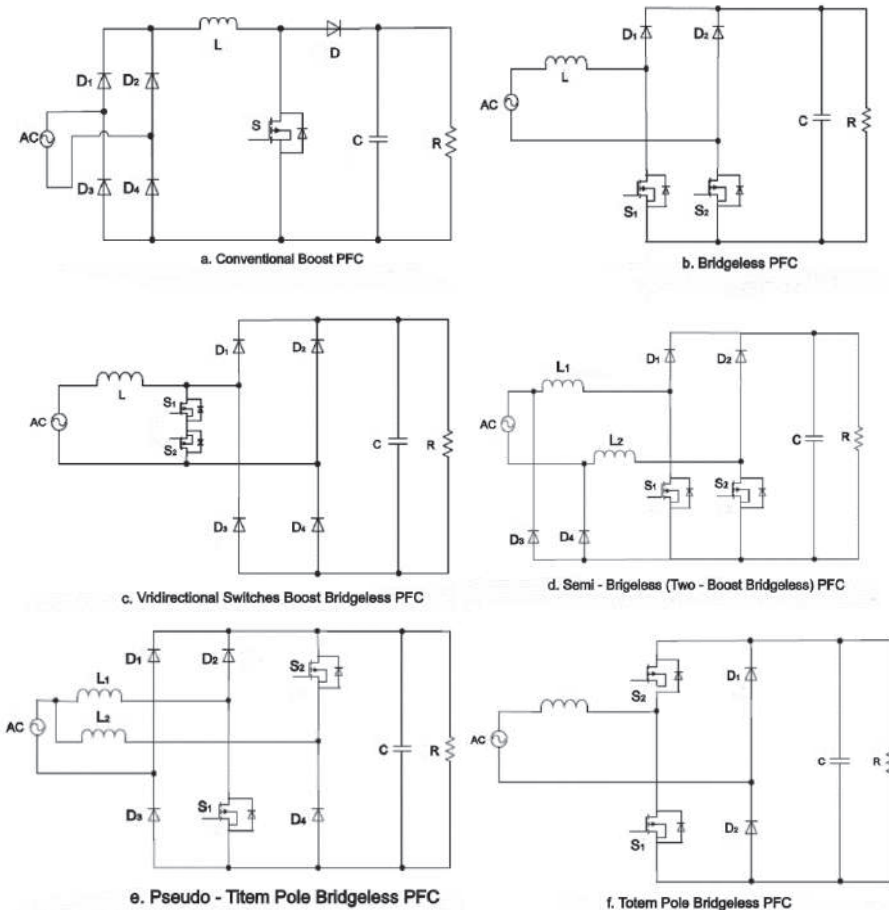


Fig. 9.22 Schematic of the PFC converters investigated in [35].

In [35], a systematic review of the Bridgeless PFC Boost Converter (BLPFC) family is presented; the conduction losses and the common mode (CM) EMI performances are analysed compared with the conventional Boost PFC.

The PFC converters investigated in [35], Fig. 9.22, are:

- the Conventional Boost PFC;
- the Bridgeless PFC Boost Converter;
- the Bidirectional Switches Boost PFC;
- the Semi-Bridgeless (Two-Boost Bridgeless) PFC;
- the Pseudo-Totem Pole PFC;
- the Totem-Pole PFC.

Simulation and experimental results show that low EMI and high efficiency can be realised by the Two-Boost Bridgeless and Pseudo-Totem Pole Bridgeless PFC topologies.

An overview of the classification and the comparison of the conducted EMI mitigation techniques used in switching power converters is done in [36], Fig. 9.23. It can be concluded that the interleaving approaches represent feasible solutions to reduce the conducted EMI.

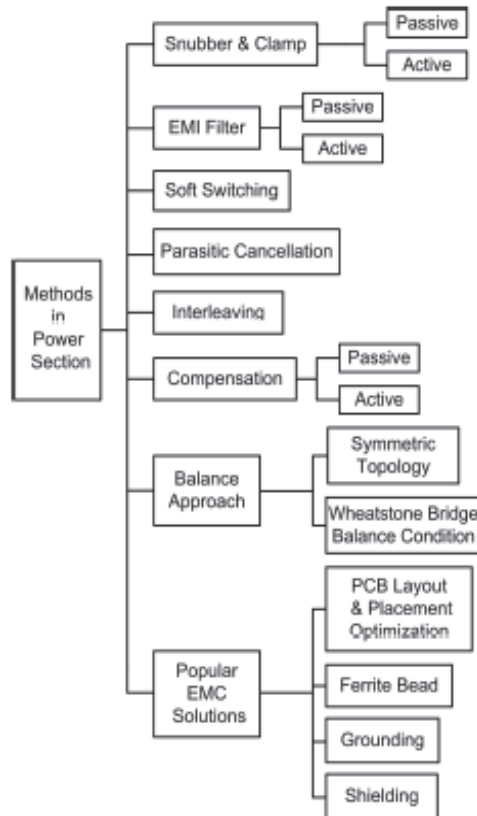


Fig. 9.23 EMI mitigation methods to converter power section [36].

## 9.4 Evaluation of the relevant publications

### 9.4.1 Design of the decisional matrix

The target of the study done by the research team at the Department of Electrical Engineering was to build a decisional matrix able to provide the best topology choice with respect to the desired requirement.

The criteria the decisional matrix was built on are low component costs, high energy efficiency, easy to scale power levels (1.5 kW, 2.2 kW, 4 kW) with the same platform (PCB), high quality, high reliability, compact design (kW/dm<sup>2</sup>). As power density has a low priority, also passive PFC and low-frequency active topologies (100 Hz) were considered in the matrix composition.

The selection of the topologies has been done being also based on the evaluation of the number of switching devices and passive components, which has to be as low as possible in order to minimise the size and the cost.

Comparable topologies have been selected in order to fulfill the requirements.

Regarding the calculations, a fair value of 0.95 for efficiency has been chosen, for all the variants.

The decisional matrix prepared for different topologies based on the above-mentioned criteria is presented in Table 9.9.

Table 9.9. Decisional matrix

	Passive PFC	Boost	Boost Interleaved	Bridgless	Semi – Bridgless	Bridgless – Interleaved	Boost – Buck	SE PIC	Conventional Sheppard-Taylor
EMI	Best	Fair	Good	Poor	Fair	Fair	Fair	Fair	Poor
Inductor Cost	Fair	Good	Best	Good	Fair	Good	Fair	Fair	Fair
Capacitor Cost	Fair	Good	Best	Good	Good	Best	Fair	Fair	Fair
	--	> 20 kHz	> 20 kHz	20 kHz	> 20 kHz	> 20 kHz	> 20 kHz	> 20 kHz	> 20 kHz
PF	Poor	Good	Good	Good	Good	Good	Good	Good	Good

Active Switch	0	1	2	2	2	4	2	1	2
Bridge Diode Quantity	4	4	4	2	2	2	4	4	4
Fast Diode	0	1	2	0	4	2	2	1	4
Efficiency	Poor	Poor	Fair	Fair	Fair	Best	Poor	Poor	Poor
Power Rating	< 1000 W	< 1000 W	< 3000 W	< 2000 W	< 2000 W	> 3000 W	< 1000 W	< 1000 W	< 1000 W
Magnetic Size	Very Large	Large	Small	Medium	Large	Small	Large	Large	Large

The design of the decisional matrix shown in Table 9.8 took into account the following considerations:

- The efficiency can be optimised by attention to several details. Switching losses can be minimised by choosing not only a fast power switch, but by using the lowest possible gate drive resistor in accordance with the current capabilities of the drive circuit. It is necessary to ensure that the drive circuit has sufficient local capacitance to provide the needed current. Selecting the fastest diode possible will also improve efficiency, but at increased cost; a compromise in diode speed may be required to meet cost targets.
- There are two types of noise problems to contend with: the conducted and the radiated EMI to the outside world, and self interference from the circuit. The first issue is as much a system problem as a PFC design problem and is normally addressed by using power line filters and proper shielding. The fast switching of voltages and currents in a multi-kilowatt PFC yields to crippling interference to the circuit itself. It is necessary to perform a careful layout to minimise the proximity of the control circuitry to high current paths, to minimise high current loop areas and to use generous ground planes.
- The proper design of the inductor is the key to long term reliability in a PFC. The iron powder cores typically used in a PFC suffer from thermal core aging if operated at a too high temperature. The circuit will function properly for several hundred to several thousand hours, whereupon it will fail rapidly. It is important to evaluate when the core losses exceed the copper losses or when a fan is needed; it is very

easy for the internal core temperatures to exceed maximum ratings. It is preferable to drop to a lower permeability core material that provides lower core losses, even through the winding losses will increase due to the increased number of the turns required.

- Boost Inductors play a critical role in the Boost type PFC converters. On one hand, it affects the system efficiency through increasing or reducing semiconductor and magnetic losses depending on its value. On the other hand, assuming a fixed energy store, in the optimised design, the maximum flux density and the winding factor of the core are both on the boundary of limitations; and the volume of the inductor, which dominates the power density of a PFC, will be determined by the inductance. Facing the biggest challenge in the PFC design today – high efficiency vs. high power density, it is necessary to investigate the PFC inductor's operating characteristics and find out how it affects the system's efficiency and power density. However, this has been difficult all the time, due to the lack of an effective way for designers to evaluate the overall performances of the PFC inductors.
- The magnetic design is always a critical and complex part of the PFC converters. A proper inductor design will not only increase the efficiency of the whole system, but give a more compact and reliable PFC. However, the method for the inductor design has been ambiguous for a long time due to the lack of an effective way to evaluate the overall performances of the PFC inductors.
- It is well-known that the inductor losses come from core losses and winding losses. In order to predict the inductor losses, the first step is the core selection. A good core for the Boost inductor must have high flux saturate limitation, low core losses and an acceptable price.
- It is well-known that, in all the magnetic cores, the operation temperature needs to be controlled in order to retain its magnetic properties and limit the losses. The switching frequency and the input current ripple values have important influence in such losses. Therefore, there are values of the switching frequency and of the input current ripple where the advantage of the inductor volume reduction is lost, due to the excessive temperature rise. Furthermore, the switching frequency also has effect on the commutation losses and on the EMI filter requirements. The current ripple also has effect on the commutation losses, on the conduction losses and on the EMI filter requirements. A higher ripple tends to increase the RMS current in the main switch, and hence, can increase the conduction losses if a MOSFET is being used.
- The ratings of the decisional matrix result from a comparison done for a reference power of  $P = 1000 \text{ W}$ .

### 9.4.2 The Matlab/Simulink model implementation of the most relevant chosen single-phase PFC converters. Simulation results

The aim of this research study was to select the four relevant single-phase power factor correction (PFC) topologies for the power range of 1.5 kW up to 4 kW and to analyse and evaluate them. The evaluation has been done with regard to the electromagnetic compatibility (EMC) requirements, which are crucial for the residential ambient. The investigated topologies are the **Conventional PFC Boost Converter, the Bridgeless PFC Boost Converter, the Boost Interleaved PFC Boost Converter and the Bridgeless Interleaved PFC Boost Converter.**

Before proceeding with the performance analysis of the four converters' topologies, the following assumptions were made:

- The unity power factor achievement, meaning that the input line current is in phase with the input line voltage, and has a sinusoidal waveform;
- The output voltage regulation, with minimum ripple.

To solve the EMI noise issue, an EMI noise reduction circuit should be introduced. Information about the EMI model building of Boost and Bridgeless PFC circuits are also given in [37]. Based on the EMI requirements and methods met in the literature, the EMI filters for the simulation models have also been developed. The schematic of the common mode and the EMI filters is depicted in Fig. 9.24 and the parameters used for modelling the filters are presented in Table 9.10.

The passive elements that built up the CM filter and the EMI filter were designed using the equations below [38].

$$A_{ttdB} = 20 \cdot \log \left( \frac{V_{in}}{10^{-6}} \right) - V_{max} \text{ [dB]} \quad (9.6)$$

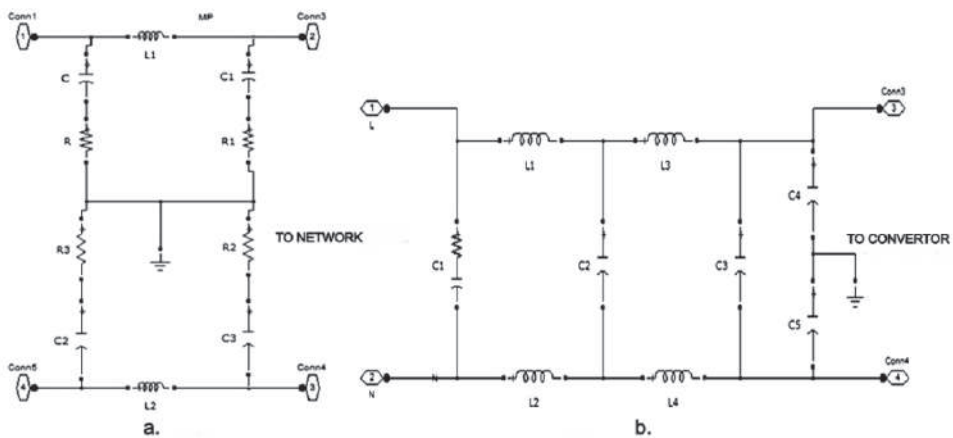


Fig. 9.24 a) Matlab/Simulink Implementation of the Common Mode and b) EMI filters.



Table 9.10. CM & EMI Filters Parameters

CM Filter Parameters		EMI Filter Parameters	
R	50 Ω	C <sub>1</sub>	1.5 μF
R <sub>1</sub>	50 Ω	C <sub>2</sub>	1.5 μF
R <sub>2</sub>	50 Ω	C <sub>3</sub>	0.47 μF
R <sub>3</sub>	50 Ω	C <sub>4</sub>	4.7 nF
C	10 μF	C <sub>5</sub>	4.7 nF
C <sub>1</sub>	0.1 μF	L <sub>1</sub>	3.3 mH
C <sub>2</sub>	10 μF	L <sub>2</sub>	3.3 mH
C <sub>3</sub>	0.1 μF	L <sub>3</sub>	3.3 mH
L <sub>1</sub> = L <sub>2</sub>	50 mH	L <sub>4</sub>	3.3 mH

$$C_{fa} = \frac{C_{in}}{C_{in} \cdot L_f \left( 2 \cdot \pi \cdot \frac{f_s}{10} \right)^2} [F] \quad (9.7)$$

$$C_d \geq 4 \cdot C_{in} [F] \quad (9.8)$$

$$R_d = \sqrt{2.1 \left( \frac{L_f}{C_d} \right)} [\Omega] \quad (9.9)$$

where:

A<sub>ttdB</sub> is the required attenuation;

f<sub>s</sub> is the switching frequency;

L<sub>f</sub> is the filter inductor;

C<sub>f</sub> is the filter capacitor;

C<sub>d</sub> is the damping of the capacitor;

R<sub>d</sub> is the damping of the resistor.

### 9.4.2.1 Boost PFC Converter Topology Matlab/Simulink Implementation

The hardware implementation of the Conventional Boost PFC Converter topology, Fig. 9.25, as well as of its controller design was carried out in the Matlab/Simulink environment, by the research team at the Department of Electrical Engineering of the University Politehnica Timisoara and is depicted in Fig. 9.26. The resonant filters used to diminish the common-mode EMI noises are also employed (the filters inductances are all equal to  $60\ \mu\text{H}$ , while the capacitances are all equal to  $22.7\ \text{nF}$ ). Its functionality is described below.

The measured DC bus voltage is compared with the prescribed voltage value. The resulting voltage error is then fed into the PI voltage controller for zero error DC bus voltage regulation. The output of the controller is, then, taken as amplitude of the reference current and is fed into the inner controller.

An analogue multiplier is used for sensing the inductance current, which is then subtracted from the reference current. The inner controller is chosen to be a hysteresis control type with  $0.1\ \text{A}$  width.

According to this control technique, the switch is turned on when the inductor current decreases below the lower reference and is turned off when the inductor current increases above the upper reference, giving rise to a variable frequency control.

To achieve smaller ripple in the input current, a narrow hysteresis band is needed. However, the narrower the hysteresis band, the higher the switching frequency. The hysteresis control scheme provides excellent dynamic performance because it acts quickly. To ensure a high stability of the control system, the outer loop is designed to be slower enough than the inner one.

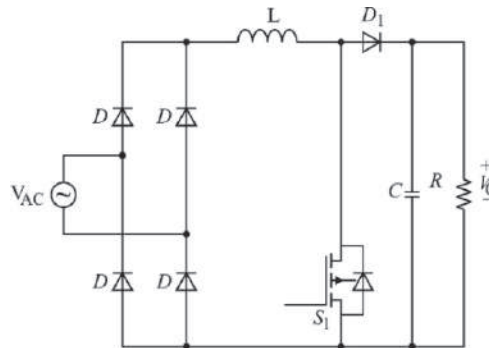


Fig. 9.25 Boost PFC converter topology.

The following operation conditions and parameters were set from the beginning: the input AC voltage is set to  $230\ \text{V}$  (RMS), the switching frequency is  $48\ \text{kHz}$ , the DC link capacitor voltage is controlled by a PI type controller to around  $380\ \text{V}$ , the DC capacitance  $C$  is set to  $780\ \mu\text{F}$ , the magnetically coupled inductances  $L = 100\ \mu\text{H}$ , the resistive load is set to  $57.76\ \Omega$ , the parameters of the PI controller are:  $k_p = 0.545\text{e-}3$ ,  $k_i = 0.0073$  and the hysteresis band is  $\pm 0.1$ .

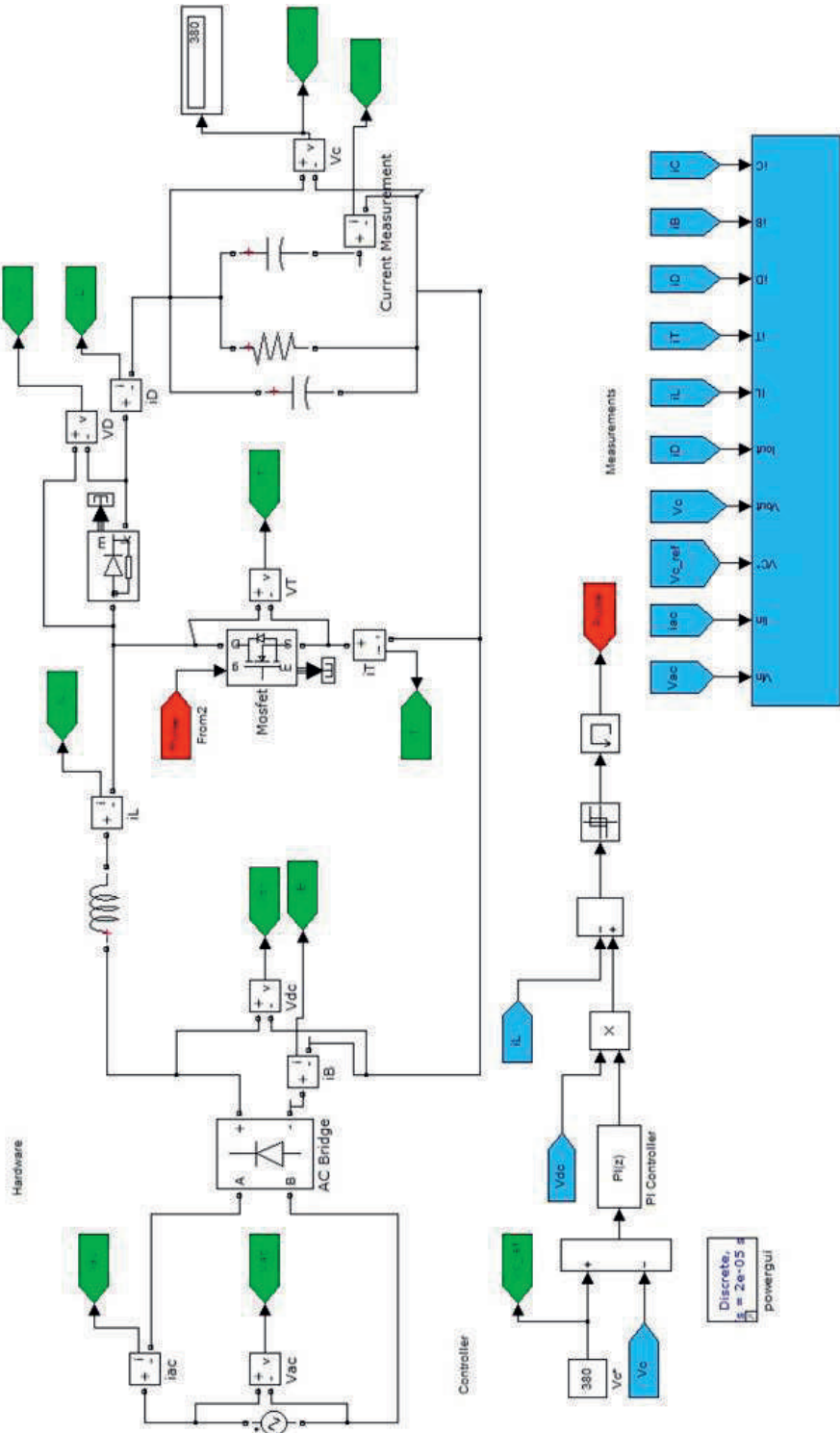


Fig. 9.26 Boost PFC Converter model implementation in Matlab/Simulink.

The simulation results, obtained for operation at  $P = 2.5 \text{ kW}$  are presented in what follows (see Fig. 9.28 – Fig. 9.32).

The simulation results, for different load values in order for the efficiency versus the power curve to be drawn, are as depicted in Fig. 9.33.

The Fast Fourier analysis of the input current waveform, of the input voltage waveform, respectively, is presented in Fig. 9.34- Fig. 9.37. The current measured between the DC capacitor C and the ground is also analysed and its Fast Fourier analysis is depicted in Fig. 9.38 and in Fig. 9.39, respectively. The analysis was done for 25 cycles of the selected signal and for two frequency ranges: from 0 to 1 kHz, and from 1 kHz to 150 kHz, respectively.

Table 9.10 presents the RMS and average values for the MOSFET current ( $I_{\text{MOSFET}}$ ), diode current ( $I_{\text{DIODE}}$ ) and inductance current ( $I_{\text{ac}}$ ).

The losses for the simulated Conventional PFC Boost Converter model, as presented in Table 9.11, were computed-based on the catalogue parameters for the MOSFET, diode and inductance devices, as follows:  $R_{\text{MOSFET}} = 0.38 \Omega$ ,  $R_{\text{DIODE}} = 0.98 \Omega$  and  $R_{\text{Copper}} = 0.075 \Omega$ .  $P_{\text{MOSFET COND}}$  and  $P_{\text{MOSFET SW}}$  stand for the conducting losses and for the switching losses, respectively.

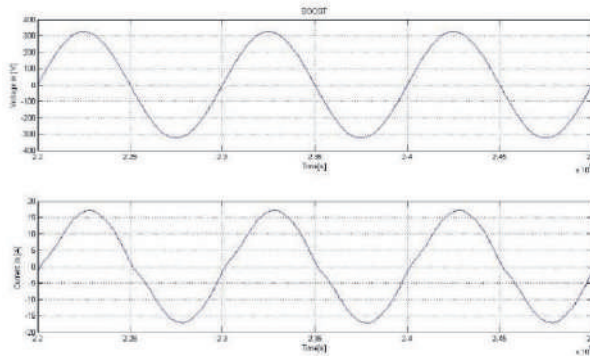


Fig. 9.27 Zoom on the input voltage & input current waveforms for the Conventional Boost PFC Converter topology.

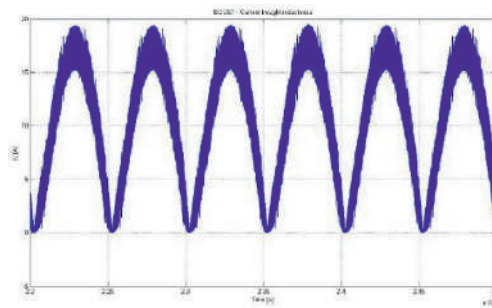


Fig. 9.28 Zoom on the inductance current waveform for the Conventional Boost PFC Converter topology.

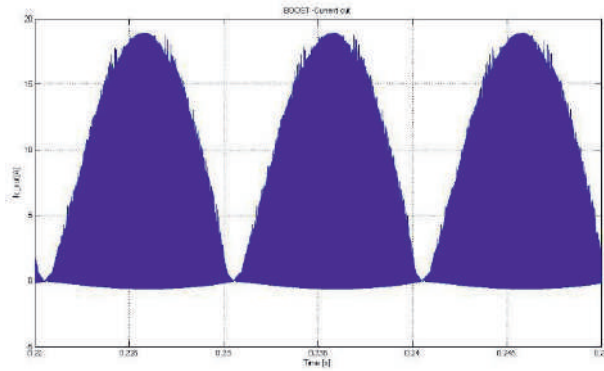


Fig. 9.29 Zoom on the capacitor current waveform for the Conventional Boost PFC Converter topology.

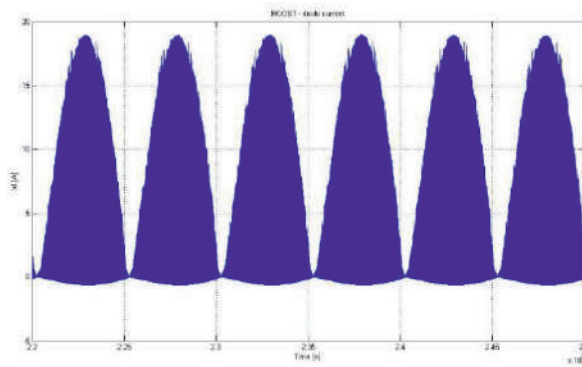


Fig. 9.30 Zoom on the diode current waveform for the Conventional Boost PFC Converter topology.

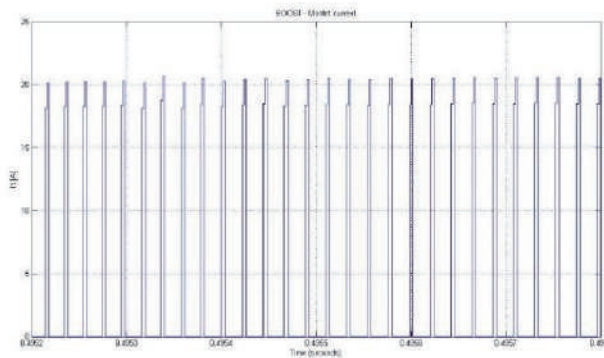


Fig. 9.31 Zoom on the MOSFET current waveform for the Conventional Boost PFC Converter topology.

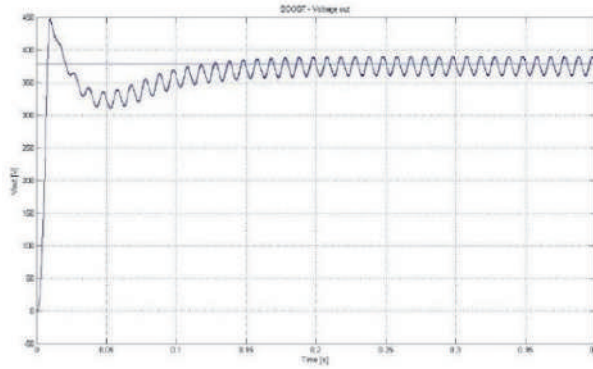


Fig. 9.32 Voltage output waveform for the Conventional Boost PFC Converter topology.

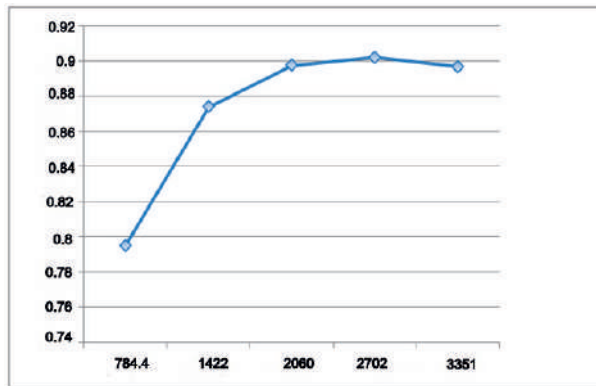


Fig. 9.33 Efficiency versus power curve for the Conventional Boost PFC Converter topology.

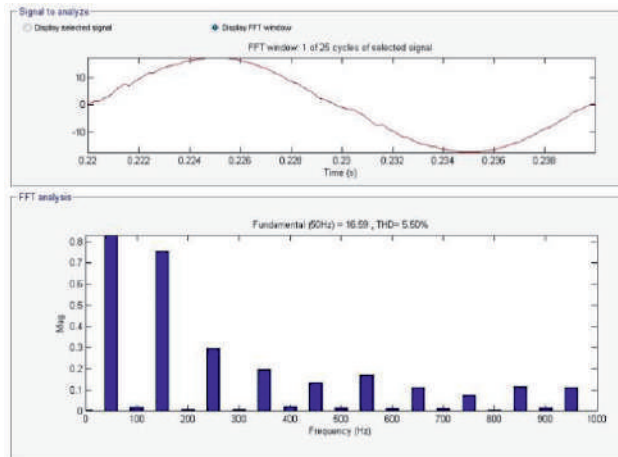


Fig. 9.34 FFT of the input current range from 0 to 1 kHz for the Conventional Boost PFC Converter topology.

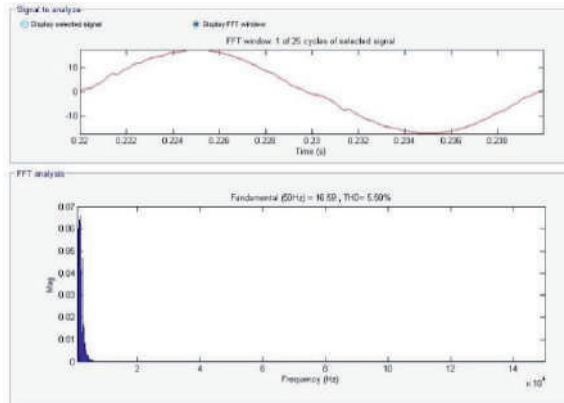


Fig. 9.35 FFT for the input current range from 1 kHz to 150 kHz for the Conventional Boost PFC Converter topology.

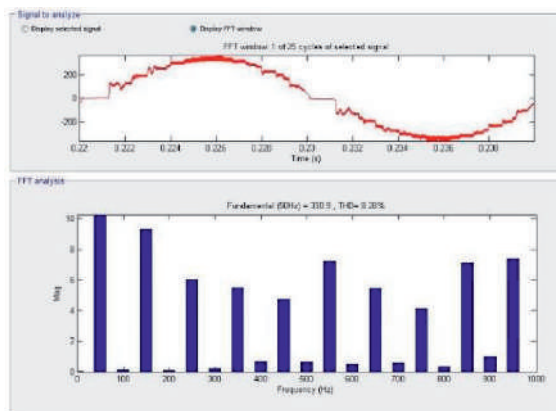


Fig. 9.36 FFT for the voltage measured after the EMI filter within 0 and 1 kHz range for the Conventional Boost PFC Converter topology.

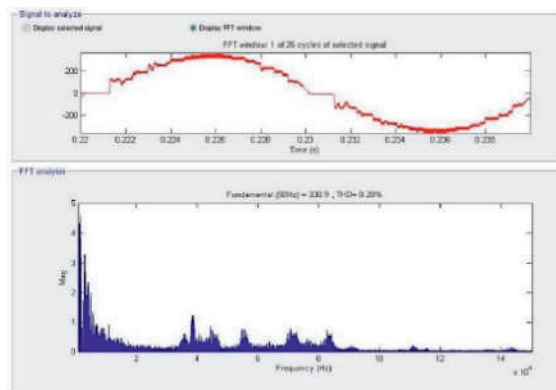


Fig. 9.37 FFT for the voltage measured after the EMI filter within 1 and 150 kHz for the Conventional Boost PFC Converter topology.

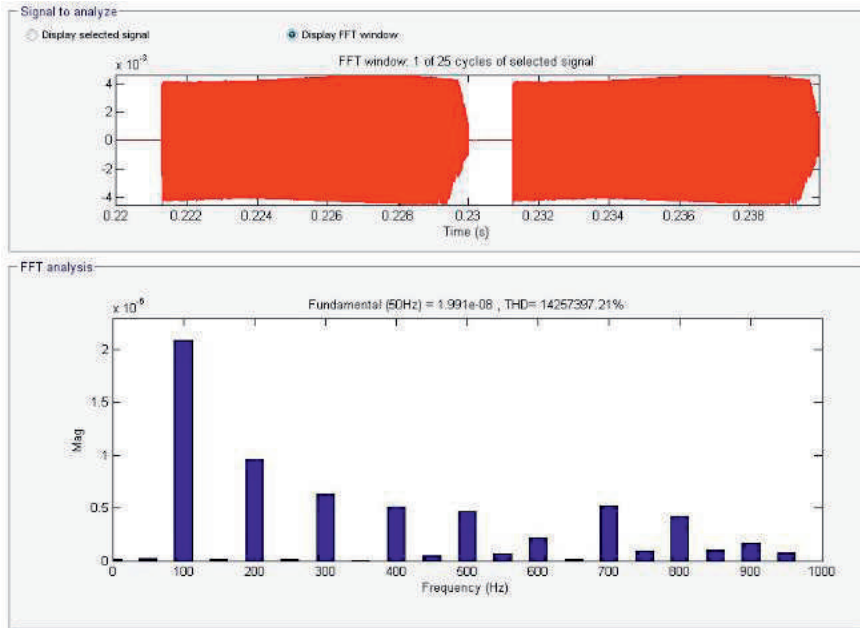


Fig. 9.38 FFT for the current measured between C and the ground within 0 and 1 kHz for the Conventional Boost PFC Converter topology.

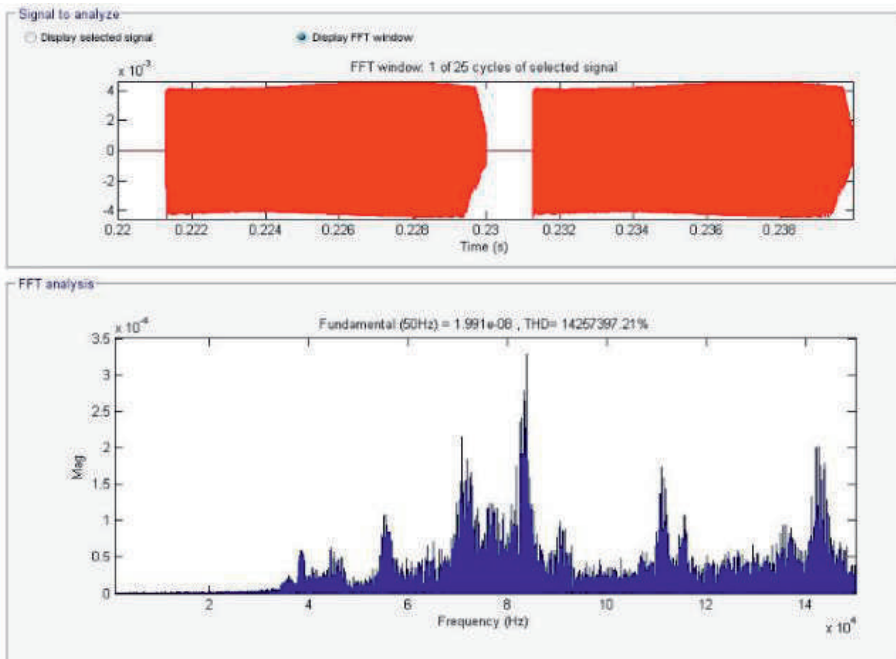


Fig. 9.39 FFT for the current between the capacitor C and the ground within 1 kHz and 150 kHz for the Conventional Boost Converter topology.



Table 9.11. RMS & Avg current values [A]

	RMS	AVG
$I_{MOSFET}$ [A]	7.063	4.201
$I_{DIODE}$ [A]	9.546	6.263
$I_{ac}$ [A]	9.76	0.009468

Table 9.12. Losses breakdown at nominal load [W]

$P_{DIODE}$ [W]	$P_{MOSFET\ COND}$ [W]	$P_{MOSFET\ SW}$ [W]	$P_{Copper}$ [W]	$P_{out}$ [W]	$P_{in}$ [W]
10.75	18.95	2.743	10.55	2438	2702

### 9.4.2.2 Bridgeless PFC Boost Converter Topology Matlab/Simulink Implementation

In the Bridgeless PFC Boost Converter configuration topology, the need for the converter input bridge is avoided, yet the classic Boost topology is maintained. This is done by making use of the intrinsic body diode connected between the drain and the source of the MOSFET switch. A simplified schematic of the Bridgeless PFC Boost Converter configuration is shown in Fig. 9.40, while its implementation in Matlab/Simulink, by the research team at the Department of Electrical Engineering of the University Politehnica Timisoara, is depicted in Fig. 9.41. As for the Boost PFC case implementation, here, also, resonant filters are being used to suppress the common-mode EMI noises (the filters inductances are all equal to 60  $\mu$ H, while the capacitances are all equal to 22.7 nF).

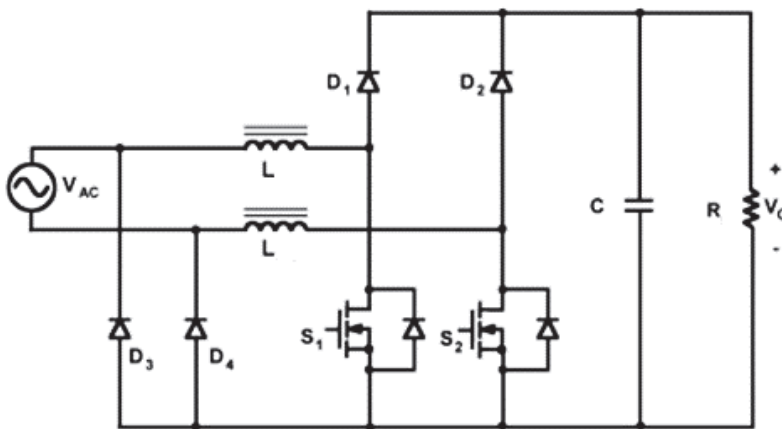


Fig. 9.40 Bridgeless PFC Boost Converter topology.

In the traditional Boost PFC Converter topology, the current flows through two of the bridge diodes connected in series. In the Bridgeless PFC Boost Converter, the current flows through only one diode with the MOSFET switches providing the return path.

The gate commands for the two switches are provided by the logic signals which are generated by comparing the current error signal with a triangular carrier of 48 kHz. The 180° phase-shift is obtained by comparing the former resulted signal with the measured AC voltage signal.

Compared to a conventional Boost PFC Converter topology, the losses due to the bridge converter are eliminated, but the diode of the inactive MOSFET must be taken into account for the Bridgeless PFC Boost Converter configuration.

Thus, in a Bridgeless PFC Boost Converter topology, there are only the conduction losses from one diode to be taken into account. As a conclusion, there is some efficiency gain for this topology, if compared with the Boost topology, by eliminating the voltage drop of one diode in the line-current path. Similar operation conditions and parameters as for the Conventional Boost PFC Converter case are also assumed here, with the only mention that now the inductances  $L_1$  and  $L_2$  are 300  $\mu\text{H}$  each. The parameters of the PI controller are:  $k_p = 0.05e-3$ ,  $k_i = 0.01$ .

The waveforms of the input voltage, of the input current through one inductor ( $I_{ac}$ ), of the Boost current through one diode ( $I_{DIODE}$ ), of the sensed current through one MOSFET device ( $I_{MOSFET}$ ) and the DC bus voltage of the converter are provided in Fig. 9.42 ÷ Fig. 9.48.

The reference and the regulated DC voltage are shown in Fig. 9.47.

The efficiency versus the power curve of the simulated model is depicted in Fig. 9.48.

A Fast Fourier analysis of the input current waveform, of the input voltage waveform and of the current measured between the DC capacitor  $C$  and the ground is provided as depicted in Fig. 9.49 - Fig. 9.53. Similar conditions for the FFT were employed: 25 cycles of the selected signal and two frequency ranges: from 0 to 1 kHz and from 1 kHz to 150 kHz, respectively, were taken into consideration.

Table 9.12 presents the RMS and the average values for the MOSFET, the diode and the inductance currents.

The losses for the Bridgeless PFC Boost Converter model, as per Table 9.13, were computed based on the same catalogue parameters as used in the previous paragraph:  $R_{MOSFET} = 0.38 \Omega$ ,  $R_{DIODE} = 0.98 \Omega$  and  $R_{Copper} = 0.075 \Omega$ .  $P_{MOSFET COND}$  and  $P_{MOSFET SW}$  stand for the conducting losses and for the switching losses, respectively.

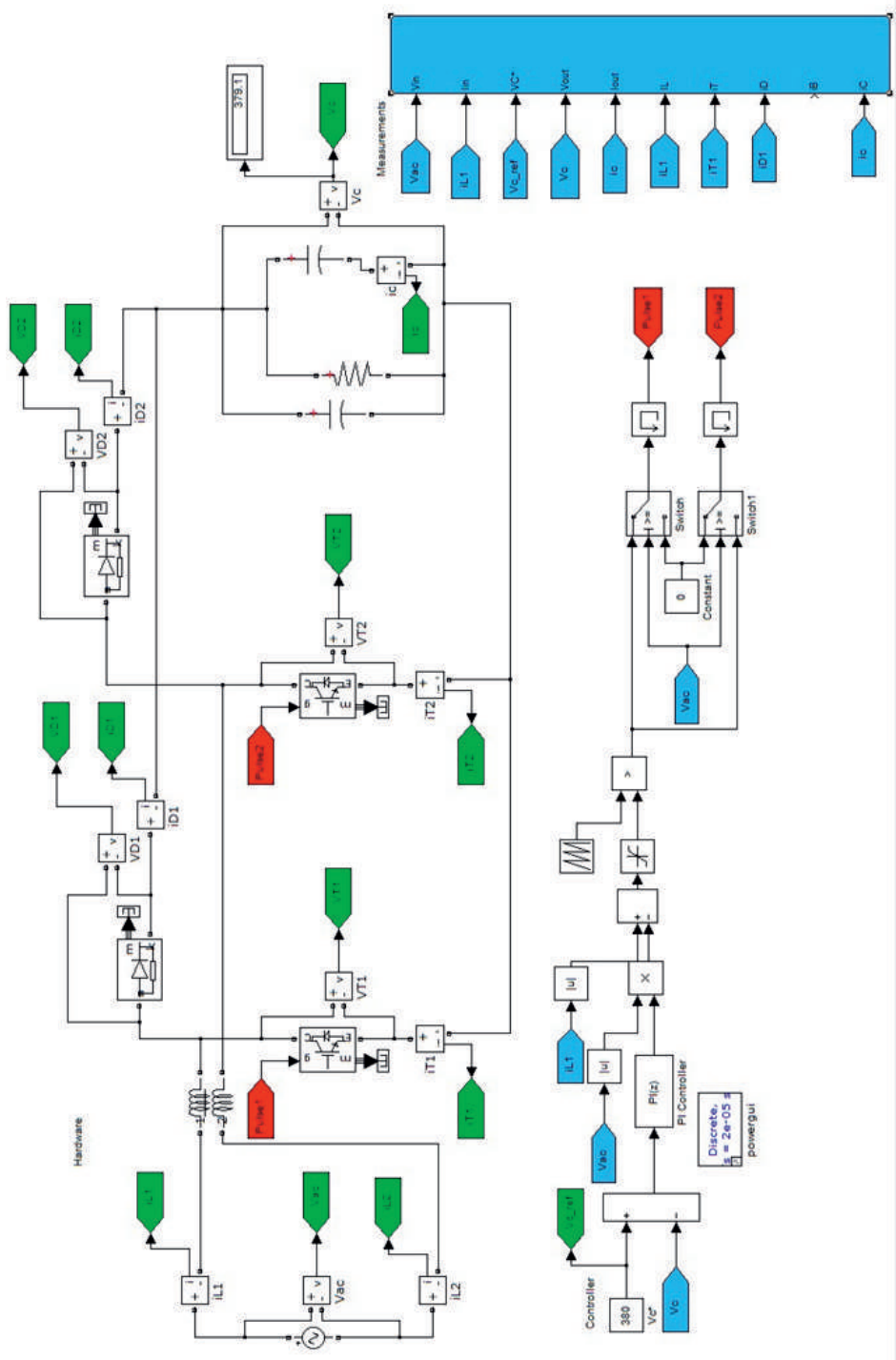


Fig. 9.41 Bridgeless PFC Boost Converter model implementation in Matlab/Simulink.

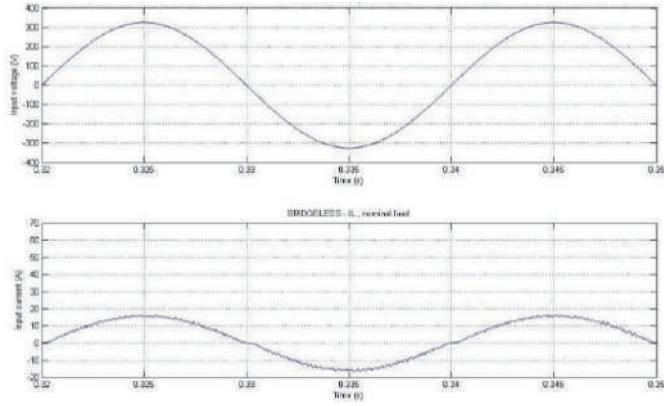


Fig. 9.42 Zoom on the input voltage & input current waveforms for the Bridgeless PFC Boost Converter topology.

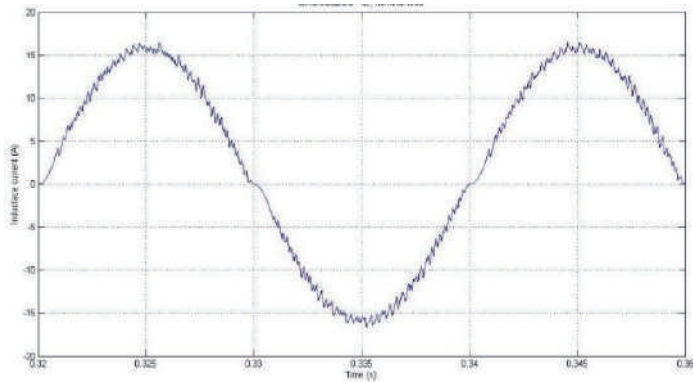


Fig. 9.43 Zoom on the inductance current waveform for the Bridgeless PFC Boost Converter topology.

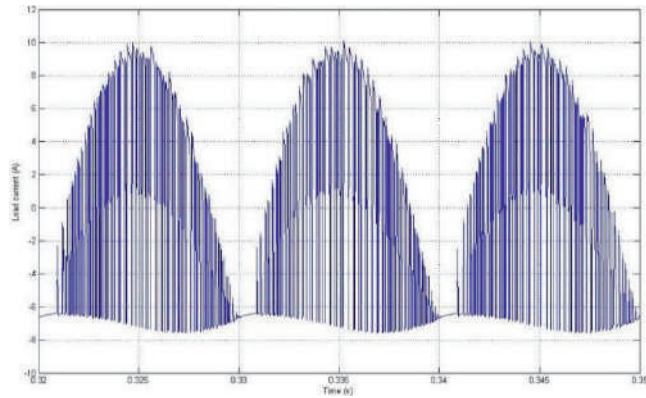


Fig. 9.44 Zoom on the capacitor current waveform for the Bridgeless PFC Boost Converter topology.

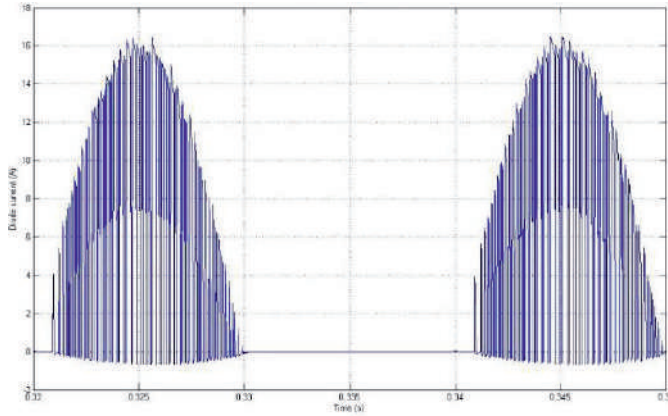


Fig. 9.45 Zoom on the diode current waveform for the Bridgeless PFC Boost Converter topology.

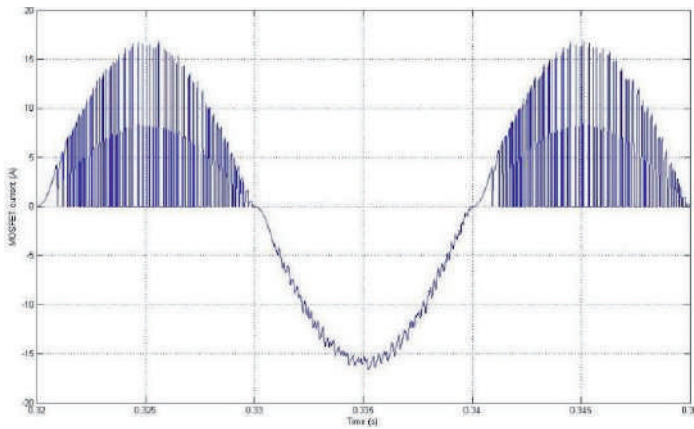


Fig. 9.46 Zoom on the MOSFET current waveform for the Bridgeless PFC Boost Converter topology.

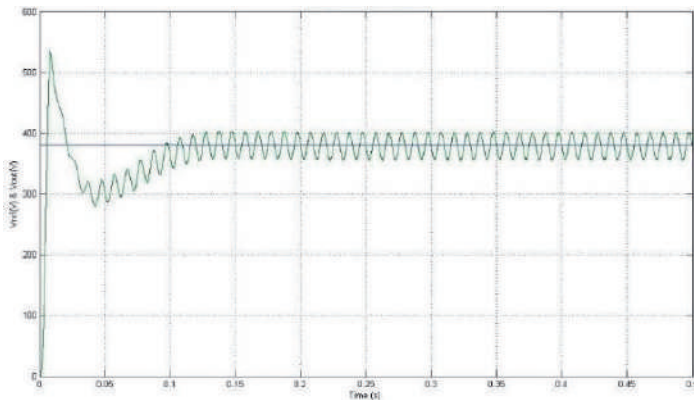


Fig. 9.47 Voltage output for the Bridgeless PFC Boost Converter topology.

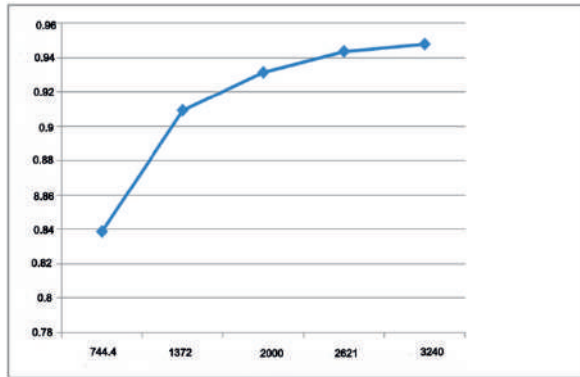


Fig. 9.48 Efficiency versus power curve for the Bridgeless PFC Boost Converter topology.

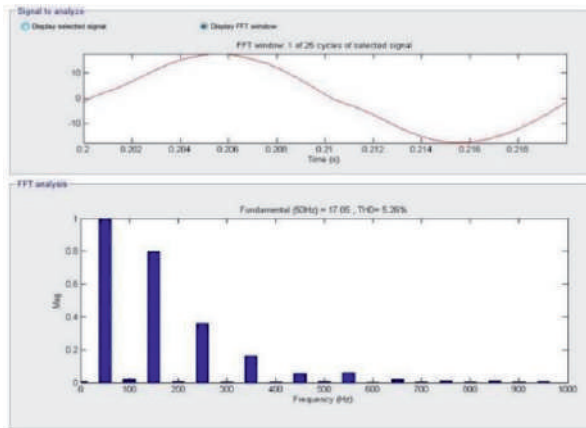


Fig. 9.49 FFT for the input current within 0 and 1 kHz range for the Bridgeless PFC Boost Converter topology.

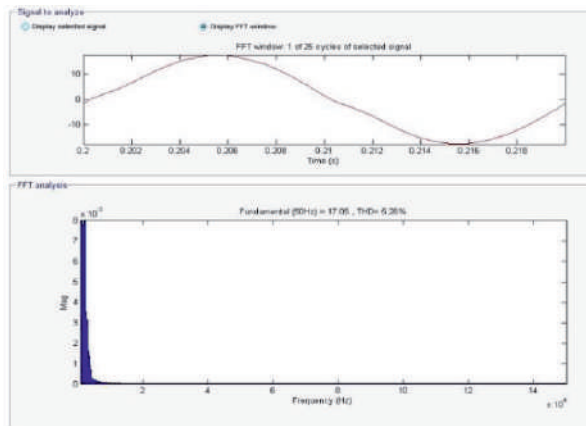


Fig. 9.50 FFT for the input current within 1 kHz and 150 kHz range for the Bridgeless PFC Boost Converter topology.

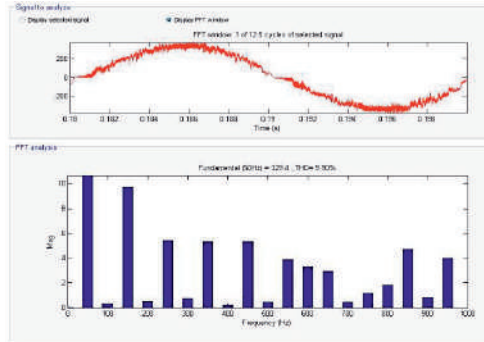


Fig. 9.51 FFT for the voltage measured after the EMI filter within 0 and 1 kHz range for the Bridgeless PFC Boost Converter topology.

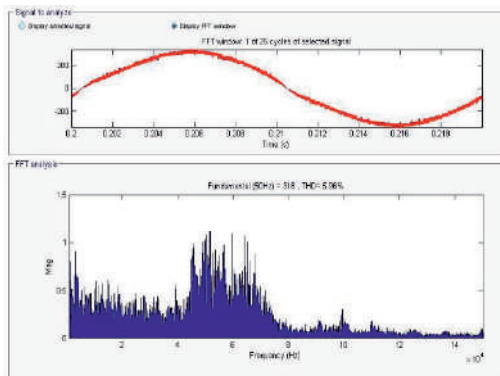


Fig. 9.52 FFT for the voltage measured after the EMI filter within 1 kHz and 150 kHz range for the Bridgeless PFC Boost Converter topology.

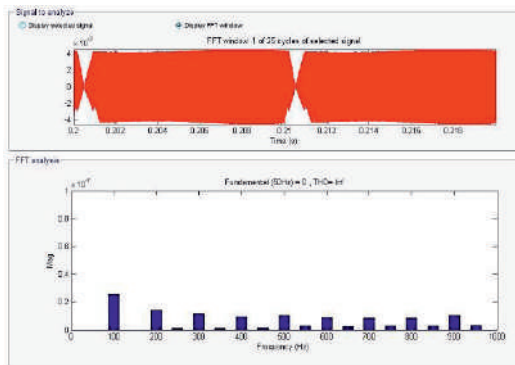


Fig. 9.53 FFT for the current measured between the capacitor C and the ground within 0 and 1 kHz range for the Bridgeless PFC Boost Converter topology.

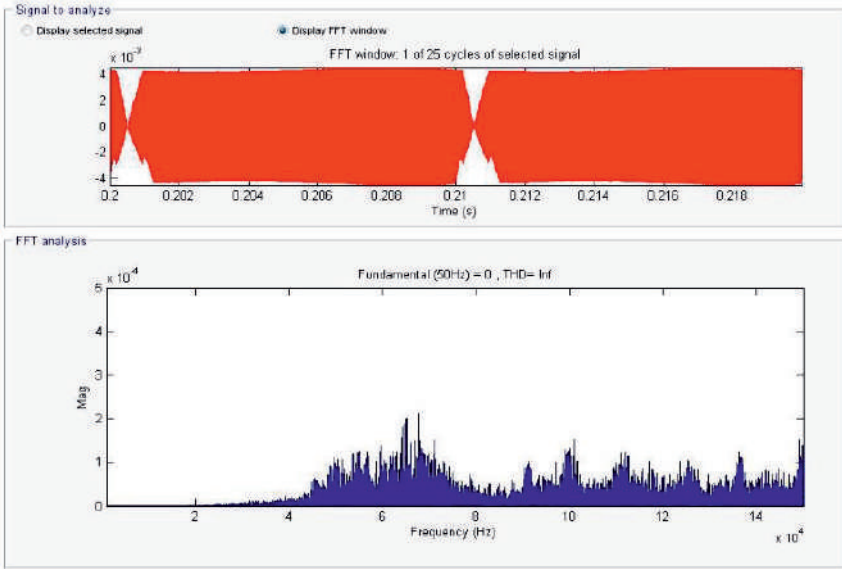


Fig. 9.54 FFT for the current measured between capacitor C and the ground within 1 kHz and 150 kHz range for the Bridgeless PFC Boost Converter topology.

Table 9.13. RMS & Avg current values [A]

	RMS	AVG
$I_{MOSFET}$ [A]	5.258	0.26
$I_{DIODE}$ [A]	6.956	3.447
$I_{ac}$ [A]	9.91	0.01249

Table 9.14. Losses breakdown at nominal load [W]

$P_{DIODE}$ [W]	$P_{MOSFET\ COND}$ [W]	$P_{MOSFET\ SW}$ [W]	$P_{Copper}$ [W]	$P_{out}$ [W]	$P_{in}$ [W]
5.715	10.5	2.341	5.61	2576	2737

### 9.4.2.3. Interleaved PFC Boost Converter Topology Matlab/Simulink Implementation

The Interleaved PFC Boost Converter, illustrated in Fig. 9.55, consists of two Boost converters in parallel, operating with a 180° phase-shift. The input current is the sum of two inductor currents.



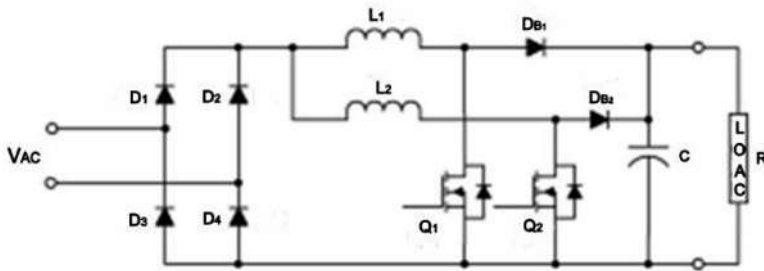


Fig. 9.55 Interleaved PFC Boost Converter topology.

It has the advantage of parallel semiconductors. It also reduces the output capacitor high frequency ripple, but it still has the problem of heat management for the input diode bridge.

To evaluate the benefits of interleaving two phases, the Interleaved PFC Boost Converter was implemented in the Matlab/Simulink environment, as depicted in Fig. 9.56. The resonant filters used to diminish the common-mode EMI noises are also employed (the filters inductances are all equal to  $60 \mu\text{H}$ , while the capacitances are all equal to  $22.7 \text{ nF}$ ).

Its control, up to one point, is the same as for the Conventional Boost PFC Converter. The exception is that here, the reference current is compared with two triangular carriers of  $48 \text{ kHz}$  ( $180^\circ$  phase-shifted from each other), and, thus, the gate commands for the  $Q_1$  and for  $Q_2$  MOSFET devices are generated.

Similar operation conditions and parameters as for the Boost PFC Converter case are also assumed here, with the only mention that now the two inductances  $L_{B1} = L_{B2} = 150 \mu\text{H}$ . The parameters of the PI controller are:  $k_p = 0.05e-3$ ,  $k_i = 0.01$  and the hysteresis band is  $\pm 0.8$ .

The simulation results showing the Interleaved PFC Boost Converter performances are presented as follows (see Fig. 9.57 – Fig. 9.60). They were obtained for operation at  $P = 2.5 \text{ kW}$ .

The efficiency versus the power curve is shown in Fig. 9.60.

A Fast Fourier analysis of the input current waveform and of the input voltage waveform, respectively, is done, as presented in Fig. 9.61 – Fig. 9.64. The current measured between the DC capacitor C and the ground is also analysed and its Fast Fourier analysis is depicted in Fig. 9.65 and in Fig. 9.66, respectively. The analysis was done for 25 cycles of the selected signal and for two frequency ranges: from 0 to  $1 \text{ kHz}$  and from  $1 \text{ kHz}$  to  $150 \text{ kHz}$ , respectively.

Table 9.14 presents the RMS and the average current values for one MOSFET ( $I_{\text{MOSFET}}$ ), one diode ( $I_{\text{DIODE}}$ ) and one inductance ( $I_{\text{ac}}$ ).

The losses for the simulated Conventional Boost PFC Converter model, as per Table 9.15, were computed based on the catalogue parameters for the MOSFET, diode and inductance devices, as follows:  $R_{\text{MOSFET}} = 0.38 \Omega$ ,  $R_{\text{DIODE}} = 0.98 \Omega$  and  $R_{\text{copper}} = 0.075 \Omega$ .  $P_{\text{MOSFET COND}}$  and  $P_{\text{MOSFET SW}}$  stand for the conducting losses and for the switching losses, respectively.

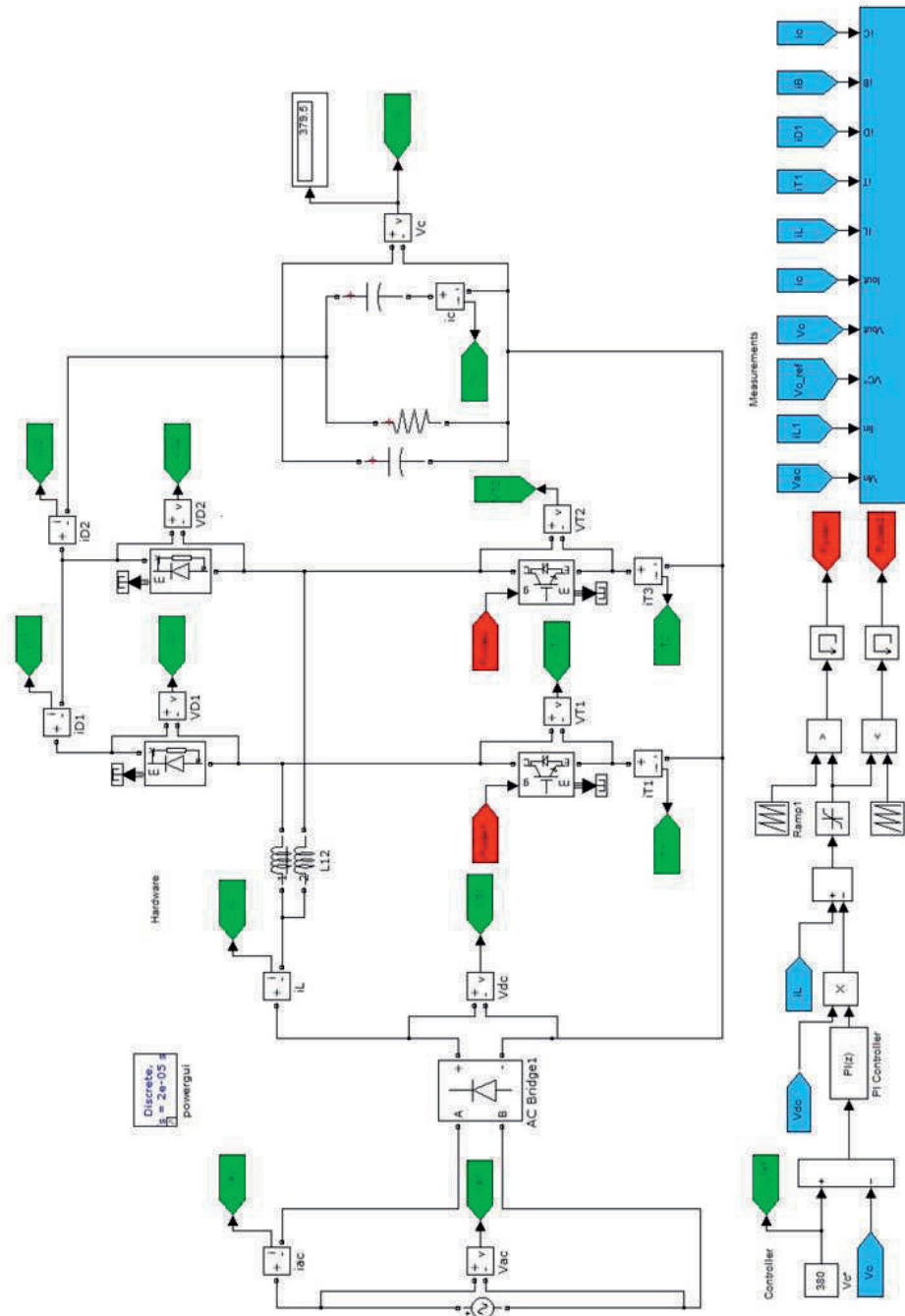


Fig. 9.56 . Interleaved PFC Boost Converter model implementation in Matlab/Simulink.

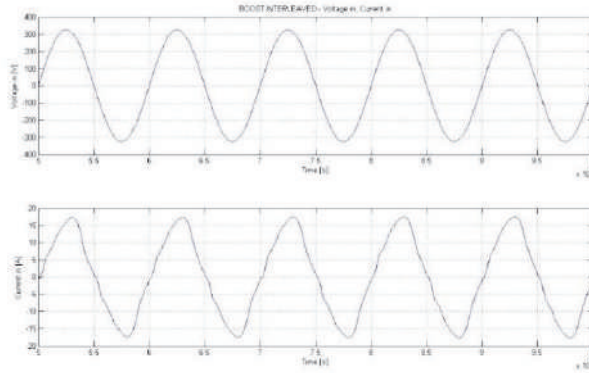


Fig. 9.57 Zoom on the input voltage & input current waveforms for the Interleaved PFC Boost Converter topology.

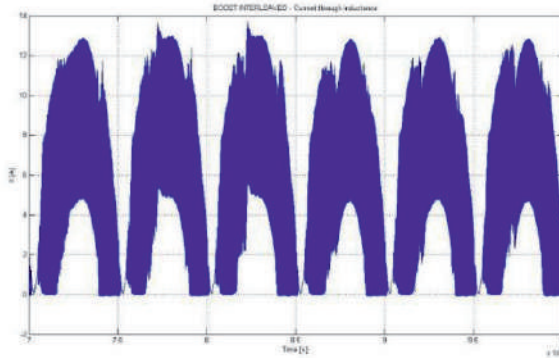


Fig. 9.58 Zoom on the inductor current waveform for the Interleaved PFC Boost Converter topology.

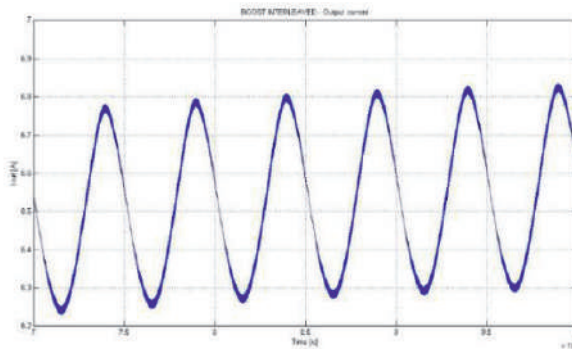


Fig. 9.59. Zoom on the capacitor current waveform for the Interleaved PFC Boost Converter topology

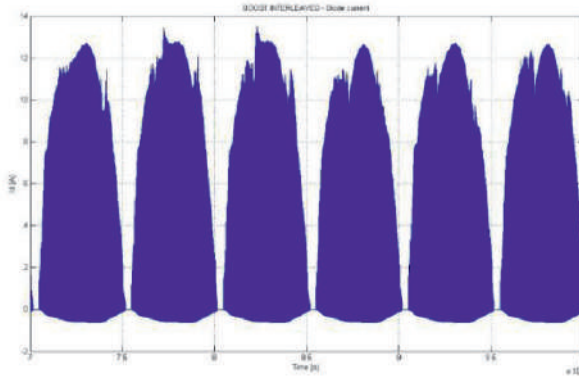


Fig. 9.60 Zoom on the diode current waveform for the Interleaved PFC Boost Converter topology.

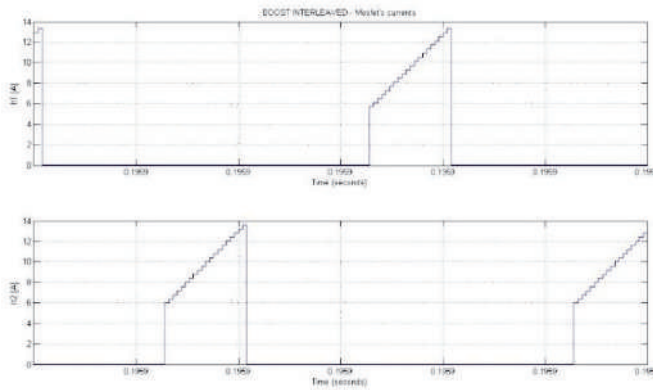


Fig. 9.61 Zoom on the two MOSFETs currents waveforms for the Interleaved PFC Boost Converter topology.

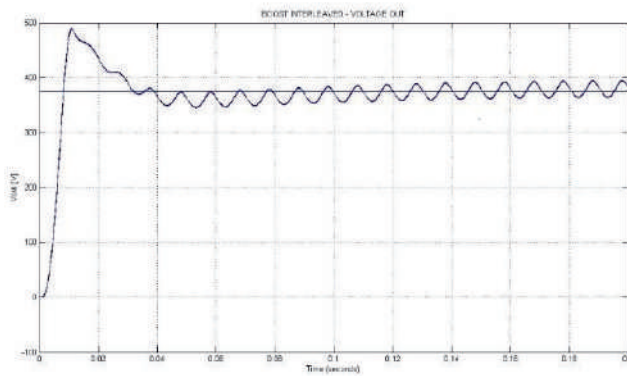


Fig. 9.62 Voltage output for the Interleaved PFC Boost Converter topology.

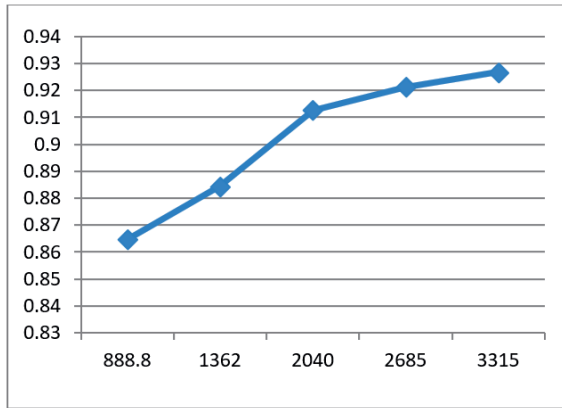


Fig. 9.63 Efficiency versus power curve for the Interleaved PFC Boost Converter topology.

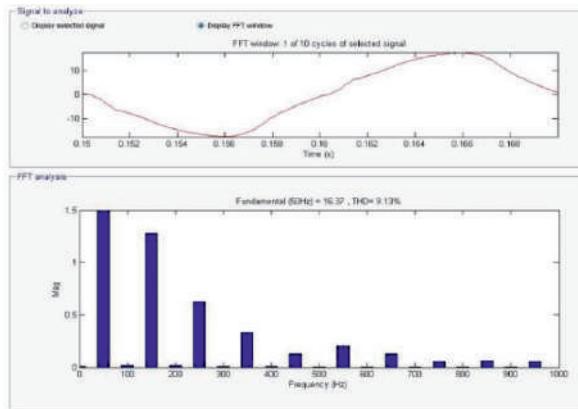


Fig. 9.64 FFT for the input current within 0 and 1 kHz range for the Interleaved PFC Boost Converter topology.

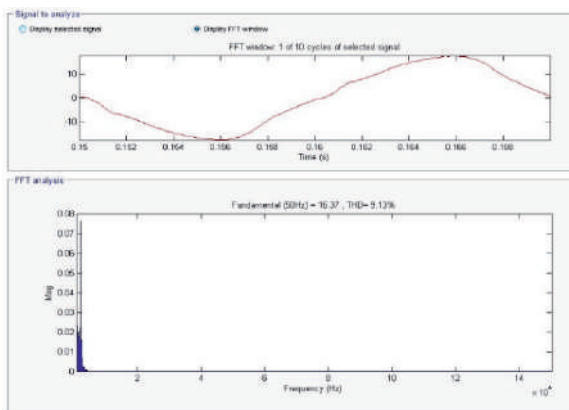


Fig. 9.65 FFT for the input current within 1 kHz and 150 kHz range for the Interleaved PFC Boost Converter topology.

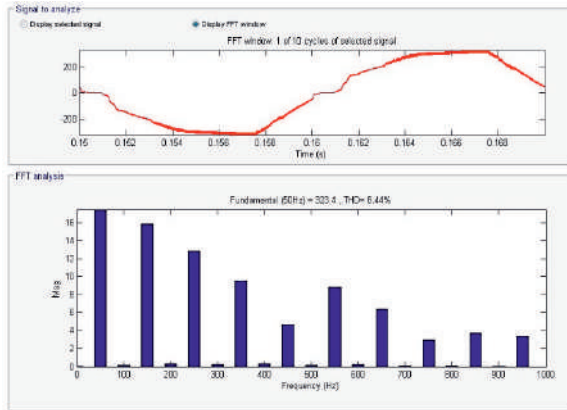


Fig. 9.66 FFT for the voltage measured after the EMI filter within 0 and 1 kHz range for the Interleaved PFC Boost Converter topology.

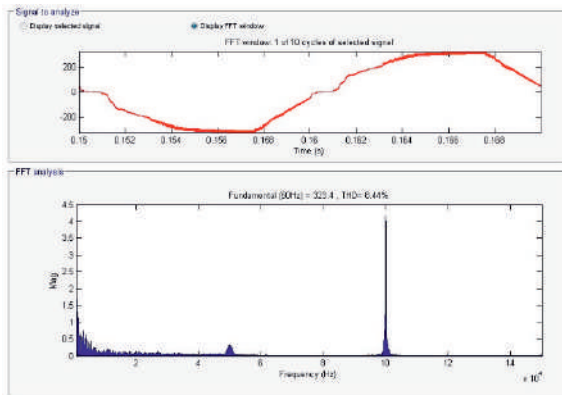


Fig. 9.67 FFT for the voltage measured after the EMI filter within 1 kHz and 150 kHz range for the Interleaved PFC Boost Converter topology.

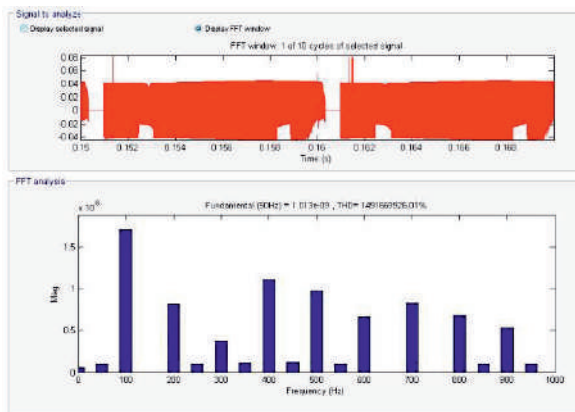


Fig. 9.68 FFT current measured between the capacitor C and the ground within 0 and 1 kHz range for the Interleaved PFC Boost Converter topology.

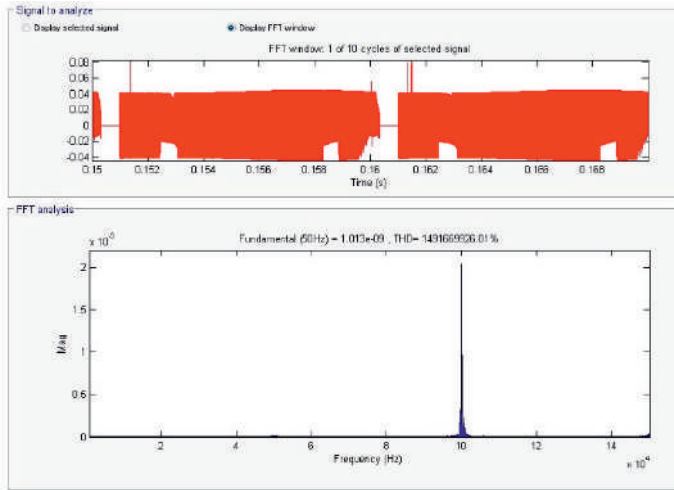


Fig. 9.69 FFT current measured between the capacitor C and the ground within 1 kHz and 150 kHz range for the Interleaved PFC Boost Converter topology.

Table 9.15. RMS & Avg current values [A]

	RMS	AVG
$I_{MOSFET}$ [A]	4.088	9.226
$I_{DIODE}$ [A]	0.4393	0.3881
$I_{ac}$ [A]	9.68	0.007998

Table 9.16. Losses breakdown at nominal load [W]

$P_{DIODE/1device}$ [W]	$P_{MOSFET COND/1device}$ [W]	$P_{MOSFET SW/1device}$ [W]	$P_{Copper/1device}$ [W]	$P_{out}$ [W]	$P_{in}$ [W]
0.02277	6.349	2.07	6.85	2474	2705

#### 9.4.2.4 Bridgeless Interleaved PFC Boost Converter Topology Matlab/Simulink Implementation

The Bridgeless Interleaved PFC topology, used in the front-end AC.–DC. converter applications, is shown in Fig. 9.70. Two more MOSFETs and two more fast diodes are inserted replacing the four slow diodes used in the input bridge of the Boost Interleaved PFC Converter. It retains the same semiconductor device count as the Boost Interleaved PFC Converter presented in the previous paragraph.

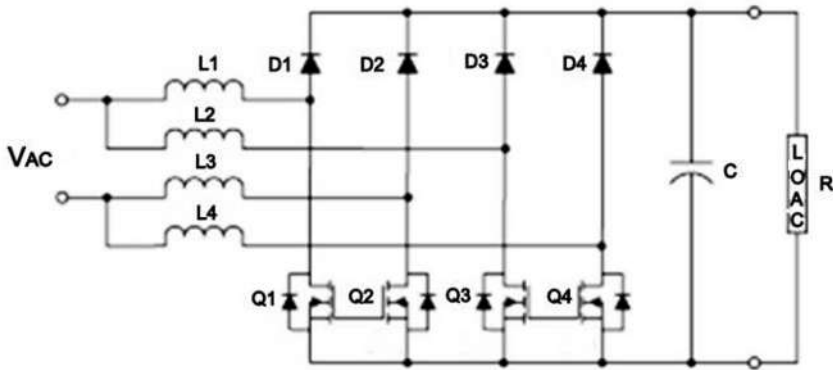


Fig. 9.70 Bridgeless Interleaved PFC Boost Converter topology.

Its control consists of two control loops: a slow outer control loop is used to regulate the output voltage  $V_o$  to a constant reference voltage and to generate a reference current signal for the fast inner current control loop with similar waveform shape as of the rectified input voltage. Its Matlab/Simulink implementation was done by the research team at the Department of Electrical Engineering of the University Politehnica Timisoara and is shown in Fig. 9.71. The filters inductances used here are all equal to  $60 \mu\text{H}$ , while the capacitances are all equal to  $22.7 \text{ nF}$ .

Further, the current error signal is compared with a triangular carrier of  $48 \text{ kHz}$  and the resulted signal is then compared with the AC voltage signal, providing the gate commands for  $Q_1$  and  $Q_3$  MOSFET devices. The gate commands for the other two switches  $Q_2$ , and for the  $Q_4$ , respectively, are generated by comparing the current error signal with a second triangular carrier of  $48 \text{ kHz}$ , which is  $180^\circ$  phase-shifted from the first one.

Similar operation conditions and parameters as for the Conventional Boost PFC Converter case are also assumed here, with the only mention that now the four inductances  $L_1 = L_2 = L_3 = L_4 = 300 \mu\text{H}$ . The parameters of the PI controller are:  $k_p = 0.05e-3$ ,  $k_i = 0.01$ .

Waveforms of the input voltage, the input current, the current through one inductor, the current per one diode, the sensed current per one MOSFET device and the DC bus voltage of the converter are provided in Fig. 9.72 – Fig. 9.78.

The reference and the regulated DC voltage are shown in Fig. 9.77.

The efficiency versus the power curve of the simulated model of the Interleaved PFC Boost Converter is depicted in Fig. 9.78.

A Fast Fourier analysis of the input current waveform, of the input voltage waveform and of the current measured between the DC capacitor  $C$  and the ground is provided as depicted in Fig. 9.79 – Fig. 9.84. Similar conditions for the FFT were employed: 25 cycles of the selected signal and two frequency ranges: from 0 to  $1 \text{ kHz}$ , and from  $1 \text{ kHz}$  to  $150 \text{ kHz}$ , respectively, were taken into consideration.



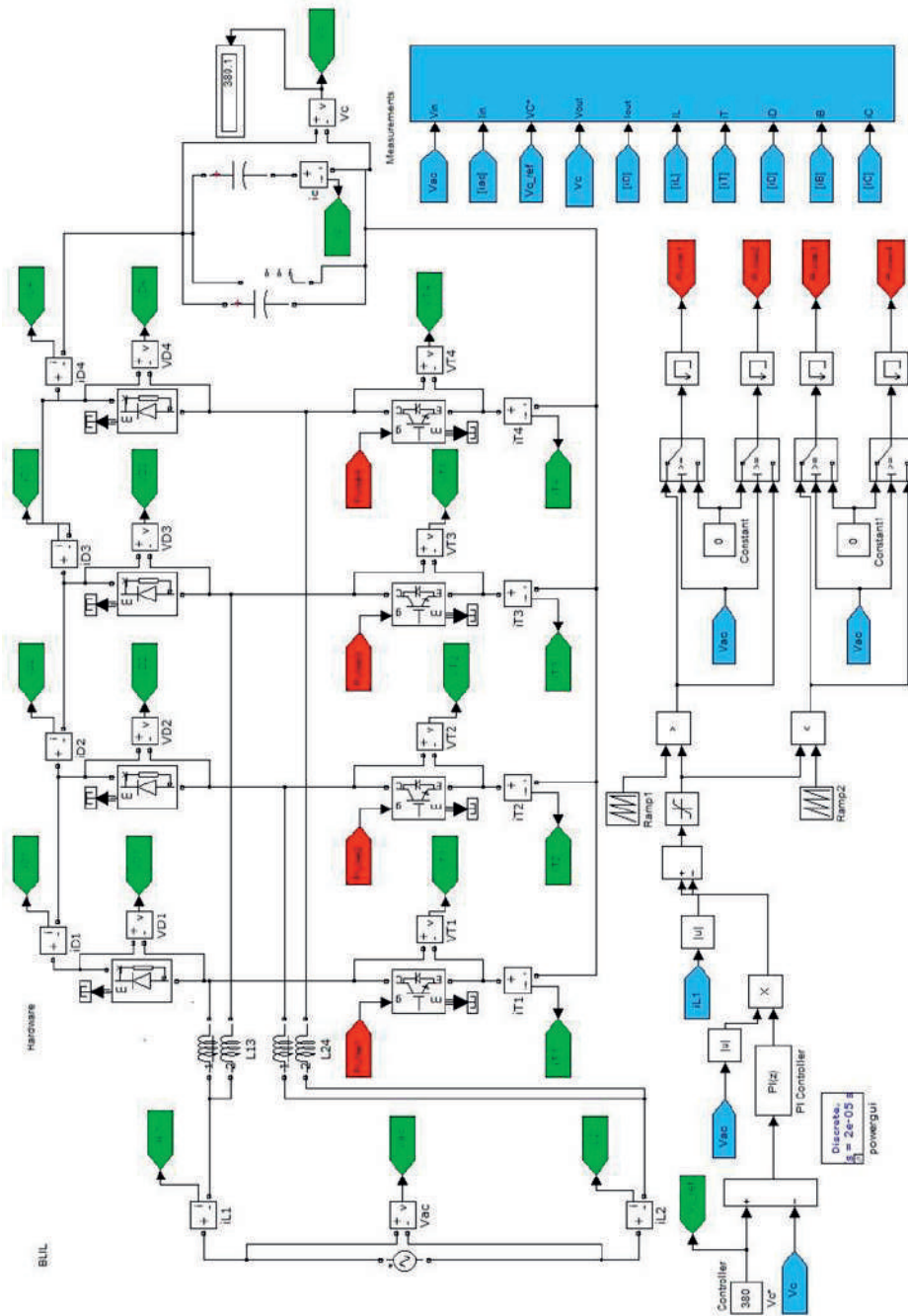


Fig. 9.71 Bridgeless Interleaved PFC Boost Converter model implementation in Matlab/Simulink.

Table 9.16 presents the RMS and average values for the MOSFET, the diode and the inductance currents. The losses for the Bridgeless Interleaved PFC Boost Converter model, as per Table 9.17, were computed based on the same catalogue parameters for the MOSFET, the diode and the inductance devices, as used in the previous paragraph:  $R_{\text{MOSFET}} = 0.38 \Omega$ ,  $R_{\text{DIODE}} = 0.98 \Omega$  and  $R_{\text{Copper}} = 0.075 \Omega$ .  $P_{\text{MOSFET COND}}$  and  $P_{\text{MOSFET SW}}$  stand for the conducting losses, and for the switching losses, respectively.

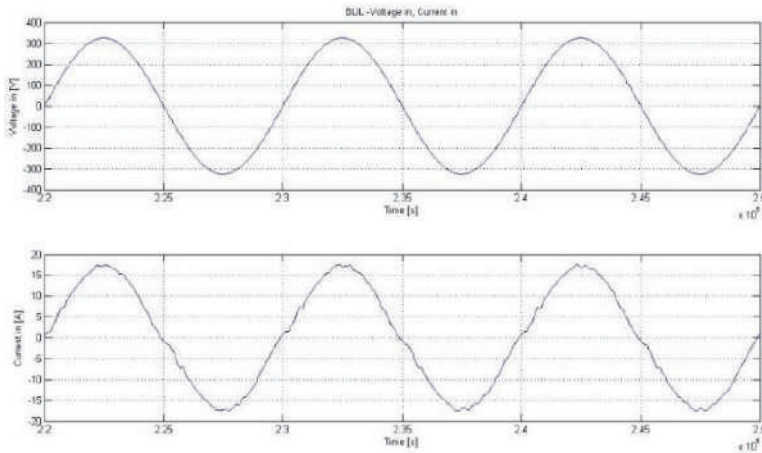


Fig. 9.72 Zoom on the input voltage & input current waveforms for the Bridgeless Interleaved PFC Boost Converter topology.

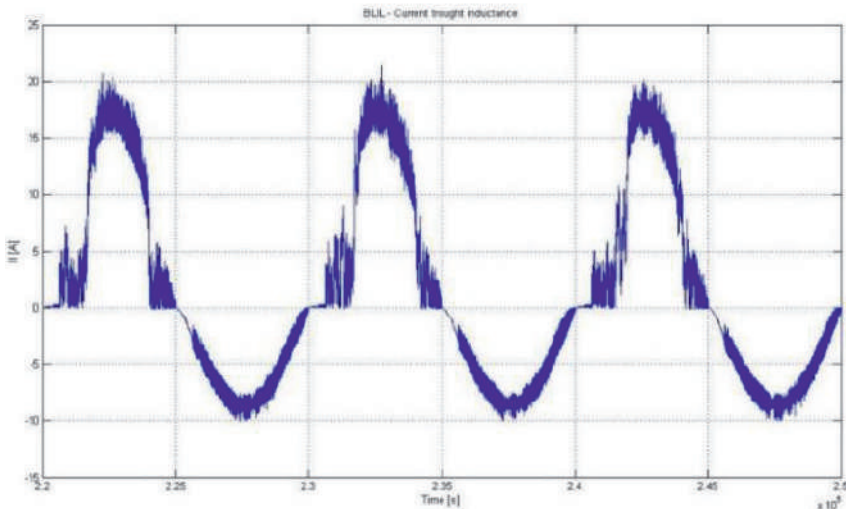


Fig. 9.73 Zoom on the inductance current waveform for the Bridgeless Interleaved PFC Boost Converter topology.

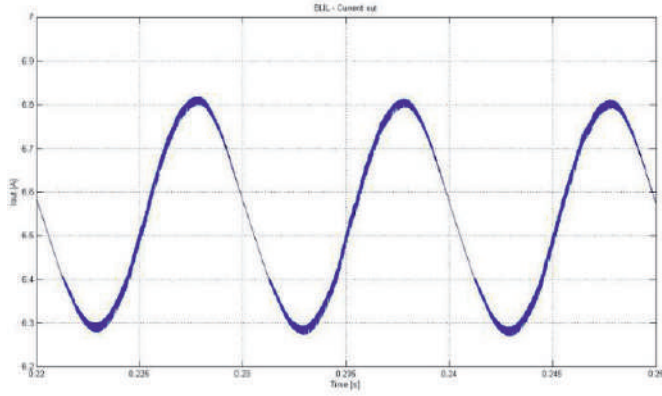


Fig. 9.74 Zoom on the capacitor current waveform for the Bridgeless Interleaved PFC Boost Converter topology.

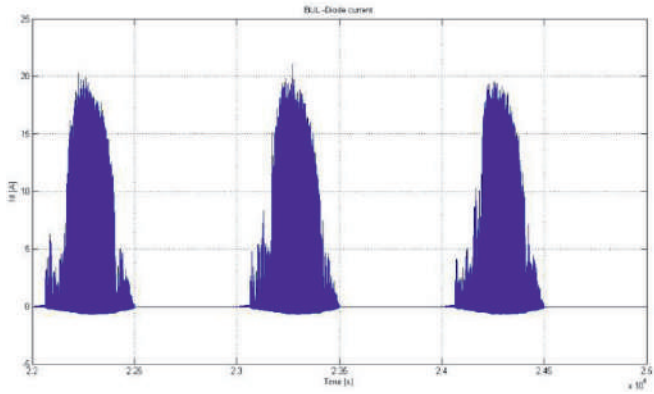


Fig. 9.75 Zoom on the diode current waveform for the Bridgeless Interleaved PFC Boost Converter topology.

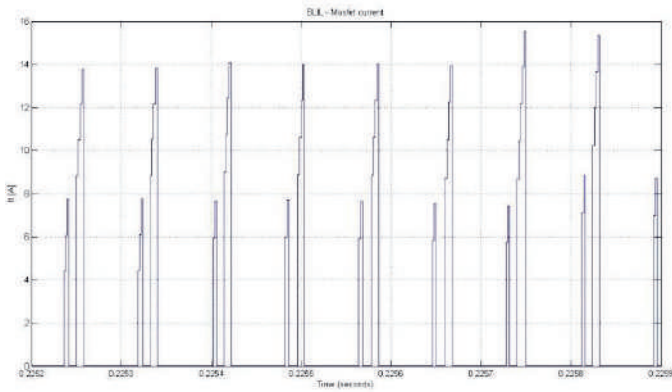


Fig. 9.76 Zoom on the MOSFET current waveform for the Bridgeless Interleaved PFC Boost Converter topology.

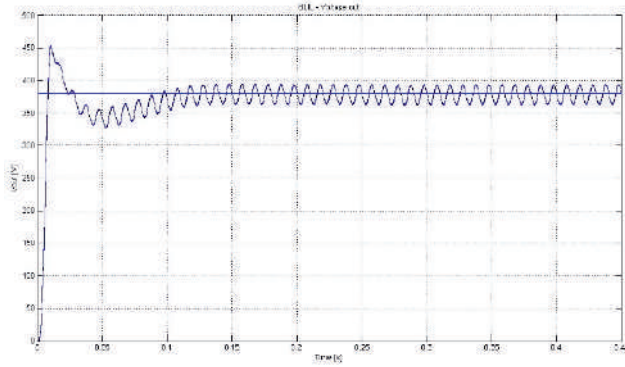


Fig. 9.77 Voltage output for the Bridgeless Interleaved PFC Boost Converter topology.

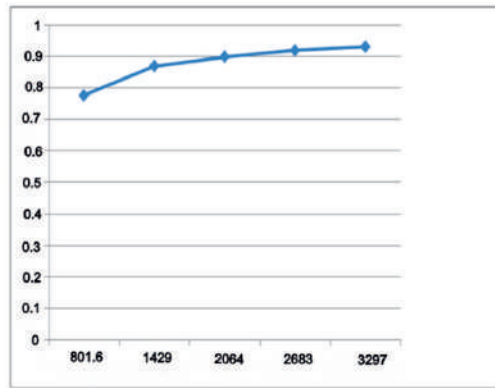


Fig. 9.78 Efficiency versus power curve for the Bridgeless Interleaved PFC Boost Converter topology.

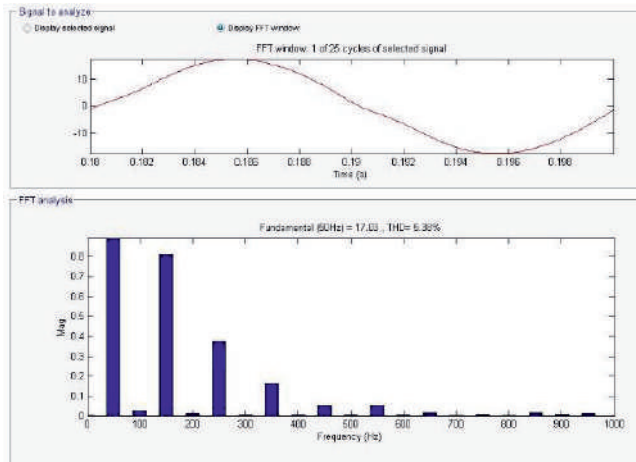


Fig. 9.79 FFT for the input current within 0 and 1 kHz range for the Bridgeless Interleaved PFC Boost Converter topology.

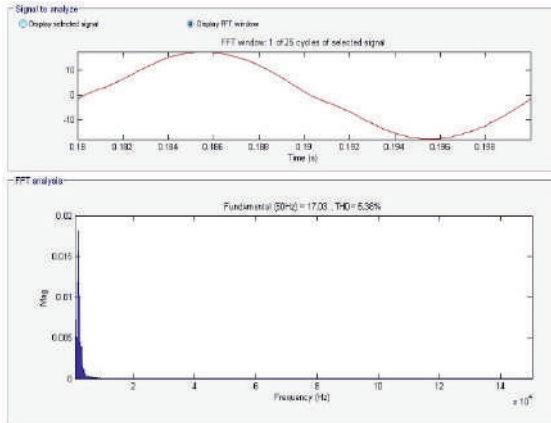


Fig. 9.80 FFT for the input current within 1 and 150 kHz range for the Bridgeless Interleaved PFC Boost Converter topology.

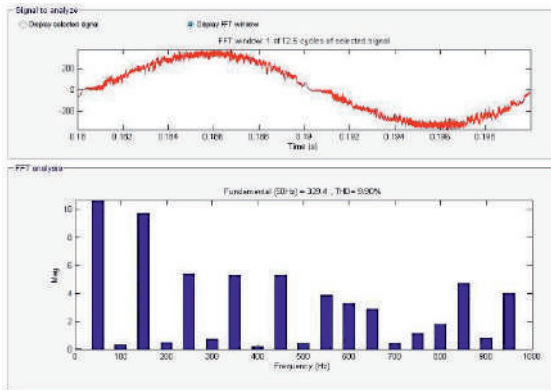


Fig. 9.81 FFT for the voltage measured after the EMI filter within 0 and 1 kHz range for the Bridgeless Interleaved PFC Boost Converter topology.

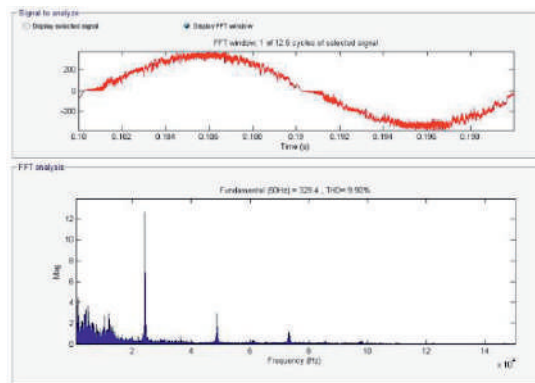


Fig. 9.82 FFT for the voltage measured after the EMI filter within 1 kHz and 150 kHz range for the Bridgeless Interleaved PFC Boost Converter topology.

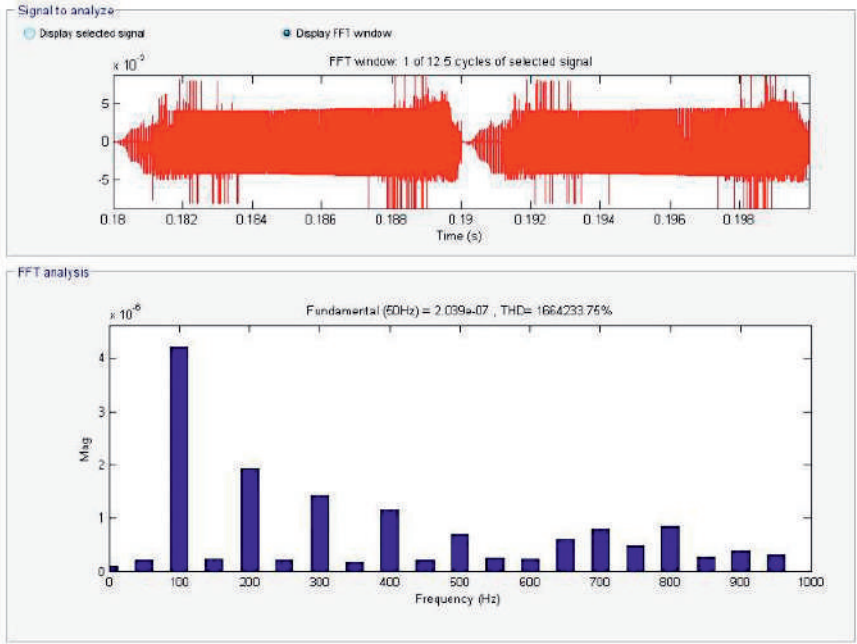


Fig. 9.83 FFT for the current measured between the capacitor C and the ground within 0 and 1 kHz range for the Bridgeless Interleaved PFC Boost Converter topology.

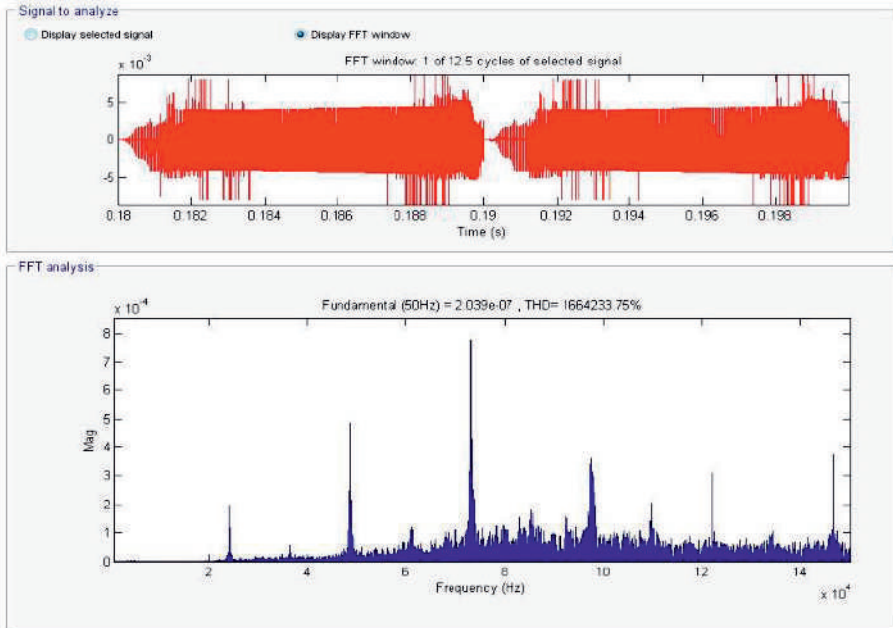


Fig. 9.84 FFT for the current measured between the capacitor C and the ground within 1 kHz and 150 kHz range for the Bridgeless Interleaved PFC Boost Converter topology.

Table 9.17. RMS & Avg current values [A]

	RMS	AVG
$I_{MOSFET}$ [A]	5.535	1.482
$I_{DIODE}$ [A]	6.229	2.539
$I_{ac}$ [A]	9.88	0.0202

Table 9.18. Losses breakdown at nominal load [W]

$P_{DIODE/1device}$ [W]	$P_{MOSFET COND/1device}$ [W]	$P_{MOSFET SW/1device}$ [W]	$P_{Copper/1device}$ [W]	$P_{out}$ [W]	$P_{in}$ [W]
4.578	9.64	2.412	5.178	2538	2730

## 9.5 Conclusion

In this paragraph, firstly, a study of the existent PFC topologies has been done by the research team at the Department of Electrical Engineering of the University Politehnica Timisoara. The result of the study indicated that four topologies seemed to be the suitable for power application ranges up to 4 kW and, thus, they have been chosen to be further investigated. These topologies are the Boost PFC converter, the Bridgeless PFC Boost Converter, the Interleaved PFC Boost Converter and the Bridgeless Interleaved PFC Boost Converter.

The next step in the research dealt with their design implementation of both the hardware and the control parts in Matlab/Simulink simulation environment and, finally, with their performance evaluation and the EMI Fast Fourier analysis.

The family of Bridgeless PFC Boost converters has been widely used since it allows considerable reduction in conduction losses providing increased global efficiency of the converter structure. In terms of the control principle and implementation, the Bridgeless PFC Boost Converter is equivalent to Conventional Boost PFC Converter.

The simulation results, run for the same operation mode, show that the input current is in phase with the input voltage and that its shape is nearly perfectly sinusoidal, as expected. This was the case for all the four topologies.

It can also be seen that the RMS and the average values for the current through the output capacitor are constant—independent of the topology (either for the Boost or for the Bridgeless PFC Boost Converter configuration).

Also, it can be noted that, in the Bridgeless PFC Boost Converter topology, a new loss has been introduced in the intrinsic body diodes of the MOSFETs, but since input bridge

converters were eliminated, there is some efficiency gain for the Bridgeless PFC Boost Converter topology in comparison with the Boost topology. This feature makes the Bridgeless PFC Boost Converter more useful in high power applications.

For the interleaved topologies, the input current is the sum of two inductor currents for the Interleaved PFC Boost Converter topology and the sum of four inductor currents for the Bridgeless Interleaved PFC Boost Converter topology, respectively. For the Interleaved PFC Boost Converter topology, the currents flowing through the two inductors are 180° phase-shifted. Thus, the total input current has smaller ripple than in each individual inductor.

Interleaving, if it is done correctly, could decrease the size of the EMI filter without increasing the size of the Boost inductor volume compared to a single stage pre-regulator approach. A common design practice is to select the switching frequency of the power converter below the EMI lower limit of 150 kHz.

Comparing the efficiency versus power curves for all four topologies, it results that for the Bridgeless Interleaved PFC Boost Converter topology there is a slightly gain in efficiency. So, in conclusion, interleaving and paralleling power converters can increase the efficiency of the power converter; as long as, the inductor ripple currents are kept within reason. The semiconductor switching losses will remain roughly the same.

Another reason to employ PFC in many of today's power supplies is to comply with regulatory requirements. Nowadays, in Europe, the electrical equipment must comply with the European EN 61000-3-2, or EN 61000-3-4 standards. This requirement applies to most of the electrical appliances. The harmonics absence is desired, thus, minimizing the electromagnetic interference (EMI) with other devices being powered from the same source.

Choosing the right parameters of the common mode and EMI filters, based on literature, is also provided, as well as their implementation in Matlab/Simulink. Simulation results show that all all four topologies are compliant with the international standards.

From the comparison between the Interleaved PFC Boost Converter and the Bridgeless Interleaved PFC Boost Converter (at equal power), it resulted that the reduced ripple in the input current for the Bridgeless Interleaved PFC Boost Converter decreases the conducted-EMI noise and helps reducing the EMI filter size.

## 9.6 References

[1] V. Grigore, "Topological Issues in Single-Phase Power Factor Circuits", Dissertation for the degree of Doctor of Science in Technology, Helsinki University of Technology, Institute of Intelligent Power Electronics, Otamedia Oy, Espoo, 2001, ISBN 951-22-5735-1.

[2] K. S. Mallika, "Topological Issues in Single Phase Power Factor Correction", Thesis for Master Degree, Department of Electrical Engineering, National Institute of Technology, Rourkela, 769008, 2007.



- [3] C. Qiao, K.M. Smedley, "A Topology Survey of Single Stage Power Factor Corrector, IEEE 2000, 0-7803-5864-3/00.
- [4] H.Z. Azazi, E. E. EL-Kholy, S.A. Mahmoud, S.S. Shokralla, "Review of Passive and Active Circuits for Power Factor Correction in Single Phase, Low Power AC-DC Converters", Proceedings of the 14th International Middle East Power Systems Conference (MEPCON'10), Cairo University, Egypt, December 19-21, 2010, Paper ID 154.
- [5] B.J.G. Zhang, K. Zhou, S. Yuvarajan, G. Miller, D.F. Weng, "Low-Cost PFC Design Meets Regulatory Standards", Power Electronics Technology, August, 2005, pp. 14-21, [www.powerselectronics.com](http://www.powerselectronics.com).
- [6] M. Savithri, "AC-DC Converter with Quasi-Active Power Factor Correction", Proceedings of the Int. Conf. on Computing and Control Engineering, ICCCE 2012, April 2012.
- [7] W.H. Wölfle, W.G. Hurley, "Quasi-Active Power Factor Correction with Variable Inductive Filter: Theory, Design and Practice", IEEE Trans. on Power Electronics, Vol. 18, No. 1, pp. 248-255, Jan. 2003.
- [8] H.S. Athab, K. Ramar, D.D.-C. Lu, "An Efficient Quasi-Active Power Factor Correction Scheme", Proceedings of the 2009 Symposium on Industrial Electronics and Applications, ISIEA 2009, pp. 536-541.
- [9] H.S. Athab, D.D.-C. Lu, "A High-Efficiency AC/DC Converter with Quasi-Active Power Factor Correction", IEEE Trans. on Power Electronics, Vol. 25, No. 5, pp. 903-909, May 2010.
- [10] S. Basu, M.H.J. Bollen, T.M. Undeland, "PFC Strategies in light of EN 61000-3-2, Paper ID A123656, pp. 1-9.
- [11] M.-Y. Cheng, Y.C. Hsu, C.-H. Chen, M.-K. Hou, M.-C. Tsai, "An Assymmetric PWM for Low Switching Frequency Power Factor Correction Circuit", 978-1-4244-1706-3/08, IEEE, 2008.
- [12] B. Keogh, "Power Factor Correction Using the Buck Topology—Efficiency Benefits and Practical Design Considerations", Topic 4.
- [13] H. Y. Kanaan, A. Hayek, R. El-Solh, K. Al-Haddad, "A New Single-Phase Power Factor Corrector Based on the SEPIC and Sheppard-Taylor Topologies", ISBN 978-1-4244-1628-8, IEEE, 2007.
- [14] H. Y. Kanaan, Al-Haddad, "A Comparative Study of Single-Phase Power Factor Correctors: Modeling, Steady-State Analysis, Tracking Ability and Design Criteria", International Symposium on Power Electronics, Electrical Drives, Automation and Motion, 2012, ISBN 978-1-4673-1301-8/12.
- [15] Y. Zhao, "SINGLE PHASE POWER FACTOR CORRECTION CIRCUIT WITH WIDE OUTPUT VOLTAGE RANGE", Thesis submitted to the Faculty of the Virginia Polytechnic Institute and State University in partial fulfillment of the requirements for the degree of Master of Science in Electrical Engineering, 1998, Blacksburg, Virginia.
- [16] H. Y. Kanaan, K. Al-Haddad, "A Unified Approach for the Analysis of Single-Phase Power Factor Correction Converters", ISBN 978-1-61284-972-0, 209.
- [17] U. Moriconi, "A bridgeless PFC configuration based on L4981 PFC controller", Application Note AN 1606, ST Microelectronics, pp. 1-18, Nov. 2002.
- [18] Y.Q. Durrani, E.C. Aeloiza, L. Palma, P. Enjeti, "An Integrated Silicon Carbide (SiC) Based Single Phase Rectifier with Power Factor Correction", Proceedings of the 36 Int. IEEE Power Electronics Specialists Conference, PESC '05, pp. 2810-2816.
- [19] L.X. Chao, W.Z. Hao, "UCC 28070 Implement Bridgeless Power Factor Correction (PFC) Pre-Regulator Design", Application Report SLUA517, Texas Instruments, pp. 1-13, July 2009.

- [20] B. Lu, B. Brown, M. Soldano, "Bridgeless PFC Implementation Using One Cycle Control Technique", APEC'05, International Rectifier, 2005.
- [21] P. Kong, S. Wang, F.C. Lee, "Common Mode EMI Noise Suppression for Bridgeless PFC Converters", IEEE Trans. on Power Electroncis, Vol. 23, No. 1, pp. 291-297, January 2008.
- [22] Y. Deng, X. He, "Novel Passive Soft Switching Schemes for High Power Single-Phase PFC Rectifiers, Proceedings of the 7th Annual IEEE Applied Power Electronics Conf. and Exposition, APEC 2002, Vol. 2, pp. 957-961.
- [23] Y. Liu, K. Smedley, "A New Passive Soft-Switching Dual-Boost Topology for Power Factor Correction", Proceedings of the 34th Annual Power Electronics Specialists Conf., PESC '03, 2003, Vol. 2, pp. 669-676.
- [24] F. Musavi, W. Eberle, W. G. Dunford, "A High-Performance Single- Phase Bridgeless Interleaved PFC Converter for Plug-in Hybrid Electric Vehicle Battery Chargers", IEEE Trans. on Ind. App., Vol. 47 , Issue: 4 , July-Aug. 2011, Page(s): 1833 - 1843.
- [25] Q. Li, M. A. E. Andersen, O. C. Thomsen, "Conduction Losses and Common Mode EMI Analysis on Bridgeless Power Factor Correction", PEDS 2009, pp. 1255-1260.
- [26] R. Ye, "Single Phase Two-Channel Interleaved PFC Converter Using MC56F8006, Freescale Semiconductor Application Note AN3843", Rev. 0, 04/2009.
- [27] M.M. Jovanović, Y. Jang, "State-of-the-Art, Single-Phase, Active Power-Factor-Correction Techniques for High-Power Applications – An Overview, IEEE Trans. on Industrial Electronics, Vol. 52, No. 3, pp. 701-708, June 2005.
- [28] L. Huber, Y. Jang, M.M. Jovanović, "Performance Evaluation of Bridgeless PFC Boost Rectifiers", IEEE Transactions on Power Electronics, Vol. 23, No. 3, May 2008, pp. 1381-1390.
- [29] E.H. Ismail, "Bridgeless SEPIC Rectifier with Unity Power Factor and Reduced Conduction Losses", IEEE Trans. on Industrial Electronics, Vol. 56, No. 4, pp. 947-957, April 2009.
- [30] L. Rossetto, S. Buso, G. Spiazzi, "Conducted EMI Issues in a 600-W Single-Phase Boost PFC Design", IEEE Trans.on Industry Applications, Vol. 36, No. 2, pp. 578-585, March/April 2000.
- [31] K. Raggl, T. Nussbaumer, J.W. Kolar, "Guideline for a Simplified Differential-Mode EMI Filter Design", IEEE Trans. on Industrial Electronics, Vol. 57, No. 3, pp. 1031-1040, March 2010.
- [32] R.H. Randall, "Improving Power Factor Correction & Reducing EMI in Switch-Mode Power Supply Design", ECN Magazine, May, 2001, pp. 59-60, www.ecnmag.com.
- [33] S. Wang, F.C. Lee, "EMI Research Nuggets", Research Report, Center for Power Electronics Systems, Virginia Polytechnic Institute and State University, 2008.
- [34] F. Beltrame, L. Roggia, J.R. Pinheiro, "Comparative analysis of electromagnetic interference produced by high power single-phase power factor correction pre-regulators", Proceedings of COBEP'09, Brazil, Nov. 2009, pp. 816-823.
- [35] F. Beltrame, L. Roggia, A.R. Abaide, L. Schuch, J.R. Pinheiro, "EMI Investigation Yield by Single-Phase PFC Pre-Regulators", Proceedings of IECON'09, Brazil, Nov. 2009, pp. 4128-4133.
- [36] Walther P., A new rectifier system high efficient, high dense, modular, quick to install and superior for service, in Proc. 15th Int. Telecom.Energy Conf., Sep. 27–30, 1993, vol. 2, pp. 247–250.
- [37] M.R. Yazdani, H. Farzanehfard, J. Faiz, "Classification and Comparison of EMI Mitigation Techniques in Switching Power Converters – A Review", JPE 9-5-18, pp. 767-777, 2009.



POLITEHNICA UNIVERSITY TIMISOARA  
1920-2020

ISBN: 978-606-35-0393-1